Study of interfaces and nanometric structures by ToF-SIMS : upon a spatially resolved quantitative analysis

Matthieu Py

UNIVERSITÉ DE GRENOBLE

THÈSE

Pour obtenir le grade de

DOCTEUR DE L'UNIVERSITÉ DE GRENOBLE

Spécialité : **Matériaux, Mécanique, Génie civil, Electrochimie**

Arrêté ministériel : 7 août 2006

Présentée par

Matthieu Py

Thèse dirigée par **Jean-Michel Hartmann**

préparée au sein du **Laboratoire de Caractérisation Physique Off-line du CEA-Léti à Grenoble**
dans **l'École Doctorale I-MEP2 de l'INP Grenoble**

A study of interfaces and nanostructures by time of flight mass spectrometry: towards a spatially resolved quantitative analysis

Thèse soutenue publiquement le **30 septembre 2011**,
devant le jury composé de :

Pr. Sorin CRISTOLOVEANU
Président
Pr. Didier LEONARD
Rapporteur
Dr. Maurice QUILLEC
Rapporteur
Pr. Wilfried VANDERVORST
Membre
Dr. Jean-Paul BARNES
Membre
Dr. Jean-Michel HARTMANN
Membre

TABLE OF CONTENTS

ABBREVIATION INDEX

AFM: Atomic Force Microscopy
AR-XPS: Angle Resolved X-ray Photoelectron Spectroscopy
CMOS: Complementary Metal Oxide Semiconductor
CMP: Chemical Mechanical Polishing
CVD: Chemical Vapour Deposition
EELS: Electron Energy Loss Spectroscopy
EOT: Equivalent Oxide Thickness
ERDA: Elastic Recoil Detection Analysis
EXLE: Extremely Low Energy
FET: Field Effect Transistor
FIB: Focused Ion Beam
FWHM: Full Width Half Maximum
GAA: Gate All Around (designates devices whose channel is cylindrical and completely surrounded by a tubular gate stack)
HAXPS: Hard X-ray Photoelectron Spectroscopy
HBT: Heterojunction Bipolar Transistor
HK: High-K
HKMG: High-K Metal Gate
HRBS: High resolution Rutherford BackScattering
HR-TEM: High Resolution Transmission Electron Microscope
IL: Insulating Layer
I_{ON}: Current passing trough the device channel in ON mode
I_{OFF}: Current passing through the device channel in OFF mode
IPA: IsoPropyl Alcohol
ITRS: International Technology Roadmap for Semiconductors
LEIS: Low Energy Ion Scattering
LMIS: Liquid Metal Ion Source
MCP: Multi Channel Plate
MCs: protocol for SIMS concentration calibration using detection of the MCs_n^+ secondary ions, M being an element of interest
MEIS: Medium Energy Ion Scattering
MOCVD: Metal Organic Chemical Vapour Deposition
MOSFET: Metal Oxide Semiconductor Field Effect Transistor
nMOS: negative channel Metal Oxide Semiconductor
NW: Nano Wire
pAR-XPS: parallel Angle Resolved X-ray Photoelectron Spectroscopy
PCBM: Phenyl-C61-Butyric acid Methyl ester
PDMS: PolyDiMethylSiloxane
PECVD: Plasma Enhanced Chemical Vapour Deposition
PMMA: PolyMethyl MethAcrylate
pMOS: positive channel Metal Oxide Semiconductor
ppb: parts per billion
ppm: parts per million
PVD: Physical Vapour Deposition
RBS: Rutherford BackScattering
RMS: Root Mean Square
ROI: Region Of Interest
RP-CVD: Reduced Pressure-Chemical Vapour Deposition
RRAM: Resistive Random Access Memory
RSF: Relative Sensitivity Factor

SCM:	Scanning Capacitance Microscopy
SEM:	Scanning Electron Microscope
SF:	Sensitivity Factor
SIMS:	Secondary Ion Mass Spectrometry
SL:	SuperLattice
SOI:	Silicon On Insulator
SR:	Sputter Rate
S-SIMS:	Static Secondary Ion Mass Spectrometry (referring to SIMS for surface analysis only, with a low primary ion dose)
sSiGe:	strained Silicon Germanium
SSRM:	Scanning Spreading Resistance Microscopy
TDEAH:	TetrakisDiEthylAmino Hafnium
TDMAS:	TetrakisDiMethylAmido Silicon
TEM:	Transmission Electron Microscope
TMAH:	TetraMethyl Ammonium Hydroxide
ToF-SIMS:	Time of Flight Secondary Ion Mass Spectrometry
TRIM:	TRansport of Ions in Matter
UHV:	Ultra High Vacuum (below 10-8 mbar)
USJ:	Ultra Shallow Junction
UV:	Ultra Violet
VSR:	Variable Sputter Rate
XPS:	X-ray Photoelectron Spectroscopy
XRD:	X-Ray Diffraction
XRR:	X-Ray Reflectivity

INTRODUCTION

For over half a century the microelectronics industry has incessantly strived to produce smaller, cheaper and more efficient devices. In order to achieve this, more and more materials were introduced in to devices. Device structures have evolved from simple, silicon based planar stacks to elaborate, multi-material stacks in three-dimensional architectures. This evolution has led to the apparition of nanometre scale features and of co-integration of different materials within the same device structure. In order to further improve device performance, one often needs to understand the device properties from a material science point of view. An accurate knowledge of local chemical composition is therefore essential. In this context, the requirements for physical/chemical characterization become extremely difficult to fulfil.

SIMS, and more particularly dual beam ToF-SIMS, is particularly well adapted for the characterisation of advanced microelectronic devices. It is already a standard tool in a semiconductor characterisation laboratory because of its capacity to perform quantitative analysis of virtually any element with sensitivities in the ppm to ppb range and depth resolutions down to the nanometre level. However many difficulties arise when the user intends to obtain accurate quantification of more complex materials and structures such as those that we propose to study here. This thesis work therefore concentrates on setting up the right experimental conditions to enable accurate quantification of materials and structures for next generation devices using a standard R&D dual beam ToF-SIMS.

In the first chapter we will review the different concepts and notions needed for the understanding of the following chapters. In particular, an overview of the evolution of microelectronic devices since the beginning of the semiconductor industry will be given. Some of the critical evolutions encountered in the last decade will be presented more into detail. These led to the introduction of new materials and structures and therefore require particular efforts to achieve their accurate characterization. Of those, we can highlight SiGe and high-k based material stacks, ultra shallow implants and materials for organic electronics. We will then present the ToF-SIMS instrument used in this study and give a review of the different underlying physical mechanisms involved in analysis. This will allow us to introduce the different limitations in conventional use of ToF-SIMS for accurate quantification of the different materials and structures described above.

The second chapter will thus be devoted to the description of the different solutions considered in this thesis work for improvement of ToF-SIMS analytical abilities. We will divide them into four categories, namely sample preparation, experimental conditions, data treatment and comparison/complementarities with other cutting-edge characterization techniques. At this stage only a theoretical description of the different solutions will be performed, as their practical setup necessarily requires specific adjustment according to the application. We will also review, in each of the categories, the expected improvements and/or complementary information of interest for our study. In the following chapters we will present the practical setup of the solutions developed in this chapter for each of the materials and structures of interest.

Chapter III will thus focus on the solutions developed for quantitative analysis of SiGe based material stacks. After a comprehensive description of the different protocols developed for improvement of our instruments analytic abilities in such alloys, we will verify the accuracy of each protocol and assess improvements in analysis quality. We will use the developed solutions to yield quantitative information on materials and structures relevant for actual device manufacture.

Similarly, the following chapters IV, V and VI will follow the same structure, describing the work performed on high-k materials, USJ and organic electronics respectively.

CHAPTER I
Challenges in ToF-SIMS characterisation for advanced microelectronic devices

I. 1. Core issue

Since the invention of the first transistor in 1947 by Bardeen, Schockley and Brattain [1-2], the microelectronics industry has continuously improved the basic concept of the transistor to match market demands of performance and price. A first standard structure, baptised CMOS for Complementary Metal Oxide Semiconductor and composed of a doped silicon region under a silicon dioxide insulator layer and a metal gate was established (see also Figure I.1 for a schematic CMOS structure) [3]. Then for the next half century, the same structure was progressively scaled down in size, allowing design of ever more complex chips integrating more and more functions. Meanwhile this enabled production at lower costs and in industrial quantities. This evolution quickly inspired Gordon Moore to propose in 1965 the well-known "Moore's law", which predicts a reduction in device size by a factor two every 12 months. It was then revised in 1975 by modifying the period to 18 months [4-5].
Today industry is still following Moore's precept established more than 40 years ago, which has led microelectronics to be one of the most dynamic fields of research of the late 20th and the early 21st century. The size of the devices has evolved from tens of microns in 1971 (Intel's first commercial microprocessor), to the micrometer scale in 1988, and below the 100 nanometre barrier in 2004 (see Figure I.1) [6]. The latest devices, in production since 2009, have characteristic dimensions (gate half-pitch) below 50 nanometres [7]. Due to the industrial production cycles, the evolution of the devices' size is not continuous but incremental, leading to the apparition of "generations", also called "technological nodes" and often associated to the average size of the CMOS gate half pitch. An international committee, called International Technology Roadmap for Semiconductors (ITRS), sets every two years the requirements to progress to future nodes, at short (5-10 years) and long term.

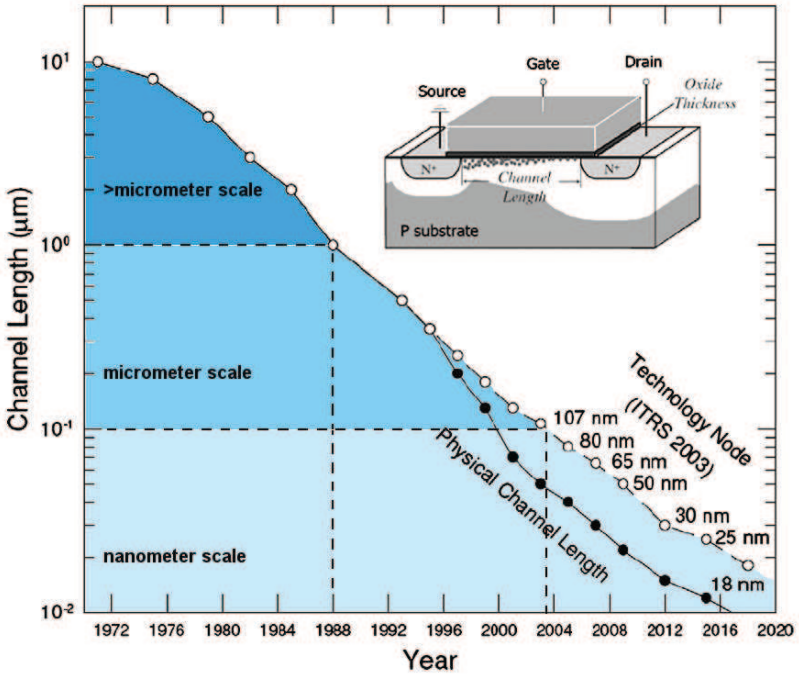

Figure I.1 Evolution of the technological nodes with time, extracted and adapted from Wong *et al.* [6].

However in the past decade or so, the requirements have became increasingly difficult to fulfil, given that further dimensional device scaling is often hindered by physics. The dimensional requirements have become so aggressive (see Figure I.1) that further scaling would present more drawbacks than gains in terms of electrical performance [7]. Alternative solutions are

thus needed to continue improvement. Several solutions have been proposed, of which we can highlight the following points (the others being beyond the scope of this thesis):

(i) Continue the miniaturisation effort in domains which still present an improvement margin,

(ii) Introducing alternative materials to the standard silicon dioxide used as insulator between the gate and the channel in CMOS devices, and alternative gate materials to replace Poly-Si and to better match the new dielectrics,

(iii) Radically change CMOS design to allow fabrication of non planar devices and stacking more CMOS on the same surface, and

(iv) Use new materials in place of Si, such as SOI, Ge, or alloys containing elements from the third and fifth columns of the Mendeleev table (more simply referred as III-V) as substrates to boost the electron and holes mobility and thus obtain faster devices. Alternatively, use organic materials in niche applications to increase efficiency and diminish production costs.

These four points are all prominent in the 2009 ITRS executive summary [7]. Some of them are already used in production such as (i) and (ii), but (ii) is still at the development stage, while (iv) needs more research and is expected to reach production in 2016-2020 [7]. Point (i) consists mainly in continuous improvement of techniques and instrumentation involved in device production, such as lithography, implantation, layer growth and metrology [7], while keeping the same process flow. Such improvements are necessary, but do not provide an important progress margin [7]. Point (ii), (iii) and (iv) involve the introduction of new higher performance materials (greater mobilities, higher dielectric constant…) to replace the original ones that had reached their limit in dimensional scaling, and eventually the structure of the device itself. These new materials and structures are promise significant progress in both device size and electrical performance, and have therefore been the focus of intense research and development efforts in these past few years.

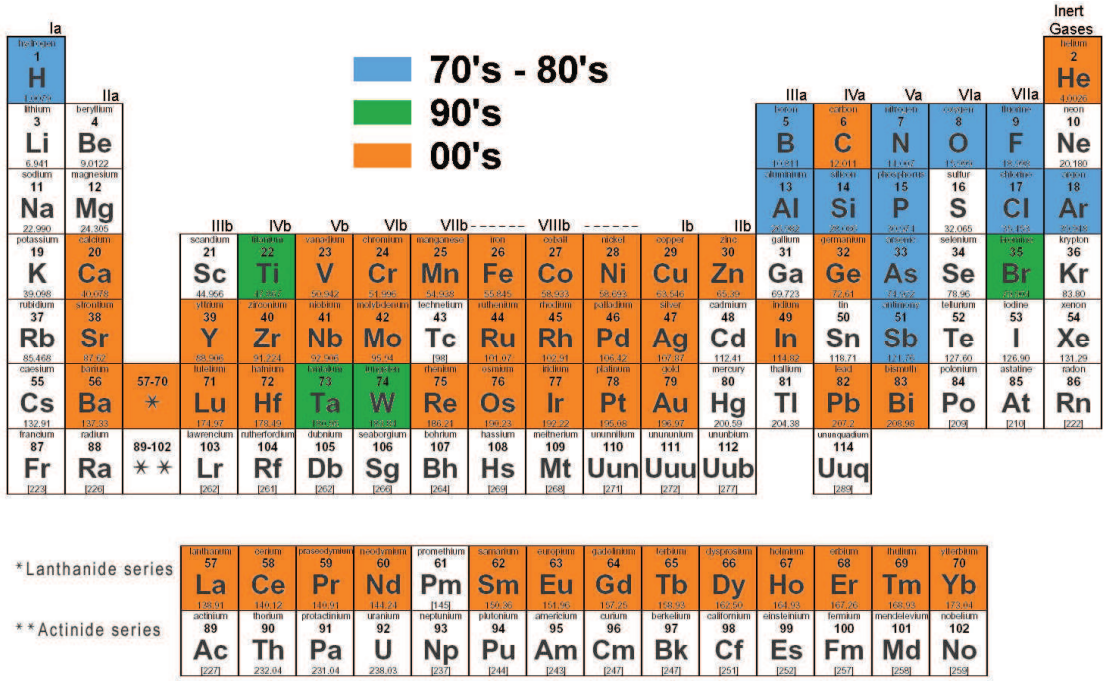

Figure I.2 Materials in use in semiconductor industry in the 70's-80's (in blue), and extensions made in the 90's (green) and 00's (orange). Compiled from data in Fan *et al.* [8].

Thus, if we consider the evolution of the elements used in devices from the 70's, we observe that the last decade has seen the introduction of approximately half of the periodic table (see

Figure I.2) [8]. Aside from purely material considerations, structures have also evolved, with the apparition of bi-axially or uni-axially strained heterostructures, three dimensional structures, all with a continuous effort on scaling. This of course induces an increase in the complexity level of the physics behind the devices, and by consequence a need for comprehension, which electrical characterisation alone cannot provide. Physical and chemical characterisation are thus required in order to analyse in the most precise manner possible the devices in terms of chemical composition, structure, layers thickness and conformity, strain level, temporal and thermal stability. Given the complexity of the devices in terms of chemical composition as well as in dimension, their accurate characterisation requires the association of many advanced characterisation techniques. Of these, mass spectrometry techniques and more particularly ToF-SIMS is an interesting candidate.

I. 2. Why ToF-SIMS? Historical aspects and performances

The first experimental observation of particle emission from a surface hit by an ion beam was reported by Thomson in 1910 [9]. He showed that particles were emitted in all directions and that they were mostly uncharged, with only a small fraction of charged ones. Later, these findings were used by Arnot and Milligan [10] who studied the yields and the energy distribution of ions induced by the impact of an ion beam on a surface. However it is only in 1949 that the first prototype SIMS instrument was reported by Herzorg and Viehboeck [11]. Several teams participated in the improvement of the concept and produced instruments adapted for analysis applications [12-14], and a first commercial prototype was released in 1967 by Herzog [15] under a NASA funded program. The main purpose of the instrument was to fulfil the need at that time to allow examination of mineral material from space missions by performing composition analysis and isotope studies. However the possibilities of the instrument for profiling of thin film and semiconductor samples issued from microelectronics industry (also growing exponentially at that time) were soon revealed [16-17]. The latter became one of the most important fields in SIMS applications due to the combined growth of demand (in parallel with growth of semiconductor industry) and supply (in parallel with instrumental developments). It yielded numerous break-through studies well summarised by Werner in his review addressing both theory, instrumentation and potential applications of SIMS [18].

Soon enough, the developments of the instrumentation allowed SIMS to be used for extreme surface analysis. Works from Benninghoven in 1970 showed indeed that surface monolayer composition could be studied with SIMS by using extremely low doses of primary ions through pulsed primary ion beams, giving birth to the Static SIMS mode [19-20]. The development of this mode leaded to the evolution from quadrupole or magnetic sector analysers (allowing observation of only a few ions in one analysis) to time of flight analysers (allowing parallel acquisition of all ions within a given mass range). First ToF-SIMS instruments were developed in the early 80's [21-22] and soon commercialised, quickly becoming a popular instrument in analysis laboratories.

The performance of the technique is indeed impressive, since it features high abilities in terms of sensitivity, depth resolution and elemental detection, all in one instrument. When compared to other techniques [23] these abilities have lead to the widespread use of SIMS in modern characterisation laboratories. Detailed and recent compilations of the performances of SIMS and ToF-SIMS in various applications reviewed by Bacon et al. [24-25]. Out of those we can point out the most important ones, for SIMS:

- Detection of every element from hydrogen (Z=1) to plutonium (Z=94) and of compound ions up to masses 300 - 500 u
- High mass resolution allowing isotopic studies, but also separation of isobaric secondary ions such as $^{30}SiH^{-/+}$ (30.9816 u) and $P^{-/+}$ (30.9738 u)
- Depth profiling of samples from a few nanometres thickness up to a few micrometers
- Depth resolution of the nanometre range
- Quantification of all elements from the parts per billion or million (ppb or ppm) concentration range up to the sub-percent range (see reference [26] for detection of various elements in Si, and more particularly [27] and [28] for ppb detection of As and B in Si respectively)
- Possibility to analyse any sample supporting Ultra High Vacuum (UHV) without special sample preparation
- Imaging capacity with sub-micron scale lateral resolution

And in addition, for ToF-SIMS:

- Parallel acquisition of all ions within a given mass range and of compound ions up to masses ~10000 u
- Possibility to perform monolayer analysis: during an analysis each primary ion hits a virgin surface by imposing an upper limit on primary ion dose
- Sample holder configuration at ground potential, allowing analysis of thick insulator samples
- Acquisition of molecular information on organic samples

These are standard capabilities of the technique, which can all be reached in routine operation. One can therefore see the interest of ToF-SIMS as a characterisation technique: given its performance, one can hold high expectations on its ability to take on the challenge of next generation microelectronics device characterisation.

I. 3. « Dual beam » ToF-SIMS principle, instrumentation and physics

In this section we will briefly review the principle and instrumentation of ToF-SIMS to give a basic overview of the technique, for a more comprehensive review please refer to Vickerman *et al.* [29]. More precisely, we will focus on the instrument used in this thesis work; the dual beam ToF-SIMS which is a particular type of SIMS, equipped with a time of flight detector and two primary ion beams, one dedicated to analysis and the other one to sputtering. Note that if principle and instrumentation differ somewhat from magnetic and quadrupole SIMS, the physics of the technique remain identical, in particular ion-solid interactions and ionisation processes.

I. 3. a- Principle

Dual beam ToF-SIMS relies, as for other SIMS instruments, on the analysis by mass spectrometry of the “secondary ions” which emanate from the sample thus giving information

on the chemical and elemental composition of the extreme surface layers. These secondary ions are a small fraction of the matter emitted when bombarding a sample surface with energetic "primary ions". However in magnetic or quadrupole SIMS, secondary ions are accelerated to a given potential and analysed as a function of their energy and velocity (depending only on their mass) by magnetic or electrostatic prisms or deflectors. This implies that only a few selected mass ranges can be observed at a time. On the contrary, ToF-SIMS makes use of a time of flight analyser. In this configuration, the secondary ions are also accelerated to a given potential, but then enter a free flight chamber under UHV in which they are subject to no exterior force, gravity being neglected given the low masses and the high velocity of the ions; and collision events with other atoms being scarce given the UHV in the free flight chamber. The duration of this free flight is then directly dependent on the mass of the ion itself:

$$t_{ToF} = L \cdot \sqrt{\frac{m}{2q(E_0 + U)}} \qquad \text{(I.1)}$$

Where t_{ToF} is the free-flight duration, L the chamber length and U the acceleration potential are known parameters, E_0 is the initial energy of the ion (right after ionisation and before acceleration) and m is the mass of the ion. Measurement of t_{ToF} can be easily performed since secondary ions all come from a single, short ion pulse (a few tens of nanoseconds). The output of this technique is therefore a secondary ion intensity diagram as a function of time, which is converted to mass to charge ratio using equation (1) and called a mass spectrum. The mass resolution of such a spectrum is expressed by the unit-less ratio $m/\Delta m = t_{ToF}/2\Delta t_{ToF}$, Δt_{ToF} comprising start pulse width, precision of the secondary ion detector and, mainly, of the difference in free drift duration for ions of same mass induced by their original energy distribution ΔE_0 which has a width of a few eV. Usual mass resolutions are of a few thousand. The measurement process and output spectra are shown schematically in Figure I.3.

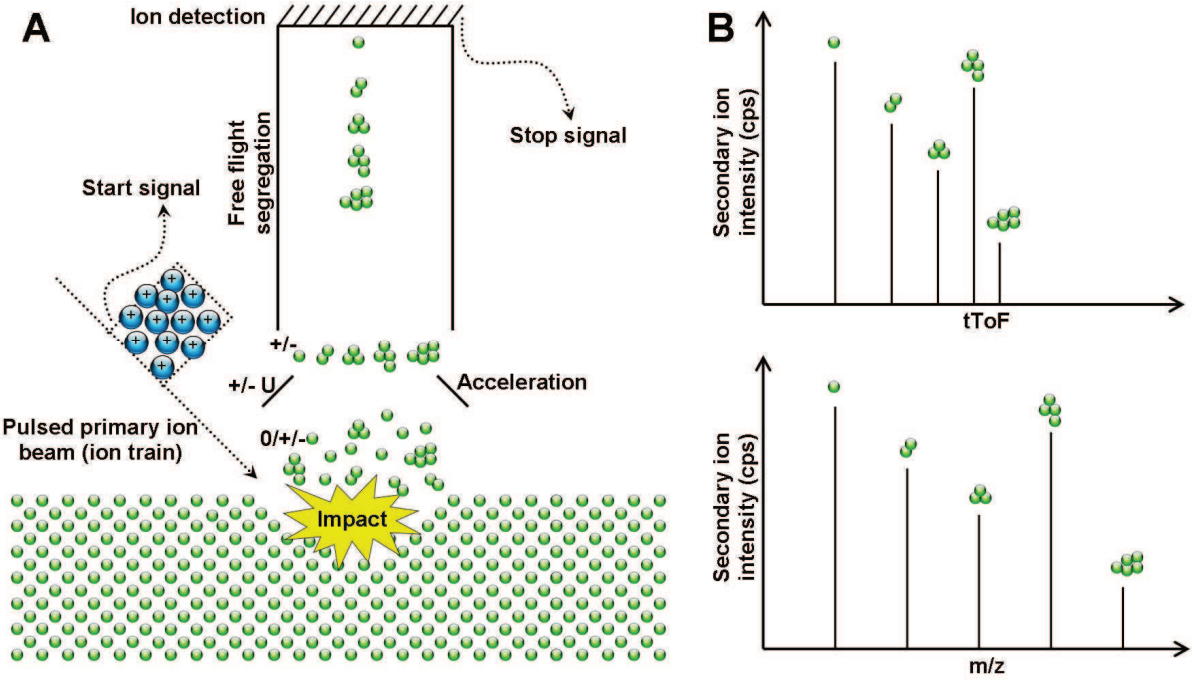

Figure I.3.A Simplified view of an analysis event: after being bunched, a train (pulse) of primary ions enter in collision with a target and induce emission of electrons, neutrals and ions. The bunching signal also serves (with delay) as a start signal for detection, while secondary

ions are accelerated by a given potential +/-U and enter the free drift chamber in which segregation as a function of mass-to-charge ratio will occur.

B Mass spectrum generated by the single pulse analysis event seen in **A**. Each ion of different mass presents a different free flight duration re-interpreted in terms of mass-to-charge ratio using equation (1). The intensity of each signal, in counts per second, is directly linked to the corresponding element surface concentration and to the instrument's sensitivity to this element. Notice that the abscise scale is not strictly speaking linear, since free flight duration shows a square root dependency on m/z. A given mass increment between two ions of low mass will thus have a more important impact on their free drift duration than the same increment between two ions of higher masses. As a result, abscise scale appears compressed for higher mass compounds. For this reason, most spectra are represented as a function of m/z and not as a function of t_{ToF}, the primary output of the technique.

In addition, dual beam ToF-SIMS makes use of two primary ion beams to bombard the sample surface: one consisting of low energy ions (from ~100 eV to a few keV) for sputtering of material and the other one consisting of energetic ions (a few tenth of keV) for analysis, while in other instruments the same ion beam is used for both purposes [29].

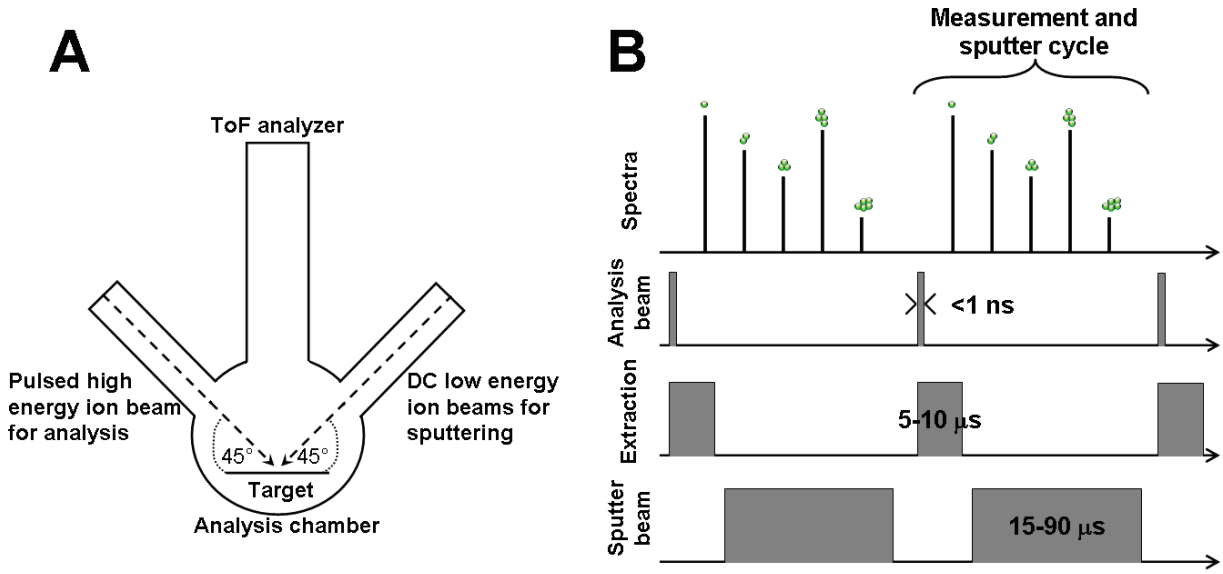

Figure I.4.A Basic diagram of our instrument configuration.

B Data acquisition routine in "interlaced" dual beam configuration for depth profiling. In some cases charge compensation can be performed while sputter beam is on by means of a low energy electron beam. For thick insulators or other samples difficult to analyse in this configuration even with charge compensation, a "non-interlaced" routine exists. It allows longer sputter cycles (a few seconds) and analysis to be performed in a successive fashion and not in parallel, while pauses (around a second long) between sputter and analysis allow for charge compensation with the electron beam.

Such a configuration has the advantage of offering high secondary ion yields through the energetic analysis beam while allowing slow sputtering and reduced damage depth through the low energy sputter beam, thus providing better resolved depth profiles. A simplified diagram of the instrument configuration is displayed in Figure I.4.A. It has also the advantage of being versatile, featuring several functions:

- Static SIMS (S-SIMS): for surface (monolayer) analysis [30]. In this mode only the analysis beam is used and the output is a spectrum as displayed in Figure I.3.B. The important parameter is usually the mass resolution, thus very short pulses of high current densities are preferred in this mode.

- Depth profiling: for bulk analysis. Here both analysis and sputter beam are turned on and hit the sample in an alternative fashion as represented in Figure I.4.B. The output is a series of spectra taken at different depth points, forming a depth profile.
- Imaging: for surface imaging [31]. Here the analysis beam is electronically rastered over the sample surface and spectra are sequentially acquired for a given number of adjacent points which become the pixels of a secondary ion image of the sample. Although this mode is used in a routine fashion in the two precedent modes, the lateral resolution is not optimised and yield poorly resolved images (~µm order). To gain in resolution, highly spatially focused analysis beam is required. This however induces drastic drop in primary ion current and thus of secondary ion yield.

These three functions will be routinely used in this thesis work.

I. 3. b- Instrumentation

The laboratory instrument is a TOF SIMS V from Ion Tof GmbH, equipped with a bismuth cluster ion beam for analysis and caesium or oxygen beams for sputter. We will now quickly review the properties of its different components, starting with the primary ion beams, then considering the analysis chamber and sample holder, and finally the ToF analyser.

Primary ion beams: ion sources and optical columns

Both analysis and sputter beams are constituted of an ion source and of acceleration, chopping and focusing column optics. The ion source for the analysis beam is a bismuth Liquid Metal Ion Source (LMIS), a source which satisfies the high brightness condition necessary for obtaining high currents even in focused, pulsed mode. This source consists of a Bi reservoir and a needle coated with Bi metal, mounted on a heater filament which is in turn held by two support legs serving as electrical contacts. When heated by the Joule effect, the Bi melts and forms a film covering the needle. When a high negative potential is applied to the extractor placed near the needle and on the same axis, metal ions near to the tip move forward as electrons move backwards, hence liquid metal at the tip will extend and form a cone. At equilibrium, ion emission is held at the extreme tip of the cone [29, 32]. This source has the particularity of allowing mono- or multi-charged mono-atomic (Bi^+, Bi^{++}) and cluster ion emission (Bi_3^+, Bi_3^{++}, Bi_5^+, Bi_7^+). For sputtering, two sources are available: one is an electron bombardment source for O_2^+. Here, gas is fed into a chamber where it is cationised by electrons emitted from a heated filament cathode. The oxygen cations are then captured and accelerated by the protruding electric field created by the extractor at the extremity of the chamber [29]. For Cs, the source is also an LMIS one.
For all beams the optical columns comprise similar elements, while their design and settings are adapted for high energy ions (for the analysis beam) or for low energy ions (for the sputter beam). After ionisation, a planar electrode with a small aperture is used to accelerate the beam to the desired energy. Depending on the application, several hundred volts to several kV can be applied at this stage, thus creating a workable ion beam for analysis. However this beam will have tendency to expand, reducing drastically the precision of our system: as beam spot size increases, chromatic aberrations will also increase and spatial resolution will be clearly worse. Current losses will also occur. The next step then is to treat the beam in order to obtain a sufficiently small and energy (mass) coherent beam. After being accelerated, the beam will travel through series of electromagnetic lenses and electrostatic plates, which can be assimilated to the optical lenses of a microscope: by analogy with optical science, we can say that the spot created by ionisation needs to be imaged at the plane constituted by the sample.

The columns contain several types of lenses and plates, each of them participating to the collimation and the coherence of the beam. Out of these, Einzel lenses are used to focus the beams. They are composed of three annular electrodes, out of which only the central one is supplied in voltage, creating electric field in the interstitial spaces separating it from the two others. Ions that were deviated from the optical axis will be focused at an imaging point whose distance from the lens can be regulated by adjusting the lens voltage [33]. Otherwise, Wien filters are used to ensure mass coherence of the beams (for example to select a given Bi cluster ion for analysis). A Wien filter will produce electric and magnetic fields arranged perpendicularly in a plan normal to the beam axis. Being under UHV, the only forces applying to the ions are the two fields, so that for set values, only ions of a certain velocity (thus mass) will pass through the filter without modification of their trajectory. Apertures of desired sized are placed after this kind of filter to blank the other ions [33]. Lastly, rastering of the beams over a defined surface of the sample is performed by electronically controlled scanning plates.
The standard energy settings are 25 keV for the analysis beam (50 keV for doubly charged ions) and between 250 and 2000 eV for both sputter beams. In terms of DC current, 15 nA is routine for analysis, while it can vary between 15 nA to a few hundred nA for sputter beams, depending on the energy and focusing. Finally spot size at the sample surface is commonly sub micrometric for analysis but can reach ~50 nm albeit at the expense of reduced beam current due to the extreme focus, while sputter beams present much less focused spots of the order of several tens of microns. The typical raster sizes for data acquisition are therefore around a hundred microns wide for analysis and a few hundreds of microns for sputtering

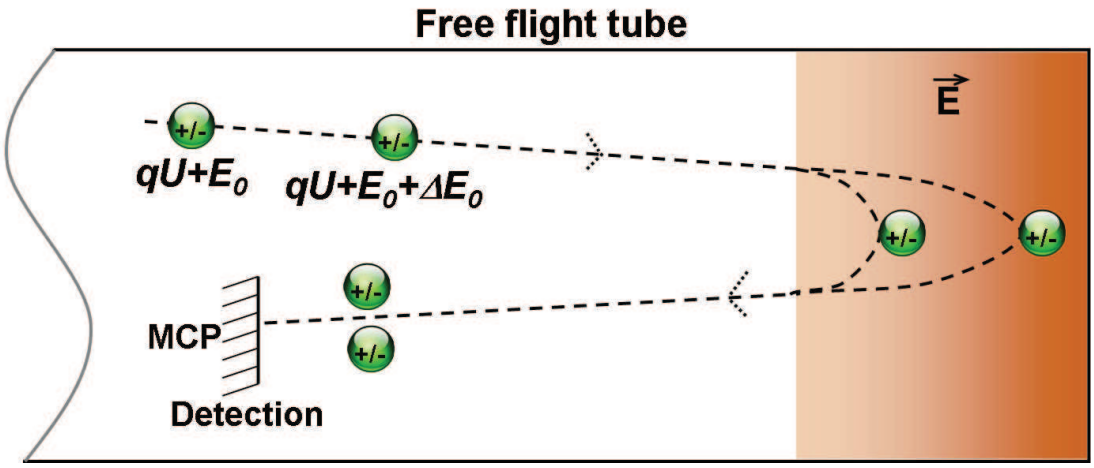

Figure I.5 Schematised view of a reflectron and of its action on two ions of same mass but slightly different initial energy (E_0 or $E_0 + \Delta E_0$).

Analysis chamber and sample holder

This part consists in an UHV chamber allowing a sample holder to be introduced through a load-lock chamber. Several options are available to allow sample temperature control (heating or cooling), sample charge state control (low energy electron beam) and atmosphere control (vacuum level, oxygen flooding). Both incident beams (analysis and sputtering) are incident at 45° to the sample normal as shown in Figure I.4.A. This configuration allows in many cases a good compromise in terms of sputtering properties. When the analysis beam hits the sample, secondary ions are extracted by an electrode brought to a high potential (typically +/- 2 kV) for a short time and propelled into the ToF analyser.

ToF analyser

The ToF analyser is composed of a chamber of known length under UHV, in which secondary ions will experience free drift, naturally segregating them as a function of their mass. Our instrument is equipped with a reflectron, which was first reported in1957 [34] but was only put to use thirty years later in SIMS instruments [35-36]. It is constituted of an electrostatic mirror placed at one extremity of the drift tube, repelling the ions and sending them back towards the detector as shown in Figure I.5. This system presents a double advantage in terms of mass resolution. First, it increases the free drift length as compared to a simple tube, which helps segregating ions of different masses without changing the actual dimensions of the free drift chamber. Second, it will compensate for ΔE_0, the difference in initial energy between two ions of same masses. The ions of higher velocity will penetrate deeper in the electrostatic field than the ions of lower velocity, thus travel longer: both ions will finally hit the detector simultaneously (see Figure I.5). The latter is constituted of a Multi Channel Plate (MCP) with a dead time around a few nanoseconds, corrected by a Poisson law. The intensity of the secondary ion signals thus detected is formalised in the following formula:

$$I_m = I_p \cdot Y_m \cdot \alpha_m^{+/-} \cdot \theta_m \cdot \eta \qquad \text{(I.2)}$$

With I_m being the secondary ion intensity for the specie m, I_p the primary ion density, Y_m the sputter yield (in number of m elements sputtered for one impinging primary ion), $\alpha_m^{+/-}$ the ionisation probability, θ_m the concentration of the element m at the surface of the sample and η the transmission rate of our instrument and detector. Typically η is quite high (90-95%) in our instrument and I_p can be changed at will; however Y_m and more particularly $\alpha_m^{+/-}$ are often extremely low and subject to important variation. The physical aspect of the impact and sputtering phenomenon will be further explained in the next subsection.

I. 3. c- Basics of ToF-SIMS

As we saw, ToF-SIMS consists in analysing secondary ions generated by the impact of a primary ion beam on a solid target. In this process, two distinct phenomena intervene: material sputtering and ionisation. In this subsection we will be briefly review these phenomena, already comprehensively addressed in numerous works. In particular refer to [37-41] for theory of sputtering and secondary ion formation, and [42-44] for applications to practical analysis cases. We will then explain how the different parameters interact and interfere with the need for quantitative measurements.

Ion-solid interactions: sputtering

In the energy and angle range considered for ToF-SIMS, from around a hundred eV to a several tens of keV and from sample normal to grazing angles [45-48], the main effect of ion bombardment is sputtering, i.e. removal of atoms from the target material. It is the result of the energy transfer from the incident ion to the target, principally through nuclear interactions (nuclear stopping power), the importance of electronic interactions (electronic stopping power) being negligible in the ~100 - 10000 eV energy range. The energy of the impinging ion is transferred by collision to the target atoms and transmitted successively (with losses) from an atom to another until becoming inferior to the cohesion energy of the

lattice. The result of this process is multiple: implantation of the impinging ion, damage or modification of the target material near surface layers, and for some atoms of these layers whose energy is sufficient, sputtering [18, 37, 49]. The amount of ejected material depends on several parameters, and primarily on the impinging ion energy, angle and nature (mono-atomic or cluster). It is characterised by the sputter yield *Y* defined as the number of ejected atoms by incident ion. Depending on the energy and nature of the impinging ion, we can distinguish three types of collision regimes.

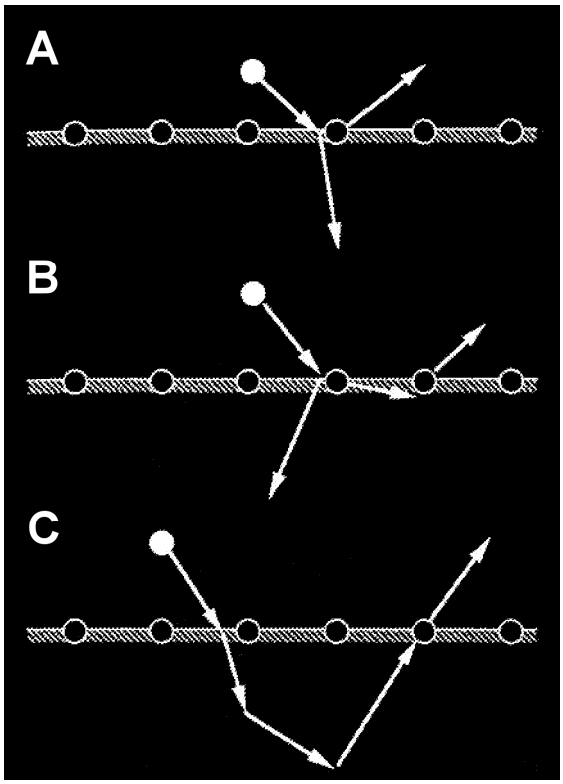

Figure I.6. Simplified representation of the different interaction mechanisms in the single knock-on regime, taken from reference [50]:

A The first recoil atom is sputtered directly on impact with the impinging ion.

B At higher energies, the first recoil atom is displaced in the target lattice and sputters a neighbouring atom.

C The first recoil atom undergoes several collisions and is backscattered towards the surface where it sputters a surface atom.

The first one, described in Figure I.6, is predominant at very low incident energies (a few tens to a few hundred eV) [50-51]. It therefore describes quite well the reaction of a target under extremely low energy bombardment with Cs^+ or O_2^+ in our experimental setup. In this regime, very few target atoms are displaced and sputtered. The impinging particle interacts with a first atom through elastic collision (primary recoiled atom) and loses enough energy to be stopped after this interaction. The primary recoiled atom is either sputtered immediately as shown in Figure I.6.A (when impinging ion energy is low), or is in turn put in movement and displaced in the target material lattice (when impinging ion energy is higher). In this case, it can either cause the next surface atom to be sputtered as in Figure I.6.B, or undergo several collisions before being backscattered and sputter a surface atom as in Figure I.6.C. In all cases, collisions are triggered in a successive fashion and displace only an atom at a time, which is why this regime is called the “single knock-on” regime. The sputter yields in this regime are generally quite low.

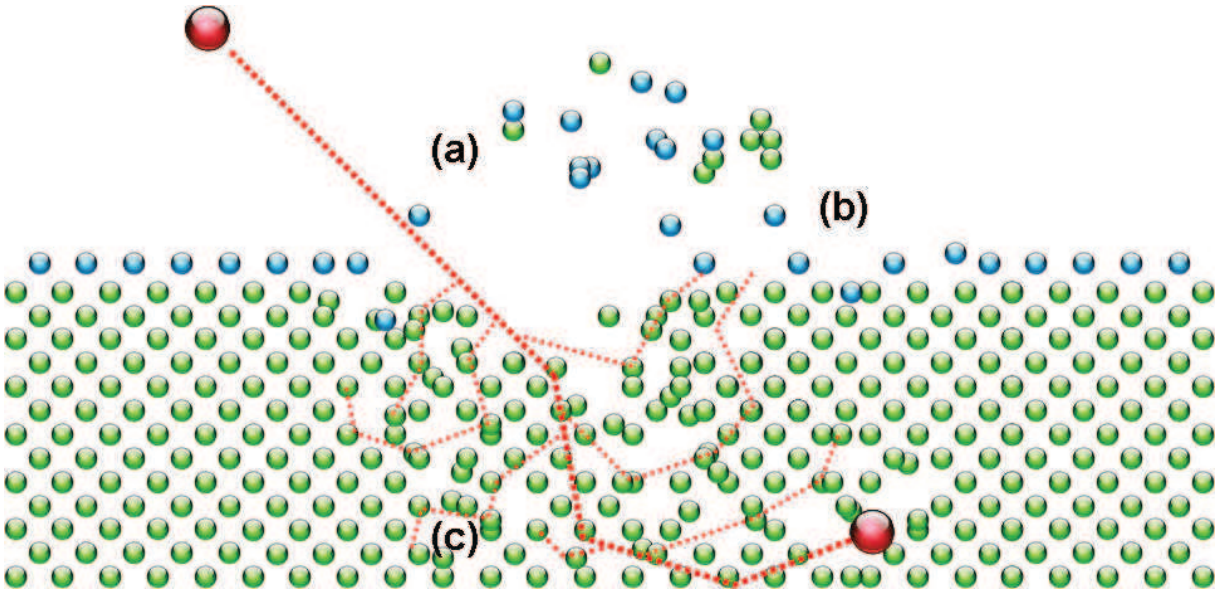

Figure I.7 Simplified diagram of a collision cascade in the linear cascade regime. Some atoms and compounds are sputtered on impact (a) but a vast majority of the sputtered material is issued from collisions with backscattered underlying atoms (b). Extensive damage is inflicted to the lattice through the numerous successive collisions between target atoms (c).

The second one, schematised in Figure I.7, becomes significant above 1 keV. It corresponds to the reaction of a target under higher energy bombardment with Cs or O_2 for sputtering, or with Bi for analysis in our experimental setup. In this regime, more atoms are displaced and sputtered upon impact than in the single knock-on regime. After the first interaction, both impinging ion and primary recoiled atom have indeed enough energy to provoke several successive collisions with environing lattice atoms before loosing all their energy. This leads to the development of a collision cascade with atoms displaced in a successive fashion, hence the name of linear collision cascade regime. At first, the collision cascade is directed in the same direction as the original direction of the impinging ion, but then many collisions take place and a fraction of the displaced atoms are backscattered towards the surface and will still have enough energy to sputter surface, or near surface atoms [52-53]. Notice that in this regime important damage can be inflicted on layers beneath the surface (see Figure I.7), but that sputtered particles come almost exclusively from the first mono-layers since only atoms of those layers are subject to ejection after a collision with rather low energy, backscattered atoms from the collision cascade. Given the important volume of displaced atoms in this regime, this regime has enhanced sputter yields relative to the first one.
The third regime explains sputter phenomena observed for heavy, cluster impinging ions. It describes the reaction of a target under bombardment with Bi clusters in our experimental setup. In this regime, called non-linear cascade regime (also spike regime), at the first interaction several atoms are displaced either because of the size of the impinging ion of because (in the case of a cluster ion) its constituents were fragmented on impact. The following collisions are therefore triggered no longer in a successive fashion but in parallel, and we observe collisions between atoms in movement, similarly to thermal agitation in a gas [54-56], as shown in the simulation results displayed in Figure I.8 [57]. This triggers drastic enhancement of the sputter yield in a non-linear fashion. That is, when compared to the sputter yield obtained with a primary ion of mass m, the sputter yield enhancement obtained with a cluster ion constituted of n elements of mass m is more important than the sputter yield enhancement obtained with an incident ion of mass $n \times m$ [58-61].

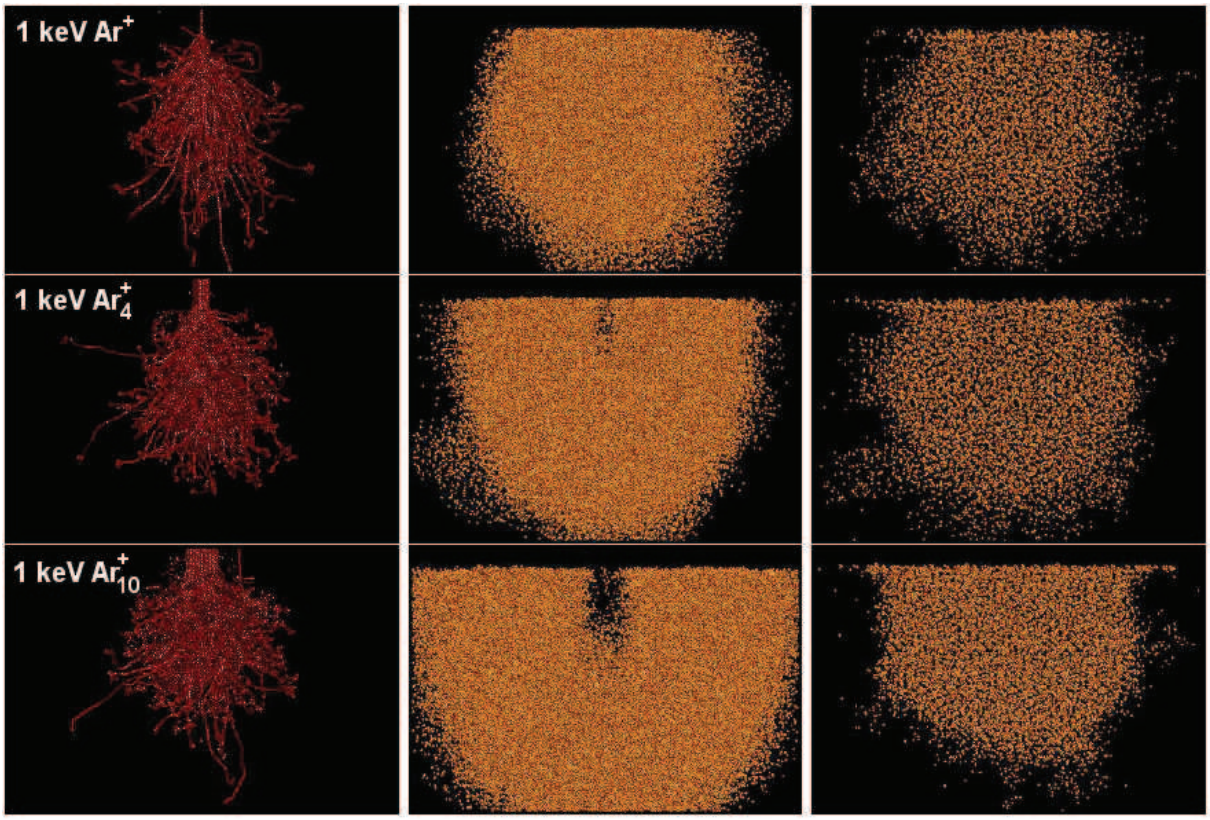

Figure I.8 Simulated collision cascades for 1 keV Ar^+, Ar_4^+ and Ar_{10}^+ in amorphous Si [57]. Each row represents the extent of the collision cascade obtained for a same number (270) of impacting Ar atoms. First column shows the trajectory impacting Ar atoms. Second column shows the amount of atoms displaced after more than two collisions with other lattice atoms. Third column shows initial position distributions of atoms displaced more than 1.5Å during the cascade development. Frames are 14 nm wide and 10 nm high.

The sputter yield is thus extremely dependent on the primary ion beam parameters, and primarily on its energy, as it tends to rapidly increase with it. Typically in the energy range which interests us in this study *Y* will vary between 0.01-0.02 at ~100 eV and 1-10 at a few tens keV [62-64] (see also [48] and references therein). But it shows also an important dependence on angle, with generally a maximum sputter yield around 60° with respect to the sample normal, quickly decreasing towards grazing angles and slowly decreasing towards the normal [65]. Other parameters of great influence on sputtering yields are the mass of the primary ion, or rather the mass ratio between the target atom and the primary ion (lighter target atoms being preferentially sputtered), and the binding energy of the target atoms which (at equal masses, atoms of lower binding energy will be preferentially sputtered) [48, 66-67]. The balance between mass ratio and binding energy is therefore particularly important when sputtering targets constituted of several chemical elements, where preferential sputtering phenomena can appear. Lastly, as parameters of lesser influence, we can cite target related parameters, such as its density, its crystalline state, its temperature or its surface roughness [68].

Another aspect of ion bombardment, common to all regimes, is the implantation or adsorption of a part of the primary ions. In the case of chemically inactive elements such as Ar, this effect is extremely limited since only physical implantation is occurring. However, in the case of active elements such as Cs and O_2, significant quantities are adsorbed (chemisorbed) on the sample surface. This results in a profound modification of the sample chemistry over a few monolayers (particular sputter conditions can yield Cs surface concentrations of a few tens

at% [69]). A transition is thus occurring at the first stages of sputtering since the sample surface composition changes from 0 at% to a given concentration. At first, surface concentration in the active element rapidly increases, then it diminishes while excess surface concentration is removed and finally it stabilises when the amount of sputtered atoms equals the amount of adsorbed ones [37]. The duration of this transient period depends on the sputter conditions and other experimental parameters such as atmosphere conditions in the analysis chamber.

Ionisation processes

Amongst those sputtered particles, mostly constituted of neutrals, a small fraction bears a positive or negative charge, and it is only this fraction which is observed in SIMS. The understanding of particle ionisation processes are thus of particular interest. As shown by equation (I.2), the secondary ion yield of a particular element *m* will indeed be directly proportional to its ionisation probability $\alpha_m^{+/-}$. However, if sputtering mechanisms are well known and controlled at least in the single knock-on and linear collision regime, it is (still) not the case with ionisation processes, which remain partly unexplained due to their intrinsic complexity and to the interaction between different processes. $\alpha_m^{+/-}$ can thus vary over several orders of magnitude for different species contained in the same target material (intrinsic sensitivity of the technique), depending primarily on their electron affinity or ionisation potential. Furthermore, the chemical state of the surrounding surface environment can also cause $\alpha_m^{+/-}$ variations of several orders of magnitude even for identical combination of species and target materials. This is due to the change in electronic configuration of an element when placed in different matrixes, hence the name of matrix effect [37]. Combined effects of sensitivity and matrix effects make extremely difficult the prediction of $\alpha_m^{+/-}$ without the use of almost similar, well known reference samples, and therefore precludes direct quantification with SIMS (further discussion on this subject will be provided in following sections). Nonetheless, the study of ionisation processes can help for partial understanding of experimental results. In particular it can explain secondary ion yield enhancement phenomena observed when using reactive ion beams such as caesium (for electronegative elements and positive caesium compound ions) and oxygen (for electropositive elements) [37] as it is the case usually with our experimental setup. In the following, we will only cite the most common processes, while more comprehensive reviews are available in the literature [45, 70].

The first one, called electron tunnelling (or work function) model, refers to the interaction between the charge of the impinging ion and the electron gas of the target. This model supposes that there is such an electron gas and is therefore valid only for metal or semiconductor targets where a high proportion of charge carriers are situated above the Fermi level. When a charged incident ion comes close to a target atom, below a certain distance threshold, electron exchange becomes favourable in regard to the target's Fermi level, and ionisation of a target atom is possible. The direction of the exchange depends on both target's work function and on the target atom's electron affinity or ionisation potential, with α_m^- showing an inverse exponential dependence with work function [71]. By reducing the target material's work function, one can thus obtain improvement of α_m^- values over several decades. This effect is used to favour emission of electronegative secondary ions when sputtering with Cs atoms, which have a tendency to be chemisorbed on the surface and therefore lower target's work function [71].

On the other hand, for oxides or halides no more interaction with the electron continuum is possible. The model describing the ionisation processes is then the bond breaking model [42, 51, 72]. In such materials, the ionisation is seen as the consequence of destruction of covalent

or ionic bonds within the lattice during sputtering. The sputtered atom (of electropositive nature) is ionised when leaving the surface by breaking its bond with another atom and leaving an electron behind. In this case, emission of positively charged ions is favoured, and positive ionisation probability exponentially increases with ionisation potential. At the opposite of the electron tunnelling, this effect can therefore be used to enhance secondary ion yields of electropositive elements by using oxygen sputtering or flooding so as to increase α_m^+ values of several orders of magnitude [70].
A last model, the recombination model, describes a particular type of ionisation for cluster ions in a specific element *X*-rich matrix. It assumes the recombination in the sputtered matter plume above the target surface, or directly during the sputtering process of emitted X^+ ions and M^0 neutrals to form MX^+ or MX_2^+ cluster ions [73]. In some cases the ionisation probability of such kind of compound cluster ions can be several orders of magnitude higher than this of the element M alone. This model is particularly valid for description of Cs compounds when sputtering with Cs (so called MCs mode [74-76]).

I. 3. d- Depth profile quantification procedure

Although a majority of ToF-SIMS studies focus on extreme surface analysis (such as for studies of organic materials, or contamination), it is a very versatile tool capable of a wide range of analyses. Amongst these, depth profiling is a well known technique that is often used for microelectronic related studies. It consists in recording the intensity of one or more signals in depth. In the case of dual beam ToF-SIMS, a crater is formed by rastering of the sputter beam over an area of the sample surface larger than the beam spot. Signals are gathered via secondary ions emitted on impact with the analysis beam, which is rastered over a smaller region in the centre of the crater in order to ensure analysis of a flat surface (see Figure I.9) and to avoid contributions coming from the crater side-walls. Analysis and sputter beam then work in an alternate fashion as schematised in Figure I.4.B to yield a series of surface spectra separated by a given sputter time, giving secondary ion intensity profiles as a function of sputter time.

Establishment of a depth scale

In order to quantify the secondary ion intensities in terms of concentration one first needs to convert the (sputter) time scale into a depth scale to assess the quantity of sputtered material. There are a number of different methods to achieve this, in correlation with aspects connected to the physical and chemical aspects of sputtering as seen in previous subsections. A few of them are summarised in Figure I.9. The most common applications involving sputtering a relatively thick layer of a homogeneous matrix are very simple to address. In this case, the sputter rate *SR* can be considered as constant along the whole profile and depth at any point of the profile after a sputter time *t* can be obtained through the relation $z(t) = SR \cdot t$, as in Figure I.9.A. To obtain *SR*, one has to determine the total thickness of material sputtered *Z*, which can be obtained from direct measurement with optical or contact profilometer or from calculation by taking into account material density, known sputter yield under identical sputter conditions, crater size and beam current. Another method would be to resort to a depth marker, as in Figure I.9.B. This marker can be a delta layer, an implantation or impurity related intensity peak etc, of known depth (characterised by Transmission Electron Microscope (TEM), simulated with TRansport of Ions in Matter code (TRIM) etc). In this case the constant sputter rate is estimated directly using the sputter time needed to reach the marker without having to measure or calculate total crater depth. This method is particularly

useful for shallow profiles (a few tens of nanometres) since both measurement and calculation of crater depth have high uncertainties at these depths. When sputtering through thick heterogeneous layers however, one can no more assume a constant sputter rate.

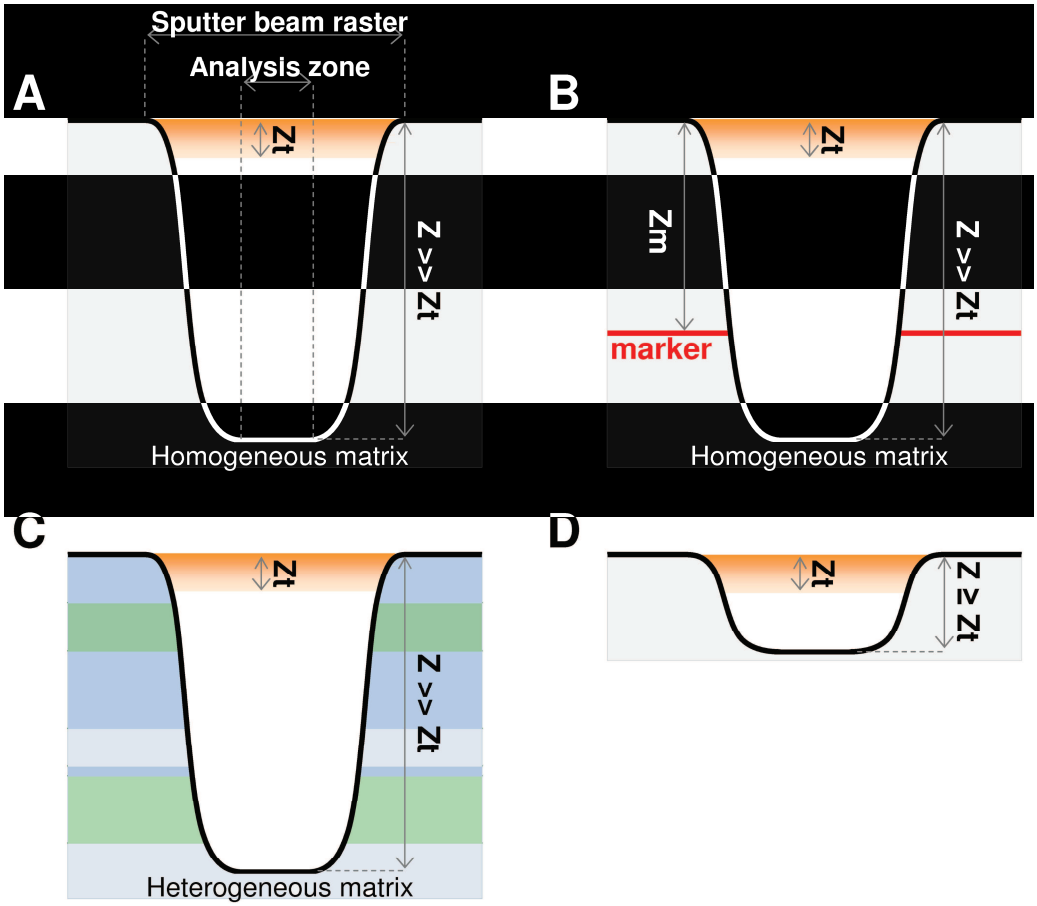

Figure I.9. Schematised cross section views of sputter craters at the end of profiling.
A In the simplest case of deep profile in homogeneous material.
B In the case of deep profile in homogeneous material with a deep enough depth marker.
C In the case of deep profile through heterogeneous materials.
D In the case of a shallow profile, in a homogeneous material or through heterogeneous layers.

Sputter mechanisms discussed in the previous subsections imply that sputter rates will indeed change from a matrix to the other (Figure I.9.C). The only valid method in this case would then to establish depth scale in sections, relying on sputter rates established from bulk reference samples of each different material. Finally and by contrast with the two first cases, when the total sputtered thickness becomes extremely thin (typically ≤10 nm) the sputter rate can no longer be assumed to be constant. Indeed (especially when sputtering with active elements), during the transient period, not only does the surface concentration change, but due to this surface modification the sputter rate also changes. If total sputtered thickness is not sufficiently important when compared to the transient region thickness *Zt* (Figure I.9.D), the variable sputter rate occurring in this region induces a non-negligible shift on the profile. An estimation of the variation in sputter rate can be obtained in some particular cases, which allows a correction for this effect. Notice that the same effect can also occur in depth, when crossing an interface between two heterogeneous materials.

Establishment of a concentration scale

According to equation (I.2) the secondary ion yield of an element depends directly on its ionisation probability. Yet in the previous paragraph this probability has been seen to vary from one element (or compound) to another, as well as with the chemical environment, and of course with the instrumental setup and parameters. As a consequence, direct quantification of secondary ion yields in terms of concentration is impossible. The only way to overcome this problem is to resort to well known reference samples that have to be profiled under exactly the same experimental conditions and preferably within the shortest time delay possible in order to obtain Relative Sensitivity Factors (RSFs). Quantification is then done at each point of the profile by normalising the signal of interest by a matrix representative signal (e.g. Si^+ in silicon) and computing the elemental concentration through the linear relationship:

$$\text{Concentration(element of interest)} = \text{RSF} \cdot \frac{\text{I(element of interest)}}{\text{I(matrix element)}} \qquad \text{(I.3)}$$

Where RSF is assumed to be constant along the profile. The RSF of an element in a particular matrix and with given experimental conditions accounts for the instrument's sensitivity for this element in the given conditions. ToF-SIMS is thus only a semi-quantitative technique, in that it does yields quantitative analysis but requires an external calibration method. Furthermore, this is valid only for the simplest case of sputtering through a homogeneous matrix, such as in Figure I.9.A and B. Similarly to the depth scale, one has to resort to several reference materials or external calibrations for quantifying impurities in heterogeneous layers. In the case of ultra thin layers close to sample surface or ultra thin layer stacks, the assumption of a constant RSF is no longer valid. One has thus to resort to extremely complex protocols to assess for the RSF variation during transient regions [77-78], but they are often limited to one experimental condition and one type of matrix. Moreover, the whole quantification protocol via RSF is only accurate for impurities up to a certain concentration (typically < 1 at%), since it requires normalisation by a matrix representative signal. If the concentration of the element of interest becomes too high, one can no longer assume a linear relationship between the intensity ratio and the actual concentration in the sample because of the matrix effects. Very specific protocols have however been developed to overcome this difficulty such as the MCs (using detection of the MCs_n^+ secondary ions, M being an element of interest) protocol for Ge quantification in SiGe [74-76], but again no general method is (yet) reported.

I. 4. Selection of materials and structures of interest for future microelectronic devices

As discussed in section I. 1, an ever increasing complexity level was introduced in semiconductor device manufacture in terms of materials and structures during the past decade. The motivation for these changes rely on (but are not limited to) improvement of electric performances (I_{ON}/I_{OFF}, frequency), power consumption, reliability and ageing, production costs etc. Numerous experimentations were thus performed on both materials and structures with device improvement objectives, yielding a large variety of new structures and interesting material uses abundantly commented in the literature. Out of these emerging devices, we selected for this thesis work a few promising ones. In this section we will therefore present the different materials and structures covered by this study from the point of view of material

science and device properties improvement, and briefly review the associated characterisation needs.

I. 4. a- Base materials and structures for Heterojunction Bipolar Transistor (HBT) and Multi Channel Field Effect Transistor (FET) devices

Interest of $Si_{1-x}Ge_x$ alloys

These devices are based on the co-integration of Si and Ge (and all available $Si_{1-x}Ge_x$ compound alloys) in the same device. Indeed Ge has very interesting properties that can be used for device improvement. These are summarised in Table I.i [79-81]. Ge is, as Si, a IV column element and has the same crystalline structure (diamond-like Face-Centered Cubic) with a relatively similar density to that of pure Si [79].

Parameter	Si	Ge
Lattice parameter (nm) [79]	0.5431	0.56575
Bandgap width (eV) [80]	1.1	0.66
Electron mobility ($cm^2/V.s$) [81]	1500	3900
Hole mobility ($cm^2/V.s$) [81]	450	1900

Table I.i. Major electronic properties of Si and Ge at ambient temperature.

Notice in particular the important gain in both electron (×2) and hole (×4) mobility for Ge with respect to values in Si [81]. These properties, already well known before the beginning of semiconductor industrial era, would place Ge as a better choice than Si in terms of device performance. Ge was used in the first transistor built at Bell labs in 1947 [1-2].

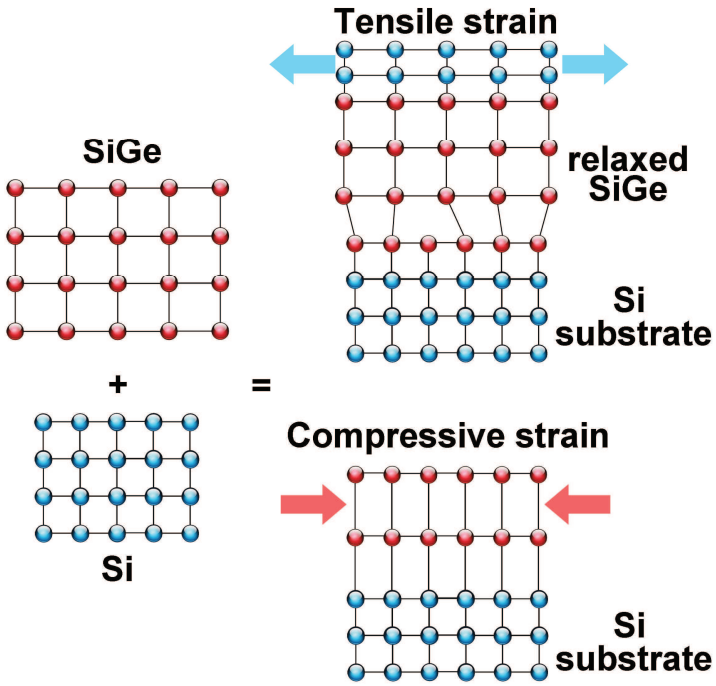

Figure I.10 Examples of strained structures that are possible by Si and SiGe co-integration. The lattice mismatch between both materials has been over-exaggerated to provide better visual understanding.

However several factors severely discouraged the use of Ge in semiconductor devices. First, its relatively small bandgap [80] makes it more subject to current leakages, and increases the difficulty to control the device through gate potential at ambient temperatures (although this could also be used as an advantage to build low resistivity contacts [82-83]). Second, its production costs are higher than those of Si, due to its low natural abundance. Finally, and most importantly, the absence of a stable Ge oxide limited its use in the basic CMOS structure [81]. However In the past few decades, instrumental developments have allowed the deposition of high quality pseudomorphic or relaxed $Si_{1-x}Ge_x$ layers of a well controlled composition on top of Si substrates [84]. This enabled Ge to be used in actual devices without bearing the usual drawbacks of pure Ge substrates. It therefore allowed improvement of device performances by making use of two intrinsic properties of Ge: (i) its higher carrier mobilities versus pure Si and (ii) its slightly higher lattice parameter presenting a 4.17% mismatch with that of Si [79]. The latter enables strain engineering inside the device by carefully choosing the co-integration scheme (for growth of Si or SiGe pseudomorphic strained or relaxed layers) and layer composition. A few examples of these are given in Figure I.10. Inducing compressive or tensile strain in the SiGe layer itself or in surrounding Si layers results in a direct improvement in carrier mobility because of the alteration of the band structure it generates [85-87]. Overall mobility enhancement with this kind of structures are reported up to ×2 for electrons and ×10 for holes [86]. For example, the tensile stress induced by a relaxed $Si_{0.8}Ge_{0.2}$ base layer on a Si channel was shown to induce ×1.5 mobilities in heterojunction devices [88]. The evolution of device performances with introduction of strain engineering is well summarised in Figure I.11. Another advantage of the use of such heterostructures relies in the reduced need for a stringent lithography [82], given that the improvement it brings is not related to dimensional scaling. This is also crucial since it represents a cost advantage for device production. All of these properties are currently exploited in so called HBT devices since the 65 nm technological node and are still subject to research for improvement in view of forthcoming nodes.

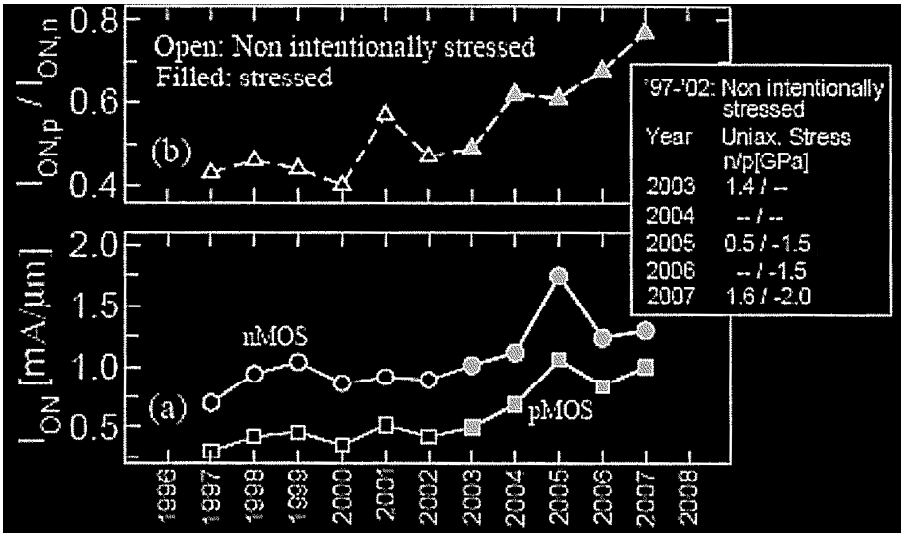

Figure I.11 Evolution of n- and pMOS carrier mobilities over time due to unintentional or intentional strain engineering.

Interest of SiGe/Si superlattice structures, in-situ doping and layer oxidation

Apart from the improvement of carrier mobilities, co-integration of heterogeneous Si and $Si_{1-x}Ge_x$ materials make completely new architectures possible. By successively growing pseudomorphic Si and SiGe layers (to form a superlattice structure) and exploiting the

different chemical etch rates between those two materials, one can build either Si or SiGe slabs surrounded by voids which will act as channels for vertically stacked Gate-All-Around (GAA) devices. A typical process flow for deposition of such multi channel devices [89], along with a cross section TEM image of a final device [90] are shown in Figure I.12. In addition to the evident gain in terms of transistor density due to their 3D architecture, excellent performances were reported for this kind of devices in the literature, with for example ×50 I_{ON}/I_{OFF} ratios relatively to planar structures [91]. Heavy in-situ doping of SiGe layers during the epitaxial growth step with impurities as carbon, or dopants as boron or phosphorous brings further improvement in two ways. First, the introduction of small elements such as C in a SiGe matrix reduces the lattice mismatch with Si and thus increases the stability of the structure and avoids strain relaxation effects when releasing the Si or SiGe channels. It therefore allows for growth of more layers and vertical stacking of more transistors [92-94]. Second, B or P doped SiGe layers would act as dopant reservoirs when an appropriate anneal is applied to them (after liberation of Si channels) and thus provide source and drain region doping without having to perform implantation. Finally, in the case of SiGe channel, optimum performance improvement can be achieved by using high Ge content layers for better mobilities. If the growth of thick enough, defect-less pseudomorphic layers of high Ge content layers on Si is impossible due to the too important lattice mismatch, one can however perform a "condensation" of the Ge content inside the SiGe layers once they have been released. The condensation technique allows the Ge enrichment of low Ge content SiGe layers by a selective oxidation of Si compared to Ge [95]. This technique has been used to fabricate high Ge content SiGe-On-Insulator substrates, with excellent hole mobilities achieved in planar pMOS devices built on top [94]. However, it can also be used to obtain Ge nanowires [96]. In [93], Saracco *et al.* proposed a new method to fabricate 3D suspended Ge-rich nanowires by Ge condensation, which is completely CMOS compatible and provides excellent electric results [97].

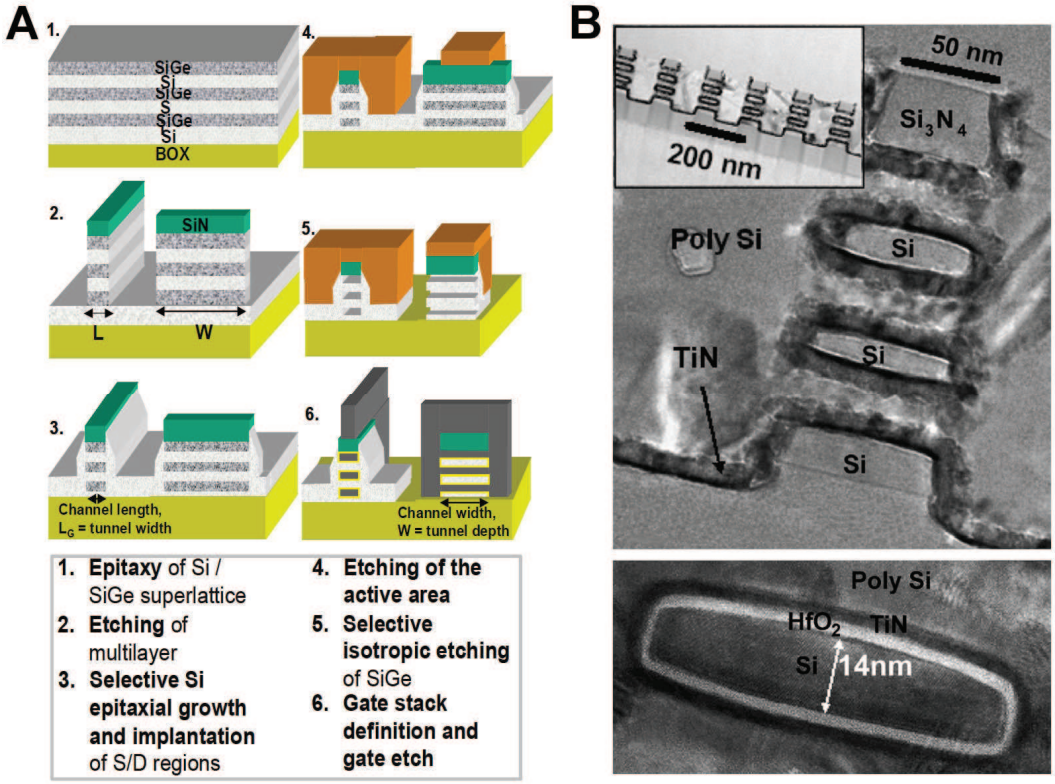

Figure I.12.A Process flow for elaboration of MCFET devices, taken from reference [89].
B Cross section SEM view of a complete device (top), focus on one channel and surrounding gate (bottom), taken from reference [90].

Not only SiGe alloys, but also doped layers deposited in an successive fashion with pure Si, and which sometimes underwent annealing or oxidising step, are therefore of interest for next generation devices. To ensure optimum control and reliability in electrical properties of such devices there is therefore a need for precise characterisation of matrix composition (Ge content) and dopant or impurity quantitative profiling, as well as layer thickness control in the most precise manner possible. Accurate characterisation of layer crystalline quality and structure behaviour under anneal and oxidation is also required.

I. 4. b- Materials and structures for sub 32 nm node planar High-K Meal Gate (HKMG) devices

Interest of high permittivity dielectrics for replacement of silicon dioxide gate dielectric

To further pursue device performance improvement according to the ITRS roadmap, dimensional scaling is an important lever. It imposes reduction of gate length, which in turn automatically forces other dimensional parameters to decrease. Along them, the reduction of the dielectric layer thickness (insulator layer between channel and gate) is problematic. The traditional material used in devices is silicon dioxide, which has excellent insulator properties, is stable and perfectly compatible with Si, but has a relatively low dielectric constant (permittivity, $\varepsilon_r = 3.9$, also referred to as Kappa). Below a certain thickness (~2 nm [98]) tunnelling effect between channel and gate becomes non negligible and the device becomes ineffective. Further reduction of oxide thickness would therefore lead to an increase of leakage currents (and I_{OFF}) and a decrease of gate potential. The solution is then to modify the gate oxide layer from SiO_2 to another material in order to obtain thicker layers with identical electric properties. The notion of Equivalent Oxide Thickness (EOT) is therefore introduced.

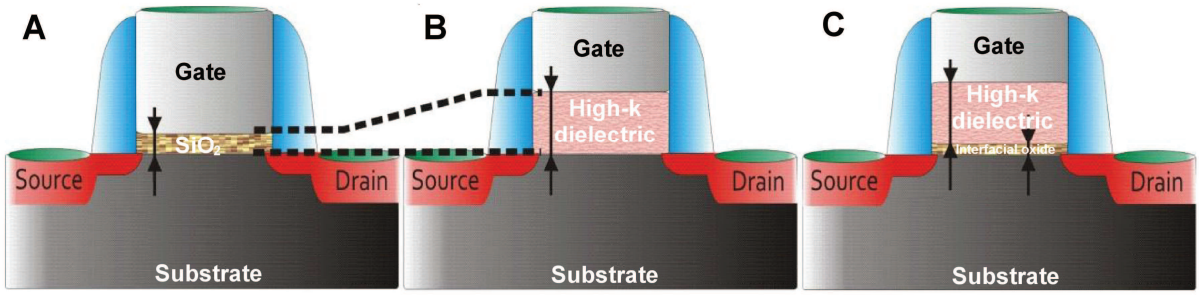

Figure I.13.A Schematic representation of a standard Metal Oxide Semiconductor FET (MOSFET) with SiO_2 pedestal oxide.
B Integration of high-k dielectric of equivalent EOT (ideal structure).
C Actual structure with formation of an interfacial oxide at the high-k material growth step. Figure extracted from [99].

The EOT of a high-k material layer represents the thickness of SiO_2 layer one would have to grow to obtain equivalent electric properties. It depends of the high-k layer thickness, and of the dielectric constant ratio $\varepsilon_r(SiO_2)/\varepsilon_r(\text{high-k})$. In order to obtain the lowest EOT possible, higher permittivity materials were thus investigated. The introduction of those materials in production lines was already performed in 65 nm generation devices, with SiO_xN_y pedestal oxides (ε_r ~5.8 [6]). Oxide nitridation also provides an excellent barrier against detrimental B diffusion towards channel during gate implant and anneal. However, depending on the N positioning in the oxide (in bulk, at interfaces, with a concentration gradient or not), its

presence can be detrimental by increasing interfacial trap density [100]. Moreover, the gain in EOT relative to SiO_2 of ×1.5 is small. Numerous materials of higher permittivity were thus investigated, and amongst them zirconium, lanthanum, aluminium, and hafnium oxides [6, 101]. Out of those, the latter is seen as the most promising for sub-45 nm nodes because of its high permittivity value (ε_r ~20), its relatively high band offset (2.3 eV) and its relatively good stability on Si [102]. Figure I.13 shows the evolution of dielectric integration in a MOSFET structure from an SiO_2 based device to a high-k one [99]. Again, this shows that is not yet a perfect: high-k material growth on pure Si yields a complex interfacial state through the apparition of a degenerated silicon oxide [103-104]. A solution to this problem is to grow high-k layers on an intentionally grown ultra thin silicon dioxide [104]. Furthermore, to avoid degradation of interfacial state quality and elemental diffusion due to gate deposition and activation anneal thermal budget, nitridation of both pedestal silicon dioxide and high-k material is required, with a good control of N composition profile though the stack. Finally the deposition of hafnium silicate in place of hafnium oxides allows a better interface quality with both silicon oxide and gate material [104]. The final dielectric structure for sub-32 nm devices studied in this work therefore consists of a HfSiON layer of several nanometres in thickness on top of a SiON pedestal oxide.

Interest of middle gap metals for the replacement of the polycrystalline-Si gate

Following the evolution of dielectric materials, the traditional doped polycrystalline (poly-Si) gate material also had to be changed to improve device properties. Integration of a poly-Si gate on top of high-k materials increases the threshold voltage of the device through a mechanism known as Fermi level pinning [105-106]. Another disadvantage of Poly-Si material is that it can be (electronically speaking) depleted at the gate/dielectric interface, which adds a few Angstroms to the device EOT and is therefore detrimental [107]. To counter these effects, metal gate electrodes have been introduced to replace poly-Si gates [108]. They have the advantage of reducing poly/high-k interaction, eliminating poly depletion, as well as reducing B penetration from the doped poly-Si into the gate dielectric, and gate resistance.

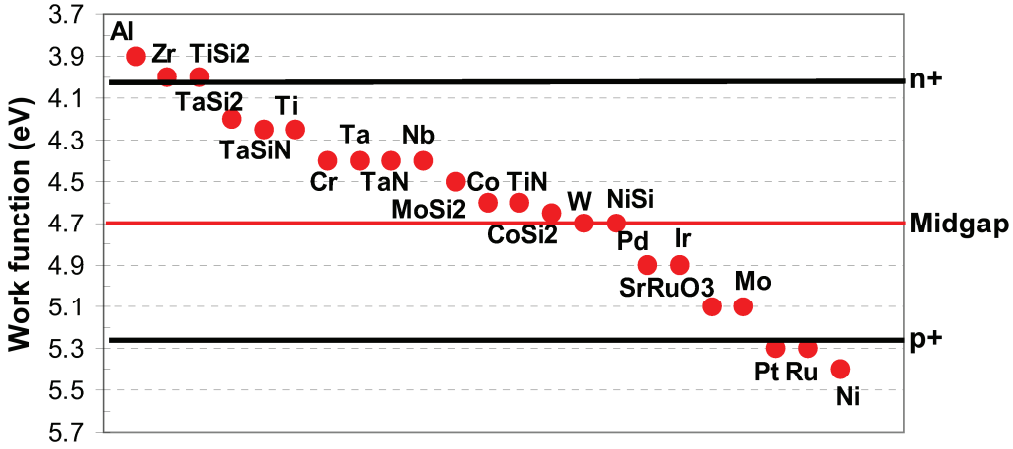

Figure I.14 Work function of different potential candidates for n or metal gates to replace poly-Si [109].

At the beginning, there has been limited consensus on the appropriate electrode material, with production ready performances. One of the role of the gate is indeed to possess an appropriate work function to match either negative or positive channel MOS (n or pMOS) devices. This was achieved by either n^+ or p^+ doping of the gate material with Poly-Si but cannot be applied to metals. A solution is then to choose different metals for n and pMOS devices, by selecting

materials with the desired work (see Figure I.14). The other solution, which is regarded as the most serious option for next generation devices, consists in using a midgap material such as TiN for both n and pMOS integration, and to modulate its work function [104, 109]. This can be done by adding ultra thin layers of Al (for pMOS) or La (for nMOS) oxide in the gate stack and making it diffuse through the gate to the gate/dielectric interface during the dopant activation anneal.
To further improve device performance, one might also want to combine HKMG technology with the SiGe based channel strain engineering technologies seen in section I. 4. a- to obtain the best characteristics possible [110].

Stacks of heterogeneous, nanometre thick hafnium silicates, silicon oxynitrides, lanthanum oxides and titanium nitride stacks which underwent (or not) consequent thermal budget are of interest for future planar CMOS devices. The properties of the final device depend principally on the composition of those layers and and on the positioning of some crucial elements such as nitrogen. To ensure optimum control and reliability in electrical properties of such devices there is therefore a need for precise quantitative depth profiling of Hf, Si, O, N, La, Ti content in ultra thin layers, as well as for accurate investigation of diffusion behaviour of all elements through the stack upon activation anneal.

I. 4. c- Ultra Shallow Junction implants for sub-32 nm planar CMOS

In order to preserve the advantages of mobility enhancement technologies (reviewed in previous paragraphs) and device scaling-down, the junction depths in next generation devices will have to be below 10 nm while achieving high dopant concentration and high levels of activation, along with extreme abruptness of ~2 nm/decade [7]. Yet, as MOSFET dimensions shrink into to sub-32 nm range, nanoscale processes engender tremendous difficulties as for instance severe short channel effects, degraded driving ability, boron penetration and poly-silicon depletion, high-field effects, direct gate tunnelling current and high series resistance [111-112]. Following Moore's law thus encounters unprecedented difficulties. The realisation of such Ultra Shallow Junctions (USJ) requires improvement of existing implant technologies, development of new dopant placement ones, along with development of thermal activation processes that have lowest possible impacts in terms of undesired dopant diffusion. In traditional ion beam implantation, the trend is to reduce implantation energy to sub keV values in order to match junction depth expectations. However this technique presents both drawbacks of (still) important defect density yield upon implantation along with a quite low throughput due to the low ion beam currents (see Figure I.15) [113]. It is therefore not well adapted to production needs. An alternative to this might be the use of gas cluster ion beams which induce less damage and show better currents [114-115] or molecular doping through monolayer dopant adsorption on Si substrate followed by surface oxidation and spike anneal [116-117]. A last, promising technique of interest is (pulsed) plasma immersion ion implantation [118-119]. It combines the advantage of high throughputs (see Figure I.15), possibility to work at extremely low energies (down to ~100 eV) and to attain high surface dose concentration, and possibility of homogenous isotropic implant on three dimensional surfaces. This is particularly important for achievement of conformal doping in non planar structures such as FinFETs, and precise ultra-shallow doping for planar FET [115]. Finally both n and p doping can be easily achieved with this technique through the use of BF_3 (for p^+) and AsH_3 (for n^+) plasmas. Upon activation anneal, different species (As and B) will feature different diffusion behaviour, in terms of the amount of diffused material, interaction with surface oxides and bulk defects, interface

segregation etc. These behaviours, which can often be detrimental to electrical properties, must also be controlled as best as possible through advanced annealing technologies [111].

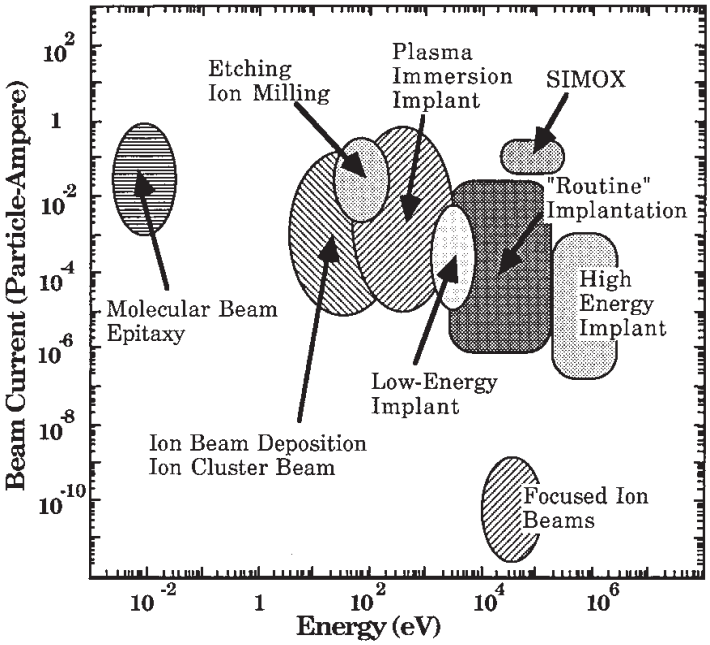

Figure I.15 Ion beam processing phase space map of the range of ion energies and beam currents used in semiconductor processing [113].

Both p^+ (B) and n^+ (As) ultra shallow implants obtained by implantation techniques are therefore of interest for future planar CMOS devices. The properties of the final device depend greatly on the amount of implanted material, especially near the surface, and on its depth distribution which must be as sharp as possible. To ensure optimum control and reliability in electrical properties of such devices there is therefore a need for precise dopant quantitative depth profiling in sub-10 nm thick layers, as well as for accurate investigation of dopant diffusion behaviour upon activation anneal. We chose to focus on As implants due to the numerous artefacts encountered in such samples.

I. 4. d- Alternative materials for future devices

Ultra low-k materials

By contrast with the core dielectric material between channel and gate, materials of ultra low permittivity are required as backend interconnection insulators. With dimensional scaling, System on Chip structure became more and more complex and delays of information circulation in interconnects became an important limitation of device circuit performance. From the 90 nm node, industry switched to Cu for interconnects and to low-k insulating materials to lower both resistance and capacitance of the interconnects. The low-k material was then a classic silicon dioxide with dedicated deposition tuning in order to obtain $\varepsilon_r \sim 3$. To further decrease this value, new materials were developed and used in production for the 45 nm device generation [7, 112]. It consists in thick, porous SiOCH layers deposited by Plasma Enhanced Chemical Vapour Deposition (PECVD) and cured through plasma, Ultra Violet (UV) or electron beam treatment. ε_r values as low as 2.2 [112, 120] are reported for such materials. However due to the porous nature of the material itself, it is still difficult to obtain reliable enough material. The properties of the materials are indeed extremely

dependent of the deposition and curing conditions, and in particular of the uniformity of layer composition [120], which therefore needs to be investigated and controlled.
Preliminary works on these materials have been performed but will not be presented in this manuscript.

Germanium and III-V materials

To further improve device performance, one has to think beyond the current strained engineered, enhanced mobility channel. One of the promising way is to switch from Si to alternative materials channel, such as Ge and III-V (InP, GaAs) compounds [7]. These indeed feature much better intrinsic mobilities than Si, as seen in Table I.i for Ge. III-V compounds feature average equivalent hole mobilities, but from 3 to 30 times enhanced electron mobilities [121]. Both Ge and III-V materials suffer from integration problems that need to be resolved, such as channel layer growth, source/drain region formation [112] or surface passivation [122]. However research devices already show promising results, both with Ge [123-124] or III-V [125-128] channels. To bring these research devices onto production lines, accurate material characterisation is necessary to address the different problems raised by these materials.
Preliminary works on these materials have been performed, and some published (see author's bibliography at the end of the manuscript) but will not be presented in this manuscript.

Organic materials

For almost forty years, the industry of electronics has focused on inorganic materials. Polymer materials have been the focus of much interest these past years for their applications in electronics. Their versatility and low production cost (spin-coating, inkjet printing) makes them serious candidates for next generation devices. A lot of practical applications were reported these past few years, especially in the optoelectronic field where their properties of electroluminescence and transparency are appreciated [129-131]. We can differentiate two kinds of molecules for electronics: polymers, which are characterised by long chains of identical repeat units and 'small molecules' which are often fullerenes or organo-metallics such as metalchelates, without repeat unit and presenting higher orders of crystalline state than polymers. Conductivity in organic materials was first reported in the 60's for anthracene single crystals [132-133]. Ten years later was reported the possibility of doping organic materials over the full range from insulators to conducting materials [134]. This discovery does not apply to all organic materials, but only to a very specific group called conjugated (or π-conjugated) materials [129]. Among them, polymer-fullerene blends present interesting properties which led to their use in optoelectronic [135] and volatile memory [136] devices. The literature contains numerous studies on polymer-C_{60} blend layers for various applications [137-139]. PolyMethyl MethAcrylate (PMMA) is an interesting choice as polymer matrix since it is an insulating material which only acts as a physical support for the C_{60} molecules without interacting at an electronic level. Furthermore PMMA is easily patternable by e-beam (and is thus used as negative electron beam resist in microelectronics industry), and thus represents a good choice for industrial microelectronics. However, electrical behaviour of these devices is tailored by their fullerene content [140] and depend on the electrode materials as well as the organic materials reaction to the activation anneal. There is therefore a strong need for accurate quantitative in-depth characterisation.

Based on the discussion above, we will focus our study on the following materials and structures:

- $Si_{1-x}Ge_x$ alloys with x varying from 0 to 1, in some cases with heavy doping and integrated in a vertical stack of heterogeneous layers which possibly undergo dedicated anneal and oxidation.
- HKMG nanometre scale layers arranged in stacks, with in some cases SiGe strained channel and which possibly undergo significant thermal budget.
- As ultra shallow junctions in Si obtained by different implantation techniques through a native or grown oxide and annealed.
- Organic materials constituted of a polymer matrix and fullerene dopants.

We will now review the difficulties encountered in ToF-SIMS analysis of such samples.

I. 5. Challenges in ToF-SIMS characterisation of advanced materials and structures for microelectronics

Before going further on the matter, we must delimit the range of action of our study. Almost all materials and structures presented in the previous section and studied in this work are intended for deep submicron technology devices. At these nanometre scales, there can be significant differences between the behaviour of a material in a full-sheet configuration and its behaviour in an actual device. This motivated the need for techniques able to provide 2D, or even 3D quantitative material characterisation with nanometre spatial resolution in order to study phenomena inside an actual device, pushed by the ITRS roadmap for characterisation [7, 141]. Techniques such as Scanning Spreading Resistance Microscopy (SSRM) or Scanning Capacitance Microscopy (SCM) were demonstrated to be able to provide 1-2 nm resolution for 2D imaging of active dopants in sub-45 nm generation devices [142-143]. This kind of performance is however impossible to obtain with our instrument, , whose extreme limit in lateral resolution is determined by the minimal analysis beam spot size attainable, measured to be 50 nm in diameter. Improved ion source and column instrumentation, compatible with our current instrument and still under development, are reported to provide 10-15 nm lateral resolution [144]. But this is still a decade more than the dimensions of actual devices. 2D mapping of actual devices is thus not possible with the current technology. The improvement of spatial resolution investigated in this study will thus be limited to the 1D dimension. The only parameter of importance for us in terms of spatial resolution is thus the depth resolution.

I. 5. a- Matrix effects

Definition

As seen previously, ‘matrix effects’ designate all effects related to the direct environment of an element or compound to analyse (during transients or due to in-situ material physical and chemical modification, due to varying matrix composition…) that influence ionisation probability of a particular element of compound and induce changes in

secondary ion yields as well as in sputter rates [37]. An example of RSFs obtained for several elements with different matrixes are displayed in Table I.ii.

Element	P	As	Ge	H	O	F	Mo
RSF (Si) $\times 10^{22}$	2.5	1	1.9	3	1.3	0.05	20
RSF (SiO_2) $\times 10^{22}$	0.052	0.036	0.19	0.03	0.02	0.005	1.3

Table I.ii. RSFs obtained in Si and SiO_2 matrixes with 1 keV Cs^+ sputter and observation of positive (M-Cs_2^+) secondary ions. Lower RSF means higher sensitivity.

In this case, the quantification of the same elements as impurities in bulk Si and in bulk oxidised matrix yields RSF variations of several decades. Experimentally, the variations are of the same range even when only the surface composition is modified (to a large extent), since most of the secondary ions come from the topmost layers. Also, RSFs are assumed to be constant over a wide concentration range from trace (ppm or ppb) to high concentrations (≤at%), but beyond this range they begin to significantly vary according to the change in matrix composition.

Consequences on analysis quality

As a direct consequence, elemental quantification of matrix elements is extremely difficult in most cases. Even in the case of very simple systems like binary alloys $Si_{1-x}Ge_x$, multiple well controlled reference samples are needed and quantification is not guaranteed over the whole concentration range. It will thus be extremely difficult to perform quantitative analysis on many of the materials of interest reviewed in the previous section. This restriction even extends to impurities (elements of concentration < at%) when quantitative profiling is required through heterogeneous matrix layers. For example, this is the case in ultra shallow implants where significant quantities of dopant are present both in the surface oxide and the Si substrate, or in HKMG samples in which La or Al diffuse through heterogeneous layers. Absence or insufficient consideration of these effects can lead to major errors. As an example, quantitative depth profiling of As through Si and SiO_2 with an RSF value only valid in Si would lead, at maximum, to a ×28 overestimation of the As content in SiO_2 (using Table I.ii values). A way to suppress or minimise matrix effects is thus required in order to yield accurate quantification in samples subject to these effects.

I. 5. b- Transient regimes

Definition

We define as transient regimes all the zones in a profile where sputter rate, ionisation probabilities or surface composition vary as a function of sputter time, in opposition to permanent regimes where all of these are stable. These mainly occur at interfaces (including the sample surface and bulk interfaces between heterogeneous materials) and their extent vary with the experimental conditions such as sputter beam energy and vacuum conditions, along with sample nature and properties (sharp or rough interfaces, reaction to oxidising environment, etc). For the energy range concerned by our study the transient regimes are often between less than a nanometer and a few nanometres.

Consequences on analysis quality

In these regimes, the ionisation probabilities vary in an uncontrolled manner, which once again precludes quantitative analysis via traditional means both for impurities and matrix elements. This particularly affects the analysis quality when quantification is needed at the near surface or around sharp interfaces, such as in ultrathin HKMG layer stacks. Furthermore they can have a significant impact on the overall analysis quality even in the permanent regime, since the interfacial variable sputter rate induces a shift on the depth scale which is reflected in the in-depth position of underlying structures. This shift will affect the profile in greater proportions if the total analysed depth is rather shallow, such as for USJs. Methods to take into account variations in both sputter rate and ionisation probabilities during the surface and interface transients is thus needed for quantitative analysis of such samples.

I. 5. c- Depth resolution

Definition

The depth resolution of an instrument is determined by observing the in-depth answer of the instrument to a stimulus constituted by a sharp structure such as an abrupt interface or a delta layer. For the simplest case of a delta layer in a homogeneous matrix, the transformation of the actual structure (close to a Dirac function) can be easily observed.

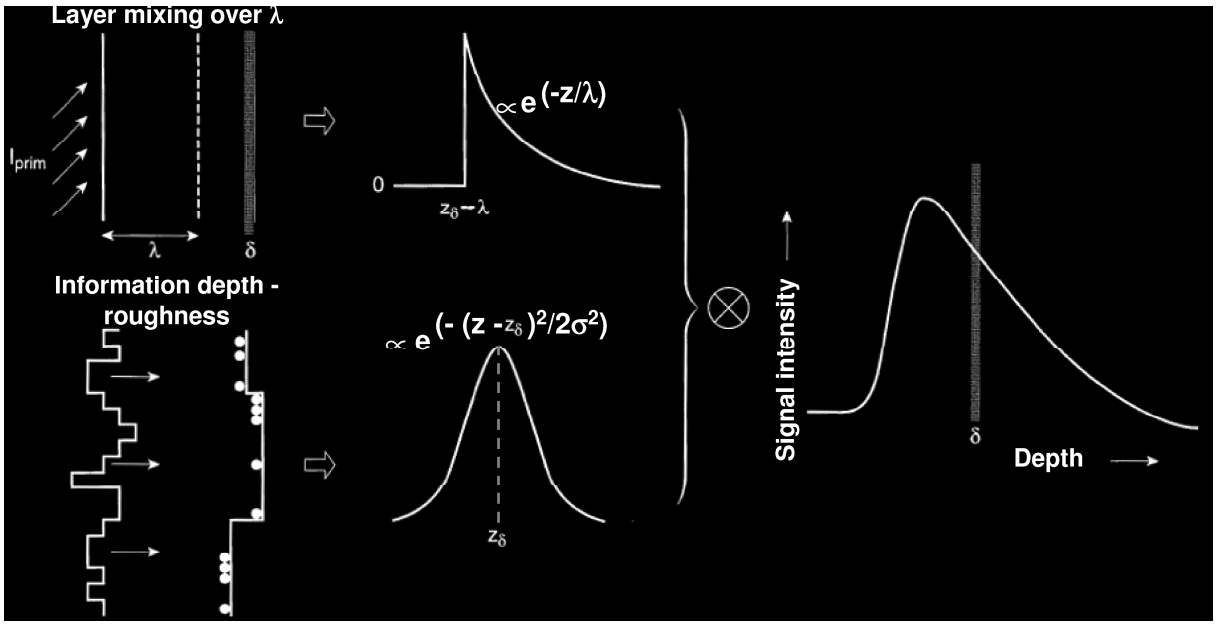

Figure I.16 Schematic representation of the ion beam mixing process explaining the shape of the instrument in-depth response to a Dirac-like stimulus. Complete and instantaneous relocation over a mixing depth λ causes a single-sided exponential redistribution. Original surface roughness and stochastic sputter process broaden the surface into a Gaussian. Adapted from [145].

Experimentally, we obtain a response as seen in the right part of Figure I.16. The characteristics of this response are a quick, Gaussian-like signal rise followed by a slower, exponential decay [146]. This is due to the combined effects of both sputtering and analysis beams induced phenomena, as schematised in Figure I.16. These can be de-convoluted in (i) a Gaussian contribution of Full Width Half Maximum (FWHM) σ due to original surface roughness and/or to roughness induced by the random nature of the sputtering process, which can be seen as the information depth of the instrument [145] and (ii) a single sided

exponential tail of decay parameter λ, which can be seen as the amount of layer mixing induced by the experimental setup [147]. The latter contribution is the dominant limitation to depth resolution, as it is reported to be at least two to three times more important than the Gaussian contribution in ideal conditions [145]. Outside ideal conditions, and particularly while sputtering with reactive elements such as oxygen, rapid roughness build-up can be observed [148]. On the other hand, when these phenomenon do not occur the contribution of depth of information to the depth resolution can be estimated to less than 0.5 nm in modern instruments. λ is also usually directly dependent on the sputter beam energy following a power law [145]. In our dual beam system, it will also depend of the analysis/sputter ratio which determines at fixed analysis and sputter beam conditions the amount of sputtering required to efficiently remove the damage (mixing) induced by the energetic analysis beam. It is thus mainly by adjusting experimental parameters such as primary beam energies to improve λ that one can improve the depth resolution. Different methods are available to measure experimental depth resolution, but widely accepted methods are the depth delta between two points for which peak intensity decays to 84% and 16% of its maximum value; and the depth delta between two points for which the signal intensity decays by a factor ten.

Consequences on analysis quality

A limited or insufficient depth resolution will hamper analysis quality in that it will preclude quantitative analysis of extremely fine structures such as monolayers, but also modify the shape of sharp features in a sample such as interfaces or concentration decays in ion implants. It affects all the different kind of structures investigated in this study, but more particularly those of critical dimensions such as nanometre thick HKMG stacks. Improvement of experimental parameters (sputter and analysis beam energy, sputter/analysis ratio, atmosphere) in view of obtaining optimised depth resolution is therefore required in each case.

I. 5. d- Physical and chemical modification of near surface layers during experiment

Definition

Ion beam analysis techniques all induce, by nature, damage and modification to the sample during the experiment. They are intrinsically destructive methods. With our instrument setup we can distinguish two kinds of modifications: (i) physical modification due exclusively to the different impacts occurring in the collision cascade and (ii) chemical modification due to the interaction of either atmosphere or primary ions with the sample. (i) corresponds in most of the cases to near surface layers mixing, as partly reviewed in the previous subsection (see also Figures I.7 and I.8) and to preferential sputtering phenomena as seen in subsection I. 3. c-). In some cases however, other effects due to physical impacts of the impinging ions on the target material modify the material well beyond the extent of mixing. This is often referred to as the knock-on phenomenon and occurs preferentially on atoms of a small size compared to the matrix material. These atoms will be implanted further in the material while they are impacted during the collision cascade [149]. (ii) covers all the effects induced by reactive elements either from atmosphere or primary ion beam on the near surface layer composition. These are multiple, the most obvious being the formation of an altered layer at the surface of the sample rich in active elements (either Cs, O or both) implying breaking of some of the original lattice bonds to form bonds with these elements. This layer alteration both directly modifies sputter rate along with ionisation yields because of the composition change and modifies ionisation yields through induced changes in surface

work function. Notice that layer alteration can also be performed on purpose to favour sensitivity to a particular element. Another effect potentially induced by this alteration is chemically induced segregation of given elements in reaction to the high concentration of active elements. This segregation can occur towards the surface (atoms tending to form bonds with active elements or with each other), such as for hafnium sputtered over a silicon rich matrix [150]. It can also occur towards bulk, such as for boron atoms sputtered with Cs^+ in a silicon matrix [151]. In either case, there is a profound modification the sample composition and nature well beyond the extent of mixing.

Consequences on analysis quality

It is quite clear that sample modification of layers deeper than depth of information during analysis will significantly affect the analysis quality. First, it will distort the elemental distribution inside the sample and thus yield erroneous profile shapes. Second, it will influence both sputter rate and ionisation yields in a dynamic way, reducing the validity of standard RSF quantification methods. These effects are also very difficult to counter balance: reducing sputter energy would decrease physical modification but in the same time increase chemically induced segregation effects (the surface concentration in active elements would increase, resulting in stronger segregation mechanisms). Their extent is also extremely difficult to evaluate, especially for chemical segregation. Specific sample preparation and/or measurement methods are thus needed.

I. 5. e- Depth and concentration scale calibration methods

ToF-SIMS is a semi-quantitative technique requiring reference materials and/or external calibration to yield quantitative analysis. Aside from the different difficulties reviewed in previous subsections, all directly dependent of the physics of the instrument and the experimental parameters, data treatment and calibration are therefore points which deserve focus. Resort to reference samples for concentration calibration is valid as soon as these are available. Since RSFs vary from an element to another in a given matrix and from a matrix to the other, one would have to possess any virtually possible (matrix + impurity) binary combination samples in order to be able to quantify any element in any kind of matrix. This of course is not practicable; but even if it was, one would still need an external, certified measure of the contents of each sample, which again is not feasible. Similarly, resort to external (measurement of crater depth by profilometry, etc) or internal methods (depth marker) for depth scale calibration is only valid as long as these are reliable and available. It thus limits their use to analysis of homogeneous, thick samples.
Furthermore, even in the ideal case of samples for which both certified reference materials and reliable depth calibration mean are available, calibration errors might still be introduced by the analyst during data treatment. Indeed, incorrect choice of the ion used to represent the matrix or impurity, insufficient background subtraction and underestimation of mass interferences are a few of the slight mistakes that could significantly hamper analysis quality by modifying profile shape and in-depth concentrations. In cases of doubt, or to verify the validity of a given data treatment protocol, externals means of control such as analysis of identical or similar samples with other characterisation techniques is thus required.

CHAPTER I Conclusion

In this chapter we reviewed the basics of dual beam ToF-SIMS, including performance, instrumentation and physics of the instrument. The standard features of the technique make it an interesting candidate for quantitative, depth resolved analysis of materials and structures for advanced microelectronic devices. We thus focus our study on a few of those, selected for their interest in terms of potential improvement of device properties or as break-through technologies. Notably SiGe based heterostructures, HKMG based ultra thin stacks, ultra shallow ion implants in silicon and organic materials were adopted. However different phenomena, directly related to the nature of the ToF-SIMS technique (ion beam sputtering, analysis of secondary ions) have effects that severely hamper its capacity to yield high quality analysis on such samples. If each of the phenomena are quite well known and thoroughly described in literature, their interaction and convolution during analysis of real samples increases the difficulty to yield precise and depth resolved quantitative analysis. We will develop in the next chapter the different solutions developed during this thesis work to subtract from or minimise unwanted effects and yield the best possible analysis.

REFERENCES

[1] W. Shockley, J. Bardeen and W.H. Brattain, *The Electronic Theory of the Transistor*, Science, 108 (**1948**) 678-679.
[2] J. Bardeen and W.H. Brattain, *The Transistor, a Semi-Conductor Triode*, Physical Review, 74 (**1948**) 230-231.
[3] F.M. Wanlass, U.S. Patent n° 3,356,858, **1967**.
[4] G.E. Moore, *Cramming More Components onto Integrated Circuits*, Electronics, 38 (**1965**) 114-117.
[5] G.E. Moore, *Progress in Digital Integrated Electronics,* International Electron Devices Meeting, 21 (**1975**) 11-13.
[6] H. Wong and H. Iwai, *On the Scaling Issues and High-[Kappa] Replacement of Ultrathin Gate Dielectrics for Nanoscale Mos Transistors*, Microelectron. Eng., 83 (**2006**) 1867-1904.
[7] International Technology Roadmap for Semiconductors: executive summary, (**2009**), http://www.itrs.net/Links/2010ITRS/Home2010.htm
[8] V. Fan, D. Harman, J. Jewett, J. Leet and D. Speranza, *Evaluation Process for Semiconductor Fabrication Materials That Are Better for the Environment*, Intel Technology Journal, (**February 2008**).
[9] J.J. Thomson, Philos. Mag. A, 20 (**1910**) 752.
[10] F.L. Arnot and J.C. Milligan, *A New Process of Negative Ion Formation*, Proceedings of the Royal Society of London. Series A - Mathematical and Physical Sciences, 156 (**1936**) 538-560.
[11] R.F.K. Herzog and F.P. Viehboeck, *Ion Source for Mass Spectrography*, Physical Review, 76 (**1949**) 855.
[12] R. Castaing and G. Slodzian, *Optique Corpusculaire - Premiers Essais De Microanalyse Par Emission Ionique Secondaire*, Comptes Rendus Hebdomadaires Des Seances De L Academie Des Sciences, 255 (**1962**) 1893-&.
[13] A. Benninghoven and F. Kirchner, *Uber Die Energieverteilung Neutraler Und Geladener Zerstaubungsprodukte*, Zeitschrift Fur Naturforschung Part a-Astrophysik Physik Und Physikalische Chemie, A 18 (**1963**) 1008-&.
[14] H. Liebl, *Ion Microprobe Mass Analyzer*, J. Appl. Phys., 38 (**1967**) 5277-5283.
[15] R.F.K. Herzog, W.P. Poschenrieder and F.G. Satkiewicz, **1967**.
[16] H.E. Beske, *Positive Sekundarionenausbeute Von 21 Elementen*, Zeitschrift Fur Naturforschung Part a-Astrophysik Physik Und Physikalische Chemie, A 19 (**1964**) 1627-&.
[17] H.W. Werner, *Developments in Applied Spectroscopy*, Plenum Press, New York, **1969**.
[18] H.W. Werner, *Theoretical and Experimental Aspects of Secondary Ion Mass Spectrometry*, Vacuum, 24 (**1974**) 493-504.
[19] A. Benninghoven, *Observing Surface Oxidation of Molybdenum with the Statical Method of Secondary Ion Mass Spectroscopy*, Chem. Phys. Lett., 6 (**1970**) 626-628.
[20] A. Benninghoven, *The Analysis of Monomolecular Layers of Solids by Secondary Ion Emission*, Die Analyse monomolekularer FestkörperoberflÄchenschichten mit Hilfe der SekundÄrionenemission, 230 (**1970**) 403-417.
[21] B.T. Chait and K.G. Standing, *A Time-of-Flight Mass Spectrometer for Measurement of Secondary Ion Mass Spectra*, International Journal of Mass Spectrometry and Ion Physics, 40 (**1981**) 185-193.
[22] P. Steffens, E. Niehuis, T. Friese, D. Greifendorf and A. Benninghoven, *A Time-of-Flight Mass Spectrometer for Static Sims Applications*, J. Vac. Sci. Technol. A, 3 (**1985**) 1322-1325.
[23] H.W. Werner and A. Torrisi, *Interface and Thin Film Analysis: Comparison of Methods, Trends*, Fresenius. J. Anal. Chem., 337 (**1990**) 594-613.
[24] J.R. Bacon, K.L. Linge and L. Van Vaeck, *Atomic Spectrometry Update. Atomic Mass Spectrometry*, J. Anal. At. Spectrom., 20 (**2005**) 763-802.
[25] J.R. Bacon, K.L. Linge, R.R. Parrish and L. Van Vaeck, *Atomic Spectrometry Update. Atomic Mass Spectrometry*, J. Anal. At. Spectrom., 23 (**2008**) 1130-1162.
[26] Y. Yaegashi and K. Inaguma, *Analysis of Semiconductors by Means of Ion Microanalyzer*, Natl Tech Rep Matsushita Electr Ind, 23 (**1977**) 116-125.

[27] P. Williams and J.C.A. Evans, *Depth Profile Detection Limit of 3 X 10^{15} Atom.Cm^{-3} for as in Si Using Cs+ Bombardment Negative Secondary Ion Mass Spectrometry*, Appl. Phys. Lett., 30 (**1977**) 559-561.
[28] S. Taya, M. Suzuki, H. Tsuyama and I. Kanomata, *Analyses of Silicon Wafers by a High-Resolution Secondary Ion Mass Spectrometer*, International Journal of Mass Spectrometry and Ion Physics, 27 (**1978**) 63-76.
[29] J.C. Vickerman and D. Briggs, *Tof-Sims – Surface Analysis by Mass Spectrometry*, SurfaceSpectra Ltd, **2001**.
[30] A. Benninghoven, *Static Sims Applications---from Silicon Single Crystal Oxidation to DNA Sequencing*, J. Vac. Sci. Technol. A, 3 (**1985**) 451-460.
[31] M.L. Pacholski and N. Winograd, *Imaging with Mass Spectrometry*, Chem. Rev. (Washington, DC, U. S.), 99 (**1999**) 2977-3006.
[32] L.W. Swanson, *Liquid Metal Ion Sources: Mechanism and Applications*, Nuclear Instruments and Methods in Physics Research, 218 (**1983**) 347-353.
[33] D. Briggs and M.P. Seah, *Practical Surface Analysis*, John Wiley & Sons, **1996**.
[34] S.G. Alikhanov, *A New Impulse Technique for Ion Mass Measurement*, Sov. Phys. JETP Letters (Translation of Pis'ma v Zhurnal Eksperimental'noi i Teoreticheskoi Fiziki), 4 (**1957**) 452.
[35] E. Niehuis, T. Heller, H. Feld and A. Benninghoven, *Design and Performance of a Reflectron Based Time-of-Flight Secondary Ion Mass Spectrometer with Electrodynamic Primary Ion Mass Separation*, J. Vac. Sci. Technol. A, 5 (**1987**) 1243-1246.
[36] X. Tang, R. Beavis, W. Ens *et al.*, *A Secondary Ion Time-of-Flight Mass Spectrometer with an Ion Mirror*, Int. J. Mass Spectrom. Ion Processes, 85 (**1988**) 43-67.
[37] A. Benninghoven, F.G. Rudenauer and H.W. Werner, *Secondary Ion Mass Spectrometry: Basic Concepts, Instrumental Aspects, Applications, and Trends*, Wiley, New York, **1987**.
[38] S. Hofmann, *Compositional Depth Profiling by Sputtering*, Prog. Surf. Sci., 36 (**1991**) 35-87.
[39] P.C. Zalm, *Ultra Shallow Doping Profiling with Sims*, Reports on Progress in Physics, 58 (**1995**) 1321.
[40] S. Hofmann, *Sputter Depth Profile Analysis of Interfaces*, Reports on Progress in Physics, 61 (**1998**) 827.
[41] T. Grehl, *Thesis Work: Improvements in Tof-Sims Instrumentation for Analytical Application and Fundamental Research*, University of Münster (**2003**).
[42] P. Williams, *The Sputtering Process and Sputtered Ion Emission*, Surf. Sci., 90 (**1979**) 588-634.
[43] K. Wittmaack, *Aspects of Quantitative Secondary Ion Mass Spectrometry*, Nuclear Instruments and Methods, 168 (**1980**) 343-356.
[44] S.P. Smith, V.K.F. Chia, C.J. Hitzman and G. Mount, *A Review of Sims Techniques for Characterization of Ultra Low Energy Ion Implants,* Ion Implantation Technology. Proceedings of the 11th International Conference on, (**1996**) 599-602.
[45] R. Behrisch and K. Wittmaack, *Sputtering by Particle Bombardment Iii*, Springer-Verlag, Berlin, **1991**.
[46] P.C. Zalm, *Some Useful Yield Estimates for Ion Beam Sputtering and Ion Plating at Low Bombarding Energies*, J. Vac. Sci. Technol. B, 2 (**1984**) 151-152.
[47] N.A. Kubota, D.J. Economou and S.J. Plimpton, *Molecular Dynamics Simulations of Low-Energy (25--200 Ev) Argon Ion Interactions with Silicon Surfaces: Sputter Yields and Product Formation Pathways*, J. Appl. Phys., 83 (**1998**) 4055-4063.
[48] V.S. Smentkowski, *Trends in Sputtering*, Prog. Surf. Sci., 64 (**2000**) 1-58.
[49] A. Benninghoven, *Surface Investigation of Solids by the Statical Method of Secondary Ion Mass Spectroscopy (Sims)*, Surf. Sci., 35 (**1973**) 427-457.
[50] G. Betz, R. Dobrozemsky and F.P. Viehböck, Ned. Tijdschr. Vacuum Tech., 8 (**1970**) 203.
[51] H. Gnaser, *Low-Energy Ion Irradiation of Solid Surfaces*, Springer-Verlag, Berlin, **1999**.
[52] P. Sigmund, *Theory of Sputtering. I. Sputtering Yield of Amorphous and Polycrystalline Targets*, Physical Review, 184 (**1969**) 383.
[53] G. Falcone, *Theory of Collisional Sputtering*, Surf. Sci., 187 (**1987**) 212-222.
[54] P. Sigmund and C. Claussen, *Sputtering from Elastic-Collision Spikes in Heavy-Ion-Bombarded Metals*, J. Appl. Phys., 52 (**1981**) 990-993.

[55] H.H. Andersen and H.L. Bay, *Nonlinear Effects in Heavy-Ion Sputtering*, J. Appl. Phys., 45 (**1974**) 953-954.
[56] H.H. Andersen and H.L. Bay, *Heavy-Ion Sputtering Yields of Gold: Further Evidence of Nonlinear Effects*, J. Appl. Phys., 46 (**1975**) 2416-2422.
[57] J. Samela and K. Nordlund, *Emergence of Non-Linear Effects in Nanocluster Collision Cascades in Amorphous Silicon*, New Journal of Physics, 10 (**2008**) 023013.
[58] D.A. Thompson and S.S. Johar, *Nonlinear Sputtering Effects in Thin Metal Films*, Appl. Phys. Lett., 34 (**1979**) 342-345.
[59] S.S. Johar and D.A. Thompson, *Spike Effects in Heavy-Ion Sputtering of Ag, Au and Pt Thin Films*, Surf. Sci., 90 (**1979**) 319-330.
[60] A. Brunelle, S. Della-Negra, J. Depauw *et al.*, *Enhanced Secondary-Ion Emission under Gold-Cluster Bombardment with Energies from Kev to Mev Per Atom*, Phys. Rev. A, 63 (**2001**) 022902.
[61] A.V. Samartsev, A. Duvenbeck and A. Wucher, *Sputtering of Indium Using Au{M} Projectiles: Transition from Linear Cascade to Spike Regime*, Physical Review B, 72 (**2005**) 115417.
[62] G.K. Wehner, *Sputtering Yields for Normally Incident Hg+ Ion Bombardment at Low Ion Energy*, Physical Review, 108 (**1957**) 35.
[63] R.V. Stuart and G.K. Wehner, *Sputtering Yields at Very Low Bombarding Ion Energies*, J. Appl. Phys., 33 (**1962**) 2345-2352.
[64] Y. Yamamura and H. Tawara, *Energy Dependence of Ion-Induced Sputtering Yields from Monatomic Solids at Normal Incidence*, Atomic Data and Nuclear Data Tables, 62 (**1996**) 149-253.
[65] A. Oliva-Florio, R.A. Baragiola, M.M. Jakas *et al.*, *Noble-Gas Ion Sputtering Yield of Gold and Copper: Dependence on the Energy and Angle of Incidence of the Projectiles*, Physical Review B, 35 (**1987**) 2198.
[66] N. Laegreid and G.K. Wehner, *Sputtering Yields of Metals for Ar+ and Ne+ Ions with Energies from 50 to 600 Ev*, J. Appl. Phys., 32 (**1961**) 365-369.
[67] H. Gnaser, *Processes in Low-Energy Ion-Surface Collisions: Preferential Sputtering, Defect and Adatom Formation*, Appl. Surf. Sci., 100-101 (**1996**) 316-328.
[68] C. Verdeil, *Thesis Work: Etude De La Pulvérisation Et De L'émission De Matière Sous Bombardement Cs+*, Institut National Polytechnique de Lorraine (**2008**).
[69] B. Berghmans, B. Van Daele, L. Geenen *et al.*, *Cesium near-Surface Concentration in Low Energy, Negative Mode Dynamic Sims*, Appl. Surf. Sci., 255 (**2008**) 1316-1319.
[70] M.L. Yu and N.D. Lang, *Mechanisms of Atomic Ion Emission During Sputtering*, Nucl. Instrum. Meth. B, 14 (**1986**) 403-413.
[71] M.L. Yu and N.D. Lang, *Direct Evidence of Electron Tunneling in the Ionization of Sputtered Atoms*, Phys. Rev. Lett., 50 (**1983**) 127.
[72] G. Slodzian, *Some Problems Encountered in Secondary Ion Emission Applied to Elementary Analysis*, Surf. Sci., 48 (**1975**) 161-186.
[73] J.E. Ortega, E.M. Oellig, Ferr *et al.*, *Cs and O Adsorption on Si(100) 2x1: A Model System for Promoted Oxidation of Semiconductors*, Physical Review B, 36 (**1987**) 6213.
[74] M. Gavelle, E. Scheid, F. Cristiano *et al.*, *Detection of Cs2ge+ Clusters for the Quantification of Germanium Atoms by Secondary Ion Mass Spectrometry: Application to the Characterization of Si1-Xgex Layers (0 <= X <= 1) and Germanium Diffusion in Silicon*, J. Appl. Phys., 102 (**2007**).
[75] P. Holliger, F. Laugier and J.C. Dupuy, *Sims Depth Profiling of Ultrashallow P, Ge and as Implants in Si Using Mcs2+ Ions*, Surf. Interface Anal., 34 (**2002**) 472-476.
[76] D. Marseilhan, J.P. Barnes, F. Fillot, J.M. Hartmann and P. Holliger, *Quantification of Sige Layer Composition Using Mcs+ and Mcs2+ Secondary Ions in Tof-Sims and Magnetic Sims*, Appl. Surf. Sci., 255 (**2008**) 1412-1414.
[77] K. Wittmaack, *Concentration–Depth Calibration and Bombardment-Induced Impurity Relocation in Sims Depth Profiling of Shallow through-Oxide Implantation Distributions: A Procedure for Eliminating the Matrix Effect*, Surf. Interface Anal., 26 (**1998**) 290-305.
[78] H.D. Witte, *Thesis Work: Fundamental Study of Ion-Substrate Interactions with Low Energy Reactive Ions*, Antwerp Univ. (**2001**).
[79] J.P. Dismukes, L. Ekstrom and R.J. Paff, *Lattice Parameter and Density in Germanium-Silicon Alloys*, J. Phys. Chem., 68 (**1964**) 3021-3027.

[80] R. Braunstein, A.R. Moore and F. Herman, *Intrinsic Optical Absorption in Germanium-Silicon Alloys*, Physical Review, 109 (**1958**) 695.
[81] E.E. Haller, *Germanium: From Its Discovery to Sige Devices*, Mater. Sci. Semicond. Process., 9 (**2006**) 408-422.
[82] E. Kasper, *Sige Alloys and Heterojunctions - Extending the Performance of Si Devices*, Current Opinion in Solid State and Materials Science, 2 (**1997**) 48-53.
[83] Y.-S. Chieh, J.P. Krusius, D. Green and M. Ozturk, *Low-Resistance Bandgap-Engineered W/Si1-Xgex/Si Contacts*, Electron Device Letters, IEEE, 17 (**1996**) 360-362.
[84] S.S. Iyer, *Molecular Beam Epitaxy of Silicon-Germanium Alloys,* Elsevier, Oxford, **2001**, pp. 5802-5806.
[85] J.L. Hoyt, H.M. Nayfeh, S. Eguchi *et al.*, *Strained Silicon Mosfet Technology,* Electron Devices Meeting, 2002. IEDM '02. Digest. International (**2002**) 23-26.
[86] M.L. Lee, E.A. Fitzgerald, M.T. Bulsara, M.T. Currie and A. Lochtefeld, *Strained Si, Sige, and Ge Channels for High-Mobility Metal-Oxide-Semiconductor Field-Effect Transistors*, J. Appl. Phys., 97 (**2005**) 011101-011128.
[87] G. Abstreiter, H. Brugger, T. Wolf, H. Jorke and H.J. Herzog, *Strain-Induced Two-Dimensional Electron Gas in Selectively Doped Si/Si_{X}Ge_{1-X} Superlattices*, Phys. Rev. Lett., 54 (**1985**) 2441.
[88] B.M. Haugerud, L.A. Bosworth and R.E. Belford, *Mechanically Induced Strain Enhancement of Metal--Oxide--Semiconductor Field Effect Transistors*, J. Appl. Phys., 94 (**2003**) 4102-4107.
[89] E. Bernard, T. Ernst, B. Guillaumot *et al.*, *Impact of the Gate Stack on the Electrical Performances of 3d Multi-Channel Mosfet (Mcfet) on Soi*, Solid-State Electron., 52 (**2008**) 1297-1302.
[90] C. Dupré, T. Ernst, V. Maffini-Alvaro *et al.*, *3d Nanowire Gate-All-around Transistors: Specific Integration and Electrical Features*, Solid-State Electron., 52 (**2008**) 519-525.
[91] E. Bernard, T. Ernst, B. Guillaumot *et al.*, *Novel Integration Process and Performances Analysis of Low Standby Power (Lstp) 3d Multi-Channel Cmosfet (Mcfet) on Soi with Metal / High-K Gate Stack,* VLSI Technology, 2008 Symposium on, (**2008**) 16-17.
[92] T. Ernst, L. Duraffourg, C. Dupre *et al.*, *Novel Si-Based Nanowire Devices: Will They Serve Ultimate Mosfets Scaling or Ultimate Hybrid Integration?,* Electron Devices Meeting, 2008. IEDM 2008. IEEE International, (**2008**) 1-4.
[93] E. Saracco, J.-F. Damlencourt, D. Lafond *et al.*, *Fabrication of Suspended Ge-Rich Nanowires by Ge Enrichment Technique for Multi-Channel Devices*, ECS Trans., 19 (**2009**) 207-212.
[94] K. Tachi, M. Casse, D. Jang *et al.*, *Relationship between Mobility and High-K Interface Properties in Advanced Si and Sige Nanowires,* Electron Devices Meeting (IEDM), 2009 IEEE International, (**2009**) 1-4.
[95] T. Tezuka, N. Sugiyama, T. Mizuno, M. Suzuki and S.I. Takagi, *A Novel Fabrication Technique of Ultrathin and Relaxed Sige Buffer Layers with High Ge Fraction for Sub-100 Nm Strained Silicon-on-Insulator Mosfets*, Jpn. J. Appl. Phys., 40 (**2001**) 2866-2874.
[96] J.F. Damlencourt, Patent N°EP1892766, **2006**.
[97] K. Ikeda, M. Oda, Y. Kamimuta, Y. Moriyama and T. Tezuka, *Hole-Mobility and Drive-Current Enhancement in Ge-Rich Strained Silicon–Germanium Wire Tri-Gate Metal–Oxide–Semiconductor Field-Effect Transistors with Nickel-Germanosilicide Metal Source and Drain*, Appl. Phys. Express, 3 (**2010**) 124201.
[98] Y. Taur and E.J. Nowak, International Electron Device Meeting proceedings, (**1997**) 215-218.
[99] T. Nguyen, *Thesis Work: Caractérisation, Modélisation Et Fiabilité Des Diélectriques De Grille À Base De Hfo2 Pour Les Futures Technologies Cmos*, INSA Lyon (**2009**).
[100] R. Katamreddy, R. Inman, G. Jursich, A. Soulet and C. Takoudis, *Nitridation and Oxynitridation of Si to Control Interfacial Reaction with Hfo2*, Thin Solid Films, 516 (**2008**) 8498-8506.
[101] G.D. Wilk, R.M. Wallace and J.M. Anthony, *High-Kappa Gate Dielectrics: Current Status and Materials Properties Considerations*, J. Appl. Phys., 89 (**2001**) 5243-5275.
[102] M. Houssa, L. Pantisano, L.Å. Ragnarsson *et al.*, *Electrical Properties of High-[Kappa] Gate Dielectrics: Challenges, Current Issues, and Possible Solutions*, Materials Science and Engineering: R: Reports, 51 (**2006**) 37-85.
[103] H. Wong, Integrated Circuits and Solid-State Technol., (**2004**) 378.

[104] G. He, L. Zhu, Z. Sun, Q. Wan and L. Zhang, *Integrations and Challenges of Novel High-K Gate Stacks in Advanced Cmos Technology*, Progress in Materials Science, 56 (**2011**) 475-572.
[105] C. Hobbs, L. Fonseca, V. Dhandapani *et al.*, *Fermi Level Pinning at the Poly-Si/Oxide Interface,* VLSI Technology Digest, (**2003**) 9-10.
[106] C. Hobbs, L.R.C. Fonseca, A. Knizhnik *et al.*, *Fermi-Level Pinning at the Polysilicon/Metal-Oxide Interface-Part Ii,* Electron Devices, IEEE Transactions on, 51 (**2004**) 978-984.
[107] J.Y.-C.S. C. Y. Wong, Y. Taur, C. S. Oh, R. Angelucci, and B. Davari, *Doping of N+ and P+ Polysilicon in a Dual-Gate Cmos Process,* International Electron Devices Meeting, (**2003**).
[108] J.C. Hu, H. Yang, R. Kraft *et al.*, *Feasibility of Using W/Tin as Metal Gate for Conventional 0.13μm Cmos Technology and Beyond,* International Electron Devices Meeting, (**1997**) 825-828.
[109] D. Aime, *Modulation Du Travail De Sortie De Grilles Métalliques Totalement Siliciurées Pour Des Dispositifs Cmos Déca-Nanométriques*, INSA Lyon (**2007**).
[110] O. Weber, *Thesis Work: Etude, Fabrication Et Propriétés De Transport De Transistors Cmos Associant Un Diélectrique De Grille Haute Permittivité Et Un Canal De Conduction Haute Mobilité*, INSA Lyon (**2005**).
[111] Y. Song, H. Zhou and Q. Xu, *Source/Drain Technologies for the Scaling of Nanoscale Cmos Device*, Solid State Sci., 13 (**2011**) 294-305.
[112] R. Huang, H. Wu, J. Kang *et al.*, *Challenges of 22 Nm and Beyond Cmos Technology*, Science in China Series F: Information Sciences, 52 (**2009**) 1491-1533.
[113] E. Chason, S.T. Picraux, J.M. Poate *et al.*, *Ion Beams in Silicon Processing and Characterization*, J. Appl. Phys., 81 (**1997**) 6513-6561.
[114] K. Uejima, K. Yako, N. Ikarashi *et al.*, *Pushing Planar Bulk Cmosfet Scaling to Its Limit by Ultimately Shallow Diffusion-Less Junction,* Electron Devices Meeting, 2007. IEDM 2007. IEEE International, (**2007**) 151-154.
[115] Y. Sasaki, K. Okashita, K. Nakamoto *et al.*, *Conformal Doping for Finfets and Precise Controllable Shallow Doping for Planar Fet Manufacturing by a Novel B2h6 Helium Self-Regulatory Plasma Doping Process,* Electron Devices Meeting, 2008. IEDM 2008. IEEE International, (**2008**) 1-4.
[116] J. Nishizawa, K. Aoki and T. Akamine, *Ultrashallow, High Doping of Boron Using Molecular Layer Doping*, Appl. Phys. Lett., 56 (**1990**) 1334-1335.
[117] J.C. Ho, R. Yerushalmi, G. Smith *et al.*, *Wafer-Scale, Sub-5 Nm Junction Formation by Monolayer Doping and Conventional Spike Annealing*, Nano Lett., 9 (**2009**) 725-730.
[118] A. Anders, *Handbook of Plasma Immersion Ion Implantation and Deposition*, John Wiley & Sons, New-York, **2000**.
[119] J. Pelletier and A. Anders, *Plasma-Based Ion Implantation and Deposition: A Review of Physics, Technology, and Applications*, Plasma Science, IEEE Transactions on, 33 (**2005**) 1944-1959.
[120] L.L. Chapelon, V. Arnal, M. Broekaart *et al.*, *Characterization and Integration of a Cvd Porous Sioch (K < 2.5) with Enhanced Mechanical Properties for 65 Nm Cmos Interconnects and Below*, Microelectron. Eng., 76 (**2004**) 1-7.
[121] O. Madelung, *Intrinsic Properties of Group Iv Elements and Iii-V, Ii-Vi, and Iv Compounds*, Springer-Verlag, Berlin, **1987**.
[122] S. Takagi, T. Iisawa, T. Tezuka *et al.*, *Carrier-Transport-Enhanced Channel Cmos for Improved Power Consumption and Performance*, Electron Devices, IEEE Transactions on 55 (**2008**) 21-39.
[123] C. Henkel, S. Abermann, O. Bethge *et al.*, *Ge P-Mosfets with Scaled Ald Zro2 Gate Dielectrics*, Electron Devices, IEEE Transactions on, 57 (**2010**) 3295-3302.
[124] Y. Kamata, *High-K/Ge Mosfets for Future Nanoelectronics*, Materials Today, 11 30-38.
[125] M. Heyns and W. Tsai, *Ultimate Scaling of Cmos Logic Devices with Ge and Iii-V Materials*, MRS Bull., 34 (**2009**) 485-492.
[126] H. Ko, K. Takei, R. Kapadia *et al.*, *Ultrathin Compound Semiconductor on Insulator Layers for High-Performance Nanoscale Transistors*, Nature, 468 (**2010**) 286-289.
[127] S. Oktyabrsky and P.D.Y. (Eds.), *Fundamentals of Iii-V Semiconductor Mosfets*, Springer, New York, **2010**.
[128] M. Radosavljevic, B. Chu-Kung, S. Corcoran *et al.*, *Advanced High-K Gate Dielectric for High-Performance Short-Channel In0.7ga0.3as Quantum Well Field Effect Transistors on Silicon Substrate for Low Power Logic Applications,* Electron Devices Meeting (IEDM), 2009 IEEE International, (**2009**) 1-4.

[129] R.H. Friend, R.W. Gymer, A.B. Holmes *et al.*, *Electroluminescence in Conjugated Polymers*, Nature, 397 (**1999**) 121-128.
[130] Y. Hino, M. Yamazaki, H. Kajii and Y. Ohmori, *Fabrication and Characteristics of Increased Efficiency of Layered Polymeric Electroluminescent Diodes*, Jpn. J. Appl. Phys. Part 1 - Regul. Pap. Short Notes Rev. Pap., 43 (**2004**) 2315-2319.
[131] S. Kirchmeyer and K. Reuter, *Scientific Importance, Properties and Growing Applications of Poly(3,4-Ethylenedioxythiophene)*, J. Mater. Chem., 15 (**2005**) 2077-2088.
[132] M. Pope, H.P. Kallmann and P. Magnante, *Electroluminescence in Organic Crystals*, The Journal of Chemical Physics, 38 (**1963**) 2042-2043.
[133] W. Helfrich and W.G. Schneider, *Recombination Radiation in Anthracene Crystals*, Phys. Rev. Lett., 14 (**1965**) 229.
[134] C.K. Chiang, C.R. Fincher, Y.W. Park *et al.*, *Electrical Conductivity in Doped Polyacetylene*, Phys. Rev. Lett., 39 (**1977**) 1098.
[135] H. Jin, Y.B. Hou, F. Teng *et al.*, *Effect of Molecular Aggregation by Thermal Treatment on Photovoltaic Properties of Meh-Ppv: Fullerene-Based Solar Cells*, Sol. Energy Mater. Sol. Cells, 93 (**2009**) 289-294.
[136] S. Baek, D. Lee, J. Kim *et al.*, *Novel Digital Nonvolatile Memory Devices Based on Semiconducting Polymer Thin Films*, Adv. Funct. Mater., 17 (**2007**) 2637-2644.
[137] H.J. Kim, J.H. Jung, J.H. Ham and T.W. Kim, *Effect of Fullerene Concentration on Flat-Band Voltage Shift of Capacitance-Voltage Curve in Organic Memory Devices Fabricated Using Hybrid Poly(4-Vinyl Phenol) Active Layer Containing Fullerene*, Japanese Journal of Applied Physics, 47 (**2008**) 5083-5085.
[138] S. Paul, *Realization of Nonvolatile Memory Devices Using Small Organic Molecules and Polymer*, Nanotechnology, IEEE Transactions on, 6 (**2007**) 191-195.
[139] Q.-D. Ling, D.-J. Liaw, C. Zhu *et al.*, *Polymer Electronic Memories: Materials, Devices and Mechanisms*, Prog. Polym. Sci., 33 (**2008**) 917-978.
[140] H.S. Majumdar, J.K. Baral, R. Österbacka, O. Ikkala and H. Stubb, *Fullerene-Based Bistable Devices and Associated Negative Differential Resistance Effect*, Organic Electronics, 6 (**2005**) 188-192.
[141] N. Duhayon, P. Eyber, M. Fouchier *et al.*, *Assessing the Performance of Two-Dimensional Dopant Profiling Techniques*, Journal of Vacuum Science & Technology B, 22 (**2004**) 385-393.
[142] P. Eyben, T. Janssens and W. Vandervorst, *Scanning Spreading Resistance Microscopy (Ssrm) 2d Carrier Profiling for Ultra-Shallow Junction Characterization in Deep-Submicron Technologies*, Materials Science and Engineering: B, 124-125 (**2005**) 45-53.
[143] M.J. Brukman and D.A. Bonnell, *Probing Physical Properties at the Nanoscale*, Physics Today, 61 (**2008**) 36-42.
[144] *Ion Tof Gmbh, Presentation at Ion Tof User's Meeting (Unpublished Work)*, **2010**.
[145] P.C. Zalm, *Dynamic Sims: Quantification at All Depths?*, Microchim. Acta, 132 (**2000**) 243-257.
[146] S. Hofmann, *Cascade Mixing Limitations in Sputter Profiling*, J. Vac. Sci. Technol. B, 10 (**1992**) 316-322.
[147] Z.L. Liau, B.Y. Tsaur and J.W. Mauer, *Influence of Atomic Mixing and Preferential Sputtering on Depth Profiles and Interfaces*, Journal of Vacuum Science and Technology, 16 (**1979**) 121-127.
[148] B. Fares, B. Gautier, P. Holliger *et al.*, *Surface Roughening and Erosion Rate Change at Low Energy Sims Depth Profiling of Silicon During Oblique O2+ Bombardment*, Appl. Surf. Sci., 253 (**2006**) 2662-2670.
[149] S. Hofmann, *Depth Resolution in Sputter Profiling*, Applied Physics A: Materials Science & Processing, 13 (**1977**) 205-207.
[150] W. Vandervorst, J. Bennett, C. Huyghebaert *et al.*, *On the Reliability of Sims Depth Profiles through Hfo2-Stacks*, Appl. Surf. Sci., 231-232 (**2004**) 569-573.
[151] R. Wilson, F. Stevie and C. Magee, *Secondary Ion Mass Spectrometry*, John Wiley, Sons, New York, **1989**.

CHAPTER II
Solutions explored to answer ToF-SIMS characterisation needs

In this chapter we will exhaustively review the solutions envisaged in this study to improve analysis quality provided by our ToF-SIMS instrument in terms of depth resolution, quantitativity and reliability. We will particularly focus on the reasons of these choices from a theoretical point of view, highlighting physical or chemical phenomena which induce potential beneficial effects on analysis quality. The practical setup of the solutions reviewed here will be examined case by case in the following chapters. We have classified the different solutions in their logical chronologic order from the point of view of the experimenter: from sample preparation to experimental conditions, data treatment and finally to comparison with complementary techniques. Thus it does thus not necessarily reflect the importance of each solution in this study.

II. 1. Sample preparation

This option is often disregarded or neglected in SIMS or ToF-SIMS since usually, no sample preparation is required for standard applications; any UHV compatible sample being a potential candidate for analysis without prior preparation. In the case of samples sensitive to contamination or oxidation for example, minimising the time between sample production and introduction into the analysis chamber under vacuum is often sufficient to ensure high quality analysis. However, in particular cases sample preparation can minimize surface / interface artefacts or simply attain structures of interest and enable their analysis.

II. 1. a- Surface cleaning

For extreme surface analysis or for samples requiring precise analysis of the topmost layers, surface contamination may need to be removed. The latter can be organic, inorganic or even both. It can be removed by several methods, such as low temperature desorption annealing, ultrasonic treatment in various solutions, plasma irradiation or even direct sputtering with a primary ion beam with a sufficient dose.

Expected improvements

The main detrimental effect of surface organic contamination is the increased risk of mass interferences. Unlike inorganic materials, the fragmentation of these soft materials (mainly polymers and small molecules) upon primary ion irradiation yields a large variety of intense secondary ions, constituted of mainly carbon, hydrogen and oxygen. This allows for massive coverage of any mass range corresponding to a possible combination of those elements. It might therefore interfere with a secondary ion of interest in the first moments of an analysis (e.g. $CO^{-/+}$ m = 27.9949 u and $^{28}Si^{-/+}$ m = 27.9769 u, even though in this case sufficient mass resolution should allow resolution of the two peaks). It also brings numerous unknown compound secondary ions, which increases the difficulty of data interpretation by yielding complex mass spectra. Similar effects can be expected in the case of inorganic contamination but to a lesser extent, since only slight fragmentation is foreseen. Inorganic contamination is also easier to identify, particularly with ToF-SIMS which allows parallel observation of large mass ranges.
Surface contamination can also produce effects much deeper than the topmost layers when incriminated elements or compounds tend to be implanted upon ion beam irradiation. In this

case, contamination induced detrimental effects can extend to part of or all of the profile. This is more likely to happen for inorganic contamination, as for example when islands of Ge oxide are present at the surface of a Ge substrate, as illustrated in Figure II.1.

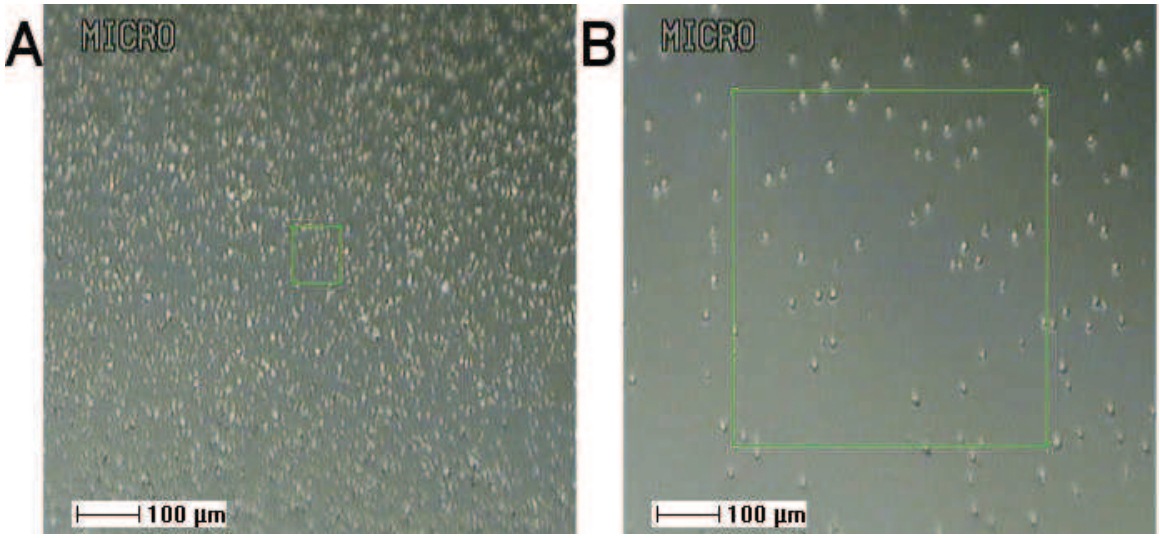

Figure II.1 Surface state of B or P implants in bulk germanium after sub-melt laser annealing in standard atmosphere observed in the instrument analysis chamber with the in-situ camera.
A Boron implant.
B Phosphorous implant. Anneal duration is lower than in case **A**.

As a side-effect, the length of the transient region is also often increased when surface contamination is present, particularly in the case of heavy organic contamination, since the instrument has to go through two interfaces: void → organic → sample instead of only one: void → sample when no contamination is present.
Partial or total removal of surface contamination would therefore reduce the extent of the transient region, diminish mass interferences and suppress unknown contributions not only in the topmost layers but also deeper in the bulk.

II. 1. b- Thin layer deposition or removal

On the same principle, on might want to remove thin layers (1~100 nm thick). These layers differ from contamination in that they are of known composition (such as native silicon dioxide layers on silicon surfaces) or even deposited on purpose for process means (thick thermal oxides, Si capping layers…). Their removal is often performed by (wet) chemical etching.
On the other hand, in some particular cases one might want to deposit thin layers on a sample. An example of this is the deposition of a metallic layer on organic samples to increase secondary ion yields, which in this case is performed via a simple sputter coater.

Expected improvements

On one hand, a thin layer on a sample surface can have detrimental effects. If the layer is very thin, it induces an increase of the transient region length as seen in the previous subsection. For thicker layers this is no more the case since both void → layer and layer → sample interfaces are distant enough to be seen as two separate interfaces separated by a permanent ionisation regime (>~10 nm, <~100 nm). However even in this case it can still

have detrimental effects on depth resolution either because of the physical interface roughness, or by increase of surface roughness due to integration of sputter induced effects on longer times. Thin layers placed on top of the layers of interest in a sample might therefore deteriorate the quality of, or even prohibit depth resolved analysis of the layers of interest. In such cases the removal of these layers is beneficial to analysis quality since it will at least minimise or completely suppress the detrimental effect associated to them.
On the other hand, analysis "as received" of some samples can be sometimes difficult because of (i) their dimensions or (ii) the difficulty to yield characteristic secondary ions. In this case, the deposition of (i) a thin, high quality, similar matrix material can displace the initial transient region from the layers of interest to the deposited layer (such as Si capping for USJ samples) or (ii) a thin metallic layer which will help improve secondary ion yields of particular elements or compounds (principally used for surface analysis of organics).

II. 1. c- Backside sample preparation

When extremely precise analysis is needed on the deepest part of a structure in a sample, or when the feature of interest for analysis is situated well below the surface of a sample, buried under other material layers which might increase analysis difficulty, one might want to analyse the sample the other way around. This approach, referred to as the backside approach or backside analysis in opposition to standard (frontside) analysis, requires removal of all or part of the substrate beneath the layers of interest while keeping smooth and flat surface state suitable for ToF-SIMS analysis. Backside preparation can be performed by physical means (grinding, polishing, plasma induced erosion), chemical means (wet etching) or by combination of the two approaches.

Expected improvements

While classic sample profiling from surface towards bulk yields satisfying quality analysis for standard applications, there are some cases where the physical limitations of the technique do not allow sufficiently quantitative, depth resolved analysis. These limitations, reviewed in the last chapter, can be related to the sample properties or nature (surface or interface roughness) or are intrinsic to the technique itself (sputter induced roughening, mixing, ion implantation). Those induce analysis artefacts which tend to increase with sputter time due to the in-situ modification of the physical and chemical nature of sub-surface layers during analysis. In practice, slowly decreasing signal tails, unrealistic interface peaks might appear on the profile, masking features of interest and deteriorating analysis quality. An example of this phenomenon is given in Figure II.2 [1], presenting SIMS profiles of a 200 eV boron implant in silicon. The combined effects of mixing and boron implantation upon sputtering in the conventional frontside profile, result in a shift of the boron distribution tail towards the bulk. In this particular case, accurate characterization of dopant distribution in the profile tail is extremely important to be able to accurately determine the junction depth. Even in very low energy sputtering conditions such as here, SIMS is unable to provide the correct junction depth value (assuming 100% activation in low dopant concentration region). By using backside profiling one is able with identical experimental conditions to observe more accurately the dopant distribution in the same part of the profile. On the other hand, one can observe mixing and implantation related artefacts on the backside profile in the left part of the profile which are of the same kind than the effects observed in the tail of the boron distribution with the frontside profiles. Backside preparation therefore allows for complete suppression of analysis artefacts observed in a conventional ToF-SIMS profile related to

potential surface/interface roughness or sputter induced effects by turning the sample the other way around. However since the physics of the instrument is unchanged, the same artefacts may still be present in the analysis direction (although the layer sequence may affect this).

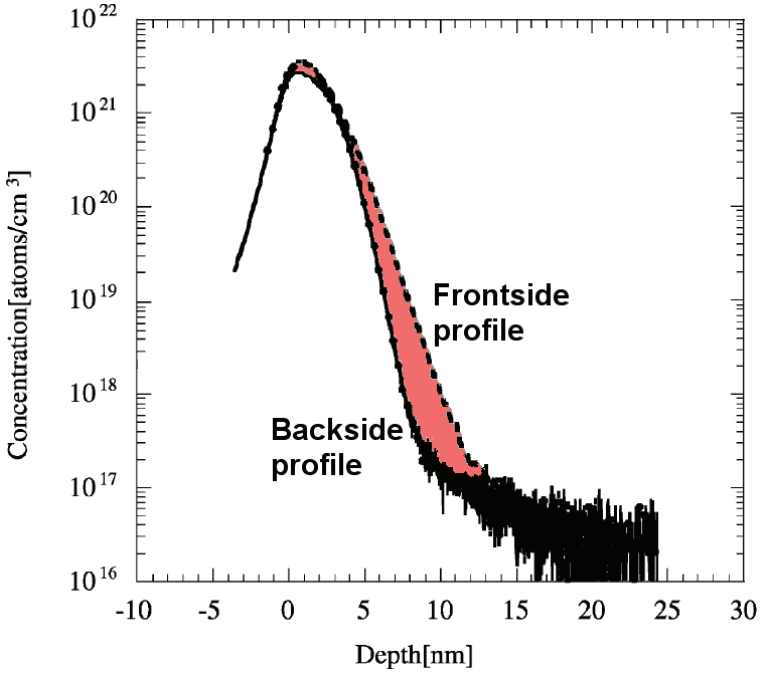

Figure II.2 SIMS frontside and backside depth profiles of a 200 eV B implant in Si obtained with 500 eV O_2^+ abrasion. Differences between profiles are highlighted in light red. Adapted from [1].

Another potential improvement brought by backside preparation is also observed in Figure II.2. The intensity of boron peak concentration is indeed seen as quite different between both profiles. The few first nanometres of a conventional analysis are often difficult to use for quantitative analysis given that the sputter transient modifies both sputter and ionisation yields in this region. Profiling a sample by its backside would allow efficient suppression of these effects in the same region.

II. 2. Optimisation of experimental parameters

In this work, a large variety of materials and structures are studied. No given experimental parameter set can reasonably be assumed to provide best analysis quality in all cases. Each of the experimental parameters needs to be studied separately in order to investigate their effects on analysis quality. This will allow us to make the right experimental parameter choices for each particular application. In this section we will therefore review the expected effects of the experimental parameter choices on analysis quality. We will also limit ourselves to the different parameters accessible for optimisation on our TOF SIMS V instrument.

II. 2. a- Primary ion nature

Primary ions in SIMS can be classified according to their chemical nature (active or inactive) and to their physical nature (monoatomic or cluster). Dual beam ToF-SIMS allows however to dissociate sputter and analysis beams by using two different primary ion beams. Our instrument enables two different active primary ion species: caesium (Cs^+) and oxygen (O_2^+) for sputtering, and one inactive specie: bismuth and bismuth clusters (Bi^+, Bi_3^+, etc) for analysis.

Effects on analysis

The choice of Cs or O_2 and thus of the chemical nature of the sputter beam primary ion will modify the chemical composition of the sample's topmost layers and induce a variety of different effects. First, and most obvious, the implantation of these elements at the surface of the sample will mask their original concentration in the sample. If caesium is not a common element in microelectronics, many applications require the O distribution in a sample to be known. The use of an oxygen primary ion beam (unless a specially prepared gas bottle is used such as isotopically homogeneous ^{18}O bottle) would therefore exclude its quantitative analysis. Second, active ions are chosen expressly for their ability to modify the sample's composition in order to exalt particular secondary ion yields. As shown in the previous chapter, oxygen and caesium produce opposite effects: the first allows improvements in positive ion yields of electropositive species, the latter tends to increase negative ion yields of electronegative species. Furthermore, ionization processes will differ greatly as a function of the primary ion used for sputtering. One can therefore expect, in addition to the usual ion yield increases for specific species, different behaviours during transient regions at surface and interfaces and thus different artefacts.
On the other hand, changing the physical nature of the primary ion for analysis, one will change the ion cascade regime on impact, as seen in the previous chapter. When increasing the number of constituents within the primary ion without changing its total energy, one also increases the deposited energy density [2-3]. This leads to enhanced sputtered volume per impact and therefore to a net increase in overall secondary ion yields (see Figure I.10). When only a small number of constituents is concerned (2 or 3), the different atoms of the original ion are still close from each other after ion fragmentation on impact. This induces multiple impacts in parallel on the same atoms or compounds of the target's lattice. These non-linear (i.e. non successive) collisions allow for more efficient energy transfer in the near surface region and an increase in the number of secondary ions, especially compound, molecular or heavier element ions, ejected from the surface [3-5]. This behaviour is notably put to use to improve the yields of MCs_n^+ secondary compound ions for the MCs quantification method. When further increasing the number of constituents however one observes only small improvements in heavier fragment yields [3]. As a side-effect small clusters also induce more damage since the sputtered volume is enhanced [6]: even though most of the secondary ions come from the topmost surface layers, the extent of mixing is expected to be greater with small cluster than monoatomic projectiles. Due to this, and particularly during organic materials analysis, sampling depth can also increase when using small cluster projectiles instead of monoatomic ones [7].

II. 2. b- Primary ion energy

In our system, the sputter column optics enable well focused, high current density beams from 250 eV to 2000 eV in standard mode. With a degradation of both current and

focusing one can however go down to ~100 eV. Similarly, analysis beam is usually operated at 25 keV, but can also be switched to 15 keV for specific applications, with only a very slight current loss. By adjusting the chopping delays, multiply charged bismuth ions can be selected instead of simply charged ones, thus multiplying the beam energy by the same amount.

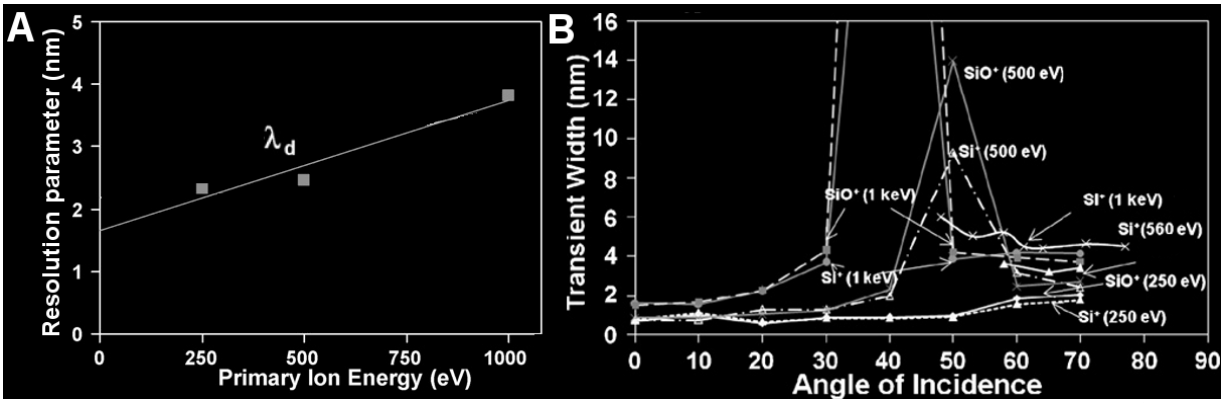

Figure II.3.A Decay length λ_d obtained on Ge delta doping layers in Si matrix with Cs^+ abrasion normal to the sample surface. Adapted from [8].

B Transient width measured in pure Si using O_2^+ sputtering and monitoring SiO^+ or Si^+ secondary ions. Adapted from [8].

Effects on analysis

Modification of sputter beam energy will have a direct impact on sputter rates because of the combined effect of the reduced impact energy and current density at lower energies. As higher energies are better suited for profiling of thick samples, lower energy sputtering is mandatory for visualisation of thin structures. Typically, for 300 × 300 μm^2 sputter craters in pure silicon, the sputter rate can vary from ~0.1 $nm.min^{-1}$ at lower energies to ~10 $nm.min^{-1}$ at higher energies. Lower sputter energy also signifies lower extent of mixing and damage to the material and thus enhanced depth resolution. Since we are sputtering with active elements, it also means higher content in primary ion specie at the surface of the sample and therefore enhanced chemically induced ion yield modification [9-10]. Finally, as sputter rates are lower, the sputter time needed to reach permanent regime at surface or after interfaces are approximately the same, which mechanically reduces the thickness of the transient regions when using lower sputter energies. This is illustrated in Figure II.3 [8, 11] for sputtering of silicon with oxygen at different angles and at various energies, along with depth resolution obtained at different energies with caesium sputtering of silicon. The appropriate compromise between depth resolution, transient region-less analysis and fast sputter rates has therefore to be performed by the experimenter according to the sample analysis requirements.

On the other hand, modification of the energy of the analysis beam to 15 keV will principally modify the penetration depth of the bismuth ions inside the target material, with only a slight diminution of the secondary ion yield. This will induce diminution of both depth of information and damage induced to the material.

II. 2. c- Sputter / analysis ratio

The sputter / analysis ratio *R* is a unit-less number representing the ratio of amount of material sputtered by sputter and analysis beams during one {sputter + analysis} cycle. There are several ways to adjust *R* in dual beam ToF-SIMS. Repetition rate can be optimised through variation of analysis and sputter cycles individual durations. Otherwise, sputter area

on analysis area can be optimised within acceptable limits of flatness of analysis zone. Finally AC sputter current / AC analysis current can also be optimised.

Effects on analysis

The successive operation of sputter and analysis beams in our dual beam ToF-SIMS apparatus allows for very low energy sputtering - thus highly depth resolved profiling -, while enabling high energy ion impact induced secondary ion generation and analysis - thus high secondary ion yields and excellent sensitivity and dynamics. However both of these are extremely dependent on the fact that sputter primary ion dose must be greatly superior to analysis primary ion dose for one complete cycle. Indeed, the role of the active element sputtering is (i) to provide an "activated" surface for analysis with a given amount of active elements at the surface in order to improve given secondary ion yields and (ii) to remove the damage induced by the highly energetic analysis ions between two analysis cycles.

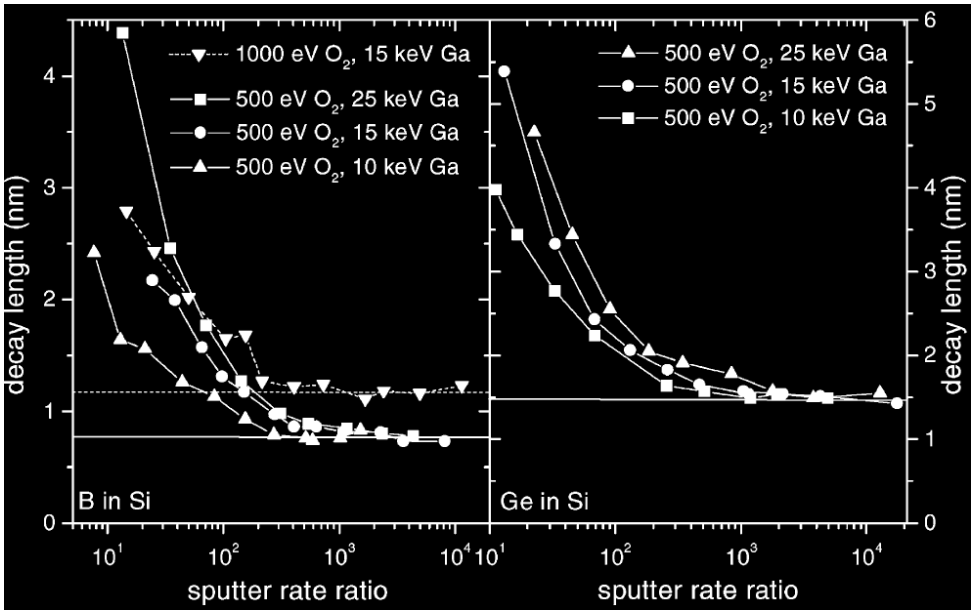

Figure II.4 Decay length evolution as a function of *R* for a B (left) or SiGe (right) delta in silicon. Under identical conditions, the higher decay found in SiGe deltas is due to Ge segregation away from the surface oxide layer [12].

If sputter primary ion dose between two analysis cycles is insufficient, one or both of these conditions might be lost, which would result in loss of secondary ion signal, depth resolution or even both. The optimisation of *R* is thus crucial, especially for applications requiring high depth resolution or visualisation of extremely thin structures. Figure II.4 shows the evolution of the depth resolution along with *R* in pure silicon. It is widely accepted that an *R* value around 100 or higher is enough to remove the risk of depth resolution degradation [12]. Such a value indeed indicates that in one cycle, the analysis beam only erodes 1% of the amount of material removed by the sputter beam. As for most applications it is easy to obtain *R* values of the order of a few hundred, for applications requiring high repetition rates (for enhanced statistics) and extremely low energy sputter rate for visualisation of thin structures with optimised depth resolution and reduced transients, this value is however difficult to achieve. In this case *R* has still to be optimised in order to find a satisfying compromise between depth resolution and repetition rate.

II. 2. d- Analysis chamber vacuum condition

The analysis chamber pressure can be controlled in two ways. First there is the possibility to adjust the vacuum level between a few 10^{-9} mbar and a few 10^{-10} mbar by simply beginning the analysis at a more or less advanced stage of vacuum pumping. In ideal conditions, the vacuum in the analysis chamber can reach ~10^{-9} mbar a few tens of minutes after the introduction of a new sample set, while it would need a few hours to reach 10^{-10} mbar (note that this can greatly depend on the samples and on the pumping efficiency). Second, one can also use O_2 flooding inside the chamber (gaseous oxygen is injected close to the sample's surface through a capillary). In this case, oxygen partial pressure (also residual pressure) can be adjusted between ~10^{-8} mbar and a few 10^{-5} mbar.

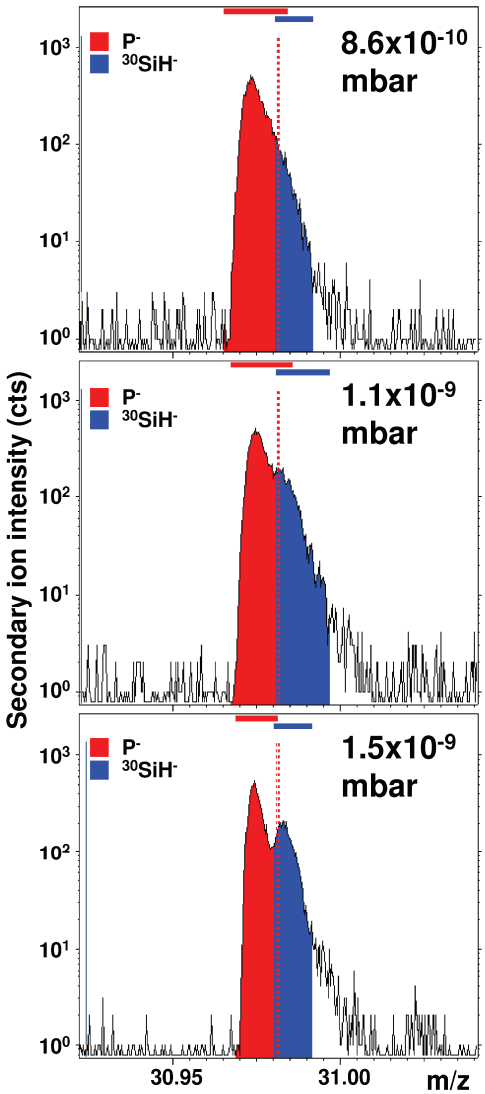

Figure II.5 Mass spectra obtained on phosphorous implants in Si around the region m/z = 31 integrated over identical primary ion doses, and with three different vacuum conditions.

Effects on analysis

A better vacuum during analysis means less hindrance from residual atmosphere contamination. Data acquired in higher vacuum conditions will show reduced background noise, but also reduced artefacts, especially at surfaces or interfaces which might react with residual oxygen in atmosphere for example. Hydrogen is another element to which ToF-SIMS

is very sensitive and which, though only present in low quantities in the already reduced pressure atmosphere, can form compound secondary ions with elements present in the sample and generate important mass interferences. A typical manifestation of this phenomenon is shown in Figure II.5. Two mass spectra taken with exactly the same conditions except for residual atmosphere show drastically different peak shape around the P^- mass region. The one acquired in poor vacuum conditions is indeed much more subject to mass interference with $^{30}SiH^-$. Improving vacuum in the analysis chamber during will therefore generally speaking reduce these undesirable effects. However, when sputtering with oxygen and especially at high energies where adsorbed oxygen content on surface is lower, one might have to resort to oxygen flooding. The latter is used to saturate the analysis chamber with oxygen, and more precisely at the vicinity of sample surface in order to create a completely oxidised layer at its surface prior to sputtering and to maintain it during the sputtering process. When this "complete oxidation" condition is achieved, maximum yield enhancement and optimised depth resolution are obtained. However, when this condition is not satisfied, severe degradation of depth resolution can occur, due to the apparition of ripples at the surface of the samples. Finally, slight oxygen flooding can also be used while sputtering with caesium in order to modify ion yields since given the affinity of oxygen with caesium, caesium surface content will tend to increase when oxygen is present too [13].

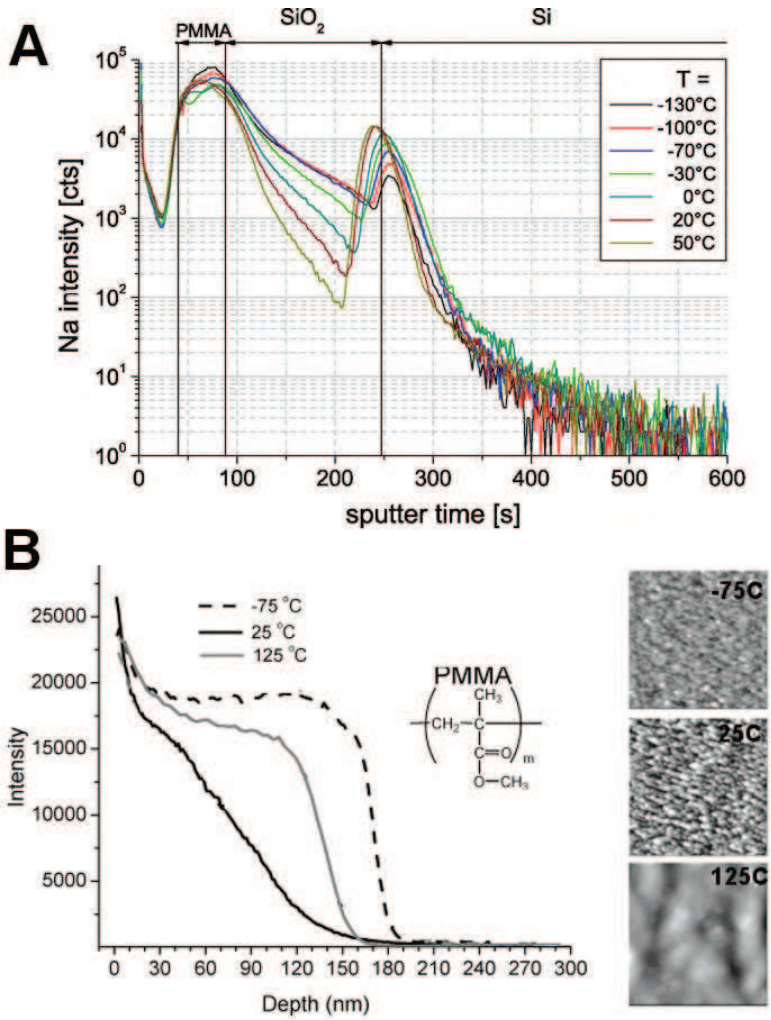

Figure II.6.A Temperature enhanced incorporation of Na in SiO_2 during depth profiling with 1 keV O_2^+. Initially, Na is located only in the surface PMMA layer with no Na in the SiO_2 layer. During sputtering through SiO_2, one can observe a temperature dependent Na transport (migration), enhanced at higher temperatures [14].

B Positive secondary ion depth profiles of m/z = 69, PMMA characteristic fragment, in ~160 nm thick PMMA films deposited on Si. Depth profiles were acquired at different temperatures (left). A strong dependence of signal sustainability on temperature is observed, in relation with important sputtered surface morphology changes as observed with AFM (right). RMS are found to be of 5.2, 2.6 and 2.7 nm at 25°C, -75°C and 125°C respectively [15].

II. 2. e- Sample temperature

The final variable parameter in our experimental setup is the sample temperature during analysis. A special sample holder equipped with resistances and with a dedicated zone for contact with a metallic tip connected to an external liquid nitrogen reservoir is indeed available. It allows either heating or cooling of the sample holder (and thus sample itself) during analysis from -150°C to +600°C.

Effects on analysis

A modification of the sample temperature in this range during profiling will in most cases modify only the (thermodynamic) reaction of the target to primary ion irradiation. These temperatures are indeed insufficient to modify the sample in itself (except for some particular organic materials such as low glass transition temperature polymers). Out of the potential effect of a temperature variation, those of main interest for us are the modification of sputter rates (due to the enhanced cohesion of target materials at lower temperatures), of surface states (apparition or smoothing of sputter induced roughness) and of temperature dependent sample sub-surface composition modification (such as migration kinetics of given elements). A few examples of these are given in Figure II.6 [14-15]. Thermally enhanced migration of some elements, such as Na here but also potentially N, B or others upon irradiation with rather low energy active primary ions is more likely to occur in inorganic materials. On the other hand, roughness development or smoothing as a function of temperature is more critical in organic materials, where extreme roughening of the surface can be observed under ambient temperature analysis conditions.

II. 3. Data treatment

The output of a ToF-SIMS analysis is extremely rich in information, comprising at each depth point both information on the secondary ion yields over a large mass range and lateral position of each mass spectra recorded; all of these being easily accessible through the instrument's software. This opens opportunities for improvement in analysis quality through post-experiment data treatment, which we will review in this section.

II. 3. a- Selection of a region of interest, partial area profile reconstruction

Within the area rastered with the analysis beam during a depth profile, there might be some zones featuring contamination or two or three dimensional structures present in the sample such as metallic line or grain boundaries. In order to either remove unwanted zones or to select only a zone of interest for analysis inside the analysis zone (called Region Of Interest (ROI)), the reconstruction software allows ROIs to be defined within the original analysis

crater. Secondary ion intensities maps can help the user to choose the appropriate zone for analysis.

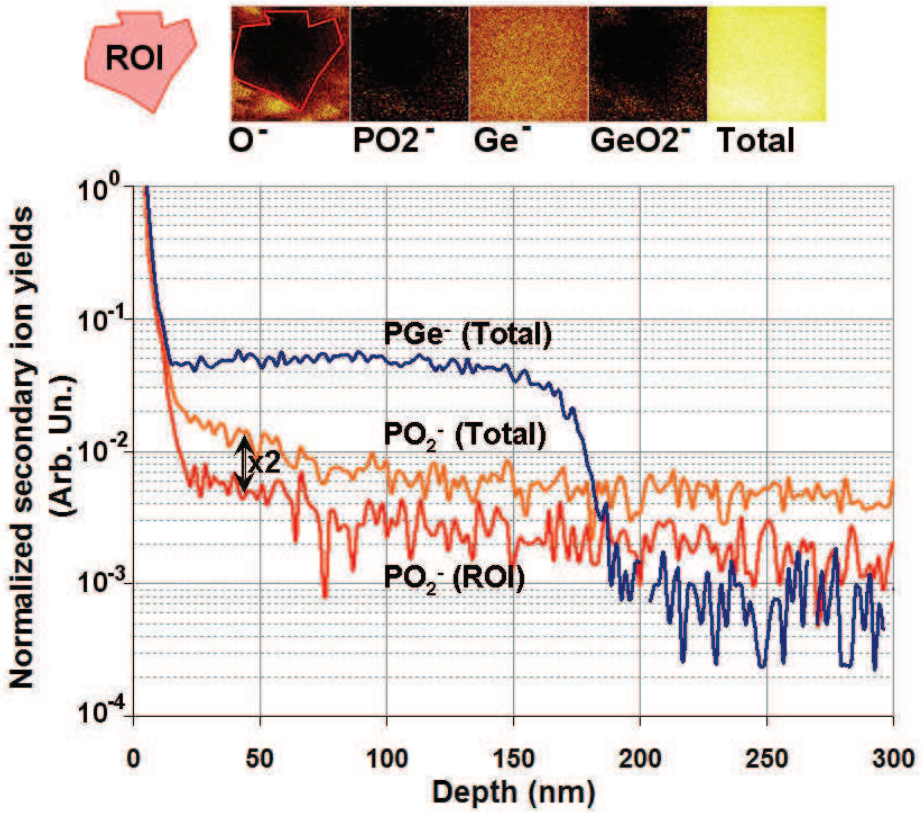

Figure II.7 Data corresponding to the depth profile of a P implant in Ge with annealing in oxidising atmosphere. Top: selected secondary ion maps integrated over the whole profile and ROI shape. Bottom: Depth profiles before data treatment (Total) and after data treatment (ROI) for characteristic secondary ions. Normalised P^- profiles after and before data treatment being almost identical, only profile before treatment is represented for clarity purposes. The level of in-depth oxygen contamination is divided by two after treatment.

Effects on analysis

Reduction of the analysis area reduces the number of total secondary ion counts per analysis cycle, thus affecting sensitivity. However it also allows, when needed, to reject zones unsuitable for analysis, be it because of the presence of contamination, of sample damage or even of sample structure. An example of this is given in Figure II.7, which shows a depth profile of a selection of secondary ions of a P implant in Ge whose surface was contaminated with Ge oxide islands (see also Figure II.1). Looking at the reconstructed secondary ion intensity maps, one can observe that a few islands containing oxygen are present on the borders of the analysis region. By selecting a zone without oxygen secondary ion counts (ROI drawn in light red) and reconstructing the profile using the points within this region only, the level of in-depth PO_2^- secondary ion counts is reduced. Reconstruction of depth profiles on well chosen ROI therefore yields enhanced precision and reliability when confronted to inhomogeneous, two or three dimensional material distribution within the analysis zone.

II. 3. b- Selection of representative secondary ions

In comparison with magnetic sector or quadrupole SIMS instruments, ToF-SIMS allows exhaustive post-experimental analysis of the mass spectra in order to select the monoatomic or compound ions most representative of the element of interest and/or of the matrix composition in the specific experimental conditions used. Resorting to systematic studies of a wide range of secondary ions and of different normalisation methods with samples calibrated with an external method is therefore the best way to improve the quality of an analysis in terms of concentration accuracy, detection limit or reliability. Literature abounds on such studies, especially for As or B USJ applications [16-17]. Figure II.8 shows a study on normalisation patterns (ratio between an impurity representative secondary ion intensity by a matrix representative one) for depth profiling of an As implant in Si through a thin silicon dioxide with Cs^+ sputtering [16]. The obtained distributions are almost identical in the Si region but can differ by several decades in the SiO_2 region. The interest of the study on a well known sample is here clear: the most accurate calibration method can be selected simply by comparing the total As dose obtained with each method to the dose obtained with an absolute dose evaluation technique such as Rutherford BackScattering (RBS).

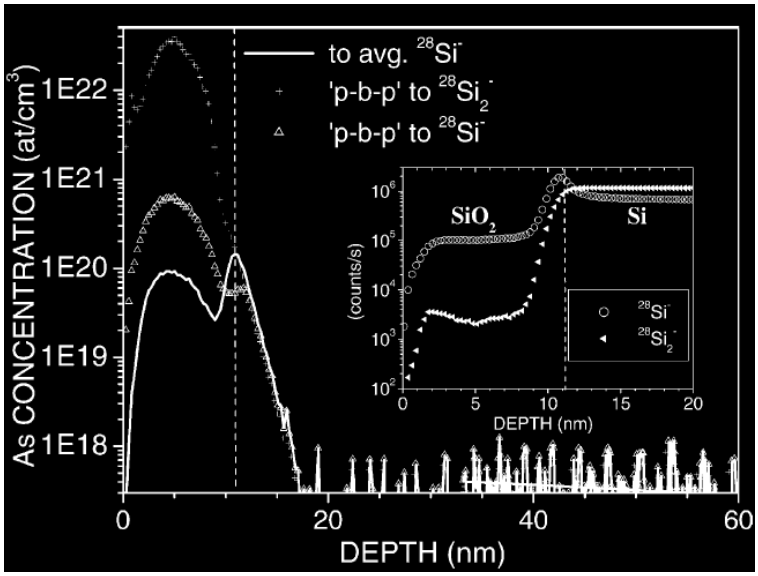

Figure II.8 Arsenic depth profile obtained on a 3 keV As implant in 11 nm SiO_2/Si stack by using 500 eV Cs+ sputtering, with three different normalisation methods for RSF calculation. $^{28}Si^-$ and $^{28}Si_2^-$ matrix profiles are represented in the inset. Avg. means normalisation to the average value of matrix signal in Si region, while p-b-p means point by point normalisation to the corresponding matrix signal [16].

II. 3. c- Specific quantification methods: combination of experimental parameters and selection of particular secondary ions

A few methods combine both experimental aspects and selection of most representative ions in order to minimise matrix effects. These are often developed for application on one type of material only (such as SiGe or III-V alloys…) through systematic studies of the role of experimental parameters (primary ion nature, energy, angle of impact…) and of different calibration strategies (secondary ion selection, normalisation procedure…). Because of this they are also often restricted to the type of materials for which they were developed. These methods often take advantage of the modification of the sample surface

obtained by sputtering with active elements such as Cs or O_2. Of these, we can mention for example the MCs method [18-22] and the Jiang *et al.* method [23].

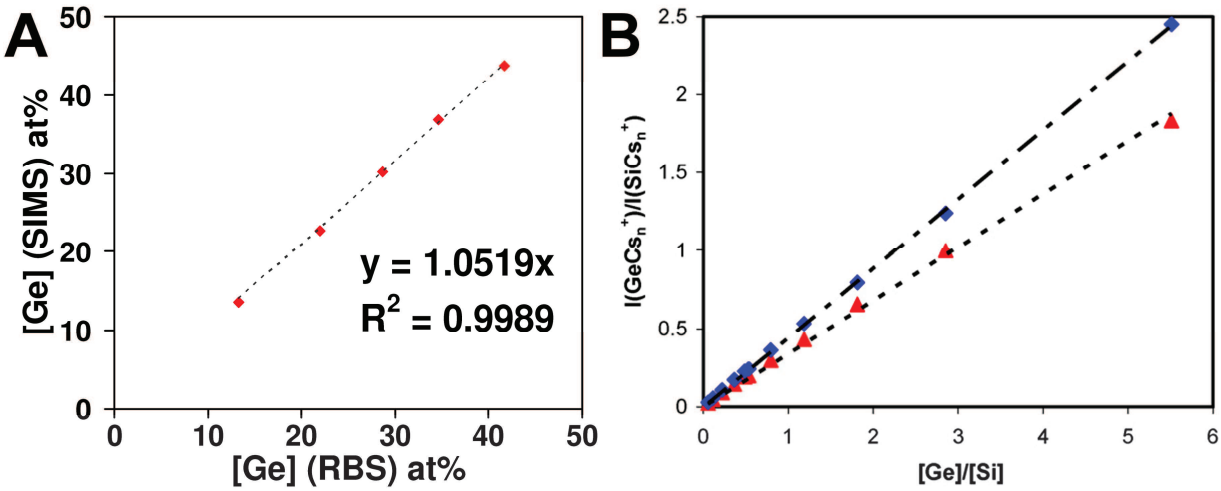

Figure II.9.A Comparison of Ge contents in SiGe films on Si bulk wafers as measured with SIMS and RBS. SIMS profiles were acquired with a 1 keV O_2^+ beam at normal incidence, detecting positive secondary ions $^{30}Si^+$ and $^{70}Ge^+$. Quantification was performed using the relation $x = \alpha \cdot I(Ge^+)/(I(Si^+) + \alpha \cdot I(Ge^+))$, x being the layer Ge content and α scaling factor. Data are extracted from [23].

B Variation of the intensity ratio $I(GeCs_n^+)/I(SiCs_n^+)$ as a function of the composition ratio [Ge]/[Si] for MCs_2^+ (♦) and MCs^+ (▲) ions. Data acquired on an ION-TOF ToF-SIMS V instrument with a 2 keV Cs^+ sputter beam and a 25 keV Bi_3^+ cluster analysis beam both incident at 45°. Vacuum during experiments was better than 10^{-9} mbar. Graph extracted from [22].

Effects on analysis

While sputtering with an active element, the surface content in primary ion species depends only on the sputter rate of the target material. In permanent regime conditions (for Cs sputtering) or in complete oxidation conditions (for O_2 sputtering) this favours stabilised emission of monoatomic or compound matrix ions, as their emission only depends on the primary ion surface concentration. It is therefore possible to solve the usual problems in matrix element quantification by appropriate secondary ion selection and normalisation. In the case of Cs^+ sputtering, selection of MCs_n^+ (n = 1 or 2) ions instead of $M^{+/-}$ was proven to minimise or totally suppress matrix effects in a wide range of materials such as III-V or SiGe alloys [18-19, 21-22], while improving sensitivity to particular elements such as noble gases [20]. In the case of O_2^+ sputtering, on the other hand, one has to pay more attention to the experimental conditions in order to conserve a smooth surface while providing full oxidation of the surface. The selection of secondary ions has then to be performed case by case through systematic studies. For $Si_{1-x}Ge_x$ alloys, it was proven that Ge quantification could be achieved within x=0.15 to 0.65 by following the Si^+/Ge^+ intensity ratio [23]. An example of the results obtained with each method on SiGe alloys is shown in Figure II.9. These methods have the advantage of being simple, well documented in the literature and require monitoring of only a limited number of secondary ions, which makes them feasible even on quadrupole or magnetic sector SIMS instruments. However the requirements on experimental conditions limit their application to a selection of materials (linear regime for Ge quantification is only obtained within x=0.15 and 0.65 with O_2^+ sputtering) and/or hamper the simultaneous quantification of impurities (such as B or C for which MCs shows a low sensitivity).

II. 3. d- The Full Spectrum approach: consideration of the whole mass spectrum

This approach, although relatively unknown and scarcely represented in the literature, is interesting because it capitalises on the specificity of ToF-SIMS (parallel monitoring of numerous secondary ions in one large range mass spectra). It indeed consists in taking into account as much information as possible from the ToF-SIMS mass spectra by following all of the secondary ions containing the element of interest, in contrast to all other approaches which usually focus on no more than one or two secondary ions. Precisely, for a given element *A*, one will sum the contributions of all $A_xR_y^-$ secondary ions normalised by x and by their isotopic abundances to obtain a new quantity corresponding to the atomic quantity of element *A* in the secondary ion beam. Instead of depth distributions of secondary ions intensities, the depth profiles are transformed into depth distributions of normalised sums of secondary ion intensities, somewhat equivalent to envelope functions.

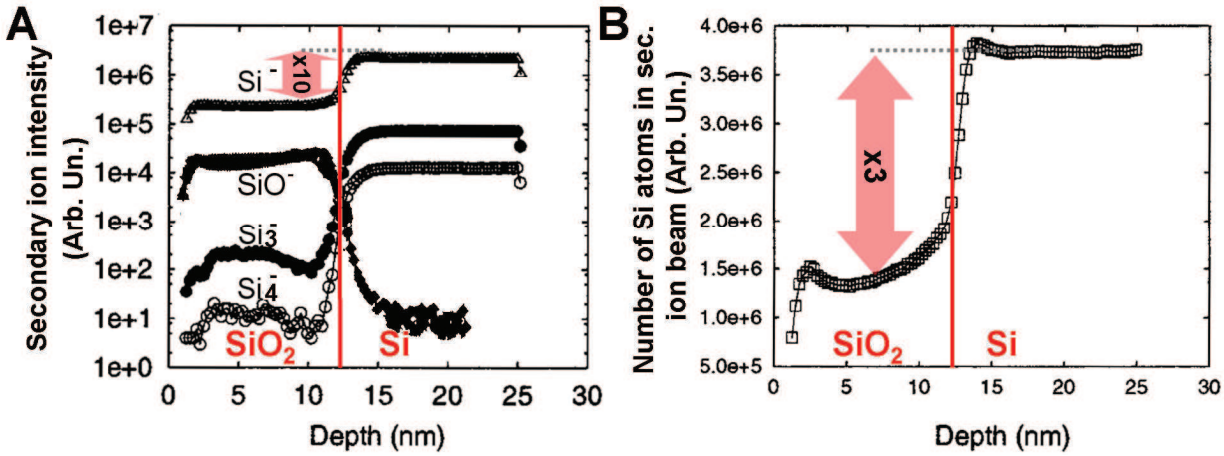

Figure II.10.A Intensity of different negative signals containing silicon as a function of depth. Signals are separated between those decreasing from oxide to silicon (mainly $Si_xO_y^-$), and those increasing in silicon (mainly Si_x^-). Adapted from [24].

B Depth distribution of the number of silicon atoms in the secondary ion beam. Note that the graph is in linear scale, whereas graphs of **A** are in log scale. Adapted from [24].

As a result, this approach shows better statistics and is more representative of matrix element depth distribution in heterogeneous stacks. The latter is represented in Figure II.10, showing the distributions of different Si based secondary ions (Figure II.10.A) and of the Si representative signal after data treatment (Figure II.10.B) obtained by analysis of a SiO_2/Si stack [24]. None of the secondary ions gives a distribution representative of silicon concentration: Si_x^- ions have too low intensities in the oxide region, while $Si_xO_y^-$ ion intensity is almost zero in the silicon substrate region. However, after data treatment, the Si representative signal shows a distribution close to the (expected) actual Si distribution in the material, with only a ×3 intensity difference between plateau in SiO_2 and Si regions. This clearly demonstrates an important minimization of matrix effects. Another feature of this approach is that the signals it yields for matrix elements is directly proportional (although not equal) to the material composition. This is shown in Figure II.11.A, where one can see that Ge content in the secondary ion beam varies in a linear fashion with actual Ge content in SiGe alloys [25]. This approach was therefore used by Ferrari *et al.* [24] and Perego *et al.* [25] in pioneer works on quantification of nitrogen in silicon oxy-nitride stacks and of germanium in silicon-germanium alloys, respectively.

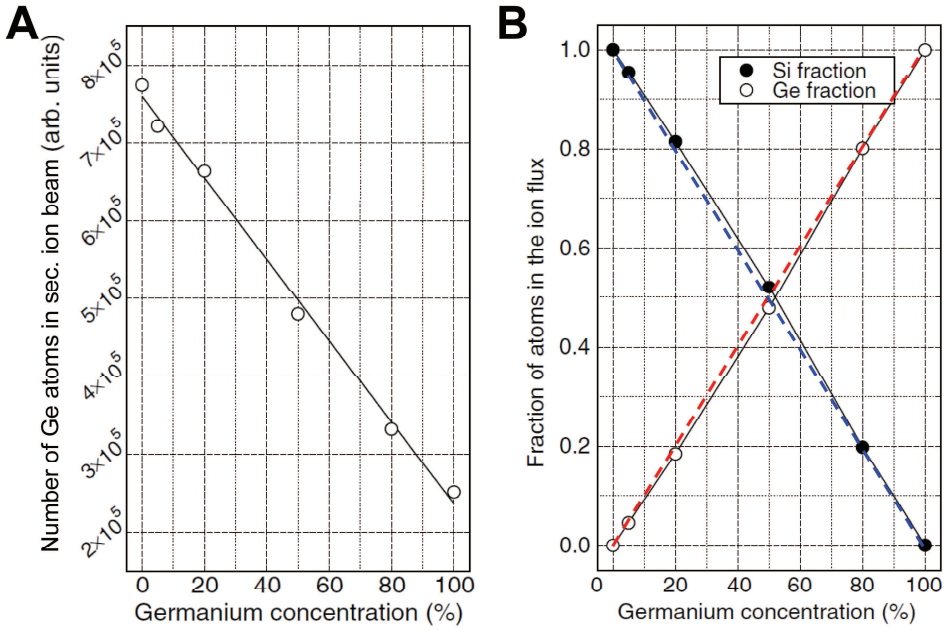

Figure II.11.A Total number of Ge atoms in the secondary ion flux as a function of the germanium concentration in SiGe alloys. The values have been determined in steady state conditions. A linear variation is observed. Adapted from [25].

B The fractions of silicon and germanium atoms in the secondary ion flux are reported as a function of the germanium concentration in SiGe alloys. It is found that the elemental composition of the secondary ion beam is very close to the elemental distribution in the actual material. Adapted from [25].

Effects on analysis

If quantitativity of the method were to be proven on different materials and through systematic studies and/or cross characterisation studies, this approach will present the advantage of enabling quantification for all matrix elements in one depth profile. Furthermore, since this ability only results from data treatment and not from instrumental or experimental condition changes, one still keeps the ability of ToF-SIMS to simultaneously quantify impurities or dopants if present. This would be completely new, as no SIMS based method is able to yield such profiles up to now. One can also expect due to the increased statistics, more reliable, reproducible and less noisy profiles. For the particular case of very thin (<10 nm) samples, and based on previous studies by Ferrari et al., one can even expect to be able to provide quantitative profiling without resorting to reference samples (through cross characterisation) [24]. However, quantification is not guaranteed without feasibility studies, as shown by Figure II.11.B for Ge quantification in SiGe alloys: although secondary ion beam composition in both Si and Ge is close to this of the actual material, it does not show a perfect match.

II. 4. Correlation and complementarity with other techniques

Though ToF-SIMS is able to yield quantitative and depth resolved chemical information on a large variety of materials and structures, in many cases this information alone is either not reliable enough or simply insufficient to describe the material's overall

properties. Additional measurements are therefore needed, either with instruments of a different nature than ToF-SIMS but giving information of the same nature (quantitative in-depth chemical composition) or with instruments giving complementary information. In this study, those measurements have been performed with a range of different instruments we will present in this section. Some of them were available at the same lab, but for a few of them, international collaborations with laboratories or directly with the equipment manufacturer were set-up. This was an important part of the thesis work which does not appear in this manuscript since it is not of a technical nature. However an important part of the interesting results obtained during the thesis couldn't have been achieved without these collaborations, which permitted access to state-of-the-art instruments in order to assess the accuracy of ToF-SIMS results.

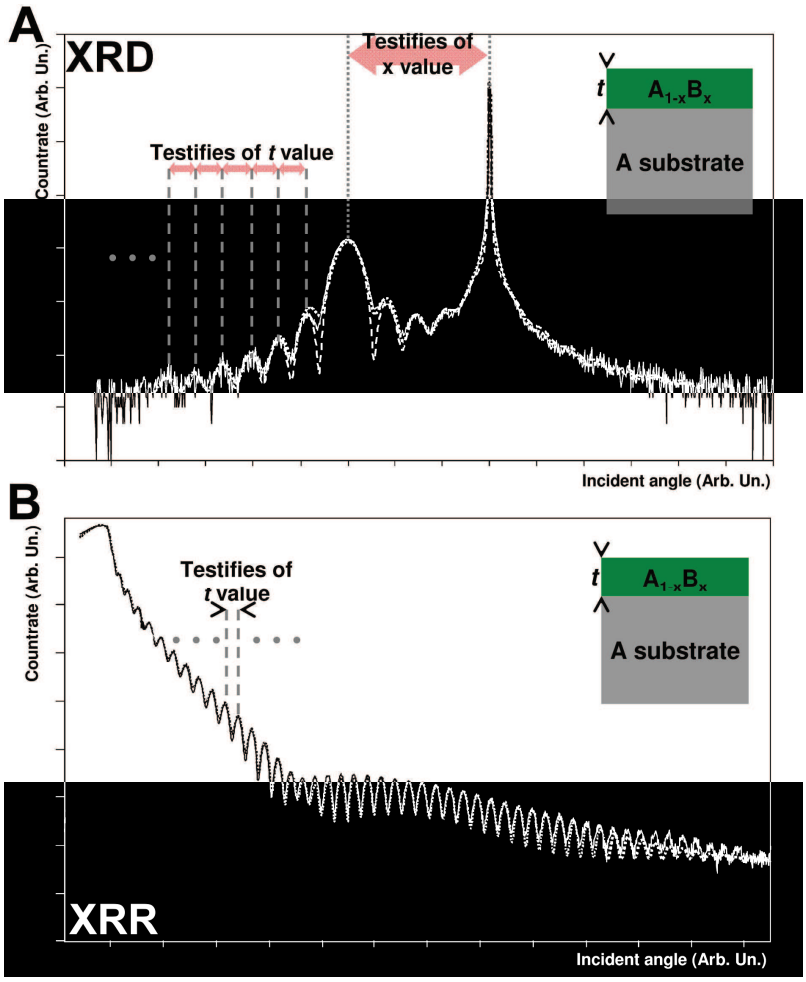

Figure II.12 XRD and XRR ω-2θ scans of a sample constituted of a substrate *A* and an overlayer of thickness *t* and of composition $A_{1-x}B_x$, *B* being an element of same crystallographic structure but higher lattice parameter in its pure form, and of lower density than *A*. Both graphs are adapted from [26].

A XRD spectrum. Experimental (solid line) and simulated (dashed line) diffraction patterns around a substrate crystallographic direction. The simulation based on a single layer does not match all measured details. The assumption of a compositional gradient significantly improves the match (square dotted).

B XRR spectrum. Measured data (solid line) and simulated reflectivity (dotted). Closely spaced thickness oscillations are resolved over the most of the curve, but a modulation of their amplitude is observed. This is attributed to the presence of a very thin layer on surface of the sample, the best-fit simulation to the experimental reflectivity curve being achieved by adding a low density top native oxide layer.

II. 4. a- X-Ray scattering: X-Ray Diffraction (XRD) and X-Ray Reflectivity (XRR)

When X-Rays go through a material, they interact with its atomic electron cloud. For inorganic materials constituted of regularly spaced series of atoms, scattering of the incident X-Rays occurs: due to the interaction between radiation and matter, incident photons are forced to change direction while keeping the same energy according to the principle of Rayleigh scattering. Since the wavelength of X-rays is close to lattice inter-plane distances (a few Angstrom), constructive and destructive interference between scattered rays can occur as well. Depending on the angular direction, both of those alternatively occur, yielding either high (for constructive interferences) or low (for destructive interferences) X photon flux. The angular spacing between directions of high flux is determined by a simple Bragg law and therefore constitutes a direct indication of the inter-atomic distances in the direction normal to the sample surface. X-Ray scattering techniques use this phenomenon to quantitatively infer the properties of pure, mono and polycrystalline material since each material (in its crystallographic form) has a unique lattice parameter. When a sample is constituted of several, heterogeneous materials layers, the different orders of reflexion *n* of the rays on the interfaces may also show oscillations with a given wavelength (similar to Fabry-Pérot effect), which contain information on the thickness of the layers. XRD or XRR spectra are obtained by illuminating a sample with an X-ray monochromatic beam and then rotating the sample. X-Ray source is fixed while both sample and detector are moved in such a way that the angle of incidence of the X-Rays is always equal to the angle of the measured scattered rays. This way one obtains a scan of intensity of scattered X-Rays as a function of their incident angle, as shown in Figure II.12 [26]. The difference between both settings consists in their angular range: while XRD measurements are obtained using rather wide incident angles (typically 30-40 degrees), XRR measurements are obtained at shallow angles (0-5 degrees) since the intensity of reflected X-Rays exponentially decreases with the incident angle (as seen on Figure II.12.B). Using XRD, the overall spectrum is dominated by the intense and narrow substrate peak, the other well-defined features are attributed to the overlayer peak (second peak in intensity) and its thickness fringes (smaller peaks). The angular separation between substrate and overlayer peaks corresponds to a given x content for the overlayer material alloy. Similarly, regular fringe spacing yields a given thickness for this layer. Attenuation of the oscillations around the overlayer material peak can suggest a non-uniform composition of the layer (see Figure II.12.A). Using XRR, an intensity plateau is obtained at low angles, corresponding to total reflection of the beam on the sample surface. The critical angle for intensity drop is characteristic of the material density. Once again, angular spacing between two peaks contains information about layer thickness, while attenuation and modulation of the oscillations with increasing incident angle allow quantitative measurement of interface roughness and of the presence of surface (or interfacial) layers (see Figure II.12.B). Such ω-2θ scans, so-called "double-axis rocking curves" are easily simulated using fundamental X-ray scattering theory. By fitting composition, number of layers, thickness and composition of the overlayer(s) in XRD or density, thickness and interfacial roughness in XRR one can fit experimental data to theoretical spectra and therefore quantitatively infer interface roughness, layer crystalline quality (in particular strain state or degree of relaxation) and presence of potential thin layers such as surface native oxides. In the case of multiple overlayers, the main features of the scans remain unchanged but spectra are more complex, due to the presence of multiple order diffraction (or reflection) peaks. For a more comprehensive overview or X-Ray scattering techniques principles and applications particularly concerning Si and SiGe epitaxial layers, please refer to references [26-31]

Both of these techniques are therefore very useful for precise determination of epitaxial, defect-less layer properties. Since these techniques are non-destructive they would preferably be used prior to any other measurement. Precisely, we are interested in the following parameters which can be provided by XRD and XRR:

- Absolute layer thickness (quantitative)
- Precise epitaxial alloy composition (quantitative)
- Interfacial roughness (qualitative)
- Layer strain state (qualitative)
- Layer crystalline quality (qualitative)

The absolute determination of layer thickness constitutes an interesting property for us since it allows direct determination of ToF-SIMS profile depth scale for both single or multiple heterogeneous material layers samples. Interfacial roughness measurement is also quite useful since it can be used to understand interface width obtained in a depth profile or to understand depth resolution worsening effects after sputtering through multiple interfaces. Finally, indications on layer strain state and crystalline quality can help in understanding of some effects observed on sputter rates or ionisation yields in particular materials.

II. 4. b- Spectrosopic ellipsometry

Light is composed of a wide variety of electromagnetic waves differing in phase and amplitude. The electric fields of these waves can be decomposed into two components, orthogonal to each other and always normal to the light's propagation direction.

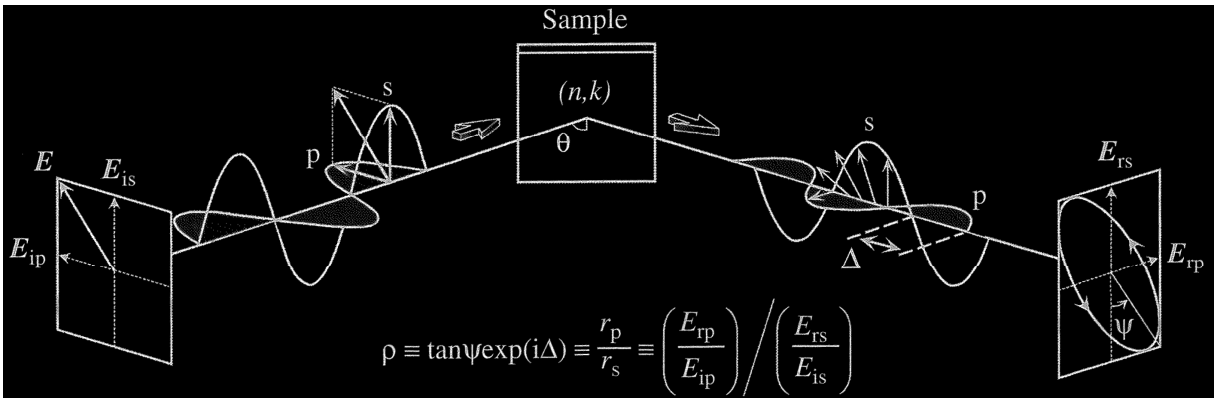

Figure II.13 Measurement principle of ellipsometry. Extracted from [32].

This results in an electric field orientation, which is random (and varying in a stochastic manner) for natural light. However also this field can also have a preferential orientation (polarized light), and can be either linear (if component waves are equal in phase and in amplitude), circular (if component waves are opposed in phase but equal in amplitude) or elliptic (composed of waves of random phase and amplitude), the latter being the most common as it is the natural state of light. When light hits a surface of different refraction index, it is partly reflected, and its polarisation is modified. Ellipsometry measures the change in polarisation occurring at such events. To achieve such a measurement, one has to produce polarised light through the use of a polariser, which is then directed to a sample. The linearly polarised light reflects on the sample surface, becomes elliptically polarised, and travels through an analyser usually composed of a continuously rotating polariser. The polarisation change is represented as the amplitude ratio, tan(Ψ), and the phase difference, Δ, as shown in

Figure II.13 [32]. The measured response depends on optical properties and thickness of individual materials. Thus, ellipsometry is primarily used to determine film thickness and optical constants through comparison with theoretical calculations using Fresnel's equations. However, it can also be used to characterise composition, crystallinity, roughness, doping concentration, and other material properties associated with a change in optical response. The film thickness is determined by interference between light reflecting from the surface and light traveling through the film. Depending on the relative phase of the reflected light, interference can be constructive or destructive. The interference involves both amplitude and phase information. The phase information from Δ is very sensitive to films down to sub-monolayer thickness [32].

In our study, we have only used this technique to obtain precise layer thickness measurements for thin (<10 nm) to ultra thin (~nm) layers. Compared to X-Ray scattering techniques, ellipsometry has the double advantage of precise measurement even for ultra-thin layers combined with efficiency on any type of material, be it crystalline, amorphous or even for organic materials.

Accurate thickness measurements on ultra-thin layers are often measurable only by ellipsometry. Based on these thicknesses one can either assess the accuracy of the depth scale of a ToF-SIMS profile or, more simply, directly infer sputter rates in single or double overlayer systems by affecting ellipsometry measured experimental thicknesses to ion intensity half signals or particular peaks characteristics of interfaces.

II. 4. c- Transmission Electron Microscopy techniques

TEM techniques make use of the transformation of the energy, direction or phase of electrons sent through a thin lamella of a given sample. Electrons, as theorised by De Broglie [33], can indeed be seen both as particles or waves and will therefore show both behaviours when interacting with the sample. On the same principle as for light microscopes, this feature can be used for magnifying and revealing properties of samples. Compared to most photons, electrons however have much smaller wavelengths. This gives electron microscopes much higher spatial resolutions than with any conventional light microscope, enabling examination of extremely fine details such as atomic columns in advanced instruments (maximum resolution of state-of-the-art TEMs being of ~0.05 nm against a few tens of nanometres for best light microscopes) [34]. For this reasons TEM is (in microelectronics) most used for direct visualisation of the cross-section of nanometric or deca-nanometric structures such as heterogeneous layer stacks of actual transistors. The information given by such simple analysis are sample conformity (i.e. thickness of the different layers/size of the different regions, interface widths) and crystalline state of each component (mono- or polycrystalline, amorphous, stacking faults) along with qualitative information on layer composition. In conventional imaging mode, TEM image contrast is indeed due to absorption of electrons in the material [35]. In this mode, called the bright field imaging mode, thicker regions of the sample, or regions with a higher atomic number will appear darker. The observed image can be explained as the two dimensional projection of the sample following the optic axis. En example of such bright field imaging is given in Figure II.14.A. However there are many other uses of TEM, yielding a variety of different information depending on the contrast method. We will now present a few of those, which found application in our study. At high magnifications, image contrast is no more dominated by absorption of electrons but by the phase difference between electron waves of different paths.

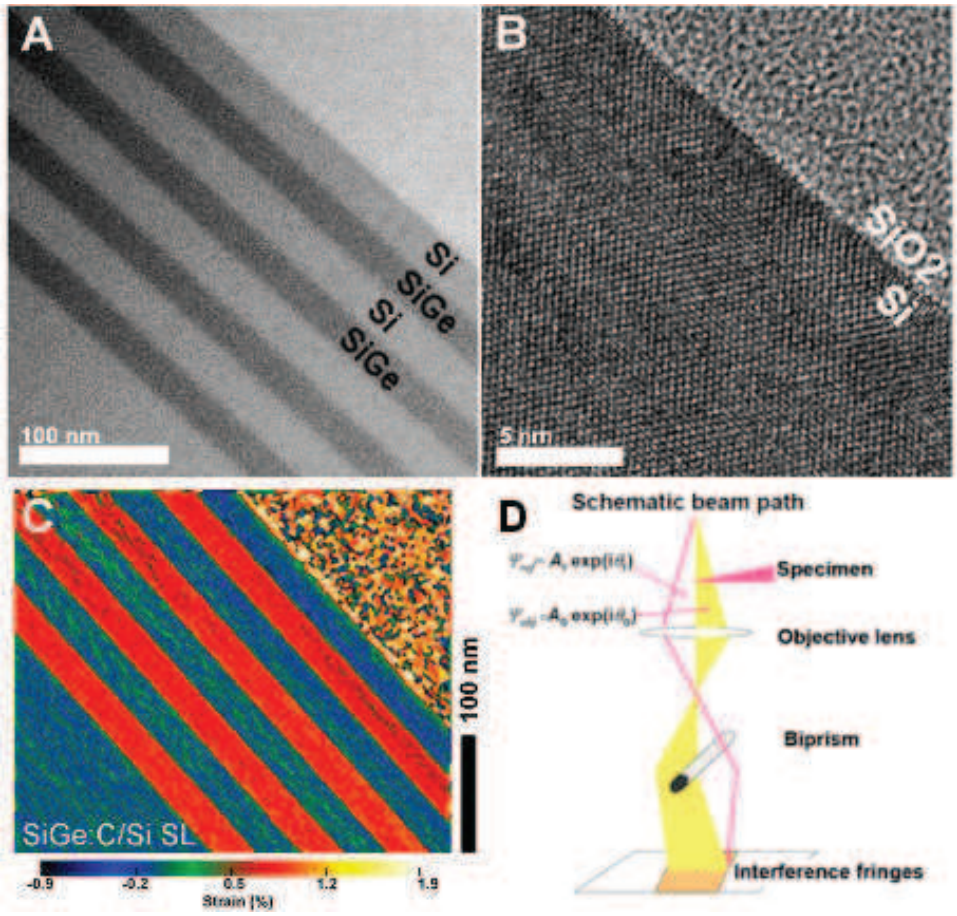

Figure II.14.A Bright field TEM image of a Si/SiGe:C superlattice. Ge containing zones appear darker. The brightest zone, in the top right corner, corresponds to a low density oxide deposited prior to lamella preparation for the purpose of measurement.

B HRTEM imaging of the oxide/silicon interface of the same sample than in A. Crystallographic organisation of Si is clearly visualised, in contrast with amorphous Si where atoms are disordered. The interface between both materials is seen as perfectly sharp (inferior to a monolayer).

C Strain mapping of the same sample obtained by Dark Field Electron Holography. Si zones appear as unstrained, while SiGe layers are compressively strained.

D Schematic representation of the instrumental setup for electron holography measurements.

The image is therefore greatly influenced by the complex modulus of the electron waves [36-37]. Complex phase retrieval is the basis of phase contrast TEM, also known as High Resolution TEM (HRTEM), and allows investigation of crystal structure because of its lateral resolution, inferior to the lattice parameter. Depending on the orientation of the specimen relative to the electron beam, atomic columns (crystallographic arrangement), stacking faults and dislocations can therefore be imaged. An example of HRTEM imaging is given in Figure II.14.B. Another way of making use of the phase modification of electron waves passing through a sample is electron holography. TEM allows, by superposition of a coherent reference wave, and of waves which underwent phase modification by going through a specimen, to record holograms, from which the image wave can be completely reconstructed in amplitude and phase. The specimen is thus quantitatively described by two separate images: one representing the amplitude, the other the phase. From the amplitude image one can perform “conventional” TEM imaging; while from the phase image, electric and magnetic

fields, but also sample strain state can be quantitatively determined (provided that beams pass through a reference sample at the same time) [38-41]. An example of strain mapping obtained via electron holography technique is displayed in Figure II.14.C. Lastly, due to inelastic collisions between electrons from the beam and electron clouds of the specimen's atoms, the original electron beam loses some of its energy by going through the sample. Different elements, having different electronic layer filling will therefore yield different energy losses in the beam after the sample. Although this usually results in chromatic aberration, it can also be used to obtain laterally resolved information on the elemental composition of a sample by recording the electron beam energy loss. This technique is thus called Electron Energy Loss Spectroscopy (EELS) [42]. However, due to its high detection limit (~10^{19} at.cm^{-3} for As in Si), the impossibility to monitor crucial elements such as boron or phosphorous (the energy loss provoked by B being too low and the ionisation level of P being too close to that of Si), this technique will only be used for monitoring of major matrix element in this study. The spatial resolution in this mode being reduced to ~2 nm, this technique couldn't either be applied to the quantitative analysis of ultra-thin layers.

These techniques necessitate heavy sample preparation in order to obtain either thin parallel sided lamellae of between a few tens to a few hundreds of nanometres width, or ultra thin bevels. The analysis quality being strongly dependent of the quality of sample preparation, only a few of these analyses were performed during this thesis work. Within these, we focused on obtaining the following information:

- Absolute layer thickness (quantitative)
- Interfacial roughness (quantitative)
- Layer stress mappings (quantitative)
- Layer composition in matrix elements (qualitative, quantitative in EELS)

Similarly to techniques presented in the two previous subsections, determination of layer thickness is a matter of prime interest to ensure accurate evaluation of ToF-SIMS sputter rates, or to serve as cross characterisation for a depth scale established via other means. Direct determination of interfacial roughness by TEM also helps in the interpretation of depth profile broadening effects due to roughness pile-up phenomena. Otherwise, stress mapping gives complementary information and provides understanding on the structural properties of some samples (such as strained samples undergoing annealing) which ToF-SIMS alone could not.

II. 4. d- Atomic Force Microscopy (AFM)

AFM is a popular near-field technique for high resolution non destructive measurement of surface topography. The principle is based on the mechanical interaction of an atomically sharp tip at the end of a flexible cantilever with the sample surface. At nanoscale, different kinds of interacting forces can be probed depending on the tip-surface distance. The main attractive interactions are induced by electrostatic, capillarity and Van der Waals forces while the repulsive interaction is dominated by elastic forces that arise due to surface indentation. Basically, these result in a repulsive contribution proportional to L^{-3} and an attractive contribution proportional to L^{-2}, L being the tip-sample surface distance.

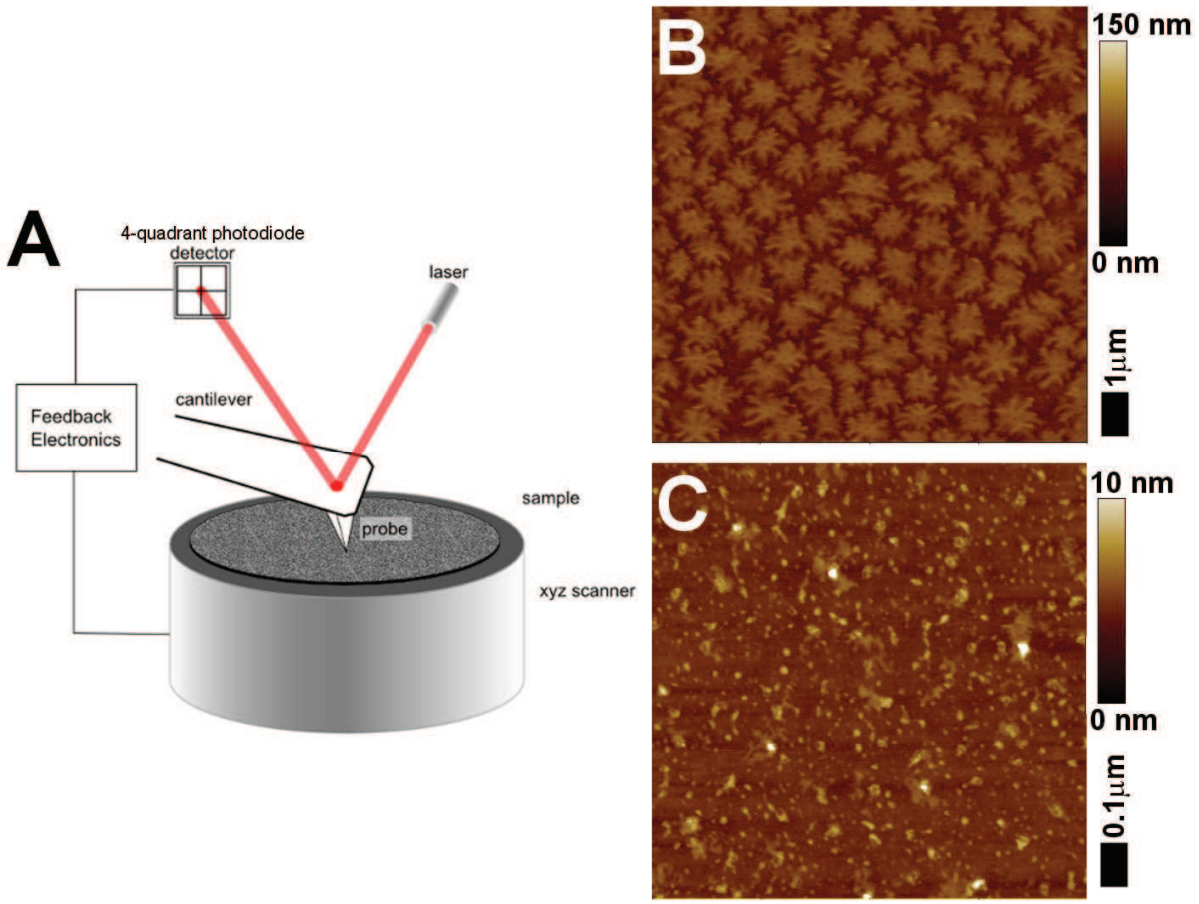

Figure II.15.A Schematised AFM instrumentation setup [43].

B 10 µm × 10 µm AFM topography mapping of PMMA irradiated with 250 eV Cs+ ions to a dose of ~5×10^{16} at/cm^2.

C 1 µm × 1 µm AFM topography mapping of a Si after removal of thick silicon oxide layer lying on top with HF.

A detailed review of such tip-surface interactions along with a consistent compilation of the intervening forces can be found in [44]. Therefore, when the tip approaches the surface, it will be either attracted or repulsed by it, depending on the tip-surface distance. The principle of AFM, as roughly schematized in Figure II.15.A [43], is to have a tip attached to the free extremity of a micrometric cantilever and to approach a sample surface with the whole system. In AFM techniques, two modes can be used: the contact mode (not discussed here) and the dynamic mode (Tapping®). In this latter mode, the cantilever is mechanically driven by a piezo-electric actuator, very close to its resonance frequency with an oscillation amplitude of several nanometres. During an oscillation, the tip undergoes intermittent contacts with the surface of the sample, hence this mode is known as the intermittent contact mode or Tapping mode. Therefore, in every cantilever oscillation period, the tip traverses both the attractive and repulsive force regimes. The oscillation amplitude is monitored by a lock-in amplifier via an optical detection of a laser beam reflected on the backside of the cantilever. In the so-called tapping mode measurement, a setpoint amplitude (smaller than the free oscillation amplitude) is kept constant through a feed-back loop. The tip is then scanned over the sample surface over square surfaces of between a few hundred nanometres and a few micrometers width using piezoelectric ceramic materials. The piezoelectric ceramic imposes a three dimensional displacement to the sample and the z-movement of the stage needed for accomplishing constant setpoint amplitude during x-y sweeping is monitored. From this one obtains an interaction map, which is translatable into a topographic map. The advantage of this mode is

that it reduces to a minimum the contact duration between the tip and the sample surface, avoiding modification of the sample morphology during analysis and deterioration of tip shape. This allows acquisition of topography maps on samples with either important topography up to a few hundreds of nanometres (by lowering surface sensitivity) or very flat surfaces (by increasing surface sensitivity). Examples of such maps are shown in Figure II.15.B and C, respectively.

Since AFM is able to provide accurate (although on a small lateral scale when compared to ToF-SIMS craters) topography mapping of a sample surface it can be used to obtain crucial parameters such as surface Root Mean Square (RMS) or peak-to-valley roughness. It can also be used to obtain a qualitative description of surface features (intended or not) and compare different samples and/or experiments. In particular, this kind of studies can be performed prior to ToF-SIMS analysis to simply investigate the surface roughness such as in Figure II.15.C, but also after analysis to assess sputter induced morphology in the sputter crater such as in Figure II.15.B. To summarise, the information of interest for us are:

- Surface RMS roughness (quantitative)
- Surface morphology (qualitative)

As explained in the previous chapter, the quality of a ToF-SIMS depth profile will strongly depend on the sample's surface state. Information such as RMS roughness of a sample can therefore be extremely useful to understand the features of a depth profile, especially in samples with thin layers or numerous buried material interfaces. Similarly, such information is needed to assess the surface state after a sample preparation in order to ensure that the preparation went well. Furthermore, qualitative description of the surface morphology can be useful to understand the reaction of a given material to high doses of primary ions and investigate roughness build-up mechanisms.

II. 4. e- X-ray Photoelectron Spectroscopy (XPS)

When energetic photons go through a material, a small part will be absorbed following Beer's law. Three types of interactions can occur between these photons and the material: Compton scattering, creation of electron-hole pairs and emission of photoelectrons. Photoelectrons arise from the ionisation of an atom and are ejected from one of its core level. They bear the energy corresponding to the transition between the neutral atom's original state with Z electrons and its final, ionised state with $Z-1$ electrons. The emission of such photoelectrons occurs only if the energy of the incident photons is superior to the binding energy of the electron. This phenomenon is largely dominant for photon energies under ~100 keV, while the two other effects are more important at higher energies (above the MeV range). XPS uses laboratory AlKα X-Ray sources emitting around 1.5 keV to excite target atoms and induce the emission of photoelectrons, which kinetic energy is measured by an hemispherical analyzer. Given the (almost) unique energy signature of the core level transitions, an XPS energy spectrum is a direct indication of the sample's composition: each orbital of each different element can emit photoelectrons whose binding energy is known and tabulated [45]. An example of such spectra is given in Figure II.16.A [46]. This allows compositional analysis of a sample without matrix effects, via the use of sensitivity factors primarily dependent of the element's photo-ionisation cross section. An interesting feature is that small energy shifts of the range of a few eV are observed depending on the atom's environment. This energy shift reflects changes in the polarity of the atom's bonds with its atomic or molecular environment.

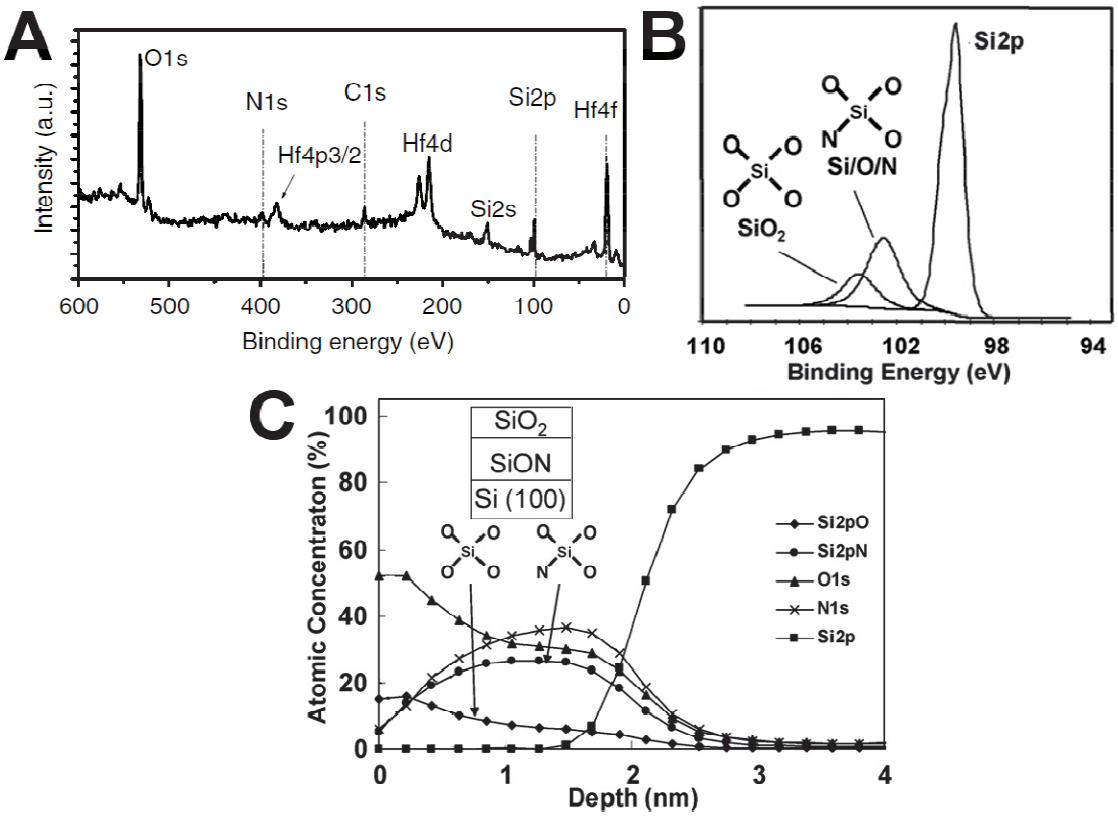

Figure II.16.A Wide scan XPS spectrum of a high-k material stack on a Si substrate. Each element present in the stack is detected by at least one peak corresponding to the best detected core level. Adapted from [46].

B Decomposition of the Si2p core level on a XPS spectrum of a SiON/Si sample. Apart from the main (substrate) peak, two other peaks corresponding to different bonding states are detected. This allows distinction of Si in SiO_2 from Si in SiO_xN_y by using chemical shifts. Adapted from [47].

C Chemical depth profiling obtained by AR-XPS of the same sample than in B. The distinction on the different chemical bonding states of Si is also observable in-depth. Adapted from [47].

As most of these energy shifts are already well identified and commented in literature for numerous applications [45, 48-50], this feature, far from being a hindrance, is extremely interesting. It indeed allows XPS to provide information not only on the sample composition, but also on the bonding states of the material. This is particularly useful in the study of heterogeneous material stacks, as illustrated in Figure II.16.B [47]. This figure represents the decomposition of the Si2p core level acquired on a SiON layer lying on a Si substrate. Although the peak is still dominated by the bulk related contribution (Si-Si bonds), one can clearly see two other peaks corresponding to an oxidised environment (O-Si-O) and to an oxy-nitridised environment (O-Si-N). The sampling depth of conventional XPS depends on parameters varying with the elemental composition of the sample, such as the mean free drift paths of the photoelectrons. XPS can be considered as a surface analysis technique, yielding information on the top ~10 nm of a sample, with most of the signal coming from the near-surface layers and little signal from the deeper layers. This value can be changed by adjusting either the photoelectron collection angle (grazing angles meaning shallower information depth) or directly the X-ray photon energy (however this requires the use of synchrotron radiation, as all laboratory sources are monochromatic). In order to obtain depth profiles one can either use ion beam induced sputtering (with inactive elements such as argon, in order to

conserve similar surface composition) or acquire spectra at different angles (so called Angle Resolved-XPS (AR-XPS)). The former inducing roughness, it might be preferred for rather thick samples, while the latter yields only (at maximum) information about the first 10 nm and is therefore preferred to study ultra thin samples [45]. An example of such depth profile is provided in Figure II.16.C [47]. Note that, in addition to quantitative elemental depth profiling, one also has access to the in-depth distribution of the different bonding states.

XPS is able to yield chemical information relative to the topmost surface layers of a sample. This information is easy to interpret through tabulated values (and abundant literature) and has few measurement artefacts. It yields quantitative layer composition for any element heavier than He (H having only 1 electron and He core level being extremely difficult to ionise), with an accuracy of ±20% and a detection limit of ~0.1 at% for light elements. It can also yield qualitative information on the bonding states of a given atom in a molecular or ionic environment. Lastly it can provide in-depth distribution of all these information via the use of ion beam sputtering (destructive, low depth resolution) or multiple angle acquisition (AR-XPS, non destructive, higher depth resolution). It is therefore a technique of great interest for the study of matrix elements in very thin layers. We will therefore focus on the acquisition of the following information:

- Surface layer chemical composition (quantitative)
- Surface layer bonding states (qualitative)
- In-depth matrix element composition (quantitative)
- In-depth bonding states (qualitative)

This information can be used in correlation with ToF-SIMS depth profiles to cross-characterise a sample. This will help assess the accuracy of ToF-SIMS analysis. It will also complete information obtained with ToF-SIMS with indications on bonding states which ToF-SIMS cannot provide. This might help understanding some effects observed on ionisation probabilities with ToF-SIMS by providing, for example, information about possible chemical changes in the atom's environment.

II. 4. f- Ion beam analysis techniques: energy loss spectrometry

When a beam of energetic, light element ions such as H^+, He^+, Ne^+ or Ar^+ irradiates a material, a proportion of the incident ions are backscattered upon collision with a target atom. The energy of the backscattered ions or neutrals is directly dependent on their mass, their initial energy, their scattering angle (which are all known parameters) and the mass of the target atom as specified by the theory of binary collision [51-52]. The measurement of this energy is therefore a direct indicator of the sample composition, free from matrix effects.

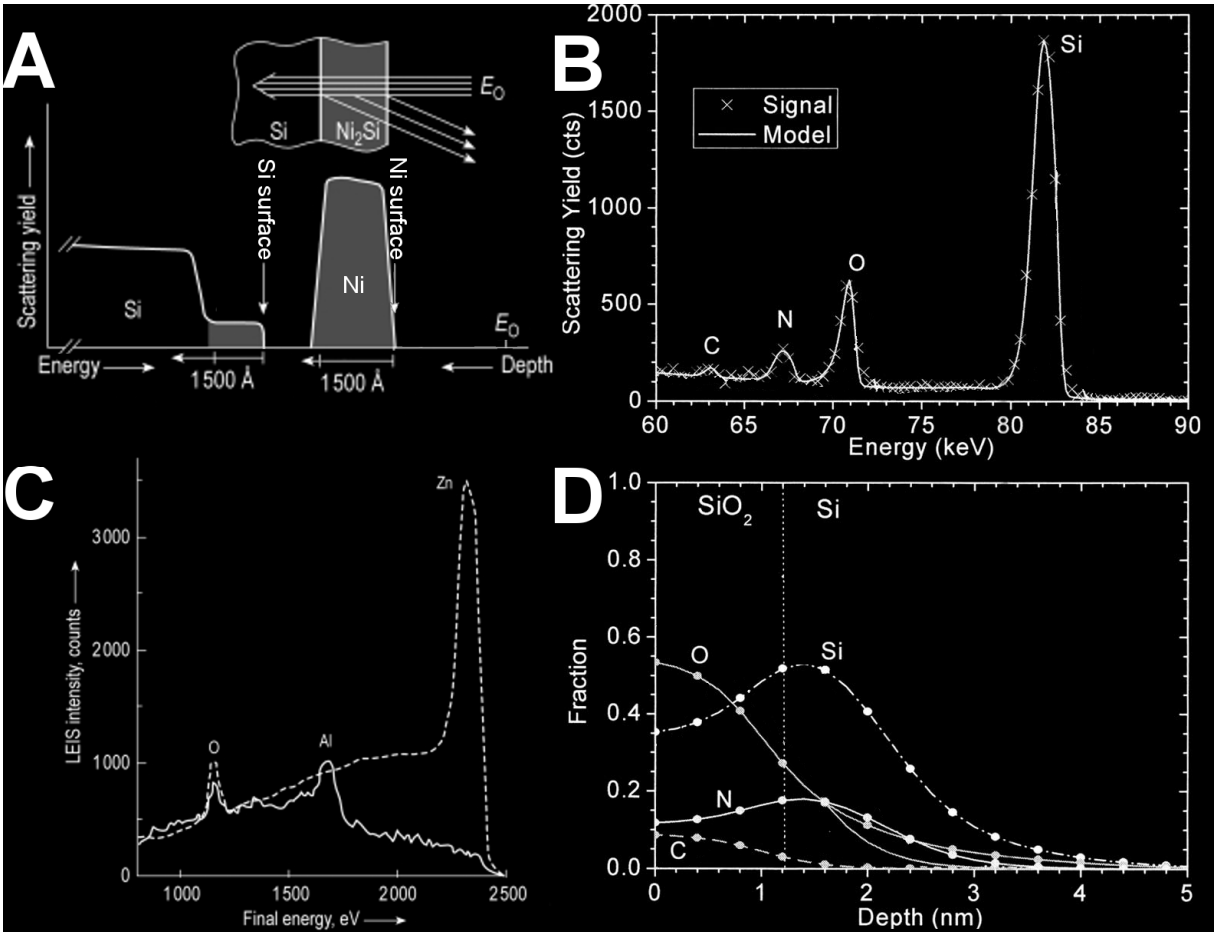

Figure II.17.A Schematic RBS spectra of a ~100 nm thick Ni_2Si film lying on a Si substrate in random angle conditions (no channeling or blocking) with ~MeV primary ions. The abscise axis is reversely graduated in energy, the highest energy possible for backscattered ions being E_0, the incident beam energy. Heavier elements appear on the right of the spectrum because of the higher energy of backscattered ions. Similarly, depth scale is always in opposition with energy scale since for a given element, ions backscattered in the bulk would loose more energy than ions backscattered at the surface. Adapted from [51].

B MEIS energy spectrum and model obtained on an ultra-thin SiON layer grown on a Si substrate. Experimental conditions were: 100 keV He^+ beam entering along the [−1−11] channel and the scattered ions being detected along the [111] blocking direction. This scattering configuration was chosen to provide an optimum between scattered yield per bombardment dose, depth, and mass resolution while still resolving peaks as low as C because of the low level of crystalline Si related counts. The effective near-surface depth resolution for these conditions is better than 0.8 nm, as determined from the slope of the leading edge of the Si peak recorded on a clean Si surface. Adapted from [53].

C LEIS energy spectra obtained with 3 keV He+ scattering on $ZnAl_2O_4$ spinel (solid line) and ZnO (dashed line). Zn is known to be unstable in $ZnAl_2O_4$ alloys and to segregate below the surface in the first sub-surface monolayer [54]. These two spectra show that although in ZnO, Zn is detected with a very high count rate, in the spinel it is almost undetected because shielded under a first Al- and O-rich monolayer, showing the extreme surface sensitivity of the LEIS technique. Extracted from [55].

D Depth profile reconstructed from MEIS spectrum in B. Depth distribution of all elements in random sites is obtained. This profile gives, in addition to absolute quantification of the elements in the surface oxide, an indication on the effect of process thermal budget on the quality of the Si substrate layers right below the oxide. Indeed in this configuration only interstitial Si can be detected in the crystalline Si substrate, and the Si peak situated right after the oxide layer indicates that the thermal oxide growth and/or nitridation step did inflict some

damage to the substrate. Adapted from [53].

Figure II.17.A [51] displays such a typical energy loss spectrum. Ions backscattered on heavier elements are more energetic because of the increased kinematic factor. This also implies that techniques based on light ion energy loss are significantly more sensitive to heavy elements than to light ones, given the reduced probability to yield backscattered ions on elements of lower atomic number. Furthermore, ions lose energy via interactions with the material's electronic cloud (electronic stopping power, see chapter I) when they penetrate in the bulk and (if they are backscattered) on their way back towards the surface. Therefore, such energy spectra also bear information on the sample's elemental distribution: the width of a peak is directly dependent of the film thickness and its density, while its shape reflects the elemental distribution. Consequently, peak area can be converted into total, absolute elemental dose in at/cm^2 and peak intensity into atomic concentration by taking into account the different cross sections. Due to the low probability of a backscattering event the detection limit reachable by such measurement is ~1 at% for light elements up to a few hundred ppm for heavy elements. Finally, by playing both on the incident beam angle (channeling) and on the angle of detection for backscattered ions (blocking), it is possible to change the amount and the nature of the atoms taken into account during analysis of crystalline materials. If the target atoms are regularly ordered, there are necessarily several incidence angles under which most of the primary ions will mostly encounter only empty zones between two atomic columns, therefore reducing backscattered ions to a minimum. Similarly, there are also necessarily several backscattering angles under which ions backscattered in the bulk will be occulted by atomic columns and do not reach the detector. Therefore, by adjusting the channeling and blocking conditions, one is able to detect the position of a given set of atoms in a crystalline lattice (substitutional or interstitial) as well as the potential faults within the lattice itself. The analysis of such spectra is thus very interesting for quantitative material analysis. Numerous techniques are based on such analysis, out of which we can cite RBS, Medium Energy Ion Scattering (MEIS) and Low Energy Ion Scattering (LEIS) which were used in this study, and Elastic Recoil Detection Analysis (ERDA) which was not used. Each of these techniques features specificities inherited from instrumental setups: RBS and ERDA use beams of 0.4 to 2.5 MeV and analysis of high (low) backscattered angle ions for RBS (ERDA). Using forward recoil scattering (at low scattering angles) allows the detection of light elements (compared to the incident ion mass). This feature of ERDA helps improve the detection limit of light elements, extremely difficult to detect in RBS due to the low backscattering energy and the weak cross section. Otherwise, MEIS uses beams of 0.05 to 0.4 MeV while LEIS uses beams of a few keV. As one can imagine, the main difference between these techniques will therefore be the depth of information and depth resolution. As conventional RBS or ERDA instruments yield a depth of information of a few hundred nanometres with a depth resolution of ~10 nm (see Figure II.17.A [51]), MEIS has high depth resolution (0.3 nm) for a depth of information of 10 nm maximum (see Figure II.17.B and D [53]). Notice that High resolution RBS (HRBS) also exists, although recent and not widespread [56]. They yield resolution of ~0.1 nm for a depth of information equivalent to that of MEIS. On the other hand, LEIS uses an energy too low to yield bulk signal for most of the elements except for the heaviest ones (see Figure II.17.C [55]) and can therefore be considered as a technique only sensitive to the first one or two atomic layers. For the latter, depth profiles cannot be acquired by a simple energy spectra and one has to resort to sample abrasion such as with XPS. For more comprehensive reviews of the theoretical and practical aspects on these techniques please consult [57-58] and references therein.

As we have seen, there are various techniques using measurement of the energy loss during light ion backscattering. These techniques present the interest of being quantitative and not subject to matrix effect for major elements (in contrast to ToF-SIMS) and depth resolved in some particular cases. We will therefore focus on the acquisition of the following information:

- Absolute layer thickness measurement (quantitative)
- Absolute elemental dose measurement (quantitative)
- Matrix element depth profiling (quantitative)
- Interstitial/substitutional atoms distribution (quantitative)

Once again, this information can be used in correlation with ToF-SIMS depth profiles to cross-characterise a sample. This will help assess the accuracy of ToF-SIMS analysis. It will also complete information obtained with ToF-SIMS with indications the position of the different atoms inside the crystalline lattice.

II. 4. g- Simulation

The physics behind microelectronics processes is nowadays sufficiently well known and documented to be accurately simulated in a number of situations. Out of these, ion implantation and diffusion processes in crystalline matter (mainly silicon) are particular fields of focus (see [59] and references within). Various models were developed and are available, explaining the physical mechanisms behind the process itself and verified with experimental data. These mathematical models are often used for design of devices in an optimal way with respect to several criteria and in identifying relevant material properties (see for example [60-62]). The quantity to be identified or optimised is the dopant depth distribution, the junction depth, the damage inflicted to the substrate during ion implantation processes; and the amount of diffused atoms along with characteristic diffusion parameters. Also of interest is the profile shape before and after annealing. The former can be obtained using Monte Carlo simulation models such as TRIM or Crystal-TRIM [63]. An example of depth profile obtained with Crystal TRIM is displayed in Figure II.18.A. Simulation of diffusion is more complex, since it is strongly dependent on element-, matrix- and environmental specific behaviours such as for instance pairing mechanism (with either vacancies or interstitials), solid solubility in various matrixes and ambient atmosphere (oxidising, wet or dry…). However the physical process itself can always be assimilated to a Fickian mechanism with Arrhenius-like diffusion coefficients [59] including these elemental-, matrix- and environmental-dependent specificities. For example let us consider intrinsic or doped SiGe heterostructures with complex geometries and strain configurations in the nanometric or deca-nanometric scale. The spatial (one dimensional) distribution of both alloy composition and dopants depend on Si, Ge and dopant diffusion upon thermal budget, which are, in turn, determined by the diffusion of point-defects (vacancies and interstitials). The phenomenology of these diffusion processes in SiGe structures can be very complex. In SiGe alloys the lattice parameter is a function of the Ge composition, which implies strain and therefore coupling of strain and compositional effects on diffusion. The diffusion behaviour of such structures upon annealing can be simulated with complete software such as S-Process [64] allowing the user to implement his own parameters to the classical diffusion equations. Ge profiles in SiGe:C/Si superlattices after annealing obtained through use of S-Process are presented in Figure II.18.B.

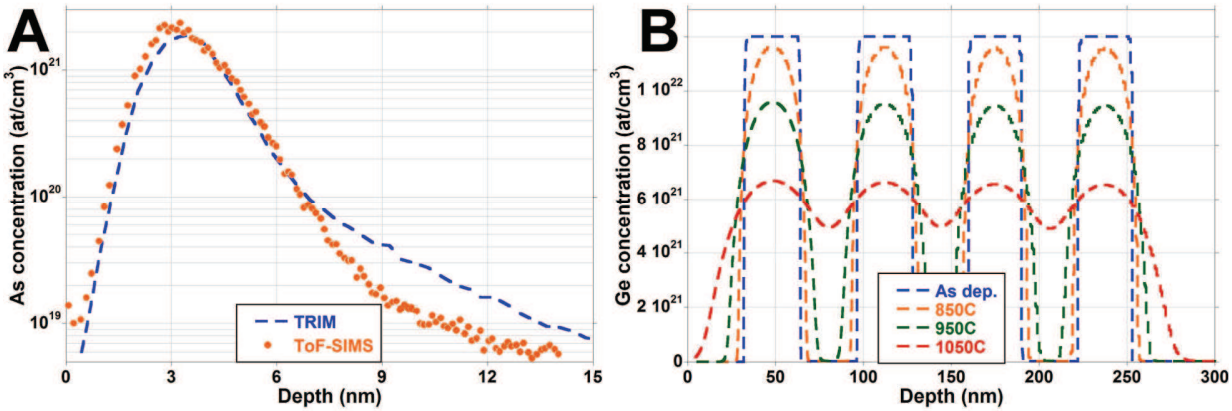

Figure II.18.A C-TRIM and ToF-SIMS profile of a 1 keV, 5×10^{14} at/cm^2 As implant in (110) Si with a tilt of 7 degrees relative to sample surface normal. ToF-SIMS profile was obtained with 250 eV Cs^+ for sputtering and 25 keV Bi^+ for analysis.

B Ge concentration profiles of a four-period SiGe:C/Si superlattice sample annealed for 2 minutes in inert atmosphere at 850, 950 and 1050C obtained with S-Process.

Various models can be applied to the simulation of semiconductor processes. They yield an extremely rich panel of information out of which only the extraction of physical parameters is of use in our study. Furthermore, although in actual nanometric devices three dimensional effects are observed, in full sheet structures in which those can be negligible. We are thus interested in the acquisition of the following, one dimensional information:

- Junction depth and dopant profile (quantitative)
- Major elements distribution after annealing (quantitative)
- In-depth stress distribution (quantitative)

This information can be used in correlation with ToF-SIMS (or any other technique) depth profiles to cross-characterise a sample. This will help assess the accuracy of ToF-SIMS analysis. It will also bring physical comprehension of some of the phenomena observed in ToF-SIMS profiles, such as chemically- or strain-enhanced diffusion behaviours.

CHAPTER II Conclusion

In this chapter we comprehensively reviewed all the solutions used in this thesis work to enhance the quality of a ToF-SIMS analysis. These are either specific to a particular kind of sample or can be applied to any kind of material and structures. Particularly data treatment and comparison with other techniques will be widely used in the following applicative chapters. Although for clarity each option was treated separately in this chapter, in reality they were used together in order to meet the characterization needs. In the next chapters we will therefore describe the practical setup of those measures in the different materials and structures presented in chapter I, the improvements they could bring and the interpretation of the improved ToF-SIMS measurements in terms of material science and device process understanding.

REFERENCES

[1] C. Hongo, M. Tomita and M. Takenaka, *Accurate Depth Profiling for Ultra-Shallow Implants Using Backside-Sims*, Appl. Surf. Sci., 231-232 (**2004**) 673-677.
[2] M. Medvedeva, I. Wojciechowski and B.J. Garrison, *Effect of Mass and Incidence Angle of Kev Energy Polyatomic Projectiles in Silicon Sputtering*, Surf. Sci., 505 (**2002**) 349-357.
[3] G. Nagy and A.V. Walker, *Enhanced Secondary Ion Emission with a Bismuth Cluster Ion Source*, Int. J. Mass Spectrom., 262 (**2007**) 144-153.
[4] G. Nagy, L. Gelb and A. Walker, *An Investigation of Enhanced Secondary Ion Emission under Aun+ (N=1–7) Bombardment*, J. Am. Soc. Mass Spectrom., 16 (**2005**) 733-742.
[5] S. Harper and K.D. Krantzman, *Molecular Dynamics Simulations to Explore the Role of Mass Matching in the Kev Bombardment of Organic Films with Polyatomic Projectiles*, Appl. Surf. Sci., 231-232 (**2004**) 44-47.
[6] J. Samela and K. Nordlund, *Emergence of Non-Linear Effects in Nanocluster Collision Cascades in Amorphous Silicon*, New Journal of Physics, 10 (**2008**) 023013.
[7] D. Wells, H. Moon and J. Gardella, *Time of Flight Secondary Ion Mass Spectrometric Determination of Molecular Weight Distributions of Low Polydispersity Poly(Dimethyl Siloxane) with Polyatomic Primary Ions*, J. Am. Soc. Mass Spectrom., 20 (**2009**) 1562-1566.
[8] A.R. Chanbasha and A.T.S. Wee, *Ultralow-Energy Sims for Shallow Semiconductor Depth Profiling*, Appl. Surf. Sci., 255 (**2008**) 1307-1310.
[9] J. Brison, R.G. Vitchev and L. Houssiau, *Cesium/Xenon Co-Sputtering at Different Energies During Tof-Sims Depth Profiling*, Nucl. Instrum. Meth. B, 266 (**2008**) 5159-5165.
[10] K. Wittmaack, *Secondary Ion Yield Variations Due to Cesium Implantation in Silicon*, Surf. Sci., 126 (**1983**) 573-580.
[11] Z.X. Jiang and P.F.A. Alkemade, *The Surface Transient in Si for Sims with Oblique Low-Energy O2+ Beams*, Surf. Interface Anal., 27 (**1999**) 125-131.
[12] T. Grehl, R. Möllers and E. Niehuis, *Low Energy Dual Beam Depth Profiling: Influence of Sputter and Analysis Beam Parameters on Profile Performance Using Tof-Sims*, Appl. Surf. Sci., 203-204 (**2003**) 277-280.
[13] B. Berghmans, B. Van Daele, L. Geenen *et al.*, *Cesium near-Surface Concentration in Low Energy, Negative Mode Dynamic Sims*, Appl. Surf. Sci., 255 (**2008**) 1316-1319.
[14] S. Krivec, T. Detzel, M. Buchmayr and H. Hutter, *On the Temperature Dependence of Na Migration in Thin Sio2 Films During Tof-Sims O2+ Depth Profiling*, Appl. Surf. Sci., 257 (**2010**) 25-32.
[15] C.M. Mahoney, A.J. Fahey, G. Gillen, C. Xu and J.D. Batteas, *Temperature-Controlled Depth Profiling of Poly(Methyl Methacrylate) Using Cluster Secondary Ion Mass Spectrometry. 2. Investigation of Sputter-Induced Topography, Chemical Damage, and Depolymerization Effects*, Anal. Chem., 79 (**2006**) 837-845.
[16] M. Barozzi, D. Giubertoni, M. Anderle and M. Bersani, *Arsenic Shallow Depth Profiling: Accurate Quantification in Sio2/Si Stack*, Appl. Surf. Sci., 231-232 (**2004**) 632-635.
[17] S.G. Simakin and V.K. Smirnov, *The Features of Using of Bo2- Secondary Ions for Sims Depth Profiling of Shallow Boron Implantation in Silicon*, Appl. Surf. Sci., 203-204 (**2003**) 314-317.
[18] H. Gnaser, *Improved Quantification in Secondary-Ion Mass Spectrometry Detecting Mcs+ Molecular Ions*, J. Vac. Sci. Technol. A, 12 (**1994**) 452-456.
[19] Y. Gao, *A New Secondary Ion Mass Spectrometry Technique for Iii-V Semiconductor Compounds Using the Molecular Ions Mcs+*, J. Appl. Phys., 64 (**1988**) 3760-3762.
[20] M.A. Ray, J.E. Baker, C.M. Loxton and J.E. Greene, *Quantitative Analysis and Depth Profiling of Rare Gases in Solids by Secondary-Ion Mass Spectrometry: Detection of (Csr)[Sup +] Molecular Ions (R=Rare Gas)*, J. Vac. Sci. Technol. A, 6 (**1988**) 44-50.
[21] M. Gavelle, E. Scheid, F. Cristiano *et al.*, *Detection of Cs2ge+ Clusters for the Quantification of Germanium Atoms by Secondary Ion Mass Spectrometry: Application to the Characterization of Si1-Xgex Layers (0 <= X <= 1) and Germanium Diffusion in Silicon*, J. Appl. Phys., 102 (**2007**).

[22] D. Marseilhan, J.P. Barnes, F. Fillot, J.M. Hartmann and P. Holliger, *Quantification of Sige Layer Composition Using Mcs+ and Mcs2+ Secondary Ions in Tof-Sims and Magnetic Sims*, Appl. Surf. Sci., 255 (**2008**) 1412-1414.
[23] Z.X. Jiang, K. Kim, J. Lerma *et al.*, *Quantitative Sims Analysis of Sige Composition with Low Energy O2+ Beams*, Appl. Surf. Sci., 252 (**2006**) 7262-7264.
[24] S. Ferrari, M. Perego and M. Fanciulli, *Characterization of Gate Oxynitrides by Means of Time of Flight Secondary Ion Mass Spectrometry and X-Ray Photoelectron Spectroscopy. Quantification of Nitrogen*, J. Vac. Sci. Technol. A, 20 (**2002**) 616-621.
[25] M. Perego, S. Ferrari and M. Fanciulli, *Negative Cluster Emission in Sputtering of Si1-Xgex Alloys: A Full Spectrum Approach*, Surf. Sci., 599 (**2005**) 141-149.
[26] J.F. Woitok, *Application of X-Ray Scattering Methods to the Analysis of Si-Based Heterostructures*, Thin Solid Films, 450 (**2004**) 138-142.
[27] D.G. Stearns, *The Scattering of X Rays from Nonideal Multilayer Structures*, J. Appl. Phys., 65 (**1989**) 491-506.
[28] J.M. Hartmann and Et Al., *Gas-Source Molecular Beam Epitaxy of Sige Virtual Substrates: Ii. Strain Relaxation and Surface Morphology*, Semicond. Sci. Technol., 15 (**2000**) 370.
[29] J.M. Fernández, L. Hart, X.M. Zhang *et al.*, *Silicon/Silicon-Germanium Multiple Quantum Wells Grown by Gas-Source Molecular Beam Epitaxy: Hydrogen Coverage and Interfacial Abruptness*, J. Cryst. Growth, 164 (**1996**) 241-247.
[30] J.M. Hartmann, A. Abbadie, D. Rouchon *et al.*, *Structural Properties of Tensile-Strained Si Layers Grown on Si1-Xgex Virtual Substrates (X = 0.2, 0.3, 0.4 and 0.5)*, Thin Solid Films, 516 (**2008**) 4238-4246.
[31] P.M. Mooney and J.L. Jordan-Sweet, *High Resolution X-Ray Diffraction Applied to Strain Relaxation of Lattice Mismatched Semiconductor Films*, JCPDS-International Centre for Diffraction Data, (**1999**).
[32] H. Fujiwara, *Spectroscopic Ellipsometry: Principles and Applications*, New-York, **2007**.
[33] L.D. Broglie, *Recherches Sur La Théorie Des Quanta (Researches on the Quantum Theory)*, Ann. Phys. (Paris), 3 (**1925**) 22.
[34] R. Heintzmann and G. Ficz, *Breaking the Resolution Limit in Light Microscopy*, Briefings in Functional Genomics & Proteomics, 5 (**2006**) 289-301.
[35] B. Fultz and J. Howe, *Transmission Electron Microscopy and Diffractometry of Materials*, Springer, **2007**.
[36] E. Kirkland, *Advanced Computing in Electron Microscopy*, Springer, **1998**.
[37] D.B. Williams and C.B. Carter, *Transmission Electron Microscopy: A Textbook for Materials Science*, Plenum Press, New-York, London, **1996**.
[38] M. Hytch, F. Houdellier, F. Hue and E. Snoeck, *Nanoscale Holographic Interferometry for Strain Measurements in Electronic Devices*, Nature, 453 (**2008**) 1086-1089.
[39] D. Cooper, J.-P. Barnes, J.-M. Hartmann, A. Beche and J.-L. Rouviere, *Dark Field Electron Holography for Quantitative Strain Measurements with Nanometer-Scale Spatial Resolution*, Appl. Phys. Lett., 95 (**2009**) 053501.
[40] M.J. Hÿtch, E. Snoeck and R. Kilaas, *Quantitative Measurement of Displacement and Strain Fields from Hrem Micrographs*, Ultramicroscopy, 74 (**1998**) 131-146.
[41] H. Lichte and M. Lehmann, *Electron Holography—Basics and Applications*, Reports on Progress in Physics, 71 (**2008**) 016102.
[42] R.F. Egerton, *Electron Energy-Loss Spectroscopy in the Electron Microscope*, Springer, **1996**.
[43] P. Eaton and P. West, *Atomic Force Microscopy*, Oxford University Press, Oxford, **2010**.
[44] J.N. Israelachvili, *Intermolecular and Surface Forces*, Academic Press, New York, 2nd edition, **1992**.
[45] D. Briggs and J.T. Grant, *Surface Analysis by Auger and X-Ray Photoelectron Spectroscopy*, IM Publications and SurfaceSpectra Limited, **2003**.
[46] L. Sygellou, S. Ladas, M.A. Reading *et al.*, *A Comparative X-Ray Photoelectron Spectroscopy and Medium-Energy Ion-Scattering Study of Ultra-Thin, Hf-Based High-K Films*, Surf. Interface Anal., 42 (**2010**) 1057-1060.

[47] C.R. Brundle, G. Conti and P. Mack, *Xps and Angle Resolved Xps, in the Semiconductor Industry: Characterization and Metrology Control of Ultra-Thin Films*, J. Electron Spectrosc., 178-179 (**2010**) 433-448.
[48] K. Siegbahn, C. Nordling, A. Fahlman *et al.*, *Esca, Atomic Molecular and Solid State Structure Studied by Means of Electron Spectroscopy*, Almquist and Wiksells, Uppsala, **1967**.
[49] D.A. Shirley, *Esca*, John Wiley & Sons, Inc., **2007**.
[50] H. Basch, *Theoretical Models for the Interpretation of E.S.C.A. Spectra*, J. Electron Spectrosc., 5 (**1974**) 463-500.
[51] L.C. Feldmann and J.W. Mayer, *Fundamentals of Surface and Thin Film Analysis*, North Holland, New York, **1986**.
[52] J.A. Leavitt, L.C. Mcintyre and M.R. Weller, *Hanbook of Modern Ion Beam Materials Analysis,* Materials Research Society, Pittsburgh, **1995**, pp. 37-81.
[53] M.A. Reading, J.A. Van Den Berg, P.C. Zalm *et al.*, *High Resolution Medium Energy Ion Scattering Analysis for the Quantitative Depth Profiling of Ultrathin High-K Layers*, J. Vac. Sci. Technol. B, 28 (**2010**) C1C65-C61C70.
[54] H.C. Yao and M. Shelef, *Nitric Oxide and Carbon Monoxide Chemisorption on Cobalt-Containing Spinels*, The Journal of Physical Chemistry, 78 (**1974**) 2490-2496.
[55] H.H. Brongersma and J.-P. Jacobs, *Application of Low-Energy Ion Scattering to Studies of Growth*, Appl. Surf. Sci., 75 (**1994**) 133-138.
[56] K. Kimura, S. Joumori, Y. Oota, K. Nakajima and M. Suzuki, *High-Resolution Rbs: A Powerful Tool for Atomic Level Characterization*, Nucl. Instrum. Meth. B, 219-220 (**2004**) 351-357.
[57] H. Bubert and H. Jenett, *Surface and Thin Film Analysis: Principles, Instrumentation, Applications*, Wiley-VCH Verlag, **2002**.
[58] C.R. Brundle, C.A. Evans and S. Wilson, *Encyclopedia of Material Characterization: Surfaces, Interfaces, Thin Films*, Buttetworth-Heinemann / Manning Publications Co., Greenwich, **1992**.
[59] S. Selberherr, *Analysis and Simulation of Semiconductor Devices*, Springer-Verlag, Wien, New-York, **1984**.
[60] M. Stockinger, R. Strasser, R. Plasun, A. Wild and S. Selberherr, *A Qualitative Study on Mosfet Doping Profiles,* SISPAD 98, (**1998**) 77-80.
[61] W. Fang and E. Cumberbatch, *Inverse Problems for Metal Oxide Semiconductor Field-Effect Transistor Contact Resistivity*, SIAM Journal on Applied Mathematics, 52 (**1992**) 699-709.
[62] P. Pichler, H. Ryssel, R. Ploss, C. Bonafos and A. Claverie, *Phosphorus-Enhanced Diffusion of Antimony Due to Generation of Self-Interstitials*, J. Appl. Phys., 78 (**1995**) 1623-1629.
[63] M. Posselt and J.P. Biersack, *Computer Simulation of Ion Implantation into Crystalline Targets*, Nucl. Instrum. Meth. B, 64 (**1992**) 706-710.
[64] *Synopsys Tcad Tools*.

CHAPTER III
Analysis of materials and structures for « 3D integration » multichannel transistors

In this chapter we will principally deal with the analysis of SiGe binary alloys materials. In addition these materials will feature varying dopant or impurity concentrations and might be surrounded by silicon dioxide. In order to match with structures encountered in actual devices, studies will be performed on full sheet, deca-nanometric layer stacks sometimes arranged in superlattices and with various annealing conditions. Given the thicknesses of the different layers, depth resolution is needed but not critical for the analysis, thus no attempt was performed to enhance depth resolution on these structures. However there is a strong need for accurate measurement of layer thicknesses because these will determine the final device properties such as channel width. Establishment of an accurate depth scale applicable to any of the structures described above is therefore a necessity. Moreover, Ge dose and depth distribution are parameters which require a precise control in those structures since they will determine the device electrical properties such as carrier mobilities but also physical properties such as strain level. ToF-SIMS being conventionally subject to heavy matrix effects in $Si_{1-x}Ge_x$ alloys with varying *x*, characterisation of such alloys by standard protocols can be difficult unless precaution is taken and well characterised reference samples used. The setup of an accurate Ge quantification protocol is thus required. In addition, the presence of high concentrations of dopants, impurity inside those layer or of surrounding oxides call for the establishment of measurement protocols specific to each case. In this chapter we will review the practical setup of all these, and show the improvements they brought in comparison with classic ToF-SIMS analysis. We will assess their accuracy using other characterisation techniques and simulation and use the analysis results to yield information and understand the physical processes encountered.

III. 1. Setup of a protocol for accurate measurement of *x* in $Si_{1-x}Ge_x$

As ToF-SIMS is very sensitive to matrix effects, quantification of Ge in these layers is hindered because RSFs required for calibration may not be constant as a function of Ge concentration. Solutions to this problem have been brought by following positive secondary MCs_n^+ ions with a Cs^+ primary ion beam, where M is the element of interest combined with one or two Cs atoms. Quantification of Ge concentration in SiGe using MCs_n^+ ions has already been shown at sputtering energies as low as 2 keV on both magnetic and ToF-SIMS instruments for Ge concentrations ranging from 0 to 85% [1]. With the development of low energy primary ion beams, this protocol even allows Ge quantification for very thin SiGe layers on both instruments [2, 3]. However one of its drawbacks is its very weak sensitivity to doping elements [4]. Similarly, Jiang *et al.* investigated both best experimental conditions and best secondary ion selection for accurate characterisation of Ge concentration in SiGe alloys with O_2^+ abrasion [5]. However while showing encouraging results this protocol is also limited by its low range of application in Ge concentration and by the impossibility of monitoring oxygen species. Relying on previous works by Perego *et al.* [6], we therefore developed a protocol to characterise SiGe layer composition in negative mode ToF-SIMS with Cs^+ sputtering, which allows simultaneous profiling of doping elements such as P, B or As. The practical setup of those three protocols was performed as follows.

For calibration means, we used a set of calibration samples which Ge concentration was obtained with XRD (± 0.1 at%) [7].

To obtain Ge concentration with the *Jiang et al.* protocol (i.e. with oxygen sputtering), we depth profiled the calibration samples, followed $^{30}Si^+$ and $^{70}Ge^+$ ions and fitted the average of the secondary ion intensity ratio $I(^{70}Ge^+)/I(^{30}Si^+)$ in the permanent regime to *x, x* being the Ge at% concentration obtained by XRD for each sample. We thus obtain a scaling factor α, which we use to calculate the Ge concentration at each point [5]:

$$[Ge]_{Jiang} = \frac{\alpha \cdot I(^{70}Ge^+)}{I(^{30}Si^+) + \alpha \cdot I(^{70}Ge^+)} \quad \text{(III.1)}$$

To obtain Ge concentration with the MCs protocol, we profiled all calibration samples, followed $SiCs_2^+$ and $GeCs_2^+$ ions and plotted the average of the secondary ion intensity ratio $I(GeCs_2^+)/I(SiCs_2^+)$ in permanent regime against *x/(100-x)*, *x* being the Ge at% concentration obtained by XRD for each sample. We thus obtain a calibration curve of slope *K*, which we use to calculate Ge concentration at each point [1]:

$$[Ge]_{MCs_2} = \frac{I(GeCs_2^+)/I(SiCs_2^+)}{K + I(GeCs_2^+)/I(SiCs_2^+)} \quad \text{(III.2)}$$

The two previous methods make use of only a few secondary ions out of the whole spectra provided by ToF-SIMS. In SiGe, the intensity of each $Si_nGe_m^-$ ion presents a different evolution with Ge content variation. This translates into non linear behaviour of each ion taken separately and overall secondary ion counts with Ge content. However, a linear dependence with Ge content is obtained by monitoring atomic quantities of Ge in the secondary ion beam instead of simply secondary ion counts [6]. This linearity might reveal proportionality between the secondary ion beam atomic content and the actual sample stoichiometry. To obtain the calibration curve of the full spectrum protocol we profiled all calibration samples and followed every negative secondary ion up to Ge_6^-.We then calculate the total quantity of Si and Ge atoms in the secondary ion beam Q_{total} using the following formula:

$$Q_{total} = \sum_{n=0}^{6}\sum_{m=0}^{6}(n+m)\cdot Y_{Si_nGe_m} \quad \text{(III.3)}$$

$Y_{Si_nGe_m}$ being the intensity of the $Si_nGe_m^-$ cluster ion divided by its isotopic abundance. Sums are performed only on secondary ions with sufficient intensity and without major mass interferences. For instance, $Si_3Ge_3^-$ is not intense enough to be taken into account; $Si_0Ge_2^-$ is otherwise detected as $^{70}Ge^{72}Ge^-$. The atomic fraction of Ge in the secondary ion beam T_{Ge}: can be deduced from (3) thanks to:

$$T_{Ge} = \frac{\sum_{n=0}^{6}\sum_{m=0}^{6} m \cdot Y_{Si_nGe_m}}{Q_{total}} \quad \text{(III.4)}$$

We then plot T_{Ge} against *x*, *x* being the at% Ge concentration of each sample as determined by XRD, to obtain a slope value *L*. Slope values obtained for the whole range of primary energies available in our instrument are displayed in Table III.i. One advantage of this

protocol is its excellent reproducibility: calibration does not need to be re-run over several months unless the instrument undergoes a major maintenance [8]. To allow comparison with XRD measurements (which give the *mean* Ge concentration of each layer) we average the $Y_{Si_nGe_m}$ values over at least 30 points in the steady state part of the profile. By plotting T_{Ge} against XRD determined at% Ge, an excellent linear correlation is obtained, as shown in Figure III.1, with a correlation factor R^2 superior to 0.995 at each energy, proving the quantitativity of the protocol over the whole concentration range concerned.

Sputter Energy (keV)	2	1	0.5	0.25	0.15
Calibration curve slope (Arb. Units)	0.9126	0.8912	0.8569	0.8006	0.7707

Table III.i Evolution of the slope value *L* with sputtering energy (±0.0025)

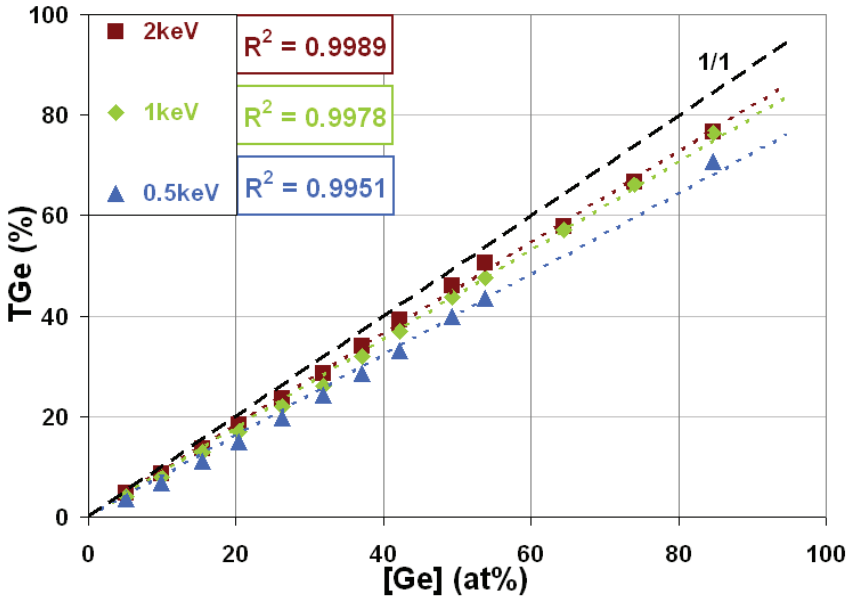

Figure III.1 T_{Ge} against [Ge] as determined by XRD. The black dotted curve represents a 1/1 perfect fit.

III. 2. Setup of a protocol for accurate measurement of dopant and O concentration profiles in $Si_{(1-x-y-z)}Ge_xO_yA_z$, A being a dopant or impurity

In O_2^+ abrasion mode, B profiling was carried out simultaneously with Ge profiling, following B^+ ions and using a reference implant in $Si_{0.5}Ge_{0.5}$. Due to low sensitivity, simultaneous profiling of P and C was not performed in this mode; and obviously oxygen concentration was not monitored either. Given the very weak sensitivity of the MCs protocol (especially when using a ToF-SIMS) to B as dopant [4] and to O, simultaneous profiling of these elements was therefore not performed. A correct sensitivity to C as CCs_2^+ and to P as PCs_2^+ is however achieved, allowing acquisition of quantitative C profiles using a simple C implant reference in Si and of P profiles using a P implant reference in SiGe, using the acquired RSFs.

A first version of Germanium depth profiles issued from the full spectrum protocol is obtained by dividing point by point values of T_{Ge} by *L* for each sample. As for dopants, depth profiles are obtained by using a RSF acquired with a known implant of each species, in $Si_{0.5}Ge_{0.5}$ for P and B and in Si for C. These profiles however take only partially advantage of the full spectrum protocol. Indeed its purpose is to switch from secondary ion quantities to

total atomic quantities in the secondary ion beam, which considerably reduces matrix effects and signal/noise ratio [8]. It would then be natural to extend the previous protocol to doping elements when they are present. These first versions of profiles which we will name $[Ge]_{FS}$ and $[A]_{FS}$, A being either B, P or C, will thus serve as references for those obtained with the extended Full Spectrum (extended FS) protocol which we will describe now. With this enhanced version of the full spectrum protocol, we calculate the total quantity of Si, Ge, O and dopant atoms (i.e. B, C and P) in the secondary ion beam Q'_{total} using the following formula:

$$Q'_{total} = \sum_{n=0}^{6}\sum_{m=0}^{6}\sum_{p=0}^{3}\sum_{q=0}^{4}(n+m+p+q)\cdot Y_{Si_nGe_mO_pA_q} \quad \text{(III.5)}$$

$Y_{Si_nGe_mO_pA_q}$ being the intensity of the $Si_nGe_mO_pA_q^-$ cluster ion divided by its isotopic abundance (same remark as for equation (III.3) concerning intensity and mass interferences). The atomic fractions of Ge and dopant in the secondary ion beam T'_{Ge} and T'_A: can be obtained from equation (III.5) using the following expression:

$$T'_{Ge} = \frac{\sum_{n=0}^{6}\sum_{m=0}^{6}\sum_{p=0}^{3}\sum_{q=0}^{4} m\cdot Y_{Si_nGe_mO_pA_q}}{Q'_{total}} \quad \text{(III.6)}$$

$$T'_{A} = \frac{\sum_{n=0}^{6}\sum_{m=0}^{6}\sum_{p=0}^{3}\sum_{q=0}^{4} q\cdot Y_{Si_nGe_mO_pA_q}}{Q'_{total}} \quad \text{(III.7)}$$

and similarly for the O fraction T'_O. Quantified profiles $[Ge]'_{FS}$ and $[A]'_{FS}$ are finally obtained by point by point multiplication of T'_{Ge} and T'_A by sensitivity factors (summarised in Table III.ii) chosen to fit $[Ge]_{FS}$ and $[A]_{FS}$ profiles in their permanent regime regions. T'_O is then quantified using a sensitivity factor obtained in pure SiO_2 (in average, 0.65). The last step of data treatment is the transformation of concentration values from at% to at/cm^3. This is done by applying the following formula which multiplies point by point layer density by the desired specie concentration:

$$[Z]_{at/cm^3} = (\rho_{Ge}\cdot[Ge]_{at\%}/100 + \rho_{Si}\cdot(1-[Ge]_{at\%}/100))\cdot[Z]_{at\%} \quad \text{(III.8)}$$

With ρ_{Ge} and ρ_{Si} the densities of pure Germanium and Silicon (ρ_{Ge} = 4.42×10^{22} at/cm^3, ρ_{Si} = 5.00×10^{22} at/cm^3 [9]). For SiO_2 we used a 6.6×10^{22} at/cm^3 density [10]. Layer stress is not taken into account at this step since its effect on layer density is still unclear as well as its variation with dopant nature and diffusion.

	SiGe	SiGe: B	SiGe: P	SiGe: C
Ge	1.5	1.45	1.45	1.5
Dopant	-	0.6	0.9	0.5

Table III.ii Sensitivity Factors (SF) for extended FS protocol. Smaller SF means better sensitivity. All SFs are close to unity, meaning that in the extended FS protocol matrix elements and impurities signals have similar total intensities, thus similar "detection" probabilities.

III. 3. Setup of a protocol for accurate measurement of thicknesses in SiGe and SiO_2

To ensure an accurate depth scale, experiments were done to assess the variation of the sputter rate in strained SiGe layers with Ge content from 0 to 55 at% and its reproducibility. Profiles of all calibration samples and of a Boron delta sample were taken with different current conditions and at several months of interval. SiGe Sputter Rate (SR) was calculated for each sample by positioning the SiGe/Si interface as determined from ToF-SIMS depth profiles at the layer thickness measured by XRR. Si SR was calculated by setting the depth of the first and second Boron peaks of the Boron delta sample as seen by ToF-SIMS to depths determined by HR-TEM (± 0.3 nm) [11]. The end of the SiGe layer was defined as the $[Ge]_{FS}$ half signal (and set equal to the thickness determined by XRR, as mentioned above). This protocol allows more precise determination of the interface, since the 50% intensity points of $[Si]_{FS}$ and $[Ge]_{FS}$ signals coincide, which is not the case for ionic signals such as $^{30}Si^-$ and $^{70}Ge^-$. This is also confirmed by recent works from Kim *et al.* for O_2^+ abrasion in SiGe [12].

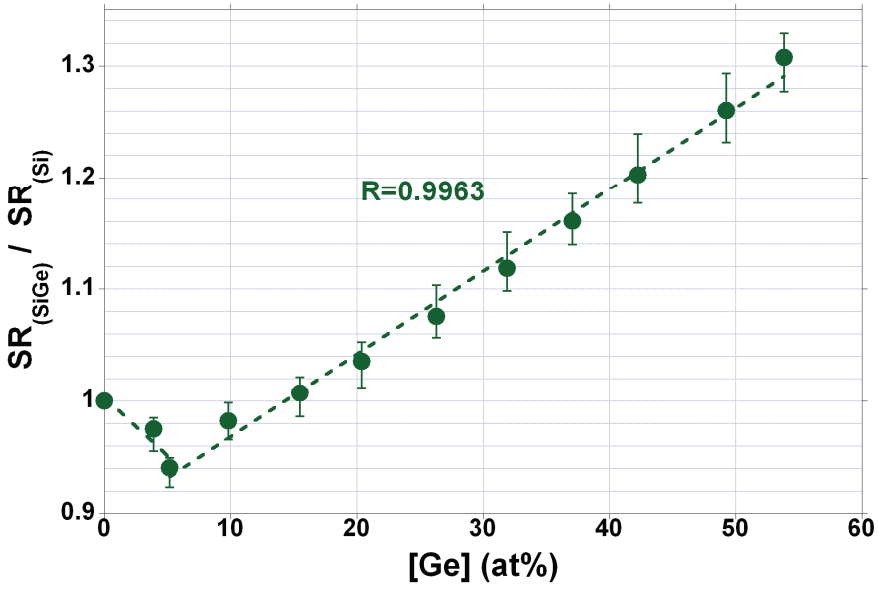

Figure III.2 Variation of the $SR_{(SiGe)}/SR_{(Si)}$ sputter rates ratio versus Ge content from 4 data sets obtained with different currents and at several months of interval. Divergence of experimental values (error bars) from their average (points) never exceeds 3.5 %.

The result of these experiments is presented in Figure III.2. Two distinct behaviours can be distinguished, below or above 5 at%. At first, the sputter rate falls. It then increases in a linear fashion up to 55 at%. This tendency was never reported before, neither for Cs^+ nor for O_2^+ abrasion. Only studies of SIMS sputter rate in *relaxed* SiGe can indeed be found in the literature, which always show a monotonous increase of the sputter rate when switching from pure Si to higher Ge content SiGe, this even for low Ge concentrations [1, 13]. Thus the sputter rate trend observed here is assumed to be directly related to the structural properties of the SiGe layers. Two different hypotheses can be proposed to explain this phenomenon. A first one would be that the compressive stress in the SiGe layers increases their local surface density compared to a relaxed layer of identical Ge content. This would induce an increase of the energy needed to break atomic bonds in the plane of analysis, which in turn would reduce the sputter rate compared to a relaxed layer. Another explanation would be that, as opposed to strained layers (pseudomorphic and thus defect-free), threading dislocations are present in relaxed layers. These dislocations might act as preferential sites for sputtering, which would then enhance the sputter rate of relaxed SiGe layers compared to strained ones of identical Ge

content. The usual threading dislocation density in state of the art relaxed SiGe layers is typically around 10^5 cm^{-2} [14]. This means that we have approximately 100 emerging dislocations in our 250×250 µm^2 sputter crater. Both hypotheses are therefore credible. The sputter rate on the entire range is simulated by two first degree polynomial functions which precisely fit experimental results as follows:

$$\begin{cases} x \leq 5 \Rightarrow SR_{(Si_{1-x}Ge_x)} = (-11.5 \cdot 10^{-2} x + 1) \cdot SR_{(Si)} \\ x > 5 \Rightarrow SR_{(Si_{1-x}Ge_x)} = (7.36 \cdot 10^{-3} x + 0.895) \cdot SR_{(Si)} \end{cases} \quad \text{(III.9)}$$

x being the at% Ge concentration. For each series of experiments, the Boron delta sample is profiled beforehand to determine the Si sputter rate. A variable sputter rate is then calculated at each point from equation (III.9) using *[Ge]'$_{FS}$* as the Ge concentration input. Doping elements such as C, B or P are assumed to have a negligible influence on the sputter rate. Using the same measurement protocols, similar behaviour of the sputter rate is observed under 1 keV O_2 bombardment. In addition, the sputter rate in SiO_2 was determined using a reference layer measured by spectroscopic ellipsometry. The difference in sputter rate between oxide and $Si_{1-x}Ge_x$ regions was accounted for using an erfc function running for ±2 nm around the interface (assumed to be at half O concentration point).

III. 4. Improvements brought by the proposed solutions applied to materials and structures representative of actual devices

In this section we will investigate the quality of the developed protocols in terms of ability to obtain simultaneous quantification of all major elements and impurities, reliability and accuracy. We will also compare the results obtained with the extended FS protocol to those obtained with more conventional ones such as the MCs and O_2^+ abrasion ones and with those obtained by complementary techniques.

III. 4. a- Accuracy of Ge concentration measurement in bulk of strained or relaxed single SiGe layers

For this study we needed SiGe layers of various compositions going through all the available alloy range and with different strain conditions in order to ensure that strain would not influence the ToF-SIMS quantification. Two types of samples were therefore used. The first consists of pseudomorphic SiGe layers of 20 nm minimum thickness with variable Ge concentration from 5% to 55% (5% increments) grown by Reduced Pressure-Chemical Vapour Deposition (RP-CVD) on Si(100) substrates [15]. The second is a step-graded SiGe virtual substrate grown at high temperature on a Si(100) substrate. In this sample, the Ge concentration is increased in steps towards the surface to form a staircase structure of 85, 75 and 65 at% Ge concentration (from top layer to bottom layer) in which each step is roughly 500 nm thick. The increment in Ge concentration between each step is low enough to have nearly fully relaxed crystalline layers with low misfit dislocation densities. A thick, linearly graded SiGe layer is grown first to reduce misfit dislocation densities and have nearly fully relaxed layers on top. The Ge concentration of the samples is determined thanks to the

Takagi-Taupin dynamical diffraction theory fitting of (004) high resolution rocking curve XRD ω-2θ curves to obtain the lattice parameter which, using a modified Vegard's law [9], is then converted to Ge concentration [16]. This method gives concentration with a precision of ± 0.1%.

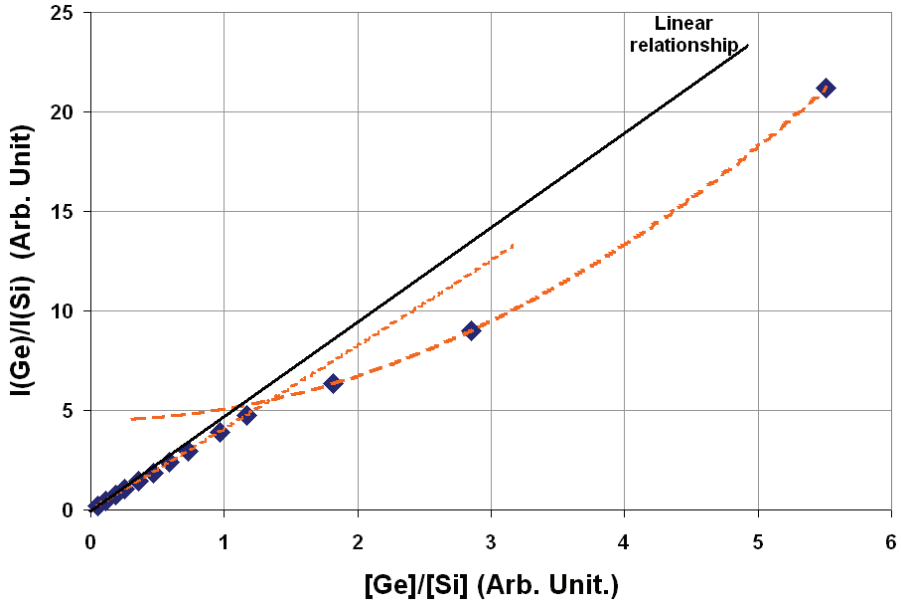

Figure III.3 Intensity ratio $^{70}Ge^-/^{30}Si^-$ obtained at 1 keV Cs+ sputtering. We observe deviation from a linear relationship from point [Ge]/[Si] = 0.5, i.e. ~33 at% Ge.

In a first approach, we tried to transpose the MCs method to negative mode analysis, i.e. to characterise Ge concentration by simple ion ratios. The advantage of such a method, if accurate, would consist in its ability to profile doping elements simultaneously. By plotting the intensity ratio of $^{70}Ge^-$ over $^{30}Si^-$ against XRD determined concentration ratio, we obtain a fairly linear approximation with R^2 values of 0.98 as shown in Figure III.3. However there are clearly two non-linear regimes observed and thus quantitativity is not guaranteed on the whole concentration range, or at least not using a simple linear approximation. The development of another measurement protocol is thus required. The full spectrum protocol that was presented in section III. 1 provides accurate Ge quantification in the permanent regime, as shown by Figure III.1, with linear behaviour or T_{Ge} against XRD determined concentrations for the whole range. Though, if we look closer at the curves displayed in Figure III.1, we observe that some points are not perfectly in agreement with their linear regression. However this induces a maximum error of only 1.5 at% Ge over the whole concentration range. Aside from this error, one of the major advantages of this protocol is that it averages the measurement error over more than twenty ion species, reducing it to less than 0.1% of the T_{Ge} value. Reproducibility tests were performed at different sputter currents and at several months of interval for each sputtering energy. They showed excellent results with no more than ±0.0025 variation in slope values, inducing less than ±0.25 at% Ge error over the total considered range. For comparison, variability of the I(Ge)/I(Si) calibration protocol over a day leads to ±1 at% Ge error over the same range. Thus a very interesting feature of the full spectrum protocol is that its calibration curves allow Ge quantification with a maximum 1.5 at% error on Ge concentration without requiring new calibration prior to each analysis. Another conclusion of the reproducibility tests is that sputter beam properties (current, crater size) at equal energy do not influence the composition of the secondary ion flux. However the analysis beam plays an important role in the composition of the secondary

beam. Indeed using Bi_3^+ instead of Bi^+ induces a significant decrease of the slope value, leading to an underestimation of the Ge content in the layer.

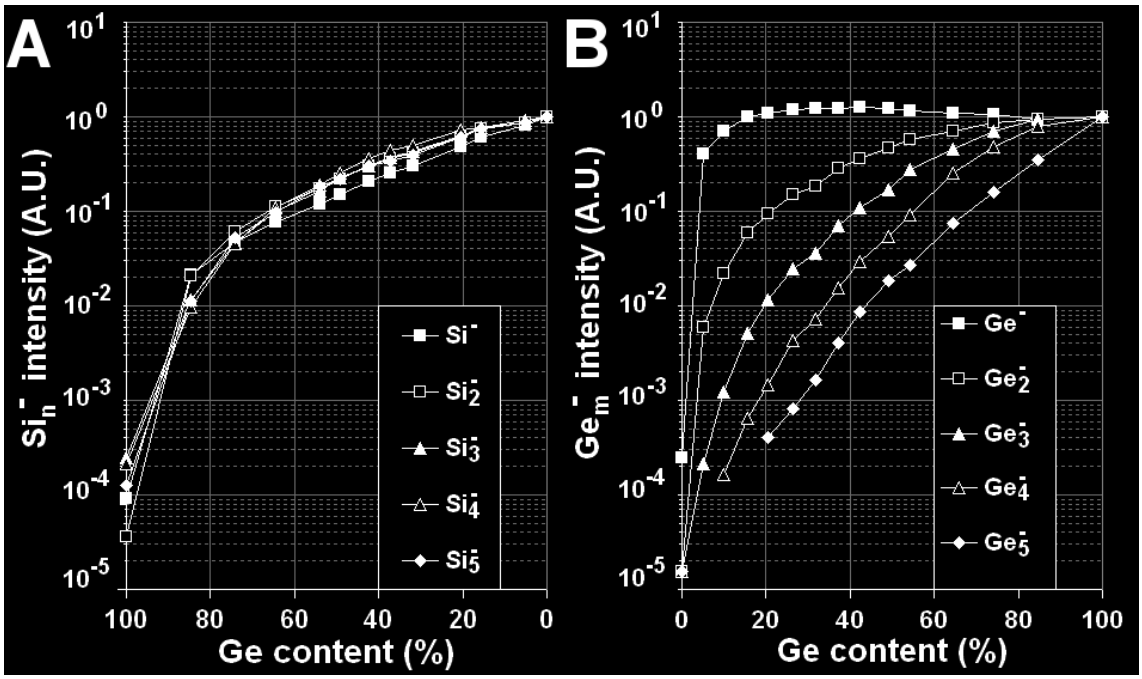

Figure III.4.A Intensities of Si_n^- cluster secondary ions in function of Ge content for 1 keV Cs^+ sputtering. Values have been normalised to Si_n^- intensity in pure silicon.
B Intensities of Ge_m^- cluster secondary ions in function of Ge content for 1 keV Cs^+ sputtering. Values have been normalised to Ge_m^- intensity in pure germanium.

However, when using the full spectrum protocol, there is only proportionality and not equality between T_{Ge} and the actual sample concentration, since the slope of the linear regression is slightly inferior to unity (see Table III.i). This means that the secondary ion beam is not perfectly representative of the actual material even if it is quite close to. For pure Ge however, calculations give a secondary ion beam composition of 99.6 at% ± 0.5 at%, showing that this behaviour is not due to interferences but more likely to ionisation behaviours. To understand this we can have a look at the tendencies of homonuclear ions Si_n^- and Ge_m^- displayed in Figure III.4. The Si_n^- ion intensity increases exponentially with increasing Si content. Meanwhile, the Ge_m^- ion intensity increases more in a linear fashion. Furthermore, Ge^- intensities reach a maximum at 50% Ge before decreasing. Thus the Ge content of the secondary ion beam increases slower than the Si content does. This could explain why less germanium than expected is obtained for high Ge contents and why slopes are slightly inferior to 1. Furthermore, we can observe that the slope values also increase as the sputter energy increases, as summarised in Table III.i. This is in agreement with the increase of the surface caesium concentration with decreasing sputter yield that is believed to emphasize differences between ionisation behaviours of Si and Ge clusters. In Figure III.5 we investigate the relation between the slopes values obtained at 2, 1 and 0.5 keV and the quantity 1/(1+Y), which is proportional to caesium concentration. Evolution is found to be close to a linear relationship, which confirms that the diminution of the slope is induced by the variation of caesium surface concentration. Increasing sputter energy (thus reducing Cs concentration) should therefore yield calibration curve slopes closer to unity. As increasing the sputter gun impact energy beyond 2 keV was not possible with our instrument, we investigated secondary ion beam composition using only the bismuth analysis beam. That is, after a DC Bi gun surface cleaning, we acquired spectra for each sample with identical ion

dose and use the spectra data to calculate T_{Ge}. Therefore we virtually reduced surface Caesium concentration to zero. The calibration curve obtained with this method had a slope of 0.9327 which is superior to all previous ones.

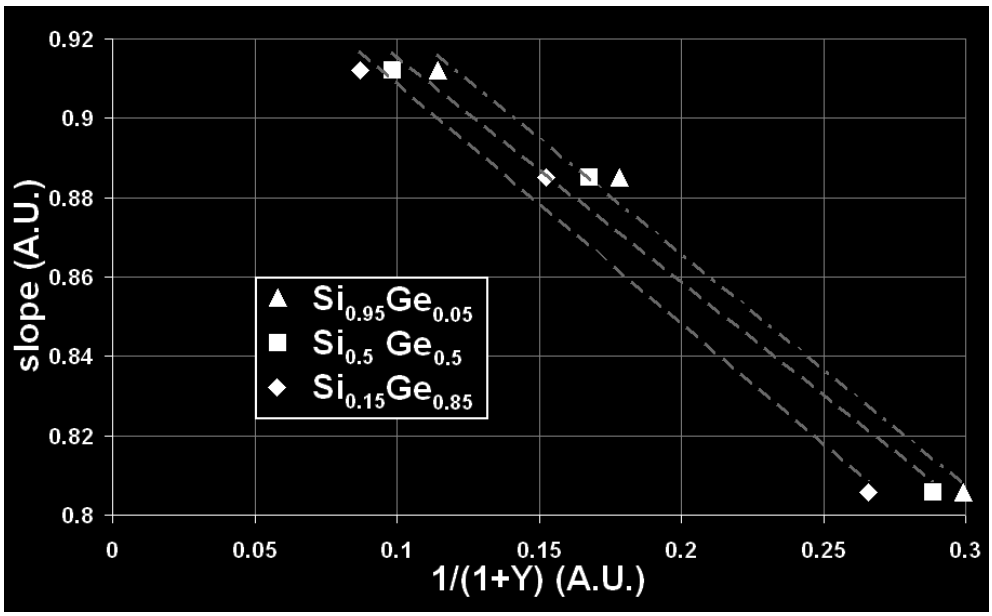

Figure III.5 Correlation between caesium concentration represented by 1/(1+Y) and curve slope for $Si_{0.95}Ge_{0.05}$, $Si_{0.5}Ge_{0.5}$ and $Si_{0.15}Ge_{0.85}$. $R^2 > 0.985$ for each.

This result confirms that slope variation with sputter energy is due to a difference of ionisation behaviour between Si_n^- and Ge_m^- ions emphasized by surface Caesium concentration. It also shows that secondary ion beam composition will never totally match material's composition. None the less, since linear correlation is excellent, the obtained linear relationships at 2, 1, 0.5, 0.25 and 0.15 keV can be used as calibration curves for Ge quantification in SiGe layers (at the condition that parameters potentially influent on the surface Cs concentration such as extraction bias are kept at the same value).

III. 4. b- Accuracy of the depth scale in SiGe/Si superlattice structures

The quantification of Ge in SiGe in permanent regime is therefore ensured by the full spectrum protocol. Strained SiGe layers, apart from being used as sacrificial layers in superlattices, can advantageously be used as the channels of p-type MOS devices. Hole mobility is indeed two to three times higher and the threshold voltage hundreds of mV lower in strained SiGe than in Si [14, 17]. Precise thickness measurement of such strained SiGe layers or stacks has been the subject of extensive studies [12, 18, 19]. It is therefore important to obtain quantitative depth profiles (i.e. concentration distribution) and not only average concentration values. To provide this one has to establish an accurate depth scale. To check the accuracy of the depth scale establishment protocol presented in section III. 3, we used four sample series, grown at 650°C on 200 mm (100) Si wafers with an RP-CVD industrial cluster tool. The samples consist of four epitaxially grown periods (Si ~30 nm / strained $Si_{0.8}Ge_{0.2}$ ~25 nm) pseudomorphic SuperLattices (SLs), the SiGe layers being either intrinsic or in-situ heavily doped with B, P, or C following the procedure detailed in [7]. Five wafers of each kind were prepared and analysed by XRR to assess layer thicknesses. Out of those, one wafer was kept as-deposited and four were annealed for 2 minutes in a H_2 atmosphere at

750°C, 850°C, 950°C and 1050°C. HR-TEM images were acquired on cross-sections of all as deposited SLs at ×74450 (×287000) magnification for whole sample (one SL period) imaging.

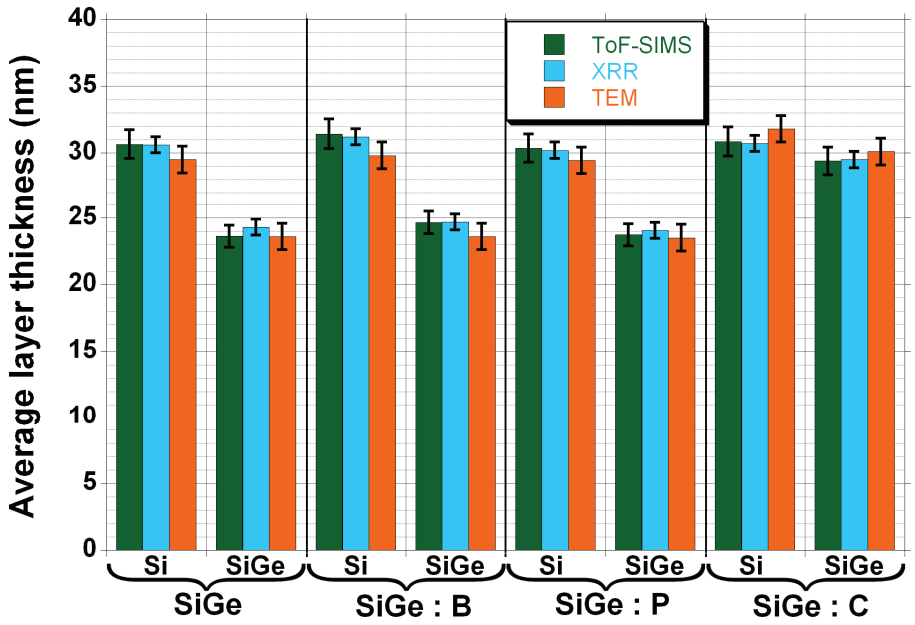

Figure III.6 Layer thicknesses as seen by ToF-SIMS, XRR and HR-TEM for all SL types.

In our case, we need a depth scale an as accurate as possible, which is why we have used several thickness measurement techniques in complement to ToF-SIMS. The total depth of the profiles obtained with the protocol presented in section III. 3 is compared to the experimental value of crater depths as determined for each sample by stylus profilometry (average of 4 values obtained in two orthogonal directions). Mismatch between both never exceed the measurement error of the profilometer (15 nm). Average layer thicknesses obtained by ToF-SIMS, XRR and HR-TEM are displayed in Figure III.6. Interface depths were determined in ToF-SIMS profiles using the 50% intensity points of the $[Ge]'_{FS}$ signal for each SLs. An excellent agreement is achieved between ToF-SIMS and XRR thicknesses, but there is a slight discrepancy with the HR-TEM measurements. This discrepancy is however never exceeding the measurement uncertainty and is likely due to sample preparation and to the low intensity contrast between Si and SiGe layers, especially in doped samples. The good agreement between the three techniques attests to the high level of accuracy of the ToF-SIMS depth scale. The Si (the SiGe) layer thicknesses are however slightly overestimated (underestimated) by ToF-SIMS compared to XRR. The maximum Si layer thickness overestimation is found to be of 0.2 nm, while the maximum SiGe layer thickness underestimation is of 0.7 nm. Although this is within the measurement error of both techniques, it is systematically observed on each sample. Such a behaviour was already observed in reference [20], which indicates a slight difference in Si and SiGe layer thickness determination by ToF-SIMS and XRR or XRD. We would suggest that it is due in our case to the depth resolution of the ToF-SIMS instrument which is not high enough to render the SiGe layers correctly. It thus distorts the actual layer shapes by broadening (shrinking) artificially the Si (the SiGe) layers. The choice of the 50% intensity points as interface markers might thus be questioned. Discrepancy between thicknesses was however judged to be low enough to keep this definition of ToF-SIMS layer thickness. To further investigate the accuracy of our depth scale, we can interest ourselves to the depth distribution of Ge in annealed samples. Indeed, the as deposited samples constitute “ideal” samples with alternate slabs of

heterogeneous materials with sharp interfaces. As this will not always be the case in real samples, it is required to test the accuracy of our depth scale on samples featuring important interpenetration of the Si and SiGe slabs in order to provide smooth interfaces.

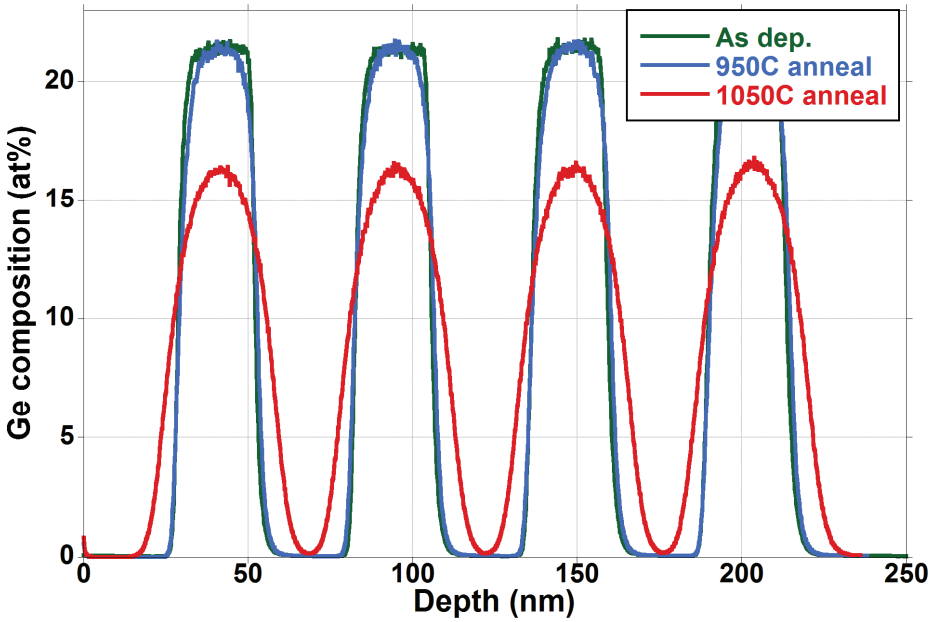

Figure III.7 ToF-SIMS full spectrum profiles of Ge concentration in as deposited, 950 and 1050C annealed SiGe / Si SLs.

This is the case in intrinsic samples annealed at 950 and 1050C. Profiles of those along with profile of the as deposited wafer are presented in Figure III.7. The strong interdiffusion of the layers observed after high temperature annealing yield important changes in the obtained concentration profiles. However we can take for grant that the total Ge dose does not evolve with annealing, as no exo-diffusion seems to occur (no Ge peak close to the surface). Therefore, and since the point to point Ge quantification is guaranteed using the full spectrum protocol (see previous subsection), the Ge dose as calculated from the full spectrum ToF-SIMS profiles using the depth scale established in section III. 3 should not vary either. The result of the dose calculations for all intrinsic samples has been reported in Table III.iii. There is no significant variation of Ge dose observed with annealing, which proves the accuracy of our depth scale.

	As dep.	750	850	950	1050
Ge dose (*10^{16} at/cm^2)	9.78	9.78	9.78	9.77	9.78
Dose variation (%)	-	-0.06	-0.06	-0.09	0.02

Table III.iii Ge dose variation with annealing temperature in intrinsic SiGe/Si SLs as calculated from full spectrum ToF-SIMS profiles

III. 4. c- Improvements in depth profiling of intrinsic or doped SiGe/Si SLs

In this subsection we investigate the improvements brought by the depth profiles obtained with the extended Full Spectrum protocol on quantification of both Ge and dopants. For this part of the study we used the sample series presented in III. 4. b-.

Precision of the extended FS protocol for determination of Ge and dopants concentration

Ge contents of the SLs as determined by ToF-SIMS are provided in Table III.iv, along with the apparent Ge concentrations obtained by XRD. The latter were assessed by a careful fitting of the XRD profiles using dynamical diffraction theory supposing the presence of binary SiGe only. Good agreement of the two techniques is found for SiGe (SiGe:P) / Si SLs: 21.6% (26.5%) by XRD ⇔ 21.4% (26.5%) by ToF-SIMS. By opposition, significantly lower values are obtained in XRD than in ToF-SIMS in SiGe:B / Si and SiGe:C / Si SLs. This is due to the fact that substitutional C and B atoms, being much smaller than Si and Ge atoms, partially compensate the compressive strain in the SiGe layers. A simple linear extrapolation between the lattice parameter of SiGe and the theoretical one that can be associated to pure B (C) can help us retrieve the actual Ge concentrations in these SLs, which are close to those seen by ToF-SIMS, as already extensively shown in references [7, 21, 22]. A good agreement is thus achieved between XRD and ToF-SIMS for all SLs.

SL type	Apparent Ge concentration by XRD (%, ± 0.6%)	Ge concentration by ToF-SIMS (%, ± 1%)
SiGe / Si	21.6	21.4
SiGe:B / Si	18.35	21.0
SiGe:P / Si	26.5	26.5
SiGe:C / Si	14.8	23.5

Table III.iv Apparent Ge concentration in the SiGe layers as measured by XRD and ToF-SIMS (extended FS protocol) in the four types of SLs.

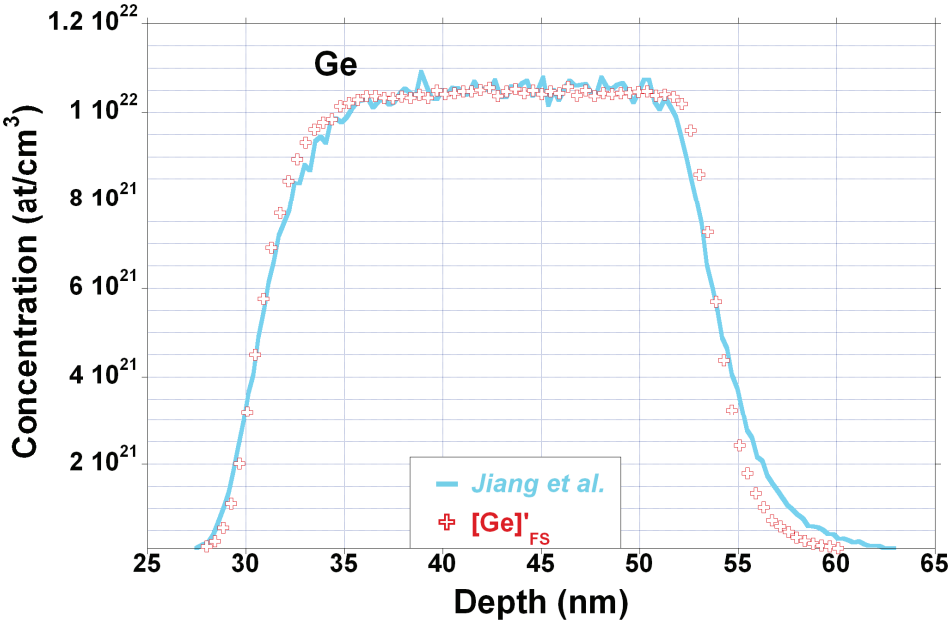

Figure III.8 Germanium profiles of the first SiGe layer of the intrinsic as-deposited SLs obtained with Jiang *et al.* (1 keV O_2 sputter) and extended FS protocols. Ordinate scale is linear.

To judge the quality of the extended FS profiles it is useful to compare them to other SIMS measurements. For Ge quantification, we used both the MCs and the Jiang *et al.* protocols as their accuracy is well established [1-3, 5]. Ge depth profiles obtained with the Jiang *et al.* (MCs) protocol and the extended FS protocols are provided in Figure III.8 for SiGe / Si SLs (and in Figure III.9 for SiGe:C / Si SLs). The agreement between the Ge concentrations

obtained by each protocol is excellent. The mean Ge concentration in the intrinsic SiGe (the SiGe:C) layers is indeed equal to 1.04×10^{22} (1.18×10^{22}) at/cm^3 with the extended FS protocol, versus 1.05×10^{22} (1.22×10^{22}) at/cm^3 with the Jiang *et al.* (MCs) protocol.

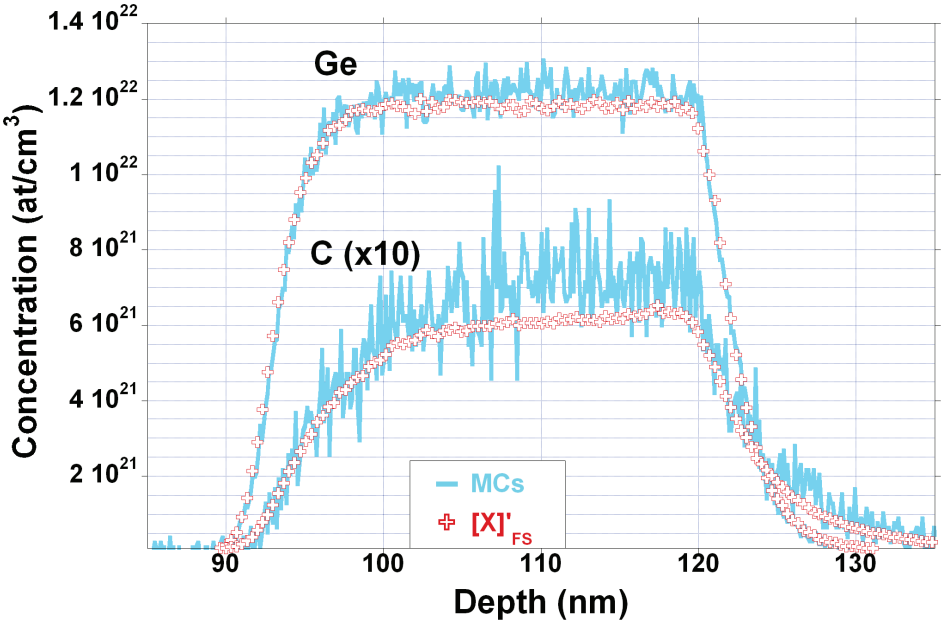

Figure III.9 Germanium and Carbon profiles of the second SiGeC layer of the Carbon doped as-grown SLs obtained with either the MCs or the extended FS protocols. Carbon profile has been multiplied by a factor of ten to increase its visibility. Ordinate scale is linear.

A similar agreement with the other protocols was obtained for all SL types. The extended FS boron dopant concentration was compared with the one deduced by O_2^+ sputter profiling (observation of B^+ secondary ions). The MCs protocol was otherwise chosen for C and P profiling, through the observation of CCs_2^+ and PCs_2^+, in order to benchmark the extended FS value. A rather good agreement (within 10%) was achieved for all. For instance, a P concentration of 1.42×10^{20} atoms/cm^3 was obtained with the extended FS protocol, versus a 1.36×10^{20} atoms/cm^3 concentration with the MCs protocol. We can thus assume that the Ge and dopants concentrations given by the extended FS protocol through depth profiling are reliable, given the excellent agreement found with the other protocols.

Accuracy of the ext. FS protocol profiles: noise level, detection limit, profile shape

We have seen in the last subsection that both the Jiang *et al.* and the extended FS protocols agreed on average Ge content in intrinsic or doped SiGe layers. The noise level in the Jiang *et al.* protocols profile is however higher than with the extended FS protocol (see Figure III.8). Moreover, there is with the Jiang *et al.* protocol a distortion of the profile shape due to a loss of depth resolution. This phenomenon, which is detectable after the sputtering of just 50 nm, increases with the sputtered depth (as shown below). This results in the impossibility to resolve the Ge plateau in the second SiGe layer and layers below with this protocol. Although the Ge detection limit is approximately one decade better with this protocol than with the extended FS protocol, its lower dynamics prevents reaching this limit in the Si spacers between the SiGe layers. The properties of each protocol in terms of stability of the Ge concentration found in the four SiGe layers and noise level are quantified in Table III.v. Signal/noise ratio is found to be quite high for Jiang *et al.* compared to the MCs or the single negative ion detection, due to its good sensitivity to Ge. It is however ~1.8 times

lower than with the extended FS protocol. MCs signals are plagued far more by noise than those obtained with the extended FS protocol (see Figure III.9). This is mainly due to a lesser sensitivity to Ge, although detection limits are approximately the same than with the extended FS protocol. Profile shapes are however in almost perfect agreement, with only a slight mismatch as far as C concentration is concerned, attesting to the accuracy of our extended FS protocol. MCs signal/noise ratios are ~3.5 times less than those obtained by the extended FS protocol for Ge, and ~10 times less for C and P.

	Extended Full Spectrum	MCs	Jiang *et al.*	$Ge^-/^{30}Si^-$	$Ge_2^-/^{30}Si^-$	$Ge_3^-/^{30}Si^-$
Standard deviation of the mean Ge concentration value through the four SiGe layers (% of mean value)	0.27	0.35	1.5	0.28	0.9	2.05
Average Ge signal/noise ratio in the 4 SiGe layers (a.u.)	54.7	14.85	29.75	21.4	12.1	3.1

Table III.v Properties of the profiles of the SiGe / Si as-grown SLs obtained with each quantification protocol. Calculations are made on the signal relevant to Ge concentration.

It is instructive to look at different negative secondary ion signals to understand how they contribute to the final extended FS signal. For this purpose, profiles of some normalised Ge negative secondary ion signals and the normalised Ge profile obtained with the extended FS protocol are shown in Figure III.10. The main contributions to the final signals are $^{70}Ge^-$, $^{70}Ge^{72}Ge^-$, Ge_3^- and the $Si_aGe_b^-$ negative ions, with *a* and *b* varying between 1 and 2.

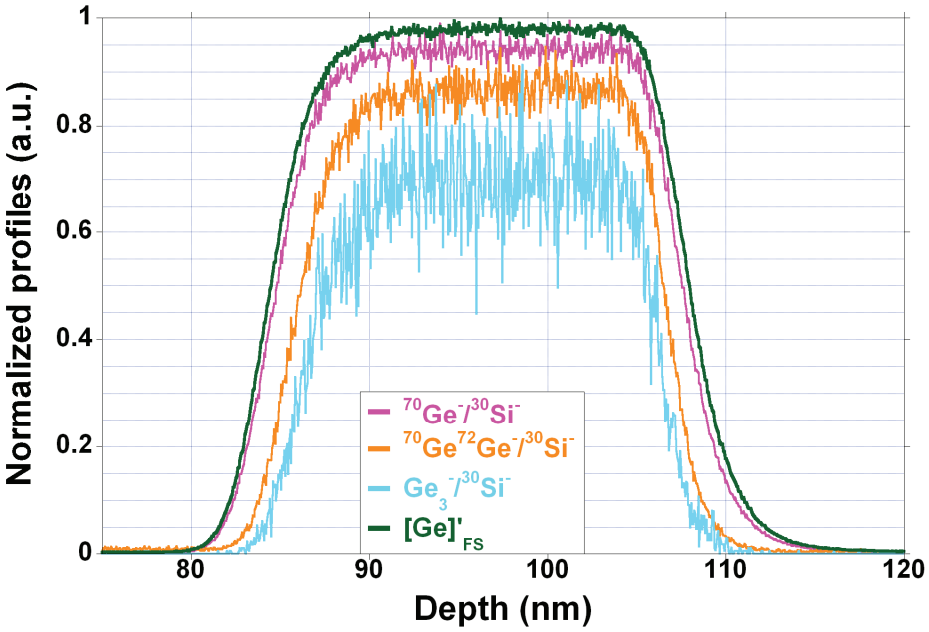

Figure III.10 Normalised profiles of several negative ionic signals and extended FS signal from the second SiGe layer of the intrinsic as-grown SLs. Ordinate scale is linear.

The latter are not shown in Figure III.10 for clarity purposes, given that their distributions are similar to the one of $^{70}Ge^-$. In our case, the Ge distribution obtained with the extended FS protocol is close to the $^{70}Ge/^{30}Si^-$ distribution, with a peak FWHM which is however slightly larger. This is due to the integration of the contributions from all the other Ge relevant signals,

which, while having much lower ionisation yields, feature smaller FWHMs and better depth resolutions. Signal decays are indeed found to be 4.3, 4.1, 2.8 and 2.7 nm / decade for $[Ge]'_{FS}$, $^{70}Ge^-/^{30}Si^-$, $^{142}Ge_2^-/^{30}Si^-$ and $Ge_3^-/^{30}Si^-$, respectively. This observation is in agreement with a recent paper by Drozdov *et al.* [23]. Signal increases are however the same for all SiGe layers whatever the negative ion followed, with a 4.3 nm / decade. This would confirm, as suggested by HR-TEM data (not shown), that the SiGe/Si interface is less abrupt when Si epitaxy is performed on SiGe than when SiGe is grown on Si. This phenomenon is likely due to a SiGe growth front which slightly undulates in order to elastically minimise the compressive strain accumulated in the layer. The Ge detection limit with $[Ge]'_{FS}$ is mostly determined by the instrument sensitivity to secondary ions such as $^{70}Ge^-$ or $Si_aGe_b^-$. However, there is a clear diminution of the noise level when comparing signals associated to single secondary ions and $[Ge]'_{FS}$. The signal/noise ratio is more than two times lower when following $^{70}Ge^-$ (4 times lower with Ge_2^-, 15 times lower with Ge_3^-) than with the extended FS protocol (see Table 3). The stability of the Ge signal through the four SiGe layers is also slightly better with the extended FS protocol.

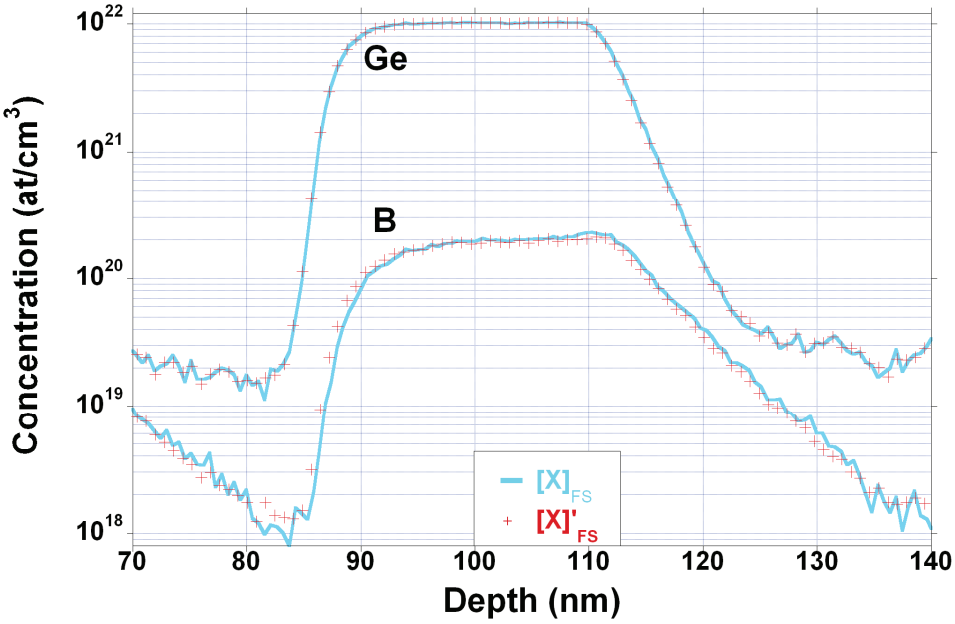

Figure III.11 $[Ge]_{FS}$, $[B]_{FS}$, $[Ge]'_{FS}$ and $[B]'_{FS}$ profiles of the second SiGe layer of the Boron doped as-deposited SLs. Profiles from other samples show similar behaviour (not shown).

Let us finally focus on the comparison of $[X]_{FS}$ and $[X]'_{FS}$ profiles, i.e. the profiles obtained with the full spectrum and the extended FS protocols. The latter are set to fit to the formers in the permanent regime within the SiGe layers of the as-grown samples. We thus expect almost no difference between the Ge profiles obtained by both protocols on all SLs types. This is attested by Figure III.11 which displays the Ge and B distributions of the second SiGe layer in the as-grown SiGe:B / Si SL. Similar behaviour is observed for the other types of SLs (not shown). As far as C and B atoms are concerned, we observe a good agreement between $[B]_{FS}$ ($[C]_{FS}$) and $[B]'_{FS}$ ($[C]'_{FS}$). A slight improvement in terms of noise level (especially at low concentrations) and depth resolution is noticed with the extended FS protocol. The good agreement obtained between the two protocols for B and C profiles is assumed to be due to the high secondary ion yields of SiB^- and SiC^- used for dopant profiling in the full spectrum protocol. This is also attested by the low B and C sensibility factors of the extended FS protocol, respectively 0.6 and 0.5, provided in Table III.ii. However, for elements with lower

ionisation yields such as phosphorous (usually detected as P^-), there is a clear difference between $[P]_{FS}$ and $[P]'_{FS}$ profiles, as illustrated in Figure III.12. As-grown SiGe:P / Si SL profiles exhibit similar shapes with slightly less noise on the $[P]'_{FS}$ profile. More importantly, the detection limit is improved by a factor ~5 when switching from the full spectrum to the extended FS protocol. In the case of annealed SiGe:P / Si SLs, the P distribution obtained with the two protocols is quite different. Indeed, it would seem from the $[P]_{FS}$ profile that P atoms diffuse very quickly towards the Si rich regions, depleting the Ge rich regions.

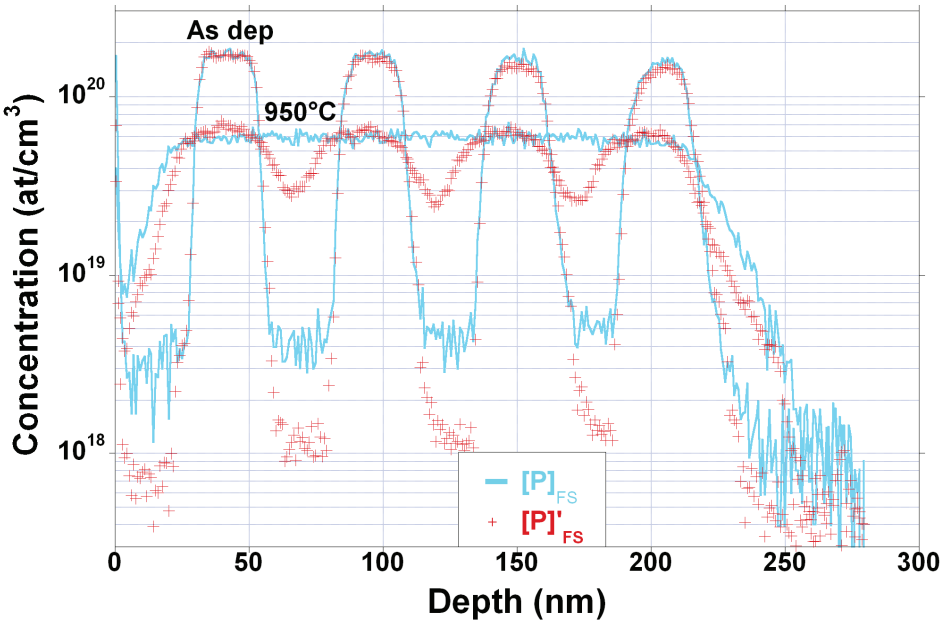

Figure III.12 $[P]_{FS}$ and $[P]'_{FS}$ profiles of the SiGe:P / Si SLs as deposited and after 950°C anneal.

In contrast, the $[P]'_{FS}$ distribution is more box-like upon annealing, i.e. there is more (less) signal in the Ge rich (the Si rich) regions. This behaviour is observed in the SLs annealed at 850°C and higher. It is most striking in the SL annealed at 950°C, whose profiles are shown in Figure III.12. We thus obtain, depending on the quantification protocol, quite different P distributions upon annealing. This is assumed to be an effect of the relatively low ion yields for P^-, the classical ion used for P quantification. Indeed, when switching to the extended FS protocol, an important number of secondary ions participating to the final P relevant signal exhibit higher intensities i.e. contribute more to the final signal than P^-. A comparative profile of the distribution of some of those secondary ions is provided in Figure III.13 for the SiGe:P / Si SL after a 950°C anneal. Given that P (m= 30.974 u) is subject to mass interference with ^{30}SiH (m= 30.982 u), one has to be particularly careful when selecting mass ranges of P secondary ions. Mass resolution is usually high enough to clearly separate P^- and $^{30}SiH^-$ in most instruments. However, this is not the case anymore for heavier ions such as SiP^- or GeP^-. One has thus to (i) reduce the pressure in the analysis chamber to minimise the influence of residual hydrogen, (ii) select isotopes to minimise mass interferences or (iii) proceed to an appropriate background substraction using a reference sample. In our case, we performed (i) and (iii), using the as-grown SiGe:C / Si SLs as a reference, since it has approximately the same Ge concentration than in P doped SLs. For instance, $^{30}Si^{30}SiH^-$ was totally absent in the mass spectra in this sample (a few tens of counts in the whole profile), while $Ge^{30}SiH^-$ was found to have a more than 5 times lower intensity compared to GeP^- in the as-grown SiGe:P / Si SL, allowing us to perform a successful background substraction.

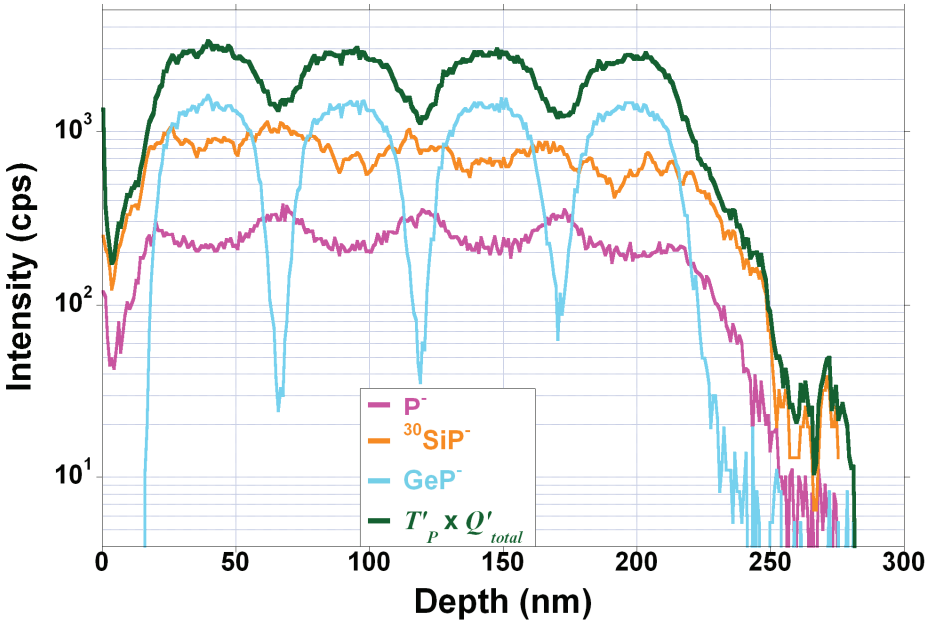

Figure III.13 Overlaid profiles of several secondary ions participating to the final P signal in the extended FS protocol and of the quantity $T'_P \times Q'_{total}$. The latter represents the number of P atoms in the secondary ion beam as defined in equations (III.5) and (III.7).

As shown in Figure III.13, considering the contribution of ions other than P^- to the final signal completely changes the shape of the profile. The apparent P out-diffusion into the Si rich regions in the conventional profile is believed to be due to the variation of the P^- ionisation yield in $Si_{1-x}Ge_x$ with variation of x. Since the usual method for P quantification with SIMS consists in following P^-, one can thus doubt of the accuracy of the profiles obtained by this method in samples such as ours, which have P doping in adjacent layers of different matrix composition.

Depth resolving power and dynamic range

Although depth resolution is not crucial for the analysis in this case, it is still a parameter of interest when comparing ToF-SIMS analysis protocols. The evolution with sputtered thickness of the so-called Ge depth resolution, defined in all types of SLs as the difference in depth for which the Ge content is equal to 16% and 84% of the maximum Ge content in the SiGe layer, is shown in Figure III.14. As expected, the Ge depth resolution degrades in a linear fashion more or less rapidly depending on the SiGe layer's nature (i.e. intrinsic or doped with B, P or C). Given the knock-on effect associated to C atoms (because of their small size) and the segregation of boron atoms towards the substrate during profiling with Cs^+ ions [24], one would have thought that these samples would present the worst depth resolutions, because of modification/destruction of layers beneath the surface producing topography. This is however not the case, as depth resolution is the worst in SiGe:P / Si SLs. Depth resolution degradation is thus likely due to a more or less important development of topography during sputtering, which depends mainly on the nature of the dopants. By extrapolation to the origin, we find that the depth resolution at depth = 0 nm is similar (2.1 ± 0.3 nm) for all samples, which is in agreement with the hypothesis of a SIMS crater roughening during sputtering (topography pile-up). The Ge and dopant normalised signal decays with depth are presented in Figure III.15. In B doped samples, B segregates under Cs^+ bombardment, leading to a huge, steady normalised B signal decay right from the start, which

is more or less unaffected by topography development (which causes the Ge signal decay to definitely increase). The normalised C signal decay in SiGe:C / Si SLs , which is at the beginning much higher than the one of Ge (knock-on effect), increases slightly with the sputtered depth, at a far lesser pace than the normalised Ge signal decay, however.

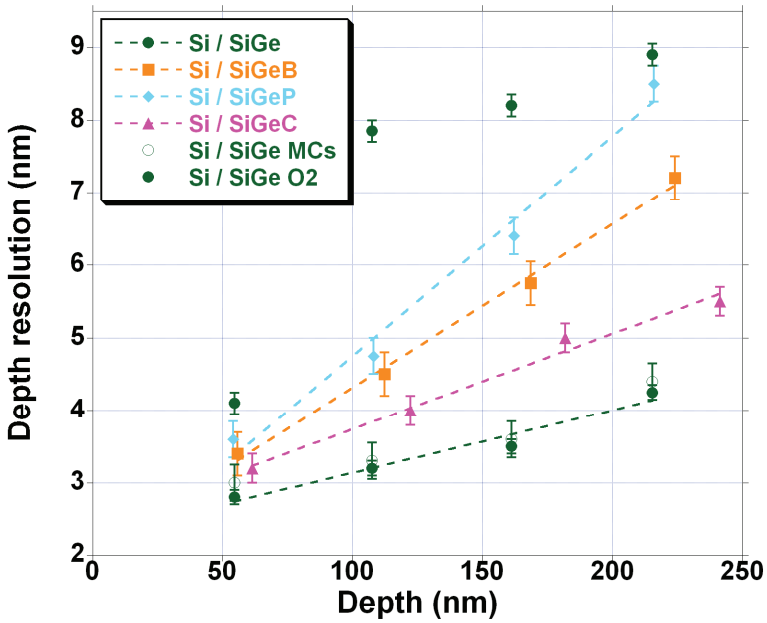

Figure III.14 Depth resolution calculated from the depth difference of the points corresponding to 84% and 16% of the SiGe layer's Ge concentration. Calculation was carried out on the decreasing slopes of the Germanium signal coming from the extended FS protocol. Depth resolutions obtained with the MCs protocol and with the Jiang *et al*. protocol (O_2 sputtering, 1 keV) for the intrinsic SL sample are provided for comparison purposes.

In contrast, Ge and P signal decays increase with a similar slope as the sputtered depth increases. This may indicate that topography development alone is responsible for the decay length increase (and thus the depth resolution loss) with sputtered depth in P doped layers. The mechanism leading to this topography increase in presence of P atoms is still unclear and under investigation. Figure III.14 also features depth resolution values for the two other protocols used in this study: MCs and Jiang *et al.*. The depth scale for MCs profiles was obtained using equation (III.9), and for O_2 sputtering with its own calibration equation (similar to equation (III.9)). Profiles were found to fit well with the profiles obtained with the extended FS protocol in terms of layer thicknesses. As expected, we obtain very poor depth resolution with the Jiang *et al.* protocol, since it involves 1 keV oxygen sputtering, which is expected to rapidly roughen the SIMS crater as the surface layers' oxygen content stabilises (because of the non-full-oxidising experimental configuration, chosen purposely to get conditions close to the Jiang *et al.* experimental setup and to avoid Ge oxidation during profiling). A typical manifestation of this is the non-linear depth resolution evolution with sputtered thickness, with a rapid build-up followed by a more linear topography development. In our case, the natural proclivity of materials under O_2 bombardment (without oxygen flooding) to topography development is enhanced by the succession of Si and SiGe layers which have different sputtering yields [25-27]. Finally, depth resolution with the MCs protocol is slightly worse than with the extended FS protocol, while having similar sputtering conditions: 500 eV Cs^+ and same primary currents. This is likely due to the higher noise level in the Ge MCs concentration profiles, as discussed in the previous section.

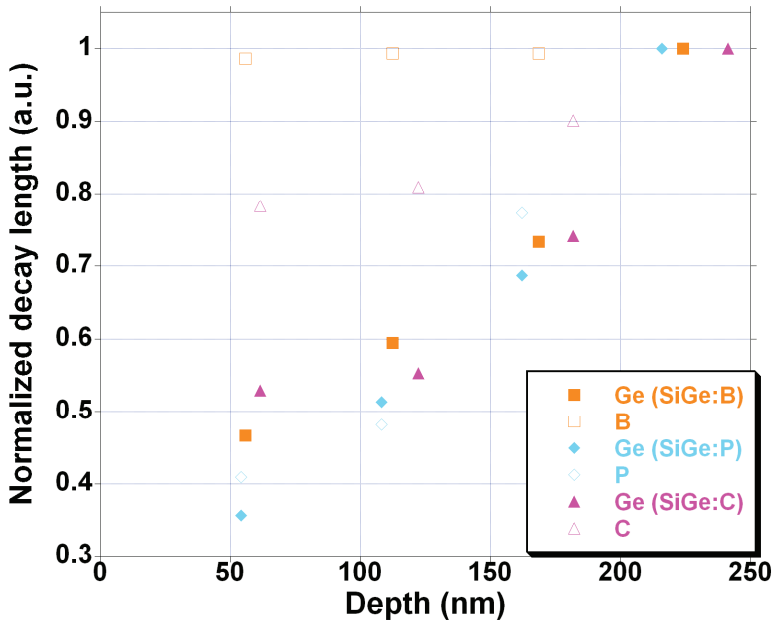

Figure III.15 Normalised decay lengths (to that of Ge, B, P or C in the fourth, deepest SiGe:B, SiGe:P or SiGe:C layer of the SLs) of $[X]'_{FS}$ (Ge, B, P and C) signals in as-grown SiGe:B / Si, SiGe:P / Si and SiGe:C / Si SLs.

The extended FS protocol we have developed is thus able to provide the best quantitative profiles out of the three different protocols proposed in this study, with a lower noise, an accurate shape and a similar or better detection limit along with better depth resolution, this simultaneously for matrix elements (Si or Ge) and dopants (C, P and B). The reduced noise level of this protocol is due to its better statistics compared to more classical protocols, where single secondary ions are followed, instead of more than fifty different secondary ions in the case of the extended FS protocol. Following simultaneously a large number of various ions (mono- and poly-atomic, homo- and hetero-nuclear ions) provides a better stability of the overall atomic concentrations, an enhanced reproducibility (less sensitive to slight changes in experimental settings). It also provides a more quantitative analysis not only of matrix elements such as Si or Ge [6, 8], but also of dopants, given that their concentration is high enough to be considered as matrix components (from 0.1-0.2 at% approximately). We would venture that this is due to a better consideration of the actual atomic distribution of elements in the material by taking into account all their associations with other elements. The extended FS protocol also provided different phosphorus in-depth distributions as compared to the classical protocols. This was likely due to the observation of several relevant secondary ions with the extended FS protocol, in opposition to classical protocols where usually only one secondary ion mass is followed. The extended Full Spectrum protocol is thus the preferred protocol for precise quantitative profiling of most SiGe/Si heterostructures. The following subsection will therefore further investigate the accuracy of this protocol in samples comprising both doped SiGe/Si and silicon oxide layers, such as the ones obtained after the use of the Ge condensation technique for the production of 3D nano-wires [28].

III. 4. d- Improvements in depth profiling of oxidised SiGe layers

As we saw in the first chapter of this work, CMOS planar technology presents limits in terms of scaling, performance and power consumption. Nanowire (NW) technology appears to be an attractive alternative [29]. It allows the improvement of electrostatic gate control and, consequently, the reduction of short channel effects. Nevertheless, the small diameters of NWs limit the current density in devices. To overcome this issue, nanowires can be stacked one upon the other, with a current density gain per area [29]. Rather high electron mobilities have been achieved in Si NW-based nMOS transistors [29]. Hole mobility in p-type MOS devices can be slightly improved by switching from Si to compressively strained $Si_{0.8}Ge_{0.2}$ NWs, as shown in reference [30]. Higher Ge content SiGe (up to 60%) should yield higher hole mobilities and thus higher performance pMOS devices [31]. The condensation technique allows the Ge enrichment of low Ge content SiGe layers by a selective oxidation of Si compared to Ge [32]. It can be used to obtain Ge nanowires [28]. In [33], Saracco *et al.* proposed a new top-down method to fabricate 3D suspended Ge-rich nanowires by Ge condensation, which is completely CMOS compatible. In-situ alloying with C atoms of the SiGe layers during epitaxy can help reduce the compressive strain in these layers and thus avoid strain relaxation during the fabrication process [33, 34]. Otherwise, in the case of nMOS, one might keep the Si slabs as channels and perform in-situ doping of SiGe slabs with B or P so as to make them diffuse towards the surrounding Si layers (S/D regions) during a suitably high temperature anneal in order to avoid ion implantation step. An in-depth knowledge of the behaviour of intrinsic or C, B or P doped SiGe layers during oxidising anneal would in that respect be most useful for process optimisation. We will investigate in this subsection the improvements brought by the extended FS protocol for quantitative analysis of such samples. For this study, three identical samples were grown on different wafers by RP-CVD. Samples consist of epitaxially grown, ~70 nm thick $Si_{0.82}Ge_{0.16}C_{0.02}$ layers following the procedure described in [15]. Samples were grown at 650°C, 20 Torr on SOI wafers with a ~70 nm thick Si layer on top of the buried oxide (BOX). SiH_2Cl_2, GeH_4 and $SiCH_6$ were used as gaseous precursors for the epitaxy of the SiGeC layers. The SiGeC layer thickness was chosen lower than critical thickness of plastic relaxation to guarantee that the structure is strained and without any crystalline defects [35]. One sample was kept as deposited, and the two other were then annealed in a Tempress horizontal furnace for 30 min or 60 min at 900°C in dry oxygen, in order to initiate the Ge enrichment process. The oxidation temperature used was lower than the Ge melting temperature (T_{Ge} = 937°C) in order to preserve crystalline quality during the whole process. Previous studies have shown that the process used to enrich the SiGe layer led to a conservation of the total amount of Ge [36]. Eventually, a HF dip was performed on parts of the wafers to remove the oxide layer produced during enrichment (or to remove the native oxide layer on the as deposited sample) prior to ToF-SIMS analysis.

Profiles of the wafer oxidised for 30 minutes in dry oxygen at 900°C (with and without HF removal) obtained with the extended FS protocol are displayed in Figure III.16. These profiles display features that are typical of the extended FS protocol: a simultaneous quantification of all matrix elements combined with a good signal/noise ratio. Briefly, from what we can observe in Figure III.16 (full lines), the extended FS protocol succeeds in quantifying all matrix elements in the successive layers. Precisely we can list:

(i) A SiO_2 layer, where the average composition is found to be 66.8 at% O and 33.1 at% Si, remaining 0.1 at% being Ge and C related noise (this region is only observed as a native layer on the as deposited sample);

(ii) Then, a Ge enriched SiGeC layer, with a varying Ge composition as a function of depth, typical of condensation processes;

(iii) Then, a SiGeC layer with stable Ge and C concentrations, of average composition 16.2 at% Ge and 2.2 at% C, corresponding to the original SiGeC layer;

(iv) And finally, the Si layer underneath, where the average composition is found to be 99.8 at% Si, the remaining 0.2 at% being Ge, O and C related noise.

Enrichment is clearly observed on the Ge profile. By contrast, no such behaviour is seen on the C profile. The profile of the sample oxidised for 60 minutes (not shown in Figure III.16) exhibits similar features. The region of interest for this study is the (i)-(ii) interface between the SiO_2 layer and the Ge enriched SiGeC layer and its evolution with annealing time.

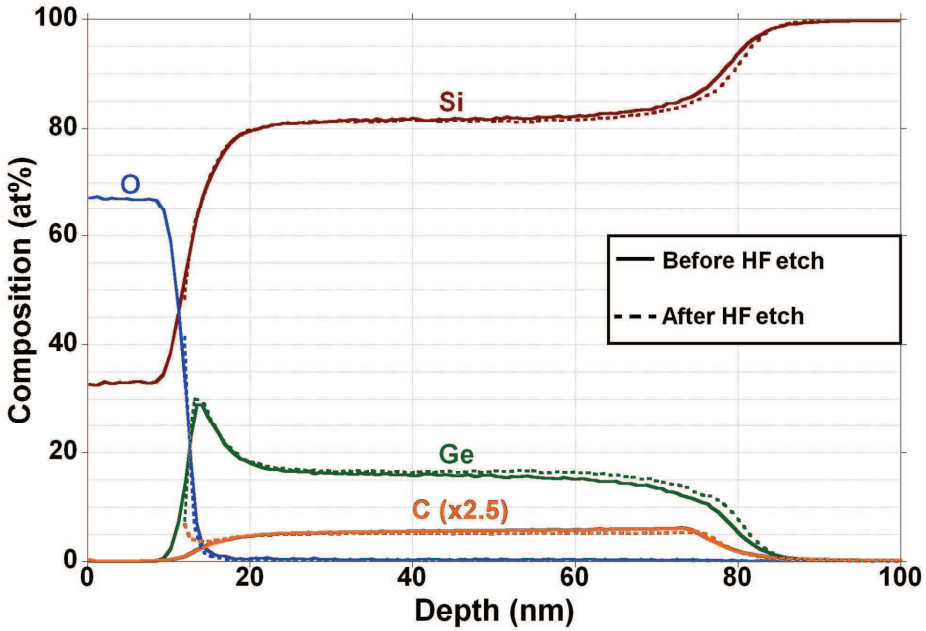

Figure III.16 Extended FS ToF-SIMS profiles of the Si, the Ge and the C atoms in the SiGeC layer oxidised for 30 minutes under dry oxygen at 900°C without (full lines) or with (dashed lines) a full HF etching of the oxide layer. The depth scale of the latter sample has been shifted so that the depth of the Ge peak is the same for both configurations. Notice the ordinates, in at% and in linear scale.

The accurate quantification of Ge in this region is indeed most difficult due to significant matrix effects. To verify the accuracy of the extended FS protocol, we acquired the profiles of all samples with two other protocols, namely the MCs and the Jiang *et al.* protocols. The profiles obtained with all three protocols are shown in Figure III.17. As expected, we obtain a satisfying agreement in the bottom part of the SiGeC layer (i.e. in region (iii)). The average Ge compositions for the three samples are indeed equal to 16.2, 16.6 and 17.5 at% with the extended FS, the Jiang *et al.* and the MCs protocols, respectively. The discrepancy between the different protocols is within their measurement error (±~1 at%). A rather good agreement is also obtained for the C composition, with an average of 2.2 and 2.3 at% with the extended FS and the MCs protocol, respectively (not shown in Figure III.17). However, important differences between profiles are observed in the interface region. Depending on the protocol, region (ii) indeed exhibits a more or less important Ge composition peak and a more or less rounded shape. Compared to the extended FS, the MCs profile shows a higher Ge peak value and a more abrupt shape. Meanwhile, the Jiang *et al.* profile presents a rounder shape with a lower Ge peak composition. Several effects can be at the origin of these differences, such as a Ge sensitivity variation close to the (i)-(ii) interface (also observed in the as deposited sample, due to the native oxide layer) and more or less important transients after the end of the SiO_2

layer. A matrix change is indeed expected to generate sputter rate and ionisation yield variations together with transients in Cs or O_2 piled-up quantities at the surface of the sample.

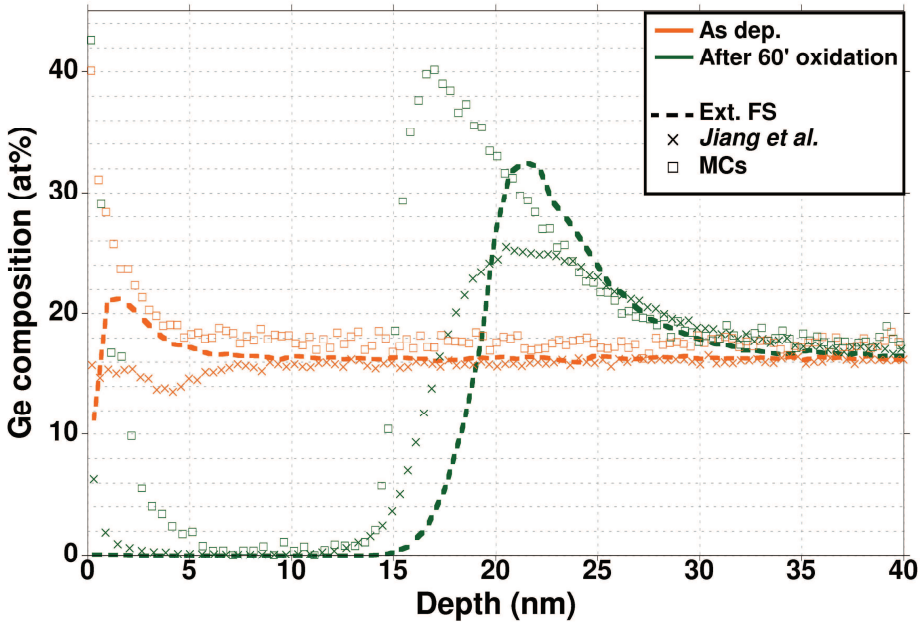

Figure III.17 Overlay of Ge composition profiles obtained on the as deposited and 60 minutes annealed samples for the three ToF-SIMS protocols. Profiles of the 30 minutes annealed sample exhibit similar features (not shown for clarity).

We can thus expect to have artefacts hampering the accurate quantification of Ge in these stacks, which will depend on the sputter beam. With Cs abrasion, we should observe an artificially high Ge related signal after the interface (as it is the case in the as deposited sample with MCs protocol and, to a lesser extent, with the extended FS protocol) resulting in an overestimation of the total Ge dose in the sample. On the other hand, with O_2 abrasion, we should have a more broadened profile due to the long transient after the interfaces between (i)-(ii), (ii)-(iii) and (iii)-(iv), inducing an underestimation of the dose in region (ii) but a global overestimation of the Ge dose.
These assumptions can be verified by calculating the Ge doses obtained with the different protocols. The results of these calculations are displayed in Figure III.18.A. At first glance, we can say that the above assumptions are true for the MCs and Jiang *et al.* protocols. Indeed, the total Ge dose found with these protocols increases with the oxidation time (+9.3% after 30 minutes and +11.1% after 60 minutes for the MCs protocol, +7.4% after 30 minutes and +15.4% after 60 minutes for the Jiang *et al.* protocol). It is not the case with the extended FS protocol. There are indeed no significant variations of the total Ge dose with the oxidation time (-2.3% after 30 minutes, +2.5% after 60 minutes). This first result indicates that the extended FS protocol seems not to be affected by matrix effects and provides accurate profiles, since we know from previous studies that the Ge condensation process is characterised by a conservation of the total initial Ge dose in the final enriched SiGe layer [36]. By looking more closely at Figure III.18.A, we notice that the extended FS protocol is the only one to testify of a significant diminution of the Ge dose contained in the original SiGeC layer after oxidation (by conversion of a few nm of this layer into silicon dioxide) partly counter-balanced by an excess Ge dose in zone (ii) coming from the enrichment process itself. The contribution of "enriched" Ge has been calculated by subtracting from the region (ii) peak area the area of a theoretical region of identical thickness and of the same Ge content than the original SiGeC layer. This contribution is more important with the MCs

protocol (7.7% after 30 minutes, 12.1% after 60 minutes) than with the extended FS protocol (7.2% after 30 minutes, 9.4% after 60 minutes). Meanwhile, the Jiang *et al.* protocol yields the lowest contribution of "enriched" Ge (2.3% after 30 minutes, 7.3% after 60 minutes) of all three. Those results highlight the fact that, as expected, the Ge contribution of region (ii) is overestimated with the MCs protocol, while it is underestimated with Jiang *et al.*.

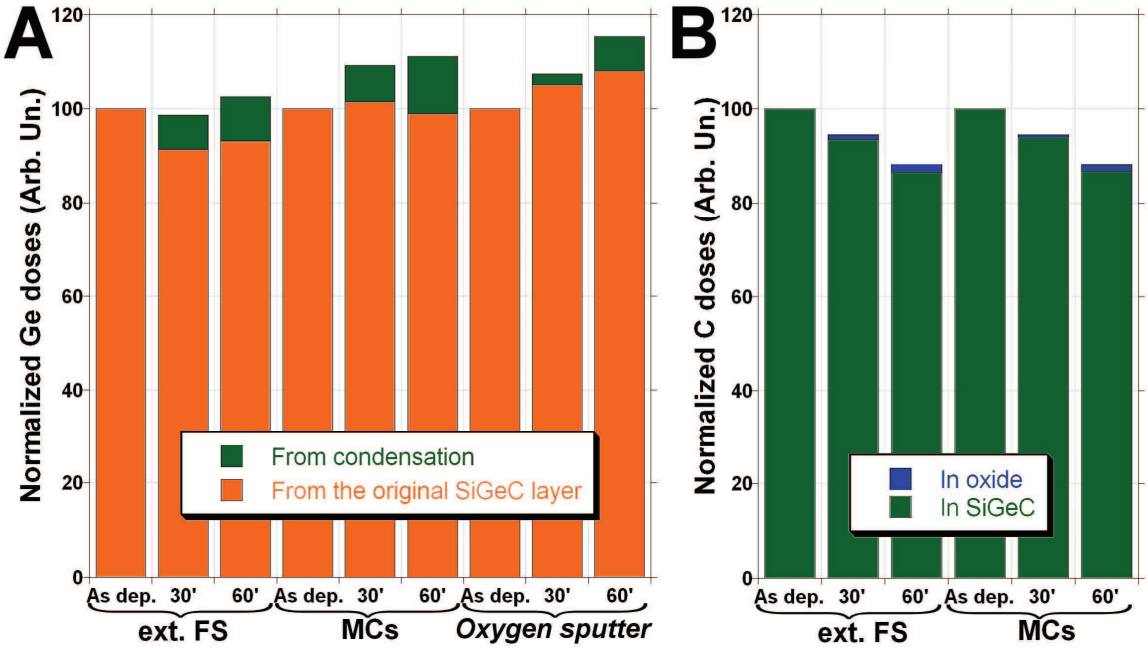

Figure III.18.A Ge doses in all samples, normalised to doses found with each protocol in as-deposited samples (%).

B C doses in all samples, normalised to doses found with each protocol in as deposited samples (%).

The global overestimation of the dose after annealing is therefore mainly due to a broadening of the SiGeC layer when profiling with Jiang *et al.* protocol. The MCs protocol is more ambivalent, with a slight broadening of the SiGeC layer (still within the measurement error) combined with an increase of the "enriched" Ge contribution. To further investigate the origin of the Ge excess found in region (ii) by the different protocols, we can proceed differently, i.e. get back to the original thickness of the SiGeC layer that has been consumed during oxidation from the data contained in the various profiles,. This cannot be done directly by measuring the thickness variation of the SiGeC layer (from the Ge signal) before and after oxidation since significant Ge diffusion also takes place at the bottom SiGeC/Si interface, due to the important thermal budget of the oxidation process. However, C does (almost) not diffuse in SiGe at 900°C [22], allowing us to measure the layer thickness variation T_{iC} directly from the C composition signal. This can also be performed by calculating the equivalent thickness of the SiGeC layer with the same composition than in region (iii) that can be obtained with the excess Ge dose in region (ii) thanks to the following formula:

$$T_{i1} = "condensed\ \ "GeDose \Big/ x \cdot \rho_{Si_{1-x}Ge_x} \qquad \text{(III.10)}$$

T_{i1} being the original thickness and ρ the density of the original SiGeC layer (supposed equal to the one of a same Ge content SiGe layer) [37]. A second method would involve measuring

the oxide thickness (determined at half intensity of the Ge signal) and calculating the original SiGeC thickness from it using the following approximation:

$$T_{i2} = T_{SiO_2} \cdot {}^{V_{SiO_2}}\!/_{V_{Si}} \cong {}^{T_{SiO_2}}\!/_{2.25} \qquad \text{(III.11)}$$

T_{i2} being the original thickness, T_{SiO2} the measured oxide thickness and V_{Si}, V_{SiO2} the Si contribution to the density of bulk Si and SiO_2, respectively [10, 37]. This method is likely to be more accurate than the previous one since it involves fewer approximations (the SiO_2 thickness can easily be measured on the ToF-SIMS profiles, while the SiO_2/Si density ratio is well known). The results obtained with each protocol on the three samples are given in Table III.vi. With the extended FS protocol, we have a rather good agreement (±1 nm) between T_{i1}, T_{i2} and T_{iC}. Meanwhile, T_{i2} is approximately two times lower than T_{i1} with the MCs protocol. With the Jiang *et al.* protocol, the opposite is true: T_{i2} is approximately two times higher than T_{i1}. This again indicates that the Ge peak in region (ii) is overestimated with the MCs protocol, while it is underestimated with the Jiang *et al.* protocol, confirming our previous assumptions. It also confirms the accuracy of the extended FS protocol.

	extended FS			MCs			Jiang *et al.*		
	As dep.	30' anneal	60' anneal	As dep.	30' anneal	60' anneal	As dep.	30' anneal	60' anneal
T_{i1}	1.3	6.3	8.1	1.8	7.9	11.4	-	1.7	5.3
T_{i2}	0.2	5.3	8.6	0.1	3.7	6.5	-	4.2	7.5
T_{iC}	-	6.5	9	-	7	9.5	-	-	-

Table III.vi Equivalent original $Si_{0.82}Ge_{0.16}C_{0.02}$ thickness corresponding to the amount of condensed Ge in region (ii), in nm.

Let us now have a look at Table III.vi results for the as deposited sample. At first glance, it would seem that the slight Ge "enrichment" observed at the surface of this sample (see Figure III.17) is an artefact. Indeed, T_{i1} is then roughly 6 times greater than T_{i2} with the extended FS protocol. The same phenomenon is observed with the MCs protocol. No such Ge "enrichment" is however observed with the Jiang *et al.* protocol. This potential artefact would then be due to a transient in Cs composition of the surface during the first nanometres of the profiling, leading to important Ge related secondary ions ionisation yield variations. To investigate the influence of this hypothetical transient, we removed with a HF dip the thermal oxide sitting on top of the "enriched' samples. Region (ii) was then just below the surface. If the surface transient did temporarily increase the yields of Ge compound secondary ions, we would have then observed a more important Ge peak in those samples than in samples with SiO_2 on top. This is however not the case. Indeed, Ge profiles of SiO_2 covered and bare samples are in good agreement in region (ii) (see Figure III.16; similar results were obtained on the 60 minutes annealed sample, not shown here). Surface transient artefacts thus seem not to play a major role with the extended FS (or the MCs) protocol. This would in turn mean that the slight Ge "enrichment" observed on the as-deposited sample might partly be real (due to the formation in air of the native oxide). This point however still needs more investigation. Finally, the extended FS and MCs protocols are in very good agreement as far as the C dose reduction during oxidation is concerned, as shown by Figure III.18.B. This testifies to the accuracy of the extended FS protocol for C quantification in the whole stack.

To summarise, the extended FS protocol allows, with a good depth resolution and an improved signal/noise ratio, the simultaneous quantitative profiling of Ge and C [38]. Moreover, it is found to be the most accurate of the three protocols explored here, because it reduces detrimental matrix effects to a minimum, with only a slight hypothetical artefact at the surface of as deposited samples (covered with a native oxide layer). It is thus well suited for a quantitative study of samples containing SiGe and oxides.

III. 4. e- Improvements brought by extended FS in doped strained SiGe… and limitations

In-situ doped recessed and raised sources and drains are extensively used nowadays in order to boost the performances of sub 100 nm gate length devices. Tens to roughly one hundred nanometres thick recessed SiGe:B Sources and Drains (S/Ds) enable, as a result of the uniaxial tensile strain in the Si channel induced by the compressively-strained SiGe layers nearby [39-42] and by the low contact resistance provided by high B doping levels (typically a few 10^{20} at/cm^3) to significantly increase the electrical performances of p-type MOSFETs. The benefits of using SiGe:B recessed S/Ds were conclusively demonstrated for p-MOSFETs built on a variety of substrates [43, 44]. The Ge concentration in the SiGe:B recessed S/Ds is ~35 at% in current 32 nm technology node transistors.

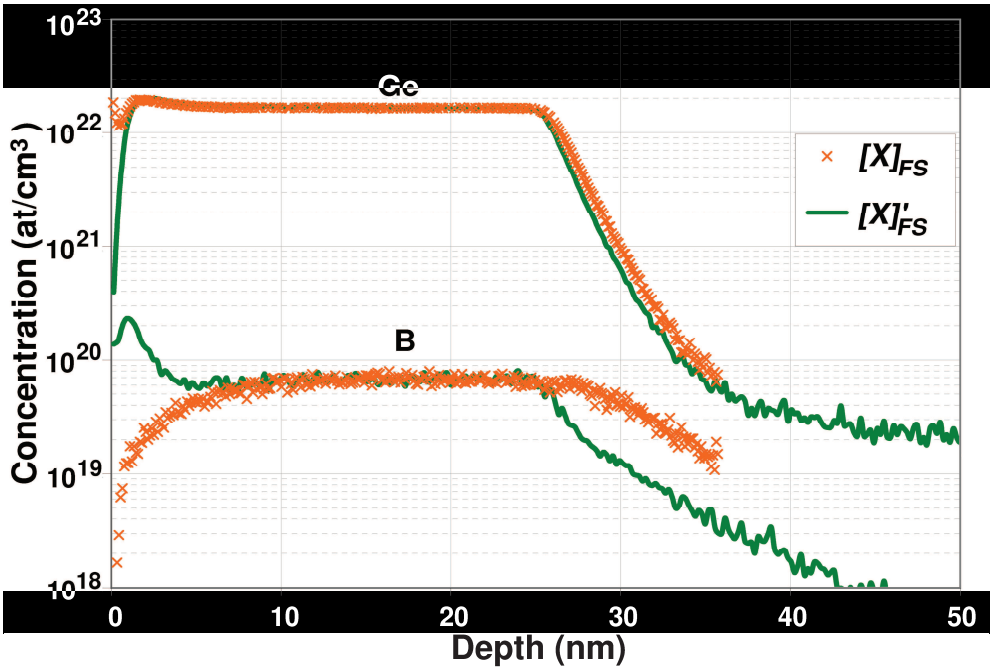

Figure III.19 *[Ge]$_{FS}$, [B]$_{FS}$, [Ge]'$_{FS}$* and *[B]'$_{FS}$* profiles of one of the B doped SiGe samples. Profiles from other samples show similar behaviour (not shown).

We have therefore investigated the low temperature boron doping of nominal $Si_{0.65}Ge_{0.35}$ with a dichlorosilane + germane + hydrochloric acid chemistry, in order to be selective not only versus SiO_2 (i.e. the isolation in-between individual transistors) but also versus Si_3N_4 (the sidewall spacers of MOS transistors). We have used RP-CVD to grow such samples, using dichlorosilane as the source of Si and germane as this of Ge. Diborane (B_2H_6) and phosphine (PH_3) were used as the sources of B and P. Thanks to mixers we were able to gain access to a wide range of dopant concentrations in the gases mass-flows from 5.54 to 2000 ppm. Quantitative depth profiles of this kind of samples would be most useful for the understanding of selective epitaxial growth of several tens of nm thick, in-situ B doped SiGe layers in the

S/D regions of short gate length 3D MOSFETs. Extended FS protocol is expected to give the best results for depth profiling of such samples, as provided by conclusions drawn from the previous subsections. However this protocol was conceived for profiling of matrix elements only, with the purpose of minimising the variation of ToF-SIMS sensitivity factors relative to major elements with variation of matrix composition. It is therefore not optimised for profiling of an elemental composition varying from trace to major element (from ~10 ppm to a few at%). In that regard, the observation of the behaviour of extended FS protocol boron sensitivity factors with different boron concentrations will be of prime interest.
The comparison of full spectrum ($[Ge]_{FS}$, $[B]_{FS}$) and extended FS ($[Ge]'_{FS}$, $[B]'_{FS}$) profiles for a sample with a rather high B composition (~0.14 at%) is given in Figure III.19. As expected, since the latter is set to fit the former in permanent regime, we observe no difference in permanent regime Ge or B concentration. Furthermore, we obtain quite close sensitivity factors as compared to those obtained for the SiGe SLs samples, with 1.31 for Ge and 0.55 for B (whilst those were 1.45 for Ge and 0.6 for B in SiGe SLs, see Table III.ii) although both experiments were spaced by almost a year and several heavy maintenance processes.

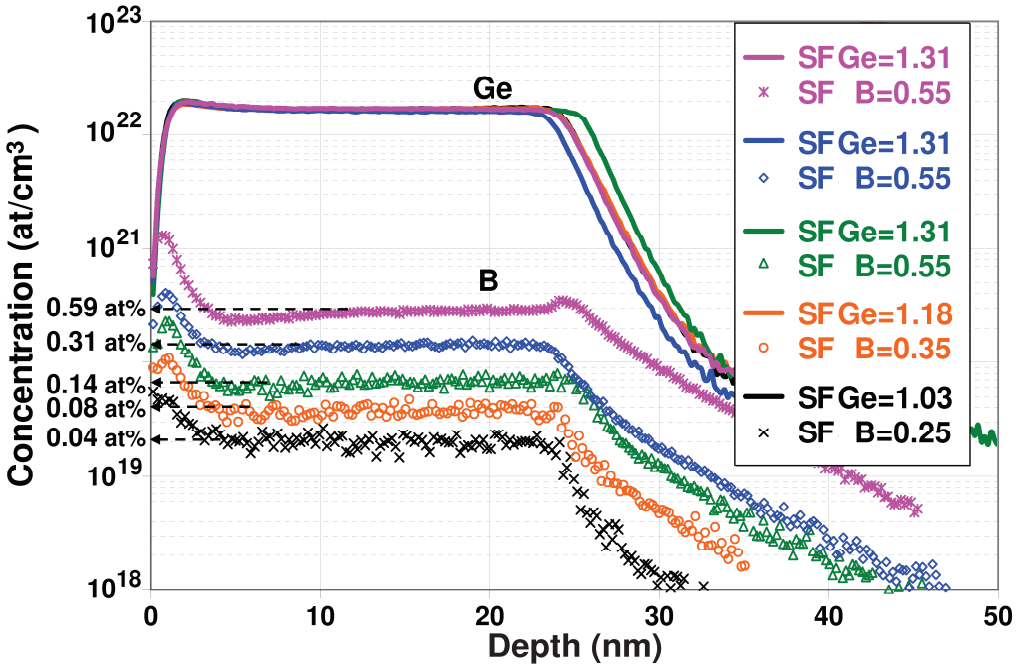

Figure III.20 Overlay of Ge and B composition profiles obtained with the extended FS protocol on all samples. Sample feature identical Ge nominal concentration but varying B nominal concentration, as highlighted by labels on the ordinate scale. Both Ge and B sensitivity factors are found to be lower than normal for the two samples featuring sub-0.1 at% boron concentration.

As expected from previous observations, we obtain important improvements by using the extended FS protocol. First, a lower noise level is found in permanent regime for both Ge and B signals. Then, we observe differences in profile shapes for the first few nanometres. This is due to the presence of a native oxide, which is not taken into account in full spectrum profiles. For $[Ge]_{FS}$, it yields erroneous Ge concentration at the surface (where there should be no Ge because of the native oxide) while the extended FS protocol accurately show there is no Ge at the surface. For $[B]_{FS}$, it results in an erroneous drop of the near-surface concentration, principally due to the drop of Si^- secondary ion yields in the native oxide while extended FS profile features no such artifact. The latter even shows segregation of boron in (or at the

interface of) SiO_2, which is known to occur in such layers. After the oxide region, one can observe also that the extended FS signal for B reaches more rapidly its permanent regime value than the conventional profile obtained by RSF (around 6 nm with extended FS against ~10 nm). Profiles obtained on other samples feature similar results (not shown). Finally, and more surprising is the difference in signal tails for both Ge and B, where extended FS is shown to improve signal decay slightly for Ge but significantly for B. This is definitely not testifying neither of an improvement of physical depth resolution nor of a diminution of B segregation process, as both profiles are issued from the same experimental acquisition. It is therefore a direct effect of the data treatment which induces, for Ge, improvements in signal yields and diminution of noise and for B, better statistics. Looking at the profiles of other samples, we indeed observe that this effect is enhanced at lower boron nominal concentrations and decreased at higher concentrations. This is also the reason why such an improvement was not observed while profiling SiGe:B / Si SLs since the B concentration in those samples was of ~0.41 at% (see Figure III.11).

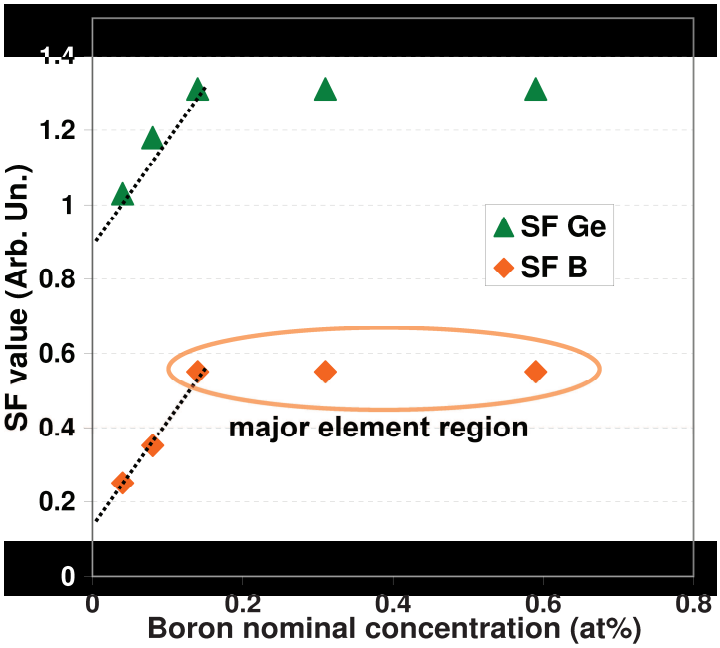

Figure III.21 Variation of Ge and B sensitivity factors with boron nominal concentration. Both SF are stable for B nominal concentration >0.1 at% and show a linear dependency with B nominal concentration below this limit.

When comparing the extended FS profiles obtained in all samples as shown in Figure III.20, we observe relatively homogeneous properties in terms of noise level and profile shape. Ge nominal concentration almost does not vary within the different samples (within the +-1 at% error margin) and B concentration increases linearly with the flux of diborane in the epitaxial chamber [45]. However, we can see that the sensitivity factors vary within the sample set. More precisely, while dopant concentration is superior to ~0.1 at%, nothing changes, but as soon as it goes below this limit, both Ge and B SF decrease. This result shows that extended FS protocol (and more generally ToF-SIMS, since data treatment in the extended FS protocol allows us to deal with atomic concentrations of B in the secondary ion beam, which are determined by the physics of the instrument) becomes more and more sensitive to boron (and by extension to other impurities) and germanium when boron (impurities) concentration decreases below matrix composition. This is coherent with ToF-SIMS extreme sensitivity to trace elements and matrix effects conventionally encountered using this technique. This also shows that the total yields of B and Ge atoms (present in the secondary ion beam as ionised

compounds) significantly increase when dopant amount becomes minute, while Si atomic yield obviously does not or not in equivalent proportions. As a consequence, the use of extended FS protocol should be restricted to matrix element of concentration superior to ~0.1 at%. In this concern, the extended FS protocol features the exact inverse behaviour than conventional measurements, which should be restricted to trace analysis. Nonetheless, it is worth to take a look at the variation of the SF in function of boron nominal concentrations, as reported in Figure III.21. One observes two main zones: the first, featuring constant FS values and corresponding to boron as a major element, and the second, featuring a somewhat linear dependency of SF with boron composition. Precisely, the slope of this linear relationship seems to be identical between Ge and B SFs. This feature, if confirmed for other species would allow the use of the extended FS protocol below the "major element" region, thus taking advantage of the improved statistics of the protocol.

III. 5. Results exploitation: useful knowledge earned through quantitative analysis

In this section we will try, starting from the best ToF-SIMS analysis on given samples (i.e. extended FS profiles), to yield useful information for understanding of materials and structures during selected processes. Precisely, we will in a first subsection interest ourselves to the superlattice samples described in subsection III. 4. b- and c-. In a second subsection we will investigate SiGe oxidation mechanisms using, within others, the samples presented in III. 4. d-.

III. 5. a- In annealed intrinsic and doped SiGe / Si SLs

In-depth chemical composition quantification

Depth profiles acquired by ToF-SIMS with the extended FS protocol are shown in Figures III.22, III.23, III.24 and III.25 for SiGe / Si, SiGe:B /Si, SiGe:P / Si and SiGe:C / Si SLs respectively. Some samples exhibit divergence between layer position before and after thermal anneals. For example, the Ge depth profile of the SiGe:P / Si SL annealed at 750°C is shifted towards the substrate compared to the profile of the as-deposited sample (Figure III.24). On the other hand, the Ge profile of the SiGe:B / Si SL annealed at 950°C is shifted towards the surface compared to the profile of the as-deposited SLs (Figure III.23). This phenomenon, which does not depend on the annealing temperature or the nature of the SLs, is assumed to be due to slight wafer-to-wafer variations during epitaxy.
The ToF-SIMS Ge concentrations and the *apparent* Ge concentrations from XRD for all SLs types are presented in Table III.vii. There is an almost perfect match between the values obtained with both techniques in the SiGe / Si and SiGe:P / Si as-grown SLs. A difference is however seen in the SiGe:B / Si as-grown SL, XRD values being slightly lower than the ToF-SIMS ones. This supports the assumption that small B atoms reduce the strain level in the SiGe layers, resulting in underestimation of the Ge concentration compared to intrinsic layers. The real Ge content is indeed almost the same in intrinsic and B doped SiGe layers. The same phenomenon is occurring in the as-grown SiGe:C / Si SL. The C concentration in the SiGe:C layers is indeed quite high at $\sim 6.0\times10^{20}$ at/cm^3, resulting in a large reduction of the compressive strain and thus to a severe Ge content underestimation by XRD.

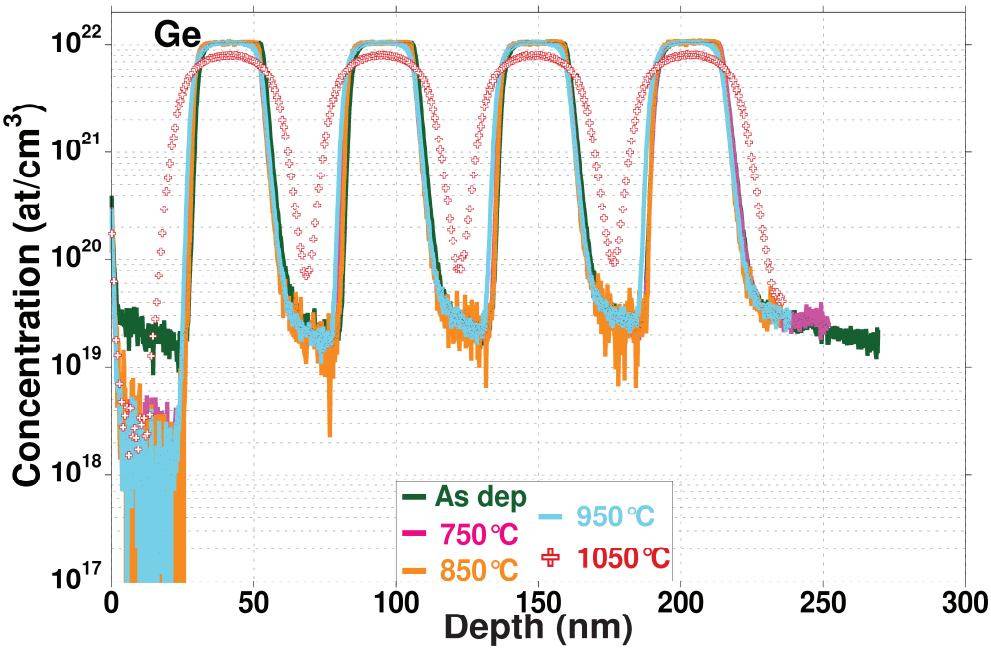

Figure III.22 Ge concentration profiles for as-grown and annealed SiGe / Si SLs.

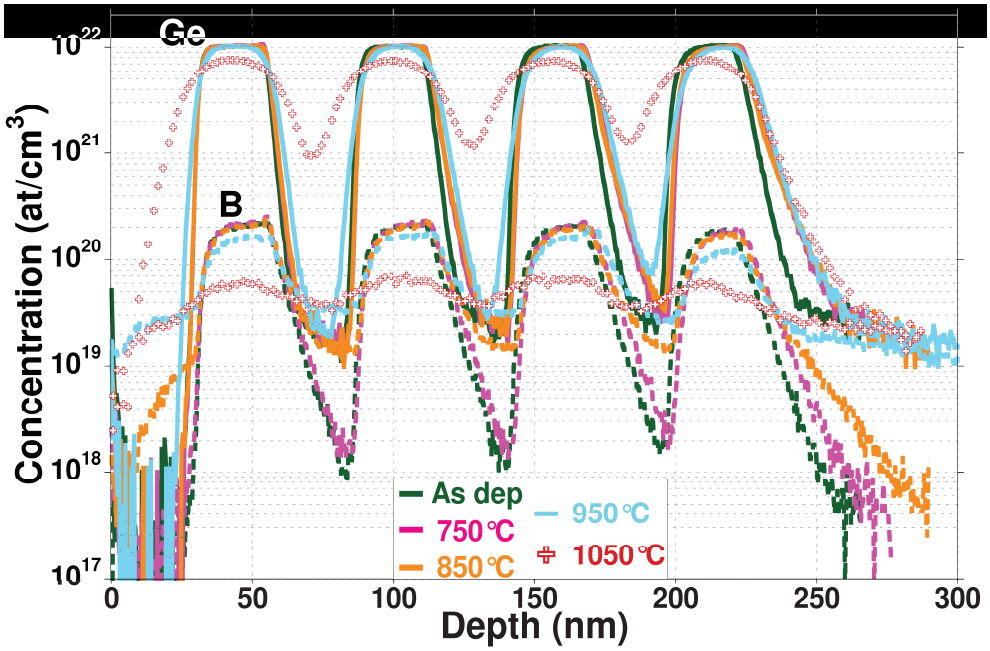

Figure III.23 Ge and B concentration profiles for as-grown and annealed SiGe:B / Si SLs.

Indeed, the real Ge content from ToF-SIMS is quite stable at 24.5%, compared to a 14.8% apparent Ge concentration from XRD, whereas 24.45% was expected from growth parameters. Measured dopant concentrations in the as-grown SiGe:B / Si and SiGe:P / Si SLs are quite high with ~2×10^{20} at/cm^3 and ~1.5×10^{20} at/cm^3 atomic concentrations for B and P, respectively, which also support this assumption. C concentration (~6×10^{20} at/cm^3) is however much higher than the one which one could expect based on XRD measurements, supposing that all C atoms are in substitutional sites. This difference is assumed to be related to the presence of a significant amount of C atoms in interstitial sites, making them invisible in XRD. This observation is in agreement with previous results on C incorporation in Si and SiGe with dichlorosilane as the Si gaseous precursor [46].

SL type	SiGe layer thickness (Å)	Si layer thickness (Å)	Mean Ge concentration in a SL period (%)	Apparent Ge concentration (%) (XRD)	Ge concentration (% - at.cm^{-3}) (ToF-SIMS)
SiGe / Si	243	306	9.6	21.6	21.4 - 1.05×10^{22}
SiGe:B / Si	247	312	8.1	18.35	21.0 - 1.02×10^{22}
SiGe:P / Si	240	302	11.7	26.5	26.5 - 1.3×10^{22}
SiGe:C / Si	295	307	7.3	14.8	24.5 - 1.2×10^{22}

Table III.vii Mean SiGe and Si layer thickness (XRR) together with the apparent Ge concentration in the SiGe layer and the mean Ge concentration in a period (XRD) in the four types of SLs and the real Ge concentration in the SiGe layer (ToF-SIMS).

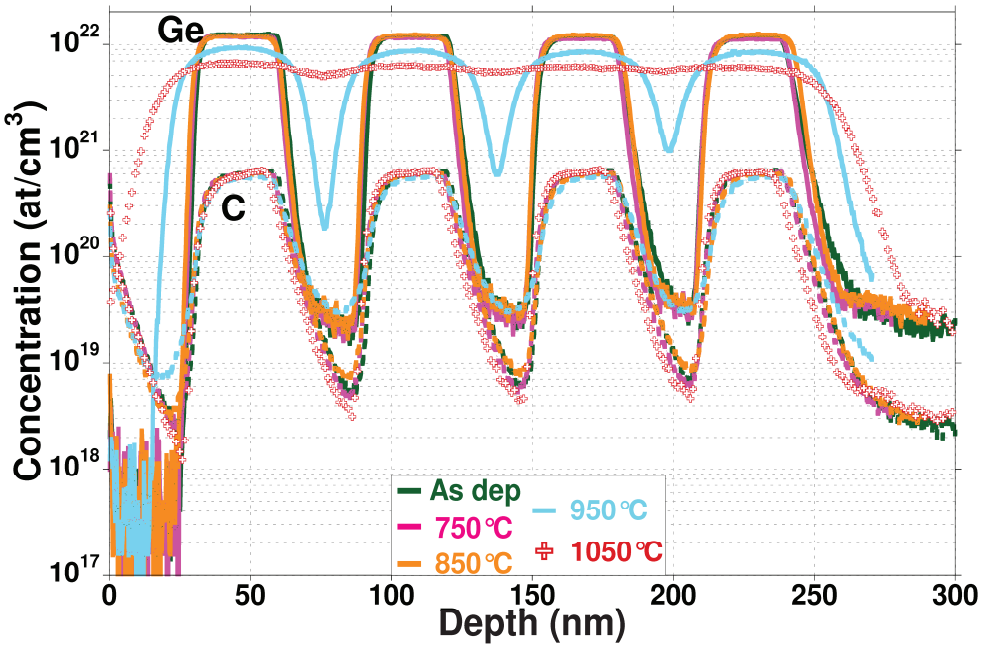

Figure III.24 Ge and P concentration profiles for as-grown and annealed SiGe:P / Si SLs.

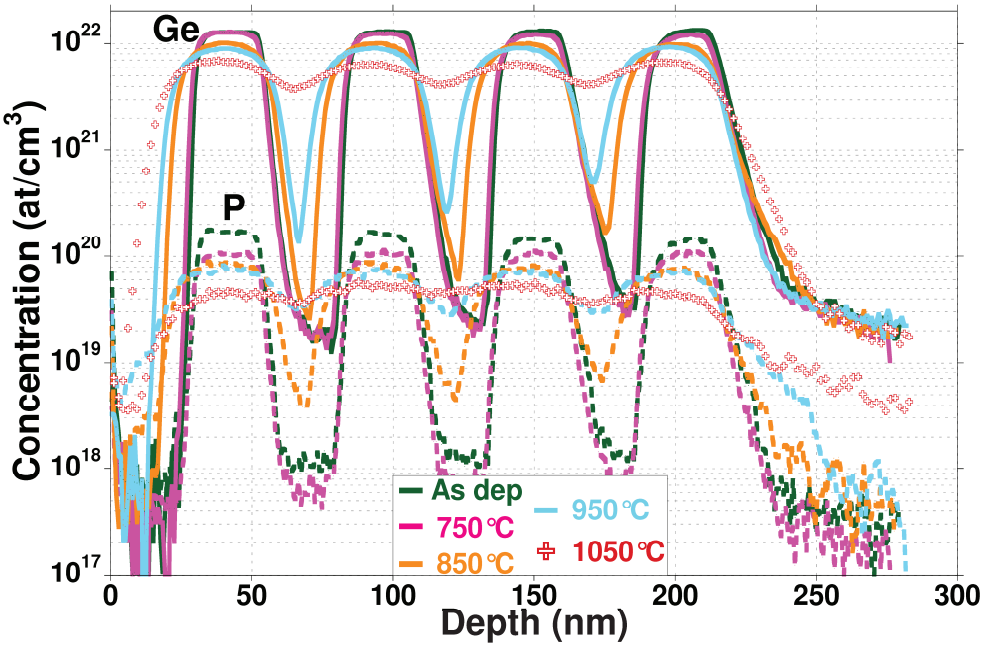

Figure III.25 Ge and C concentration profiles for as-grown and annealed SiGe:C / Si SLs.

Let us now discuss the evolution of the total elemental doses of Ge, B, P and C in our SLs with the annealing temperature. As seen in Figure III.26, the Ge dose is not impacted by the various annealings: there are indeed no more than ±2.5% variations around its value in as-grown intrinsic or B, P and C doped SLs. The same behaviour is observed for C in SiGe:C / Si SLs samples, with no more than ±3% dose variations. On the other hand, B and P doses are subject to dramatic drops. We observe a ~12% B dose loss after the 950°C anneal and a ~40% loss after the 1050°C one. The P dose drops by ~30% after the 750°C anneal and then stays approximately stable. This is likely due to a significant out-diffusion by desorption of those dopants during annealing, a phenomenon which is observed from 700°C for P in Si [47, 48] and at higher temperatures for B in Si under a H_2 rich anneal atmosphere [49, 50].

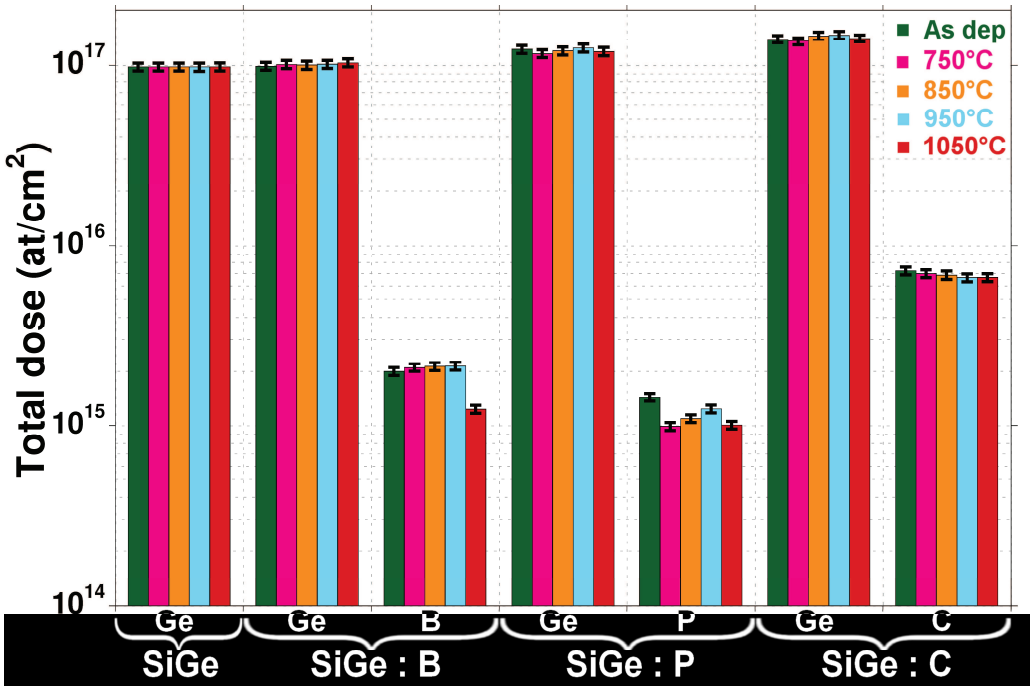

Figure III.26 Total elemental doses extracted from ToF-SIMS profiles for Ge and doping elements.

The concentration profiles displayed in Figures III.22 to III.25 allow us to quantify the diffusion of Ge, C, B and P atoms upon annealing in such SLs. Different behaviours are noticed depending on the SL nature, which we will divide into different stages:

(i) No significant diffusion is detected compared to the as-grown SL.

(ii) Top edges of each layer become slightly rounded, i.e. there is slight diffusion at high concentrations (peaks). No clear diffusion is observed for low concentrations (valleys). The ascending or descending slopes associated to each layer are slightly less important than for the as-grown SL.

(iii) Definitely rounded peaks plus larger slope modification. Larger diffusion: atoms from peak *n* reach the atoms from peak *n+1* in the valley between.

(iv) Extreme inter-diffusion with almost no distinction between peaks and valleys.

As far as Ge diffusion is concerned, SiGe / Si and SiGe:B / Si SLs (Figures III.22 and III.23) behave somewhat similarly, staying at stage (i) up to 850°C, switching to stage (ii) at 950°C and stage (iii) at 1050°C. Ge diffusion is however larger in SiGe:B / Si than in SiGe / Si SLs (be it at 950°C or 1050°C). ToF-SIMS profiles thus show that Ge diffusion is enhanced in the presence of B atoms, whereas B diffusion follows a different evolution, staying at stage (i) up to 850°C and moving directly to stage (iii) at 950°C and 1050°C. Compared to these,

diffusions of both Ge and P atoms in SiGe:P / Si SLs evolve much more rapidly (Figure III.24). They indeed move from stage (i) to (ii) at 750°C, shift to stage (iii) at 850°C and finally move over to stage (iv) at 1050°C. The presence of P significantly enhances Ge diffusion in such SLs. Moreover, Ge and P diffusion behave rather similarly, which would imply that their diffusion mechanisms are somehow related at high P concentration. Finally, Ge and C atoms diffuse very differently in SiGe:C / Si SLs (Figure III.25). C profiles are almost not affected at all by the tested thermal anneals. Meanwhile, Ge diffusion is promoted by the presence of C atoms and is faster than in any of the other SLs. Indeed, Ge profiles shift from stage (i) to stage (ii) at 850°C, to stage (iii) at 950°C and finally to stage (iv) at 1050°C. Carbon profiles stay at stage (i) up to 950°C and shifts to stage (ii) only at 1050°C. The difference of diffusion behaviour in those SLs can most likely be explained by the different diffusion mechanisms of present impurities. In next part, we will thus focus on the quantitative extraction of diffusion parameters from the ToF-SIMS profiles.

Interpretation of ToF-SIMS profiles in terms of diffusion mechanisms and extraction of diffusion parameters by experimental and simulation methods

For a start, we extracted Ge diffusivity from the ToF-SIMS profiles with the Boltzmann-Matano method [51-53]. This method is known to provide rather precise diffusivity values in the case of semi-infinite inter-diffusion, i.e. at the interface between two large adjacent blocks with different compositions, each behaving as a semi-infinite reservoir. It has already proven its accuracy for the determination of Ge diffusivity in thick, relaxed SiGe and Si layers [48]. We are however here in the case of thin, stacked layers. The accuracy of the method is then reduced (especially when significant diffusion is taking place), this because of the rather arbitrary and subjective choice of boundary conditions. Indeed, one has to determine the Matano plane, the depth at which equal amounts of species have diffused in both directions. In our case, this requires the integration of the amounts of Ge given by the ToF-SIMS profiles, by setting lower and higher boundary limits for integration, materialised by the maximum and minimum Ge concentrations. The setting of these boundaries plays an important role in the establishment of the position of the Matano plane, which in turn determines the accuracy of the extracted diffusivity values at each point. When important diffusion is taking place, the positioning of these boundaries becomes highly subjective because we are no longer able to identify the reservoir concentration regions: we are no longer in the case of semi-infinite layers (stages (iii) and (iv) in previous ToF-SIMS profiles description). Therefore the appreciation of diffusivities with this method becomes highly approximate. Our second approach was to model the Ge diffusion in three SiGe / Si periods by an error function (erf) series, as detailed in reference [54]. This method has the advantage of an easy setup through standard spreadsheet calculations. However, it does not take into account the stress-enhanced diffusivity that is occurring in our samples and thus provides diffusivity values that do not evolve with the Ge content. Both fitting protocols also suffer from the fact that, at low annealing temperatures, modification to the initial Ge distribution in the SLs is limited compared to the ToF-SIMS instrumental resolution. Accurate diffusivity values in the whole temperature range covered here can thus not be achieved with methods based on the fitting of experimental profiles only.
Therefore, we used the S-Process simulation tool. Ge diffusion computations were carried out in the so-called “one-stream” fashion, which is the only one currently available for Ge. The underlying hypothesis is that Ge atoms diffusion occurs almost solely through vacancies (V) by formation of mobile Ge-V pairs, with negligible direct interaction with interstitials (I) or dopants (such as B, P or C atoms, in our case). A “one stream” computation of Ge atoms diffusion is thus quite representative of the actual diffusion mechanisms in intrinsic SiGe / Si

SLs. We can however expect divergences between simulated and ToF-SIMS profiles in doped SLs. Simulation of diffusion in SiGe:P / Si SLs is from that point of view expected to be particularly difficult, as Ge and P diffusion processes were found in Section II to be closely related. A phenomenological description of the results thanks to this "one stream", already quite complex approach will nevertheless enable us to quantify with a reasonably small error the Ge diffusivity. Indeed, a more complete description of the various diffusion mechanisms is in progress by the study of Vacancy point defect generation from different dopant-defect clusters. Dopants such as B, P and C were integrated in a "5-stream" computation, (i.e. interaction with I, V and other potential dopants taken into account), allowing a precise simulation of their diffusion profiles. In particular, B-Ge cluster formation and kick-out rate are incorporated in calculations for SiGe:B / Si SLs. C diffusion is integrated as a typical neutral diffusion with a very short range migration length.

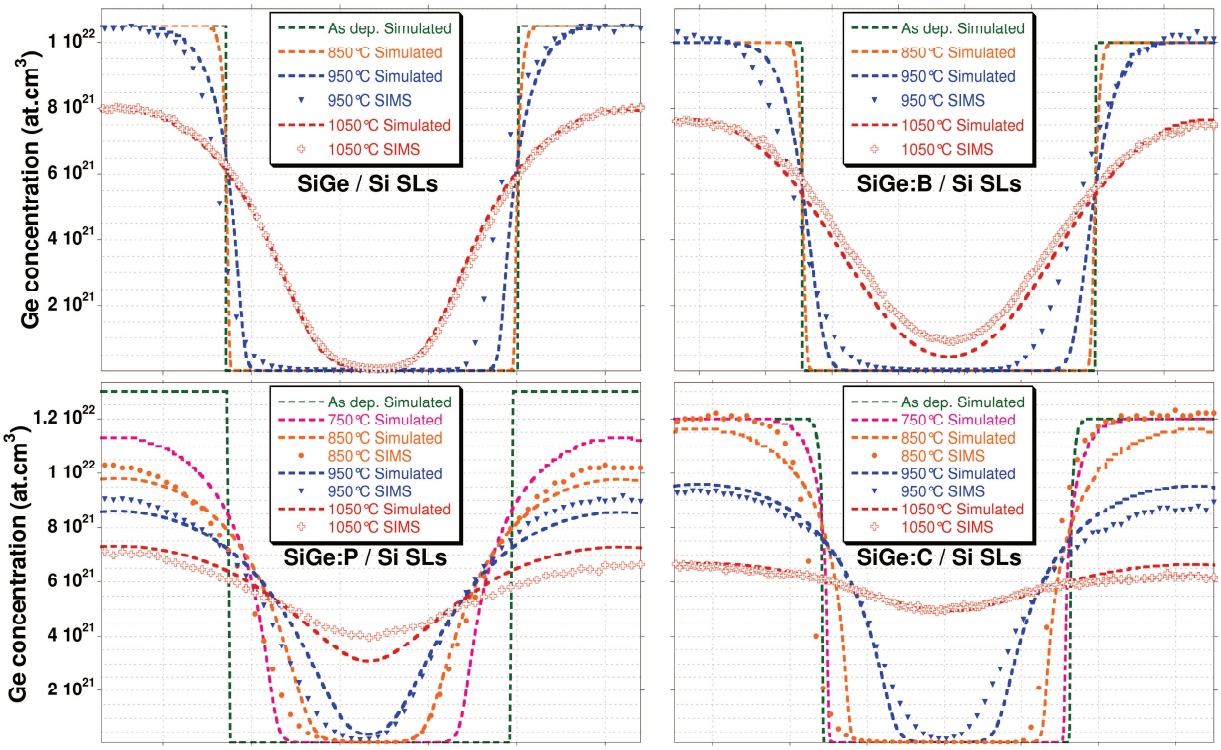

Figure III.27 Overlaid simulated and ToF-SIMS profiles for all SLs types (focus on the region around the first valley). ToF-SIMS profiles for SiGe / Si and SiGe:B / Si SLs (SiGe:P / Si and SiGe:C / Si SLs) as-deposited and 850°C annealed (as-deposited, 750°C and 850°C annealed) are not shown for clarity purposes.

Our simulation routine consisted first in the two dimensional modelling of 4 periods (SiGe, SiGe:B, SiGe:P or SiGe:C / Si) SLs on a Si substrate using the individual layer thickness and atomic concentrations extracted from ToF-SIMS profiles. Compressive strain was supposed to be equal to 0.0425 × Ge concentration at each point, corresponding to a linear extrapolation of the lattice mismatch between pure Si and Ge. Then, each annealing was modelled by a temperature ramping from 630°C up to the desired anneal temperature with a 2.5°C.s^{-1} ramp rate, followed by a two minutes anneal at the targeted temperature and a ramping-down to 600°C at a slow -10°C.s^{-1} rate. Annealing simulation was done in an inert H_2 atmosphere. Ge and dopant concentration profiles along with stress profiles were then extracted in the centre part of the simulation set-up. Ge diffusion pre-factor and activation energy were modified and stress impact on diffusivity of both Germanium and dopants was taken into account through

an Arrhenius law (similarly to Xia *et al*. in [55]) in order to accurately fit ToF-SIMS profiles. Ge "one stream" diffusivity computation is thus carried out using the following formula:

$$D_{Ge} = D_0 \cdot e^{(-E_a / kT)} \cdot e^{(B\varepsilon / kT)} \quad \text{(III.12)}$$

D_0 being the diffusion pre-factor, E_a the activation energy, B a factor characteristic of the importance of stress-enhanced diffusion and ε the stress component along the diffusion axis. As only one Ge-point defects mobile pairs are considered in S-Process, interstitial and vacancy fraction, respectively f_I and f_V, are included in the diffusion pre-factor D_0. Thus, we consider that $D_0 = f_I \times D_0^I \times [I]/[I^*] + f_V \times D_0^V \times [V]/[V^*]$ where D_0^I and D_0^V are respectively the interstitial related diffusion pre-factor and the vacancy related diffusion pre-factor, *[V]* or *[I]* are the actual point defects concentrations and *[V*]* or *[I*]* their corresponding equilibrium value at the diffusion temperature. D_0, *Ea* and *B* values obtained for best fit between simulated and actual ToF-SIMS profiles for each SLs type are provided in Table III.viii. Simulated profiles are displayed in Figure III.27. Notice that our system does not make the distinction between active or inactive atoms (i.e. between free atoms and interstitials, clusters…). A diffusivity value for a given element thus corresponds to the averaged diffusivity of all its states, i.e. to its *effective diffusivity*.

SL type	Element	D_0 ($cm^2.s^{-1}$)	*Ea* (eV)	*B* (a.u.)
SiGe / Si	Ge	10	4.22	40
SiGe:B / Si	Ge	10	4.11	20
	B	2.88×10^{3}	4.42	-40
SiGe:P / Si	Ge	1×10^{-11}	1	40
	P	1	3.5	30
SiGe:C / Si	Ge	2×10^{-5}	2.6	52.5

Table III.viii Input parameters of equation (III.12) during simulation process for each type of SLs. In S-Process, B and P diffusivities vary depending on their charge state (1, 0, -1 or -2) and on the associated defect (V or I). To simplify we present in this table parameters issued from a fit to the sum of all these contributions by an expression identical to equation (III.12). Divergence between diffusivities as simulated by S-Process and diffusivities calculated from parameters in this table never exceeds 3%.

Ge diffusivities in intrinsic Si/SiGe SLs obtained with the Boltzmann-Matano, the Erf series and the S-Process methods for a 10% Ge content are displayed in Figure III.28. We clearly observe (as foreseen and explained at the beginning of this section) that neither the Boltzmann-Matano nor the Erf models allow diffusivity value extraction for annealing temperatures below 950°C. However, values obtained by the three methods for the two highest anneal temperatures (i.e. 950°C and 1050°C) are quite close. This most likely indicates that our values obtained by the Erf and the S-Process methods are reliable on these points. It also means that, for high temperature anneals where long-hop diffusion mechanisms are not driving the diffusion profiles, one does not need to resort to advanced diffusion process simulation tools to obtain acceptable diffusivity values in this kind of sample. Our Ge diffusivity values are ~ 10 times (~ 2 times) higher than values found by Xia *et al.* [55] (Hasanuzzaman *et al.* [56]) with experimental settings approaching ours. Meanwhile, the slope of the Arrhenius plots are approximately the same. Results from the pioneer works of Zangenberg *et al.* [57] deal with the self diffusion of Ge in SiGe. They are thus less correlated with ours, especially at low temperatures since they relate the diffusion of Ge in SiGe as we are relating the diffusion of Ge in Si (at low temperature) and in varying Ge content SiGe (at

higher temperature, when the Ge atoms from two different layers meet in the bottom of a valley region). Notice that Hasanuzzaman *et al.* used a 5-stream model for the simulation, providing *a priori* the most accurate extracted values. This shows that even with our rough model we can extract quite reliable diffusivity values. A comparison between Ge diffusivity values in the whole temperature range and for all SLs types is displayed in Figure III.29, along with B and P diffusivities.

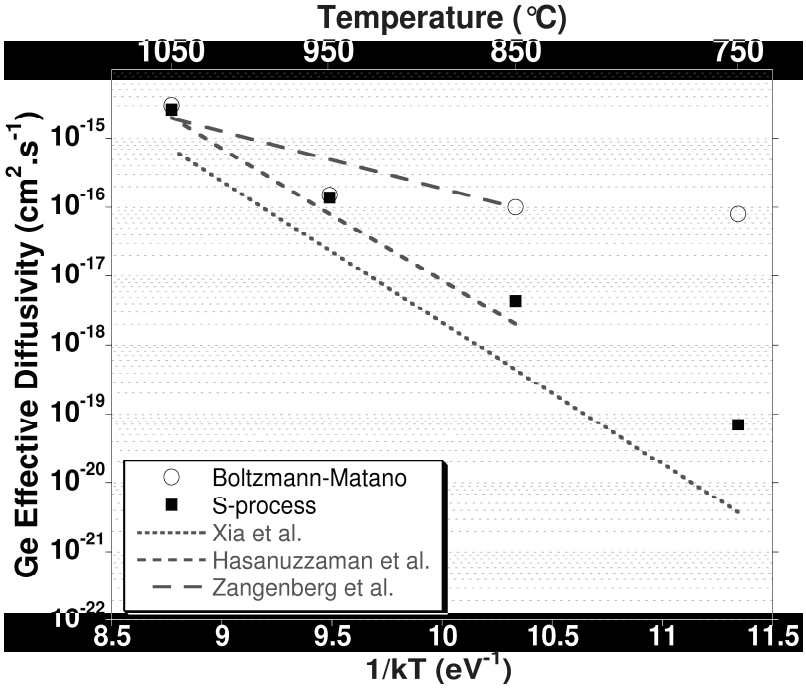

Figure III.28 Comparison between Ge diffusivity values in SiGe / Si SLs obtained with the Boltzmann-Matano, the Erf model and the S-process simulation tool at 10 at% Ge content. Dotted lines represent data extracted from Xia *et al.* [55], Hasanuzzaman *et al.* [56] and Zangenberg *et al.* [57].

As expected from ToF-SIMS profiles, Ge diffusivity is slightly higher in B doped than in intrinsic SLs. The main difference between the two is a smaller stress-enhanced diffusion in B-doped SLs (50% decrease of parameter *B*). This is in good agreement with the lower level of built-in compressive strain due to the presence of significant amounts of small B atoms. E_a is otherwise slightly lower for B doped than for intrinsic SLs (see Table III.viii). B atomic concentration in the SiGe layers is well above its solubility limit (few 10^{19} at/cm^3), which is ideal for the formation upon annealing of Boron-Interstitial Clusters (BICs). Most B atoms in our SLs are thus contained in BICs, which prevents their diffusion. At low annealing temperatures, only the diffusion of substitutional "free" B atoms occurs, the presence of typical kick-out mechanism "skirts" on Figure III.23 boron profile after the 850°C anneal. Diffusion of such B atoms would not induce any additional Ge diffusion. However, after 950 and 1050°C anneals, we observe (see Figure III.23) some skirts in the first twenty nanometres of the B profile and due to "free" B atom diffusion. in addition to this, a B concentration loss is occurring in the SiGe layers which is likely due to the breaking-up of boron interstitial clusters (BICs) into interstitial and "free" boron atoms which will in turn diffuse [58, 59]. It is also at these temperatures that we observe a faster Ge diffusion. We therefore suggest that the diffusivity enhancement observed in the SiGe:B / Si SLs is due to the interaction of Ge atoms with interstitials released by BICs clusters during thermal annealing. Considering that Ge is known to diffuse almost entirely with V and that the fraction *fI* of Interstitial diffusion of Ge is small, the relatively weak enhancement is explained.

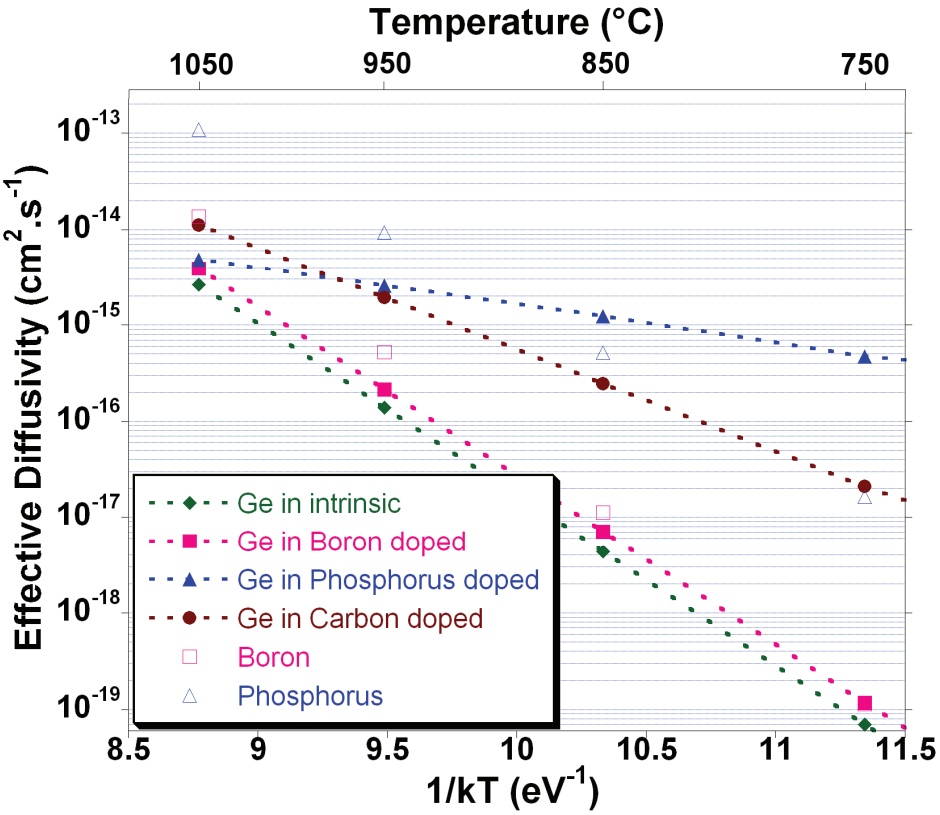

Figure III.29 Diffusivity values for Ge and dopants in all SL types, at 10 at% Ge content.

In contrast, Ge diffusion in presence of phosphorus is much faster and starts at a much lower temperature, as indicated by an activation energy E_a more than four times lower than in intrinsic or B-doped SLs. Stress-enhanced diffusion is however the same as in intrinsic SLs. The Ge diffusion in Figure III.24 is thus mainly enhanced by the presence of high levels of P atoms and to a much lesser extent by the increased built-in stress. The only credible explanation for such a huge change in diffusion parameters would be, as was the case for B doped layers, an indirect interaction between Ge and point defects released by phosphorus-defect clusters formed at high P concentration. Similar conclusions were drawn by Pichler *et al.* concerning the role of a high P concentration on the diffusivity of antimony [60]. It is known that P diffuses with I at low concentrations (up to ~3×10^{19} at/cm^3), its diffusion for higher concentrations being still under investigation. We can however already state that (i) it is activated even at low temperatures (ii) the defect release rate and/or quantity is much more important than the one induced by BICs. As this could not be taken into account in our present simulation routine, it explains why the fit of simulated and actual profiles of SiGeP / Si SLs was not as good as in the previous cases (see Figure III.27).
Finally, Ge diffusion in SiGe:C / Si SLs is quite well described by our simulations. This is likely due to a significant indirect interaction between C and Ge atoms. In our model, C atoms have a very short migration length (between 3 and 30×10^{-5} nm), and thus almost no diffusion occurs during annealing (see Figure III.25). They will instead move from substitutional to interstitial sites, as suggested previously. A significant amount of vacancies are then released, significantly accelerating Ge diffusion [61, 62]. Activation energy E_a and pre-factor D_0 are consequently much lower in SiGe:C / Si than in SiGe/Si SLs (see Table III.viii). This results in Ge diffusivity in SiGe:C / Si SLs being the highest one at high temperatures.

Let us now deal with B and P dopants. Phosphorus is characterised by diffusivities about one decade higher than B, with however a lower activation energy as shown by a lesser dependence on the annealing temperature (see Table III.viii and Figure III.29). P diffusivity increases with the Ge content (stress enhanced diffusivity), while B diffusivity diminishes. The latter is likely due to weak interactions between B and Ge atoms leading to a B migration energy increase in the presence of the Ge atoms, thereby reducing their diffusivity [63]. Literature data are scarce on dopant diffusion in strained SiGe. We can nevertheless refer to Christensen *et al.* [64] and Rajendran *et al.* [65] for P and B, respectively. We obtain in both cases diffusivities within an order of magnitude of their values (~ 10 times higher values for P, ~ 2 times lower for B), with a similar dependence on annealing temperature. Both of these works however dealt with lower dopant concentrations (inferior to 1×10^{19} at/cm^3) than in our case. As dopant-defects clusters controls the diffusion behaviour of dopants at high concentration, an extensive study of the clusters formed is needed in order to enhance the accuracy of our results. Nevertheless, the effect of these clusters on germanium diffusion seen in our experience can be useful for their study.

In depth quantitative strain analysis

The evolution of in-depth strain level in SLs is of great interest for device purposes. We will focus here on local stress mapping by dark field holography and by simulated pressure profiles issued from previous simulations, based on ToF-SIMS profiles. Dark field holography is a recently developed transmission electron microscopy-based technique which is particularly well suited for measuring the strain in nanometre-scale semiconductor structures [41, 66] and the ability of this technique for studying SiGe [67] as well as SiC [68] strained structures has already been demonstrated. For dark field holography, an electron biprism is used to form an interference pattern from coherent electrons that have passed through the strained region of interest with electrons that have passed through a reference region, such as the substrate. A dark field electron hologram uses only a diffracted beam that corresponds to the lattice planes that are of interest. This interference pattern, referred to as the hologram, contains information about the phase of the electrons. The phase of an electron is sensitive to magnetic fields, electrostatic potentials and strain fields in the sample. Therefore, information on the difference between the reciprocal lattice vectors of these two regions can be obtained by using geometrical phase analysis to provide a strain map [69].
Strain mapping was performed on selected samples, prepared into parallel-sided lamellas with a dual-beam Focused Ion Beam (FIB). Holograms were acquired with a probe corrected field emission gun TEM operated at 200 kV. The objective lens was switched off and a dedicated Lorentz lens was used for larger field of view. An ellipse-shaped beam was projected onto an electrostatic biprism unto which a voltage of 180 V was applied. Strain information in the [001] growth direction was obtained by selecting the (004) diffracted spot in dark field mode with an objective aperture. Holograms with a fringe spacing of 2 nm were acquired during 64 s for signal-to-noise improvement [41, 66]. These interference patterns were treated using a home-made geometrical phase analysis plug-in for DigitalMicrograph^{TM}, allowing calculation of the strain map.

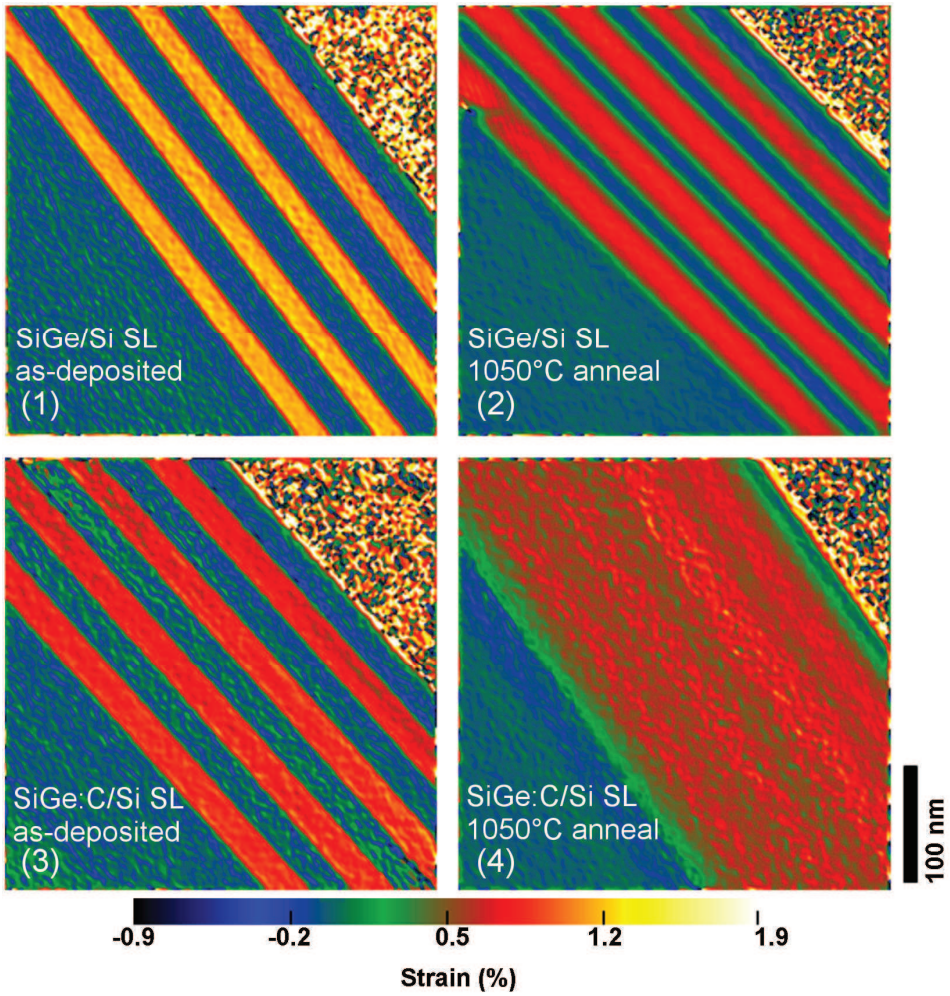

Figure III.30 Dark field holography strain maps acquired on SiGe / Si SLs (top row) and SiGe:C / Si SLs (bottom row) after either their epitaxy at 650°C ((1) and (3) : left column) or a after a 2 min. anneal at 1050°C ((2) and (4) : right column). The sample substrate is on the bottom left-hand corner of each image. The top right-hand corner corresponds to a resist layer deposited prior to preparation in order to protect the sample surface.

Strain maps obtained on as-deposited and 1050°C annealed SiGe and SiGe:C / Si SLs are shown in Figure III.30. The strain colour scale is defined as follows:

$$\varepsilon = \frac{a_{ROI} - a_{Si}}{a_{Si}} \qquad \text{(III.13)}$$

where a_{ROI} is the lattice parameter in the region of interest (SLs) and a_{Si} is the lattice parameter measured in the silicon substrate. Positive values therefore represent tensile strain compared to the substrate lattice. SiGe layers appear in yellow or red, whereas Si is in blue-green. Strain profiles (averaged over 20 nm) extracted from the maps are represented in Figure III.31, along with pressure profiles issued from simulation. For intrinsic samples, it is observed that after annealing, SiGe layers strain peaks have decreased from 1.2 to 0.8 % and they have also broadened due to Ge diffusion, in agreement with Section I conclusions. For both techniques, the shape of strain distribution is closely related to the Ge profiles (Figure III.22). We observe an overall good agreement between both techniques, which that our simulation process is accurate. Moreover, it underlines the strong impact of Ge diffusion on the strain distribution and confirms the conclusions of previous sections on stress evolution

during annealing. For both samples, the first SiGe layer stress level is found to be slightly lower in dark field holography. However, according to the ToF-SIMS profiles, the Ge content is the same in the four layers. Therefore, this difference can be related to the sample preparation or to the fact that this layer is close to sample surface. Indeed, strain relaxation phenomena occurring in a thin lamella might be different for a layer close to the surface and for layers placed deeper in the sample. Besides, the high strain levels (negative or positive) that can be seen at some interfaces and just below the surface are artefacts due to phase discontinuities.

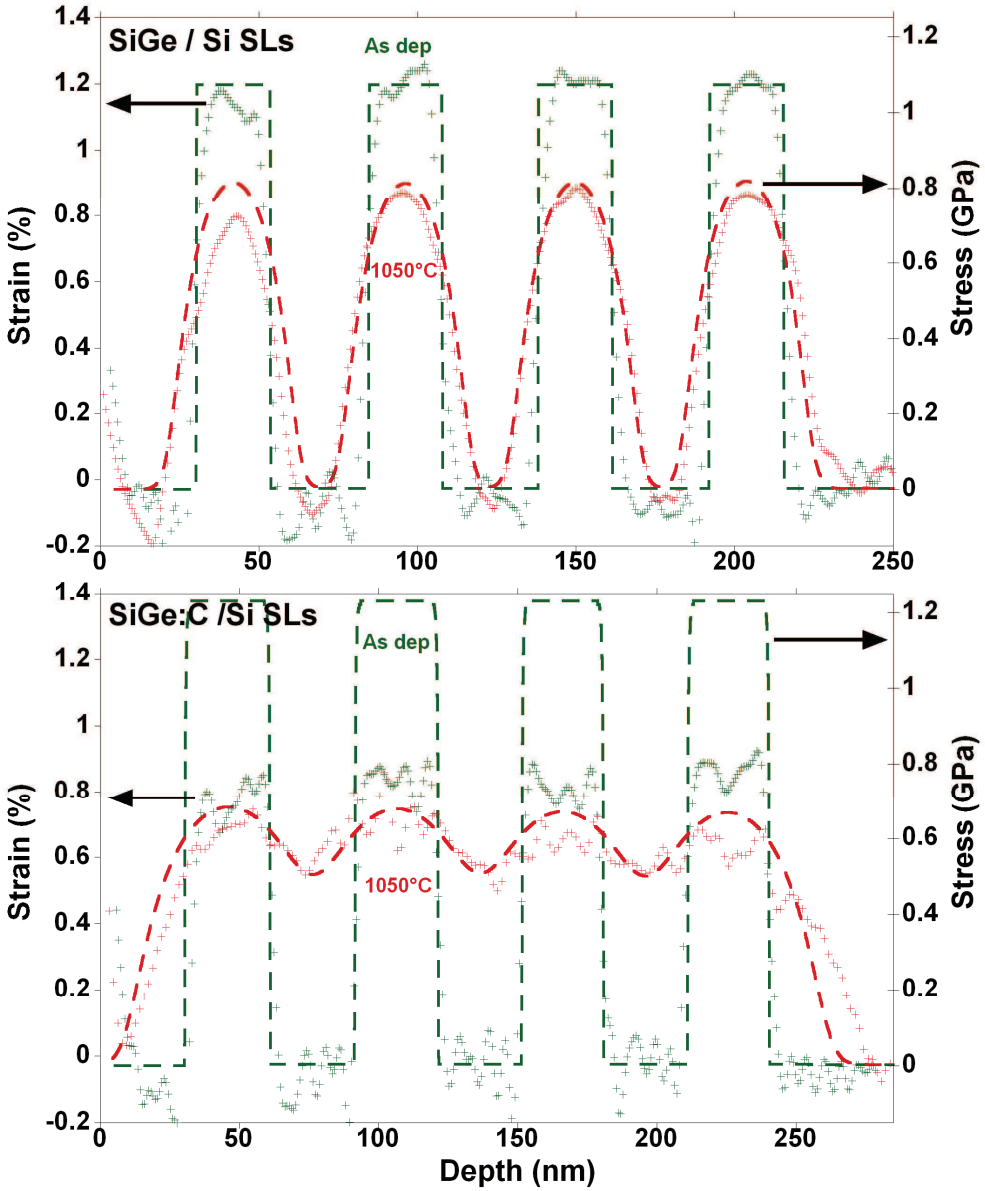

Figure III.31 Dark field holography strain profiles (crosses) and pressure profiles from S-Process simulations (dotted lines) for as-grown (at 650°C) and annealed (at 1050°C for 2 min. in H_2) SiGe / Si SLs (top) and SiGe:C / Si SLs (bottom). The huge discrepancy between experimental strain profiles and stress simulations in the case of as-grown SiGe:C / Si SLs is due to the fact that the S-Process software is not able to take into account the strain compensation by substitutional C atoms in SiGe:C layers. The reason why the simulated stress is higher in the SiGe:C layers than in the SiGe layers is then fairly simple: the Ge concentration is equal to 24.5% in the former, versus 21.4% in the latter (see Table III.vii).

The effect of the strain compensation by C doping can be seen by making a comparison between the maps (1) and (3). As expected, heavy C doping leads to an important decrease of the strain from approximately 1.2 to 0.8 %. After annealing at 1050°C, the strain peaks have almost disappeared and have merged in a single large strained area of 0.6 - 0.7 % in map (4). The shape of this area is in good agreement with the extreme Ge diffusion observed in the ToF-SIMS profile (Figure III.25). The decrease of the strain level after annealing is less important in these SLs (-0.15 %) than in the intrinsic ones (-0.4 %) on dark field holography profiles (Figure III.31). This tendency is not observed on simulated stress profiles. Profiles obtained with both techniques in the annealed samples are in good agreement, and they exhibit similar shape in the as-deposited SLs. However the simulated nominal strain value in SiGe:C layers for the as-deposited samples is very high compared to the experimental data. This is due to the fact that substitutional dopants in the SiGe matrix are not taken into account for stress calculations in S-Process and thus the strain level found by simulation in the as deposited SLs is representative of a corresponding intrinsic SiGe only. However as suggested by previous observations, C atoms massively move from substitutional to interstitial sites during annealing, which reduces their role in strain compensation. The agreement between simulated and measured strain profile after the 1050°C anneal shows then that almost all C atoms have moved to interstitial positions after this anneal. This is in agreement with recent results in [70]. As a consequence of the over-estimation of the simulated strain in doped SLs, the factor B in equation (III.12) is thought to be under-estimated as compared to the real role of stress enhanced diffusion.

We have studied the strain state, in-depth chemical composition and diffusion behaviour of Ge and dopants in SiGe / Si SLs with 4 periods. The SLs were epitaxially grown at 650°C. The SiGe layers were either intrinsic or highly boron, phosphorus or carbon doped. They were characterised with XRD, XRR, ToF-SIMS and Dark Field electron Holography. In addition, simulation was used to quantify the diffusion of the different elements along with the strain distribution in the layers. The complementarities of the different characterisation techniques allowed a complete study of the stacks properties and yielded conclusions in agreement with simulation results.

ToF-SIMS profiles acquired using the extended FS protocol enabled simultaneous quantification of matrix elements and dopants. They allowed a rather good quantification of inter-diffusion. A clear dependence of Ge diffusivity on the presence of dopants and their nature was evidenced. Ge diffusivity significantly decreased when moving from SiGe:C to SiGe:P to SiGe:B SLs. In contrast, Ge diffusivity in the latter type of SLs was barely higher than in intrinsic SiGe SLs.

Extraction of the diffusion parameters and diffusivity values from ToF-SIMS compositional profiles was performed by simulation. Ge diffusivity was found to be enhanced by the compressive stress present in the SiGe layers and, at a much larger scale, by dopant induced defects injection (little enhancement with Boron, definite increase with phosphorus and carbon respectively at low and high temperatures). Different mechanisms for enhanced diffusion in each type of SLs were proposed.

Eventually, strain profiles at the nanometre scale were obtained in selected samples using dark field holography and compared to simulated profiles. A good agreement was obtained between both techniques on intrinsic SLs, validating the ToF-SIMS results on the strain evolution during thermal annealing. It was found that simulation overestimated the nominal strain level of carbon doped as-deposited samples, which was no longer the case for the 1050°C annealed sample. This is related to the massive displacement of carbon from substitutional to interstitial sites after high temperature annealing.

III. 4. b- In intrinsic and doped SiGe layers upon dry or wet oxidising anneal

As we saw in section III. 3. d-, Ge oxidation mechanism can be used to obtain high Ge concentration Ge NW for three dimensionally stacked transistors. Understanding of the behaviour of intrinsic or C, B or P doped SiGe layers under different oxidation anneals (dry or wet) is therefore needed for process optimisation. In this study, we used the same samples than in section III. 3. d- (dry oxidised), along with a second set of samples. This second series involved four samples grown with the same RP-CVD tool, consisting in 30 nm $Si_{0.78}Ge_{0.22}$, $Si_{0.79}Ge_{0.21}B_{0.004}$, $Si_{0.78}Ge_{0.21}C_{0.01}$ and $Si0._{74}Ge_{0.26}P_{0.04}$ layers on SOI substrates. These samples were annealed for 35 min at 750°C in wet oxygen atmosphere.

Behaviour of SiGeC layers under dry oxidation

Given the reduced number of samples available, we do not intend to perform an exhaustive study of the properties of SiGeC under dry oxidation; some works are available in literature for that purpose [71, 72]. However, the extended FS ToF-SIMS profiles can still provide some useful information which we will detail now.
First of all, the most important feature of the Ge "enrichment" process seems preserved on SiGeC. Indeed, there is no Ge dose evolution with annealing (or within the measurement error of the extended FS protocol, see Figure III.18.A), which means that the Ge overall dose is conserved during the oxidation process. The amount of Ge originally present in the consumed SiGeC layer is rejected at the oxidation front and thus participates in the Ge content enrichment of a 10-15 nm thick region. The Ge peak concentration and FWHM of this region increase with the oxidation time, with 28.9 and 32.5 at% peak concentrations and 2.6 and 3.5 nm FWHM after 30 minutes and 60 minutes anneals, respectively.
No such behaviour is observed for C, however. This is made clear in Figure III.32, which displays the Ge and C concentration profiles for all samples. The bump on the Ge profiles at the SiO_2/SiGeC interface is clearly visible, while the C profiles exhibit no such feature. Furthermore, we observe a significant dose loss during the annealing, as shown in Figure III.18.B. This was already reported by Cuadras *et al.* in [71]. They however used an optical characterisation technique for their study, which is sensitive to substitutional C atoms only. Yet C atoms are known to move from substitutional to interstitial sites during annealing [22, 61, 62]. In order to obtain reliable data on the overall C dose after annealing, it is thus necessary to be able to probe both substitutional and interstitial C. ToF-SIMS does have this ability since the chemical information it gives for an element is independent of its crystallographic location. By looking at the evolution of the C dose with annealing (Figure III.18.B) we thus have an idea of the total C consumption throughout the process. The dose loss is found to be directly proportional to the oxidation time (5.10^{14} at/cm^2 after 30 minutes, 1.10^{15} at/cm^2 after 60 minutes). Moreover, a part of the remaining C is situated in the oxide, as testified by the shoulder on the C profiles in Figure III.32 (1% of the remaining dose after 30 minutes anneal, 1.7% after 60 minutes). The addition of this contribution to the dose loss gives (with a ± 30% error bar) the original C dose present in the consumed SiGeC layer (as calculated with a 2.2 at% C content and with T_{i1}, T_{i2} or T_{iC} as the consumed layer thickness). This would indicate that C atoms do not diffuse towards the oxidation front, but are instead consumed as the oxidation front goes deeper and deeper. Once in the oxide, the C forms C-C or C-O complexes which either out diffuses as CO or segregates just before the oxidation front [71] (shoulder in C profiles, Figure III.32).

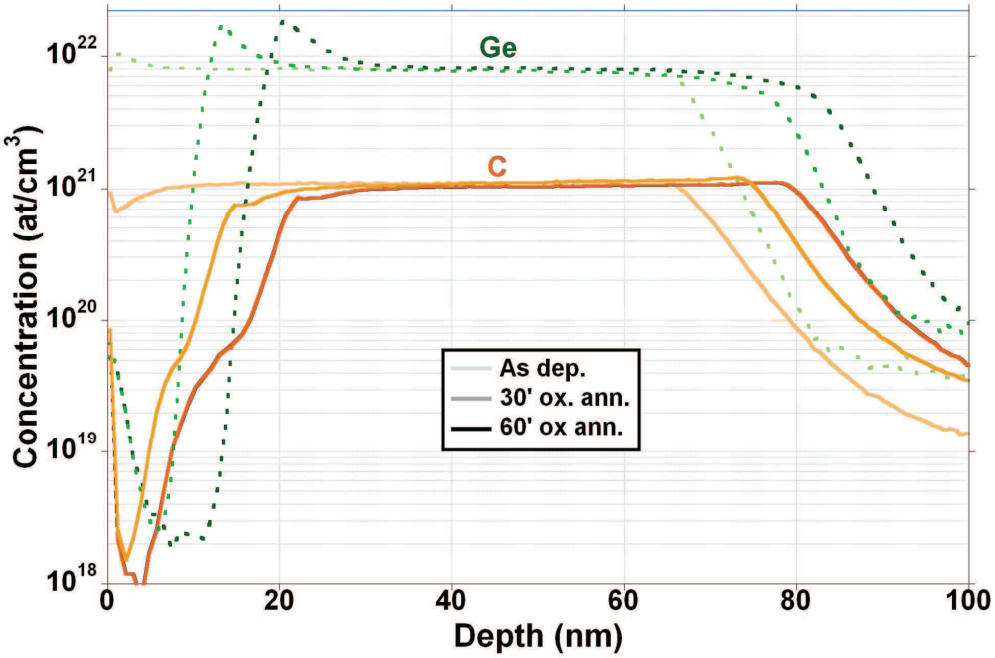

Figure III.32 Extended FS ToF-SIMS Ge and C concentration profiles in as-deposited and in dry oxidised SiGeC layers.

Another interesting feature of the SiGeC "enrichment" process is its oxidation rate. The measurement of the oxidation rate can be performed either by measuring directly T_{SiO2} or by using T_{i1} or T_{iC} (see section III. 3. d-) and by multiplying them by 2.25. All methods give approximately the same result, with a ±1.5 nm discrepancy. T_{SiO2} is found to be 12 nm and 19.5 nm after 30 and 60 minutes oxidation, respectively. Due to relatively short oxidation times, we stay in the thin oxide regime, where the Deal and Grove law for thermal oxidation can be approximated to a linear relationship [73]. We find a linear rate constant B/A of 0.25 nm.min^{-1} with an initial offset (initial oxide width, due the furnace ramp-up) of 4.5 nm. Literature is scarce on dry oxidation kinetics of SiGe at 900°C. To our knowledge, no such data is available for SiGeC at these temperatures. The comparison is however possible with values coming from a previous paper from our laboratory [74], where $Si_{0.9}Ge_{0.1}$ dry oxidation at 900°C was studied. A linear rate constant of 0.298 nm.min^{-1} with an initial oxide width of 7.9 nm were found. These values are higher than those found in our samples, meaning that the oxidation kinetic is significantly slower in our case. Although the oxidation rate is usually reported to increase with the Ge fraction in SiGe [75], we observe the opposite here (the Ge fraction in our samples being ~0.16 compared to 0.1 in [74]). This would mean that the presence of C atoms in the layer reduces the oxidation kinetics. This behaviour has already been observed by *Cuadras et al.* at 1000°C in [71]. The authors proposed two possible reasons for the reduced kinetics in SiGeC: (i) the injection of excess Si interstitials in SiGeC layers compared to SiGe and (ii) the formation of C-O complexes at the oxide/SiGeC interface (before its out- diffusion as CO), acting as an obstacle for the oxidant diffusion to the SiGeC layer interface. The latter is corroborated by the extended FS ToF-SIMS profiles shown in Figure III.32, in which a small amount of C is detected in the oxide layer, right before the oxidation front.

Behaviour of SiGe, SiGeB, SiGeC and SiGeP layers under wet oxidation

Extended FS ToF-SIMS profiles of samples of each dopant type after 35 min anneal are shown in Figure III.33. Again, we observe Ge condensation as in dry oxidised samples. In particular, intrinsic and carbon doped layers show similar features than layers which underwent dry oxidation, with a conservation of total Ge dose and no oxidation of Ge. Furthermore, carbon is not subject to condensation and is partially consumed (with a dose loss of ~13%) and partially integrated in the oxide as in the dry oxidation case. However the oxidation kinetics seem much faster, with an observed oxide thickness of 36, 49, 25 and 60 nm for SiGe, SiGeB, SiGeC and SiGeP respectively. For SiGeC, we have thus a ×2 enhancement of oxidation rate as compared to dry oxidation, which agrees with results from [76] (although this is to be nuanced since the C content in the samples is half that of the dry oxidised samples). These results also confirm the fact that the presence of C in SiGe decreases the oxidation rate. Moreover, SiGeC layers have the lowest oxidation rate of all, followed by intrinsic SiGe, SiGeB and SiGeP which have the highest rate. Higher oxidation rates are observed in the case of B and P doping, which is in agreement in results in Si [77]. The oxidation is so fast in the two latter ones that it almost consumed the entire original SiGeX layer: indeed an oxide thickness of 49 nm (60 nm) corresponds to a consumption of 49/2.25=22 nm (60/2.25=26 nm) of the original SiGeB (SiGeP) layer thickness [10, 37].

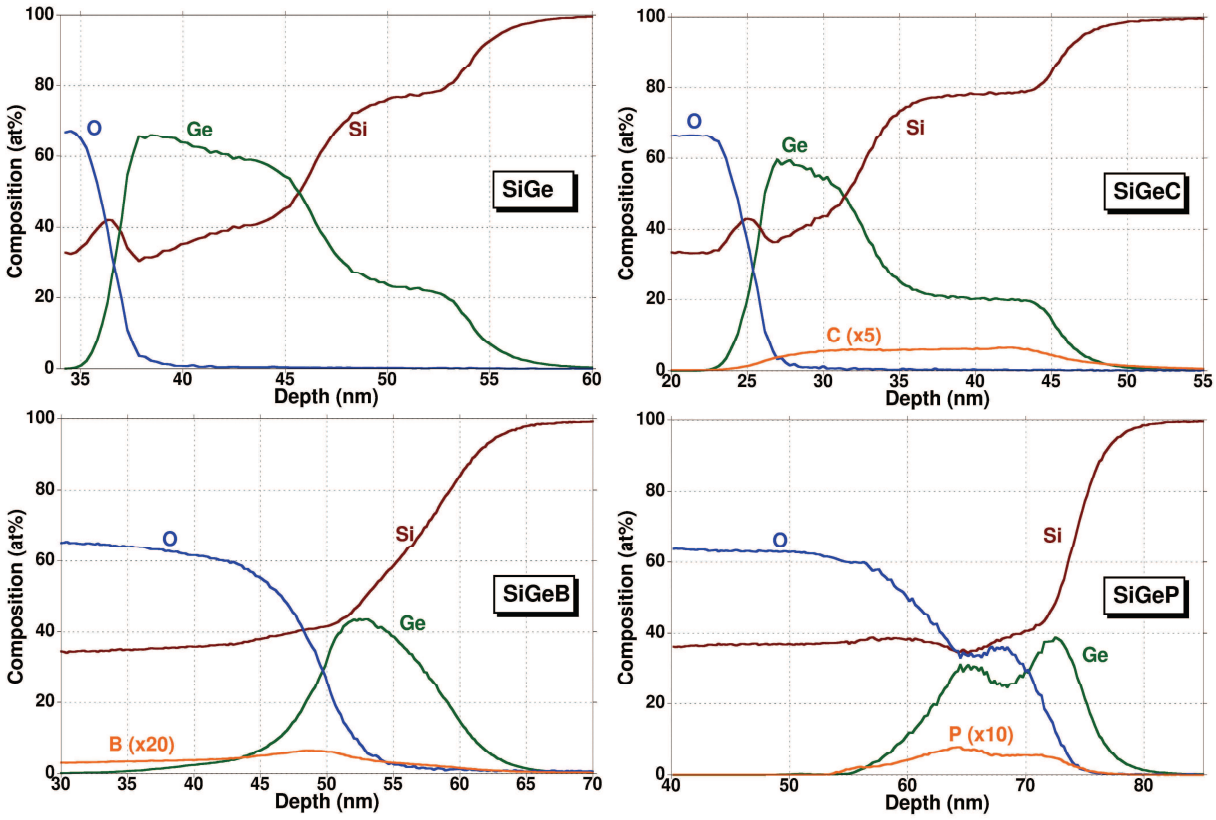

Figure III.33 Extended FS ToF-SIMS of the SiGe, SiGeC, SiGeB and SiGeP layers oxidised in a wet atmosphere for 35 minutes at 750°C.

As seen on the SIMS profiles, this clearly deteriorates the interfacial oxide quality. When Si content of the SiGe condensed layers becomes low, oxidation of Ge instead of Si becomes energetically possible and some Ge is oxidised. This phenomenon is observed on the SiGeP sample, and at a lesser extent on the SiGeB sample profile (see Figure III.33). Furthermore, the Ge profile in the SiGeP oxidised layer features a double peak, as if the layer was 'split'

and allowed oxide regrowth just behind (see the inverse bumps on Ge and O content between 60 and 70 nm in the ToF-SIMS profile). HR-TEM cross section imaging of this sample shown that this was indeed the case (see Figure III.34). A bright thin layer corresponding to silicon dioxide appears between two dark zones corresponding to Ge rich zones. This phenomenon is however not constant along the interfaces: at small scale (right image) it appears as a continued layer but at larger scale, one can see that it is not the case. This also explains the relatively bad resolution of these layers with ToF-SIMS: as the analysed region is 80×80 µm wide, both 'split' regions and 'non split' regions are taken into account at the same time.

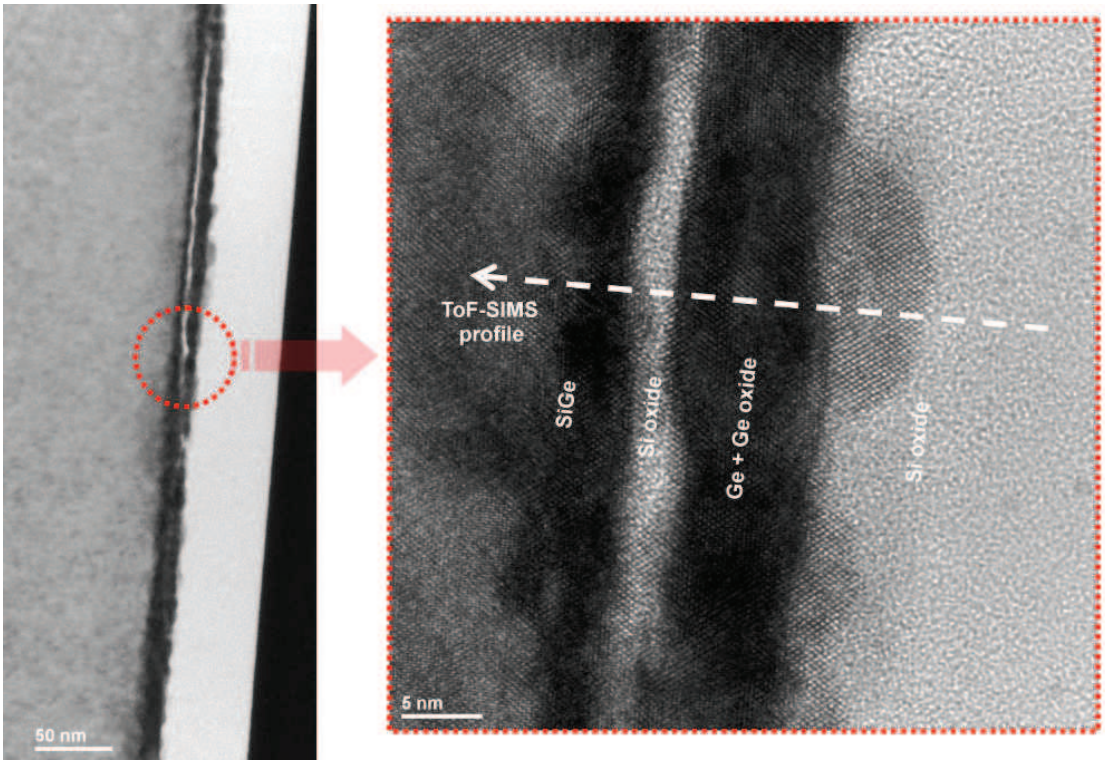

Figure III.34 HR-TEM images of the SiGeP sample oxidised in a wet atmosphere for 35 minutes at 750°C, at a large scale (left) and at a smaller scale (right).

To verify if Ge oxidation really occurred in this case we thus performed XPS analysis on both a sample with 'split' SiGe interface (which underwent fast oxidation) and on one with a clean interface (which underwent slow oxidation), after complete oxide removal with HF. The comparison of the Ge core levels [78], shown in Figure III.35, proves that the contribution of Ge oxide bonds is much stronger in the case of the fast oxidised sample. The area ratio of the Ge3d on GeO_2 is indeed of 6×10^6 in the case of slow oxidation against only 4 in the case of fast oxidation. This proves that although it is usually very unfavourable energetically, Ge oxidation really occurs in this case.
The role of dopants is thus crucial in the (wet) oxidation kinetics: as C slows down the oxidation rate and is consumed through the process, B enhances it and massively segregates in the oxide, and P drastically enhances it while staying in the Ge rich regions. These observations correlate well with those of behaviour of wet or dry oxidation of B or P rich silicon [79-81].

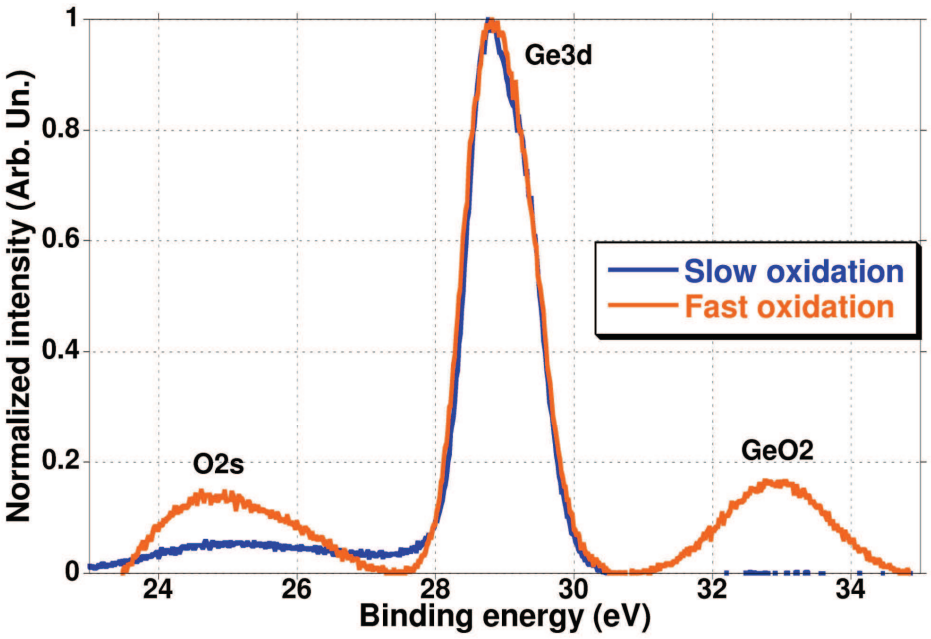

Figure III.35 XPS spectra of the Ge3d core level for samples which underwent fast or slow wet oxidation.

The extended FS protocol has allowed the revelation or confirmation of a few specific behaviours of SiGeC layers under dry oxidation, such as the conservation of Ge and the consumption of C through the enrichment process, and the decrease of oxidation rate compared to SiGe layers. Similarly, features of wet oxidation of SiGe, SiGeB, SiGeP and SiGeC layers were revealed. Specifically, layers doped with P yielded the highest oxidation rates. In some cases, the creation of germanium oxide islands separated from the original layers was evidenced. Fast oxidation rate combined to almost entire consumption of the original alloy layer is proposed as an explanation for this behaviour.

CHAPTER III Conclusion

In this chapter we detailed the different practical solutions we developed for improvement of the quantitative analysis capacities of our ToF-SIMS instrument in SiGe based materials and structures. Precisely, we focused on data treatment and experimental conditions, setting up an original protocol for signal quantification and another for depth scale establishment. The data treatment protocol, based on a full spectrum approach of the ToF-SIMS data sets, was optimised for depth profiling of intrinsic or doped SiGe layers, and adjacent oxide layers when present.
The accuracy of the proposed solutions was investigated in various structures representative of actual device structures by comparison with more conventional ToF-SIMS measurement protocols. Each time, the proposed solutions revealed to yield the best properties out of the other characterisation means in terms of accuracy, reliability, reproducibility, noise level, depth resolution and accuracy of depth scale. The developed measurement protocol was therefore used to understand the behaviour of some particular structures under typical device elaboration processes such as annealing or oxidation. Based on the ToF-SIMS profiles we were able to yield quantified information on elemental interdiffusion mechanisms in SiGe/Si

superlattices under annealing as well as on diffusion and segregation occurring in doped and intrinsic SiGe layers during oxidation. By using cross-characterisation with complementary techniques, we were also able to yield understanding on the stress relaxation processes during annealing of the superlattices and on Ge condensation mechanisms during SiGe oxidation. All this information, that the accuracy of the developed ToF-SIMS quantification protocols has made available, can contribute to a better understanding of the physical processes occurring during device manufacture and thus ultimately lead to performance gains.

REFERENCES

[1] D. Marseilhan, J.P. Barnes, F. Fillot, J.M. Hartmann and P. Holliger, *Quantification of Sige Layer Composition Using Mcs+ and Mcs2+ Secondary Ions in Tof-Sims and Magnetic Sims*, Appl. Surf. Sci., 255 (**2008**) 1412-1414.
[2] P. Holliger, F. Laugier and J.C. Dupuy, *Sims Depth Profiling of Ultrashallow P, Ge and as Implants in Si Using Mcs2+ Ions*, Surf. Interface Anal., 34 (**2002**) 472-476.
[3] M. Gavelle, E. Scheid, F. Cristiano *et al.*, *Detection of Cs2ge+ Clusters for the Quantification of Germanium Atoms by Secondary Ion Mass Spectrometry: Application to the Characterisation of Si1-Xgex Layers (0 <= X <= 1) and Germanium Diffusion in Silicon*, J. Appl. Phys., 102 (**2007**).
[4] G. Prudon, B. Gautier, J.C. Dupuy *et al.*, *Quantification of Germanium and Boron in Heterostructures Si/Si1-Xgex/Si by Sims*, Thin Solid Films, 294 (**1997**) 54-58.
[5] Z.X. Jiang, K. Kim, J. Lerma *et al.*, *Quantitative Sims Analysis of Sige Composition with Low Energy O2+ Beams*, Appl. Surf. Sci., 252 (**2006**) 7262-7264.
[6] M. Perego, S. Ferrari and M. Fanciulli, *Negative Cluster Emission in Sputtering of Si1-Xgex Alloys: A Full Spectrum Approach*, Surf. Sci., 599 (**2005**) 141-149.
[7] J.-M. Hartmann, A.-M. Papon, J.-P. Colonna, T. Ernst and T. Billon, *Growth and Thermal Stability of Sige/Si Superlattices on Bulk Si Wafers*, ECS Trans., 16 (**2008**) 341-351.
[8] M. Py, J.P. Barnes and J.M. Hartmann, *Quantification of Germanium in Si1−Xgex Alloys by Negative Mode Tof-Sims: The Interest of the Full Spectrum Method*, Surf. Interface Anal., 43 (**2011**) 539-542.
[9] J.P. Dismukes, L. Ekstrom and R.J. Paff, *Lattice Parameter and Density in Germanium-Silicon Alloys*, J. Phys. Chem., 68 (**1964**) 3021-3027.
[10] K.E. Petersen, *Dynamic Micromechanics on Silicon: Techniques and Devices*, Electron Devices, IEEE Transactions on, 25 (**1978**) 1241-1250.
[11] N. Baboux, J.C. Dupuy, G. Prudon *et al.*, *Ultra-Low Energy Sims Analysis of Boron Deltas in Silicon*, J. Cryst. Growth, 245 (**2002**) 1-8.
[12] K.J. Kim, J.S. Jang, D.W. Moon and H.J. Kang, *A Method to Determine the Interface Position and Layer Thickness in Sims Depth Profiling of Multilayer Films*, Metrologia, 47 (**2010**) 253-261.
[13] R.J.H. Morris and M.G. Dowsett, *Ion Yields and Erosion Rates for Si1-Xgex(0 <= X <= 1) Ultralow Energy O-2(+) Secondary Ion Mass Spectrometry in the Energy Range of 0.25-1 Kev*, J. Appl. Phys., 105 (**2009**).
[14] Y. Bogumilowicz, J.M. Hartmann, F. Laugier *et al.*, *High Germanium Content Sige Virtual Substrates Grown at High Temperatures*, J. Cryst. Growth, 283 (**2005**) 346-355.
[15] J.M. Hartmann, L. Clavelier, C. Jahan *et al.*, *Selective Epitaxial Growth of Boron- and Phosphorus-Doped Si and Sige for Raised Sources and Drains*, J. Cryst. Growth, 264 (**2004**) 36-47.
[16] J.M. Hartmann, L. Baud, G. Rolland, J.M. Fabbri and T. Billon, *Very High Temperature Growth of Sige Virtual Substrates (15% < [Ge] < 45%)*, ECS Trans., 3 (**2006**) 219.
[17] F. Andrieu, T. Ernst, O. Faynot *et al.*, *Co-Integrated Dual Strained Channels on Fully Depleted Ssdoi Cmosfets with Hfo₂/Tin Gate Stack Down to 15nm Gate Length,* SOI Conference, 2005. Proceedings. 2005 IEEE International, (**2005**) 223-225.
[18] L. Gomez, P. Hashemi and J.L. Hoyt, *Enhanced Hole Transport in Short-Channel Strained-Sige P-Mosfets*, Electron Devices, IEEE Transactions on, 56 (**2009**) 2644-2651.
[19] S. Koelling, M. Gilbert, J. Goossens *et al.*, *High Depth Resolution Analysis of Si/Sige Multilayers with the Atom Probe*, Appl. Phys. Lett., 95 (**2009**) 144106.
[20] J.M. Hartmann, P. Holliger, F. Laugier *et al.*, *Growth of Sige/Si Superlattices on Silicon-on-Insulator Substrates for Multi-Bridge Channel Field Effect Transistors*, J. Cryst. Growth, 283 (**2005**) 57-67.
[21] J.M. Hartmann, F. Gonzatti, F. Fillot and T. Billon, *Growth Kinetics and Boron Doping of Very High Ge Content Sige for Source/Drain Engineering*, J. Cryst. Growth, 310 (**2008**) 62-70.
[22] M. Py, J.P. Barnes, P. Rivallin *et al.*, *Characterisation and Modelling of Structural Properties of Sige/Si Superlattices for Multi-Channel Devices Upon Annealing*, Submitted for publication in Journal of Applied Physics, (**2011**).

[23] M.N. Drozdov, Y.N. Drozdov, D.N. Lobanov, A.V. Novikov and D.V. Yurasov, *Secondary Cluster Ions Ge (2) (-) and Ge (3) (-) for Improving Depth Resolution of Sims Depth Profiling of Gesi/Si Heterostructures*, Semiconductors, 44 (**2010**) 401-404.
[24] R. Wilson, F. Stevie and C. Magee, *Secondary Ion Mass Spectrometry*, John Wiley, Sons, New York, **1989**.
[25] K. Elst, W. Vandervorst, J. Alay, J. Snauwaert and L. Hellemans, *Influence of Oxygen on the Formation of Ripples on Si*, J. Vac. Sci. Technol. B, 11 (**1993**) 1968-1981.
[26] H. Oechsne, Applied Physics, 8 (**1975**) 185.
[27] D. Gui, Z.X. Xing, Y.H. Huang *et al.*, *Roughness Development in the Depth Profiling with 500 ev O2+ Beam with the Combination of Oxygen Flooding and Sample Rotation*, Appl. Surf. Sci., 255 (**2008**) 1433-1436.
[28] J.F. Damlencourt, Patent N°EP1892766, **2006**.
[29] C. Dupré, T. Ernst, V. Maffini-Alvaro *et al.*, *3d Nanowire Gate-All-around Transistors: Specific Integration and Electrical Features*, Solid-State Electron., 52 (**2008**) 519-525.
[30] K. Tachi, M. Casse, D. Jang *et al.*, *Relationship between Mobility and High-K Interface Properties in Advanced Si and Sige Nanowires,* Electron Devices Meeting (IEDM), 2009 IEEE International, (**2009**) 1-4.
[31] Q.T. Nguyen, J.F. Damlencourt, B. Vincent *et al.*, *High Quality Germanium-on-Insulator Wafers with Excellent Hole Mobility*, Solid-State Electron., 51 (**2007**) 1172-1179.
[32] T. Tezuka, N. Sugiyama, T. Mizuno, M. Suzuki and S.I. Takagi, *A Novel Fabrication Technique of Ultrathin and Relaxed Sige Buffer Layers with High Ge Fraction for Sub-100 Nm Strained Silicon-on-Insulator Mosfets*, Jpn. J. Appl. Phys., 40 (**2001**) 2866-2874.
[33] E. Saracco, J.-F. Damlencourt, D. Lafond *et al.*, *Fabrication of Suspended Ge-Rich Nanowires by Ge Enrichment Technique for Multi-Channel Devices*, ECS Trans., 19 (**2009**) 207-212.
[34] J.F. Damlencourt, E. Saracco and T. Poiraux, Patent N°FR0904321, **2009**.
[35] J. Huang, Z. Ye, H. Lu and D. Que, *Calculation of Critical Layer Thickness Considering Thermal Strain in Si1-Xgex/Si Strained-Layer Heterostructures*, J. Appl. Phys., 83 (**1998**) 171-173.
[36] B. Vincent, J.F. Damlencourt, P. Rivallin *et al.*, *Fabrication of Sige-on-Insulator Substrates by a Condensation Technique: An Experimental and Modelling Study*, Semicond. Sci. Technol., 22 (**2007**) 237-244.
[37] S. Schaffler, *Properties of Advanced Semiconductor Materials Gan, Aln, Inn, Bn, Sic, Sige*, John Wiley & Sons, Inc., New York, **2001**.
[38] M. Py, J.P. Barnes, D. Lafond and J.M. Hartmann, *Quantitative Profiling of Sige/Si Superlattices by Time-of-Flight Secondary Ion Mass Spectrometry: The Advantages of the Extended Full Spectrum Protocol*, Rapid Commun. Mass Spectrom., 25 (**2011**) 629-638.
[39] K.-W. Ang, K.-J. Chui, V. Bliznetsov *et al.*, *Lattice Strain Analysis of Transistor Structures with Silicon--Germanium and Silicon--Carbon Source/Drain Stressors*, Appl. Phys. Lett., 86 (**2005**) 093102-093103.
[40] P. Zhang, A.A. Istratov, E.R. Weber *et al.*, *Direct Strain Measurement in a 65 Nm Node Strained Silicon Transistor by Convergent-Beam Electron Diffraction*, Appl. Phys. Lett., 89 (**2006**) 161907-161903.
[41] M. Hytch, F. Houdellier, F. Hue and E. Snoeck, *Nanoscale Holographic Interferometry for Strain Measurements in Electronic Devices*, Nature, 453 (**2008**) 1086-1089.
[42] D. Cooper, A. Béché, J.M. Hartmann, V. Carron and J.M. Rouvière, *Strain Mapping for the Semiconductor Industry by Dark-Field Electron Holography and Nanobeam Electron Diffraction with Nm Resolution*, Semicond. Sci. Technol., 25 (**2010**) 095012.
[43] S. Baudot, F. Andrieu, O. Weber *et al.*, IEEE Electron. Dev. Lett., 31 (**2010**) 1074.
[44] S.E. Thompson, S. Guangyu, C.Y. Sung and T. Nishida, IEEE Trans. Electron. Dev., 53 (**2006**) 1010.
[45] J.M. Hartmann, M. Py, J.P. Barnes *et al.*, *Low Temperature, Boron and Phosphorous Doped Sige for Recessed and Raised Sources and Drains*, Submitted for publication in Journal of Crystal Growth, (**2011**).

[46] V. Loup, J.M. Hartmann, G. Rolland *et al.*, *Reduced Pressure Chemical Vapour Deposition of Si/Si1-X-Ygexcy Heterostructures Using a Chlorinated Chemistry*, Semicond. Sci. Technol., 18 (**2003**) 352-360.
[47] P.B. Griffin, S.W. Crowder and J.M. Knight, *Dose Loss in Phosphorus Implants Due to Transient Diffusion and Interface Segregation*, Appl. Phys. Lett., 67 (**1995**) 482.
[48] R. Duffy, V.C. Venezia, J. Loo *et al.*, *Low-Temperature Diffusion of High-Concentration Phosphorus in Silicon, a Preferential Movement toward the Surface*, Appl. Phys. Lett., 86 (**2005**) 1-3.
[49] L. Zhong, Y. Kirino, Y. Matsushita *et al.*, *Outdiffusion of Impurity Atoms from Silicon Crystals and Its Dependence Upon the Annealing Atmosphere*, Appl. Phys. Lett., 68 (**1996**) 1229-1231.
[50] B.J. Pawlak, N.E.B. Cowern and W. Vandervorst, *B Profile Alteration by Annealing in Reactive Ambients*, Appl. Phys. Lett., 94 (**2009**) 022104-022103.
[51] L. Boltzmann, Ann. Phys., 289 (**1894**) 959.
[52] C. Matano, Jpn. J. Physiol., 8 (**1933**) 109.
[53] S. Kailasam, J. Lacombe and M. Glicksman, *Evaluation of the Methods for Calculating the Concentration-Dependent Diffusivity in Binary Systems*, Metallurgical and Materials Transactions A, 30 (**1999**) 2605-2610.
[54] M.E. Glicksman, *Diffusion in Solids: Field Theory, Solid-State Principles, and Applications*, Wiley Inter Science, **2000**.
[55] G. Xia, J.L. Hoyt and M. Canonico, *Si--Ge Interdiffusion in Strained Si/Strained Sige Heterostructures and Implications for Enhanced Mobility Metal-Oxide-Semiconductor Field-Effect Transistors*, J. Appl. Phys., 101 (**2007**) 044901-044911.
[56] M. Hasanuzzaman, Y.M. Haddara and A.P. Knights, *Modeling Germanium Diffusion in Si[Sub 1 - X]Ge[Sub X]/Si Superlattice Structures*, J. Appl. Phys., 105 (**2009**) 043504-043505.
[57] N.R. Zangenberg, J. Lundsgaard Hansen, J. Fage-Pedersen and A. Nylandsted Larsen, *Ge Self-Diffusion in Epitaxial Si_{1-X}Ge_{X} Layers*, Phys. Rev. Lett., 87 (**2001**) 125901.
[58] L. Pelaz, M. Jaraiz, G.H. Gilmer *et al.*, *B Diffusion and Clustering in Ion Implanted Si: The Role of B Cluster Precursors*, Appl. Phys. Lett., 70 (**1997**) 2285-2287.
[59] G. Mannino, N.E.B. Cowern, F. Roozeboom and J.G.M. Van Berkum, *Role of Self- and Boron-Interstitial Clusters in Transient Enhanced Diffusion in Silicon*, Appl. Phys. Lett., 76 (**2000**) 855-857.
[60] P. Pichler, H. Ryssel, R. Ploss, C. Bonafos and A. Claverie, *Phosphorus-Enhanced Diffusion of Antimony Due to Generation of Self-Interstitials*, J. Appl. Phys., 78 (**1995**) 1623-1629.
[61] R.F. Scholz, P. Werner, U. Gosele and T.Y. Tan, *The Contribution of Vacancies to Carbon out-Diffusion in Silicon*, Appl. Phys. Lett., 74 (**1999**) 392-394.
[62] H. Rucker, B. Heinemann, D. Bolze *et al.*, *The Impact of Supersaturated Carbon on Transient Enhanced Diffusion*, Appl. Phys. Lett., 74 (**1999**) 3377-3379.
[63] J. Bang, J. Kang, W.-J. Lee, K.J. Chang and H. Kim, *Chemical Bonding Effect of Ge Atoms on B Diffusion in Si*, Physical Review B, 76 (**2007**) 064118.
[64] J.S. Christensen, H.H. Radamson, A.Y. Kuznetsov and B.G. Svensson, *Diffusion of Phosphorus in Relaxed Si[Sub 1 - X]Ge[Sub X] Films and Strained Si/Si[Sub 1 - X]Ge[Sub X] Heterostructures*, J. Appl. Phys., 94 (**2003**) 6533-6540.
[65] K. Rajendran and W. Schoenmaker, *Measurement and Simulation of Boron Diffusivity in Strained Si1-Xgex Epitaxial Layers*, Vlsi Design, 13 (**2001**) 317-321.
[66] D. Cooper, A. Beche, J.-M. Hartmann, V. Carron and J.-L. Rouviere, *Strain Evolution During the Silicidation of Nanometre-Scale Sige Semiconductor Devices Studied by Dark Field Electron Holography*, Appl. Phys. Lett., 96 (**2010**) 113508-113503.
[67] F. Hue, M. Hytch, F. Houdellier, E. Snoeck and A. Claverie, *Strain Mapping in Mosfets by High-Resolution Electron Microscopy and Electron Holography*, Materials Science and Engineering B-Advanced Functional Solid-State Materials, 154 (**2008**) 221-224.
[68] F. Hue, M. Hytch, F. Houdellier, H. Bender and A. Claverie, *Strain Mapping of Tensiley Strained Silicon Transistors with Embedded Si[Sub 1 - Y]C[Sub Y] Source and Drain by Dark-Field Holography*, Appl. Phys. Lett., 95 (**2009**) 073103-073103.
[69] M.J. Hÿtch, E. Snoeck and R. Kilaas, *Quantitative Measurement of Displacement and Strain Fields from Hrem Micrographs*, Ultramicroscopy, 74 (**1998**) 131-146.

[70] T. Denneulin, J.L. Rouvière, A. Béché *et al.*, *Evaluation of the Substitutional Carbon Content in Annealed Si/Sigec Superlattices by Dark-Field Electron Holography,* MSM XVII proceedings, (**2011**).
[71] A. Cuadras, B. Garrido, C. Bonafos *et al.*, *Optical Characterisation of Thermally Oxidised Si1-X-Ygexcy Layers*, Thin Solid Films, 364 (**2000**) 233-238.
[72] J. Xiang, N. Herbots, H. Jacobsson *et al.*, *Comparative Study on Dry Oxidation of Heteroepitaxial Si[Sub 1 - X]Ge[Sub X] and Si[Sub 1 - X - Y]Ge[Sub X]C[Sub Y] on Si(100)[Sup +]*, J. Appl. Phys., 80 (**1996**) 1857-1866.
[73] B.E. Deal and A.S. Grove, *General Relationship for the Thermal Oxidation of Silicon*, J. Appl. Phys., 36 (**1965**) 3770-3778.
[74] B. Vincent, J.-F. Damlencourt, Y. Morand, D. Rouchon and M. Mermoux, *Ge Enrichment Technique on Sige/Soi Mesa Islands: A Localized Geoi Structures Fabrication Method*, ECS Trans., 13 (**2008**) 235-242.
[75] M. Spadafora, A. Terrasi, S. Mirabella *et al.*, *Dry Oxidation of Mbe-Sige Films: Rate Enhancement, Ge Redistribution and Defect Injection*, Mater. Sci. Semicond. Process., 8 219-224.
[76] J.P. Zhang, P.L.F. Hemment, S.M. Newstead *et al.*, *A Comparison of the Behaviour of Si0.5ge0.5 Alloy During Dry and Wet Oxidation*, Thin Solid Films, 222 (**1992**) 141-144.
[77] C.P. Ho and J.D. Plummer, *Si/Sio2 Interface Oxidation Kinetics: A Physical Model for the Influence of High Substrate Doping Levels*, J. Electrochem. Soc., 126 (**1979**) 1523-1530.
[78] P.W. Wang, Y. Qi and D.O. Henderson, *Oxygen Bonding in Geo2 Glass*, J. Non-Cryst. Solids, 224 (**1998**) 31-35.
[79] H. Sakamoto and S. Kumashiro, *A New Diffusion Algorithm During Oxidation Which Can Handle Both Phosphorus Pile-up and Boron Segregation at Si-Sio2 Interface,* Simulation of Semiconductor Processes and Devices, 1997. SISPAD '97., 1997 International Conference on, (**1997**) 81-84.
[80] O. Aleksandrov and N. Afonin, *Effect of Thermal Oxidation on the Segregation of Phosphorus Implanted into Silicon*, Inorganic Materials, 41 (**2005**) 972-980.
[81] K. Shimakura, T. Suzuki and Y. Yadoiwa, *Boron and Phosphorus Diffusion through an Sio2 Layer from a Doped Polycrystalline Si Source under Various Drive-in Ambients*, Solid-State Electron., 18 (**1975**) 991-996.

CHAPTER IV
Analysis of materials and structures for advanced dielectric/gate stacks in sub-32 nm generation CMOS

In this chapter we will examine high-k dielectric material stacks as described in chapter I. Contrary to the samples used in the previous chapter, which were specifically designed for ToF-SIMS analysis while being inspired from actual device structures, the samples studied here are directly issued from pre-production lines for sub-32 nm devices. The materials of interest are hafnium and lanthanum oxides or silicates, silicon dioxide and silicon oxy-nitride for the dielectric, titanium nitride for the gate and of course Si and SiGe as channel materials. All of these are integrated vertically as a stack, each layer thickness being of the order of the nanometre (slightly thicker for the gate material). We have therefore to study stacks of heterogeneous materials with nanometre or sub-nanometre scale thicknesses. Depth resolution will thus be critical in these structures, requiring the use of extremely low sputter energies and/or analysis beam energy. It will thus be interesting to explore the lowest sputter energies attainable with our ToF-SIMS instrument with a reasonable current and to develop an EXtremely Low Energy (EXLE) depth profile acquisition protocol (with sputtering energy <250 eV). Similarly, in such thin heterogeneous stacks, the determination of the depth scale will greatly influence the quality of the analysis: therefore requiring a dedicated protocol, along with specific ways to verify its accuracy. Dealing with heterogeneous stacks also means dealing with heavy matrix effects. To succeed in quantifying the depth profiles of all major elements, we have to develop an original protocol, since no known single SIMS protocol currently allows this. Consequently, and in contrast to the SiGe materials discussed in the previous chapter, assessing the accuracy of the newly developed ToF-SIMS protocol will require the use of other techniques able to yield similar quantified depth profiles. The need for oxygen monitoring in these samples also rules out O_2 abrasion. Finally, specific effects of chemical segregation of some elements during profiling (in particular N and Hf as discussed in chapter I) hinder quantification abilities and need to be measured. In order to study these phenomena, a backside sample preparation protocol adapted to the dimensions of the stacks and the requirements of the analysis has to be developed.

IV. 1. Development of an EXLE depth profiling protocol with Cs^+ sputtering

In our instrument, the primary ion column optics are already adapted to low energy beams: they enable standard operation between 2 keV and 250 eV. The ion focusing optics are better adapted to lower energies (500 eV), as shown on the chart displayed in Figure IV.1.A. Indeed the DC Cs^+ current as measured in a Faraday cup situated on the sample holder evolves almost linearly with the primary ion energy below 500 eV while its increase is much slower for energies above this limit. Each working point (250, 500, 1000 and 2000 eV) is defined by a set of parameters such as extraction voltage, various focus lens voltages and lateral deflection voltages. To set up a new working point, the simplest method is to start from an existing set of parameters (corresponding to the closest energy) and to slightly modify the extraction voltage while keeping the DC current at its maximum by adjusting the other parameters. Performing this protocol several times in an iterative manner, we were able to obtain working points for sputter beam energies as low as 120 eV. However, even though our instrument is equipped with a very bright caesium LMIS, the maximum current obtained at energies this low never exceeds 2 nA, which does not yield substantial sputter rates in Si. The first “useful” energy with our system configuration was found to be 150 eV, which routinely provided 7-8 nA current (see Figure IV.1.A). Such results are in agreement with the values found in literature for similar systems [1-2]. However the DC current measurement is done in a millimetre large Faraday cup and thus does not account for the lateral dispersion of

the beam (focusing). Yet, focusing of the beam on the sample surface becomes difficult with decreasing energy, as shown in Figure IV.1.B. Having a less focused spot also means that the minimum raster size required for a flat crater bottom also increases with decreasing energy, from ~100 µm at 2000 eV to ~400 µm at 150 eV.

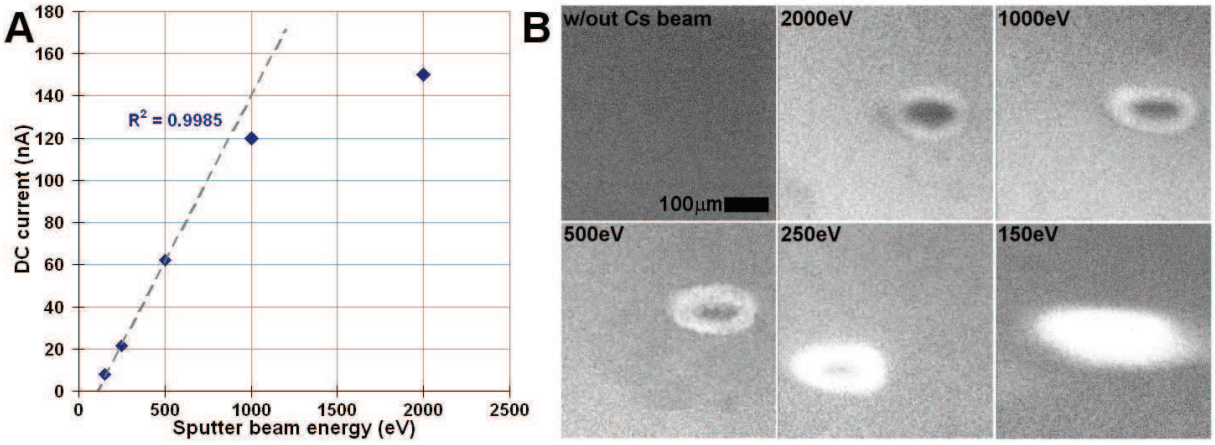

Figure IV.1.A Evolution of DC Cs^+ beam current as a function of energy. Linear behaviour of the current with beam energy is observed up to 500 eV. Beyond this limit, the increase in current becomes slower. Extrapolation of the linear tendency (dashed curve) shows that current falls to zero at 105 eV.

B Total secondary ion images of a metallic sample surface obtained with 25 keV Bi^+ beam rastered over 500×500 µm. Focused spot marks are observed as bright ovals whose size and shape varies with energy, the lower the energy the broader the spot.

The EXLE mode enabled by the procedure above therefore yields very slow depth profiles, the relatively low sputter rate of 150 eV Cs^+ in Si (~0.05 at/incident ion [2]) being further hampered by the low current and necessity to raster over large areas. Typical abrasion rate in Si, measured with a known B delta sample in Si was found to be of ~0.1 nm/min, once again in agreement with literature [2].

Due to these very low sputter rates and to the dual beam architecture of our instrument, there is a risk to inflict too much damage to the underlying layers during analysis and thus to loose all the advantages of EXLE mode in terms of depth resolution. To avoid such undesirable effects, the analysis beam in EXLE mode was operated at 15 keV instead of 25 keV in standard mode. Profiling was always performed in non interlaced mode (see chapter I), with 10 s sputtering and 0.75 s pause between two analyses. With this setup and by adjusting analysis beam raster size, we ensured a sputter/analysis ratio R>50 for every profile.

IV. 2. Depth scale establishment protocols

For simple systems consisting of thin, single layers of well known materials, with no or little modification of the elemental distribution inside the layer, direct measurement of the layer thickness with an external calibration method is the best option. In this work we performed such measurements with spectroscopic ellipsometry (see subsection II. 4. b-). The thickness of the layer obtained with ellipsometry is then used for depth scale establishment by supposing constant sputter rate throughout the whole layer and sharp bottom interface. The layer thickness divided by the sputter time required to reach the interface as determined by the

half intensity of a relevant signal (e.g. oxygen signal for a SiO_2/Si interface). The results obtained on a set of four thin SiO_2 layers which underwent nitridation anneal in a classic furnace (providing an N distribution centred on the SiO_2/Si interface and thus a relatively homogeneous composition close to SiO_2 through the layer) are displayed in Figure IV.2.A. We observe a good correlation between the time needed to reach the interface and the layer thickness as determined by ellipsometry at both sputtering energies. This means that, at least in the EXLE regime, the influence of the transient region (see Figure I.9.D) is still negligible when profiling homogeneous samples such as these. Furthermore, linear regression R^2 is found to be slightly better at 150 eV than at 250 eV, showing that our protocol for 150 eV sputtering depth profile allows reduction of the transient regime as well. Using the same protocol on a sample of thick thermal oxide, we were able to define the variation of sputter rate between SiO_2 and Si at various energies (the sputter rate in the latter being measured using a known B delta in Si). The sputter rate ratio $SR(SiO_2)/SR(Si)$ was found to be of 1.35, 1.5 and 2.4 at 500, 250 and 150 eV respectively.

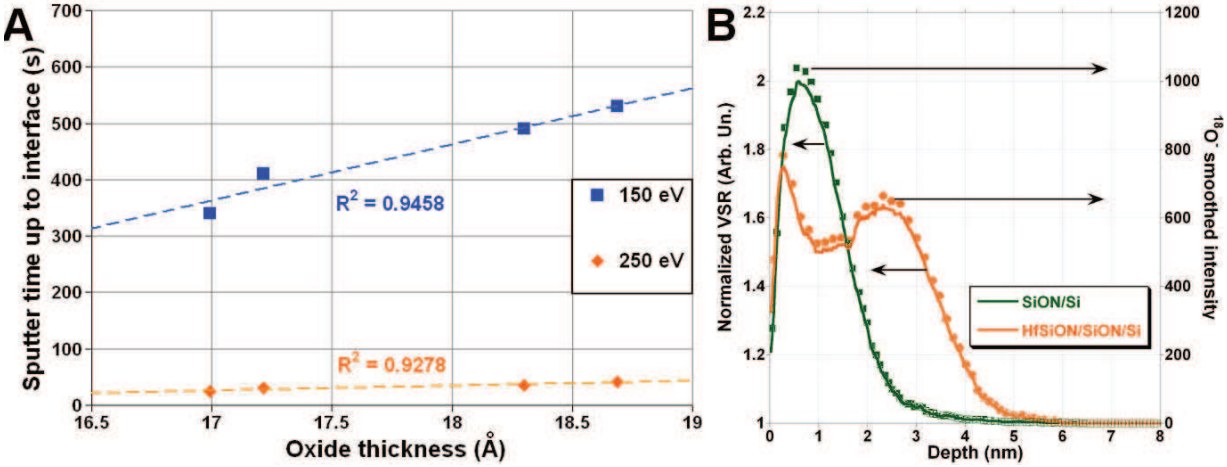

Figure IV.2.A Correlation between sputter time up to interface and layer thicknesses as measured by spectroscopic ellipsometry obtained with 250 and 150eV Cs^+ sputtering on furnace nitridised SiO_2 samples.

B $^{18}O^-$ smoothed distributions (symbols) and VSR deducted from those signals (curves) obtained at 250 eV Cs^+ sputtering (and 15 keV Bi^+ for analysis) on a silicon oxy-nitride layer (green) and on a hafnium silicate/ silicon oxy-nitride stack (orange).

However for more complex systems constituted of several heterogeneous layers, or even single layers whose composition is varying with depth such as plasma nitridised SiO2 layers, this simple method does not work because (i) layer thicknesses become difficult to assess with ellipsometry du to the composition inhomogeneity and (ii) interfaces become difficult to assess with the method of secondary ion intensity half-signal (all layers containing appreciatively the same elements but featuring different composition). In this case the use of a Variable Sputter Rate (VSR) function comes to help in order to assess sputter rate variation throughout the layers. Establishment of such a VSR can be performed, as proposed in [3], by associating the variation of an oxygen representative signal to the variation of sputter rate. In our protocol the oxygen representative signal is normalised and smoothed to obtain the VSR function which is then multiplied by SR(Si) to obtain the actual SR along the whole sample (see Figure IV.2.B). This second protocol, which results were already shown to be accurate in a variety of samples [3], is also advantageous in that it does not require any external calibration (except from the measurement of SR(Si)), since the ToF-SIMS profile itself is used for depth scale calibration.

IV. 3. Development of a protocol for quantification of major elements in high-k dielectric material stacks

As no existing ToF-SIMS protocol enables, in one profile, the quantification of all matrix elements in such samples, we tried to develop a new one. The principle of a full spectrum approach for quantification of major elements has already been described in the previous chapter. Briefly, the essence of the Full Spectrum protocol consists in the summation of all contributions from mono-atomic and poly-atomic ions containing a particular element. This improves the counting statistics and allows a better description of the material's composition [4-5]. It also takes full advantage of the parallel mass detection over a large mass range of the ToF-SIMS. We therefore adapted this protocol for use on high-k dielectric materials. In this version, we consider Q_{Si}, Q_{Hf}, Q_O and Q_N, the atomic quantities of Si, Hf, O and N in the secondary ion beam, using the following formula:

$$Q_{Si} = \sum_{n=0}^{6}\sum_{m=0}^{1}\sum_{p=0}^{5}\sum_{q=0}^{1} n \cdot Y_{Si_nHf_mO_pN_q} \qquad \text{(IV.1)}$$

$YSi_nHf_mO_pN_q$ being the intensity of the $Si_nHf_mO_pN_q^-$ cluster ion divided by the $Si_nHf_mO_pN_q$ compound isotopic abundance. Only one isotopic configuration is taken into account for each cluster. To obtain Q_{Hf}, Q_O and Q_N, one has simply to replace n by m, p and q, the equation format being the same. Sums are performed on secondary ions with sufficient intensity, hence the upper limits for each elements in the sum. Some combinations are also "forbidden", meaning the corresponding compound would not be chemically relevant and/or the correspondent mass range presents no significant intensity. The secondary ions are selected to avoid major mass interferences. For instance, Hf^- is almost not detected and thus not intense enough to be taken into account; $Si_2Hf_0O_0N_0^-$ is followed using a particular isotopic cluster $^{29}Si^{28}Si$.

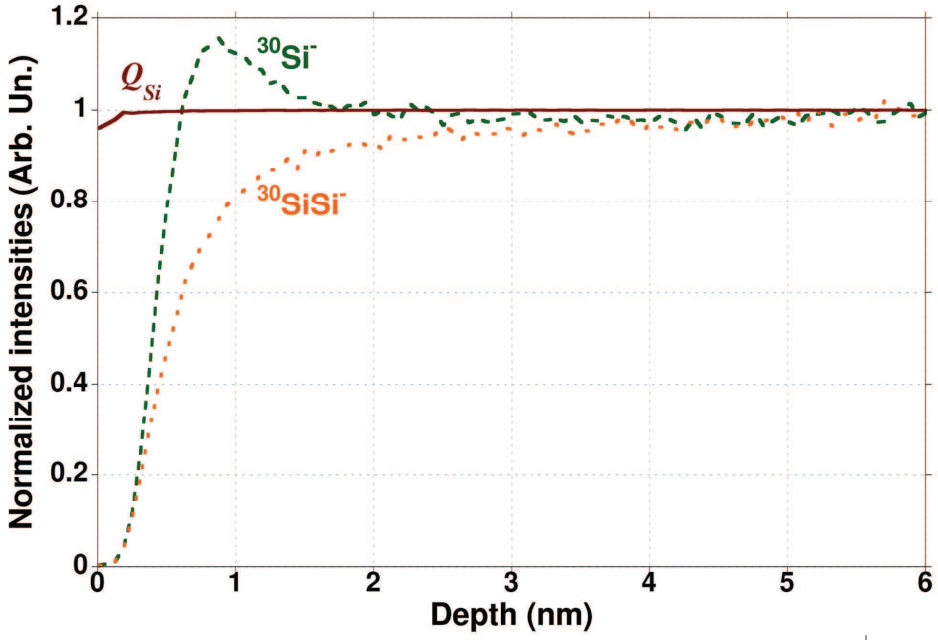

Figure IV.3 Transient in pure (bulk) Si wafer obtained with a 250 eV Cs^+ beam for sputtering and a 15 keV Bi^+ beam for analysis.

The use of these quantities offers several advantages over that of more usually followed secondary ion signals. Of these, two are critical for the application we discuss in this study: (i) the reduction of effects due the surface transient region and (ii) the minimisation of matrix effects. Point (i) is illustrated in Figure IV.3, which shows the first few nanometres of profiles obtained on a bulk, clean Si wafer with a thin native oxide at its surface. Several usual secondary ion signals such as Si^- and Si_2^- are represented along with Q_{Si}. All signals are normalised to their intensity in the 6 nm to 10 nm region. The depth scale was not corrected for sputter rate variations in the near surface region. The observation of the transient reduction provided by the use of Q_{Si} instead of usual secondary ion signals is very straightforward in this case, since the material is composed only of Si as a matrix element and of a sub-nanometre thick native oxide layer. If we define the permanent regime of a signal as the instant from which it undergoes only monotonous variation within 5% of its bulk value, we can define indicative transient lengths for each signal. We thus find a 3.7 nm, 2.6 nm and 0.55 nm transient for Si_2^-, Si^- and Q_{Si} respectively, while the native oxide thickness as estimated from SiO_2^- half signal in Figure IV.3 is approximately 0.6 nm. The permanent regime of the Q_{Si} signal is therefore reached just after the native oxide, while it takes 5 to 7 times longer for the single ion signals to reach it. While the physical transient period due to Cs pile-up at the surface of the sample remains unchanged, we observe a reduction of its effects on the stabilisation of Q_{Si} as compared to single ion signals. Therefore, in a simple model layer like the one we have here, the use of Q_{Si} allows an artificial reduction of transient effects. This is due to the fact that Si^- or Si_2^- ion yields are indeed rather representative of the bulk Si substrate only, while Q_{Si} takes into account the $Si_xO_y^-$ ions, quite intense in the native oxide.

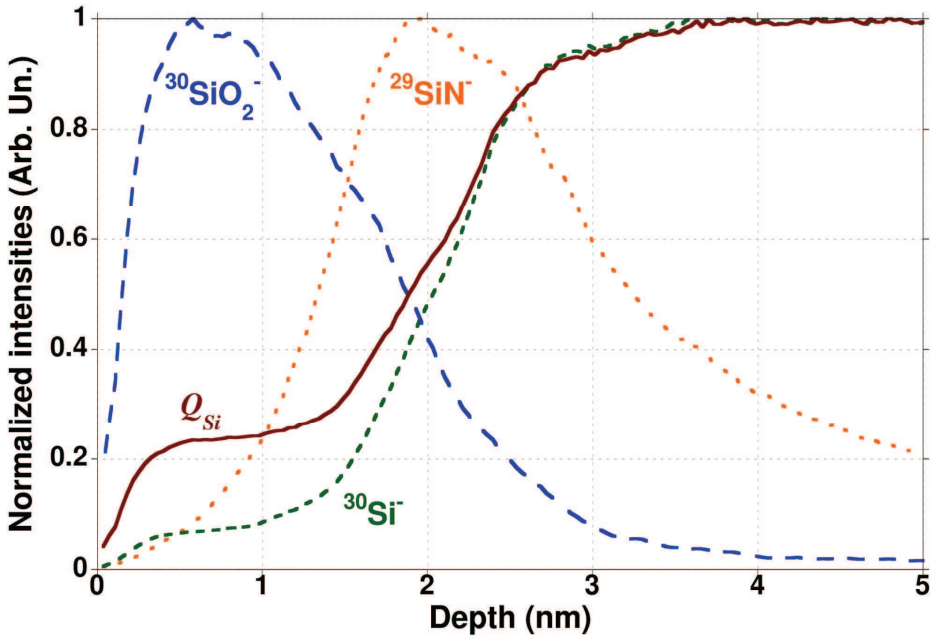

Figure IV.4 Profile of a 1.9 nm thick SiON layer on a Si substrate, obtained with a 150 eV Cs^+ beam for sputtering and a 15 keV Bi^+ beam for analysis.

Figure IV.4 shows the depth profile of a 1.9 nm thick SiON layer on Si obtained with a 150 eV Cs^+ primary beam energy. Again, several classic normalised secondary ion signals such as Si^-, SiO_2^- and SiN^- are represented along with Q_{Si}. From these profiles, we can draw the conclusion that none of the secondary ions observed alone are representative of the Si distribution through the entire stack. However Q_{Si} shows a high intensity plateau in the SiON

region, followed by a transient region before reaching its bulk value. The different secondary ions predominantly participate in the final Q_{Si} signal at different steps: SiO_2^- in the SiON layer, SiN^- at the interface, and finally Si^- in the bulk. A plateau is also observed in normalised Si^- or Si_2^- signals in the SiON region, but of much lower intensity than Q_{Si}. Their average value in the SiON region is found to be 0.08 and 0.01 for Si^- and Si_2^- respectively, while that of Q_{Si} is 0.26. The latter is thus much closer to the actual Si composition of the layer (estimated to be 0.33) than the first two. This shows that Q_{Si}, Q_{Hf}, Q_O and Q_N quantities, by taking into account several secondary ions representative of each element in each different layer, help minimise artefacts and matrix effects through the transient periods at surfaces and interfaces. They provide more representative signals through all layers of a heterogeneous stack compared to single secondary ion signals. However, these quantities, even if they are more representative of the elemental distribution than classic secondary ion signals, correspond only to the number of atoms in the secondary ion beam, which, as seen in previous works, is always slightly divergent from the number of atoms in the actual material [6]. This is why one needs to calibrate those signals in order to obtain quantitative profiles. The usual approach in ToF-SIMS is to refer to well calibrated samples and to use them as reference samples for the quantification of one element in a particular matrix. However, for ultra thin high-k applications, this approach seems difficult to implement since it would require (i) a series of samples with a range of certified, typical concentrations for each element (Si, Hf, O, N) and (ii) samples with a time-stable composition, i.e. bulk layers, making such an approach less adapted to ultra-thin layers. We thus chose another approach, originally proposed by Ferrari *et al.* [4], which consists in calibrating the SIMS profiles with XPS data. The area of a XPS spectra peak for a particular element A can be calculated using the following expression [4, 7]:

$$\mathrm{I_A(XPS)} = \mathrm{I_0} \cdot SF_A^{XPS} \int_0^{\infty} \frac{D_A(z) \cdot \exp\left(-\frac{z}{\lambda \cos(\theta)}\right)}{\cos(\theta)} dz \qquad \text{(IV.2)}$$

Where $I_A(XPS)$ is the area of the XPS spectra peak for the element A, I_0 the unattenuated intensity, SF_A^{XPS} the XPS sensitivity factor for element A in a particular matrix, $D_A(z)$ the depth distribution of the material composition in element A, θ the photoelectron take-off angle, λ the average attenuation length for all considered elements in the considered matrix, and z the depth. The different SF_A^{XPS} were estimated from tabulated values in Scofield [8] corrected to take into account the instrument geometry. A unique value of λ is used for all elements. It is obtained by averaging the different λ values for each element in a SiO_2 matrix for the SiON/Si sample and in an HfO_2 matrix for the other two samples [9-10]. Despite the simplicity of the model, the theoretical error is below 10% [4, 11] which is still satisfactory for our experiment. When the XPS probing depth is superior to the total stack thickness (which is the case in our samples), the distribution $D_A(z)$ in equation (IV.2) can be modelled by the following equation:

$$D_A(z) = Q_A(z) \cdot SF_A^{SIMS} \qquad \text{(IV.3)}$$

Where $Q_A(z)$ is one of the quantities defined in equation (IV.1), and SF_A^{SIMS} is the ToF-SIMS sensitivity factor for the corresponding element. If we implement equation (IV.3) in equation (IV.2), every parameter of the equation is known except from I_0 and SF_A^{SIMS}, which is the parameter we want to quantify. We then proceed through ratios, considering the

quantities $I_{Hf}(XPS)/I_{Si}(XPS)$, $I_O(XPS)/I_{Si}(XPS)$ and $I_N(XPS)/I_{Si}(XPS)$. This allows us to discard I_0 and to quantify all SIMS sensitivity factors relative to Si ($SF_{Si}^{SIMS} = 1$). The different SIMS sensitivity factors found using the ratios are then used as input parameters in equation (IV.3) to retrieve the concentration profiles. This approach has the advantage of providing self-consistent profiles, i.e. the measured sample is used as its own reference. Moreover, since the XPS information depth is greater than the total stack thickness, the calibration of Full Spectrum ToF-SIMS profiles by XPS data allows establishment of constant SIMS sensitivity factors throughout the entire profile, which would not have been the case if thick layers of each material had been used for calibration.

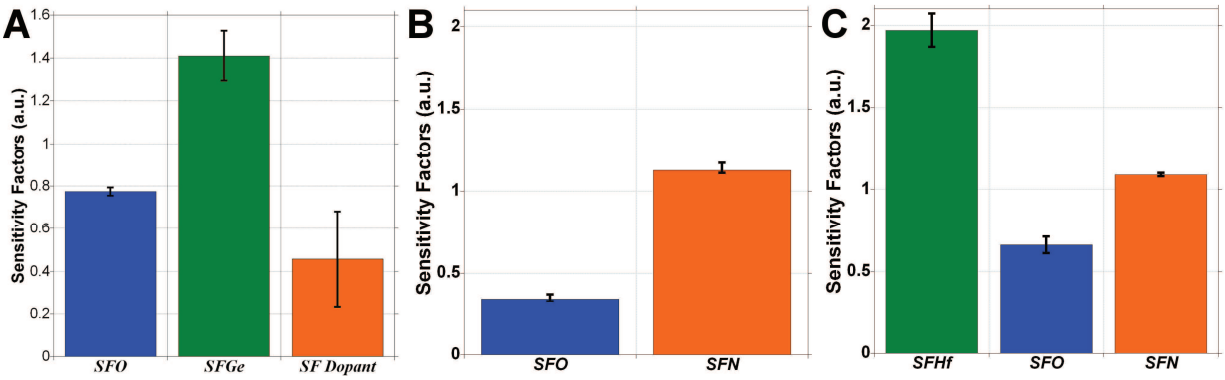

Figure IV.5. Variation of the sensitivity factors obtained with equation (IV.3) over several months interval and with several samples of varying composition within the following:

A Doped SiGe surrounded with oxide (dopants are: C, B and P).

B Silicon oxy-nitride thin layers on Si substrate.

C Hafnium silicate/silicon oxy-nitride on Si substrate.

IV. 4. Extension of the full spectrum protocol to thicker stacks

However in samples too thick for XPS to be able to yield signals up to the substrate, the replacement of $Da(z)$ in equation (IV.2) by its expression in equation (IV.3) is not valid anymore. Indeed, the substitution done in previous section can be operated only of the XPS depth of information is more than the total thickness of the stack, i.e. if the XPS peak for element A renders its distribution over a more important thickness than the layers of interest. Otherwise, the assumption of constant ToF-SIMS sensitivity factors along the whole layers becomes false and the calibration protocol cannot be applied. This rules out from the start the use of such a protocol on samples whose layers of interest thicknesses sum up to ~8 nm or more. Therefore, samples such as complete high-k dielectric/metal gate stacks, or high-k stacks on Si/SiGe heterogeneous (stressed) channel cannot be directly quantified using XPS calibration. To circumvent this limitation, we performed reproducibility studies on several samples of close, but different composition and at several months of interval. By looking at the evolution of SF_A^{SIMS} factors in groups of similar materials (e.g. hafnium silicates, silicon oxy-nitrides, doped/oxidised strained SiGe (sSiGe), etc) we found that there was an extremely good reproducibility in time and with compositional differences. These results are displayed in Figure IV.5 for the various groups of materials studied. Within a given group of materials, the reproducibility is good enough for ToF-SIMS profile quantification to be made without the need for an XPS calibration. Therefore, for thicker samples, the quantification of full spectrum profiles will be performed simply by multiplying the Q_A profiles by the corresponding average SF_A^{SIMS} value in a similar material.

IV. 5. Development of a backside sample preparation protocol adapted to ultra thin high-k/metal gate stacks

Over the past decade it has become increasingly common to resort to backside analysis to overcome weaknesses such as ion mixing and preferential sputtering in SIMS depth profiling, or to bring the layer of interest as close as possible to the surface for XPS analysis [12-17]. The introduction of new materials in the gate stack combined with aggressive dimensional scaling imposed by the 32 nm node and below in microelectronics, means that is is increasingly difficult to draw accurate conclusions from a conventional front-side analysis [18-19]. Backside preparation is one of the potential solutions that to this problem. However in the case of such thin layers, the sample preparation remains challenging since, starting from the whole sample on thick substrate (700 μm for a 300 mm wafer), only a few tens of nanometres corresponding to the layers of interest must remain while maintaining a smooth and flat surface suitable for analysis. Recent developments have used SOI substrates where preparation is performed by a selective plasma etch, with the buried thick oxide acting as an etch stop layer [20]. This method, although providing sufficient etch selectivity against metals or oxides, lacks accurate endpoint detection, implying consequent over-etching thus requiring an etch stop layer of several tens of nanometres. It is therefore impractical for the preparation of samples grown on bulk Si substrates with nanometre or sub-nanometre ultrathin pedestal oxides as etch stops. On the other hand, the work from Hantschel *et al.* investigates a procedure allowing extremely precise preparation for samples featuring sub-nanometre etch stop layers [17]. However the latter presents several drawbacks: (i) it requires a complex mechanical polishing step, involving counting interference fringes at low remaining Si thicknesses, (ii) the useful area yield per sample is quite small and (iii) the obtained surface quality is poor, with a 5 nm RMS roughness for a 30 × 30 μm AFM scan.

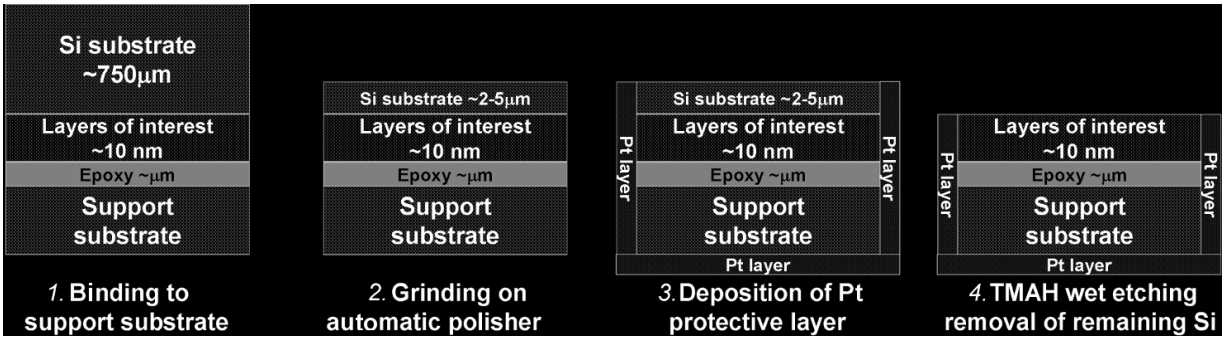

Figure IV.6 Schematic representation of the different steps in the backside preparation process. *1.* Sample is fixed to a support substrate of approximately the same size, and the four sides of the stack are polished. *2.* Si substrate is ground with diamond lapping film disks of varying grade until 2 to 5 μm of Si remains. *3.* Pt protective layers are deposited on the four sides and on the bottom of the support substrate. *4.* Remaining Si is etched in TMAH.

Here we propose a simple method for backside sample preparation adapted to samples grown on Si substrates with nanometre or sub-nanometre ultrathin pedestal oxides. It consists of mechanical polishing to remove all but a few remaining microns, followed by a dedicated TetraMethyl Ammonium Hydroxide (TMAH) etch. This method has the advantage of being simple to perform, since the polishing step does not require high precision; while the optimised conditions for TMAH etch make it compatible with ultra-thin etch stop layers. We therefore used it to prepare samples consisting of high-k/metal gate stacks for 32 nm node CMOS devices. On these samples the etch stop layer consists of a 1.5 nm thick SiON layer. Several full sheet samples representative of the structures of actual high-k/metal gate nMOS

devices were prepared on (100) Si wafers. The samples structure starting from the Si substrate is (i) a thin SiON (1.5 nm) layer, (ii) an HfSiON (1.7 nm) layer, (iii) a 0.4 nm lanthanum oxide layer, (iv) a 6.5 nm thick TiN gate and (v) a 60 nm thick Poly Si capping. SiO_2 was formed by oxidation of the silicon substrate with in-situ steam generation at 1025°C and hafnium silicate was deposited by Metal Organic Chemical Vapour Deposition (MOCVD) with an industry state of the art fab tool. Nitridation of both pedestal SiO_2 and hafnium silicate was carried out by a plasma nitridation followed by a 1000°C rapid thermal anneal. LaO_x capping layers were formed by Physical Vapour Deposition (PVD). The metal gate was also deposited by PVD, and the following Poly-Si by CVD. In order to perform analyses, Poly-Si top layers were chemically removed with TMAH.

G2 resin and hardener epoxy glue was used to bond the sample to a support wafer. A 20 min anneal at 120°C in a dedicated incubator was used to cure the epoxy. Physical polishing was performed with a Centar Frontier from Gatan, using 3M diamond abrasive lapping film disks of 30, 6, 3 and 1 µm grade. Prior to wet etch, a protective Pt film was deposited on the sides and on the bottom of the polished sample/support wafer sandwich by sputter coating. Finally wet etching was performed using small volumes of a 25% concentrated TMAH solution heated at 90°C to ensure fast Si etching rate, smooth surface state and high selectivity versus oxides and metal (5000:1 assumed) [21].

The backside preparation proposed in this work features four main process steps, illustrated in Figure IV.6. The first one consists in the preparation of the sample and of its support substrate see (Figure IV.6, *1.*). Both are cleaved into approximately (±0.5 mm) identical sized pieces using a diamond tip. The dimensions are dictated by the polishing machines sample holder, from 3 mm minimum to 7 mm maximum in both width and length. The support substrate can be any piece of a standard wafer, but for optimised visualisation of the preparation advancement in the final etch step, it is better if the surface has coloured patterns. The surface should also be as flat as possible so as to optimise the final surface quality. In this study, we therefore used a substrate with various metallic lines and patterns planarised by Chemical Mechanical Polishing (CMP). The maximum topography of this substrate was measured to be ±50 nm by contact profilometry. Both pieces are then cleaned in Acetone and Isopropyl Alcohol (IPA) to remove any surface contamination, and carefully glued together, taking care to avoid gas inclusions in the glue. After which, the four sides of the stack are polished to ensure (i) the absence of cleaving residues, glue traces, particles and edge mismatches on all of them, to prevent from degradation of the sample's surface quality during backside polishing by scratches created by particles coming from the edges of the sample and (ii) provide an optimised visualisation of the grinding progress on one of them. The latter will indeed be observed in cross section view during the physical polishing step with a ×50 or ×100 magnification. All sides are therefore polished roughly, using 30 µm and 6 µm grade lapping film disks, while one is finished using using 3 µm and 1 µm grade disks.

The second step consists in grinding the Si substrate until only a microns of material remain, typically 2 to 5 µm. This is performed in a semi-automatic fashion by the mechanical polisher. The manual manipulations are limited to the replacement of the lapping disks from one grade to another, and to check the sample alignment periodically. Most of the substrate is first removed using 30 µm disks (up to ~60 µm remaining Si), while the following steps are performed with finer abrasives, with 6 µm (3 µm, 1 µm) grade disks up to 15 µm (5 µm, 2 µm) remaining Si. However this is only indicative, as the right moment to stop this polishing step is for the user to decide, knowing that one has to provide the thinnest remaining Si layer in order to reduce chemical etch duration, but that over-polishing might degrade surface quality with appearance of scratches and/or bevel.

After demounting the substrate, the stack is once again cleaned with Acetone and IPA. Then, a metallic Pt layer of typically ~100 nm thickness is deposited on the 4 sides of the stack as well as on the bottom side of the support substrate. This step is crucial because it avoids side etch of the sample and delamination of the layers of interest during the etch step. To deposit Pt on one side of the stack, we use a dedicated Teflon sample holder to immobilise the stack during deposition, and protecting all the sides except the one on which the deposition is to be performed. The procedure is then repeated for the other sides, and finally Pt is deposited on the bottom of the support substrate.

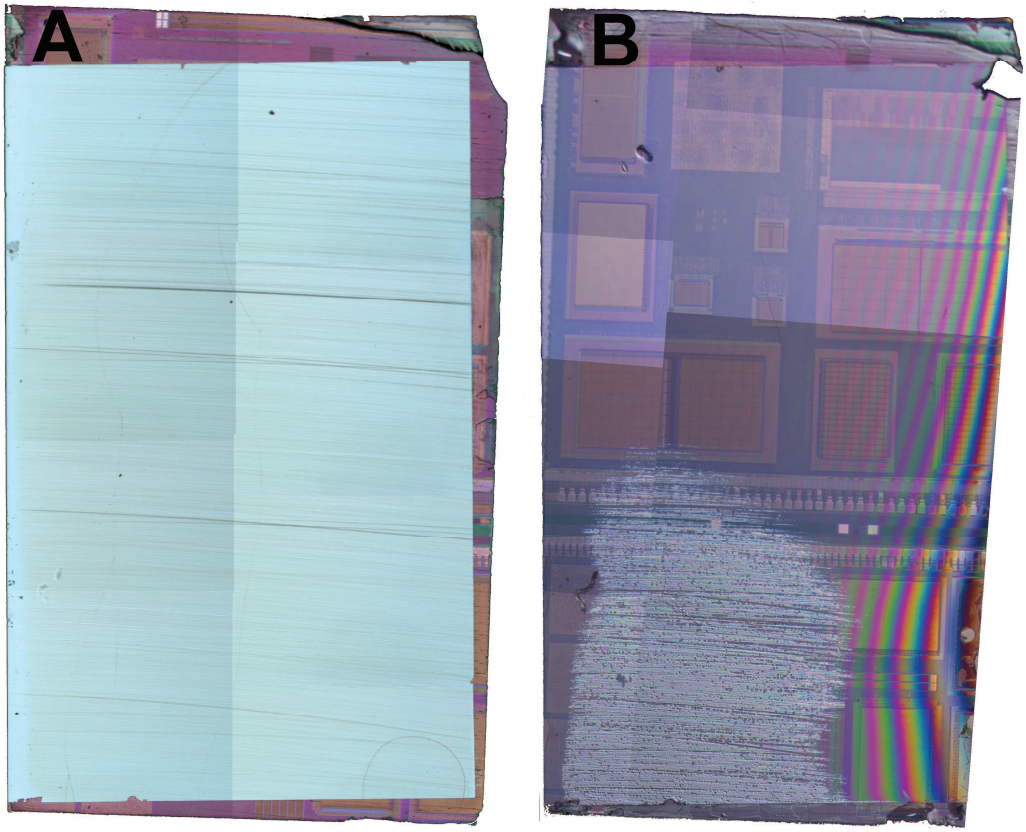

Figure IV.7 Optical image of a sample before (**A**) and after (**B**) chemical etch step, composed from several ×2.5 magnification snapshots. Patterns are clearly visible by transparency, except on the top left corner where Si is still remaining. Interference fringes are assumed to be related to inhomogeneity of the glue thickness (given that the layer of interest thickness is inferior to 15 nm).

The last step of the preparation is the TMAH etch, performed in small volumes and for a short time, given the small remaining Si thickness. If all the previous steps are performed in good conditions, it becomes easy to determine the appropriate moment to stop the etch, since when the silicon is totally removed, the sample colour changes to pink/reddish depending on the glue thickness. Even if substantial over-etch was to be performed the expected effects are thought to be small, given the high selectivity over oxide of TMAH etch in our configuration. To further determine the surface quality, one can use an optical microscope to visualise the underlying support substrate patterns by transparency (hence the importance of the support substrate choice). A typical good surface state is displayed in Figure IV.7. The total duration of the whole preparation does not exceed half a day.

Surface quality

One advantage of this preparation method is its high useful surface yield. Figure IV.7 shows optical views of a sample before and after TMAH etch step, corresponding respectively to the end of step *2.* and the end of step *3.* as presented in Figure IV.6. On the left image we can observe a light grey surface corresponding to the sample to analyse, and a darker, patterned region surrounding the former on three sides, corresponding to the surface of the support substrate. Some scratches are visible on the polished sample surface, and the support substrate is not visible by transparency. On the right image, displaying the same sample after TMAH etch, we observe the same structure, the support substrate now being visible through a semi-transparent layer corresponding to the layers of interest. On the bottom left corner, some Si remains from the substrate, and we can still observe some of the scratches present before etching. However, the integrity of the sample seems preserved, i.e. the layers of interest were not delaminated during the etch process, as corroborated by the fact that the shape of the thin, transparent film corresponding to the layers of interest matches well with the shape of the light grey region in the left image. Given the extremely small thickness of the remaining layers of interest (~10 nm), the interference fringes are assumed to be due to a variation of the glue thickness over the sample surface and not to a bevel on the layers of interest themselves. The average throughput of "clean" surface on a 25 mm² original surface was found to be 17.5 mm². This preparation method therefore allows achievement of a ~70% useful surface by sample, which is largely sufficient for multi-technique analysis.

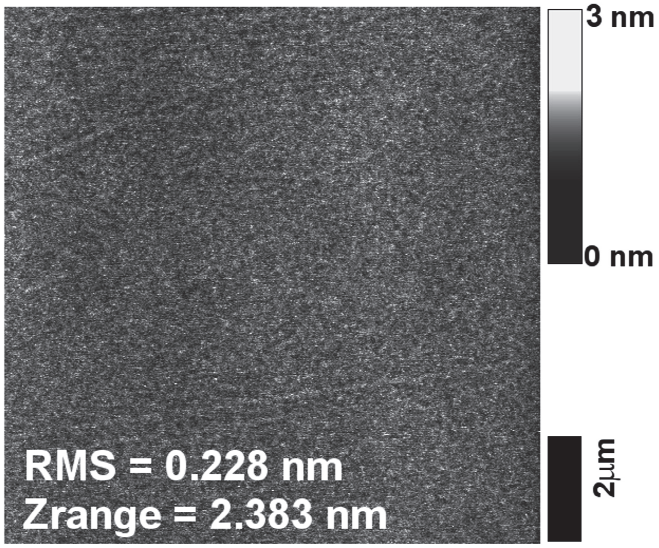

Figure IV.8 10 × 10 µm AFM scan of a sample surface after TMAH etch. The given RMS and Z range (Peak to valley maximum distance) values are averaged over five acquisitions on the same sample at different locations.

The other advantage of this method is the high quality of the surface state it can yield. No three dimensional features (such as pyramids issued from TMAH anisotropic etching properties) can be seen on the surface of the layers of interest in Figure IV.7, which seems perfectly smooth. This can be further investigated by Scanning Electron Microscope (SEM) and by AFM. As SEM observation confirms the smoothness of the surface, it does not give any additional information on its quality (not shown). On the other hand, AFM images give useful information on the topography at small (~1 µm²) and large scale (~100 µm²). The acquisition of 10 × 10 µm scans on several samples and at five different spots on the surface yielded an average RMS roughness of 0.228 nm and a peak to valley maximum distance of

2.383 nm, which is almost as good as an unprepared Si wafer surface. Figure IV.8 shows one such image. In conclusion, the surface state yielded by our backside preparation method seems to be excellent, with a large percentage of useful, flat and smooth surface. However this would be meaningless if the layers of interest were etched during preparation. The next point we will investigate is thus the amount of remaining etch stop layer after preparation.

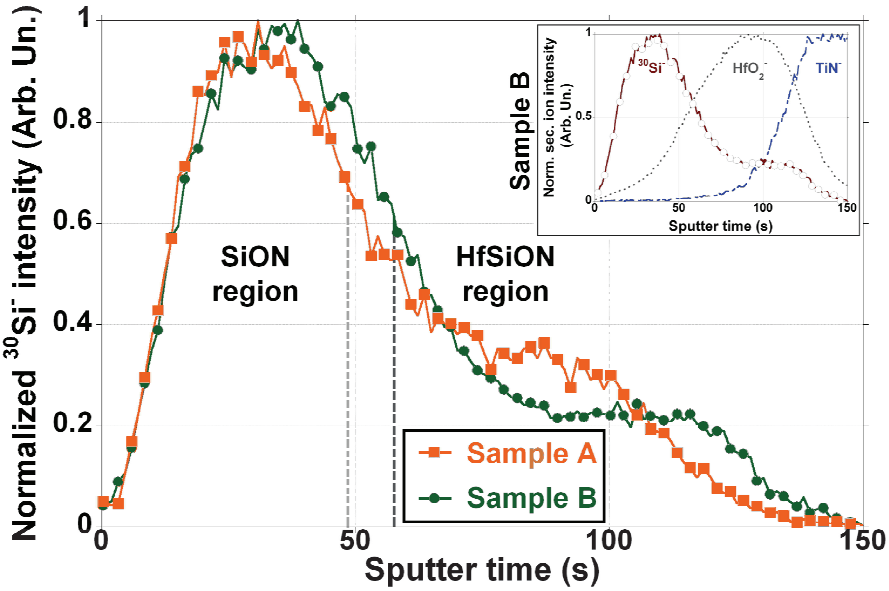

Figure IV.9 $^{30}Si^-$ distribution in the ToF-SIMS backside approach profiles of two similar high-k/metal gate samples. The top right frame shows the succession of the layers in the profile of one of the samples through $^{30}Si^-$, HfO_2^- ant TiN^- secondary ions.

Remaining thickness of the etch stop layer

We will first verify the presence of a SiON layer at the surface of the samples. ToF-SIMS profiles, such as the one shown on the top-right in Figure IV.9 tell us that the near surface region is rich in Si, N and O (only Si is shown in Figure IV.9 for clarity), followed after ~50 s sputtering by a region dominated by hafnium compounds. This corresponds perfectly to the nominal description of the stack and confirms the presence of SiON at the sample surface. Parallel AR-XPS has also been used to assess the depth repartition of the chemical components in the backside prepared samples. The plot shown in Figure IV.10 uses the relative sensitivity to each chemical component with respect to the detection angle, which allows the classification of the components as a function of depth. The high number of angles acquired, improves the significance of the depth information [22]. In the same way than with ToF-SIMS, we observe a phase evolution (due to the vertical stacking of heterogeneous layers) with depth in AR-XPS, with a strong Si / Si-O signature at the surface of the sample (increasing when using shallower detection angles) and a Hf compound signature deeper in the sample (increasing when using steeper angles). Finally, MEIS spectra (Figure IV.11) show a two-step Si distribution, with a more intense Si signal step starting from the surface of the sample and a less intense signal step at higher depths, corresponding to successive Si-rich and Si-poor layers, characteristic of SiON and HfSiON layers respectively. In order to measure the remaining SiON thickness, we used several calculation methods. With ToF-SIMS, we neglected the near-surface sputter rate variation due to Cs pile-up transient and assumed a constant yield in SiON, equal to the bulk SiO_2 sputter rate. Then we defined the end of the SiON layer as the $^{30}Si^-$ half signal between SiON and HfSiON regions (see Figure IV.9). The sputter time necessary to reach this limit is then converted into nanometres using the bulk

SiO_2 sputter rate obtained with our reference sample. As observed in Fig. 4, there is a slight evolution of the sputter time needed to completely remove the SiON layer.

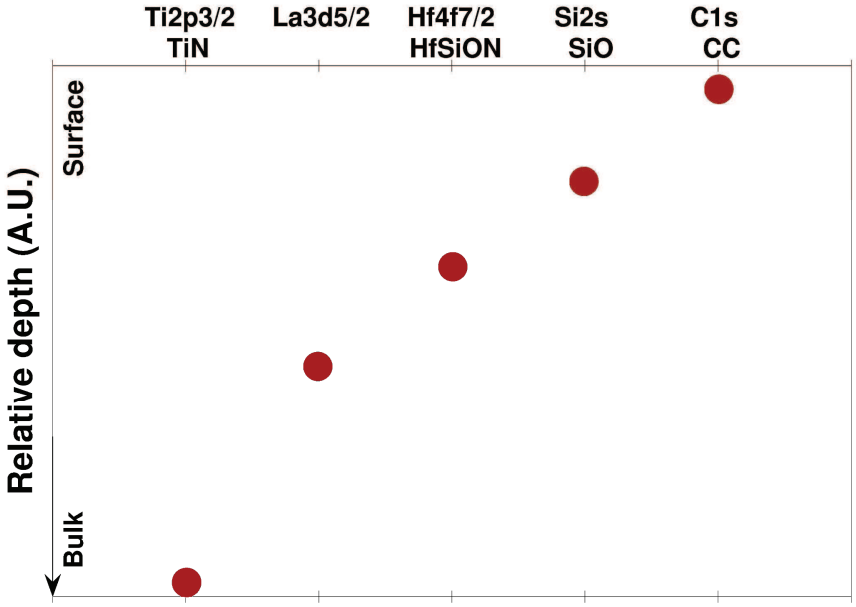

Figure IV.10 Relative depth plot of chemical components in AR-XPS for a backside prepared sample.

This implies a small variation of the over-etch duration of approximately ±12% from one sample to another. The average thickness of remaining SiON is therefore found to be 1.27 ±0.25 nm, which is close to the nominal SiON thickness of 1.5 nm, especially given the approximation of constant sputter rate in SiON. This also means that even in the worst case of extensive over-etching, more than two thirds of the original layer remain.

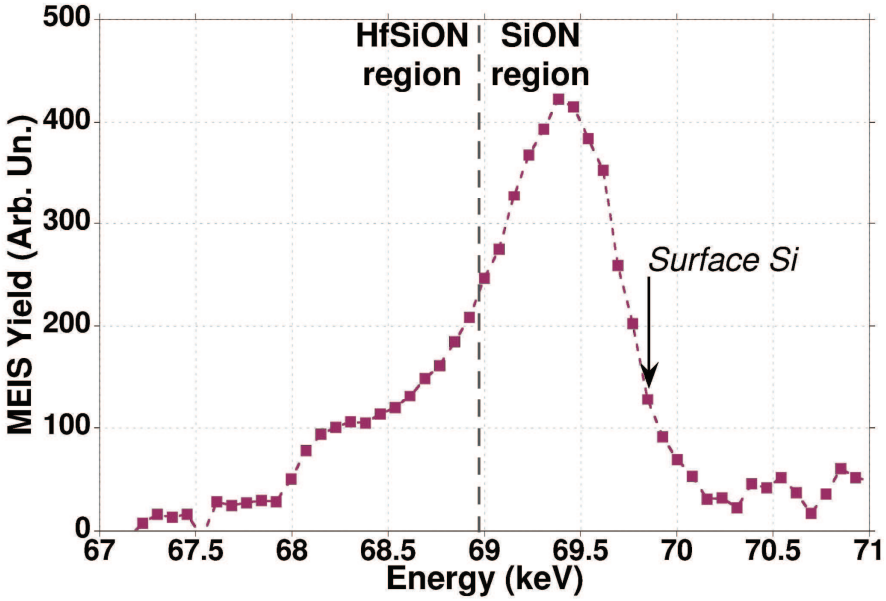

Figure IV.11 MEIS energy spectrum recorded in the Si region with He^+ 100 keV incident at 40° and using a 105° detection angle. The highest measured energy position (black arrow) corresponds to ions scattered from surface atoms while the vertical line indicates the limit between SiON and HfSiON contributions.

MEIS results agree quite well with these conclusions, with an average remaining SiON thickness measured at around 1 nm. These results were obtained by spectra simulation and measurement of Si dose in the surface layer corresponding to SiON. This Si dose was then transformed to layer thickness by assuming a 2200 kg.m^{-3} density for SiON (approximated from SiO_2 density of ref. [23]). AR-XPS results did not allow straightforward measurement of SiON thickness due to the absence of Si substrate in the backside prepared sample, making it difficult to establish an accurate depth scale.
The backside preparation method we present here is therefore shown to yield excellent surface state while preserving the layers of interest, which allows us to investigate the improvements it brings for analysis of the sample's properties with various characterisation techniques.

IV. 6. Improvements brought by the proposed solutions in application to materials and structures representative of actual devices

In this section we will evaluate the developed protocols in terms of ability to obtain simultaneous quantification of all major elements in given set of high-k related materials, reliability and accuracy. As no other known ToF-SIMS protocol can obtain such profiles and to avoid SIMS artefacts, we will use measurements obtained with external techniques (MEIS, HRBS, AR-XPS) for profile comparison and cross characterisation of the same samples.

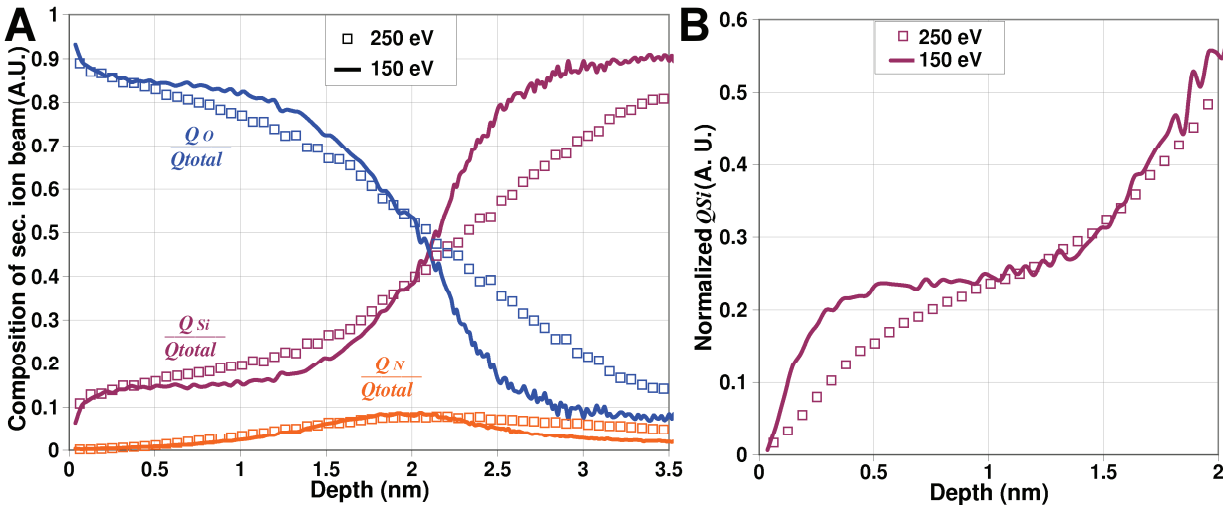

Figure IV.12.A Profiles of a 1.95 nm thick (as measured by ellipsometry) furnace-nitridised SiO_2 layer on Si substrate, obtained with 250 or 150 eV Cs^+ sputtering and 15 keV Bi^+ for analysis. The ordinate scale reflects the atomic composition of the secondary ion beam, using the values Q_A/Q_{total} as defined in equation (IV.1).
B Focus, for the same sample, on Q_{Si} profiles in the first nanometres of the profile. The increase of signals before 1 nm is found to be much slower at 250 eV than at 150 eV.

IV. 6. a- Improvements brought by EXLE mode for profiling of ultra thin SiON layers

The typical layer thickness for dielectric materials in sub-32 nm devices varies between 1 and 1.5 nm depending on its composition. This is due to the very aggressive dimensional scaling of such devices, which requires a very small EOT (~1.4 nm [24]). The

analysis of such ultra-thin layers with ToF-SIMS therefore requires both extremely high depth resolution and minimised transient region. Our EXLE profiling protocol was designed to answer these needs. In this subsection, we will investigate the improvements brought by EXLE depth profiling on a series of thin SiO_2 samples which underwent furnace nitridation (samples are different from those used in section IV. 2). Samples were profiled at 250 and 150 eV, with a 15 keV Bi^+ beam for analysis. Depth scale was established using external layer thickness measurement by ellipsometry for SiO_2 and sputter rate in Si was measured using a known B delta sample.

Depth profiles of the thickest sample (1.95 nm thick) obtained at 250 and 150 eV are presented in Figure IV.12.A. These profiles represent the depth distributions of quantities Q_A/Q_{total}, that is, composition of the secondary ion beam in element A so as defined by equation (IV.1). As discussed in section IV. 4, these quantities present distributions which are more representative of the actual distributions of the different elements than classic secondary ion intensities, but require external calibration for quantification (hence the 0.9 value for O representative signals in SiO_2). We observe quite a difference between the profiles obtained at 250 and 150 eV. In a general manner, profiles obtained at 250 eV are much broader. Specifically, inside the SiO_2 layer, Si and O plateaus are well resolved at 150 eV but less so at 250 eV. The O (Si) signal decay (raise) at interface are also much slower at 250 eV. The interfacial width as calculated by the distance in nanometres from the point of 20 to 80% intensity variation of Q_{Si}/Q_{total} was measured to be 1.2 nm at 250 eV compared to only 0.75 nm with 150 eV sputtering. Finally, inside the bulk Si substrate (at the right of a virtual line at 1.95 nm), the N signal tail is much more persistent at 250 eV. All of these features indicate that depth resolution is significantly improved when using 150 eV sputtering with the depth profiling protocol proposed in section IV. 1.

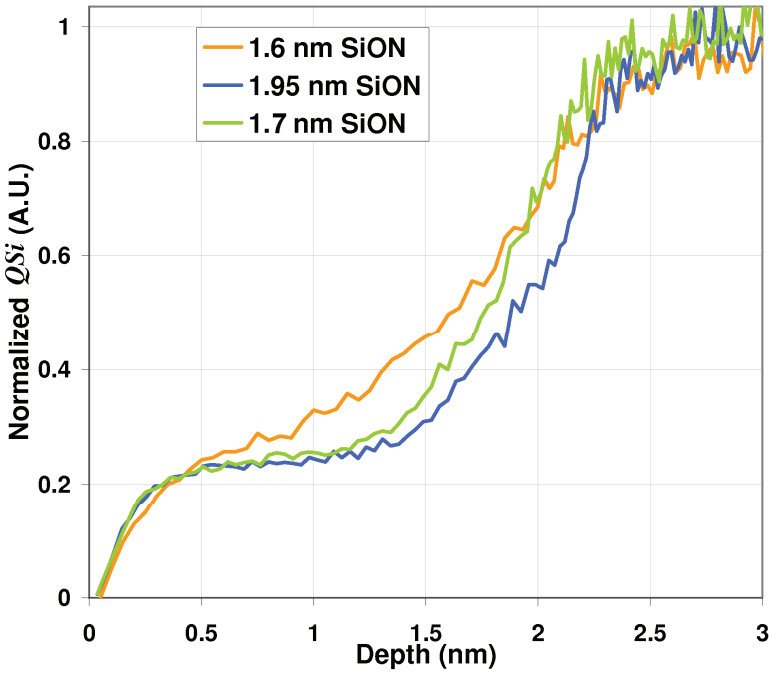

Figure IV.13 Normalised Q_{Si} profiles obtained at 150 eV profiling on nitridised SiO_2 layers of varying thickness.

We can also interest ourselves to the signal increase and stabilisation region in the first nanometres of the profiles. For this, we observe the raw Q_{Si} signals normalised by their value in bulk Si as displayed in Figure IV.12.B. Indeed in the previous profile we only displayed

values normalised by the total number of atoms in the secondary ion beam, which tends to smooth transient region by compressing the signals in the first few data points. The profiles shown in Figure IV.12.B indicate a faster signal rise (before reaching the Si plateau) at 150 eV than at 250 eV, which suggests a reduced transient region in EXLE regime. Profiling with 150 eV Cs^+ therefore provides better depth resolution and reduced transient region in practical sample analysis.
Although definitely improved, those parameters are however still finite and will therefore interfere with data analysis at a certain point. When looking at thinner samples of similar composition (see Figure IV.13), we find out that the layer definition is very good (with the same criteria than previously) up to layers of 1.7 nm thick. For thinner layers, we begin to observe the same kind of profile shape as that which is observed in Figure IV.12 with 250 eV sputtering, i.e. apparition of a slope instead of Si and O plateau, longer interfacial region, etc. The beneficial effects of our EXLE protocol for depth profiling are therefore lessened when looking at layers of 1.6 nm thickness or less.
Moreover, this regime imposes extremely slow sputter rates, given the low caesium beam current and bad focusing. Moreover, due to the obligation to perform depth profiling in non-interlaced mode in order to maintain high sputter/analysis ratio, sputter and analysis cycles are performed sequentially and second-long pauses are inserted between two cycles. These two effects imply very long acquisition times, even for ultra-thin layers such as those studied here. For example, ~30 minutes are needed to record the 3.5 nm of the profile displayed in Figure IV.12.A. Profiling of the 15 nm thick B delta in Si sample for sputter rate calibration otherwise requires approximately 3 hours. EXLE mode is therefore extremely efficient for analysis of ultra-thin samples but may not be the best practical option for analysis of thicker samples unless low energy high current sources are developed. In the following subsections, all the analyses will therefore be conducted at 250 eV Cs^+ sputtering.

IV. 6. b- Accuracy of the full spectrum protocol profiles in high-k material stacks

For this study, three samples were prepared on (100) Si wafers, each sample being representative of the different steps in the elaboration of a typical high-k stack: first a thin SiON (1.5 nm) layer, then an HfSiON (1.7 nm) / SiO_2 (1.2 nm) stack, and finally an HfSiON (1.7 nm) / SiON (1.5 nm) stack. SiO_2 was formed by oxidation of the silicon substrate with in-situ steam generation at 1025°C and hafnium silicate was deposited by MOCVD. TetrakisDiEthylAmino Hafnium (TDEAH) and TetrakisDiMethylAmido Silicon (TDMAS) were used as precursors for hafnium and silicon respectively. Nitridation of both pedestal SiO_2 and hafnium silicate was carried out by plasma nitridation followed by a 1000°C rapid thermal anneal. Nominal composition of the hafnium silicate layers was [Hf]/([Hf]+[Si])=60%, and nominal nitrogen level after nitridation was 10-14 at%. All profiles were acquired with a 250 eV Cs^+ beam, using a 300 µm×300 µm raster to allow slow sputtering of the surface (1 nm/min in silicon) and reduce surface transient. For analysis, a 15 keV Bi^+ beam was used with a relatively large 120 µm×120 µm raster in the centre part of the sputter crater in order to achieve a sputter/analysis ratio of ~80 (the absence of edge effects was observed using secondary ion images). Vacuum in the analysis chamber was kept between 7×10^{-8} Pa and 1×10^{-7} Pa while profiling to reduce the influence of residual gases (typically oxygen and hydrogen) on the analysis. Cycle time was set to 80 µs to allow observation of a sufficiently large mass range of secondary ions. Accurate depth scale calibration was performed by using a variable sputter rate indexed on oxygen signal variations, using the protocol presented in section IV.2. The sputter rate in pure Si was measured by profiling a known boron delta sample [25], while sputter rate in silicon dioxide

was measured with a thick SiO_2 layer characterised by ellipsometry. For calibration of the ToF-SIMS profiles, XPS spectra for Si_{2p}, O_{1s}, N_{1s} and Hf_{4f} core levels were acquired using incident photon energy of 1486.6 eV and collection angle of 35°. This configuration yields an average λ value in HfO_2 matrix of ~2.5 nm [10], i.e. maximum depth of information ~3λ=7.5 nm (with most information coming from the first 2.5 nm). Carbon core levels were also monitored but not taken into account in the analysis and treated as surface contamination only. The choice of a standard XPS instrument for this step was motivated by the necessity of providing a (relatively) easy access to the calibration protocol. To assess the accuracy of the quantified ToF-SIMS profiles obtained by the Full Spectrum protocol, the samples were also analysed by HRBS and parallel AR-XPS (pAR-XPS). For HRBS, a 400 keV He^+ ion beam generated by an accelerator was collimated by two 4-jaw slit systems to 2 × 2 mm^2. The divergence angle of the ion beam was less than 2 mrad. The beam was incident on the specimen mounted on a high-precision goniometer in an UHV chamber. The energy of the He^+ ions that scattered from the specimen was analysed using a 90° sector magnetic spectrometer and detected by a one-dimensional position-sensitive detector. A more detailed description of the HRBS instrument is available in Kimura *et al.* [26]. As depth scale in HRBS profiles is given in atomic doses (i.e. at.cm^{-2}), one needs to model the density profile of each stack to retrieve a depth scale. This was performed by approximating each stack to a succession of two or three layers of density 9000 kg.m^{-3} for hafnium silicate (approximated to HfO_2, density extracted from Triyoso *et al.* [27]), 2200 kg.m^{-3} for silicon oxynitride (approximated to SiO_2, density extracted from Petersen *et al.* [23]) and 2329 kg.m^{-3} for silicon (density extracted from Dismukes *et al.* [28]). Finally, for pAR-XPS, samples were profiled using a customised spectrometer with parallel angle resolved capability, allowing simultaneous acquisition of a wide angle range without sample tilt. The signal of photoelectrons corresponding to the Si_{2p}, Hf_{4f}, O_{1s}, N_{1s} core levels were simultaneously acquired from 8 angles (from 23.75° to 76.25°) using a high resolution monochromatic Al Kα X-ray source (1486.6 eV photons) and at pass energy of 100 eV. Carbon was acquired, but ignored as in the standard XPS experiment. By using a numerical procedure, spectral fitting was performed to extract the peak contributions in the acquired energy regions. Individual line shapes were simulated with a combination of Lorentzian and Gaussians functions. The background subtraction was made using a Shirley function. After correction of the lens transmission factor, each element concentration was obtained by dividing calculated peaks areas by the corresponding Scofield cross section. Reconstruction of the profiles was done using a maximum entropy minimisation algorithm, without specific optimisation of parameters and without fixing a substrate depth. The profile depth scales were scaled using a linear relationship to those obtained with the HRBS and ToF-SIMS measurements.

Properties of the Full Spectrum ToF-SIMS profiles

An interesting property of the profiles obtained with the Full Spectrum protocol is that the number of counts is optimised for each element, and that their intensity is at least of the same order of magnitude. This is not usually the case when comparing single secondary ion intensities, which may differ by several orders of magnitude. As a direct consequence, the sensitivity factors for Hf, Ge, O and N are close to that of Si, which is taken to be unity. The sensitivity factors determined using equations (IV.2) and (IV.3) in (within others) the three samples studied here are synthesised in Figure IV.5. Despite the slightly different nature of the samples, we observe a low spreading of the sensitivity factors around unity. SF_N^{SIMS} is found in all cases to be very close to one, meaning that its detection probability is close to that of Si; while SF_O^{SIMS} is found to have an average value of 0.55 (when averaging over values

found in Figure IV.5.B and IV.5.C), showing that its detection probability is twice as much as that of Si. This is in good agreement with findings in Ferrari *et al.* [4]. However, if we look in detail at Figure IV.5, we observe a clear difference between SF_O^{SIMS} values obtained in hafnium silicates and in silicon oxynitrides, the latter being approximately twice lower than the former. Thus O is detected twice as well in silicon oxynitride than in hafnium silicate. This is mostly due to the large contribution of O_x^- and $Si_xO_y^-$ signals to Q_O in SiON, compared to the much smaller contribution of $Hf_xO_y^-$ secondary ions in hafnium silicate. This might be linked to a diminution of the oxidised species ionisation probability in presence of Hf due to its segregation during profiling, which modifies the surface state into a partially metallic Hf layer [19]. SF_{Hf}^{SIMS} is otherwise found to have an average value around 2, meaning that its detection probability is half that in Si. Even if clear sensitivity factor variations are detected from an element to another, they never differ from one by more than a factor of four. This is much less than what we would expect if we were using single secondary ion signals instead of Q_A quantities, since the difference in sensitivity factor for a particular element in different matrixes (oxidised or not) can reach several orders of magnitude [29-31]. This behaviour proves that the matrix effects are minimised when using the Full Spectrum approach. Another interesting property of these sensitivity factors is their reproducibility from a sample to another, when the sample structure is similar but the composition slightly different. This was the case in the SiON layers studied in Ferrari *et al.* [4], as well as here for the two hafnium silicate samples. Those preliminary results show that it may be possible to shortcut the XPS step by performing systematic studies on samples with similar structure but slightly different composition and using average SF_X^{SIMS} values.

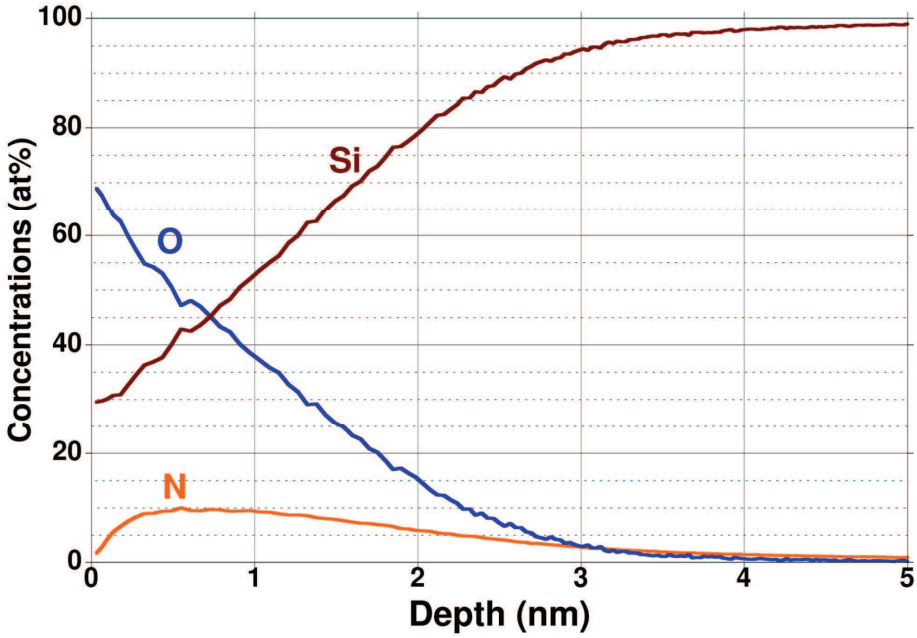

Figure IV.14 Full Spectrum ToF-SIMS profile of the SiON/Si sample.

The Full Spectrum ToF-SIMS profiles are displayed in Figure IV.14 for SiON / Si and in Figure IV.15 for HfSiON / SiO_2 / Si and HfSiON / SiON / Si. The concentration is plotted on a linear scale and in at% for all elements. This is unusual in SIMS or ToF-SIMS depth profiles, and only the works of Van Berkum *et al.* [32] and Douglas *et al.*[33] on silicon oxynitrides show similar properties. However these works differ from ours in that they use chemically inactive primary ion beams for both sputter and analysis, and standard reference samples for concentration calibration (which is no longer needed if the Full Spectrum protocol

is used). The nominal thicknesses of the SiON layers investigated in these papers are also at least 30% greater than those studied in the present work.
The linear at% scale is a direct consequence of the quantification mechanism described in equations (IV.2) and (IV.3). Indeed, the quantity $D_A(z)$ must be unitless for the equation (IV.2) to be satisfied. The Full Spectrum ToF-SIMS profiles result therefore from the point to point normalisation of the sum of all the $D_A(z)$ quantities to a hundred percent. This allows, as opposed to classic SIMS quantification methods whose output would be in at.cm^{-3}, a direct comparison with other characterisation techniques only sensitive to the relative composition of a material, such as RBS, MEIS or AR-XPS.

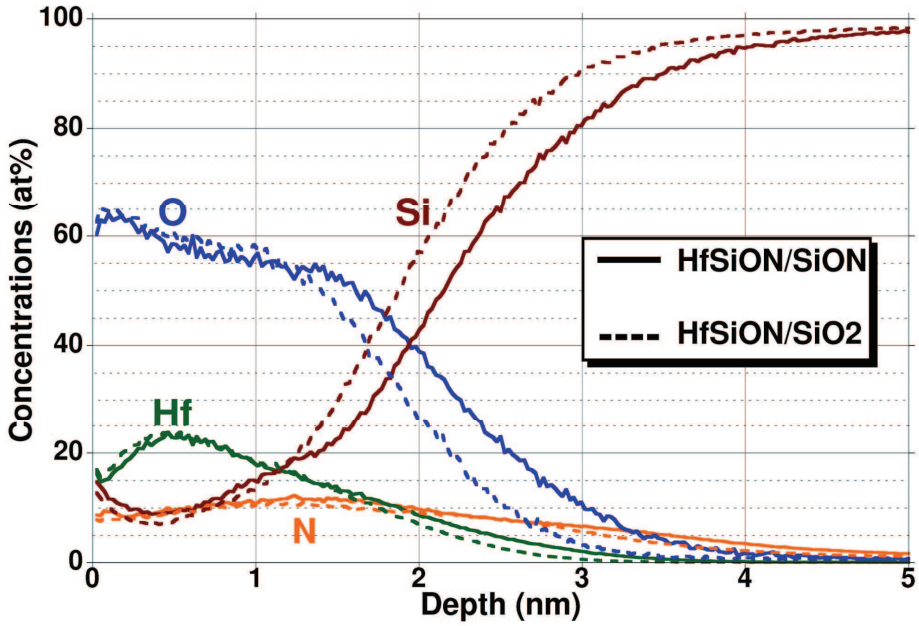

Figure IV.15 Full Spectrum ToF-SIMS profiles of the HfSiON/SiO_2/Si and HfSiON/SiON/Si samples.

Each of the profiles displayed in Figures IV.14 and IV.15 exhibits features characteristic of the corresponding stack structure. For SiON/Si we observe an O-rich (Si-poor) transient region where most of the N is situated, followed by an O-poor (Si-rich) transient region including an N tail, and finally a stable Si region. For both HfSiON/SiO_2/Si and HfSiON/SiON/Si, we observe first an O and Si plateau corresponding to the hafnium silicate layer, then a transient region corresponding to the pedestal oxide layer, and finally a stable Si region. The pedestal oxide region is observed to be thinner in the SiO_2 case than in the SiON case, which agrees well with the nominal thicknesses. The fact that important transient regions are present in these profiles shows that the Full Spectrum protocol does not modify the sputter processes. It only improves the quantification by taking better account of the elements present in the secondary ion beam, thus minimising the artefacts due to ionisation processes. However artefacts resulting from physical or chemical reaction of the material with either the sputter/analysis beam or the ambient atmosphere are still present. Typically, the N tail in the ultrathin SiON layer profile is expected to be an artefact due to N migration towards Si during profiling [34]. In this aspect, Full Spectrum ToF-SIMS profiles would not differ from classic profiles, and only a change of sputter/analysis conditions, such as the use of chemically inactive species for both sputtering and analysis as in Van Berkum *et al.* [32] or Douglas *et al.*[33], would help reduce these undesired effects. Apart from these artefacts, other parameters such as collisional mixing and depth of information also play a role in the

shape of Full Spectrum ToF-SIMS profiles as it would for classic ones. Consequently, the profile of the SiON layer does not feature any O or Si plateau as one would expect. Instead, it exhibits a transient period in O and Si compositions. Lowering the sputtering energy to 150 eV would help to partially resolve this problem, as shown in the above subsection (note however that the thickness of the SiON layer is, in our case, 1.5 nm, which is less than the lower limit for high definition of such a layer with 150 eV Cs^+ sputtering). In the same way, the pedestal oxide layer beneath the hafnium silicate layer is not resolved in both profiles of Figure IV.15. This is an intrinsic limit of the ToF-SIMS instrumentation and parameters we used in this study, such as the sputter and analysis beams energy, chosen on purpose to limit acquisition times to reasonable durations. One can therefore expect less mixing and improved depth of information using different angular configurations or by adjusting the residual atmosphere in the analysis chamber [3, 18, 35-37]. Nonetheless, data available in literature on high resolution compositional depth profiling of similar structures show rather similar profile shape. It is for instance the case in Reading *et al.*,[38] where the pedestal oxide layer in hafnium silicate on silicon dioxide stack on Si is seen only as a transient when using a model to retrieve quantified depth profiles from MEIS spectra. The same phenomenon is also observed when using HRBS [39]. It can thus be quite tricky to determine with precision the thickness of each layer in samples such as ours, based on profiles obtained with one technique only. We however performed it to obtain indicative thicknesses by using the simple and widely-used method of half-signal, consisting in using the half intensity point of a signal as an interface marker. Thickness data obtained with this method are compiled in Table IV.i. An excellent agreement is found between the nominal thicknesses of each layer and the experimental thicknesses extracted from Full Spectrum ToF-SIMS profiles. Moreover, the thickness of the pedestal oxide in both hafnium silicate stacked samples diverges of 0.25 nm, which is also very close to the nominal thickness difference between these two layers. This shows that even if the layer is not perfectly resolved, some useful information on its thickness can be extracted from the Full Spectrum ToF-SIMS profiles.

Sample	Layer	Nominal	FS ToF-SIMS	HRBS
SiON/Si	SiON	1.5	1.5	1.3
HfSiON/SiO_2/Si	HfSiON	1.7	1.8	1.6
	SiO_2	1.2	1.25	1.1
HfSiON/SiON/Si	HfSiON	1.7	1.8	1.5
	SiON	1.5	1.5	1.5

TABLE IV.i Layer thicknesses measured for the different samples, in nm. For SiON/Si sample, layer thickness was measured as the point of 66.6 at% Si composition (Si half signal from SiON layer to Si substrate). For both other samples, hafnium silicate layer thickness was measured as the point of Hf half signal, and pedestal oxide layer thickness as the point of N half signal. Layer thicknesses were not measured with pAR-XPS since its depth scale was resulting from a fit to this of the two other techniques.

Concerning the composition of the different layers, we observe a very close match to the nominal compositions specified in the experimental part of this paper. To avoid the transient regions, we averaged the compositions in the different layers in their centre parts with a 0.5 nm exclusion margin on both sides. For the SiON/Si sample, the N composition in the SiON layer is found to be 9.5 at%, in agreement with the nominal N level (10 to 14 at%). The average composition of both hafnium silicate layers is found to be of 20 ±0.2 at%, 12.6 ±0.6 at%, 56.9 ±0.8 at% and 10.5 ±0.3 at% for Hf, Si, O and N respectively, yielding a

stoichiometry of $Hf_{0.6}Si_{0.38}O_{1.7}N_{0.31}$. This implies a partial stoichiometry [Hf]/([Hf]+[Si])=61.3%, which is again very close to the 60% expected.
The Full Spectrum protocol seems therefore to provide accurate compositional profiles of the different stacks studied in this paper. However, to definitely prove it we would need to compare with results obtained with other techniques on the same samples.

Comparison with HRBS and pAR-XPS profiles

Only a few techniques are able to provide quantified elemental depth profiles of ultrathin samples such as these, and among them HRBS and AR-XPS have produced up to now the most reliable results, with various works available in the literature. We can refer in particular to the works of Kimura *et al.* [39], Ichihara *et al.* [40], Brijs *et al.* [41] (Toyoda *et al.* [42-43], Brundle *et al.* [44]) for an overview of the abilities of HRBS (AR-XPS) in in-depth elemental quantification of ultrathin high-k samples. We therefore used both of these techniques to check the reliability of our Full Spectrum ToF-SIMS profiles.

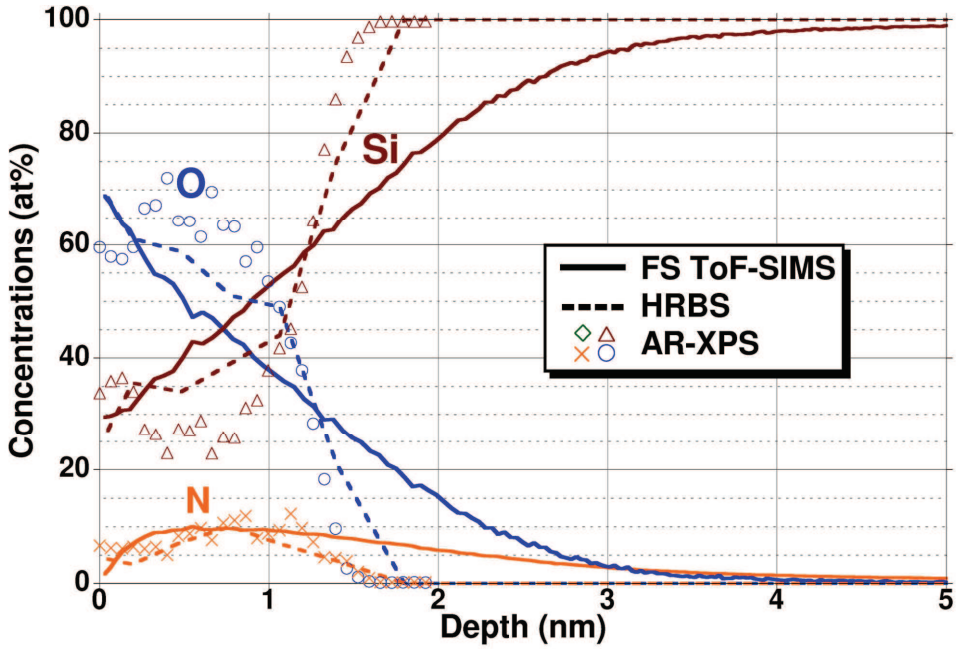

Figure IV.16 Overlaid Full Spectrum ToF-SIMS, HRBS and pAR-XPS profiles of the SiON/Si sample.

The profiles obtained with all three techniques on the SiON/Si and HfSiON/SiON/Si samples are shown in Figures IV.16 and IV.17. Firstly there is good agreement of the profiles obtained with the three techniques, in terms of layer thicknesses and order as well as in layer composition (while distortion of profile shapes and peak values of some elements are also noteworthy). This is not trivial given the inherent drawbacks of each technique, such as the loss of depth resolution with depth for HRBS, layer mixing and matrix effects for ToF-SIMS, and reduced sensitivity for layers below the surface in pAR-XPS. One would therefore expect, if the ToF-SIMS profiles were not accurate, important discrepancy with the profiles obtained with the two other techniques. This phenomenon is observed in Brijs *et al.* [41], where ToF-ERDA, RBS and ToF-SIMS ability to perform quantitative profiles of ONO structures (silicon dioxide / silicon nitride / silicon dioxide) was investigated. The authors of this paper conclude on the difficulty to obtain a *"single method available providing a complete*

composition depth profile with high depth resolution [...] and quantification accuracy". This is clearly not the case in our study, given the overall good match obtained within the three techniques. In terms of layer thickness, we indeed obtain an agreement within ±0.3 nm uncertainty between values extracted with ToF-SIMS and HRBS (see Table IV.i), the thicknesses measured by HRBS being slightly lower. In terms of layer composition, the N level in the SiON/Si sample is found to be of 8.6 at% with HRBS, against 9.5 at% for both ToF-SIMS and pAR-XPS, showing a difference of appreciation of less than 1 at%.

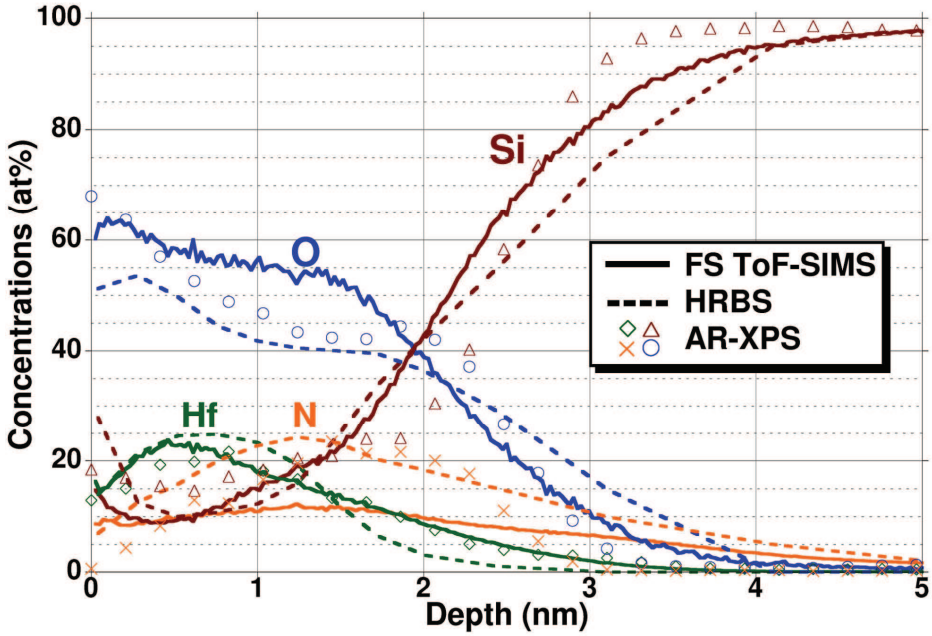

Figure IV.17 Overlaid Full Spectrum ToF-SIMS, HRBS and pAR-XPS profiles of the HfSiON/SiON/Si sample. Same agreement is achieved for the HfSiON/SiO_2/Si sample (not shown).

The composition of the hafnium silicate layer in the HfSiON/SiON/Si sample is synthesised in Table IV.ii (profiles are displayed in Figure IV.17). All techniques agree on each element concentration with a ±2 at% discrepancy for Hf and Si, and a ±5 at% discrepancy for O and N. The partial stoichiometries [Hf]/([Hf]+[Si]) obtained with the different techniques are also in agreement with each other with a ~60% ±5% value. The profiles finally agree on the fact that the N peak is situated at the interface between the hafnium silicate and the pedestal oxide layer, showing that N piles up at this interface.

Technique	Hf	Si	O	N
Full Spectrum ToF-SIMS	19.8	13.3	55.1	10.8
HRBS	22.9	12.3	44.1	20.7
pAR-XPS	19.9	16.7	49.4	13.9

TABLE IV.ii Composition of the hafnium silicate layer in the HfSiON/SiON/Si sample obtained with the three techniques, in at%. These values were obtained on the centre part of the layer, with a 0.5 nm exclusion margin on each side to avoid transient regions.

Closer observation of these profiles reveals slight differences between the techniques. First of all, on the N profile shape of the SiON/Si sample. The long tail visible on the ToF-SIMS profile over several nanometres in the Si substrate is absent for the other techniques. This

shows that the N tail is an artefact due to segregation during profiling. Moreover, on the same sample, the ToF-SIMS profile is the only one not to exhibit an O and Si plateau in the SiON region. pAR-XPS shows in this respect the widest and most stable concentration plateau, along with the sharpest interface. This is due to both a lack of resolution in ToF-SIMS at the near-surface region and to the mixing artefacts discussed in previous section. For this reason, the total N dose extracted from the ToF-SIMS profiles is largely overestimated compared to the other techniques. On both hafnium silicate samples, no such difference is observed on the different in-depth distribution shapes. However, there is a noticeable discrepancy on the O and N level obtained (see Figure IV.17 and Table IV.ii). Relative to ToF-SIMS, pAR-XPS slightly underestimates (overestimates) the O (the N) level by approximately 5 at%. This tendency is even greater for HRBS with a discrepancy of ~10 at%. Given that (i) the three techniques agree on the N concentration in the SiON/Si sample and (ii) the nitridation recipe is exactly the same for the nitridation of the silicon dioxide and the hafnium silicates (in terms of plasma energy, gas flow and duration), one would expect to obtain similar N at% (~10 at%, as obtained in the SiON/Si sample) for the hafnium silicate samples with the three different techniques. The origin of this discrepancy might therefore only be due to the conjunction of the measurement errors of each separate technique. Finally and as on the SiON/Si sample, pAR-XPS yields the best layer definition and the sharpest interfaces of all the techniques.
Apart from these differences, the profiles obtained with HRBS and pAR-XPS match correctly the Full Spectrum ToF-SIMS in terms of layer thicknesses and composition, demonstrating the feasibility of quantitative depth profiling of ultrathin high-k stacks with ToF-SIMS, using the Full Spectrum protocol.

Consistency and limits of the Full Spectrum protocol

The reliance of the quantification of the Full Spectrum profiles on modelling the stack with XPS data might cause one to consider the robustness of the protocol. There are indeed several steps where user subjectivity can influence the final profile. These are (i) the choice of the secondary ion sets for calculation of the Q_A quantities in equation (IV.1), and (ii) the approximation of several of the parameters in equation (IV.2) for calculation of the SF_A^{SIMS}. Point (i) is furthermore divided into two parts: either the omission or the improper monitoring of an ion in the list. The latter can be quickly detected, since if the followed ion relates to a different element than that of interest, the shape of the distribution will usually help the user to discriminate the ion. In the case of a mass interference, for instance, one must carefully choose a different isotope in order to avoid or minimise the intensity of the interfering ion. Compared to this, the omission of an ion is less trivial to detect. However, except if a major ion is omitted (such as for example SiN^- for the calculation of Q_N), the maximum resulting error would not exceed ±10% on the composition for each element. This error is considered reasonable, since for the HfSiON/SiON/Si sample, it would yield a maximum variation of ±2 at%, ±1.3 at%, ±5.5 at% and ±1.1 at% on the layer composition in Hf, Si, O and N, respectively. As for point (ii), the only approximation made in equation (IV.2) would be for the establishment of λ. Indeed, all other values are either known (θ) or extracted from recognised tabulated values (SF_A^{XPS}). In our model, λ is taken as a constant though the entire stack and the same average value is used for all elements. These two conditions are of course not verified experimentally, and it is therefore worth to check the robustness of the Full Spectrum protocol to an inaccurate choice of λ value. The profiles of the HfSiON/SiON/Si sample obtained through the Full Spectrum protocol with λ variations are shown in Figure IV.18. The different elements are not affected in the same way by the approximation on λ, Si being the most sensitive, with up to ±6 at% variation in the first 1.7 nm of the profile.

For the other elements, the variation is less important, with a maximum deviation from the main value of ±5 at% for O (in the transient region corresponding to the SiON layer) and of ±1.25 at% for Hf and N. These errors are acceptable, given the difficulty of the analysis. The protocol may therefore be considered robust, even in the case of slightly misguided use.

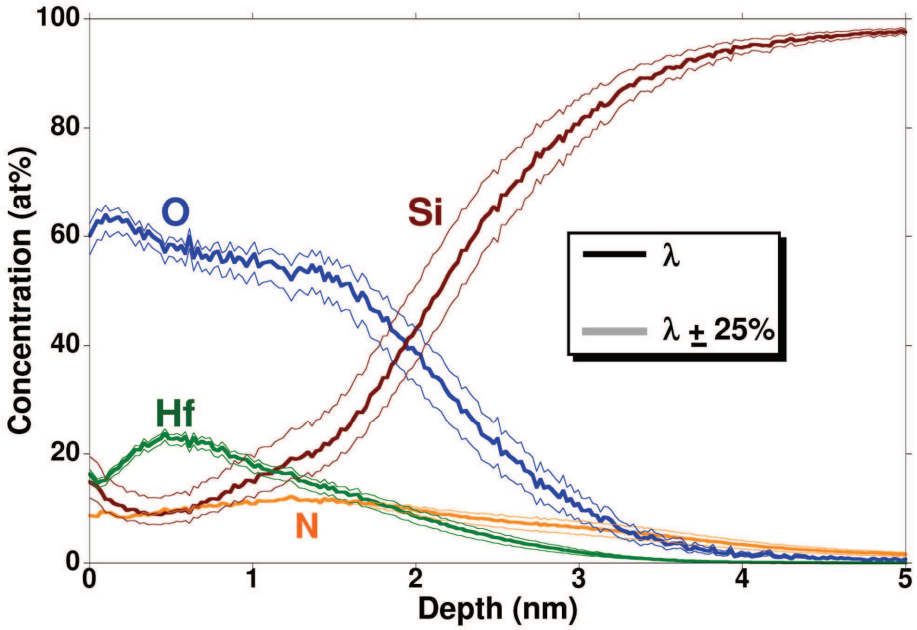

Figure IV.18 Overlaid Full Spectrum ToF-SIMS profiles of the HfSiON/SiON/Si sample obtained with a λ variation of ±25%. The full, dark lines represent the correct profile (identical to the profile presented in Figures IV.15 and IV.17), and the light areas represent the possible composition variations due to the change of λ. Same behaviour is observed for the other samples.

As for the limits of the use of the Full Spectrum in different stacks, they principally reside in the XPS calibration method. As discussed before, for the assumption of constant SF_A^{SIMS} to be true, the XPS sampling depth must be superior to the total depth of interest, i.e. the thickness of samples quantified though this protocol can usually not exceed 5 to 10 nm in the most favourable case. The analysis of thicker stacks, which would be interesting for example for studies of stack evolution with annealing, requires therefore the use of the extended protocol as presented in section IV.5.

IV. 6. c- Accuracy of the full spectrum protocol profiles in high-k/strained channel stacks

For this study, two identical samples were grown on (100) silicon substrates. They were constituted (from bottom to top) of (i) a pseudomorphic (compressively strained) SiGe layer of 20 at% nominal Ge content and of 4 nm nominal thickness, (ii) a Si cap of 3 nm nominal thickness, (iii) a SiO_2 pedestal oxide of 0.8 nm nominal thickness and (iv) a hafnium silicate layer of 2.3 nm nominal thickness either nitridised or not. sSiGe and Si cap were epitaxially grown, while SiO_2 was grown from Si using a low temperature oxidation plasma. Finally hafnium silicate was deposited by MOCVD and its nitridation was performed by plasma nitridation followed by a 950°C spike anneal in N_2 atmosphere. Samples were analysed with ToF-SIMS and HRBS using the same experimental parameters than in the previous subsection. ToF-SIMS profiles depth scale was determined by mixing both the

approach developed in section IV. 2 for sputter rate within the oxygen-rich region of the profile, and the approach developed in the previous chapter for the $Si_{1-x}Ge_x$ region.

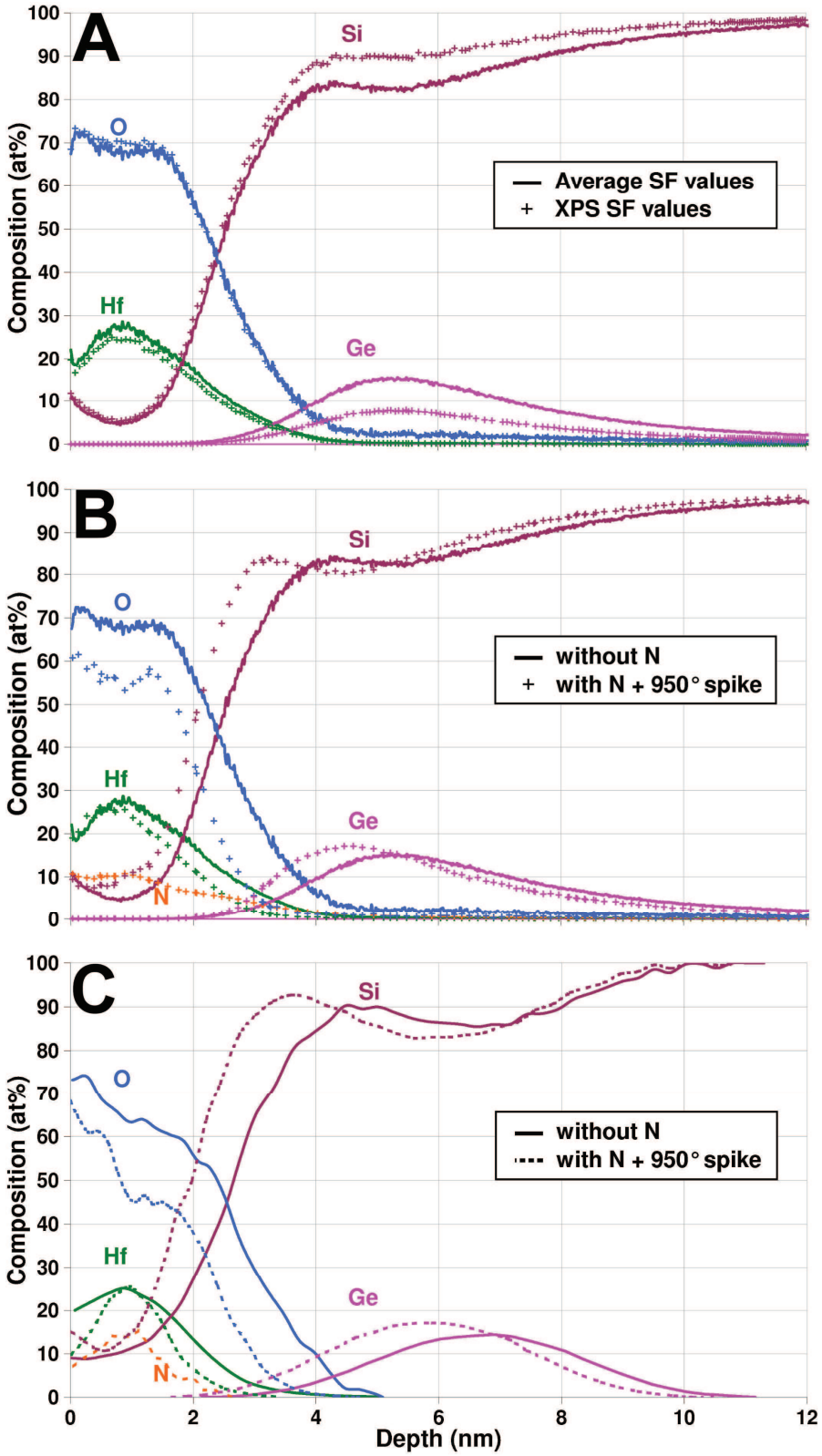

Figure IV.19.A ToF-SIMS profiles of the as deposited, high-k stack on strained SiGe channel sample. Both profiles are obtained with the Full Spectrum protocol, one using average SF values and the other using actual SF values deduced through XPS measurements and equation (IV.3). Excellent agreement is obtained until ~3 nm, but afterwards the profile

obtained with XPS cross-calibration features Ge content underestimation.

B Overlaid ToF-SIMS profiles of the as deposited and spike annealed samples, obtained with average SF values.

C Overlaid HRBS profiles of the as deposited and spike annealed samples. Similar elemental distribution, layer composition and evolution with annealing is observed.

For HRBS, it was determined by approximating material densities to tabulated values of HfO_2, SiO_2 and Si as in previous subsection for the oxygen-rich region of the profiles and by calculating the point by point $Si_{1-x}Ge_x$ material density in function of *x* from pure Si and Ge densities using a linear approximation in silicon germanium. ToF-SIMS profile calibration was performed both using XPS cross characterisation to obtain sensitivity factors as in the previous subsection, and using the average SF values for Hf, O, N and Ge displayed in Figures IV.5.A and IV.5.C. ToF-SIMS depth profiles of the as-deposited, non nitridised sample obtained with both quantification methods are displayed in Figure IV.19.A. As expected, we observe a very good fit of both profiles in their first ~3 nm: indeed this virtual layer is the one from which most XPS signal is obtained. Full Spectrum ToF-SIMS sensitivity factors can be accurately deduced from XPS peak areas since XPS is able to efficiently probe material in this region. However, when going deeper in the sample, we observe a discrepancy between both profiles, with the XPS calibrated profile showing a Ge content underestimation as compared to the average SF value calibrated profile. This can be interpreted as an effect of the under-sampling of Ge in XPS spectra, Ge appearing too deep in the sample to be efficiently probed. Similar behaviour is observed on the other sample (not shown). The Ge profiles obtained with average SF values are also closer to expectations from nominal composition of the sample. This results shows the interest of using average SF values for quantification of thick samples in that (i) average SF issued profiles show no significant difference with XPS calibrated profiles in the first few nanometres and (ii) they still yield plausible depth distributions deeper in the samples.

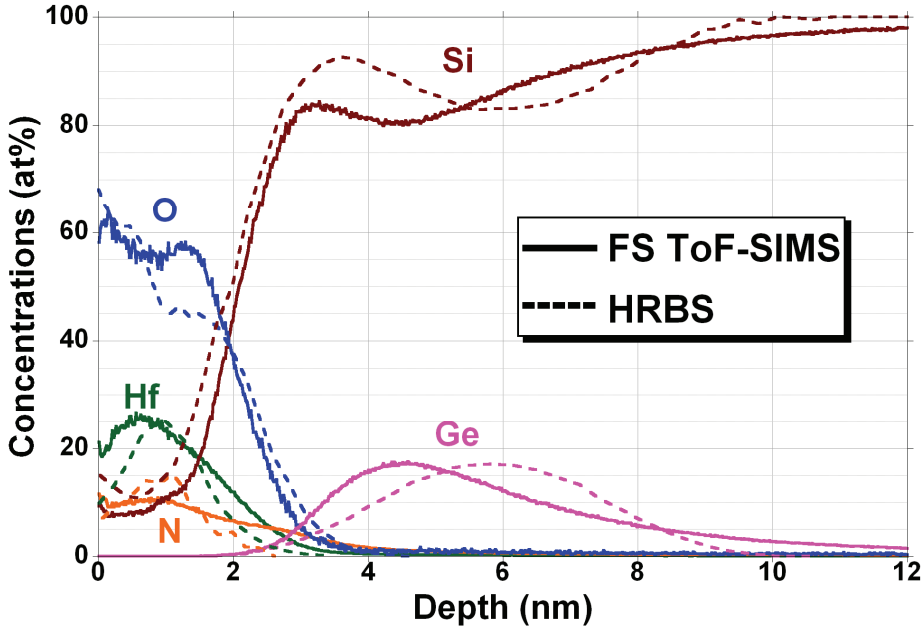

Figure IV.20 HRBS and ToF-SIMS elemental profiles of both as deposited and annealed samples. We observe excellent agreement on concentration profiles in the high-k region and on SiGe layer composition. However different shapes of the SiGe region (sharper interface with ToF-SIMS, broad with HRBS) are obtained.

To further check the accuracy of such profiles, we performed HRBS profiling on the same samples. In this case pAR-XPS profiles were not acquired because the total stack thickness was superior to the instrument's sampling depth. Overlaid ToF-SIMS (HRBS) profiles obtained for both as deposited and nitridised samples are displayed in Figure IV.19.B (IV.19.C). Both techniques yield similar profiles, with a typical Si and O plateau in the first few nanometres of the Hf-rich region, followed by a sharp signal decay and successive Si and Ge signal bumps corresponding to the ultra-thin Si cap and to the SiGe layer respectively. Both techniques reveal the same stack evolution upon nitridation and annealing, with significant oxygen dose loss accompanied by layer densification and contraction. Total dielectric thickness as measured with both techniques from O half signal give 3 nm before nitridation (in agreement with summed nominal thicknesses of hafnium silicate and silicon oxy-nitride layers) against 2.3 nm after nitridation. For further profile comparison, overlaid Full Spectrum ToF-SIMS and HRBS profiles for the nitridised sample are shown in Figure IV.20. We observe an even better agreement on concentration profiles than with the previous sample series, especially on O, Si, N and Hf distribution in the high-k dielectric region. This indicates that the discrepancy observed in Figure IV.17 on O and N level might be due to a conjunction of measurement errors, as previously supposed. Both profiles are indeed almost identical up to the thickness of ~3 nm, which proves the accuracy of the Full Spectrum approach for quantification of high-k dielectrics. Si signal sharp raise is also similar with both techniques, which indicates that at least down to 3 nm their depth resolution is equivalent. The concentration profile of the Si cap and SiGe layer beneath the high-k stack is yet somehow different. Ge doses found with both techniques are coherent with each other (3.72 at/cm² with Full Spectrum ToF-SIMS, 3.34 at/cm² with HRBS) and in satisfying agreement with nominal dose (~3.9 at/cm²). Moreover, Ge dose variation with annealing does not exceed 2% in ToF-SIMS profiles, which testifies for accuracy of both quantification protocol and depth scale. However, the Ge seems distributed differently. Since both doses are equivalent while HRBS profiles seem broadened in this region, one might conclude that this can be an artefact intrinsic to HRBS technique, in which depth resolution decreases in an important proportion with depth because of impinging ion energy loss and trajectory modification due to the material electronic stopping power. This phenomenon, called straggling, will cause the ions backscattered on Ge atoms at a depth Δ to have less energy than expected and therefore appear as ions reflected at a depth $\Delta+\delta$, which induces forward-broadening of the Ge distribution in our samples. Other potential causes for this discrepancy might rely in the relatively low Ge content in the buried layers as well as from the HRBS profile reconstruction method from energy spectra.
Given the overall agreement of the techniques, this study however assesses of the accuracy of the Full Spectrum protocol profiles extended to thicker samples using average sensitivity factors.

IV. 6. d- Accuracy of the full spectrum protocol profiles in high-k/metal gate stacks

For this study, we used the samples described in section IV. 5. To study stack behaviour under annealing, half of the samples was kept as deposited while the other half underwent spike anneal in a H_2 atmosphere at 1065°C for 1.5 s to simulate the transistor fabrication process. ToF-SIMS profiling was performed with 250 eV Cs^+ sputtering and 15 keV Bi^+ for analysis. Depth scale was obtained using ellipsometry measurement of the TiN

layer thickness (6.5 nm) in the as-deposited sample (for the TiN region) and using the protocol presented in section IV. 2 (for the dielectric material region). Similarly to the previous subsection, average sensitivity values were used, due to the too great TiN thickness, preventing XPS analysis of the whole stack. Moreover, the sensitivity factor for Ti was determined so as to obtain equal N and Ti content in the TiN region of the as-deposited sample (SF_{Ti}=1.25). Finally, as La is only present as a trace material in these stacks, it could not be accurately quantified by the Full Spectrum protocol. Therefore, SF_{La} was calculated so that the La dose in the as-deposited samples would match the nominal La dose (determined using La_2O_3 nominal layer thickness: 0.4 nm and density: 6.5 g/cm^3 [45]).

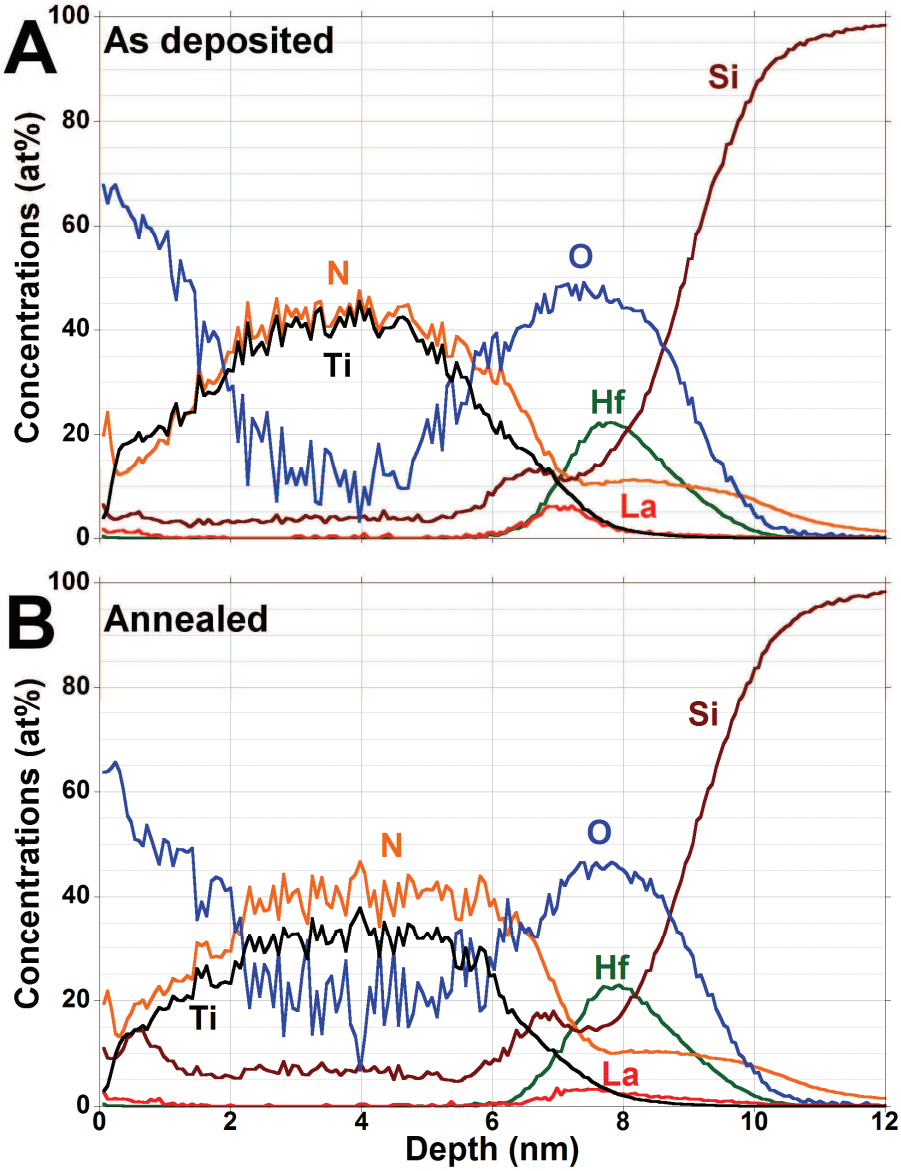

Figure IV.21 Full Spectrum ToF-SIMS elemental profiles of both as deposited (**A**) and annealed (**B**) HKMG samples.

Profiles of both samples are shown in Figure IV.21. In both cases we observe well defined layers, with a first N plateau in TiN and a second in the dielectric material region. Inside the latter, elemental composition in Hf, Si and N is very similar to that found in dielectric stacks alone (see subsection IV. 6. b-), which indicates achievement of accurate quantification. La

distribution is the only one whose shape is found to change with annealing, with a broadening towards the substrate. The compositions of O, Ti and Si are found to vary as well in the TiN region, but only in intensity and not in shape. This is tentatively explained by Si and O uphill diffusion in TiN upon annealing, as proposed by Goncharova *et al.* [46-47]. However, one can observe, as shown by Figure IV.22, that total elemental doses calculated from Full Spectrum ToF-SIMS profiles using tabulated density values do not vary with annealing (or within the experimental error of ±10%). This feature also indicates that quantification is accurate since the very short annealing step is done in an inert atmosphere and should therefore generate no change in the total elemental doses in the stack. To further investigate ToF-SIMS profiles accuracy, we acquired profiles on similar samples with Auger spectroscopy. Profiles were acquired using 250 eV Ar abrasion at an incidence angle of 32° with respect to the sample normal, without sample rotation. Due to the large beam size, sputter and analysis was performed in a successive fashion, with 15 s sputtering for one analysis cycle.

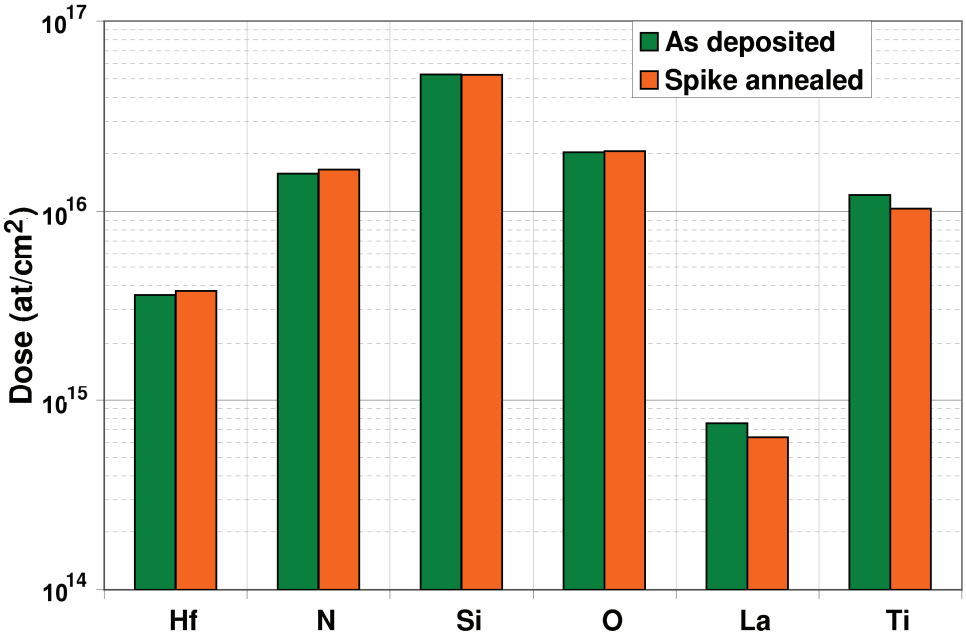

Figure IV.22 Elemental doses obtained from ToF-SIMS profiles in both samples. Experimental error (not shown) is estimated to be ±10%.

Sample were elaborated using exactly the same conditions, with the difference of TiN layer thickness which was made ~2 nm thick only in order to allow more rapid stack analysis and LaOx thickness which was made 1 nm thick in order to get more La relevant signal. Auger profiles are displayed in Figure IV.23. With the exception of the TiN region, we obtain very similar elemental distributions, with N and Si plateaus in the dielectric region, and same O and Hf peaks. La peak shape variation with annealing is also found to be very similar to that in ToF-SIMS profiles. All these factors further confirm the accuracy of the ToF-SIMS profiles in these samples. The discrepancy in TiN region is assumed to be due to the combined effects of a thinner TiN region and lack of depth resolution of the Auger profiles (Ar being much lighter than Cs, it is expected at the same impact energy to induce more mixing), does not enable the "true" composition of the TiN region to be measured because of both surface oxidation of the TiN and of the O-rich beneath layers. However, Auger can resolve chemical bonding states of any element during profiling. In this case, the observation of Hf bonding states is very helpful since it reveals the apparition of an important fraction metallic Hf, although Hf is very unlikely to form metallic layers in an oxide (and silicated)

environment. This proves that the long Hf tails obtained when profiling such stacks are indeed due to sample modification while sputtering, with the creation of a metallic Hf-rich surface.

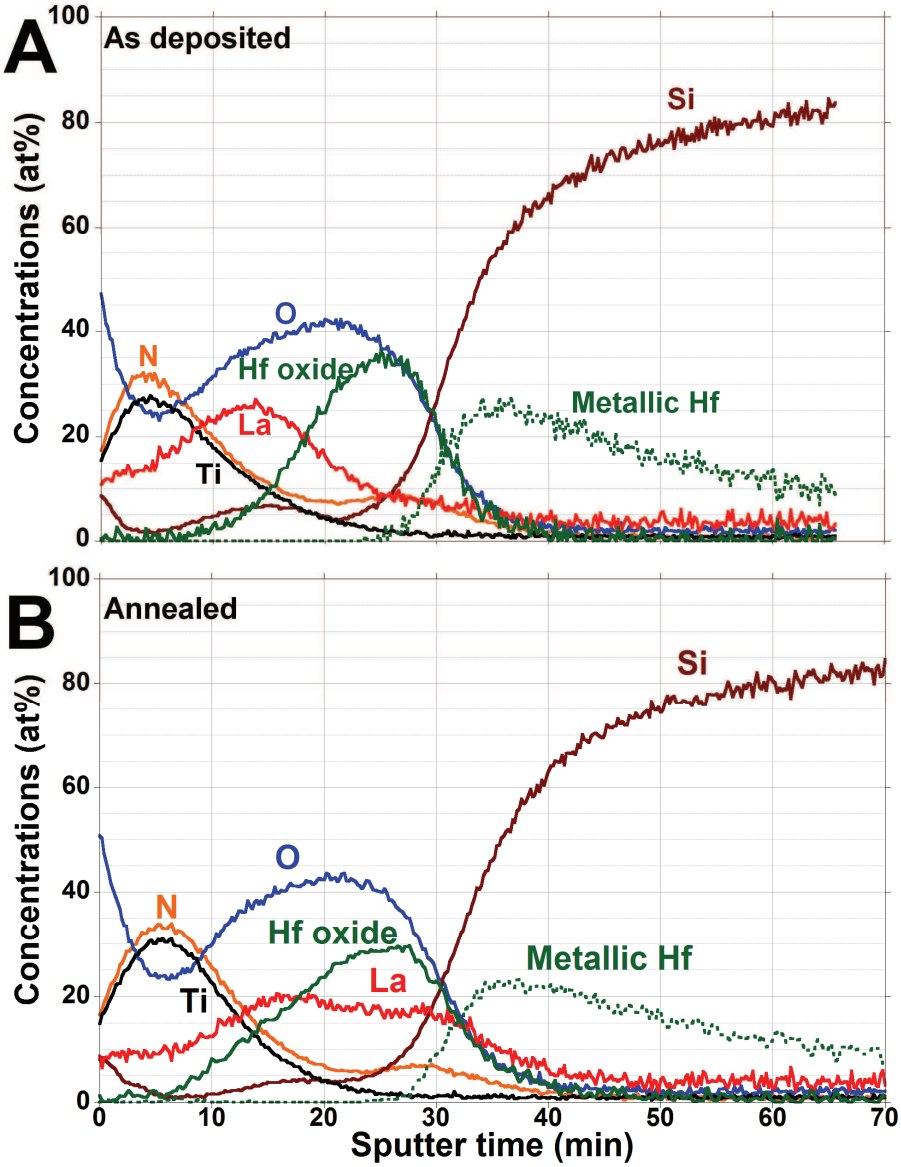

Figure IV.23 Auger elemental profiles of both as deposited (**A**) and annealed (**B**) HKMG samples.

IV. 6. e- Improvements brought by the developed backside sample preparation protocol for accurate analysis of high-k/metal gate stacks upon annealing

Even using advanced calibration protocols such as those investigated above, every characterisation technique presents some limitations intrinsically related to the physics of the instrument. Particularly, profiling by means of energetic ion beam sputtering of Hf based materials raises a problem of significant in-situ material modification, as shown by the Auger profiles in Figure IV.23. These hinder the possibility to accurately characterise samples. In the particular case of our high-k/metal gate stack, much of the recent research interest has focused on the diffusion of the different elements, and in particular La, throughout the stack during the activation anneal. What matters here is therefore the ability of a technique to resolve the La distribution in the most precise manner possible. We will now investigate the improvements

brought by backside sample preparation on the quality of analysis yielded by techniques such as ToF-SIMS, AR-XPS or MEIS on the same samples than in section IV. 5.

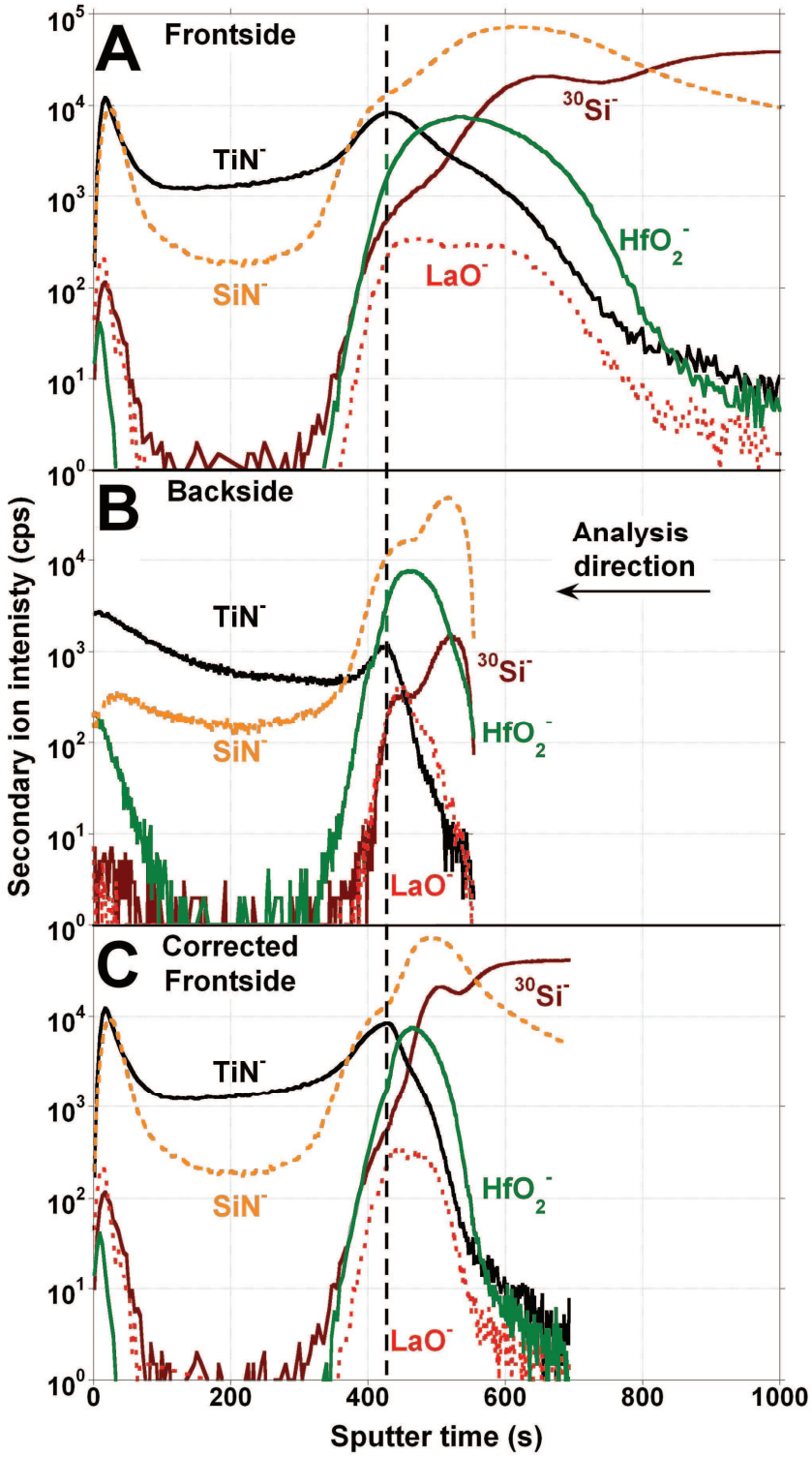

Figure IV.24 ToF-SIMS profiles of the same high-k/metal gate sample, with both frontside (**A**) and backside (**B**) approaches. The x scale of the backside profile has been inverted for ease of comparison. A vertical dotted line indicates the virtual limit between the titanium nitride region (left) and the lanthanum oxide/hafnium silicate/silicon oxynitride region (right). A corrected frontside profile is displayed in **C**.

With ToF-SIMS

Use of SIMS or ToF-SIMS implies abrasion with a more or less energetic, chemically active or not, primary ion beam. This usually generates two kind of detrimental effects: (i) physical effects: with roughness build-up during analysis or mixing of the near surface layers due to the energetic impact, and (ii) chemical effects: with modification of the chemistry of the near surface layers. The latter can occur because of shallow implantation and adsorption of the primary ion species leading to the creation of a modified surface layer (with active elements such as O or Cs), but also because of the segregation of some elements present in the sample to analyse, reacting to the energy deposited on impact (therefore unrelated to the chemically active or not character of the primary ion species). The latter is well known to happen in samples containing Hf, where Hf is expected to be implanted upon impact, and to segregate back to the surface, forming a partially modified metallic Hf layer [48]. This modification of the surface composition and nature during analysis results in dramatic change in both sputter rates and ionisation yields, increasing the difficulty of analysis [19, 48]. Figure IV.24 shows the profiles obtained by ToF-SIMS on the same high-k/metal gate sample, using frontside and backside analysis.

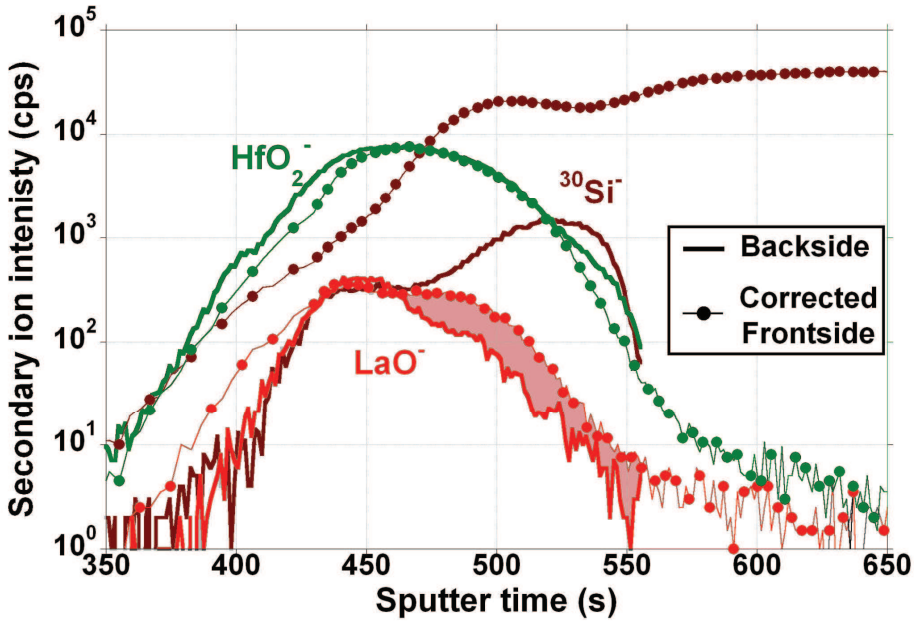

Figure IV.25 Overlaid backside and corrected frontside ToF-SIMS profiles of the same high-k/metal gate sample, focused on the high-k layer.

Both approaches yield similar profiles in the TiN region at least in terms of sputter rate, given the good alignment of the profiles in this region. However there is huge horizontal scale distortion in the right region of the image, corresponding to the HfSiON and underlying layers. This is a direct effect of the Hf segregation during analysis, discussed above. The same effect is not observed on the backside profile (there is no extensive Hf compound secondary ion tails the TiN region). This is assumed to be due to the metallic nature of the layer beneath hafnium silicate in the backside approach, avoiding the formation of another (fractional) Hf based metallic layer at the surface of the sample while profiling. Since the extent of the scale distortion is unknown, it would be extremely difficult to perform an accurate scale correction by conventional calculation approaches. There are in literature a few detailed works on this matter, such as the paper from Vandervorst *et al.* [19], but they mainly focus on depth scale

correction after the end of the hafnium containing layers (in the Si substrate), not inside or close to those layers. In our case, we want to perform the latter since we want to assess the La distribution in the stack. A very simple depth scale correction has therefore been designed in order to make HfO_2^- distribution of the frontside profile fit to that of the backside profile. It consists in dividing by 3 the time scale for all points at the right of the vertical line, i.e. all analysis points acquired in the layers beneath the HfSiON layer and in the HfSiON layer itself. As shown by the overlaid backside and corrected frontside profiles in Figure IV.25, the Hf compound secondary ion signals fit quite well, validating the horizontal scale correction. However, important differences in the depth distributions of the other elements are observed, in particular for La which distribution in frontside profile is found to be largely erroneous, showing artificial diffusion towards the substrate (light red zone in Figure IV.25). This is assumed to be due to the second effect of Hf segregation: the modification of sputter/ionisation yields for other elements. The latter would be again very difficult to assess without access to reliable depth profiles as provided by the backside analysis.
The accuracy of ToF-SIMS analysis on this kind of sample is thus greatly enhanced by using the backside preparation approach proposed in this work, yielding more realist elemental distributions in the stack and allowing quantitative studies to be done.

With MEIS

On the contrary MEIS allows matrix free analysis, that is, the output energy spectra for a particular element will only depend on its depth distribution and its abundance in the stack and not on the surrounding elements. However, the energy of the backscattered ions only depends on the masses of the incident ion and the target atom, and also on the scattering angle.

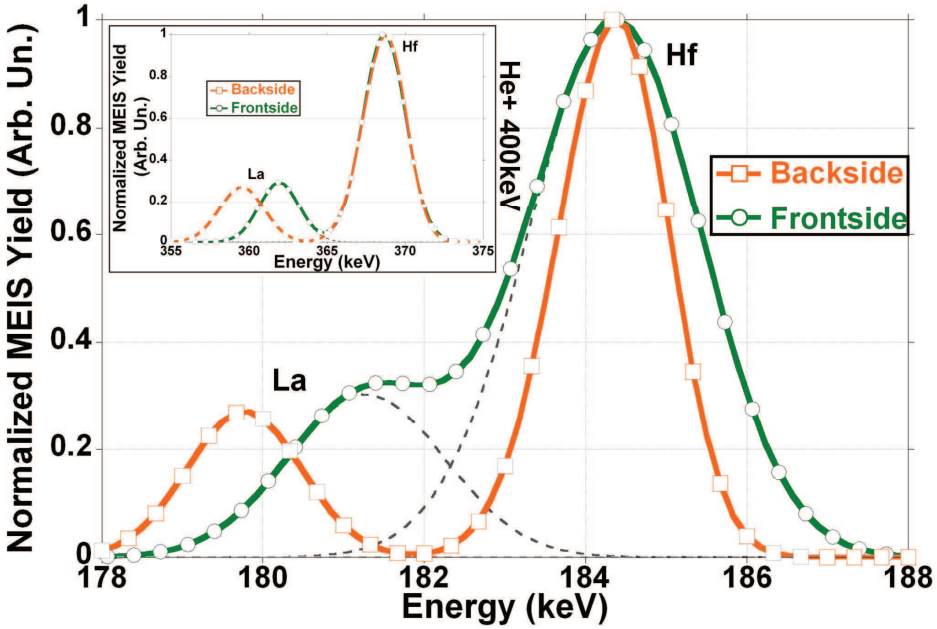

Figure IV.26 Frontside and backside simulated MEIS spectra in the Hf / La region, with a 200 or 400 keV He^+ primary beam incident at 21°, and a 131° detection angle. The structure of the simulated stack is: TiN(6.5 nm)/La_2O_3(0.4 nm)/HfSiON(1.7 nm)/SiON(1.5 nm)/Si substrate in the case of the frontside approach, and: SiON(1.5 nm)/HfSiON(1.7 nm)/La_2O_3(0.4 nm)/TiN(6.5 nm) in the case of the backside approach. Simulation was done with a home-made software program, taking into account straggling and neutralisation effects. Hf peak intensity were aligned in energy to allow better visualisation of the differences between the two approaches in terms of peak separation power.

Thus, the mass resolution obviously depends on the energy resolution ΔE of the instrumental setup, which in our case is given by ΔE/E ~ 0.35%. Mass resolution is optimised (1) for the largest scattering angles, (2) by using heavier incident ions (He^+ instead of H^+), or (3) by increasing the primary beam energy, but it remains a difficult issue to solve for heavy target elements of similar masses. In the present study, La and Hf mass difference combined to their localisation in the stack makes the spectral separation problematic. This is exactly the case of our samples, where La (Z = 57) is placed right on top of Hf (Z = 72). The simulated backscattered spectra displayed in Figure IV.26 show that in the frontside analysis configuration, the peaks corresponding to La and Hf are almost merged, which complicates the analysis, although geometry was optimised for enhanced peak separation. Since the detector was placed at the largest possible angular position, the only solution is then to increase the incident beam energy (see Figure IV.26 top left frame), but this would deteriorate energy (and thus depth) resolution, which is detrimental to the analysis of such stacks. On the other hand, in the case of the backside approach one can see that the two peaks are clearly separated. This allows diminution of the minimum incident energy needed to resolve both peaks and thus permits a more precise study of the stacks. Our backside sample preparation is therefore a crucial advantage for analysis of those samples with MEIS.

With AR-XPS

In the case of XPS or AR-XPS one can very easily understand that it would be impossible to yield useful information from a frontside analysis of such a stack. The usual depth of information with these techniques is usually of no more than 6 nm in depth (except if synchrotron sources are used), which hinders analysis of the layers situated beneath the TiN layer (6.5 nm thick). Removal of the whole TiN layer is not an option, since given the highly reactive character of La to oxygen, the composition of the stack would change. Deposition of a thinner TiN layer would also modify the stack structure, due to the modification of the thermal budget seen by the different layers during the Poly-Si deposition and activation annealing, as shown by the Auger profiles in Figure IV.23. It might also affect the stability of certain elements inside the stack. The last option would be to remove only a fraction of the TiN layer by chemical (or plasma) etch. However this would require an extreme control of the etch rate and duration and might deteriorate sample surface quality, making precise analysis of the stack more difficult. Therefore, a promising way to perform stack analysis without modifying the sample structure or composition seems therefore to be the backside approach developed in this work.

IV. 7. Results exploitation: useful knowledge earned through quantitative analysis

In this section we will try, starting from the best ToF-SIMS analysis on given samples (i.e. either Full Spectrum profiles or profiles obtained after backside sample preparation), to yield useful information for understanding of materials and structures during selected processes. In a first subsection, we will briefly study composition and layer thicknesses of high-k dielectric stacks such as those studied in subsections IV. 6. b- and IV. 6. c- and see the correlation between those features and electrical properties of the devices. In a second subsection we will focus on the evolution of HKMG stacks with annealing, and particularly on La diffusion.

IV. 7. a- In hafnium silicate based high-k dielectric stacks

As shown in chapter I, the evolution from silicon dioxide to oxynitrides and high-k materials as dielectrics was the result of the research of materials of higher ε in order to build smaller devices while keeping good electric characteristics. However as hafnium oxides present high ε values, they are also not quite stable in a gate-first approach integration environment. Upon activation annealing, they tend to crystallise, while oxygen and nitrogen are exchanged at a very rapid rate between high-k and gate material [49-50]. All of these have of course detrimental effects on the device properties, particularly on leakage currents and trap densities. As the introduction within the high-k layer of given amounts of Si and N is known to minimise these effects, it can also contribute to properties degradation if the composition is not finely tuned. Furthermore they will induce a diminution of the original layer ε and thus limit the minimum reachable device size. To build the best device possible, one has thus to find a compromise between layer thickness and layer composition [51-53]. Some elements showing the electrical properties variation in function of layer thickness and composition are shown in Figure IV.27 [49, 54]. Concerning device stacks for sub-32 nm generation devices, best properties are obtained for a hafnium silicate (HfSiON) layer of ~1.5 nm thick and of stoichiometry ratio [Si]/([Hf]+[Si])=~30%. Therefore a precise control of both layer thickness and stoichiometry is required, which can be performed using Full Spectrum ToF-SIMS profiles. As an example, hafnium silicate layers in samples observed in subsection IV. 6. b- were found to have an average thickness of 1.8 nm and a [Si]/([Hf]+[Si]) ratio ~40%. By contrast, those of the samples studied in subsection IV. 6. d- show a thickness of 1.7 nm with a [Si]/([Hf]+[Si]) ratio ~32%, closer to the ideal composition. Full Spectrum ToF-SIMS profiles can therefore help to control the stoichiometry and thicknesses of the layers in view of ensuring that the deposition processes correctly yield the desired layer conformation.

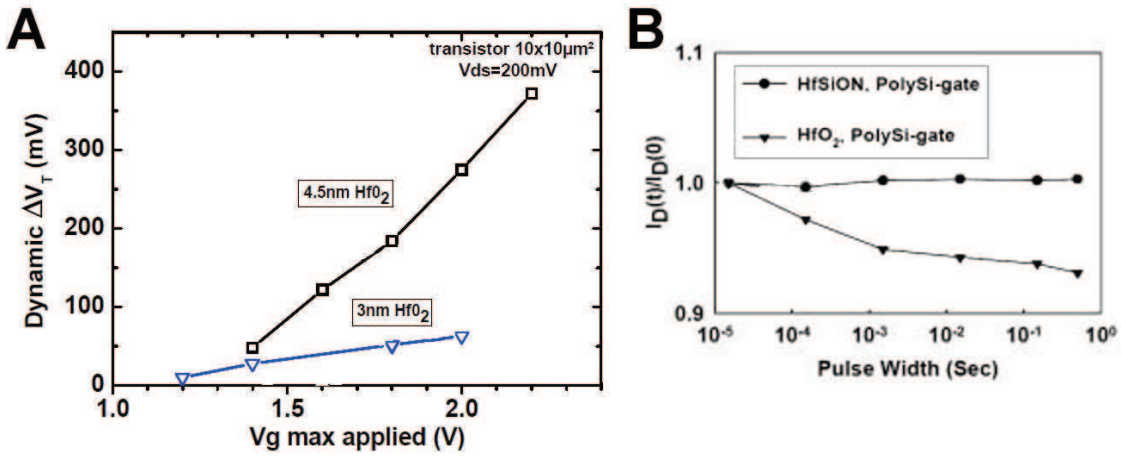

Figure IV.27.A Dynamic Vt shift for samples with same high-k materials of different thicknesses. The magnitude of shift mainly depends on the HfO_2 layer thickness, which is consistent with the fact that reducing the thickness of the high-k material reduces the number of bulk defects. Adapted from [54].

B Measurement of variation of the drive current of nFETs using HfO_2 or HfSiON as high-k dielectric upon pulse width. No significant change in the drive current was observed in the case of devices made using HfSiON films, while a 9 % degradation is observed when using HfO_2. The decrease in drive current is consistent with charge trapping within the HfO_2 layer [49].

IV. 7. b- Analysis of complete spike annealed HKMG stacks

As briefly introduced in chapter I, the easiest way in terms of process to elaborate complete HKMG devices is to chose a midgap gate material, and to selectively deposit gap modifying materials in the gate to obtain the desired work function either for nMOS or pMOS. This can be performed using lanthanum oxides for nMOS. LaO_x capping layers have indeed been reported to provide a negative threshold voltage (V_{th}) shift, yielding the necessary decrease of gate work function [55-56] while keeping the mobility sufficiently high [57-58]. The mechanism of this V_{th} shift is attributed to La-induced dipoles at the High-K/Insulating Layer (HK/IL) interface [55, 59]. The control of V_{th} is thus strongly linked to the location of LaO_x capping layer within the gate stack. Therefore, a strict control of the diffusion of La atoms towards the IL is required during the transistor gate-first process fabrication. In this work, we therefore focused on technologically relevant stacks composed of a TiN/HfSiON/SiON/Si structure where an ultra-thin LaO_x capping layer (0.4 nm) is inserted between the TiN metal gate and the HfSiON dielectric. A detailed study of La diffusion after a 1065°C spike anneal and its impact on the electronic structure, such as band alignment of the gate stacks, without removing or altering the TiN gate would then be of utmost importance to validate the whole device fabrication process. In particular, although not exclusively as other elements also play an important role, we are interested (i) in quantification of the diffused La amount, (ii) in determination of La diffusion range within the stack, and (iii) in the bonding states of La after diffusion.

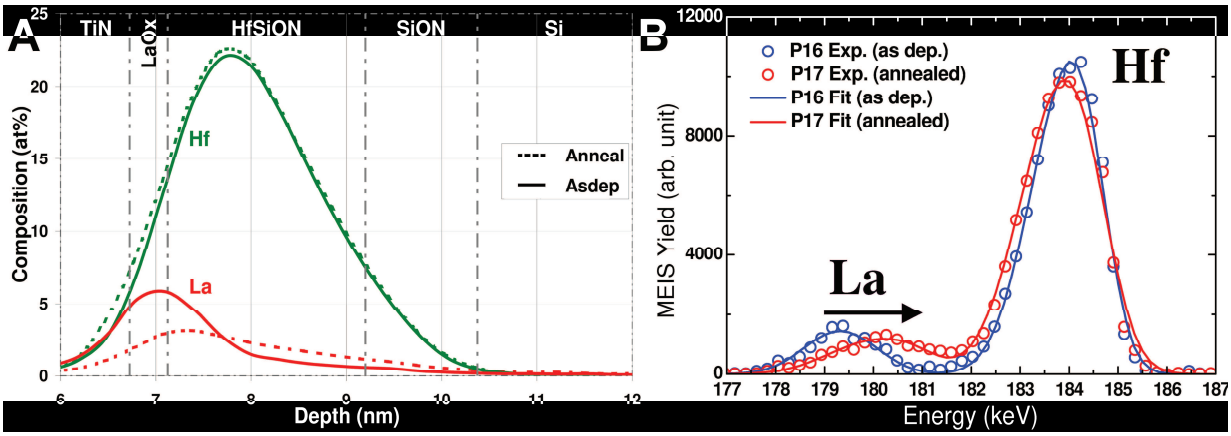

Figure IV.28.A Full spectrum ToF-SIMS profiles of the as deposited and annealed HKMG stacks described in section IV. 5, focused on the dielectric region. The boundaries between different regions are determined using ionic signals half-intensity points and indicated by vertical dashed lines.

B Backside MEIS spectra of the same samples, obtained with 200 keV He^+ primary ions incident at 21° with respect to the sample surface and analysis of backscattered ions around a backscattering angle of 136°.

Points (i) and (ii) can be directly investigated using ToF-SIMS data issued from Full Spectrum protocol analyses as described in subsection IV. 6. d-. A close-up of the high-k dielectric region of profiles shown in Figure IV.21 is displayed in Figure IV.28.A. Although a small amount of La is observed near the top surface of the TiN layer, this amount does not change upon annealing. La is thus presumed to have diffused during TiN layer growth and poly-Si deposition at 600°C, and not during annealing, in agreement with observations of Boujamaa *et al.* in [60]. The regions of interest for study of La diffusion in such stacks are therefore constituted of: the original LaO_x region, the hafnium silicate region and the SiON region, as indicated by vertical dashed lines in Figure IV.28.A. One can observe a well

defined La peak in the zone corresponding to the LaO_x layer before annealing, while overall La distribution is broadened towards the IL after annealing, with a peak concentration situated in the hafnium silicate layer. In the mean time, Hf distribution does not change at all upon annealing, which shows that La diffusion from the original LaO_x layer towards IL is indeed occurring. Looking at the backside ToF-SIMS profiles in Figure IV.25, one can obtain more precise information since these profiles show without ambiguity that very little La is present inside the SiON layer, and even after diffusion (not shown), most of this La is situated close to the HK/IL interface, with no La present at the bottom IL interface (SiON/Si interface). Since the total La dose does not vary significantly during annealing (see Figure IV.22), we can also use the La distributions displayed in Figure IV.28.A to calculate the relative amount of La in each of the respective regions. The results of these calculations are shown in Table IV.iii.

	in LaO_x	in HfSiON	in SiON	in other (noise)
Before annealing	54.2%	39.3%	3.9%	2.6%
After annealing	28.4%	55.7%	9.6%	6.3%

Table IV.iii Relative amounts of La in the original lanthanum oxide, HK and IL layers as determined in Figure IV.28.A.

This shows that although a significant part of the La is actually mixed with HfSiON (~40%) in the as deposited sample, most of it is situated, as expected, inside the LaO_x layer, while a very small part of it is detected in the SiON layer. However after annealing the La dose fractions in both HfSiON and SiON increase, while that in the LaO_x region is halved. This indicates that the diffused La primarily stays within the hafnium silicate layer while only a small amount diffuses through the HK layer to end up in the IL. This information can be verified by acquiring MEIS energy spectra on a region centred on Hf and La peaks using the backside sample preparation protocol presented in section IV. 6. Indeed MEIS allows direct identification of layer thicknesses and composition via modelling of its energy spectra (the energy of an ion backscattered on a particular element at a particular depth being known by calculation, see chapter I). MEIS analysis results are shown in Figure IV.28.B. We observe a displacement of the La peak towards higher energy regions with annealing, which suggests a La diffusion towards the surface (and in this case, towards the IL). In order to make the simulated spectra fit the experimental ones, 40% of the La dose was placed in the HK layer in the as deposited sample against 60% in the annealed sample, with in addition 15% in the IL layer. These results are very close to those obtained with Full Spectrum ToF-SIMS, which confirms our conclusions both on La diffusion direction and diffused amounts upon annealing. Cross characterisation of the same stacks with Hard X-ray Photoelectron Spectroscopy (HAXPES) using synchrotron radiation for deep probing of the material show that this diffusion up to IL is accompanied by formation of lanthanum silicates, as shown in Figure IV.29.A [60]. By increasing the original amount of LaO_x in the stack, one can easily imagine that the amount of La diffused in the IL will also increase, thus forming more La-silicate. In this case, we can observe a shift in the XPS spectra (shown in Figure IV.29.B [60]), proportional to the amount of diffused La. This shift is consistent with a modification of the gate work function in the desired direction, as shown by the Capacitance-Voltage characteristics displayed in Figure IV.29.C [60].

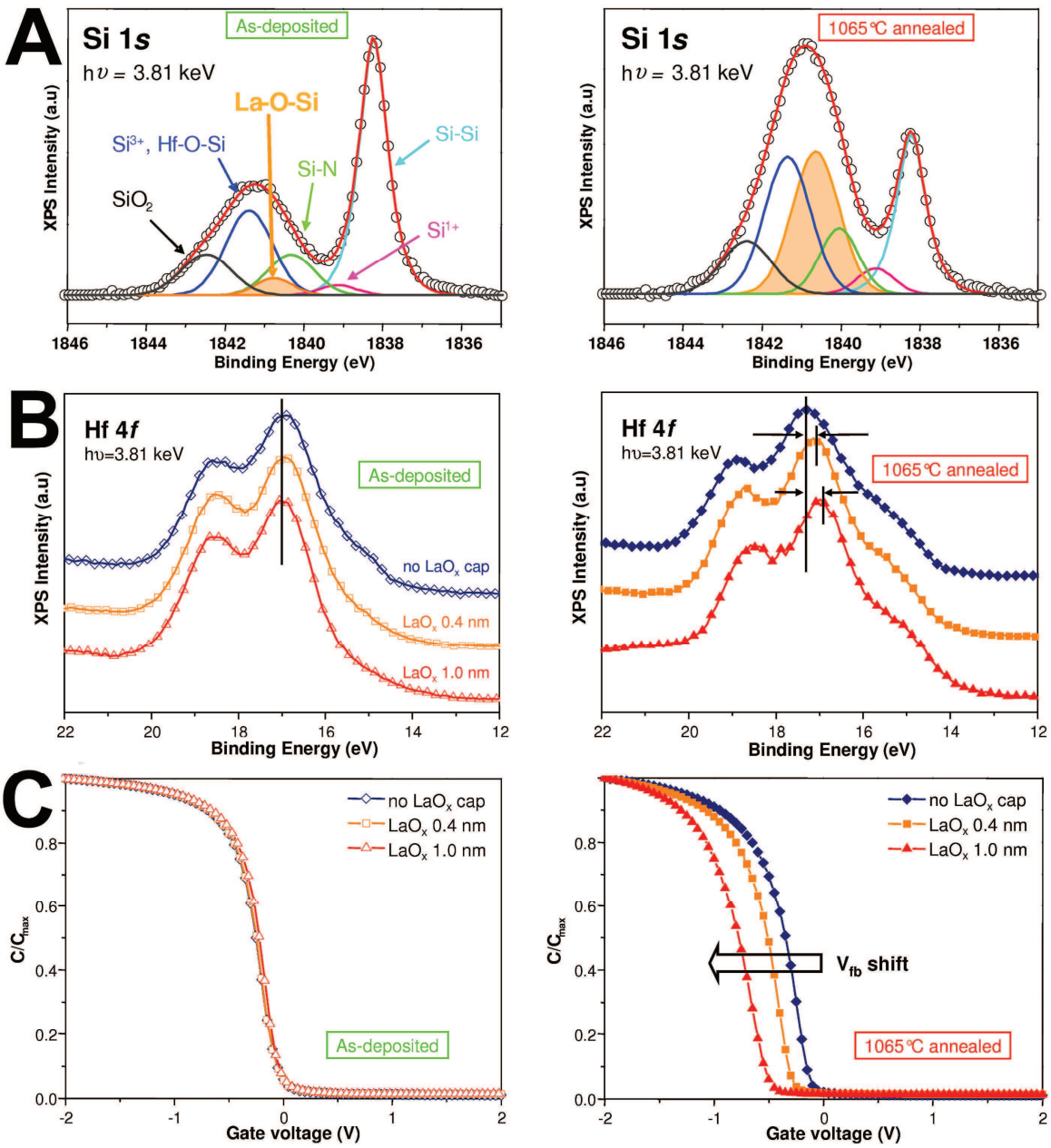

Figure IV.29.A HAXPES spectra of as deposited (left) and annealed (right) gate stacks. The Si1s core-level spectra is decomposed into various components using calibration from literature. While other components do not significantly vary, a relative increase in the O-Si-La (La silicate) bond peak is observed after annealing [60].

B Evolution of the HAXPES spectra as a function of LaO_x thickness. Hf 4f core level of annealed samples (right) is found to be shifted towards higher energies in correlation with the amount of La-silicate formed [60].

C Comparison of Capacitance-Voltage characteristics for as-deposited (left) and annealed (right) gate stacks as a function of LaO_x thickness Again, a shift correlated to the amount of La diffused in the IL is observed in the annealed samples (right) [60].

In summary, we have investigated using ToF-SIMS the impact of high temperature annealing on the chemical and electronic properties of TiN/HfSiON/SiON/Si gate stacks in which a few Angstroms of LaO_x capping is inserted between TiN and HfSiON layers. Upon high temperature annealing, we showed that La diffuses into HfSiON and that a small amount reaches the SiON IL. Here, complementary measurements indicated that La forms silicates,

thus providing a means of controlling V_{th}. The V_{fb} shifts observed by HAXPES induced by different amounts of diffused La in IL were found to be well correlated with the shifts observed in C-V characteristics of the corresponding devices.

CHAPTER IV Conclusion

In this chapter we described the different practical solutions developed for improvement of the quantitative analysis capacities of our ToF-SIMS instrument for nanometre scale, high-k material based structures In particular, we focused on data treatment and experimental conditions. To achieve the required high depth resolution, we developed a protocol for extremely low energy depth profiling. We also proposed a means to establish a depth scale through calculation of a variable sputter rate as a function of oxygen content. The data treatment protocol, based on a full spectrum approach of the ToF-SIMS data sets, was optimised for depth profiling nanometre or sub-nanometre thick stacks including high-k dielectric materials, gate materials and channel stressors such as SiGe. It was shown to allow simultaneous quantification of all matrix elements in the target materials, which is to our knowledge unique to this protocol. Finally, we proposed an original method for backside sample preparation adapted to samples comprising an ultra thin (nanometre scale) chemical etch stop layer.

The validity of the proposed solutions was investigated in various structures representative of sub-32 nm devices dielectric and gate stacks. In order to assess the improvements brought by both experimental developments and data treatment, comparison with results obtained via other techniques such as MEIS, AR-XPS and HRBS was used. The proposed data treatment protocol gave satisfactory results in terms of profile accuracy, both using XPS cross-calibration (for thinner samples) and average sensitivity factors (for thicker samples). On the other hand, the extremely low energy profiling protocol was shown to bring significant improvements in terms of depth resolution and reduction of surface transients but did show some limitations because of its too low sputtering yield. Finally the backside sample preparation was shown to yield large areas of flat and smooth surfaces without removing layers of interest, thus enabling multi-technique analysis.

The developed solutions were therefore used firstly to control the stoichiometry and thickness of high-k dielectric stacks in view of device performance optimisation. Secondly, they were used to understand the behaviour of complete high-k/metal gate stacks under activation annealing. Based on the ToF-SIMS profiles we were able to yield quantitative information on lanthanum diffusion in such samples. By using cross-characterisation, this diffusion was shown to induce a shift towards lower device work function, which was the desired effect. All these information, obtained thanks to the accuracy of the developed ToF-SIMS analysis protocols, are of great interest both for control of the physical processes in device elaboration and thus for improvement of their electric performance.

REFERENCES

[1] M.G. Dowsett, *Depth Profiling Using Ultra-Low-Energy Secondary Ion Mass Spectrometry*, Appl. Surf. Sci., 203-204 (**2003**) 5-12.
[2] W. Vandervorst, *Semiconductor Profiling with Sub-Nm Resolution: Challenges and Solutions*, Appl. Surf. Sci., 255 (**2008**) 805-812.
[3] A. Merkulov, P. Peres, S. Choi *et al.*, *Advanced Secondary Ion Mass Spectroscopy Quantification in the First Few Nanometer of B, P, and as Ultrashallow Implants*, J. Vac. Sci. Technol. B, 28 (**2010**) C1C48-C41C53.
[4] S. Ferrari, M. Perego and M. Fanciulli, *Characterization of Gate Oxynitrides by Means of Time of Flight Secondary Ion Mass Spectrometry and X-Ray Photoelectron Spectroscopy. Quantification of Nitrogen*, J. Vac. Sci. Technol. A, 20 (**2002**) 616-621.
[5] M. Py, J.P. Barnes, D. Lafond and J.M. Hartmann, *Quantitative Profiling of Sige/Si Superlattices by Time-of-Flight Secondary Ion Mass Spectrometry: The Advantages of the Extended Full Spectrum Protocol*, Rapid Commun. Mass Spectrom., 25 (**2011**) 629-638.
[6] M. Py, J.P. Barnes and J.M. Hartmann, *Quantification of Germanium in Si1−Xgex Alloys by Negative Mode Tof-Sims: The Interest of the Full Spectrum Method*, Surf. Interface Anal., (**2010**) DOI: 10.1002/sia.3535.
[7] C.J. Powell, A. Jablonski, I.S. Tilinin, S. Tanuma and D.R. Penn, *Surface Sensitivity of Auger-Electron Spectroscopy and X-Ray Photoelectron Spectroscopy*, J. Electron Spectrosc., 98-99 (**1999**) 1-15.
[8] J.H. Scofield, *Hartree-Slater Subshell Photoionization Cross-Sections at 1254 and 1487 Ev*, J. Electron Spectrosc., 8 (**1976**) 129-137.
[9] S. Tanuma, C.J. Powell and D.R. Penn, *Calculations of Electron Inelastic Mean Free Paths. V. Data for 14 Organic Compounds over the 50–2000 Ev Range*, Surf. Interface Anal., 21 (**1994**) 165-176.
[10] S. Tougaard, *Quases-Tougaard Software*.
[11] C.J. Powell and A. Jablonski, *Effects of Elastic-Electron Scattering on Measurements of Silicon Dioxide Film Thicknesses by X-Ray Photoelectron Spectroscopy*, J. Electron Spectrosc., 114-116 (**2001**) 1139-1143.
[12] F. Laugier, J.M. Hartmann, H. Moriceau *et al.*, *Backside and Frontside Depth Profiling of B Delta Doping, at Low Energy, Using New and Previous Magnetic Sims Instruments*, Appl. Surf. Sci., 231-232 (**2004**) 668-672.
[13] C. Hongo, M. Takenaka, Y. Kamimuta, M. Suzuki and M. Koyama, *Backside-Sims Profiling of Dopants in Thin Hf Silicate Film*, Appl. Surf. Sci., 231-232 (**2004**) 594-597.
[14] C. Hongo, M. Tomita and M. Takenaka, *Accurate Depth Profiling for Ultra-Shallow Implants Using Backside-Sims*, Appl. Surf. Sci., 231-232 (**2004**) 673-677.
[15] J. Sameshima, R. Maeda, K. Yamada, A. Karen and S. Yamada, *Depth Profiles of Boron and Nitrogen in Sion Films by Backside Sims*, Appl. Surf. Sci., 231-232 (**2004**) 614-617.
[16] J. Bennett, M. Quevedo-Lopez and S. Satyanarayana, *Characterizing High-K and Low-K Dielectric Materials for Semiconductors: Progress and Challenges*, Appl. Surf. Sci., 252 (**2006**) 7167-7171.
[17] T. Hantschel, C. Demeulemeester, A. Suderie *et al.*, *Backside Analysis of Ultra-Thin Film Stacks in Microelectronics Technology Using X-Ray Photoelectron Spectroscopy,* Materials Research Society, Warrendale, **2009**, pp. 185-190.
[18] T. Conard, W. Vandervorst, H. De Witte and S. Van Elshocht, *Nitrogen Analysis in High-K Stack Layers: A Challenge*, Appl. Surf. Sci., 231-232 (**2004**) 581-584.
[19] W. Vandervorst, J. Bennett, C. Huyghebaert *et al.*, *On the Reliability of Sims Depth Profiles through Hfo2-Stacks*, Appl. Surf. Sci., 231-232 (**2004**) 569-573.
[20] M.J.P. Hopstaken, J.C. Cabral, D. Pfeiffer, C. Molella and P. Ronsheim, *Towards Routine Backside Sims Sample Preparation for Efficient Support of Advanced Ic Process Development*, AIP Conf. Proc., 1173 (**2009**) 94-98.
[21] O. Tabata, R. Asahi, H. Funabashi, K. Shimaoka and S. Sugiyama, *Anisotropic Etching of Silicon in Tmah Solutions*, Sensors and Actuators A: Physical, 34 (**1992**) 51-57.

[22] B. Pelissier, A. Beaurain, J.P. Barnes *et al.*, *Parallel Angle Resolved Xps Investigations on 12 in. Wafers for the Study of W and Wsix Oxidation in Air*, Microelectron. Eng., 85 (**2008**) 1882-1887.
[23] K.E. Petersen, *Dynamic Micromechanics on Silicon: Techniques and Devices*, Electron Devices, IEEE Transactions on, 25 (**1978**) 1241-1250.
[24] International Technology Roadmap for Semiconductors: executive summary, (**2009**), http://www.itrs.net/Links/2010ITRS/Home2010.htm
[25] N. Baboux, J.C. Dupuy, G. Prudon *et al.*, *Ultra-Low Energy Sims Analysis of Boron Deltas in Silicon*, J. Cryst. Growth, 245 (**2002**) 1-8.
[26] K. Kimura, S. Joumori, Y. Oota, K. Nakajima and M. Suzuki, *High-Resolution Rbs: A Powerful Tool for Atomic Level Characterization*, Nucl. Instrum. Meth. B, 219-220 (**2004**) 351-357.
[27] D.H. Triyoso, M. Ramon, R.I. Hegde *et al.*, *Physical and Electrical Characteristics of Hfo[Sub 2] Gate Dielectrics Deposited by Ald and Mocvd*, J. Electrochem. Soc., 152 (**2005**) G203-G209.
[28] J.P. Dismukes, L. Ekstrom and R.J. Paff, *Lattice Parameter and Density in Germanium-Silicon Alloys*, J. Phys. Chem., 68 (**1964**) 3021-3027.
[29] S.W. Novak and R.G. Wilson, *Systematics of Positive Secondary Ion Mass Spectrometry Relative Sensitivity Factors for Si and Sio[Sub 2] Measured Using Oxygen and Argon Ion Bombardment*, J. Appl. Phys., 69 (**1991**) 463-465.
[30] R.G. Wilson and S.W. Novak, *Systematics of Secondary-Ion-Mass Spectrometry Relative Sensitivity Factors Versus Electron Affinity and Ionization Potential for a Variety of Matrices Determined from Implanted Standards of More Than 70 Elements*, J. Appl. Phys., 69 (**1991**) 466-474.
[31] D.Q. Yang and C.Z. Fan, *Dependence of Secondary Ion Mass Spectrometry Relative Sensitivity Factor on Matrix*, Chinese Phys. Lett., 15 (**1998**) 697-699.
[32] J.G.M. Van Berkum, M.J.P. Hopstaken, J.H.M. Snijders, Y. Tamminga and F.N. Cubaynes, *Quantitative Depth Profiling of Sioxny Layers on Si*, Appl. Surf. Sci., 203-204 (**2003**) 414-417.
[33] M.A. Douglas, S. Hattangady and K. Eason, *Depth Profile Analysis of Ultrathin Silicon Oxynitride Films by Tof-Sims*, J. Electrochem. Soc., 147 (**2000**) 1893-1902.
[34] I. Banerjee and D. Kuzminov, *Nitrogen Redistribution in Sio<Inf>2</Inf> under Ion Bombardment*, J. Vac. Sci. Technol. B, 12 (**1994**) 205-208.
[35] J. Bennett, C. Gondran, C. Sparks, P.Y. Hung and A. Hou, *Sims Depth Profiling of Advanced Gate Dielectric Materials*, Appl. Surf. Sci., 203-204 (**2003**) 409-413.
[36] Z.X. Jiang, K. Kim, J. Lerma *et al.*, *Characterization of Nitrogen Distribution in Hfo[Sub 2] with Low Energy Secondary Ion Mass Spectrometry*, J. Vac. Sci. Technol. A, 23 (**2005**) 589-592.
[37] Z.X. Jiang, K. Kim, J. Lerma *et al.*, *Characterization of Hfo2 Dielectric Films with Low Energy Sims*, Appl. Surf. Sci., 252 (**2006**) 7172-7175.
[38] M.A. Reading, J.A. Van Den Berg, P.C. Zalm *et al.*, *High Resolution Medium Energy Ion Scattering Analysis for the Quantitative Depth Profiling of Ultrathin High-K Layers*, J. Vac. Sci. Technol. B, 28 (**2010**) C1C65-C61C70.
[39] K. Kimura, K. Nakajima, M. Zhao *et al.*, *Combination of High-Resolution Rbs and Angle-Resolved Xps: Accurate Depth Profiling of Chemical States*, Surf. Interface Anal., 40 (**2008**) 423-426.
[40] C. Ichihara, S. Yasuno, H. Takeuchi *et al.*, *High-Resolution Rutherford Backscattering Spectrometry Study on Process Dependent Elemental Depth Profile Change of Hafnium Silicate on Silicon*, J. Vac. Sci. Technol. A, 27 (**2009**) 937-942.
[41] B. Brijs, T. Sajavaara, S. Giangrandi *et al.*, *The Analysis of a Thin Sio2/Si3n4/Sio2 Stack: A Comparative Study of Low-Energy Heavy Ion Elastic Recoil Detection, High-Resolution Rutherford Backscattering and Secondary Ion Mass Spectrometry*, Nucl. Instrum. Meth. B, 249 (**2006**) 847-850.
[42] S. Toyoda, H. Kamada, A. Kikuchi *et al.*, *Effect of Nitrogen Bonding States on Dipole at the Hfsio/Sion Interface Studied by Photoemission Spectroscopy*, J. Appl. Phys., 107 (**2010**) 124103-124103.
[43] S. Toyoda, H. Kamada, T. Tanimura *et al.*, *Annealing Effects of in-Depth Profile and Band Discontinuity in Tin/Lao/Hfsio/Sio2/Si Gate Stack Structure Studied by Angle-Resolved Photoemission Spectroscopy from Backside*, Appl. Phys. Lett., 96 (**2010**) 042905-042903.
[44] C.R. Brundle, G. Conti and P. Mack, *Xps and Angle Resolved Xps, in the Semiconductor Industry: Characterization and Metrology Control of Ultra-Thin Films*, J. Electron Spectrosc., 178-179 (**2010**) 433-448.

[45] *Www.Webelements.Com*
[46] L.V. Goncharova, M. Dalponte, T. Feng *et al.*, *Diffusion and Interface Growth in Hafnium Oxide and Silicate Ultrathin Films on Si(001)*, Physical Review B, 83 (**2011**).
[47] L.V. Goncharova, S.N. Dedyulin and J. Liu, *Medium Energy Ion Scattering Studies of Semiconductor-Dielectric Interfaces*, IBA 2011, Itapema, Brazil (unpublished results), **2011**.
[48] W. Nieveen, B.W. Schueler, G. Goodman *et al.*, *Analysis of High-K Hfo2 and Hfsio4 Dielectric Films*, Appl. Surf. Sci., 231-232 (**2004**) 556-560.
[49] A. Shanware, M.R. Visokay, J.J. Chambers *et al.*, *Characterization and Comparison of the Charge Trapping in Hfsion and Hfo2 Gate Dielectrics,* Electron Devices Meeting, 2003. IEDM '03 Technical Digest. IEEE International, (**2003**) 38.36.31-38.36.34.
[50] G. Ribes, J. Mitard, M. Denais *et al.*, *Review on High-K Dielectrics Reliability Issues*, IEEE Trans. Device Mater. Reliab., 5 (**2005**) 5-19.
[51] C. Fachmann, L. Frey, S. Kudelka *et al.*, *Tuning the Dielectric Properties of Hafnium Silicate Films*, Microelectron. Eng., 84 (**2007**) 2883-2887.
[52] J.H. Choi, Y. Mao and J.P. Chang, *Development of Hafnium Based High-K Materials--a Review*, Materials Science and Engineering: R: Reports, In Press, Corrected Proof.
[53] I.Z. Mitrovic, O. Buiu, S. Hall *et al.*, *Electrical and Structural Properties of Hafnium Silicate Thin Films*, Microelectronics Reliability, 47 (**2007**) 645-648.
[54] G. Ribes, *Thesis Work: Caracterisation Et Fiabilite Des Oxydes Ultra Fins Et Des Dielectriques a Forte Permittivite Issue Des Technologies Cmos 45nm Et En Deça*, (**2005**).
[55] K. Kita and A. Toriumi, *Origin of Electric Dipoles Formed at High-K/Sio2 Interface*, Appl. Phys. Lett., 94 (**2009**) 3.
[56] H.N. Alshareef, M. Quevedo-Lopez, H.C. Wen *et al.*, *Work Function Engineering Using Lanthanum Oxide Interfacial Layers*, Appl. Phys. Lett., 89 (**2006**) 3.
[57] M.A. Quevedo-Lopez, S.A. Krishnan, P.D. Kirsch *et al.*, *Ultrascaled Hafnium Silicon Oxynitride Gate Dielectrics with Excellent Carrier Mobility and Reliability*, Appl. Phys. Lett., 87 (**2005**) 3.
[58] T. Ando, M. Copel, J. Bruley *et al.*, *Physical Origins of Mobility Degradation in Extremely Scaled Sio2/Hfo2 Gate Stacks with La and Al Induced Dipoles*, Appl. Phys. Lett., 96 (**2010**) 3.
[59] P.D. Kirsch, P. Sivasubramani, J. Huang *et al.*, *Dipole Model Explaining High-K/Metal Gate Field Effect Transistor Threshold Voltage Tuning*, Appl. Phys. Lett., 92 (**2008**) 092901.
[60] R. Boujamaa, S. Baudot, N. Rochat *et al.*, *Impact of High Temperature Annealing on La Diffusion and Flatband Voltage (Vfb) Modulation in Tin/Laox/Hfsion/Sion/Si Gate Stacks*, Submitted for publication in Journal of Applied Physics (2011).

CHAPTER V
Analysis of materials and structures for arsenic ultra shallow junctions for sub-32 nm generation CMOS

This chapter will cover the field of materials and structures for USJ as defined in chapter I. More particularly we will focus the studies on arsenic implants in silicon, given the artefacts encountered in conventional SIMS profiling of such implants [1-2], are more important than those prone to occur in boron implants. Arsenic profiles are known to suffer from in conventional depth profiling conditions from a shift of the maximum concentration peak towards the surface, inaccurate profile shape in the first few nanometres and overestimation of the total dose [3-4]. Moreover, annealing of such samples produces extremely sharp concentration peaks, usually situated at (when present) the silicon dioxide /silicon interface [5-6]. These features are extremely difficult to accurately resolve with ToF-SIMS due to their small size (width ~1 nm) and high concentration range (a decade or more). These effects represent a significant hindrance to ToF-SIMS quantification of such samples, especially when looking at low energy implants designed for sub-32 nm generation devices in which most of the doping elements are implanted very close to the sample surface. The materials of interest for our study are therefore as-implanted As doped Si substrates and SiO_2 as native or intentionally deposited oxide. To allow straightforward discrimination of dopant amount in oxide and in Si, Cs^+ sputtering is preferred. To match requirements for S/D region resistivity values and thickness in advanced devices, implants have to be performed at low energies and high doses. High dopant dose can therefore be expected at surface or sub-surface, with a swift drop down to a few hundred ppm in less than 10 nm. Both high depth resolution and minimisation of surface transients is thus required, which involves the use of the EXLE regime as described in the previous chapter. To enable reduction of the usual artefacts and to provide the best possible dynamics, a systematic study of the (available) experimental conditions and data treatment protocols is also necessary. Due to the presence of heterogeneous layers (SiO_2 on Si) and to the fact that features of interest are situated at the or near the interface, particular care must be brought to the establishment of an accurate depth scale. Finally, assessing the accuracy of the ToF-SIMS profiles will require the use of other techniques able to yield similar quantified depth profiles.

V. 1. Systematic study of secondary ions, data treatment protocol

V. 1. a- Secondary ion selection

Due to the variety of existing ionisation mechanisms, different secondary ions will have different ionisation probabilities. This is particularly true for compound ions, whose components potentially come from different parts of the sample surface and with different initial charge states. Such ions are therefore expected to provide significantly different depth distributions than mono-atomic ones, especially when profiling through different materials. In the case of depth profiling of As implants, $AsSi^-$ ions are known to display no interfacial artefacts (unrealistic peak at SiO_2/Si interface) as opposed to As^- ions [5-6]. This effect is clearly observed in ToF-SIMS profiles such as that shown in Figure V.1.A. This profile corresponds to a 1 keV As implant in Si(110), without annealing. Therefore, the expected profile shape is the convolution of a Gaussian and an exponential decay. Such a round shape could correspond to the $AsSi^-$ distribution, which is round. However the As^- distribution is characterised by additional features, with a signal peak at ~100 s sputtering time (right at the SiO_2/Si interface) and a double exponential decay (a first one before ~250 s and a second one, more important, afterwards). The choice of the $AsSi^-$ ion would therefore seem wiser in order to obtain depth distributions with less artefacts, at least in pure silicon. However, given the

interest of sSiGe source and drain regions for sub-32 nm devices, it might be interesting to provide a protocol directly transposable to such materials. Even though in this study we focus only on implants in pure silicon, this ion is therefore discarded as it would not allow accurate depth profiling in SiGe materials. The selection of such an ion in a SiGe matrix would indeed require an impractically high mass resolution or important background substraction, which would in any case increase analytical uncertainty [7].

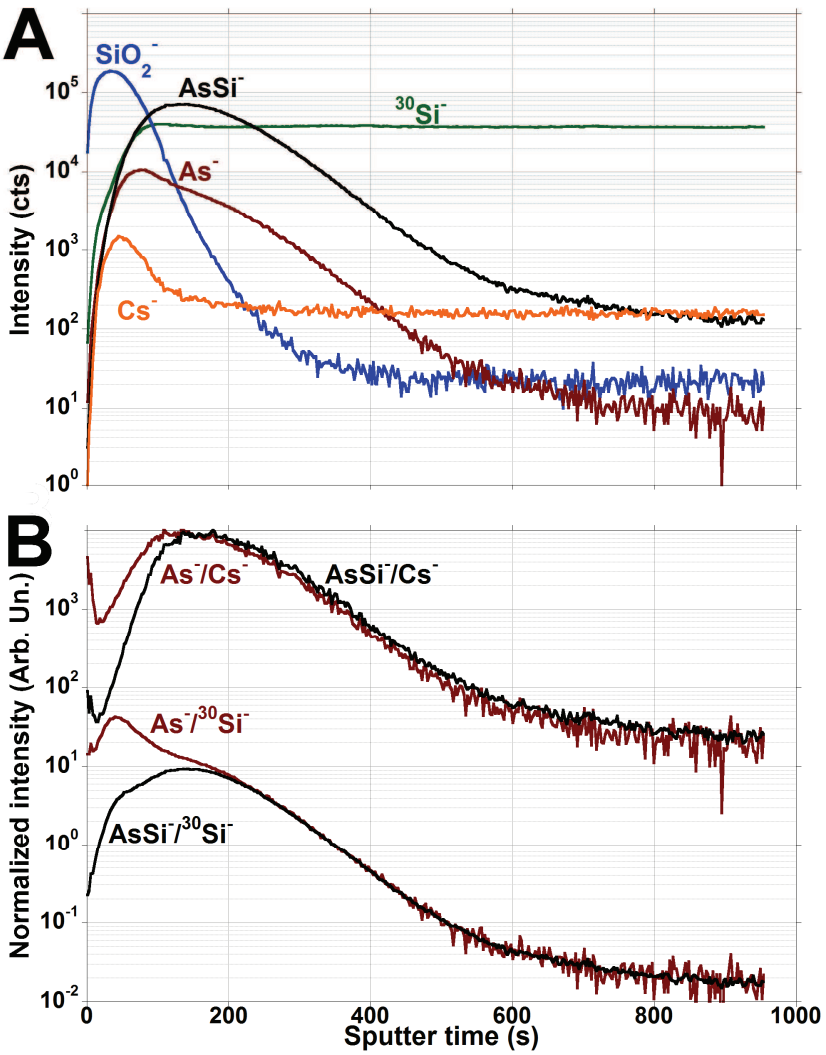

Figure V.1.A Raw secondary ion intensity profiles obtained in a 1 keV 6.5x1014 at/cm2 As implant in Si with 250 eV Cs^+ sputtering. A native oxide is present at the surface of the sample, as indicated by the strong SiO_2^- signal. The shape of As^- profile is significantly different from that of $AsSi^-$, with notably an As^- bump at the SiO_2/Si interface followed by a first rapid exponential decay. These are well known SIMS artefacts.

B Comparison of the effects on profile shapes of two different point-to-point normalisations of the ionic signals obtained in **A**. While $^{30}Si^-$ normalisation shows an increased discrepancy between both As^- and $AsSi^-$ depth distributions, Cs^- normalisation is found to contribute to the minimisation of the artefacts observed in **A**.

However, raw secondary ion signals are not necessarily representative of the shape of the quantified profile: indeed impurity signal normalisation by a matrix signal is needed (see chapter I). One can therefore try to minimise the artefact present in the As^- profile shape by selecting the right matrix secondary ion for normalisation. Point to point normalisation is necessary, as average or bulk value normalisation would not change the profile shape.

Normalisation to $^{30}Si^-$ (or to any other Si containing secondary ion, not shown here for clarity) does not provide satisfactory results, as shown in Figure V.1.B. The discrepancy between both normalised ion signals would rather seem to have been increased. This is due to the lower value of the $^{30}Si^-$ signal in the SiO_2 region than in the Si bulk region. It leads us to the assumption that higher sensitivity to As is achieved in SiO_2 than in Si. This assumption is correlated by results in Barozzi *et al.* [1]. In this work, accurate quantification of As in thick SiO_2 and Si is achieved by point to point normalisation to the Si^- signal. The RSF in SiO_2 is found to be only 1.8 times higher than in Si, while Si^- signal intensity is 11 times lower in SiO_2 than in Si. This shows that As sensitivity in SiO_2 is higher by a factor 11/1.8≈6.1 to that in Si. To minimise artefacts by point to point normalisation, use of a secondary ion featuring ≈6.1 more intense signal in SiO_2 than in Si would therefore provide the best results. However no matrix representative ion was found to feature such characteristics. Si_x^- signals indeed always feature lower intensities in SiO_2 than in Si. In the meantime, $Si_xO_y^-$ signals fall by almost four decades from SiO_2 to Si in UHV, and from at least two decades using O_2 flooding while profiling at a partial oxygen pressure of ~10^{-8} mbar. However, the distribution of Cs^- in such samples (see Figure V.1.A) is found to match quite well our requirements. This can sound strange, as Cs concentration at the surface of the sample (and thus in a first approximation Cs^- signal intensity too) is known to increase with decreasing sputter rates (see chapter I). However Cs affinity with O favours the formation of Cs-O complexes at the surface of the sample, which induces a drop in Cs removal rate and an increase of Cs surface concentration. Furthermore, such Cs concentration increase is known to enhance the negative secondary ion yields of electronegative elements (such as As). Therefore, the As sensitivity ratio between SiO_2 and Si can be (partly) explained by the ratio of Cs surface concentration between SiO_2 and Si. Despite the fact that this could be a simple coincidence, identical behaviours are observed when using other experimental parameters such as different sputtering energies and atmosphere composition (not shown). Cs^- might therefore be an interesting candidate for As^- normalisation. The results of such normalisation are displayed in Figure V.1.B. We can indeed observe a minimisation of the discrepancy between As^- and $AsSi^-$ signals after normalisation, which indicates the accuracy of our approach. This allows for quantification of As layer content through a single reference material consisting of an As implant in pure Si.

V. 1. b- Full Spectrum protocol

It can also be interesting, as another approach for quantification of such implants, to make use of the full spectrum approach, following the same procedure as in previous chapters. USJ are indeed designed to provide high dopant concentration (>1 at%) close to the surface followed by a sharp drop. Therefore, both the ability to quantify matrix elements and important dynamics are necessary for their accurate quantification. The results shown by the full spectrum approach in previous studies therefore motivated its application in this case. Once again, the full spectrum approach involves monitoring not secondary ion quantities but total atomic quantities in the secondary ion beam, which considerably reduces matrix effects and signal/noise ratio, as shown previously. With this version of the FS protocol, we calculate the total quantity of Si, O and As atoms in the secondary ion beam Q_{total} using the following formula:

$$Q_{total} = \sum_{n=0}^{6}\sum_{m=0}^{3}\sum_{p=0}^{2}(n+m+p)\cdot Y_{Si_nO_mAs_p} \qquad (V.1)$$

$Y_{Si_nO_mAs_p}$ being the intensity of the $Si_nO_mAs_p^-$ cluster ion divided by its isotopic abundance (same remark as for previous chapters concerning intensity and mass interferences (see equation (III.3)). The atomic fractions of O and As in the secondary ion beam, T_O and T_{As} can be obtained from equation (V.1) using the following expressions:

$$T_O = \frac{\sum_{n=0}^{6}\sum_{m=0}^{3}\sum_{p=0}^{2} m \cdot Y_{Si_nO_mAs_p}}{Q_{total}} \qquad (V.2)$$

$$T_{As} = \frac{\sum_{n=0}^{6}\sum_{m=0}^{3}\sum_{p=0}^{2} p \cdot Y_{Si_nO_mAs_p}}{Q_{total}} \qquad (V.3)$$

Quantified profiles are then obtained by point by point multiplication of T_O and T_{As} by sensitivity factors issued from a known, thick thermal SiO_2 layer (for T_O) and from a high energy, high dose As implant in pure Si (for T_{As}).

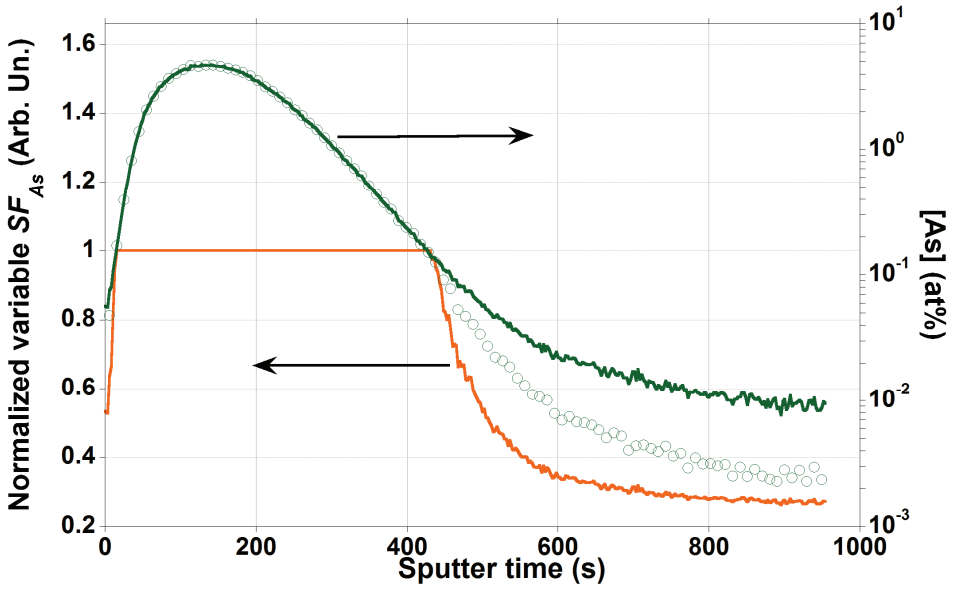

Figure V.2 Normalised variation of SF_{As} as a function of As concentration as obtained with a first FS protocol profile of As composition. The latter is shown in continuous lines, while the profile obtained with the variable SF_{As} is shown in open circles. Profiles are obtained on the same sample and with the same experimental conditions as in Figure V.1.

However we demonstrated in chapter III that such an approach yielded inaccurate results for doping elements under a given concentration (≤0.1 at%). Under this limit, an approximately linear variation of the SF with sample composition was observed (derived from data in Figure III.21), with a rough relation to the SF in "matrix element" regime given by:

$$SF_{var} = \begin{cases} SF_{matrix\_element} \times (5.5 \times [As]_{at\%} + 0.22) & \text{if } [As]_{at\%} < 0.15 \\ SF_{matrix\_element} & \text{if } [As]_{at\%} \geq 0.15 \end{cases} \qquad (V.4)$$

To take into account this variation, a first profile is built using the constant SF brought by calibration with reference material. Then, SF_{var} is calculated using this first profile. These values are then used once again to calculate the final As profile from T_{As}. The depth distribution of SF_{var} and the two As profile versions are given in Figure V.2. Modification is mainly observed in the tail region of the profile, on which constantly decreasing SF_{var} with depth induces increasing discrepancy with profiles obtained using constant SF. This is thus expected to allow better representation of the low concentration part of dopant profiles obtained with the FS protocol, which might improve the accuracy of junction depth determination (usually taken as the depth corresponding to the point of 1 or 5.10^{18} at/cm^3 As concentration). The last step of data treatment is the transformation of concentration values from at% to at/cm^3. This is done by modelling the stack density using densities of pure SiO_2 [8] and Si [9].

V. 2. Setup of depth scale establishment protocol

Similarly to the approach developed in previous chapter for single layer systems, the simplest depth scale establishment protocol in our samples (constituted of thin SiO_2 on Si) is to measure sputter rates in pure Si and SiO_2 using reference samples.

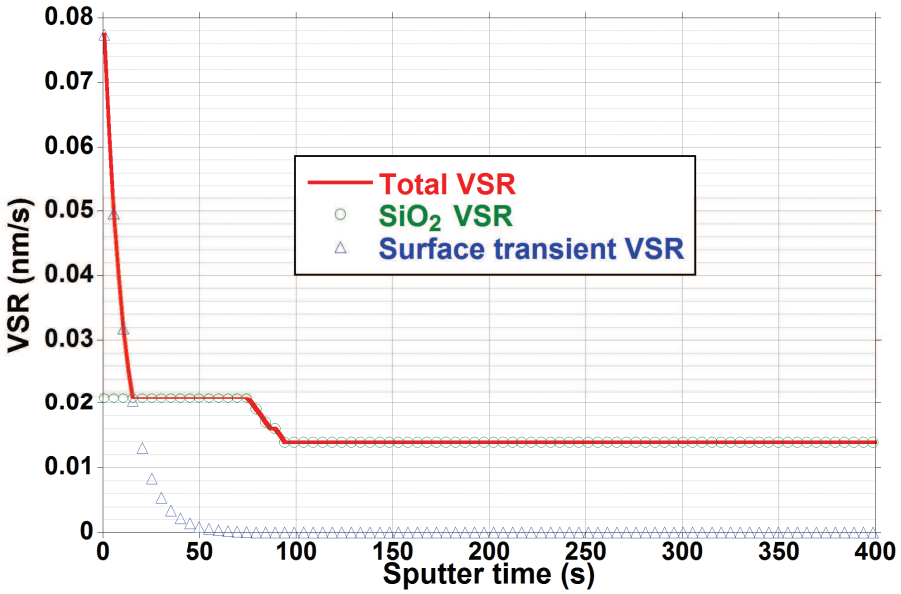

Figure V.3 Example of a VSR function obtained in a As implant in Si sample with a native oxide. The total VSR is constituted of two components: one taking into account sputter rate variation between SiO_2 and Si layers and the other rendering the surface transient as proposed in equation (V.5). The number of data points for both component VSRs has been voluntarily reduced by a factor two for clarity.

Those have already been described in previous chapters. In this study, since As is expected to pile-up at SiO_2/Si interface, particular care must be taken in the evaluation of the transient regime between both materials. The transition between the two sputter rates was therefore set to be proportional to the variation of the oxygen representative signal, in an approach similar to that of Merkulov *et al.* [10]. Establishment of such a VSR is usually enough for accurate profiling of ultra thin layers, as for example those studied in the last chapter. However for As

USJ profiling near surface non-linear effects on sputter rates due to Cs pile-up are expected to play an important role in maximum peak shift towards the surface if not corrected. To account for those, we set up an additional VSR in the first few data points. Different protocols are proposed in the literature, such as quadratic [11] or exponential [12] variation as a function of the sputter time. Both approaches were tested but the second was adopted since it gave better results (see below). The surface VSR is thus accounted for by the following formula:

$$VSR_{surface} = (SR_{SiO_2} \times M) \cdot \mathrm{e}^{-\frac{t \times SR_{SiO_2}}{D_c}} \quad \text{(V.5)}$$

where SR_{SiO2} is the SiO_2 sputter rate determined in a reference sample, M is an empirical multiplying factor and D_c an empirical critical depth for attenuation of the surface sputter rate enhancement effect. Using various experimental parameters, Merkulov *et al.* found a relatively stable M value of 4, which we will use in this study. Surface sputter rate correction was otherwise found to give best results using a D_c value of 0.23 nm. An example of VSR obtained at 250 eV sputtering in a 1 keV As implant in Si(110) is displayed in Figure V.3 along with the decomposition of surface and SiO_2 VSRs.

V. 3. Improvements brought by the proposed solutions in application to materials and structures representative of actual As USJ

In this section we will focus on comparing the results given by the developed protocols and the explored experimental conditions in terms depth resolution and ability to accurately quantify As in ultra shallow implants in Si. To investigate ToF-SIMS profiles accuracy, we will use measurements obtained with external techniques (RBS, HRBS, NRA). Crystal-TRIM implant profile simulation as well as As diffusion study with S-Process will also be of assistance.

For this study, a (110) Si wafer was implanted with 1 keV As at a nominal dose of 6.5×10^{14} at/cm^2 through a native oxide layer. While keeping one half as implanted, the other half underwent a rapid thermal anneal at 1000°C for 10 s. ToF-SIMS profiles were performed using Cs^+ sputtering at 500, 250 or 150 eV and 15 keV Bi^+ for analysis. Precautions were taken to obtain sufficiently high sputter/analysis ration in the EXLE regime. All analysis were performed under UHV ($<5\times10^{-10}$ mbar). In addition, one series of analysis were conducted at 250 eV sputtering and with an O_2 partial pressure of 1×10^{-8} mbar in the analysis chamber in order to investigate the effects of vacuum conditions on profile quality. For measurement of the sputter rates in pure Si and SiO_2, a B delta sample in Si and a thick thermal SiO_2 sample were used. For concentration scale calibration, a reference sample (3 keV As implant in Si) measured by RBS was used. RBS (using a 2 MeV He+ beam incident at 43° and detection at 160°) and NRA (using a 930 keV deuterium beam to look at $^{16}O(d,p)^{17}O$ reaction) were otherwise used on both samples concerned by this study to measure total doses of As and O, respectively. Finally, HRBS was used to obtain Si, O and As depth profiles in both samples (with the same setup as described in the previous chapter). Crystal-TRIM was performed to obtain theoretical As profiles, using As dose and native oxide thicknesses obtained by RBS and NRA respectively. Based on these profiles, S-Process simulations were performed using the "five-stream" model for As diffusion as already implemented in S-Process software [13].

V. 3. a- Depth scale accuracy

As we saw, quantification of As ultra shallow implants via ToF-SIMS profiling is compromised by the numerous artefacts observed during analysis. An accurate depth scale is therefore (amongst others) required to minimise these artefacts. However many effects can cause distortion of the As depth distribution obtained with ToF-SIMS.

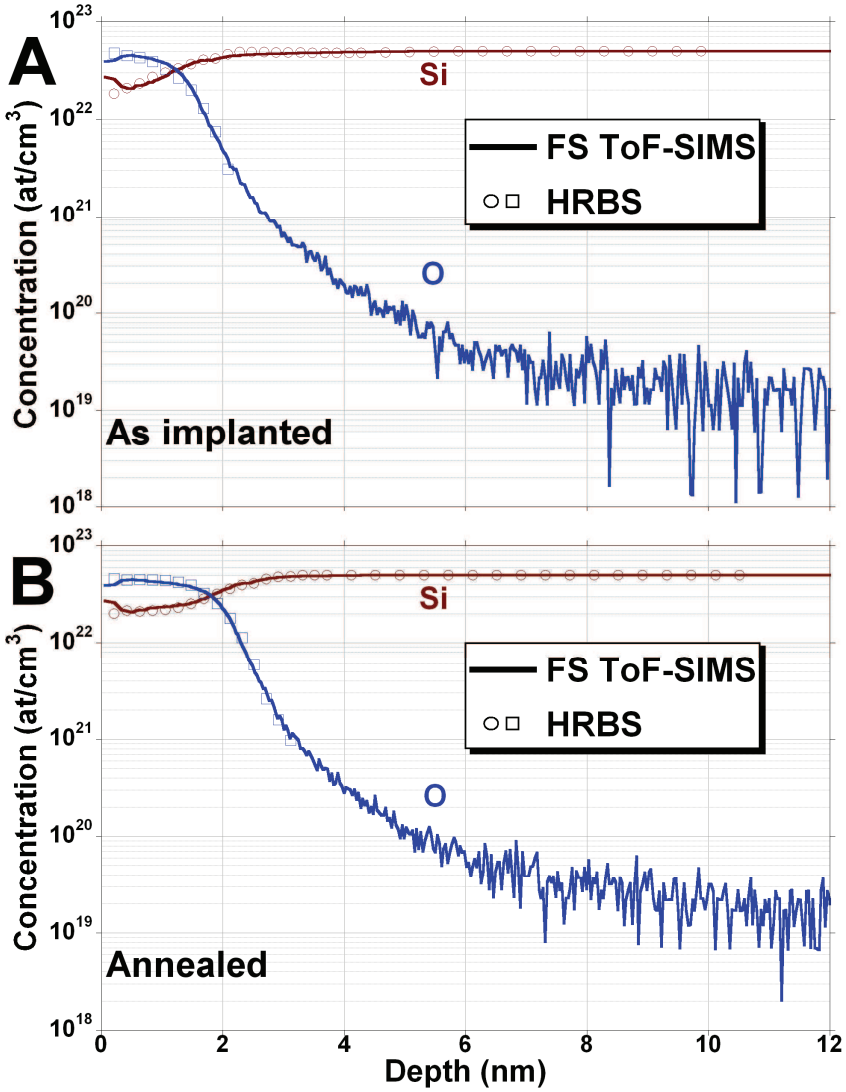

Figure V.4 Overlaid 250 eV sputtering FS ToF-SIMS (curves) and HRBS (open symbols) Si and O elemental profiles obtained in both as implanted (**A**) and annealed (**B**) samples concerned by this study.

The usually observed shift of the As maximum concentration peak position towards the surface, for example, is assumed to be due to a combination of sputter rate and ionisation yield variation within surface oxide and substrate and across the SiO_2/Si interface. It would therefore be difficult to assess the accuracy of the depth scale alone using As distribution, due to the convolution of these various effects. To check this we therefore chose to focus on oxide layer thickness assessment and on Si and O quantified depth distributions. Oxide layer thickness was obtained (i) by NRA, assuming a SiO_2 density of 2200 $kg.m^{-3}$ [8], (ii) by HRBS and ToF-SIMS (using several sputter energies), assuming that the SiO_2/Si interface was

positioned at the half intensity of oxygen signal. Note that oxide thicknesses obtained at different energies by ToF-SIMS were found to have a very small spread of ±0.15 nm around their average value. Comparison of the thicknesses obtained by the three techniques is shown in Table V.i.

	ToF-SIMS	HRBS	NRA
As implanted sample	1.46 ± 0.15	1.48 ± 0.1	1.51 ± 0.15
Annealed sample	2.02 ± 0.15	2.07 ± 0.1	1.98 ± 0.2

Table V.i Oxide thicknesses obtained with ToF-SIMS, HRBS and NRA in both as implanted and annealed samples. Values are in nm.

An excellent agreement is obtained, showing the accuracy of the developed depth scale establishment protocol for ToF-SIMS. To further investigate the matter, we can consider the shape of the oxygen and silicon distribution which can be obtained with Full Spectrum ToF-SIMS and compare them with those obtained with HRBS. This comparison is achieved in FigureV.4. Once again the excellent agreement of the profile shapes for both samples (which have significantly different oxide layer thicknesses) suggests that the accuracy of the depth scale used in ToF-SIMS is good.

V. 3. b- Improvements brought by EXLE regime, influence of residual atmosphere

As demonstrated in the previous chapter, the best depth resolution can be achieved by lowering sputter energy to 150 eV.

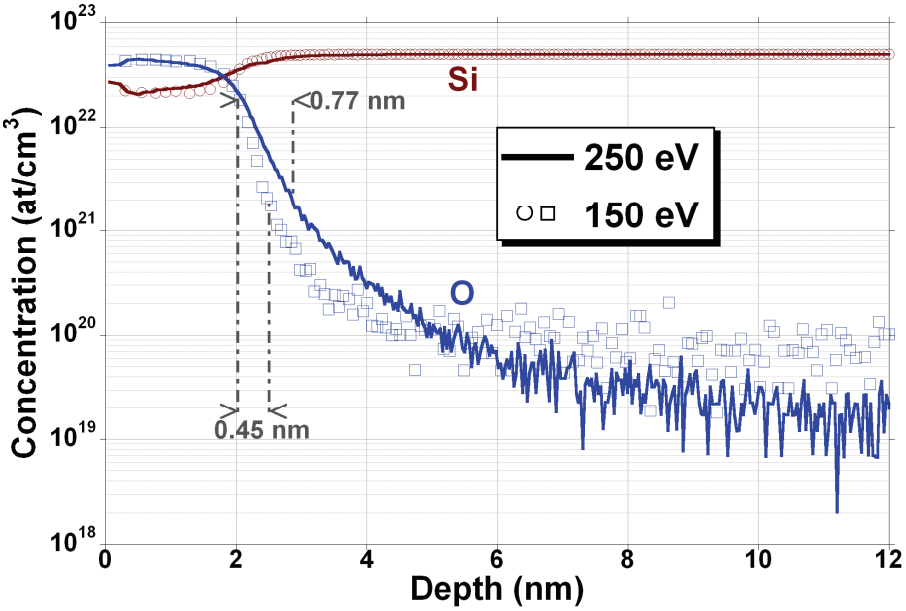

Figure V.5 Overlaid 250 eV sputtering (curves) and 150 eV sputtering (open symbols) FS ToF-SIMS Si and O elemental profiles obtained in annealed samples. The number of data points for 150 eV sputtering profile has been voluntarily by a factor four for clarity.

Profiles obtained in EXLE regime are thus expected to be significantly improved when compared to those obtained at higher energies. The sharpness of the As interfacial peak after sample annealing is indeed one of the features of interest for accurate assessment of the As depth distribution. However, for similar reasons than in last subsection, it might be difficult to

judge of the depth resolution at different energies based on the As profiles, due to the combination of several effects potentially distorting its distribution. The best way to check for depth resolution is thus to focus on the sharp physical interface constituted by the native oxide / silicon substrate system. Oxygen relevant signals should be good candidates for such a study, given that we can expect high dynamic range between their value in SiO_2 and in Si.

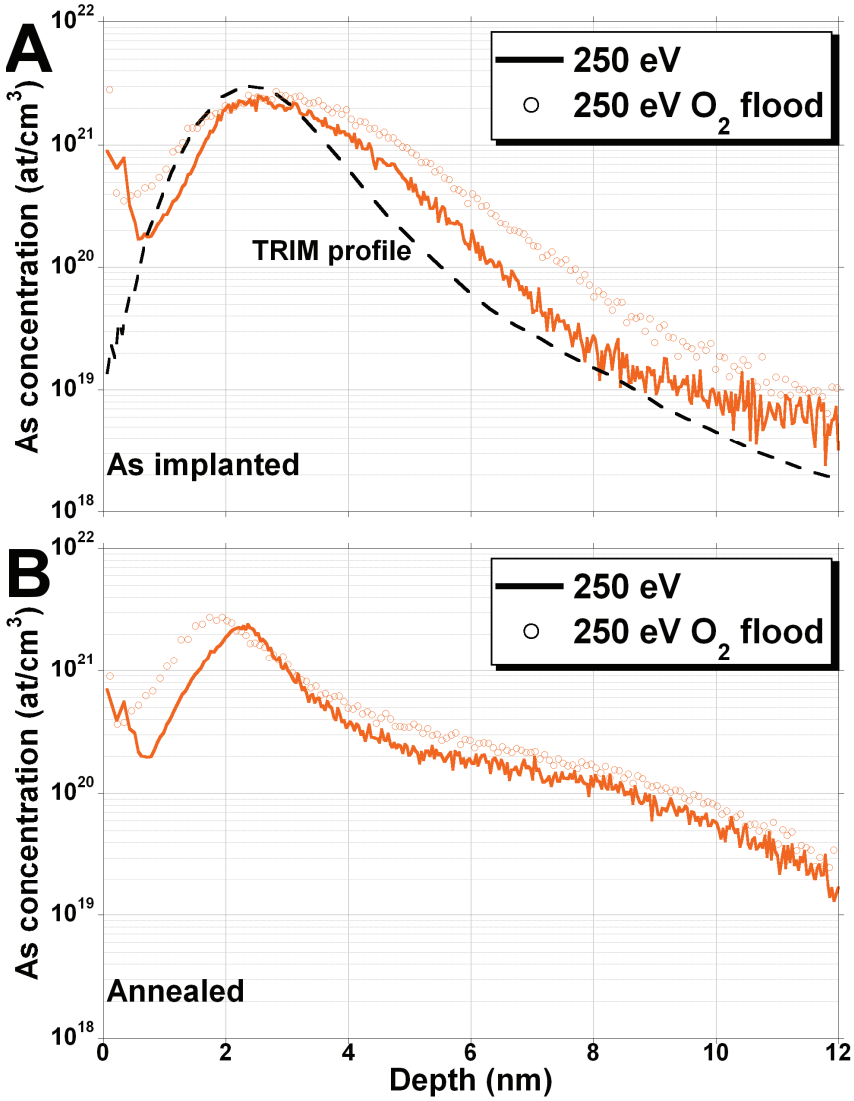

Figure V.6 Overlaid 250 eV sputtering in UHV (curves) and with O_2 flooding (open symbols) As ToF-SIMS profiles obtained via Cs^- ion normalisation in both as implanted (**A**) and annealed (**B**) samples. The number of data points for the profile obtained with O_2 flooding has been voluntarily reduced for enhanced visualisation. TRIM simulation of the As concentration distribution in the as implanted case is also given for comparison (dashed line).

Quantified Si and O profiles obtained by the FS protocol using 250 and 150 eV sputtering are shown in Figure V.5. For this figure, we deliberately chose the annealed sample as, with its thicker oxide, it allows better comparison of the profiles. We first observe that, similarly to results obtained in last chapter, Si and O plateau are better resolved in the EXLE regime, with flatter distributions inside the SiO_2 layer. The interfacial width measured by the depth delta between the points of 20% and 80% of Si signal raise are found to be of 0.5 ±0.1 nm at 150 eV against 0.9 ±0.1 nm at 250 eV. Despite this difference, O distribution obtained with both energies fit quite well each other on a region situated at the centre of the interfacial

region (between 1.8 and 2.0 nm), which justifies the good agreement obtained on oxide layer thicknesses at various energies. However, the O decay is sharper right after this point in profiles obtained at 150 eV. The decay length measured in the exponential part of the decreasing O signal (shown by dashed lines in Figure V.5) is found to be 0.45 nm at 150 eV against 0.77 nm at 250 eV. Hence, the experimental setup for EXLE depth profiling shows, once again, drastic improvements in terms of depth resolution when compared to profiles obtained at higher energies.
The effect of the analysis chamber atmosphere is also of interest, since we have to go through a two-layer system composed of oxidised and non oxidised layers. In this context, the use of slight O_2 flooding during profiling can be expected to help reduce both sputter rate and ionisation yield variations. However it also reduces the ionic contrast between oxide and pure Si regions, making it difficult to locate the interface as was performed above. Comparison between UHV and O_2 flooding protocol (both being performed with 250 eV sputtering) is thus done in Figure V.6 using As depth distributions. Crystal-TRIM issued As profile is also displayed in the as implanted sample for comparison. The profiles obtained in both samples using O_2 flooding are significantly broader that those in UHV. This broadening also results in a shift of the As peak towards the surface in the annealed sample. Profile broadening is imputed to an increased surface roughening. Sputtering experiments in presence of low pressure oxygen flooding (inducing only partial surface oxidation) indeed shown an angular dependence of crater roughness, with dense ripple apparition around 45° [14-16]. Even minute amounts of oxygen flooding are therefore detrimental to the analysis. Although experiments at lower energies were not performed, similar effects are expected.

V. 3. c- Effects of the Full Spectrum protocol

On the same principle, it is interesting to compare As quantified profiles obtained with the same experimental conditions but using both quantification protocols proposed in subsections V. 1. a- and V. 1. b-. These are presented in Figure V. 7 (only profiles obtained at 250eV are shown for clarity but same behaviour is observed at other energies). The first outcome of the FS protocol, certainly due better counting statistics, is the improved signal-to-noise ratio as compared to the Cs^- normalisation protocol. This was expected, given that similar effects were shown in other materials (see previous chapters). Also, profiles fit quite well each other most of the time in both as implanted and annealed samples. However there are a few significant differences observed in the oxide region (which includes oxide/silicon interfacial region) and in the profile tail region. In both case these differences are due to the improved statistics of the FS protocol. Indeed, in the oxide region, AsO_x^- secondary ion intensities are high enough to bring a significant contribution to the Q_{As} signal. This creates a discrepancy with the other profile in which only As^- intensity is taken into account (from ~1.5 to 2 nm in the as implanted sample and from ~0.8 to 2.2 nm in the annealed sample). The discrepancy observed in the tail region is a direct consequence of the variation of sensitivity factor used in the FS protocol at low As concentrations. Although this correction produces a somewhat unnatural profile shape (especially for the as implanted sample), it gives, if one refers to the crystal-TRIM profile, better estimation of the junction depth, usually determined at 1×10^{18} at/cm^3. Both of these discrepancies implicitly show that better dynamics can be obtained with the FS protocol due to its better statistics, however this does not tell us which of the profiles gives the most realistic As depth distribution.

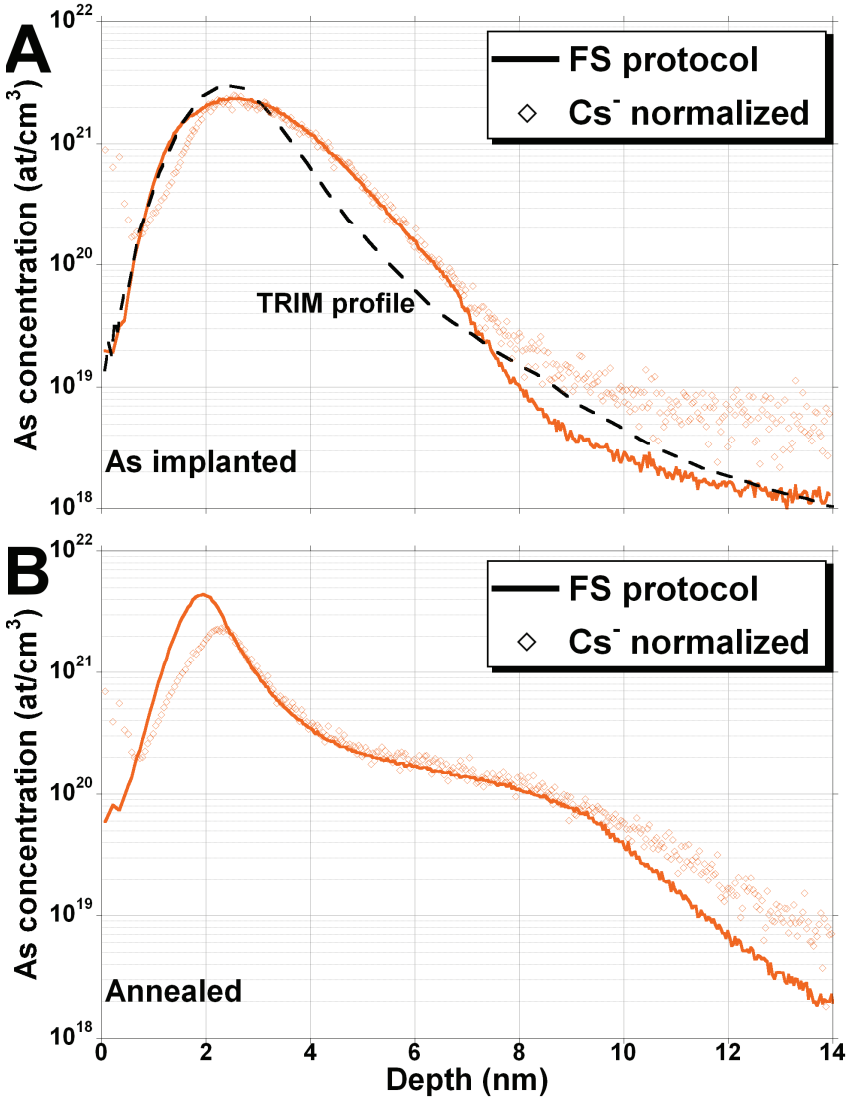

Figure V.7 Overlaid 250 eV sputtering FS protocol (curves) and Cs^- normalisation (open symbols) As concentration profiles obtained in both as implanted (**A**) and annealed (**B**) samples. The number of data points for the profile obtained with Cs^- normalisation has been voluntarily reduced for enhanced visualisation. TRIM simulation of the As concentration distribution in the as implanted is also given for comparison means.

V. 4. d- Overall comparison of the different profiling conditions

To answer this question, it is important to know with a good confidence the real As distribution in those samples, which is not trivial. The number of techniques providing sufficient sensitivity, depth resolution and matrix-free quantification for dopant depth profiles is indeed scarce. HRBS is known to provide 0.1-0.2 nm depth resolution in the first few nanometres of a depth profile and matrix-free quantification. However its sensitivity is usually insufficient to allow accurate quantification of junction depths at a few 10^{18} at/cm^3. In our case, we thus resorted to the use of HRBS and simulation (crystal-TRIM and S-Process) to provide profiles which will serve as basis to assess the accuracy of ToF-SIMS profiles.
To allow better visualisation of the different profiles, we propose an overlay of crystal-TRIM (or S-Process), HRBS and all ToF-SIMS profiles issued from Cs^- normalisation in Figure V.8;

followed by an overlay of Crystal-TRIM (or S-Process), HRBS and FS ToF-SIMS profiles in Figure V.9.

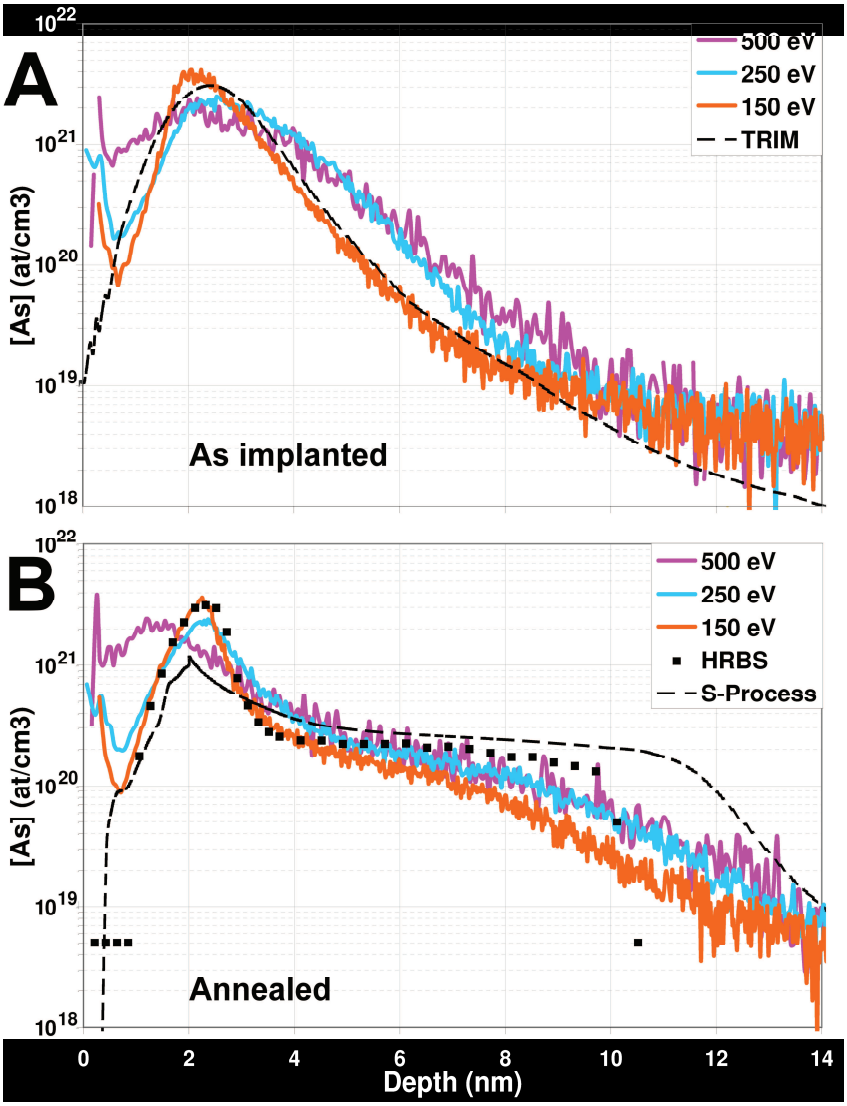

Figure V.8 Overlay of ToF-SIMS As concentration profiles issued from Cs^- normalisation at several sputtering energies, TRIM and HRBS profiles in both as implanted (**A**) and annealed (**B**) samples.

Let us first compare the different ToF-SIMS profiles without commenting on their agreement (or discrepancy) with simulation or HRBS ones. As expected from subsection V. 3. b-, higher sputtering energies yield more broadened profiles in particular around maximum As concentration peak and for both as implanted or annealed case. The most striking effects are observed on the profile obtained on the annealed sample at 500 eV sputtering, where a clear As peak is not even well resolved, as it is merged with the initial (transient induced) high As signal artefact. Apart from this exception, we can however observe a relatively good agreement on the As peak position in both as implanted and annealed samples. Another point of agreement is obtained in the profile tails (after 8-10 nm). This shows that our depth scale establishment protocol and quantification protocols (either Cs^- normalisation or FS) help to minimise artefacts. If we focus on comparison of the profiles obtained with different quantification protocols, we indeed observe, as expected from the previous subsection, higher dynamics and signal-to-noise ratio with the FS protocol. In particular, the As peak after annealing is seen at higher concentrations while a plateau is seen at similar levels (this

tendency increases at lower sputtering energies). The As plateau in Si, expected due to the usual box-shape diffusion of As in Si, is also better resolved (flatter) with the FS protocol, as well as the concentration drop after the plateau. Due to the lower noise level and the particular quantification method, the detection limit obtained with the FS protocol is also (artificially) enhanced by a factor ~4 as compared to Cs^- normalisation. As concentration at a depth of 14 nm is indeed found to be of 1.2 and 5×10^{18} at/cm^3 (2 and 8×10^{18} at/cm^3) in the as implanted (annealed) sample with the FS protocol and Cs^- normalisation protocol respectively.

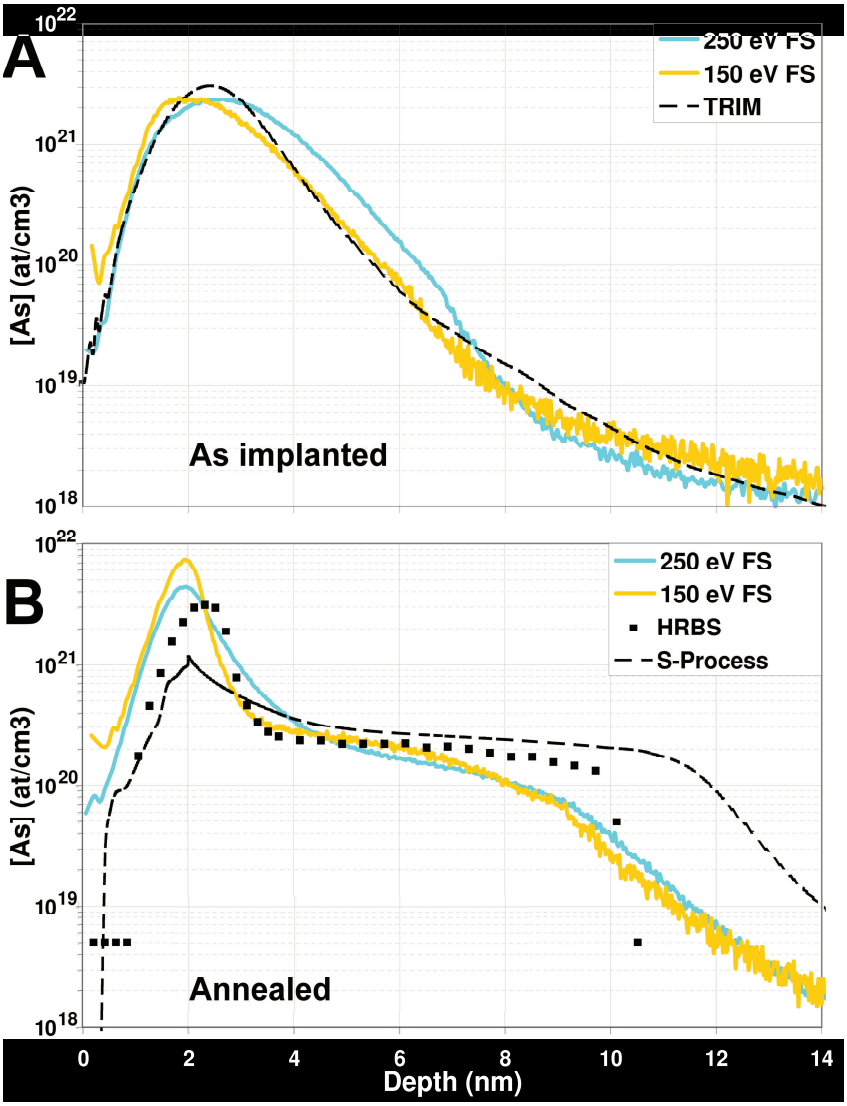

Figure V.9 Overlay of ToF-SIMS As concentration profiles issued from FS protocol at several sputtering energies, TRIM and HRBS profiles in both as implanted (**A**) and annealed (**B**) samples.

Let us now focus on the as implanted sample alone and compare ToF-SIMS profile shapes with crystal-TRIM profiles, which represent for us the real As distribution. Some uncertainty in profile shape usually arises from the fact that crystal-TRIM code does only take into account binary collisions, which causes divergence with actual profile shape up to an amount of 5-20%, particularly because of channelling of the incident ions [17-18]. However, since our study focuses on low energy implants, with As (heavy element) ion implantation in Si (110), little channelling can be expected; which justifies the use of crystal-TRIM profile as reference. With both quantification methods, the best ToF-SIMS profile shapes are obtained at 150 eV

sputtering. Profiles obtained at higher energies are, as pointed out before, broadened and/or have lower level, misplaced As concentration peaks. However, while the best fit seems to be obtained with Cs^- normalisation around As maximum, slightly better fit is obtained on the far tail-end of the profile with the FS protocol due to its better sensitivity. Thus the latter may be preferred if a realistic value of the junction depth is required. Almost the same conclusions can be drawn from the profiles obtained in the annealed sample. In this case, due to the difficulty to obtain precise profiles by simulation because of the complex phenomena occurring at SiO_2/Si interface, S-Process profiles are only used to obtain the theoretical position of the As peak (right after the SiO_2 interface) and of As plateau concentration. HRBS profile is therefore used as the reference profile for profile shape (in the high As concentration zones). All ToF-SIMS profiles agree with HRBS (and simulation) on As plateau concentration. Again, the As interfacial peak is always better resolved by going to lower sputtering energies. Improvements are particularly important on decay slope of the As peak, with 3.5, 1.9 and 0.7 nm/decade found on Cs^- normalised profiles at 500, 250 and 150 eV (roughly the same values are obtained with the FS protocol), showing a linear dependence with sputtering energy. The same depth resolution as HRBS is thus achieved at 150 eV sputtering on As profiles. Furthermore, the best fit of HRBS profile shape both in As peak and plateau are also obtained at 150 eV for both quantification protocols. However, FS protocol profiles tend to overestimate the As peak value and show slight peak shift towards the surface. This is assumed to be due to the FS protocol's improved statistics in the oxide layer (through AsO_x^- ions). It also shows that the FS protocol may not be the best choice for characterisation of such samples.

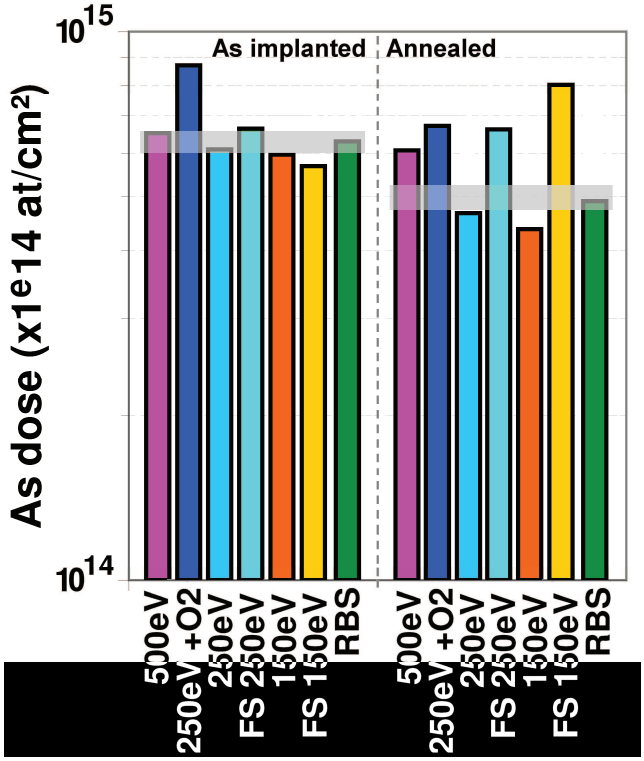

Figure V.10 Total As doses as calculated from ToF-SIMS profiles in Figures V.8 and V.9, compared to the (absolute) dose obtained by RBS for both as implanted (left) and annealed (right) samples. RBS measurement error is shown in both cases by a light grey bar. Colour code is the same as in Figures V.8 and V.9.

To further investigate these results, we can consider the total As dose calculated using ToF-SIMS profiles and compare it to RBS (absolute) doses. Precise evaluation of total dopant dose

is indeed important to assess (if any) dose loss after annealing and for correlation with sample resistivity. Such a comparison is done in Figure V.10 for both as implanted and annealed samples. Surprisingly, the ToF-SIMS profiles providing the best fit to (assumed) real sample composition do not systematically yield the best agreement in total dose. For example, 150 eV Cs^- normalised profile of the annealed sample is found to underestimate the dose when compared to RBS. On the contrary, profiles which are known to be erroneous in shape, such as 500 eV profile in as implanted sample, gives a good agreement in dose with RBS. In all of those (i.e. 500 eV or 250 eV profiles whatever the quantification protocol and 150 eV profile with FS protocol), whenever the calculated dose is close to that of HRBS it is clear that this is most likely a coincidence. That is, profile broadening or peak position and/or concentration mismatch produce an equilibrium which yields artificially the right dose. It is therefore interesting to see that in both samples, 250 eV sputtering with Cs^- normalisation yields the closest results to RBS, just before 150 eV profiles (whose shape was found to give much better fits to simulation or HRBS). The lower dose found at 150 eV can be explained by the fact that the As plateau is not as flat as in HRBS profile, which induces dose underestimation.
This leads us to the conclusion that none of the profiles performed in this study could yield realistic profiles on all three points required for accurate quantification, i.e. profile shape, junction depth and total dose. Instead, each point would require a dedicated profile. However the benefits of EXLE regime and FS protocol are clear for obtaining correct profile shape and junction depth respectively.

V. 5. Results exploitation: useful knowledge earned through quantitative analysis

In this section we will, starting from the best ToF-SIMS analysis (i.e. either Full Spectrum or Cs- normalised profiles obtained at 150 eV sputtering), extract useful information for understanding implant shape dependence on implantation process. We will thus investigate the different types of As implants relevant for device fabrication. A comparison of profile shapes obtained with classic ion beam implantation and pulsed plasma implantation will be performed. The study of the dopant profiles in plasma-implanted sample after a spike anneal (selected as giving the best electrical properties out of a panel of anneals) will be done and correlated with electrical characterisation.
For this study, two silicon (100) wafers were implanted with As using the pulsed plasma implantation technique [19]. The precursor specie for As in the plasma was AsH_3, the energy of implantation was 1 keV and the nominal dose 1.5×10^{15} at/cm^2. One of the wafers was kept as implanted, while the other underwent a 1050°C spike anneal in N_2 atmosphere. In addition another silicon (100) wafer was implanted using classic ion beam implantation, at an energy of 1 keV and to a dose of 1×10^{15} at/cm^2. All samples were profiled using the EXLE regime and quantified using the "Cs^- normalisation" protocol developed above. Resistivity measurements were performed with a conventional four point probe tool.
The profiles of as-implanted samples with both implantation techniques are displayed in Figure V.11.A. Both profiles have been normalised to their highest value to allow better comparison of their shape, although the two differ only slightly: 5.7 at/cm^3 for the ion beam implanted sample and 6.6 at/cm^3 for the pulsed plasma implanted one. Three main differences can be pointed out. First, more dopants are implanted close to the surface with the pulsed plasma technique (even if the first 3-4 points of the profile have to be neglected). Second, the maximum concentration peak is closer to the surface with pulsed plasma implantation (1.75 nm from the surface) than with ion beam implantation (2 nm from the surface). It is also

closer to the native oxide/silicon interface: 0.2 nm and 0.5 nm with pulsed plasma and ion beam implantation respectively (oxygen relevant signals are not shown in Figure V.11 for clarity). Finally, dopant concentration decay length is different, resulting in different junction abruptness. In the ion beam implanted sample, we observe a single exponential decay from 2.5 nm to ~8 nm, where sensitivity with our profiling method drops and does not allow to resolve the profile correctly. This single exponential decay is typical of ion implantation. Its decay length is found to be of 2.8 nm/decade. Meanwhile, the profile obtained on pulsed plasma implanted samples is complicated, showing two distinct exponential decays. The first one is very sharp (1.5 nm/decade) and runs from 1.8 nm to 3.2 nm. The second is slower (2.2 nm/decade) and runs from 3.2 nm to ~5.5 nm, where again sensitivity is not sufficient to resolve the actual concentration profile.

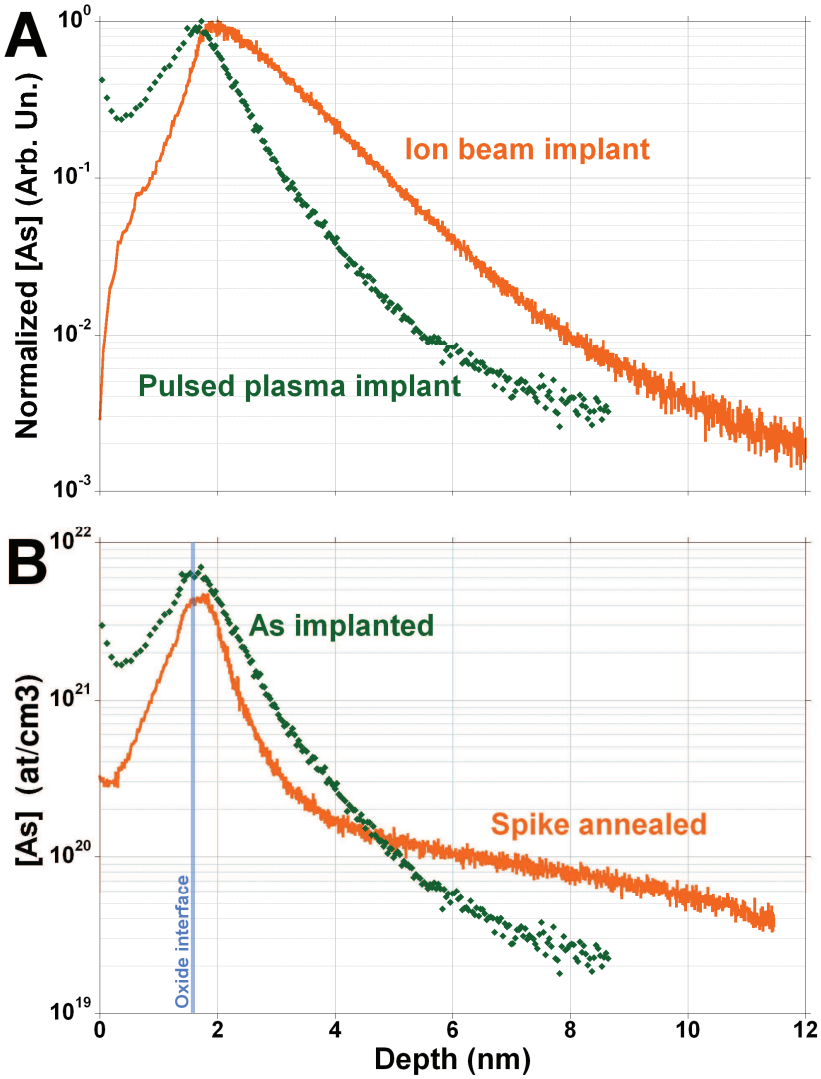

Figure V.11.A Overlay of ToF-SIMS As concentration profiles issued from Cs^- normalisation at 150 eV sputtering, in as implanted samples obtained with pulsed plasma and ion implantation techniques.

B Overlay of ToF-SIMS As concentration profiles issued from Cs^- normalisation at 150 eV sputtering, in as implanted and spike annealed samples obtained with pulsed plasma implantation technique.

These differences are all assumed to be inherent to plasma implantation. While ion beam implantation uses a mono-energetic beam (1 keV here), in plasma implantation the whole gas volume sees a different potential, with a maximum at 1 keV in our case and whose distribution depends of the transient sheath extension dynamics in the plasma [20-23]. In other terms, all the atoms and compounds in the plasma are not implanted with the same energy and a significant fraction of the implanted elements impacted the sample with energies lower than 1 keV. Thus, more atoms are implanted close to the surface with the pulsed plasma technique, which provides shallower depth distributions as described above.
After annealing, we observe roughly the same behaviour than in the ion beam implanted samples presented in the previous section. A fraction of the As atoms diffused towards the substrate, creating a box shaped profile (although here the analysis was stopped before reaching signal drop, due to a too important analysis duration) as shown in Figure V.11.B. A strong oxide/silicon interfacial peak is also observed, with a peak As concentration/plateau concentration ratio of ~30, twice to that of ion beam implanted sample studied in previous section. This indicates that in the case of plasma implantation, fewer atoms are prone to diffuse upon annealing, therefore providing sharper interfacial peaks and shorter junction depths after annealing than ion beam implantation. This phenomenon is also reported in the literature for boron USJs [19]. One explanation for this tendency would be higher levels of As clustering in the As interfacial peak, preventing their diffusion. This is often verified by the higher square resistivity of pulsed plasma implants as compared to more classic implants (provided that similar conditions of implant energy, total dose and annealing are used), as shown in [19]. In our case, the square resistivity was found to be 1005 Ω/square for the pulsed plasma implanted sample and of 539 Ω/square for the ion beam implanted sample after annealing. This might indeed indicate higher levels of clustering in pulsed plasma implanted samples.

CHAPTER V Conclusion

In this chapter we detailed the different practical solutions developed for improvement of the quantitative analysis capacities of our ToF-SIMS instrument in arsenic ultra shallow implants for source and drains of next generation devices. We focused on improvement of experimental conditions and on optimisation of data treatment to obtain both accurate depth and concentration scales. To answer the needs of high depth resolution, we used the protocol for extremely low energy profiling developed in chapter IV. We proposed a depth scale correction through a two-fold variable sputter rate corresponding to a short surface transient and to the sputter rate variation between silicon dioxide and pure silicon. Two data treatment protocols were described. The first is intended to enable arsenic quantification in presence of germanium (such as for example in SiGe based source/drains), although in this study we only worked with pure silicon wafers. It consists in the point to point normalisation of As^- signal by Cs^- and in quantification via a reference sample. The second is based on a full spectrum approach of the ToF-SIMS data sets, with an original use of the protocol's feature described in chapter III relative to the quantification of diluted elements in a matrix. Using this feature, we were able to artificially lower the detection limit of the technique.
The validity of the proposed solutions was investigated in structures representative of those found in actual devices, constituted of as implanted and annealed 1 keV As implants in silicon. In order to assess the improvements brought by both experimental and data treatment improvements, ToF-SIMS results were compared with those obtained on the same samples

with HRBS or simulation (crystal-TRIM for as implanted sample, S-Process for annealed sample). Excellent agreement of the ToF-SIMS and HRBS depth scales was obtained (measured on native oxide layer present on the different samples). Improvement of the depth resolution was found to be important when using EXLE regime, with a 0.45 nm decay length measured on oxygen relevant signal at 150 eV Cs^+ sputtering. Concerning As profile shape and agreement with reference profiles (either simulation or HRBS), best agreement was obtained in the EXLE regime. However, none of the proposed data treatment methods enabled accurate quantification of the As in-depth concentration through the whole sample thickness. "Cs^- normalisation" protocol gave the best profiles in the high As concentration region and is thus useful to visualise accurate profile shape especially after annealing. On the other hand, the Full Spectrum approach gave better profiles in the low concentration region, which is particularly useful for determination of the accurate junction depth. Yet, the combination of best experimental conditions and data treatment protocol did not always yield accurate (total) As dose when compared to RBS measurements. In conclusion, no unique method was found that enables accurate quantification of both profile shape and total dopant dose, although both are needed for process optimisation purposes.
We thus performed studies of the As profile shape using the "Cs^- normalisation" protocol in EXLE regime in USJ obtained by a recent implantation technique: the pulsed plasma implantation. Dopant distribution obtained by such implants were compared to those obtained by conventional ion beam implantation. They were found to yield shallower distributions and faster dopant concentration decay in as implanted samples. However, higher cluster concentrations led to higher concentration interfacial As peak after annealing, resulting in lower junction depth but also higher square resistivity than in the ion beam implanted samples.

REFERENCES

[1] M. Barozzi, D. Giubertoni, M. Anderle and M. Bersani, *Arsenic Shallow Depth Profiling: Accurate Quantification in Sio2/Si Stack*, Appl. Surf. Sci., 231-232 (**2004**) 632-635.
[2] M. Barozzi, D. Giubertoni, S. Pederzoli *et al.*, *Influence of Changes in the Resistivity of the Sample Surface on Ultra-Shallow Sims Profiles for Arsenic*, Appl. Surf. Sci., 252 (**2006**) 7286-7289.
[3] D. Giubertoni, M. Bersani, M. Barozzi *et al.*, *Comparison between the Sims and Meis Techniques for the Characterization of Ultra Shallow Arsenic Implants*, Appl. Surf. Sci., 252 (**2006**) 7214-7217.
[4] Y. Kataoka and T. Itani, *Ultrashallow Depth Profiling Using Sims and Ion Scattering Spectroscopy*, Surf. Interface Anal., 39 (**2007**) 826-831.
[5] P.H. Chi, D.S. Simons, J.M. Mckinley, F.A. Stevie and C.N. Granger, *High Precision Measurements of Arsenic and Phosphorous Implantation Dose in Silicon by Secondary Ion Mass Spectrometry*, J. Vac. Sci. Technol. A, 20 (**2002**) 688-692.
[6] M. Tomita, T. Hasegawa, S. Hashimoto *et al.*, *Sims Round-Robin Study of Depth Profiling of Arsenic Implants in Silicon*, Appl. Surf. Sci., 203-204 (**2003**) 465-469.
[7] A. Merkulov, F. Desse and M. Schuhmacher, Proceedings of the Third European SIMS Workshop, (**2002**) 52.
[8] K.E. Petersen, *Dynamic Micromechanics on Silicon: Techniques and Devices*, Electron Devices, IEEE Transactions on, 25 (**1978**) 1241-1250.
[9] J.P. Dismukes, L. Ekstrom and R.J. Paff, *Lattice Parameter and Density in Germanium-Silicon Alloys*, J. Phys. Chem., 68 (**1964**) 3021-3027.
[10] A. Merkulov, P. Peres, S. Choi *et al.*, *Advanced Secondary Ion Mass Spectroscopy Quantification in the First Few Nanometer of B, P, and as Ultrashallow Implants*, J. Vac. Sci. Technol. B, 28 (**2010**) C1C48-C41C53.
[11] P.A.W. Van Der Heide, M.S. Lim, S.S. Perry and J. Bennett, *A Systematic Study of the Surface Roughening and Sputter Rate Variations Occurring During Sims Ultrashallow Depth Profile Analysis of Si with Cs+*, Nucl. Instrum. Meth. B, 201 (**2003**) 413-425.
[12] A. Merkulov, P. Peres, J. Choi, F. Horreard and M. Schuhmacher, Proceedings of Frontiers of Characterization and Metrology for Nanoelectronics (**2011**).
[13] *Synopsys Tcad Tools*.
[14] K. Wittmaack, *Artifacts in Low-Energy Depth Profiling Using Oxygen Primary Ion Beams: Dependence on Impact Angle and Oxygen Flooding Conditions*, J. Vac. Sci. Technol. B, 16 (**1998**) 2776-2785.
[15] C.W. Magee, G.R. Mount, S.P. Smith, B. Herner and H.-J. Gossmann, *Sputtering Rate Change and Surface Roughening During Oblique and Normal Incidence O[Sub 2][Sup +] Bombardment of Silicon, with and without Oxygen Flooding*, J. Vac. Sci. Technol. B, 16 (**1998**) 3099-3104.
[16] P.F.A. Alkemade and Z.X. Jiang, *Complex Roughening of Si under Oblique Bombardment by Low-Energy Oxygen Ions*, J. Vac. Sci. Technol. B, 19 (**2001**) 1699-1705.
[17] K. Gärtner, M. Nitschke and W. Eckstein, *Computer Simulation Studies of Low Energy B Implantation into Amorphous and Crystalline Silicon*, Nucl. Instrum. Meth. B, 83 (**1993**) 87-94.
[18] H.Y. Chan, M.P. Srinivasan, F. Benistant, H.M. Jin and L. Chan, *Sampling Calibration of Ion Implantation Profiles in Crystalline Silicon from 0.1 to 300 kev Using Monte Carlo Simulations*, Solid-State Electron., 49 (**2005**) 1241-1247.
[19] S.B. Felch, Z. Fang, B.W. Koo *et al.*, *Plasma Doping for the Fabrication of Ultra-Shallow Junctions*, Surf. Coat. Technol., 156 (**2002**) 229-236.
[20] J. Pelletier and A. Anders, *Plasma-Based Ion Implantation and Deposition: A Review of Physics, Technology, and Applications*, Plasma Science, IEEE Transactions on, 33 (**2005**) 1944-1959.
[21] M. Carrere, F. Torregrosa and V. Kaeppelin, *Ion Behaviour in Pulsed Plasma Regime by Means of Time-Resolved Energy Mass Spectroscopy (Trems) Applied to an Industrial Radiofrequency Plasma Immersion Ion Implanter Pulsion (R),* Amer Inst Physics, Melville, **2006**, pp. 257-260.
[22] B.P. Linder and N.W. Cheung, *Modeling of Energy Distributions for Plasma Implantation*, Surf. Coat. Technol., 136 (**2001**) 132-137.
[23] X.B. Tian, D.T.K. Kwok and P.K. Chu, *Modeling of Incident Particle Energy Distribution in Plasma Immersion Ion Implantation*, J. Appl. Phys., 88 (**2000**) 4961-4966.

CHAPTER VI
Analysis of materials and structures for organic electronics: application to PPMA - C_{60} blend based Resistive RAM

In this final chapter, we will cover a very specific application of ToF-SIMS analysis of organic materials. Although ToF-SIMS was originally designed for surface studies and is nowadays widely used in surface characterisation, its huge potential in terms of depth profiling of organic materials makes it an extremely promising tool for the study of organic electronics. Indeed, in opposition to inorganic materials, the information of interest in organics is often contained in molecules (and not elements or clusters). Dual beam ToF-SIMS, with its slow sputter ions and swift analysis ions, enables both gentle abrasion without destruction of the organic structure and high molecular secondary ion yields. We chose in this study to focus on PMMA - C_{60} blends because of their numerous applications in electronics, especially in Resistive Random Access Memory (RRAM) [1-3]. The materials concerned by this study will therefore be blends of a polymer (PMMA) and small molecules (C_{60}). Both of those are mainly constituted of carbon: PMMA composition being $(C_5H_8O_2)_n$, with *n* the number of repeat units (monomers). For qualitative as for quantitative analysis of such blends, we will thus have to face very complex mass spectra, typical of organic materials. In addition, we will need to discriminate molecular information representative of both components, while both of them are mainly constituted of carbon. A careful study of the mass spectra will thus be required in order to identify the secondary ions of interest for our study. Organic materials are also very fragile and can be rapidly damaged upon ion beam irradiation, which usually results in dramatic loss of information. We will therefore have to find an experimental protocol that enables sustainable profiling of organic layers without information loss. Finally, we are also interested in quantification of the blend composition, as the latter determines the electrical behaviour of the device. As very few studies of this kind are available, we need to setup a protocol enabling in-depth quantification of the PMMA - C_{60} blend layers in a large range of compositions.

VI. 1. Study of (surface) mass spectra, selection of representative secondary ions

Since detecting fullerenes in a polymer matrix was not expected to be trivial, we investigated the ability of several primary ions to reveal the presence of C_{60} and to discriminate the information from that belonging to the polymer. We therefore acquired surface mass spectra of blends of various compositions using 25 keV Bi_x^{q+} primary ions where $x = 1, 3, 5$ and $q = 1, 2$ and monitoring positive or negative secondary ions. In agreement with results reported in [4] no particular ionisation yield enhancement was observed using doubly charged primary ions in PMMA. As regards primary ion mass, if Bi_3^+ enhances yields by a factor ten with respect to Bi^+, little improvement was brought by selecting Bi_5^+ and tremendous decrease in primary beam current was observed, in agreement with [4-5]. Thus we limited ourselves to simply charged Bi^+ and Bi_3^+ ions for analysis. Following positive secondary ions did not allow detection of any fullerene related ions with either of the selected primary ions in blends containing low concentrations of C_{60}. On the other hand, negative ion mass spectra showed a strong signature at mass-to-charge ratio 720 u, corresponding to $^{12}C_{60}^-$. The surface spectra of a PMMA - 10 wt% C_{60} sample is shown in Figure IV.1. The C_{60} mass group appears with particular high intensity in the high mass range displayed in Figure VI.1.D. The fact that high (negative) secondary ion yields are obtained while positive ions corresponding to C_{60} are not observed is not intuitive, due to the important number of applications using positive C_{60} ions, including as primary ions for SIMS ion sources [6-9]. Literature also provides ToF-SIMS studies showing high secondary ion intensities in the positive polarity, such as Kato *et al.* [10]. The difference with our study is

that those focus on pure fullerene materials. The reported mechanism of C_{60} ion formation through interaction with electrons is twofold. While high energy electrons (a few eV to a few tenths eV) tend to tear away an electron from the molecule's electron cloud, thus forming positive ions, lower energy electrons tend to attach themselves to the molecule, thus forming negative ions [11-13]. Therefore, an explanation to the absence of C_{60}^+ because can be that the energy of free electrons liberated on impact of primary ion with the target was too low, or lowered after multiple interactions with other materials. This phenomenon is not observed in [10] because samples are constituted of fullerene only, while in our case the small molecules are wrapped in polymer. Considering that the blends used in this study ranged from 0.0025 to 20 wt% C_{60}, we indeed obtain a number of fullerenes by PMMA repeat unit ranging from 3.5×10^{-4} to 2.8. However this hypothesis would require studies on blends with higher C_{60} composition to be proven.

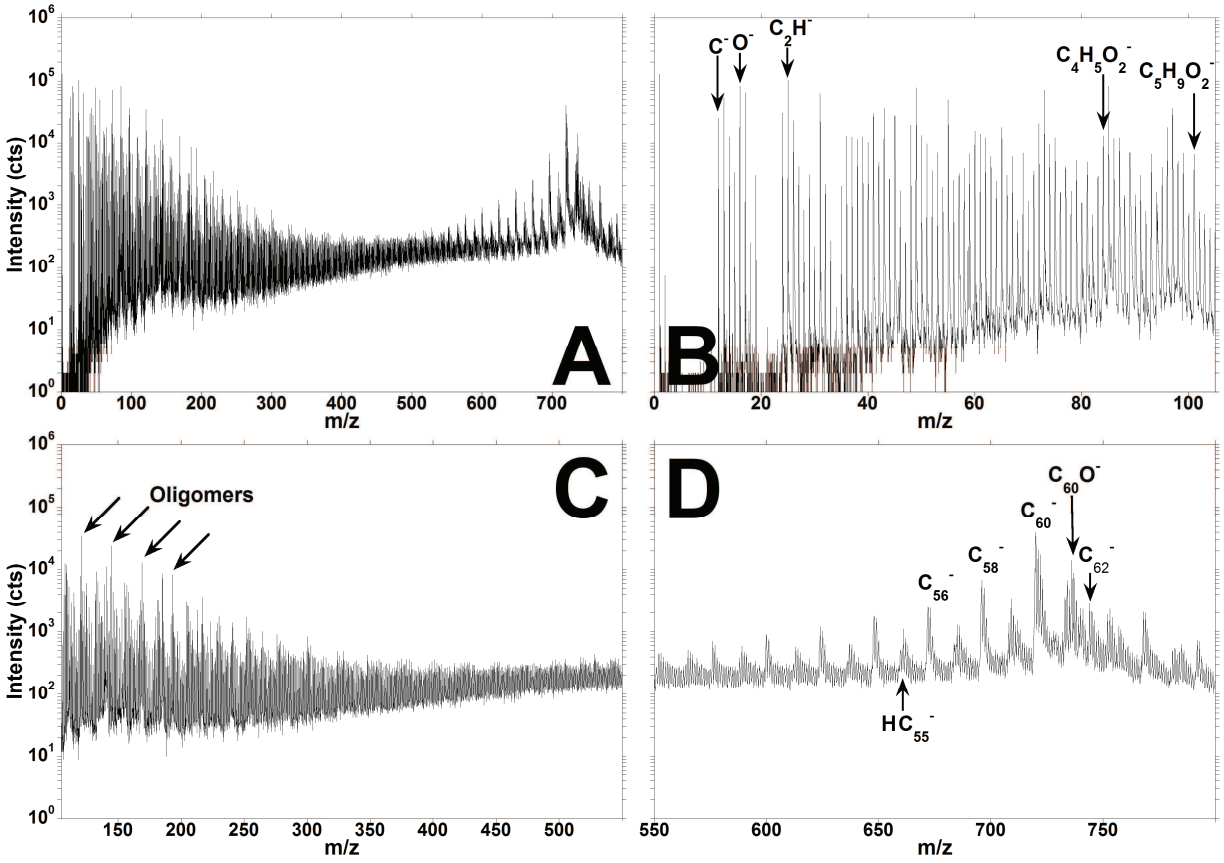

Figure VI.1.A Overall surface mass spectrum of a PMMA - 10 wt% C_{60} blend obtained with 25 keV Bi_3^+. Primary ion dose is 1×10^{12} ions/cm^2. High background (~10^2) is typical of organic materials.

B The low mass zone of the spectrum, from m/z = 0 to 105.
C The mid-mass zone of the spectrum, from m/z = 105 to 550.
D The high mass zone of the spectrum, from m/z = 550 to 800.

The fragmentation of C_{60} under irradiation with the analysis beam could also be observed, as shown by the numerous satellite peaks in Figure VI.1.D. These lower intensity peaks at m/z=720±12×2n, n being an integer between 1 and 8, correspond to C_{60-2n}^-. These C_2 depleted fullerenes are a characteristic product of C_{60} irradiation by swift heavy ions [14]. Interestingly enough, they are not the only fragmentation products, as odd numbered fullerenes are also detected. However, these are always shifted of 1 u towards heavier masses as compared to what would have been expected. That is, while C_{2n} fullerenes are detected at (12×2n) u, these

odd-numbered fullerenes C_{2n+1}, n being an entire number between 0 and 7, are always detected at (12×(2n+1))+1 u. This suggests the attachment of an H atom to the odd-numbered fullerenes and correlates the hypothesis formulated by Kong *et al.* [14] on the fact that such fullerenes are in fact constituted of open cages with a missing carbon atom. Indeed, the removal of a carbon pair is done by breaking four C-C bonds within the fullerene, which leaves an even number of "free" electrons and allows formation of two new C-C bonds. However the removal of one carbon requires breaking of three C-C bonds: while two of the remaining free electrons can form a new bond, the third one is still free and (in our experiment) is used to create a C-H bond. The secondary ion intensities of those fragmentation products are found to vary in a logarithmic fashion with the number of removed carbon atoms (for odd numbered fullerenes) or carbon atom pairs (for even numbered ones), the formers having on average half the intensities of the latter. When comparing the relative intensities of the even numbered fullerene fragments to the main (C_{50}^-) ion to those obtained in [10] with Au_3^+, we find that fragment intensities are approximately half that in our experiment. This can be explained again by the fact that experiments in [10] involved pure fullerene layers. Finally, the relatively high intensities observed on fragmentation products at masses 720+16×n u (with n = 1, 2 or 3) indicates the formation of $C_{60}O_n$- ions, already observed in aqueous solutions upon electron irradiation in [15].
To further confirm that we enabled observation of C_{60}^- ions and to remove any possibility of mass interference, we can investigate relative intensities of C_{60}^- and its isotopes at m=720,721,722,723,724,725 u as found in the ToF-SIMS spectra and compare them to theoretical isotopic abundance as calculated by:

$$\alpha(^{12}C_{60-n}\,^{13}C_n) = \alpha(^{13}C)^n \times \alpha(^{12}C) \times \frac{60!}{(60-n)!} \qquad \text{(VI.1)}$$

where $\alpha(^{13}C)$ and $\alpha(^{12}C)$ are the natural isotopic fractions of ^{13}C (0.111) and ^{12}C (0.9889) and the factorial ratio expresses the equivalence between two fullerenes containing n ^{13}C at different positions. The results of this comparison is shown in Table VI.i.

m (u)	720	721	722	723	724	725
Isotopic fraction α calculated from equation VI.1(%)	51.18	34.47	11.41	2.48	0.4	0.05
α from surface spectra (%, ±0.5)	52.3	32	11.4	3.4	0.6	0.3

Table VI.i Isotopic abundances of C_{60} isotopes as determined by peak area ratios in surface spectra and equation (VI.1).

These results reveal good correlation between spectra peak areas and isotopic abundance for the six main C_{60} isotopes, proving the absence of mass interference in the 720 to 725 u mass group and allowing us to choose C_{60}^- ion as the ion representative of C_{60} in our samples.
When looking at the entire mass spectra (see Figure VI.1.A), we observe, apart from the C60 related ions discussed above, an important number of peaks out of which we will have to identify a few characteristic ones for monitoring of PMMA. We can divide the whole spectra in three different groups: (i) $m/z < 50$ group, corresponding to elemental ion peaks (mono-atomic or polyatomic, result of heavy fragmentation and/or recombination), (ii) $50 \leq m/z \leq 105$ group, corresponding to fragments of the PMMA chain issued from breaking and recombination of different sections of the chain as well as the chain monomer at $m/z = 101$ (Figure VI.1.B) and (iii) $m/z \geq 105$ group, corresponding to oligomers containing a number n of monomers and/or chain fragments (Figure VI.1.C). Group (i) can contain

recombination products from both fullerene and polymer fragmentation (typically C_xH_y-), which prohibit their use as PMMA representative ions. Nonetheless this allows us to use C_2H^- as an ion characteristic of the organic matrix (as for example $^{30}Si^-$ would be used in silicon). Group (ii) contains heavy PMMA fragments constituted of aromatic recombination products and oligomer ions. Concerning group (iii), the higher the secondary ion mass is, the more we have mass interferences between different fragments, which makes it difficult to clearly identify a compound associated to one peak, not to mention the problem of mass resolution. Secondary ions characteristic of PMMA were thus selected in group (ii), whose spectral analysis is easier and well documented. Based on ToF-SIMS spectra available in literature [16-17] and spectra libraries, we selected fragment ion $C_4H_5O_2^-$ (m/z=85 u) and oligomer ion $C_5H_9O_2^-$ (PMMA monomer + H, m/z=101 u) as PMMA characteristic ions.

VI. 2. Setup of an experimental protocol for damage-less organic layer profiling

Due to the fragile nature of organic materials, heavy damage can be inflicted even by minute doses of energetic ions from the analysis beam. This results most of the time in loss of molecular signal. This phenomenon is revealed in Figure VI.2, which shows the evolution of the C_{60}^- ion intensity with primary ion dose. One can see that molecular signals are reduced by a factor ten after a dose of 6×10^{12} ions/cm^2, which is only six times the static limit for surface analysis. This shows how considerable the damage is in our samples. To avoid such a fast material destruction, we thus have to (i) use low energy sputtering and (b) remove as much as possible of the layers damaged by the analysis beam between two analysis cycles.

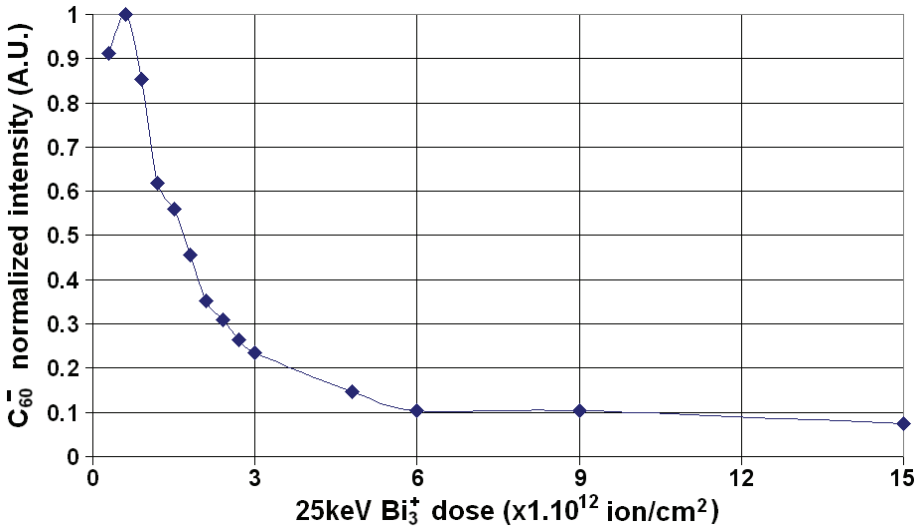

Figure VI.2 Variation of the C_{60}^- secondary ion yield as a function of the 25 keV Bi_3^+ primary ion dose (normalised to its highest value). To obtain these data, spectra were acquired in a successive fashion over the same 200×200 µm area of the sample. The primary ion dose for the first ten spectra is 0.3×10^{12} ion/cm^2.

To perform this we operated the beams in non interlaced mode with low energy sputtering. As oxygen sputtering induced, even at very low doses, complete loss of the C_{60} relevant signals, we used only caesium sputtering. Furthermore, considering the sample involved in this study were involving layers of ~60 to ~150 nm thick and that depth resolution was not a critical requirement, we did not use EXLE mode for sputtering nor 15 keV bismuth beam for analysis.

Series of profiles with various cycle time conditions and experimental parameters were performed in order to search for the best protocol in terms of molecular signal stability. The latter was obtained with the following settings for primary ion beams: 25 keV Bi^+ or Bi_3^+ analysis beam and 250 eV Cs^+ sputtering beam. Primary beam currents measured in a Faraday cup were 15 nA for sputtering (DC current) and 14 nA for analysis (DC current). Raster areas were 300 µm × 300 µm and 100 µm × 100 µm for sputter and analysis respectively. The best balance between signal stability and statistics (data sampling) was obtained alternating analysis cycle and 3 s sputtering followed by a pause of 0.5 s. This protocol was meant to be used either at ambient temperature (25°C) or at -75°C by means of a temperature controlled sample holder cooled by liquid nitrogen, in which case electron flooding was used for charge compensation. To keep atmospheric contamination to a minimum, a vacuum level $<10^{-9}$ mbar was maintained during analysis. Using this protocol, we obtained sputter rates of 0.26 ±0.02 nm/s in pure PMMA and of 0.16 ±0.04 nm/s in PMMA - C_{60} blends on the whole C_{60} composition range.

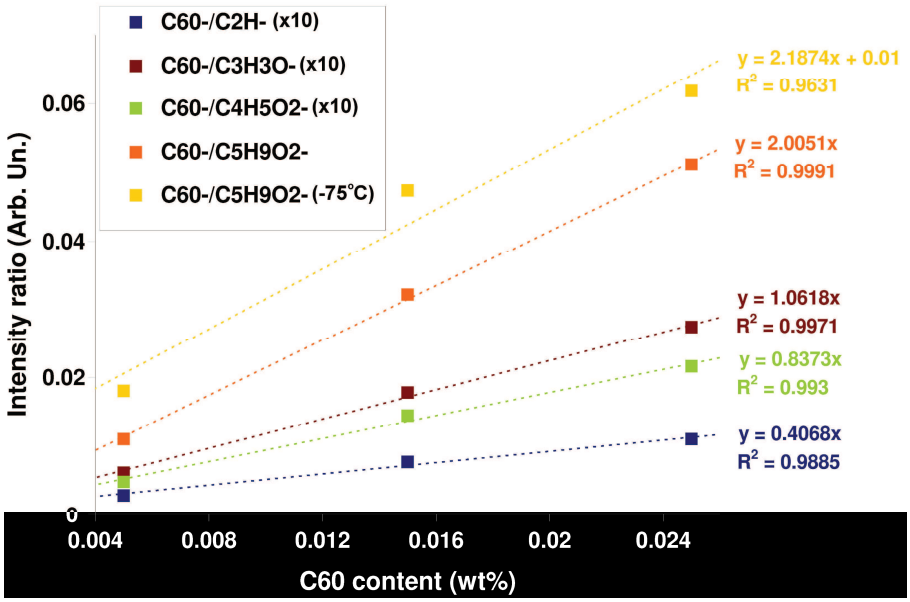

Figure VI.3 The various (assumed) linear relationships with the sample's nominal C60 concentration obtained with different secondary ion intensity ratios in the low C_{60} content region. The best linear relationship is obtained for the $I(C_{60}^-)/I(C_5H_9O_2^-)$ ratio at ambient temperature.

VI. 3. Setup of a protocol for PMMA - C_{60} blend quantification

Being able to discriminate molecular information relevant to both blend components and to obtain sustainable signals in-depth by depth profiling, the next step consists then in finding a means for quantifying the blend composition. While profiling blends of a large composition range, we notice a trend for secondary ion intensities below and beyond 0.015 wt% C_{60} for both temperatures. Beyond 0.015 wt% and below 0.04 wt%, PMMA related fragment ions intensities decrease while C_{60}^- intensity remains stable, whereas below 0.015 wt% C_{60} the opposite happens. Furthermore, beyond 0.04 wt% PMMA related fragment ions intensities stay stable while C_{60}^- intensity increases. This tendency let us suppose that it might be possible to quantify the C_{60} content of the layers by normalising C_{60}^- to a PMMA representative ion in the steady part of the profile. This possibility was therefore studied using different secondary ions and observing the evolution of the ratio $I(C_{60}^-)/I(\text{fragment ion})$ for different fragment ions. A focus on the values obtained for low composition blends with

various fragment ions is shown in Figure VI.3. All of the ratios exhibit good linear correlation with nominal layer composition, but with various degrees of accuracy, measured here by the correlation factor R^2. As expected, the ratio obtained with C_2H^- normalisation yields the worst correlation, given that (as discussed in the previous section) this ion is not well representative of PMMA. By using more massive fragment ions, we obtain better linear relationships. The best correlation factor is obtained using the monomer ion $C_5H_9O_2^-$ intensity for normalisation. The same ratio evolution is also shown when profiling at -75°C. The latter shows for an unknown reason a shift (which is also observed on other ratios obtained when profiling at low temperature) and do not yield an acceptable linear correlation factor. The quantification protocol will therefore consist in profiling the samples at ambient temperature and observing the evolution of the intensity ratio $I(C_{60}^-)/I(C_5H_9O_2^-)$.

VI. 4. Results from the proposed protocols in PMMA - C_{60} layers on silicon

In this section we will explore the results from the developed protocols in terms of useful molecular ion yield, damage-less profiling and quantification of the blend composition. To investigate ToF-SIMS quantification accuracy, we will use measurements obtained with UV visible ellipsometry.

For this study, commercial solutions of Anisole dissolved PMMA were mixed with C_{60} previously dissolved in toluene. Resulting solutions, of 0, 0.0025, 0.005, 0.015, 0.025, 0.04, 1, 2, 5, 10 and 20 wt% C_{60}, where wt% expresses the total mass ratio of C_{60} on PMMA, were spin-coated on 200 mm Silicon base-wafers, leading to smooth layers in the range of 20 nm to 150 nm in thickness. Variability on the blending procedure through microliter pipettes leads to an estimated nominal concentration error of ±0.001 wt% over the whole considered range. Thickness measurements were made by spectroscopic ellipsometry. All samples were studied with ToF-SIMS: surface spectra and depth profiles were performed using the protocol proposed in section VI. 2. In both cases analysis was performed using negative secondary ions in the m/z=0 to 800 range. Crater morphology was observed with an AFM in tapping mode. For correlation with layer content quantification obtained with ToF-SIMS, we used UV visible ellipsometry. Indeed, the layer's extinction coefficient at 261 nm is characteristic of absorption by C_{60} [18]. UV visible spectroscopy is thus a good quantitative technique in order to quantify C_{60} loading rate in the films. However it dose not give any information on C_{60} in-depth distribution within the nanocomposite layers.

VI. 4. a- The advantage of polyatomic primary ions for surface spectra analysis

Surface spectra of the PMMA - 0.025 wt% C_{60} sample obtained with both Bi^+ and Bi_3^+ are shown in Figure VI.4. The C_{60} mass group appears with higher intensity on the spectrum acquired with Bi_3^+. As foreseen, the use of a polyatomic projectile enhances intensities for heavier molecular ions as shown in the bottom frame in Figure VI.4, and in particular for the C_{60} mass group which is almost totally absent from the Bi^+ spectrum. Molecular signal is also enhanced, with higher peaks at m/z = 85 and 101 (within others), corresponding to heavy fragments of the PMMA chain. However, what is less expected is that polymer fragmentation seems to be more severe with Bi_3^+. Indeed both elemental ions (C^-, O^-) and recombination products $C_xH_y^-$ feature much more intense peaks using Bi_3^+ (see top frame).

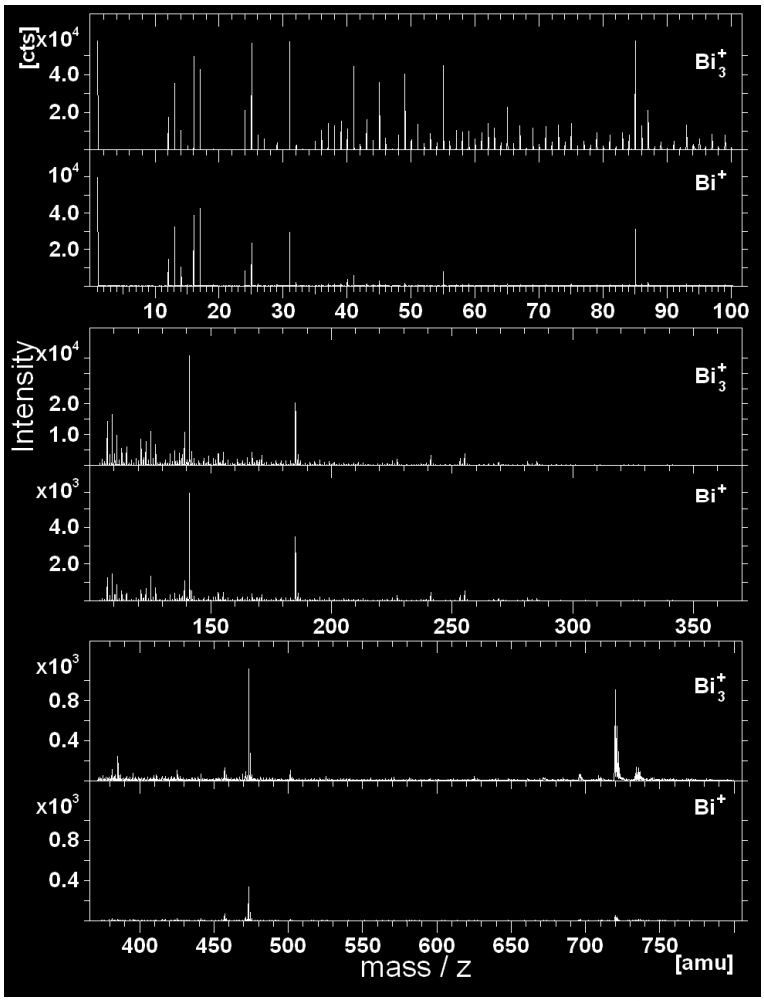

Figure VI.4 Surface spectra of PMMA - 0.025 wt% C_{60} blend with Bi^+ and Bi_3^+. Primary ion dose was 1×10^{12} ions/cm^2 for both spectra. Vertical scale is identical between spectra for each frame but changes between frames. Fragmentation is more severe with polyatomic projectile (top and middle frames up to m/z = 150). Heavier fragment intensities are enhanced with Bi_3^+. The C_{60} related mass group is only observed in the polyatomic primary ion spectrum at m/z = 720.

It might seem unnatural for a polyatomic projectile to enhance both heavy fragments and produce more small fragments at a time, but this might be explained by the differences in collision cascade discussed in the first chapter. While mono-atomic projectiles penetrate deeper in the sample than polyatomic ones, the energy they deposit at the surface of the sample is also lower and more energy is lost in the sample bulk. This reduced surface energy deposition implies less fragmentation at the surface, while fragments generated in the sample bulk would not be sputtered away and/or ionised. By opposition, the surface energy deposited by polyatomic ions is more important, which results in more fragmentation. These results are in agreement with observations of Wells et *al.* on PolyDiMethylSiloxane (PDMS) [19], although the different nature of PDMS and PMMA does not allow firm conclusions to be drawn about whether this phenomenon is due solely to the ion beam.
A focus on the C_{60} mass group obtained with both primary ions considering the same number of incident atoms is shown in Figure VI.5. This allows easy comparison of the C_{60}^- useful ion yield obtained with both primary ions. The latter was found to be ~15 times higher with Bi_3^+ than with Bi^+. For this reason, only Bi_3^+ will be used in the following for depth profiling of the layers.

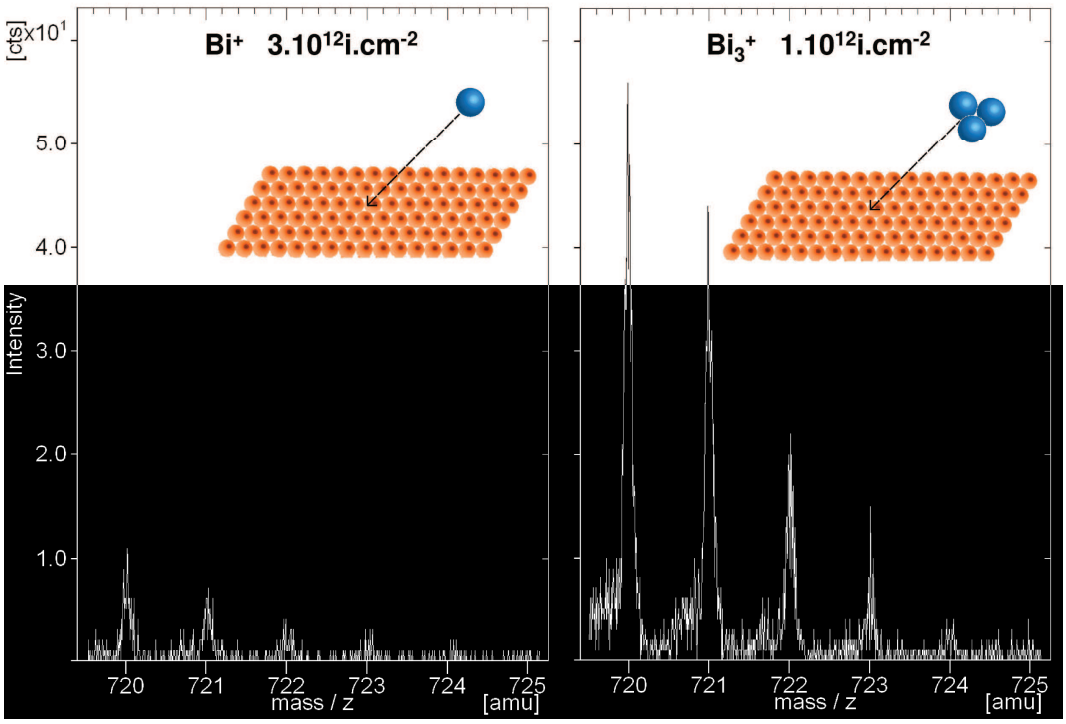

Figure VI.5 The m/z= 719 to 726 region of surface spectra of PMMA - 0.025 wt% C_{60} blend with the same number of incident bismuth atoms using both Bi^+ and Bi_3^+. C_{60}^- ion yield is found to be enhanced ~15 times when switching from Bi^+ to Bi_3^+. C_{60} isotopes are detected and intensities ratios are in good agreement with their isotopic abundances (see Table VI.i).

VI. 4. b- Properties of the depth profiles with the developed protocol

The depth profiling protocol developed in section VI. 3 allowed profiling with very stable secondary ion intensities in the organic layers. Figure VI.6 shows the profile obtained at ambient temperature for the PMMA - 0.015 wt% C_{60} sample. After a very short transient period inducing a "v" shaped dip in signal, the intensity of all the monitored organic fragments was found to be sustainable until reaching the substrate. Stability of the signals throughout the organic layer is comparable to what has been reported in recent literature [20], showing that no chemical information is lost during profiling. Damage cross sections of $C_5H_9O_2^-$ calculated in the stable part of the profiles were found to be inferior to 0.001 nm² for all samples, which is two orders of magnitude lower than values reported in [21] for 5 keV SF_5^+ sputtering.

We do however observe that substrate related signal starts to increase almost halfway though the 130 nm thick organic layer. This feature, which is clearly not ideal for the study of such blends, appears only in pure PMMA and in layers with low C_{60} content (< 1 wt%). It also appears on thinner layers of the same composition (not shown). As Si is unlikely to travel so far in the polymer we assumed this was an effect of ion beam induced roughness and tried to reduce it by lowering sample temperature during profiling following recommendations in [22-23]. Best profiles were obtained at -75°C: PMMA - 0.015 wt% C_{60} sample profile obtained in these conditions is displayed in Figure VI.7. Indeed we observe much better depth resolution features, with a sharp substrate signal slope and only slight degradation of signal stability through the organic layer. Moreover, signal decline after the substrate interface is improved by a factor two, from 2×10^{16} ions.cm^{-2}/decade at 25°C to 1×10^{16} ion.cm^{-2}/decade in the low temperature case. Further lowering of sample temperature did not show quantitative profile

improvement. AFM studies of crater bottoms confirmed that these improvements were due to reduction of beam induced roughness, which was found to be more important at ambient temperature, in agreement with more complete studies in [24]. AFM images of craters after a sputtering halfway through the layers are shown in Figure VI.8. Notice that similar results were obtained on all blends whose C_{60} composition was inferior to 0.04 wt%.

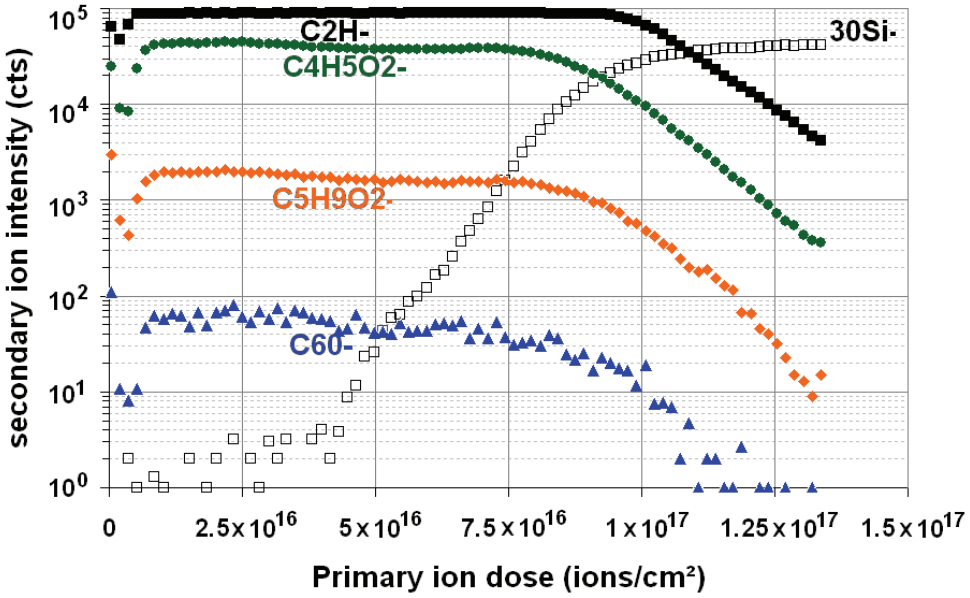

Figure VI.6 Depth profile of a PMMA - 0.015 wt% C_{60} blend layer at 25°C. Notice the short transient and the stability of organic compound ions in the first half of the profile.

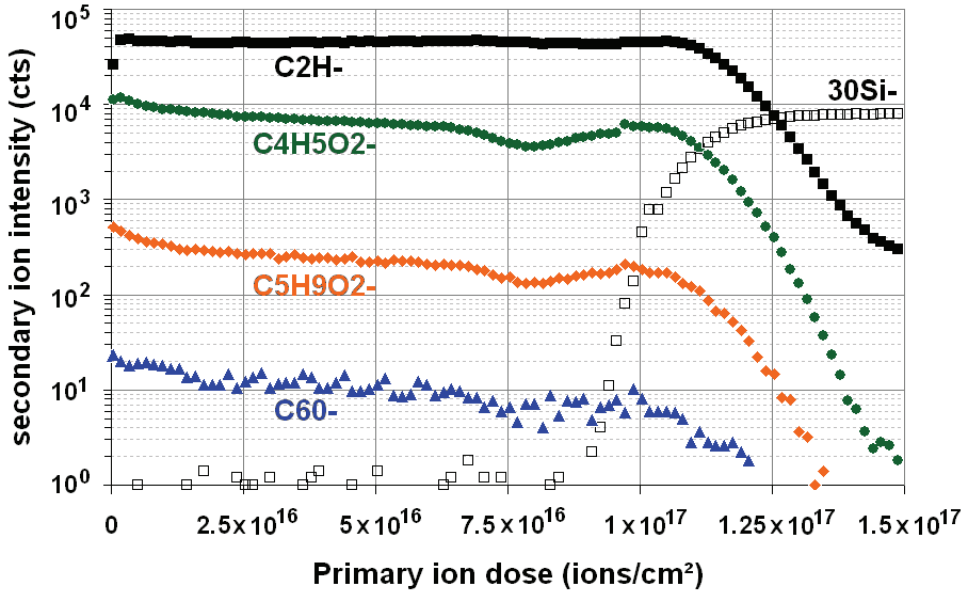

Figure VI.7 Depth profile of a PMMA - 0.015 wt% C_{60} blend layer at -75°C. Notice the sharp increase of substrate signal and the fast decrease of organic compound ions in the substrate.

On the contrary, profiles obtained on layers with higher percentage of C_{60} featured sharper interfaces. More interestingly, interface sharpness (and thus depth resolution) seems to evolve as a function of the C_{60} content, as shown by profiles in Figure VI.9. Notice that all samples did not have similar layer thickness, which explains the discrepancy in interface position. The C_{60}^- signal decay is found to vary monotonously with C_{60} content, starting from 550 s/decade

in PMMA - 0.015 wt% C_{60} blends (in lower content blends, signals were too low to be able to measure their decay lengths) to 30 s/decade in PMMA - 20 wt% C_{60} blends. The signal decay dependence on C_{60} content can be fitted trough a power law with a high degree of confidence (decay ~ $100\times(C_{60}\,wt\%)^{-0.4}$; R^2=0.9965), which shows a clear correlation between both values.

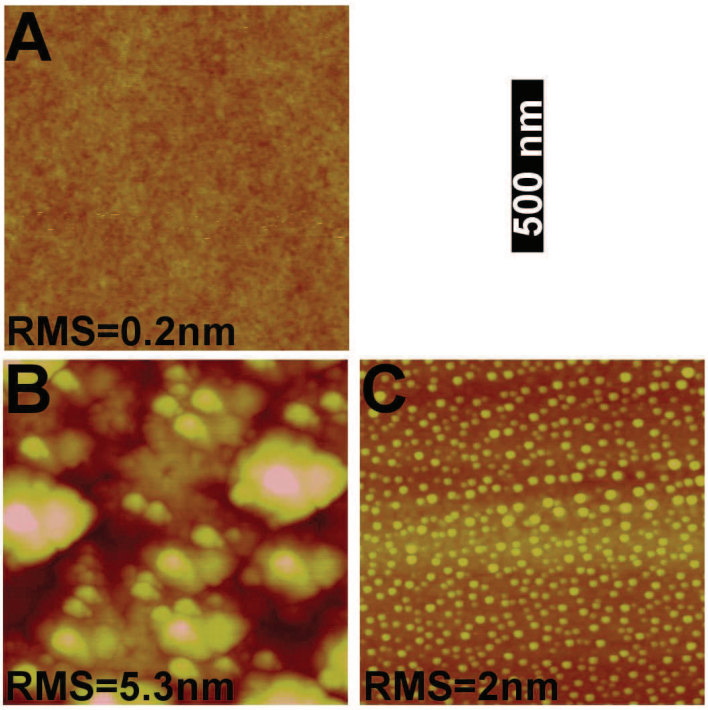

Figure VI.8.A AFM topography mapping of PMMA - 0.025 wt% C_{60} sample surface.
B AFM topography mapping of PMMA - 0.025 wt% C_{60} sample crater bottom after sputtering with 250 eV Cs^+ halfway through the organic layer at 25°.
C AFM topography mapping of PMMA - 0.025 wt% C_{60} sample crater bottom after sputtering with 250 eV Cs^+ halfway through the organic layer at -75°.

This could be interpreted as an effect of the increased conductivity of the layers with increased C_{60} content. Indeed C_{60} is, for device purposes, included in the blend to serve as an electron carrier, since PMMA is a pure insulator and does not allow charge exchange. During ToF-SIMS analysis, sample charging could thus occur during profiling of low C_{60} content layers and modify the organic matrix while profiling, creating the three dimensional structures observed after sputtering in AFM (see Figure VI.8.B), This would also explain the roughness reduction after sputtering at -75°C, since in this configuration charge compensation with low energy electron beam was performed (while it was not used when profiling at ambient temperature). However, such sample charging effects also usually have repercussions on the ToF-SIMS spectra, inducing peak shift and/or severe loss of mass resolution. As this was not the case in our study, it means the hypothesis formulated below is not valid. Another explanation would be the reaction of the PMMA polymers under low energy Cs^+ irradiation. If one looks at the features present on the AFM topography image in Figure VI.8.B and compare them to those present on the image in Figure VI.8.C, one can see repetitive structures of ~100 nm diameter, while no such structures are observed at low temperature. Such structures could be due to a thermally triggered PMMA reaction under ion beam irradiation (such as crystallisation, as suggested in [25-28]), which would explain why the phenomenon is absent (or reduced) at low temperature. As already pointed out, the number of fullerenes by repeat unit in our samples is dictated by the mass ratio and ranges from 3.5×10^{-4} (for 0.0025 wt% C_{60}) to 2.8 (for 20 wt% C_{60}). Considering that the average molecular weight of

the PMMA polymer used here was 950000 u, we can deduce the number of fullerenes by polymer chain in the blends.

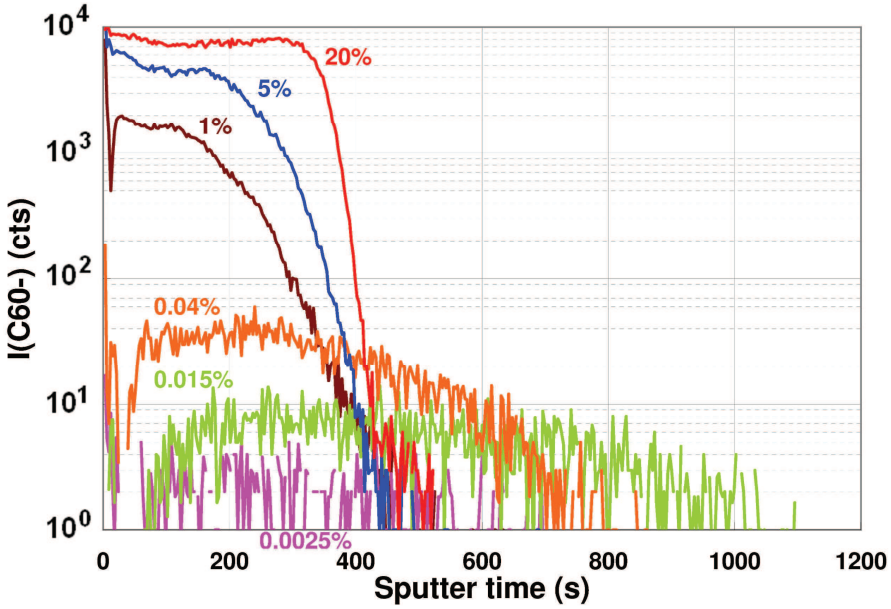

Figure VI.9 Raw C_{60}^- intensity profiles in a selection of samples. Other profiles show similar behaviour (not shown for clarity).

We find out that while for low C_{60} content blends, this number is considerably low (e.g. 20 fullerenes by chain for a 0.015 wt% content, 53 for a 0.04 wt% content), it is extremely high in high C_{60} content blends (e.g. 6600 fullerenes by chain for a 5 wt% content, 26400 for a 20 wt% content). The hypothesis is thus that the number of fullerenes is too high in these blends for the PMMA to be able to react under irradiation, thus preventing the formation of three dimensional structures (and roughness pile-up). This is confirmed by the fact that no features at all appear on crater bottom of PMMA - 20 wt% C_{60} samples, even when looking at a larger scale, as shown in Figure VI.10. As in the following, most of the samples of interest will feature high C60 content (>5 wt%), this property allows us to perform profiling at ambient temperature with improved depth resolution.
Finally, as proposed in section VI. 3, plotting the intensity ratio $C_{60}^-/C_5H_9O_2^-$ against nominal C_{60} content revealed an excellent linear correlation, as shown in Figure VI.11.A, demonstrating the ability of the protocol to quantify simply the C_{60} content of such layers. Moreover, the obtained linear relationship seems to be valid on the whole concentration range, from C_{60} as a trace element to matrix element. This is interesting because it allows for very accurate characterisation of subtle variation in blend composition. UV visible ellipsometry also allowed quantification of the blends C_{60} content, as shown in Figure VI.11.B. However one drawback of this technique is its lack of sensitivity (as seen in Figure VI.11.B, no significant signal is obtained for C_{60} contents below 1 wt%). Furthermore, it only yields average information on the layer contents and do not allow in-depth composition studies, which can be interesting for understanding device properties, as we will see below.

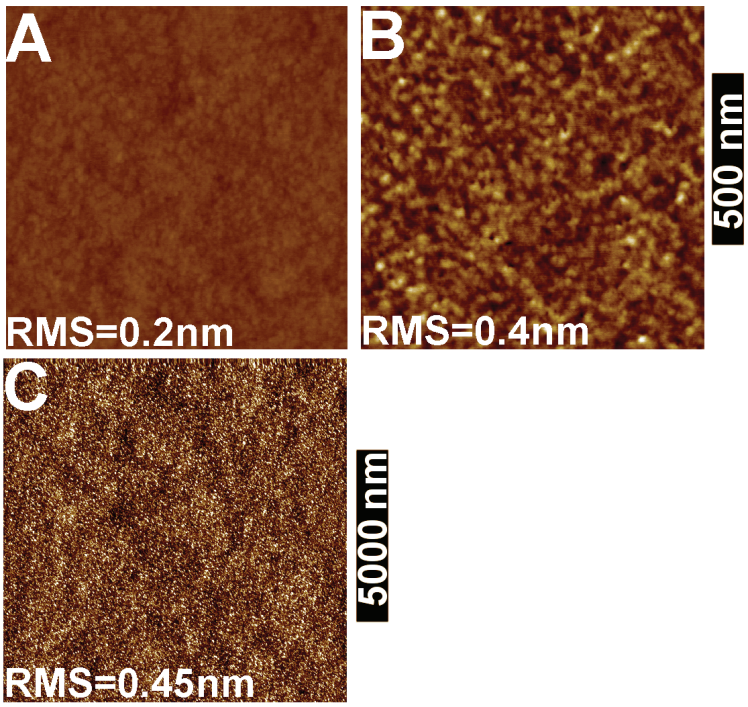

Figure VI.10.A 1×1 µm AFM topography mapping of PMMA - 20 wt% C_{60} sample surface.
B 1×1 µm AFM topography mapping of PMMA - 0.025 wt% C_{60} sample crater bottom after sputtering with 250 eV Cs^+ halfway through the organic layer at 25°.
C 10×10 µm AFM topography mapping of PMMA - 0.025 wt% C_{60} sample crater bottom after sputtering with 250 eV Cs^+ halfway through the organic layer at 25°.

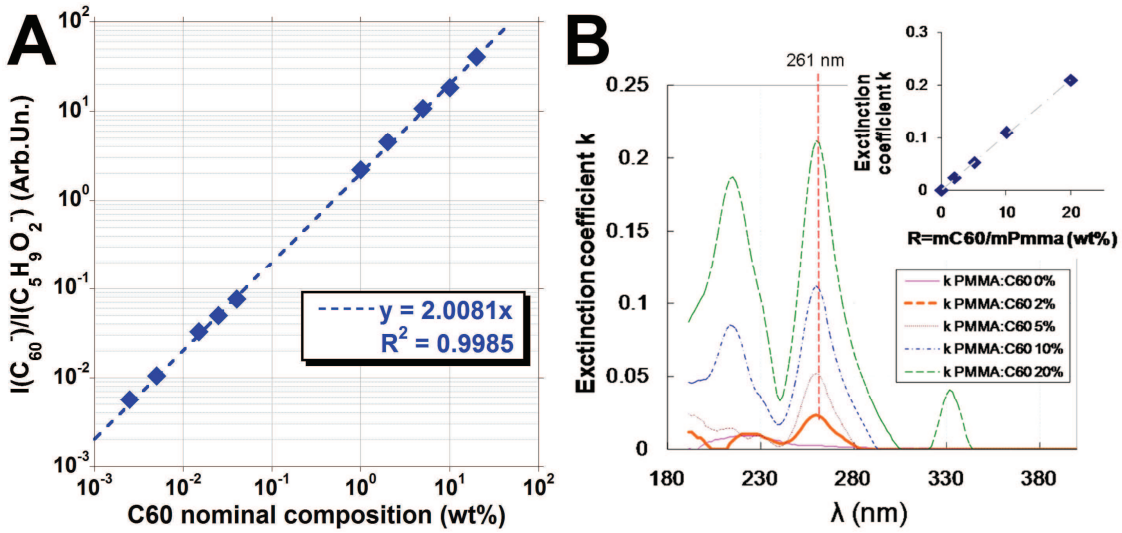

Figure VI.11.A Intensity ratios $I(C_{60}^-)/I(C_5H_9O_2^-)$ obtained at ambient temperature on the whole range of composition show an excellent linear dependence with layer content in C_{60}.
B Extinction coefficient spectra obtained by UV visible ellipsometry on various high C_{60} content PMMA - C_{60} films. Insert: extinction coefficient at 261 nm shows a linear dependence with layer content in C_{60}.

VI. 5. Results exploitation: useful knowledge earned through quantitative analysis

The growing interest in resistive memory technologies [29] and the recent developments in the field of organic electronics, have motivated research into polymer resistive memories. Their potential advantages include low fabrication cost, synthetic

tailorability [1] and self-organisation capabilities [30]. However, the electrodes often employ oxidisable metals or metal oxides (such as Al [31] or ITO [32]) being already known for their resistive switching properties. The properties of the final device can therefore be due in a large part to the electrode material's reaction to the activation anneal. Here we perform, using the protocols developed above, in depth chemical composition of PMMA - C_{60} based organic devices with inert Pt electrodes in order to understand the cause of their electric behavior. Samples consist of a device structures featuring a full sheet bottom Pt electrode, an organic layer (either pure PMMA for reference or PMMA - 10 wt% C_{60} blend), and 300 µm spaced 2500 μm^2 square top Pt electrodes. All samples were dried at 120°C for 90s. PMMA and blend layers were respectively ~130 nm and ~60 nm thick before an additional thermal treatment assimilated to an activation anneal, consisting in a 30 minutes annealing at 180°C in N_2 atmosphere, performed before deposition of the top electrodes. The study of the evolution of the organic layer composition and interaction with electrode upon annealing is thus needed for comprehension of the final device electrical properties. ToF-SIMS surface spectra and depth profiling were performed on all four samples in the space available between top electrodes in order to avoid unnecessary Pt implantation into the organic layers during profiling. Electrical characterisation was performed with double-sweep I-V measurements on both annealed and non annealed PMMA - 10 wt% C_{60} devices.

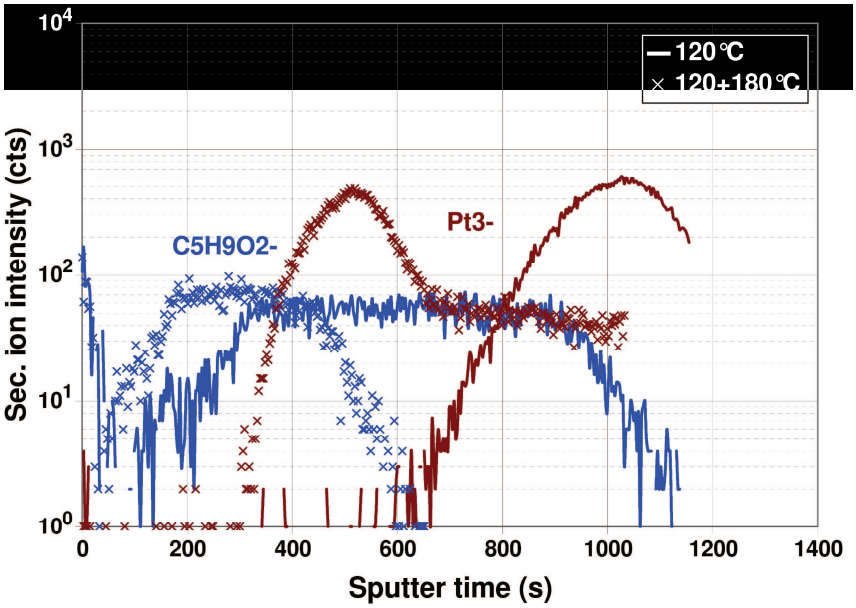

Figure VI.12 Depth profiles of the pure PMMA reference samples before and after annealing at 180°C.

VI. 5. a- Annealing behaviour of the reference PMMA layers

Profiles of the samples containing only PMMA before and after annealing are shown in Figure VI.12. Pt_3^- was preferred to Pt^- and Pt_2^- as secondary ion representative of the electrode material because of its peak is found at m/z = 585, in the region where no oligomer peaks are observed (see Figure VI.1.D) and where little mass interference can be expected (no C_n isotope being detected at mass 585 u). Intensities relative to the monomer ion $C_5H_9O_2^-$ are quite weak, but stable along the whole organic layers after a transient period due to the insulating nature of the layer. Furthermore, neither their intensity nor profile shape does vary between annealed and non annealed sample, which indicates no change in sample composition. Moreover, we do not observe any diffusion of the electrode material within the

organic layer after annealing, as shown by the fact that $C_5H_9O_2^-$ and Pt_3^- signals feature appreciably similar decay (or raise) in both samples. However, the sputter time needed to reach the electrode interface (defined as the point of maximum intensity of Pt_3^- signal) is almost halved after annealing. This phenomenon might reveal a change in material density, combined to a certain extent with layer shrinking.

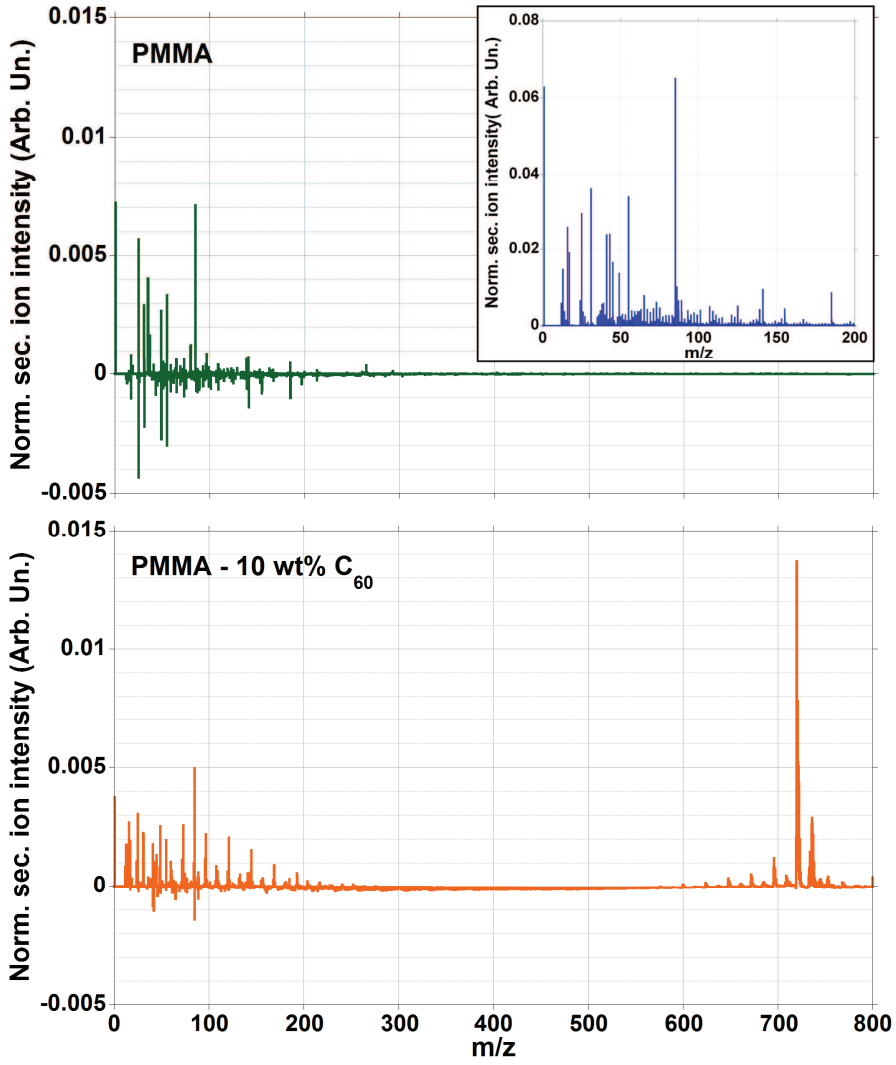

Figure VI.13 Top frame: differential mass spectrum obtained on pure PMMA samples (spectrum after annealing - spectrum before annealing). Insert: PMMA surface spectrum before annealing. Bottom frame: differential mass spectrum obtained on PMMA - 10 wt% C_{60} samples (spectrum after annealing - spectrum before annealing).

To evaluate the layer shrinking, we removed the organic layer on parts of the sample using both physical means (scratching the surface of the layer with a metallic tip) and chemical means (using partial sample dip in acetone) and measured the created steps by stylus profilometry. The results indicated that sample shrinking to half of its original thickness was indeed occurring upon annealing since the thicknesses were found to be of 130 ±5 nm before annealing and of 77.5 ±5 nm after annealing. This result correlates very well with the fact that sputter duration in annealed sample was approximately half of that in the non annealed one. Such a layer shrinkage can be explained by the fact that the annealing temperature, 180°C, is well above the glass transition temperature of PMMA, which provokes partial or total melting of the layer. During such an anneal, sample growth by-products such as excess monomer

materials, organic contamination or even residual solvents can therefore be evaporated. To make sure this layer shrinkage was not paired with changes in layer composition, especially at the sample surface, we acquired ToF-SIMS surface spectra in both samples. Comparison was performed by subtraction of both spectra as shown in Figure VI.13. In this figure, mass calibration is carefully done in both spectra using the same secondary ions to avoid excessive peak misfit. Then both spectra are normalised to their total ion counts and point to point subtraction is performed. In these spectra, positive loadings represent peaks observed after annealing but not (or less) before, while negative loadings represent peaks observed before annealing but not (or less) after. While normalised spectra without subtraction feature peak intensities of ~0.07 (see insert in Figure VI.13 top frame), no such intense peaks are found on the subtracted spectrum. Indeed most peaks feature intensities lower than 0.07, which is already ten times lower than the intensities in the original spectra. Moreover, most peaks are doubled (they are present both in negative and positive loadings) which means that there was still a slight misfit in mass calibration between both spectra. Yet, the peak at m/z = 85 seems to show higher intensity after annealing than before. Considering that this peak is associated to $C_4H_5O_2^-$, a main fragment of the PMMA polymer chain, we can consider that a slight but significant part of the original polymer was de-polymerised during annealing. Apart from this feature, no change in chemical composition is observed upon annealing.

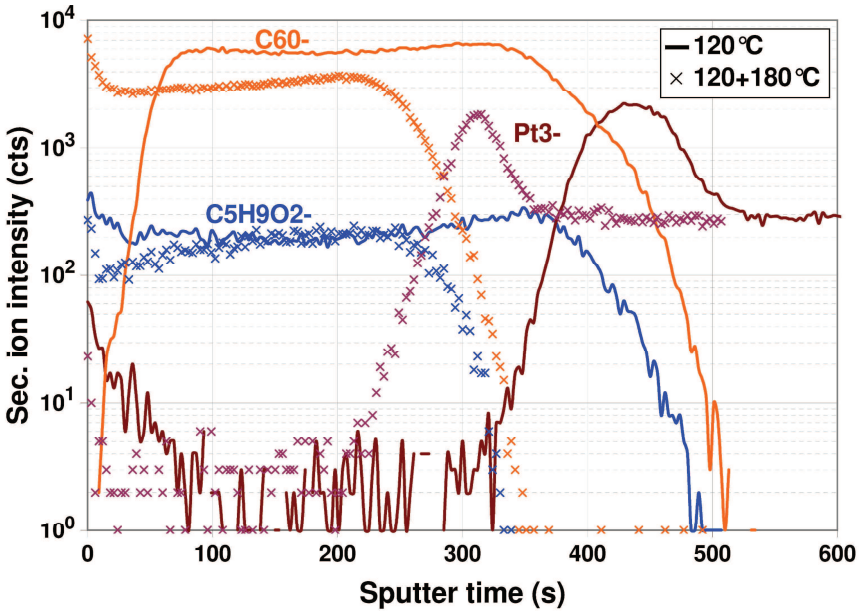

Figure VI.14 Depth profiles of the PMMA - 10 wt% C_{60} samples before and after annealing at 180°C.

On the contrary, important changes are observed on the subtracted spectra obtained in the PMMA - 10 wt% C_{60} samples, shown in Figure VI.13 bottom frame. While same features than with pure PMMA are obtained in the low mass region, there are important positive loadings in a region corresponding to the C_{60} related mass group around m/z = 720. This shows that C_{60} was absent (or in very low quantities) from the sample's surface in the non annealed sample while it is present in significant proportion after annealing. It thus implies that C_{60} segregation did occur in those samples. To better investigate this point, we can refer to the samples depth profiles displayed in Figure VI.14.

VI. 5. b- Annealing behaviour of the device structure

Concerning the polymer and electrode materials, roughly the same conclusions as for pure PMMA can be drawn. There is indeed no significant evolution of monomer ion intensity with annealing and no Pt elemental diffusion is observed, as testified by the equivalent signal decays before and after annealing. Pt signals in the first few seconds of the profiles are assumed to be artefacts. Again, we observe layer shrinkage after annealing, although to a slightly lesser extent than in pure PMMA: the measured layer thicknesses were 55 ±5 nm before annealing and of 32.5 ±5 nm after annealing. However, important differences are observed in the C_{60}^- signal. First, no C_{60}^- signal is observed for about 50-70 s sputtering at the beginning of the non annealed sample profile. This cannot be due to a transient region since none of the other organic secondary ions features similar behaviour in the same sample. Meanwhile, stable C_{60}^- signal is obtained through the whole organic layer on the annealed sample. This seems to indicate, as observed in surface spectra, important relocation of the fullerenes and segregation towards surface after annealing.

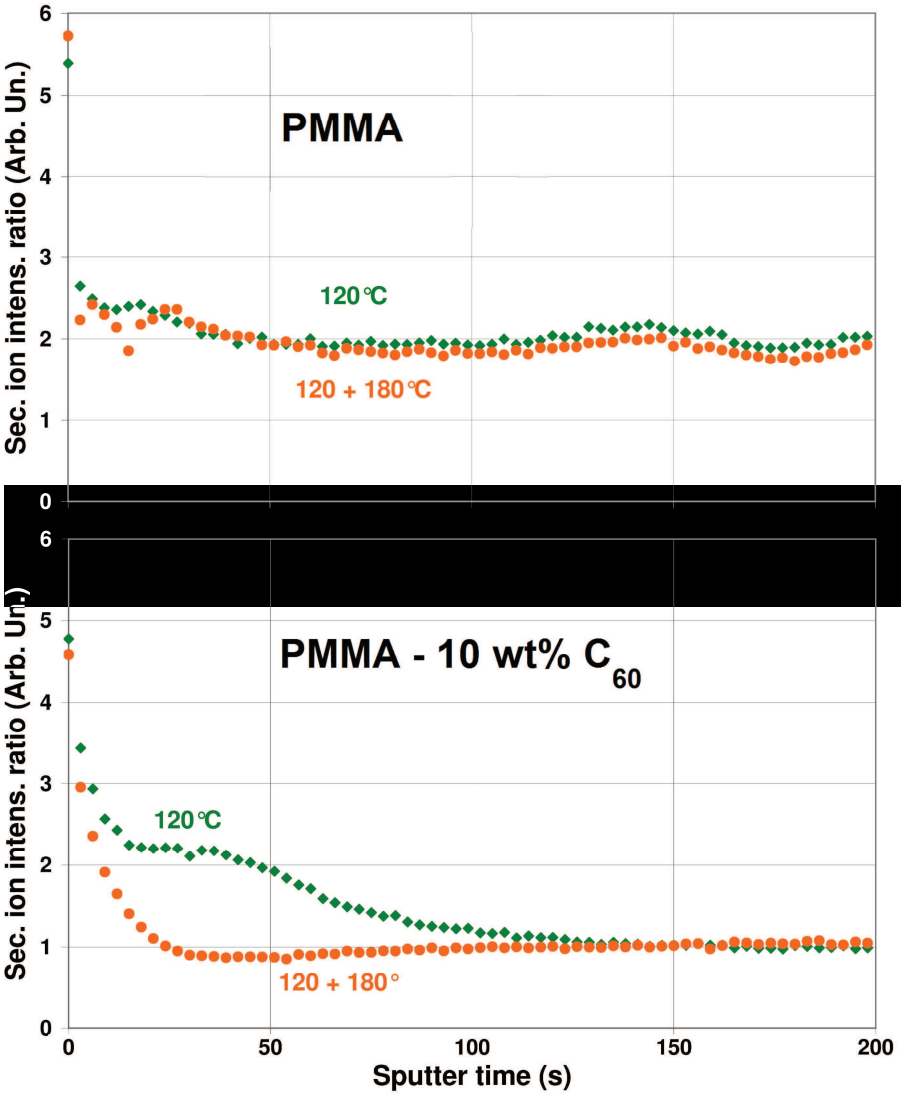

Figure VI.15 In-depth evolution of the O-/C- secondary ion intensity ratio in pure PMMA samples (top frame) and PMMA - 10 wt% C_{60} samples (bottom frame) before and after annealing.

Further confirmation of this hypothesis can be obtained by looking at the in-depth evolution of oxygen. Indeed, as PMMA contains two oxygen atoms per repeat unit, fullerenes contain no oxygen. The samples relative composition in oxygen and carbon can be monitored using appropriate ion peak ratios such as O^-/C^-, as done in Figure VI.15. As expected, no change is detected in pure PMMA layers (top frame) between annealed and non annealed sample.

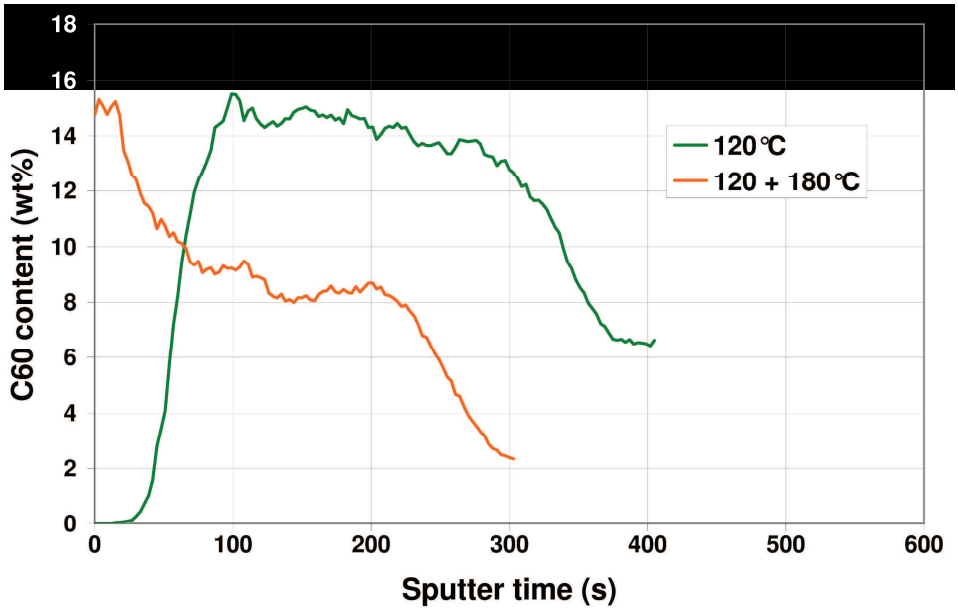

Figure VI.16 In-depth evolution of the C_{60} content in PMMA - 10 wt% C_{60} samples before and after annealing.

The relatively constant ratio value along the layer also confirms that no significant chemical composition change is occurring during annealing. Similarly, the ratio obtained in the annealed PMMA - 10 wt% C_{60} sample does not vary in depth (at the exception of a surface transient due to the residual oxygen present in the analysis chamber). However, a clear change is observed in the non annealed sample. While the ratio's bulk value is found to be similar to that after annealing, a rather stable plateau appears in the first moments of the profile, up to ~50 s sputtering as observed on the depth profiles in Figure VI.14. The ratio value in the plateau region is approximately twice that in bulk and is close to the value observed in pure PMMA. These findings support the hypothesis of C_{60} segregation in the bulk layer before annealing, with the first few nanometres actually constituted of pure PMMA. However,, after annealing there seems to be more C_{60} at the surface of the sample than in its bulk. In-depth monitoring of the C_{60} composition can be performed using the protocol developed in section VI. 3. Composition profiles of both samples are shown in Figure VI.16. In addition to the features discussed above, we also observe that the bulk layer C_{60} content has been halved after annealing. This is due to the diminution of C_{60}^- secondary ion yields while those of other organic fragments such as $C_5H_9O_2^-$ did not vary with annealing (see profiles on Figure VI.14). This phenomenon results in a C60 dose loss of approximately 50% after annealing, which would support the hypothesis that annealing leads to a partial evaporation of the organic layer, thus explaining why layer thickness was found to be lower after annealing. In addition to this material evaporation, the fullerenes seem to exo-diffuse during the annealing, which would explain their high concentration at the surface of the sample after annealing. Such phenomenon might also lead to the creation of fullerene clusters, as observed in [33] with Phenyl-C61-Butyric acid Methyl ester (PCBM), a type of functionalised fullerene.

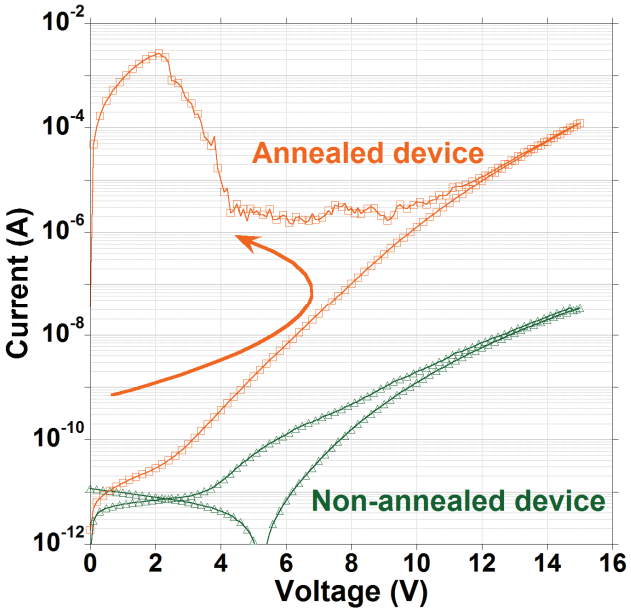

Figure VI.17 Double sweep I-V characteristics on PMMA - 10 wt% C_{60} devices before and after annealing.

Double-sweep I-V measurements performed on both annealed and non annealed samples are shown in Figure VI.17. The same measurements on both PMMA reference samples led to flat distributions of the current in function of applied voltage, characteristic of insulators (not shown). In contrast, both PMMA - 10 wt% C_{60} samples showed conductive behaviour, with a constant increase of current in function of voltage (during the first voltage increase cycle). A greater slope is observed on this part of the graph on annealed samples, indicating better sample conductivity after annealing. Furthermore, above a threshold voltage value, the annealed device exhibited a hysteresis in current with negative differential resistance behaviour [1, 34-35]. Following these observations, it was determined that by using an appropriate voltage sweep sequence, the device could be set and reset using the same voltage polarity and provide behaviour fit for memory applications [36]. In comparison, no significant hysteresis was observed in the non annealed sample. Both layer thickness reduction and C_{60} segregation in the organic layer after annealing observed with ToF-SIMS might be at the origin of the appearance of such hysteresis.

CHAPTER VI Conclusion

In this chapter we discussed the different practical solutions developed to obtain quantitative in-depth information on specific organic nanocomposite layers consisting of a polymer, PMMA, and a fullerene, C_{60}. We first performed systematic studies on experimental conditions to allow enhanced visualisation of the fullerenes inside their polymer matrix. Then we focused on the setup of a protocol enabling damage-less depth profiling of the organic layers. Finally we optimised data treatment in order to yield quantitative information on the blends composition.
Detection of C_{60} related ions was made possible even in extremely low concentration blends by the use of polyatomic projectiles Bi_3^+ for analysis and detection of negative secondary ions. This is attributed to the ability of Bi_3^+ to better sputter and ionise fullerenes (or heavy

compounds) than Bi^+, due to the different development of the collision cascade. We showed that characteristic fragmentation of C_{60} was observable, with characteristic features that helped understand the formation of odd-numbered fullerenes.
The developed depth profiling protocol, using 250 eV Cs^+ as primary ion for sputtering and operation of the beams in non interlaced mode enabled profiling of 20 to 130 nm thick layers. Organic secondary ion intensities were particularly stable through the organic layer, showing minimal loss of information during profiling. Sputter beam induced roughness did hinder the depth resolution of the profiles in the most resistive samples; however this effect was reduced when profiling the sample at lower temperature. However no extensive roughness was observed after sputtering at ambient temperature in more conductive samples (i.e. with higher C_{60} contents).
The protocol established for quantification of the blends composition was found to be very efficient and accurate, allowing quantification of C_{60} from concentrations of 0.0025 wt% to 20 wt%. Indeed the variation of secondary ion intensity ratio $I(C_{60}^-)/I(C_5H_9O_2^-)$ with nominal C_{60} content was found to be linear with an excellent correlation factor. This work therefore showed that ToF-SIMS was able to detect and quantify extremely small quantities as well as high concentrations of C_{60} in a PMMA matrix.
It was thus used to study the evolution of device structures for resistive memories upon low temperature annealing. We observed a layer contraction after annealing, associated to a segregation of the fullerenes towards the surface of the organic layer. This in-depth composition change was found to be linked with the creation of a hysteresis in I-V electrical properties of the device, leading to the creation of a memory cell.

REFERENCES

[1] Q.-D. Ling, D.-J. Liaw, C. Zhu *et al.*, *Polymer Electronic Memories: Materials, Devices and Mechanisms*, Prog. Polym. Sci., 33 (**2008**) 917-978.
[2] B. De Salvo, J. Buckley and D. Vuillaume, *Recent Results on Organic-Based Molecular Memories*, Current Applied Physics, In Press, Corrected Proof.
[3] M.F. Mabrook, A.S. Jombert, S.E. Machin *et al.*, *Memory Effects in Mis Structures Based on Silicon and Polymethylmethacrylate with Nanoparticle Charge-Storage Elements*, Materials Science and Engineering: B, 159-160 (**2009**) 14-17.
[4] G. Nagy, P. Lu and A. Walker, *An Investigation of Secondary Ion Yield Enhancement Using Bi_n^{2+} (N=1, 3, 5) Primary Ions*, J. Am. Soc. Mass Spectrom., 19 (**2008**) 33-45.
[5] G. Nagy and A.V. Walker, *Enhanced Secondary Ion Emission with a Bismuth Cluster Ion Source*, Int. J. Mass Spectrom., 262 (**2007**) 144-153.
[6] A.J. Fahey, G. Gillen, P. Chi and C.M. Mahoney, *Performance of a C60+ Ion Source on a Dynamic Sims Instrument*, Appl. Surf. Sci., 252 (**2006**) 7312-7314.
[7] S.C.C. Wong, R. Hill, P. Blenkinsopp *et al.*, *Development of a C60+ Ion Gun for Static Sims and Chemical Imaging*, Appl. Surf. Sci., 203-204 (**2003**) 219-222.
[8] R. Hill and P.W.M. Blenkinsopp, *The Development of C60 and Gold Cluster Ion Guns for Static Sims Analysis*, Appl. Surf. Sci., 231-232 (**2004**) 936-939.
[9] A.G. Sostarecz, S. Sun, C. Szakal, A. Wucher and N. Winograd, *Depth Profiling Studies of Multilayer Films with a C60+ Ion Source*, Appl. Surf. Sci., 231-232 (**2004**) 179-182.
[10] N. Kato, Y. Yamashita, S. Iida, N. Sanada and M. Kudo, *Analysis of Tof-Sims Spectra from Fullerene Compounds*, Appl. Surf. Sci., 255 (**2008**) 938-940.
[11] C.D. Finch, R.A. Popple, P. Nordlander and F.B. Dunning, *Formation of Long-Lived C60- Ions in Rydberg Atom-C60 Collisions*, Chem. Phys. Lett., 244 (**1995**) 345-349.
[12] M.Y. Amusia, A.S. Baltenkov and B.G. Krakov, *Photodetachment of Negative C60- Ions*, Phys. Lett. A, 243 (**1998**) 99-105.
[13] M. Lezius, P. Scheier, M. Foltin *et al.*, *Interaction of Free Electrons with C60: Ionization and Attachment Reactions*, Int. J. Mass Spectrom. Ion Processes, 129 (**1993**) 49-56.
[14] Q. Kong, L. Zhao, J. Zhuang *et al.*, *Formation of Odd-Numbered Fullerene-Related Species and Its Relation to the Formation of Metallofullerenes*, Int. J. Mass Spectrom., 209 (**2001**) 69-79.
[15] L. Xiao, G.G. Wildgoose, A. Crossley and R.G. Compton, *The Electroreduction Of "C60" Films in Aqueous Electrolyte Does Not Lead to Alkali Metal Ion Insertion--Evidence for the Involvement of Adventitious Poly-Epoxidated C60 (C60on)*, Sensors and Actuators B: Chemical, 138 (**2009**) 397-401.
[16] K. Endo, N. Kobayashi, M. Aida and T. Hoshi, *Spectral Analysis of Polystyrene, Polypropylene, and Poly(Methyl Methacrylate) Polymers in Tof Sims and Xps by Mo Calculations Using the Model Oligomers*, Polym. J. (Tokyo, Jpn.), 28 (**1996**) 901-910.
[17] M.S. Wagner, *Molecular Depth Profiling of Multilayer Polymer Films Using Time-of-Flight Secondary Ion Mass Spectrometry*, Anal. Chem., 77 (**2004**) 911-922.
[18] M. Charbonneau, R. Tiron, J. Buckley *et al.*, *Study on C60 Doped Pmma for Organic Memory Devices*, MRS Online Proceedings Library, 1250 (**2010**) null-null.
[19] D. Wells, H. Moon and J. Gardella, *Time of Flight Secondary Ion Mass Spectrometric Determination of Molecular Weight Distributions of Low Polydispersity Poly(Dimethyl Siloxane) with Polyatomic Primary Ions*, J. Am. Soc. Mass Spectrom., 20 (**2009**) 1562-1566.
[20] L. Houssiau, B. Douhard and N. Mine, *Molecular Depth Profiling of Polymers with Very Low Energy Ions*, Appl. Surf. Sci., 255 (**2008**) 970-972.
[21] M.S. Wagner, *Impact Energy Dependence of Sf5+-Induced Damage in Poly(Methyl Methacrylate) Studied Using Time-of-Flight Secondary Ion Mass Spectrometry*, Anal. Chem., 76 (**2004**) 1264-1272.
[22] C.M. Mahoney, A.J. Fahey and G. Gillen, *Temperature-Controlled Depth Profiling of Poly(Methyl Methacrylate) Using Cluster Secondary Ion Mass Spectrometry. 1. Investigation of Depth Profile Characteristics*, Anal. Chem., 79 (**2006**) 828-836.
[23] C.M. Mahoney, A.J. Fahey, G. Gillen, C. Xu and J.D. Batteas, *Temperature-Controlled Depth Profiling of Poly(Methyl Methacrylate) Using Cluster Secondary Ion Mass Spectrometry. 2.*

Investigation of Sputter-Induced Topography, Chemical Damage, and Depolymerization Effects, Anal. Chem., 79 (**2006**) 837-845.
[24] C.M. Mahoney, A.J. Fahey, G. Gillen, C. Xu and J.D. Batteas, *Temperature-Controlled Depth Profiling in Polymeric Materials Using Cluster Secondary Ion Mass Spectrometry (Sims)*, Appl. Surf. Sci., 252 (**2006**) 6502-6505.
[25] M. Gheorghiu, I. Rusu and G. Popa, *Surface Modification of the Poly(Ethyleneterephthalate) Foil by Reactive Ion Beam Bombardment*, Vacuum, 47 (**1996**) 1093-1102.
[26] B.C. Okerberg, H. Marand and J.F. Douglas, *Dendritic Crystallization in Thin Films of Peo/Pmma Blends: A Comparison to Crystallization in Small Molecule Liquids*, Polymer, 49 (**2008**) 579-587.
[27] H.D. Keith and J.F.J. Padden, *A Phenomenological Theory of Spherulitic Crystallization*, J. Appl. Phys., 34 (**1963**) 2409-2421.
[28] R.V. Castillo and A.J. Müller, *Crystallization and Morphology of Biodegradable or Biostable Single and Double Crystalline Block Copolymers*, Prog. Polym. Sci., 34 (**2009**) 516-560.
[29] J. Hutchby, *Itrs Summer Conference - San Francisco - 14 July 2010*.
[30] C. De Rosa, F. Auriemma, R. Di Girolamo *et al.*, *Enabling Strategies in Organic Electronics Using Ordered Block Copolymer Nanostructures*, Adv. Mater. (Weinheim, Ger.), 22 (**2010**) 5414-+.
[31] F. Verbakel, S.C.J. Meskers, R.A.J. Janssen *et al.*, *Reproducible Resistive Switching in Nonvolatile Organic Memories*, Appl. Phys. Lett., 91 (**2007**).
[32] B. Cho, T.W. Kim, M. Choe *et al.*, *Unipolar Nonvolatile Memory Devices with Composites of Poly(9-Vinylcarbazole) and Titanium Dioxide Nanoparticles*, Organic Electronics, 10 (**2009**) 473-477.
[33] A. Laiho, H.S. Majumdar, J.K. Baral *et al.*, *Tuning the Electrical Switching of Polymer/Fullerene Nanocomposite Thin Film Devices by Control of Morphology*, Appl. Phys. Lett., 93 (**2008**).
[34] H.S. Majumdar, J.K. Baral, R. Österbacka, O. Ikkala and H. Stubb, *Fullerene-Based Bistable Devices and Associated Negative Differential Resistance Effect*, Organic Electronics, 6 (**2005**) 188-192.
[35] M. Vilkman, K. Solehmainen, A. Laiho, H.G.O. Sandberg and O. Ikkala, *Negative Differential Resistance in Polymeric Memory Devices Containing Disordered Block Copolymers with Semiconducting Block*, Organic Electronics, 10 (**2009**) 1478-1482.
[36] M. Charbonneau, J. Buckley, R. Tiron *et al.*, *Ndr Controlled Multilevel Programming in Porram with All-Organic Active Layer and Inert Electrodes,* Abstract #1309, 219th ECS Meeting, (**2010, http://www.electrochem.org/meetings/scheduler/abstracts/219/1309.pdf**).

CONCLUSIONS AND PERSPECTIVES

In its search for faster, smaller, cheaper and more efficient devices, the semiconductor industry has during half a century, and especially during last decade, given birth to a diversity of architectures and introduced many complex combinations of materials. To improve the properties of devices, a detailed understanding of their composition is required. ToF-SIMS is one of the tools nowadays used for characterization of standard materials and structures. However, it does not commonly enable quantified, depth resolved characterisation of advanced samples for microelectronics. This is firstly due to its lack of depth resolution, prohibiting accurate analysis of the nanometre thick structures encountered in current generation devices. It is also due to the fact that ToF-SIMS is still a semi-quantitative technique, very sensitive to matrix effects and experimental conditions, requiring calibration for both depth and concentration scales.

In this thesis work, we thus endeavoured to address such problems using a commercially available instrument, without specific instrumental customization. We proposed an overview of the resources at our disposal, which we organized in four kinds of approaches. Namely sample preparation, experimental parameters, data treatment and comparison with other cutting edge techniques were used. For each of those, specific protocols were setup in order to answer characterisation needs. Those were used to improve the instrument's ability to yield accurate information on materials and structures characteristic of next generation devices. In particular, SiGe or high-k material based gate stacks, ultra shallow implants for reduced dimensions sources and drains, and materials for organic electronics were investigated. The combination of several approaches was performed for each application in order to enhance ToF-SIMS characterisation abilities.

For each of the studied applications, the developed solutions allowed important improvements. The use of extremely low energy regime (150 eV sputtering) provided the best depth resolution and enabled reduced transient for better quantification of ultra-thin material stacks and ultra shallow arsenic implants. Performing dedicated backside sample preparation on high-k / metal gate samples permitted minimised in-situ sample modification during depth profiling, which enabled enhanced quantitative analysis. Systematic studies of secondary ions and of different signal normalization resulted in optimisation of profile accuracy in ultra shallow arsenic implants in silicon as well as in polymer-fullerene organic blends.
Data treatment was otherwise an important part of this work. In particular, an original approach has been developed by making use of the parallel monitoring of large secondary ion mass ranges that is possible with a ToF-SIMS instrument. This approach, called the full spectrum method, is an important break-through as it enables quantification of all major chemical elements in one analysis. It was applied with success to oxides and oxy-nitrides, SiGe and high-k based materials. In particular, we showed that it enabled quantification of Ge in strained or relaxed SiGe alloys with less than 1 at% error over the whole range of available Ge content. In presence of dopants, impurities or oxygen, it was shown to be more representative of the actual sample composition while reducing noise level and improving reproducibility. It was finally shown to permit precise compositional depth profiling of major elements in ultra-thin high-k material stacks without using any reference material, through XPS cross-calibration. By performing reproducibility studies, it was shown that the latter could even be applied to thicker stacks without resorting to XPS. Such a data treatment protocol proved that analyses that were thought to be impossible with ToF-SIMS (such as simultaneous quantification of all matrix elements in one analysis without using reference samples) could actually be performed. Significant progress towards quantitative, depth resolved analysis of samples for next generation microelectronics devices was thus achieved by the different dedicated solutions developed during this thesis work in terms of optimisation of experimental parameters, sample preparation and data treatment.

However in some cases we also discovered limitations to the improvements brought by our different developments in terms of depth resolution as well as in terms of accuracy of quantification. Those can be divided into three categories.
The first one involves limitations. For example, the full spectrum protocols we developed require the following of a large number of secondary ions, which can be a source of noise or interference and requires careful studies of mass interferences. They also require the monitoring of large numbers of secondary ions at once (between 50 and 100 depending on the material), which prohibits their use in magnetic SIMS instruments. Otherwise, they are based in some cases on XPS cross-calibration, which can be a source of potential error. All of these could be overrun without modifying the instrument, by simply improving even more the data treatment protocols.
The second one is directly related to instrumental considerations. For example, the extremely low sputter rates in EXLE regime do not allow analysis of samples thicker than ~10 nm. Even for ultra-thin stack analysis, the profile duration is too long to be a practical option in everyday use. Otherwise, the complexity of ToF-SIMS spectra in organic materials is a hindrance for their quick and easy interpretation. Therefore instrumental developments are needed in different directions, to improve beam currents and focusing at extremely low energies for ultra-thin sample profiling and allow minimised damage and maximised molecular signal for analysis of organic materials.
A last fraction of those limitations is due to the intrinsic physics behind ToF-SIMS instrumentation. Even with improved ion sources and optics, a technique based on ion beam sputtering and/or analysis would never offer sufficient lateral resolution to be able to characterize real devices of a few tens of nanometres wide. Similarly, there are limits to the smallest achievable depth resolution intrinsically linked to the phenomena of ion/matter interactions (unless the ion energy is dropped to zero, in the case of zero-energy SIMS [1-2]). Even with improved experimental conditions and data treatment, matrix effects will never be completely removed when using SIMS analysis, due to the sensitivity of both sputter and ionization yields to the surrounding environment at a local scale. These limitations cannot be completely solved neither by instrumental changes nor by development of specific quantification protocols so other characterization techniques will often need to be used when accurate quantification is required.

These limitations also give rise to perspectives, which can be divided into three categories: first perspectives using the same instrument than in this study, then using the same technique but with instrumental developments; not to neglect, finally, the possibilities given by emerging characterization techniques.
To continue the study on matrix element quantification with ToF-SIMS, reproducibility studies should be performed. These could help reduce the total number of secondary ions needed to perform a full spectrum analysis and enable transposition onto magnetic SIMS instruments. They would also establish a map of sensitivity factors in various materials and structures, possibly enabling direct quantification without having to resort to calibration samples or XPS cross-calibration. They would finally help explore the capabilities of the full spectrum protocol in other materials of interest, such as metallic alloys, III-V or low-k materials.
Recent technological developments enabled elaboration of new ion sources and original instrumentation for SIMS and ToF-SIMS. The optimisation of instrument optics for extremely low energy showed the possibility to obtain highly focused, high density ion beams down to a hundred electron volts for both oxygen and caesium sputtering. This kind of progress could be very useful for improving both throughput and reliability (crater conformality, reproducibility) in analysis of ultra-thin material stacks or ultra shallow junctions [3]. New ion sources exploit heavier primary ions, such as massive argon clusters. These enable analysis of organic materials with less damage than more conventional primary ions and show interesting improvements in

molecular ion yields, which is necessary to yield relevant information, be it on polymers, small molecules or biological samples [4-6].

Finally, the emergence of new characterization techniques could help resolve some of the problems for which ToF-SIMS is inadequate. For example, matrix-effect free, easy quantification of major element depth profiles could be achieved using LEIS instruments associating extreme surface sensitivity and no sample modification during analysis, to low energy sputtering in an alternate fashion as already used in dual beam ToF-SIMS. The use of local field effect techniques such as Atom Probe Tomography could also allow atomic scale chemical quantification of real nanometre-scale devices, provided that reliable 3D volumes can be obtained by developments in sample preparation, analysis conditions and most importantly in reconstruction methods.

REFERENCES

[1] W. Vandervorst, *Semiconductor Profiling with Sub-Nm Resolution: Challenges and Solutions*, Appl. Surf. Sci., 255 (**2008**) 805-812.
[2] N. Vanhove, P. Lievens and W. Vandervorst, *Towards Quantitative Depth Profiling with High Spatial and High Depth Resolution*, Appl. Surf. Sci., 255 (**2008**) 1360-1363.
[3] A. Merkulov, P. Peres, S. Choi *et al.*, *Advanced Secondary Ion Mass Spectroscopy Quantification in the First Few Nanometer of B, P, and as Ultrashallow Implants*, J. Vac. Sci. Technol. B, 28 (**2010**) C1C48-C41C53.
[4] J.L.S. Lee, S. Ninomiya, J. Matsuo *et al.*, *Organic Depth Profiling of a Nanostructured Delta Layer Reference Material Using Large Argon Cluster Ions*, Anal. Chem., 82 (**2010**) 98-105.
[5] S. Ninomiya, K. Ichiki, H. Yamada *et al.*, *Molecular Depth Profiling of Multilayer Structures of Organic Semiconductor Materials by Secondary Ion Mass Spectrometry with Large Argon Cluster Ion Beams*, Rapid Commun. Mass Spectrom., 23 (**2009**) 3264-3268.
[6] S. Ninomiya, K. Ichiki, H. Yamada *et al.*, *Precise and Fast Secondary Ion Mass Spectrometry Depth Profiling of Polymer Materials with Large Ar Cluster Ion Beams*, Rapid Commun. Mass Spectrom., 23 (**2009**) 1601-1606.

APPENDIX LIST:

APPENDIX I : RESUME EN FRANÇAIS

PLAN

INTRODUCTION

Au cours de la dernière décennie, les dispositifs pour la microélectronique ont évolué de simples structures planaires majoritairement composées de silicium à des structures plus élaborées, comprenant plusieurs matériaux hétérogènes, dont la complexité des propriétés nécessite une compréhension du point de vue de la science des matériaux. Il y a donc nécessité d'avoir une connaissance précise de leur composition chimique. Les exigences pour leur caractérisation physico/chimique sont donc fortes et incluent une résolution spatiale et une sensibilité extrêmes, ainsi que la capacité de quantifier précisément n'importe quel élément chimique dans n'importe quelle configuration structurale.

Le SIMS, et particulièrement le ToF-SIMS, est un candidat intéressant pour répondre à ce défi du fait de ses performances sur des applications standard. Cependant il y a encore beaucoup de difficultés pour obtenir une quantification précise dans des structures aussi complexes que celles de la microélectronique actuelle et à venir. Ce travail de thèse porte donc sur la mise au point de développements expérimentaux pour permettre cette quantification avec un ToF-SIMS standard.

Dans une première partie, nous survolerons les différents concepts et notions nécessaires à la compréhension de l'étude qui suit. Nous allons aussi présenter les matériaux et structures choisis, l'outil ToF-SIMS du laboratoire, son fonctionnement et ses limitations. Notre seconde partie portera sur la description des différentes solutions envisagées pour améliorer la qualité des analyses ToF-SIMS. Ensuite nous détaillerons les protocoles développés pour chacun des matériaux étudiés dans des parties successives.

I Enjeux et perspectives: le ToF-SIMS pour la caractérisation de dispositifs pour la microélectronique avancée

I. 1. Problématique

Depuis l'invention du premier transistor, l'industrie de la microélectronique n'a jamais cessé d'améliorer le concept de base du transistor. Une première structure standard, baptisée CMOS, est composée d'une couche d'isolant en oxyde de silicium placée au dessous d'une grille en poly-silicium et métal et au dessus d'une région en silicium dopé [1]. Pendant presque cinquante ans, la même structure a été régulièrement améliorée en réduisant sa taille, ce qui a permis l'élaboration de puces de plus en plus complexes intégrant plus de fonctions. La taille moyenne d'un dispositif a évolué d'une dizaine de microns en 1971 à l'échelle micrométrique en 1988 et est passée sous la barre des 100 nm en 2004 [2]. Les dispositifs actuellement en production ont des tailles inférieures à 50 nm [3]. Mais depuis une dizaine d'années les exigences en termes de taille sont devenues difficiles à satisfaire du fait que la réduction pure de taille se heurte au mal-fonctionnement des dispositifs à cause de leurs propriétés physiques. Des solutions alternatives se doivent donc d'être développées, parmi lesquelles :

(i) Continuer la miniaturisation dans les domaines présentant encore une marge d'amélioration
(ii) Introduire des matériaux alternatifs au SiO2 (diélectrique) et au Poly-Si (grille)
(iii) Changer la structure du dispositif (vers une structure en trois dimensions)
(iv) Utiliser de nouveaux matériaux pour le substrat afin d'améliorer les mobilités.
Ces quatre points sont bien décrits dans la revue 2009 de l'ITRS [3].

De fait, si l'on observe l'évolution du nombre des éléments chimiques utilisés dans les transistors, on constate l'introduction de presque la moitié de la table des éléments dans la dernière décennie [4]. De plus, les structures des dispositifs ont-elles aussi évolué, avec l'apparition d'hétérostructures contraintes et de structures en trois dimensions. La caractérisation physico-chimique de ces dispositifs est donc nécessaire pour analyser de façon précise leur composition, leur structure, leur taille et leur forme, leur niveau de contrainte, leur vieillissement, leur réaction au budget thermique. Du fait de la complexité de la tâche, seules quelques techniques pourraient répondre à ce défi. Parmi elles, le SIMS et plus particulièrement le ToF-SIMS est intéressant.

I. 2. Pourquoi le ToF-SIMS

Les performances de cette technique sont en effet impressionnantes, avec de fortes capacités en termes de sensibilité, de résolution en profondeur et de détection chimique, le tout regroupé dans un seul instrument [5-6]. On peut citer les performances suivantes:

- Détection de tous les éléments de H jusqu'à Pu et de composés
- Grande résolution en masse permettant de résoudre des isotopes ainsi que des ions de masse similaires tells que $^{30}SiH^{-/+}$ (30.9816 u) et $P^{-/+}$ (30.9738 u)
- Profil en profondeur d'échantillons, de quelques nanomètres à plusieurs microns.
- Résolution en profondeur de l'ordre du nanomètre
- Quantification de tous les éléments à l'état de trace (ppm - ppb) comme à l'état de dopant (quelques pourcents atomique)
- Possibilité d'analyser tout échantillon supportant l'UHV sans préparation particulière
- Acquisition parallèle de tous les ions dans une gamme de masse et jusqu'à ~10000 u

- Analyse de monocouches en surface grâce à de très faible doses d'ions incidents
- Etude d'échantillons isolants comme conducteurs
- Acquisition d'information moléculaire sur les échantillons organiques
- Capacités d'imagerie avec une résolution latérale sub-micronique

qui sont toutes des performances standard, atteignables en fonctionnement de routine. On peut donc comprendre l'intérêt de la technique : du fait de ses performances, on peut en attendre beaucoup sur sa capacité à relever les défis proposés par cette étude.

I. 3. Principe, instrumentation et physique du ToF-SIMS "dual beam"

I. 3. a- Principe

Le principe du ToF-SIMS "dual beam" repose sur l'analyse par un spectromètre de masse d'ions secondaires qui donnent des informations sue la nature chimique des couches de surface d'un échantillon. Ces ions secondaires représentent une petite fraction de la matière émise lors du bombardement d'un échantillon avec des ions primaires énergétiques. Le ToF-SIMS utilise comme son nom l'indique un détecteur à temps de vol. Les ions secondaires sont d'abord accélérés grâce à un potentiel fixe et entrent dans une chambre à temps de vol dans lequel la durée de leur vol est mesurée et est reliée à leur masse par la relation:

$$t_{ToF} = L \cdot \sqrt{\frac{m}{2q(E_0 + U)}} \qquad \text{(I.1)}$$

où t_{ToF} est la durée du vol, L la longueur de la chambre et U le potentiel d'accélération qui sont des paramètres connus. E_0 est l'énergie initiale des ions secondaires (souvent négligeable) et m leur masse. Le fonctionnement de l'instrument est schématisé en Figure I.1.

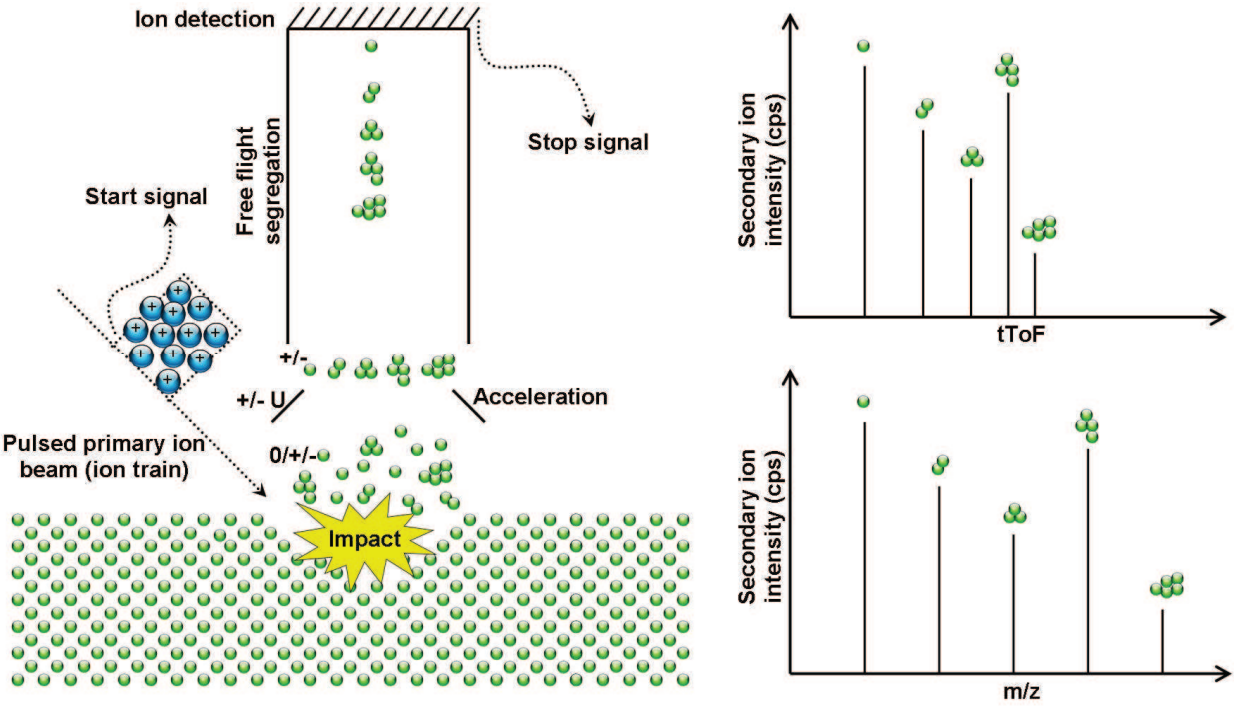

Figure I.1.Gauche: Vue simplifiée du déroulement d'une analyse: après hachage, un train d'ions primaires entre en collision avec une cible et provoque l'émission de particules neutres ou chargées. Le signal de hachage sert également d'impulsion de départ, avec délai, pour le calcul du temps de vol. Les ions accélérés par un potentiel entre dans la chambre de vol libre et ségrégent en fonction de leur masse.

Droite: Spectre de masse générée par l'analyse précédente. Chaque ion secondaire de msse différente a un tmps de vol unique et caractéristique de sa composition. L'intensité de chaque signal dépend de la concentration de l'élément en surface ainsi que de la sensibilité de la technique à cet élément.

Le ToF-SIMS « dual beam » utilise deux faisceaux d'ions distincts : le premier est constitué d'ions énergétiques (quelques dizaines de keV) pour l'analyse et le deuxième d'ions plus faiblement énergétiques (de 0.1 à quelques keV). Cette configuration permet de fort taux d'ionisation pour l'analyse combinés à une forte résolution en profondeur et à une abrasion douce. Elle permet aussi une versatilité de l'outil, qui comporte plusieurs fonctions :

- S-SIMS: pour l'analyse monocouche de surface [7]. Dans ce mode seul le faisceau d'analyse est utilisé pour obtenir des spectres de masse.
- Le profil de profondeur: pour l'analyse d'échantillons dans leur épaisseur. Les deux faisceaux sont utilisés de façon successive. En sortie, les données sont une série de spectres de masse pris à différentes épaisseurs et formant un profil en profondeur.
- Imagerie: pour obtenir une image ionique d'une surface [8]. Le faisceau d'analyse est balayé sur la surface de l'échantillon et chaque spectre de masse forme le pixel d'une image. Ce mode est utilisé de facto dans les deux précédents modes mais avec une faible résolution spatiale (plusieurs centaines de nm). Une meilleure résolution latérale peut être obtenue mais uniquement aux dépens de la résolution de masse.

Ces trois modes seront utilisés tout au long de nos travaux.

I. 3. b- Instrumentation

Les faisceaux d'analyse et d'abrasion sont tous deux constitués d'une source d'ions et

d'une colonne optique comportant accélération, hachage et lentilles de polarisation. Pour l'analyse on utilise une source d'ions bismuth LMIS, qui possède une grande brillance et permet d'obtenir de forts courants et une faible taille de spot. Cette source permet de produire des ions simplement ou multiplement chargés ainsi que l'émission agglomérats de trois, cinq ou sept atomes de Bi. Pour l'abrasion on utilise une source à ionisation par filament pour l'oxygène, et une source LMIS pour le césium. En fonctionnement standard le faisceau Bi^+ a une énergie de 25 keV tandis que les faisceaux d'abrasion O_2^+ ou Cs^+ peuvent varier entre 250 et 2000 eV. En courant continu on obtient 15 nA avec Bi^+ et de 15 à plusieurs centaines de nA avec O_2^+ ou Cs^+.
La chambre de mesure du temps de vol est un tube de longueur connue sous UHV dans lequel les ions secondaires vont ségréger en fonction de leur masse. Notre instrument est de plus équipé avec un Reflectron, qui permet d'augmenter la résolution de masse en supprimant l'influence de l'énergie initiale des ions secondaires et en augmentant la durée de vol. L'intensité des ions secondaires suit la formule suivante :

$$I_m = I_p \cdot Y_m \cdot \alpha_m^{+/-} \cdot \theta_m \cdot \eta \qquad \text{(I.2)}$$

Avec I_m l'intensité de l'ion secondaire m, I_p la densité d'ions primaires, Y_m le taux de pulvérisation, $\alpha_m^{+/-}$ le taux d'ionisation, θ_m the la concentration en élément m à la surface de l'échantillon et η le facteur de transmission de l'instrument. Typiquement ce dernier est haut (90-95%) et I_p peut être changé à volonté ; par contre Y_m et plus particulièrement $\alpha_m^{+/-}$ sont souvent très faibles et sujets à d'importantes variations.

I. 3. c- La physique du ToF-SIMS

Comme nous venons de le voir, le principe du ToF-SIMS est d'analyser des ions secondaires générés par l'impact d'ions primaires sur une cible. Au cours de ce processus interviennent deux phénomènes: la pulvérisation de matière et l'ionisation [9-16].
Dans la gamme d'énergie et d'angle concernée, l'effet principal du bombardement ionique est la pulvérisation, c.a.d. l'arrachage d'atomes du matériau cible. C'est le résultat du transfert d'énergie de l'ion incident à la cible. La quantité de matière émise dépend de l'énergie de l'ion primaire, de son angle d'incidence et de sa nature (atomique ou agrégat). Un autre aspect du bombardement ionique est l'implantation et l'adsorption d'une partie des ions primaires, qui dans le cas d'éléments actifs comme le Cs ou l'O_2 résultent en une profonde modification de la composition des couches de surface de l'échantillon.
Parmi les particules pulvérisées, seule une petite fraction est chargée ; et c'est celle-ci qui est analysée en SIMS. Cependant, le taux d'ionisation peut varier de plusieurs ordres de magnitude selon l'élément choisi ou selon son environnement chimique immédiat. Il peut également changer en fonction des conditions expérimentales. Ceci est du au changement de configuration électronique d'un élément lorsqu'il est placé dans différentes matrices à l'échelle locale : d'où le nom d'effets de matrice [9]. Ces effets rendent impossible la prédiction du taux d'ionisation d'un élément à moins d'utiliser un échantillon de référence connu, comportant le même élément dans une matrice similaire. De fait, la quantification directe n'est pas possible en SIMS.

I. 3. d- La procédure de quantification des profils en profondeur

Un profil en profondeur consiste en un enregistrement de l'intensité d'un ou plusieurs ions secondaires en profondeur. Dans le cas du ToF-SIMS dual beam, un cratère d'abrasion est formé bar balayage du faisceau d'abrasion sur l'échantillon, à l'intérieur duquel les spectres de masse sont obtenus par un balayage du faisceau d'analyse (de taille plus réduite pour éviter les

effets de bord). Pour transformer ces intensités en concentration, il est nécessaire de convertir l'échelle de temps (d'abrasion) en échelle de profondeur, ce qui peut être réalisé de différentes façons en fonction de l'application. Puisque le taux d'ionisation d'un élément n'est pas contrôlable, il est nécessaire pour effectuer une calibration en concentration d'obtenir dans les mêmes conditions expérimentales un profil dans un échantillon de référence. Ceci permettra d'obtenir un facteur de sensibilité appelé RSF. En cela, le ToF-SIMS est donc une technique uniquement semi-quantitative.

I. 4. Sélection de matériaux et structures d'intérêt

En nous basant sur leur intérêt pour une application dans les dispositifs microélectronique nouvelle génération, nous avons sélectionné les matériaux et structures suivants :

- Les alliages $Si_{1-x}Ge_x$ avec x variant de 0 à 1, éventuellement avec un fort dopage et intégrés dans une empilement vertical qui peut subir un recuit.
- Les couches nanométriques HKMG.
- Les implants ultra basse énergie d'Arsenic dans Si, à travers un oxyde natif.
- Les matériaux organiques constitués d'une matrice polymère et de fullerènes.

Nous allons maintenant décrire les difficultés rencontrées lors de l'analyse ToF-SIMS de ces échantillons.

I. 5. Difficultés associées à la caractérisation ToF-SIMS de matériaux et structures avancés

Les effets de matrice désignent tous les effets due à l'environnement immédiat d'un élément ou compose à analyser. Ceux-ci comportent : les transitoires de surface et d'interface, les effets dus à la composition de la matrice, et à la modification in-situ de la matrice par les ions primaires. Ces effets influencent la probabilité d'ionisation de l'élément ou composé à analyser. De fait, la quantification d'éléments de matrice dans les échantillons d'intérêt est difficile en fonctionnement conventionnel [9]. Il faut donc mettre au point un protocole de mesure permettant de remédier à cela.

Les régimes transitoires recouvrent toutes les zones d'un profil dans lesquelles la vitesse d'abrasion, les probabilités d'ionisation et la composition de la surface varient en fonction du temps d'abrasion ; par opposition au régime permanent où tous ceux-ci sont stables. Ils font présents aux interfaces du matériau (dont la surface fait partie) et leur étendue peut varier en fonction des conditions expérimentales telles que l'énergie des ions primaires ou les conditions de vide et bien sur en fonction de la nature et des propriétés de l'échantillon. Dans ces régimes, les probabilités d'ionisation varient d'une façon incontrôlée, ce qui ne permet pas de quantification via le moyen traditionnel des RSFs. Il est donc nécessaire de pouvoir rendre compte au mieux de ces variations afin de permettre une analyse quantitative dans ces régimes.

La résolution en profondeur d'un instrument est déterminée par la réponse de l'instrument à un stimulus bref, tel qu'une interface bien définie entre deux matériaux ou un delta. Les caractéristiques de la réponse sont une convolution d'une gaussienne fine et d'une descente exponentielle plus lente. Cette caractéristique est due aux effets du bombardement ionique sur le matériau, induisant une épaisseur de matériau endommagé. Une résolution en profondeur insuffisante détériorera la qualité de l'analyse en empêchant la caractérisation de couches fines mais aussi en modifiant la forme des structures rencontrées, par exemple lors d'interfaces entre matériaux hétérogènes. Dans chaque cas, il faut donc optimiser les paramètres expérimentaux afin d'améliorer la résolution en profondeur.

De plus le bombardement ionique inflige également des dommages au matériau, ce qui le modifie de façon physique (en mélangeant les matériaux déjà présents et détruisant l'ordre du matériau) et de façon chimique (en modifiant sa composition par implantation et adsorption d'ions primaires). Dans tous les cas cette modification est plus profonde que les quelques premières couches de surface, ce qui peut singulièrement affecter la qualité d'une analyse. La mise au point de protocoles de préparation d'échantillons ou de mesure sont donc requises pour minimiser ces effets.
Enfin, le ToF-SIMS est une technique semi-quantitative demandant des références ou une caractérisation externe pour être quantitative. En plus des difficultés citées plus haut et qui dépendent de phénomènes physiques, il est aussi nécessaire de se pencher dur le traitement de données afin de pouvoir améliorer la manière de quantifier des données et répondre à la demande.

Comme nous pouvons le voir, différents phénomènes directement liés à la physique du ToF-SIMS ont des effets néfastes sur la capacité de l'outil à donner une information quantitative fiable sur les matériaux et structures qui nous intéressent. Dans une prochaine partie nous allons donc présenter les différentes solutions que nous avons mises en place pour contrer ces phénomènes.

II Les voies explorées pour répondre au besoin de caractérisation ToF-SIMS

II. 1. Préparation 'face arrière' d'échantillon

Cette option est peu usitée en SIMS puisqu'usuellement aucune préparation n'est requise pour des applications standard. En effet n'importe quel échantillon supportant l'UHV pourra être analysé. Cependant pour certaines applications lorsque les couches d'intérêt d'un échantillon sont enterrées, ou bien se trouvent sous une succession de couches d'autres matériaux et que les conditions sont telles que l'analyse de ces couches d'intérêt ne peut se faire correctement du fait d'une modification in situ de l'échantillon ou d'un manque de résolution en profondeur, il peut être intéressant d'analyser l'échantillon dans l'autre sens ; c.a.d. en le retournant. Ceci demande toutefois de retirer tout ou partie de substrat sur lequel ces couches sont déposées tout en conservant un état de surface approprié pour l'analyse.
Une analyse face arrière permet de supprimer complètement tous les effets liés aux rugosités de surface ou d'interface du matériau, qui ne sont pus traversées avant d'analyser la couche d'intérêt. Elle permet aussi de supprimer les effets de mixing et d'implantation ionique (effets qui toutefois se retrouveront dans le sens de progression du profil).

II. 2. Optimisation des paramètres expérimentaux

On peut s'intéresser à l'optimisation de plusieurs paramètres séparément, afin de comprendre leurs effets sur l'analyse.
Tout d'abord on peut jouer sur la nature chimique (active ou inactive) et physique (atomique ou agrégat) des ions primaires. Le fonctionnement dual beam permet de dissocier faisceau d'analyse et d'abrasion. Pour ce dernier deux espèces d'ions sont disponibles : Cs et O2, toutes deux sont actives. Pour l'analyse seul le Bi est disponible, c'est une espèce inactive. Cependant on peut jouer sur la masse des ions en sélectionnant des ions atomiques ou des agrégats avec 3, 5 ou 7 atomes de bismuth. Le choix d'un des deux ions pour l'abrasion modifie de fait la composition de l'échantillon, du moins de ses couches de proche surface, en induisant des effets divers sur les vitesses d'abrasion et les probabilités d'ionisation comme vu plus haut. En fonction de ce choix,

on peut donc s'attendre à obtenir des profiles différents en forme et en intensités, en particulier durant les régions transitoires de l'analyse. En jouant sur la nature de l'ion primaire pour l'analyse, l'on modifie la cascade de collision à l'impact et donc à la fois les dommages au matériau et le taux de pulvérisation.
De plus notre instrument permet de faire varier l'énergie d'impact des faisceaux d'abrasion entre 250 et 2000 eV en mode standard, avec de forts courants d'ions primaires et une faible taille de spot. Avec une dégradation du courant et de la focalisation il est aussi possible de descendre jusqu'à une centaine d'eV. De la même façon il est possible de choisir l'énergie du faisceau d'analyse, 25 keV en mode standard et 15 keV en mode avancé. Il est également possible de former et de sélectionner des ions doublement chargés, ce qui multiplie leur énergie par deux. La modification de l'énergie du faisceau d'abrasion aura un effet direct sur les vitesses d'abrasion à cause de l'effet combiné de la variation d'énergie (un ion moins énergétique pulvérise moins de matière) et du courant (plus l'énergie est faible et plus le courant est faible en pratique). Les hautes énergies sont donc plutôt adaptées au profilage d'échantillons épais tandis que les basses énergies sont réservées pour l'analyse de structure fines dont elles permettent une meilleure visualisation. Par ailleurs la modification de l'énergie du faisceau d'analyse influera principalement sue la longueur de pénétration des ions dans le matériau mais modifie très peu le taux de pulvérisation et d'ionisation. Le choix d'une énergie plus basse permet donc de diminuer à la fois les dommages au matériau et la profondeur d'information.
Enfin, le dernier paramètre d'importance est le ratio abrasion/analyse, qui représente le ratio de matière pulvérisée dans un cycle par le faisceau d'abrasion et par le faisceau d'analyse. Si celui-ci n'est pas assez élevé, cela montre que les dommages infligés aux couches par le faisceau d'analyse n'est pas complètement enlevé lors du cycle d'abrasion, ce qui induit une dégradation de la résolution en profondeur et réduit la représentativité de l'analyse car les couches analysées sont modifiées in situ (mixing). L'optimisation du ratio est donc cruciale, plus particulièrement pour les applications demandant une grande résolution en profondeur. Il est communément accepté qu'une valeur de 100 ou plus est suffisante pour réduire presque totalement le risque de dégradation de la résolution en profondeur [17]. Cette valeur correspond à un cycle dans lequel le faisceau d'analyse pulvérise moins de 1% de la quantité de matière pulvérisée pendant la période d'abrasion.

II. 3. Traitement des données "full spectrum"

Le produit d'une analyse ToF-SIMS est extrêmement riche en information puisqu'à chaque point de données on a accès à plusieurs centaines de spectres de masse contenant chacun de larges gammes de masses et dont la position latérale est enregistrée. Toutes ces données sont accessibles facilement depuis le logiciel machine, ce qui ouvre des possibilités d'amélioration de qualité d'analyse en utilisant du traitement de donnée postérieur à l'analyse en elle-même.
L'approche « full spectrum », bien que relativement peu connue et peu présente dans la littérature, est intéressantes car elle tire parti au maximum de la spécificité du ToF-SIMS, qui est de permettre l'acquisition en parallèle de nombreux ions secondaires à l'intérieur d'une large gamme de masse.

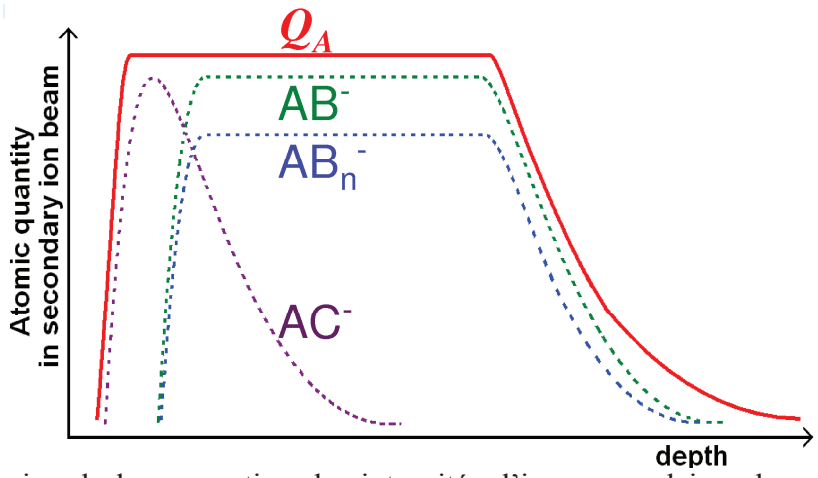

Figure II.1 Principe de la sommation des intensités d'ions secondaires dans le protocole full spectrum.

En effet, cette approche consiste à prendre en compte le maximum d'information possible en s'intéressant à tous les ions secondaires contenant l'élément à analyser, contrairement à une approche classique dans laquelle un seul ion secondaire est regardé. Plus précisément, pour un élément *A* donné, l'on va sommer les contributions de tous les ions secondaires $A_xR_y^-$, normalisées par x et par leur abondance isotopique, comme montré en Figure II.1. Ce faisant on obtient une nouvelle quantité Q_A qui est la quantité d'atomes *A* dans le faisceau d'ions secondaires. En lieu de distributions en profondeur d'intensités d'ions secondaires on a donc des profils de « fonctions enveloppe » qui prennent mieux en compte les différentes espèces ioniques. Cette approche permet donc une meilleure représentativité de la distribution des éléments de matrice en profondeur. Si la quantitativité d'une telle approche pouvait être prouvée, elle permettrait la quantification de tous les éléments de matrice en un profil, ce que demandent la plupart de nos applications. De plus, cette nouvelle capacité ne résulte que d'un traitement des données : on conserve donc toutes les propriétés standard du SIMS à savoir son extrême sensibilité ce qui permet la quantification en même temps de dopants ou d'éléments trace.

II. 4. Corrélation et complémentarité avec d'autres techniques

Bien que le ToF-SIMS permette d'obtenir des informations quantitatives et résolues en profondeur dans une large gamme de matériaux, bien souvent cette information seule n'est pas suffisamment crédible et/ou n'est pas suffisante seule pour décrire l'ensemble des propriétés du matériau. Dans ce cas il est nécessaire de faire appel à des techniques annexes pour obtenir des informations soit de même nature (profils de composition) soit de nature complémentaire.

II. 4. a- L'apport des techniques de scatterométrie X: XRR et XRD

Ces techniques utilisent l'interaction des rayons X avec le nuage électronique du matériau cible afin d'en tirer les propriétés. Elles s'appliquent aux matériaux mono ou poly cristallins et permettent leur identification car chaque matériau a un paramètre de maille unique. Si un échantillon est constitué de plusieurs couches de matériaux différents, les différents ordres de réflexion *n* des rayons aux interfaces peuvent induire des oscillations de longueur d'onde données, caractéristiques de l'épaisseur des couches. Un spectre XRD ou XRR est obtenu par illumination d'un échantillon par des rayons X monochromatique et en opérant une rotation de l'échantillon tandis que la source et le détecteur sont fixes. De cette façon on obtient un spectre d'intensité des rayons X réfléchis ou difractés en fonction de l'angle incident [18]. Ces spectres

peuvent être simulés et permettent donc de déduire, en s'approchant au mieux du spectre expérimental en faisant varier la composition, le nombre de couches et leur épaisseur, des informations quantitatives sur l'échantillon [18-23]. Dans cette étude nous nous focalisons sur :

- L'épaisseur des couches (quantitatif)
- La composition d'alliage épitaxiés (quantitatif)
- La rugosité d'interface (qualitatif)
- Le niveau de contrainte moyen (qualitatif)
- La qualité du réseau cristallin (qualitatif)

II. 4. b- L'ellipsométrie

Lorsque de la lumière frappe une surface de matériau d'un indice optique différent, elle est partiellement réfléchie et sa polarisation est modifiée. L'ellipsométrie mesure ce changement de polarisation, qui dépend des propriétés optiques et de l'épaisseur des matériaux concernés. Elle permet donc de mesurer précisément l'épaisseur de films minces en remontant aux propriétés des couches étudiées par les équations de Fresnel. Dans notre étude, nous utilisons cette technique pour la mesure d'épaisseur de couches très fines (<10 nm).

II. 4. c- La Transmission Electron Microscopy

Les techniques TEM utilisent la transformation de l'énergie, de la direction ou de la phase d'électrons envoyés à travers une fine lamelle d'échantillon. L'information donnée par une analyse simple en imagerie concerne la structure de l'échantillon (épaisseur de couches, rugosité d'interface…) et dans le cas d'analyses haute résolution, l'état cristallin de chaque couche et son orientation éventuelle. Cependant il existe d'autres usages au TEM qui donnent accès à une variété d'informations différentes en fonction du mode de contraste. Par exemple il est possible d'utiliser la modification de phase des électrons passant à travers un échantillon par holographie électronique. Par superposition d'une onde cohérente de référence et d'ondes qui ont subi une modification de phase d'obtenir des hologrammes à partir duquel on peut dé-corréler les images en amplitude et en phase. La première permet de faire de l'imagerie conventionnelle tandis que la seconde permet de déduire l'état de contrainte local [24-27]. On souhaite donc déterminer:

- L'épaisseur des couches (quantitatif)
- La rugosité d'interface (quantitatif)
- Le niveau de contrainte local en imagerie (quantitatif)
- La composition en éléments de matrice (qualitatif)

II. 4. d- L'Atomic Force Microscopy

L'AFM est une technique de champ proche utilisant les interactions faibles entre une pointe fine et la surface d'un échantillon à des distances de l'ordre du nanomètre. Le principe est d'avoir une pointe nanométrique attachée à la pointe d'une poutre micrométrique en oscillation forcée et d'approcher le système de la surface d'un échantillon. Les interactions de la pointe avec la surface vont modifier l'amplitude des oscillations. En asservissant le déplacement tri dimensionnel de l'échantillon pour obtenir une amplitude constante, on obtient une carte d'interactions directement transformable en carte topographique de la surface de l'échantillon. Les informations d'intérêt sont donc :

- La rugosité de surface (quantitatif)
- La morphologie de l'échantillon (qualitatif)

II. 4. e- La spectroscopie de photons X

Lorsque des photons énergétiques traversent un matériau, une petite partie en est absorbée. Des photoélectrons peuvent alors être émis lors de l'ionisation d'un atome par éjection d'électrons de cœur. Leur énergie correspond à la transition entre l'état de base de l'atome neutre avec Z électrons et l'état final avec Z-1 électrons. Etant donné que cette énergie constitue une signature quasi unique pour un élément, l'acquisition d'un spectre d'énergie de ces électrons donne une indication directe sur la composition d'un échantillon, ce qui permet l'analyse de la composition d'un échantillon sans effets de matrice [28]. De plus l'énergie de ces photoélectrons subira de légers shifts en fonction de l'environnement chimique de l'élément concerné. Comme ces shifts sont connus et tabulés, ils permettent également l'étude des états de liaison des éléments [28-31]. Enfin cette technique est limitée aux éléments majeurs et à une analyse de surface (maximum 10 nm), mais en faisant varier l'angle d'acquisition des photoélectrons on peut obtenir un profil sur la même épaisseur. On s'intéresse aux informations suivantes:

- La composition moyenne de la surface (quantitatif)
- Les états de liaison en surface (qualitatif)
- Le profil de composition (quantitatif)
- Le profil d'états de liaison (qualitatif)

II. 4. f- Les techniques par faisceau d'ions: spectroscopies de perte d'énergie

Lorsqu'un faisceau d'ions énergétiques légers (H^+, He^+, Ne^+…) bombarde un matériaux, une partie des ions incidents sont rétrodiffusés après collision avec un atome du réseau. L'énergie des ions rétrodiffusés dépend directement de la masse de l'atome cible selon la théorie des collisions binaires [32-33]. La mesure de cette énergie est donc un moyen direct de remonter à la composition du matériau sans effets de matrice. Cette énergie est aussi caractéristique de la distribution des éléments en profondeur puisque la largeur d'un pic d'énergie est dépendant de l'épaisseur d'une couche et de sa densité. De plus sa frome reflète directement la distribution en profondeur de l'élément dans le matériau. De nombreuses techniques utilisent cet effet comme la RBS, le MEIS, le LEIS. Chacune possède ses spécificités, conférées par leur instrumentation [34-35]. Nous nous focalisons sur l'acquisition des informations suivantes:

- Mesure absolue d'épaisseur de couche (quantitatif)
- Mesure absolue de dose d'un élément (quantitatif)
- Profil en profondeur d'éléments de matrice (quantitatif)

II. 4. g- Simulation

La simulation permet de prévoir et de comprendre les phénomènes en action au cours des procédés de la microélectronique. L'implantation ionique et les processus de diffusion atomiques sont deux champs d'étude d'importance [36]. De nombreux modèles mathématiques sont disponibles pour identifier les propriétés de matériaux et comprendre ces procédés [37-39]. La quantité à identifier est la distribution en profondeur de dopant, la profondeur de jonction, le dommage infligé au matériau, et la quantité d'atomes qui ont diffusé. Par ailleurs la distribution des éléments à l'intérieur d'un échantillon après recuit est également un domaine d'intérêt. Les informations concernant l'implantation ionique peuvent être obtenues par TRIM ou Crystal TRIM [40]. Les études de diffusion requières des modèles plus complexes tels que ceux intégrés dans S-Process [41]. On s'intéresse donc aux informations suivantes, en une dimension:

- Profondeur de junction et profil de dopants (quantitatif)
- Profil d'éléments de matrice après recuit (quantitatif)
- Profil de contraintes (quantitatif)

Dans cette partie nous avons survolé les différentes voies explorées pour améliorer la qualité des analyses ToF-SIMS. Par la suite, nous allons nous intéresser à la mise en place des solutions dans les différents matériaux et structures évoquées en partie I.

III Mise en place des solutions et résultats dans les matériaux et structures pour intégration 3D à base de SiGe

III. 1. Mise en place d'un protocole de mesure précise de *x* in $Si_{1-x}Ge_x$

A cause des effets de matrice, la quantification de Ge dans des alliages SiGe est difficile puisque la sensibilité de la technique à Ge varie avec la composition de la matrice. A partie de travaux de Perego *et al.* [42], nous avons donc développé un protocole pour permettre la caractérisation de Ge dans n'importe quel alliage SiGe. Ce protocole utilise l'observation d'ions secondaires négatifs par ToF-SIMS, avec une abrasion au césium, ce qui permet d'obtenir simultanément les profils de concentration de dopants comme P ou B.
Pour établir une courbe de calibration nous avons utilisé une série d'échantillons de concentration entre 0 et 85 at% de Ge et dont la composition a été mesurée de façon précise par XRD (précision 0.1 at%) [43]. Dans le SiGe, l'intensité de chaque ion $Si_nGe_m^-$ montre une évolution différente en fonction du contenu en Ge. Ceci induit une variation non linéaire de l'intensité de chaque ion pris séparément. Cependant, lorsqu'on s'intéresse aux quantités de Ge dans le faisceau d'ions secondaires comme proposé en partie II, on s'aperçoit que la variation est linéaire [42]. Cette linéarité peut venir d'une proportionnalité entre la quantité de Ge dans le faisceau d'ions secondaires et dans le matériau lui-même. Pour vérifier cela nous avons obtenu des profils sur les échantillons présentés plus haut. On calcule ensuite la quantité totale de Si et de Ge dans le faisceau d'ions secondaires à l'aide de la relation :

$$Q_{total} = \sum_{n=0}^{6}\sum_{m=0}^{6}(n+m)\cdot \mathrm{Y}_{\mathrm{Si_nGe_m}} \qquad \text{(III.1)}$$

$Y_{Si_nGe_m}$ représente l'intensité de l'ion $Si_nGe_m^-$ divisée par l'abondance isotopique de Si_nGe_m. Pour minimiser le nombre d'ions et éviter les erreurs, les sommes sont effectuées exclusivement sur des ions d'intensité suffisante et qui ne présentent pas d'interférence de mase. La fraction de Ge dans le faisceau d'ions secondaire est ensuite calculée grâce à:

$$T_{Ge} = \frac{\sum_{n=0}^{6}\sum_{m=0}^{6} m \cdot Y_{Si_nGe_m}}{Q_{total}} \qquad \text{(III.2)}$$

On peut ensuite tracer le graphe T_{Ge} en fonction de x, x étant la concentration de chaque échantillon en Ge déterminée par XRD. On observe une excellente relation de proportionnalité entre ces deux valeurs, ce qui permet d'utiliser cette courbe de calibration pour caractériser des alliages de SiGe inconnus. Un autre avantage de ce protocole est son excellente reproductibilité puisque la courbe de calibration n'a pas besoin d'être réitérée à chaque analyse, et sa précision car elle ne génère une erreur maximum que de 1 at% Ge sur toute la gamme de concentration concernée [44].

III. 2. Mise en place d'un protocole de quantification précise de Ge, Si, O et des dopants dans des alliages SiGe dopés ou oxydés

Une première version du profil de Ge est obtenue grâce au protocole décrit en III.1, et les profils de dopants sont obtenus grâce à une procédure classique utilisant des références dans des alliages SiGe. Ces premières versions des profils, appelées $[Ge]_{FS}$ et $[A]_{FS}$, vont servir de référence en régime permanent pour calibrer ceux obtenus avec une version étendue du protocole full spectrum permettant de quantifier également les oxydes et les dopants. Dans cette version, on calcule la quantité totale de Si, Ge, O et de dopant dans le faisceau d'ions secondaires avec :

$$Q'_{total} = \sum_{n=0}^{6}\sum_{m=0}^{6}\sum_{p=0}^{3}\sum_{q=0}^{4}(n+m+p+q)\cdot \mathrm{Y}_{\mathrm{Si_nGe_mO_pA_q}} \qquad \text{(III.3)}$$

$Y_{Si_nGe_mO_pA_q}$ représente l'intensité de l'ion $Si_nGe_mO_pA_q^-$ divisée par l'abondance isotopique de Si_nGe_m. De même que précédemment, on n'utilise que des ions secondaires intenses et sans interférence de masse. Les fractions atomiques de Ge et de dopant sont obtenues grâce à:

$$T'_{Ge} = \frac{\sum_{n=0}^{6}\sum_{m=0}^{6}\sum_{p=0}^{3}\sum_{q=0}^{4} m \cdot \mathrm{Y}_{\mathrm{Si_nGe_mO_pA_q}}}{Q'_{total}} \qquad \text{(III.4)}$$

$$T'_{A} = \frac{\sum_{n=0}^{6}\sum_{m=0}^{6}\sum_{p=0}^{3}\sum_{q=0}^{4} q \cdot \mathrm{Y}_{\mathrm{Si_nGe_mO_pA_q}}}{Q'_{total}} \qquad \text{(III.5)}$$

De même pour la fraction de O. Les profils quantifiés $[O]'_{FS}$, $[Ge]'_{FS}$ and $[A]'_{FS}$ sont enfin obtenus par multiplication de T'_O, T'_{Ge} et T'_A par des facteurs de sensibilité obtenus par fit aux premiers profils dans leur régime permanent et par utilisation d'une référence d'oxyde de silicium. La dernière étape du traitement de données consiste à transformer l'unité de ces valeurs de at% vers at/cm^3. Pour cela il est nécessaire de modéliser la densité des couches, ce qui peut être obtenu par calcul en utilisant la formule suivante :

$$[Z]_{at/cm^3} = (\rho_{Ge} \cdot [Ge]_{at\%} / 100 + \rho_{Si} \cdot (1 - [Ge]_{at\%} / 100)) \cdot [Z]_{at\%} \quad \text{(III.6)}$$

Avec ρ_{Ge} et ρ_{Si} les densités du Ge et du Si purs (ρ_{Ge} = 4.42×10^{22} at/cm^3, ρ_{Si} = 5.00×10^{22} at/cm^3 [45]). Pour SiO2, nous avons utilisé une densité de 6.6×10^{22} at/cm^3, rapportée dans [46].

III. 3. Mise au point d'un protocole précis d'établissement d'échelle de profondeur dans SiGe et SiO_2

Des expériences ont également été menées pour assurer l'exactitude de notre échelle en profondeur dans SiGe contraint. Pour cela nous avons utilisé des couches contraintes de concentration 0 à 55 at% Ge ainsi qu'un delta de Bore dans Si pour déterminer les vitesses d'abrasion dans chacun des matériaux. Pour cela les épaisseurs des échantillons de SiGe ont été mesurées en XRR et leur contenu en Ge par XRD. Le delta de Bore a quant à lui été mesuré en TEM haute résolution. La vitesse d'abrasion varie dans SiGe contraint selon la loi :

$$\begin{cases} x \leq 5 \Rightarrow SR_{(Si_{1-x}Ge_x)} = (-11.5 \cdot 10^{-2} x + 1) \cdot SR_{(Si)} \\ x > 5 \Rightarrow SR_{(Si_{1-x}Ge_x)} = (7.36 \cdot 10^{-3} x + 0.895) \cdot SR_{(Si)} \end{cases} \quad \text{(III.7)}$$

x étant la concentration de Ge en at%. Enfin la vitesse dans SiO2 est calibrée à l'aide d'un échantillon de référence épais.

III. 4. Améliorations apportées par les différentes solutions développées en application à des matériaux et structures d'intérêt

III. 4. a- Précision de la mesure de concentration de Ge dans SiGe

Pour vérifier la précision de la mesure de concentration de Ge dans SiGe avec le protocole full spectrum présenté en III.1, deux types d'échantillons ont été utilisés. Le premier consiste en des couches contraintes de concentration mesurées en XRD [45, 47]. Le deuxième en des échantillons de couches de haute teneur en Ge et relaxées. Tous les échantillons ont été élaborés par épitaxie selon l méthode RP-CVD sur des bases Si(100) [48].

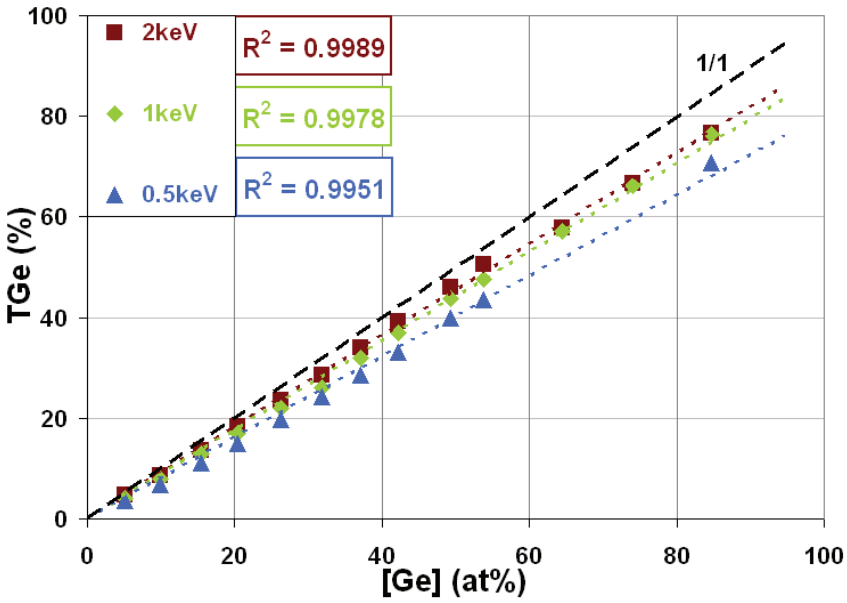

Figure III.1 T_{Ge} en function de la concentration de Ge déterminée par XRD. La courbe en pointillés correspond à une représentativité parfaite 1/1.

On observe en Figure III.1 une très bonne corrélation linéaire entre les valeurs de TGe et celles de la concentration en Ge trouvée par XRD. Des tests de reproductibilité ont été effectués à plusieurs énergies d'abrasion, plusieurs valeurs de courant et à plusieurs mois d'intervalle. Ils ont montré une excellente reproductibilité, avec une variation maximale de ±0.0025 sur la valeur de la pente de la courbe de calibration, ce qui induit une erreur de moins de ±0.25 at% Ge sur toute la gamme de concentration étudiée.

III. 4. b- Précision de l'échelle en profondeur dans des structures alternées Si/SiGe

Nous avons testé la solidité de notre modèle d'établissement d'échelle de profondeur en comparant les épaisseurs obtenues par ToF-SIMS, XRR et TEM haute résolution sur des échantillons épitaxiés multicouches de SiGe/Si, SiGeB/Si, SiGeP/Si et SiGeC/Si. Les épaisseurs obtenues sur ces échantillons sont montrées en Figure III.2. En ToF-SIMS, les interfaces ont été déterminées par le point de mi-intensité du profil de concentration obtenu par le protocole full spectrum étendu ($[Ge]'_{FS}$).On observe un excellent accord entre les valeurs obtenues par les trois techniques, bien que les épaisseurs obtenues en TEM soient légèrement différentes. Cette différence n'excède cependant jamais la marge d'erreur de chaque technique. Ceci démontre donc la précision de notre échelle de profondeur.

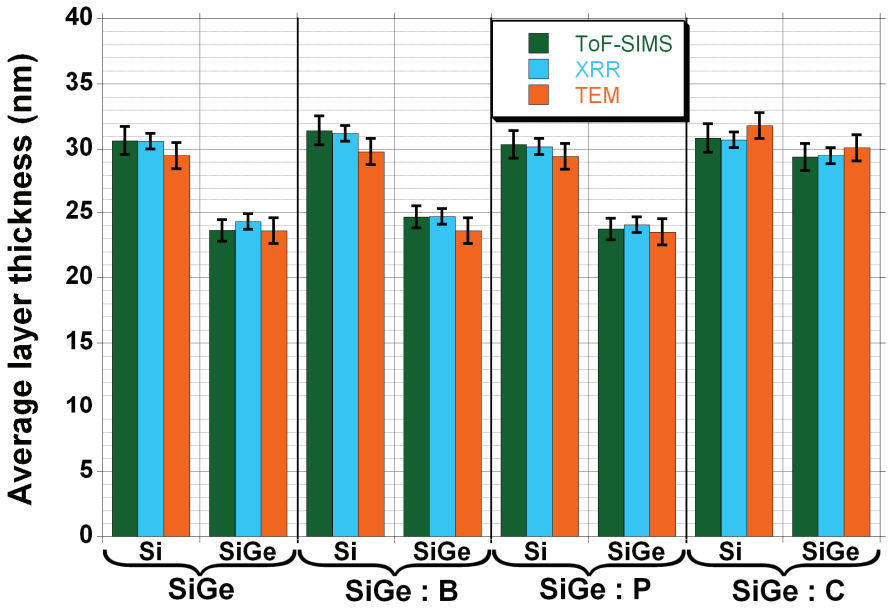

Figure III.2 Epaisseur des couches obtenues par ToF-SIMS, XRR and HR-TEM tous les échantillons.

III. 4. c- Améliorations pour le profil quantitatif de multicouches Si/SiGe dopées

Les contenus en Ge de diverses couches intrinsèques ou dopées de SiGe à l'intérieur d'échantillons multicouches one été mesurés avec le protocole full spectrum étendu. Les valeurs obtenues sont montrées dans la table III.i avec mes concentrations apparentes de Ge obtenues par XRD. On obtient un bon accord des deux techniques pour les couches SiGe (SiGe:P) / Si: 21.6% (26.5%) par XRD ⇔ 21.4% (26.5%) par ToF-SIMS. Cependant des concentrations bien plus basses qu'en TOF-SIMS sont obtenues en XRD pour les couches SiGe:B / Si and SiGe:C / Si. Ceci est dû au fait que les atomes substitutionnels de C et de B sont beaucoup plus petits que ceux de Si ou de Ge et compensent donc partiellement les contraintes dans les couches de SiGe dopées en diminuant leur paramètre de maille moyen. Une simple extrapolation linéaire entre le paramètre de maille attendu pour du SiGe pur et pour du pur carbone ou B dans la même configuration cristalline nous permet cependant de retrouver les concentrations en Ge réelles, qui sont très proches de celles trouvées en ToF-SIMS comme démontré dans les références [43, 49-50]. Nous avons donc un très bon accord des deux techniques dans tous les échantillons observés.

Echantillon	Concentration apparente en Ge par XRD (%, ± 0.6%)	Concentration en Ge par ToF-SIMS (%, ± 1%)
SiGe / Si	21.6	21.4
SiGe:B / Si	18.35	21.0
SiGe:P / Si	26.5	26.5
SiGe:C / Si	14.8	23.5

Table III.i Concentration apparente en Ge mesurée par XRD et concentration en Ge mesurée par ToF-SIMS avec le protocole full spectrum étendu dans les quatre types d'échantillons.

Pour juger plus en avant de la qualité des profiles obtenus par full spectrum étendu il est utile de le comparer avec ceux obtenus par d'autres protocoles de mesure. Pour quantifier le germanium nous avons donc utilisé les protocoles MCs et Jiang *et al*. car leur précision est connue rapportée dans la littérature [51-54]. Les profils obtenus par Jiang *et al.* et full spectrum étendu dans les échantillons intrinsèques sont montrés en Figure III.3. Ceux obtenus par MCs et full spectrum

étendu dans SiGeC sont montrés en Figure III.4. L'accord sur les concentrations en Ge est excellent entre les trois protocoles. De plus un bon accord est trouvé sur les concentrations de dopants (qui ne sont pas tous montrés pour plus de clarté). On peut donc en déduire encore une fois que le protocole permet une quantification précise de Ge et des dopants.

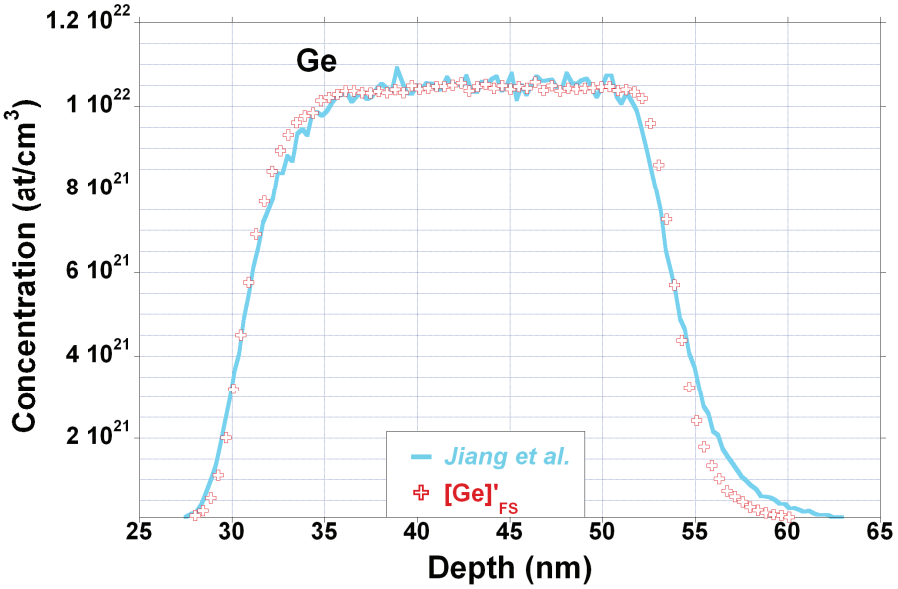

Figure III.3 profils de Ge d'une couche de SiGe non dope obtenue avec les protocoles Jiang *et al.* (1 keV O_2) et full spectrum étendu. L'échelle des ordonnées est linéaire.

Cependant le niveau de bruit des deux protocoles conventionnels semble nettement plus élevé que celui obtenu avec le protocole full spectrum étendu. Les propriétés de chaque protocole sont résumées dans la table III.ii. On s'aperçoit que le meilleur niveau de signal sur bruit est effectivement obtenu avec le protocole full spectrum étendu. De plus la variation de la concentration en Ge dans les différentes couches du même échantillon est plus importante en utilisant des protocoles conventionnels. Ceci démontre bien que les autres protocoles, en plus d'avoir une sensibilité moindre à Ge et aux dopants, sont moins représentatifs de la composition en profondeur du matériau.

	Full Spectrum étendu	MCs	Jiang *et al.*	$Ge^-/^{30}Si^-$	$Ge_2^-/^{30}Si^-$	$Ge_3^-/^{30}Si^-$
Déviation de la concentration de Ge dans les multicouches de SiGe (% de la valeur moyenne)	0.27	0.35	1.5	0.28	0.9	2.05
Moyenne du rapport signal sur bruit dans les couches de SiGe (a.u.)	54.7	14.85	29.75	21.4	12.1	3.1

Table III.ii Propriétés des différents protocoles dans l'échantillon SiGe / Si.

Le protocole « full spectrum étendu » que nous avons élaboré est donc à même de fournir de meilleurs profils que ceux obtenus avec d'autres protocoles plus conventionnels. On leur trouve une meilleure précision dans la quantification de Ge et des dopants, un meilleur rapport signal sur bruit, une limite de détection similaire ou meilleure ainsi qu'une résolution en profondeur légèrement améliorée. Il permet une meilleure quantitativité pour les éléments de matrice et les dopants grâce à la prise en compte de nombreuses espèces d'ions secondaires qui permettent une

meilleure statistique et une meilleure représentativité. Ce protocole est donc le meilleur pour analyser des hétérostructures Si/SiGe.

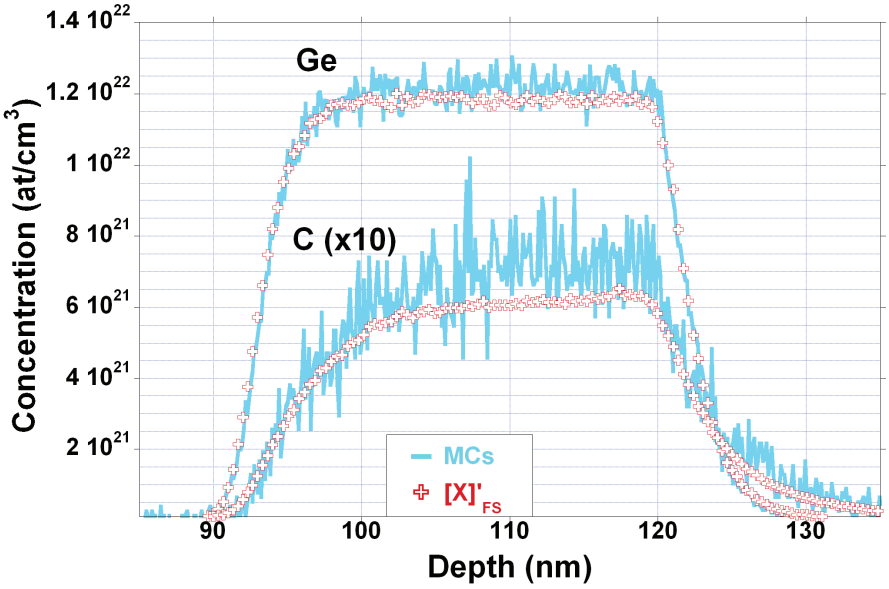

Figure III.4 Profils de Ge et C obtenus dans une couche de SiGeC avec les protocoles MCs et full spectrum étendu. L'échelle des ordonnées est linéaire.

III. 4. d- Améliorations pour le profil quantitatif de couches de SiGeC oxydées

Pour cette étude nous utilisons trois échantillons identiques de SiGeC contraintes et épaisses de 70 nm environ, élaborées par RP-CVD selon la méthode présentée dans [48]. Un échantillon a été gardé tel quel tandis que les deux autres subissaient des recuits oxydants, l'un pendant 30 minutes et l'autre pendant 60 minutes afin d'amorcer le processus connu sous le nom de « condensation du Germanium ». Le profil ToF-SIMS obtenu avec le protocole full spectrum étendu sur l'échantillon recuit pendant 30 minutes (avant et après attache HF pour supprimer l'épaisseur d'oxyde) est montré en Figure III.5. Nous observons l'enchainement des couches :

(i) Une couche de SiO_2 de composition moyenne 66.8 at% O et 33.1 at% Si, les 0.1 at% restant étant du bruit lié à Ge et à C;

(ii) Puis une couche de SiGeC enrichie en Ge avec une concentration de Ge variant en profondeur, typique de processus de condensation de Ge;

(iii) Puis une couche de SiGeC avec des concentrations stables de Ge et de C avec16.2 at% Ge et 2.2 at% C, ce qui correspond bien aux valeurs nominales;

(iv) Et enfin le substrat Si dans lequel la composition est de 99.8 at% Si, les 0.2 at% restant étant du bruit lié à Ge, O and C.

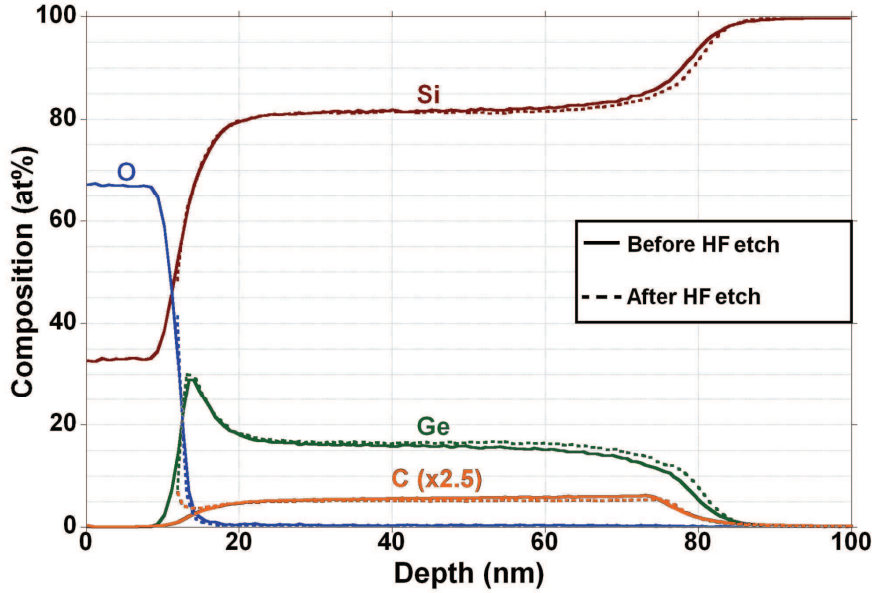

Figure III.5 Profils obtenus par le protocole full spectrum étendu dans l'échantillon recuit pendant 30 minutes sans (lignes pleines) ou avec (pointillés) attaque de l'oxyde de surface à l'HF. Notez l'échelle des ordonnées en at% et linéaire.

On observe très clairement l'enrichissement en Ge sur le profil ToF-SIMS. Par contre le profil de C ne montre pas la même forme (à noter que la même tendance est observée sur l'échantillon recuit pour 60 minutes). La région d'intérêt pour cette étude est la région (ii) et ses interfaces

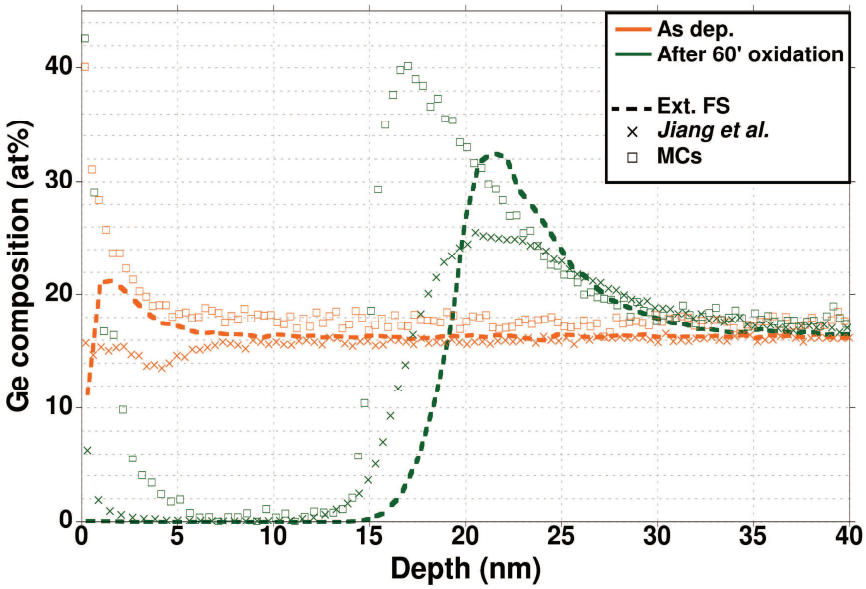

Figure III.6 Superposition des profiles quantifies de Ge obtenus dans l'échantillon recuit pour 60 minutes avec les trios protocols.

avec les régions attenantes, puisque c'est là que se déroule le phénomène de condensation du Ge. C'est aussi une région dans laquelle il est difficile d'obtenir un profil juste par des protocoles de mesure conventionnels à cause des importants effets de matrice. Pour vérifier la justesse de notre protocole, nous avons acquis les profils dans les mêmes échantillons avec deux autres protocoles réputés pour être précis : le MCs et Jiang et al.. La comparaison de ces trois protocoles est effectuée en Figure III.6. Comme attendu, on obtient un bon accord dans la zone de profil

correspondant au régime permanent (régions (iii) et (iv)), ceci pour les concentrations de Ge, Si et C. Cependant d'importantes différences sont à noter aux interfaces. Suivant le protocole utilisé, la région (ii) présente une concentration maximum plus ou moins importante et une forme de pic plus ou moins arrondie. Comparé au profil obtenu en full spectrum étendu, le profil MCs montre une valeur de concentration maximum plus élevée et une forme de pic plus abrupte. A contrario, le profil Jiang et al ; présente une forme plus ronde avec une concentration maximum plus faible. En MCs, on observe en fait une valeur de Ge artificiellement trop élevée due à un artéfact de mesure, ce qui résulte en une surestimation de la dose totale de Ge dans l'échantillon. Par ailleurs, avec Jiang et al. on a un profil plus élargi à cause d'un transitoire plus long entre les régions (i)-(ii), (ii)-(iii) et (iii)-(iv), ce qui induit une sous estimation de la quantité de Ge dans la région (ii), et donc de la cinétique de condensation du Ge mais induit également une surestimation de la dose totale de Ge. Le protocole full spectrum étendu quant à lui montre que la dose totale de Ge se conserve au cours de l'oxydation, ce qui n'est pas le cas des deux autres protocoles et qui est prédit par la théorie de la condensation du Ge. Il en résulte que le protocole full spectrum étendu permet de réduire au minium les effets de matrice dans des échantillons de SiGe oxydés, tout en optimisant les sensibilités chimiques et le niveau de signal/bruit.

En conclusion, nous avons développé différents protocoles originaux pour permettre l'amélioration de la quantitativité du ToF-SIMS pour Ge, O et pour les dopants dans des alliages SiGe intrinsèques ou dopés, et éventuellement oxydés. Nous avons également développé un nouveau protocole d'établissement d'échelle de profondeur. Nous avons testé ces protocoles dans des échantillons représentatifs de structures pour la microélectronique avancée et montré qu'à chaque fois de meilleurs résultats étaient obtenus avec les protocoles développés.

IV Mise en place des solutions et résultats dans les matériaux et structures pour empilement de grille avancés dans les nœuds post 32 nm

IV. 1. Mise en place d'un protocole de profilage EXLE avec abrasion Cs^+

Notre instrument possède de façon standard des colonnes optiques adaptées aux faisceaux basse énergie, puisqu'ils permettent une opération entre 250 et 2000 eV. Chaque point de fonctionnement (250, 500, 1000, 2000 eV) est défini par un ensemble de paramètres tels que le potentiel d'extraction, les potentiels de lentilles électromagnétiques et de déflexion latérale. Pour créer un nouveau point de fonctionnement, le plus simple est de partir d'un point déjà existant et de modifier petit à petit chaque paramètre jusqu'a arriver à l'énergie voulue tout en conservant un courant et une focalisation optimum. De cette façon et en procédant de manière itérative, nous avons pu obtenir des points de fonctionnement pour des énergies aussi basses que 150 eV. Le mode EXLE établi par cette procédure présente des vitesses d'abrasion très lentes du fait du taux de pulvérisation très faible obtenu par un faisceau de 150 eV Cs+ (~0.05 at/ion incident [55]). De plus les courants deviennent très faibles à ces énergies, ce qui augmente encore la durée d'une analyse, avec des vitesses moyennes de ~0.1 nm/min dans Si, en accord avec les valeurs trouvées dans la littérature [55].
A cause de ces taux de pulvérisation très faibles, il y a un risque non négligeable que le ratio abrasion / analyse ne soit pas suffisant et que les dommages infligés à l'échantillon au cours d'une analyse ne soit pas complètement enlevés au cours du cycle d'abrasion. Ceci ferait perdre tous les avantages du mode EXLE en termes de résolution en profondeur. Pour éviter cela, nous utiliserons les faisceaux en mode « non interlacé », c'est-à-dire avec des cycles d'abrasion et d'analyse séparés par des pauses, avec 10 secondes d'abrasion pour une analyse et des pauses de 0.5 secondes entre chaque cycle. De plus, nous avons utilisé une énergie de 15 keV au lieu de 25 keV pour l'analyse. Avec ce protocole nous avons pu avoir un ratio abrasion sur analyse supérieur à 50 pour tous les profils effectués dans ce mode.

IV. 2. Mise en place d'échelles de profondeur justes

De même que dans la partie III, il est nécessaire ici d'utiliser des VSR pour évaluer correctement la variation de vitesse d'abrasion au cours du profil. L'établissement d'une VSR peut se faire en associant la variation du signal représentant l'oxygène dans l'empilement à une variation de vitesse d'abrasion, comme proposé dans [56]. Dans notre protocole, le signal représentatif de l'oxygène est normalisé et lissé afin d'obtenir une fonction VSR, qui est ensuite multipliée par la vitesse d'abrasion dans Si obtenue dans les mêmes conditions expérimentales dans un échantillon de référence. Ce protocoles a déjà montré de bons résultats dans une grande variété d'échantillons est il est avantageux en ce qu'il ne demande aucune calibration supplémentaire au ToF-SIMS, puisque c'est le profil de l'échantillon lui-même qui est utilisé pour obtenir la calibration de l'échelle de profondeur [56].

IV. 3. Mise en place d'un protocole de quantification des éléments de matrice dans des empilements de diélectriques haute permittivité

Nous avons adapté le protocole full spectrum présenté en partie III pour pouvoir l'utiliser sur les matériaux haute permittivité et en particulier sur les silicates d'hafnium. Dans cette version, nous considérons Q_{Si}, Q_{Hf}, Q_O and Q_N, les quantités atomiques de Si, Hf, O et N dans le faisceau d'ions secondaires en utilisant la formule suivante :

$$Q_{Si} = \sum_{n=0}^{6}\sum_{m=0}^{1}\sum_{p=0}^{5}\sum_{q=0}^{1} n \cdot \mathrm{Y}_{\mathrm{Si_nHf_mO_pN_q}} \qquad \text{(IV.1)}$$

$YSi_nHf_mO_pN_q$ étant l'intensité de l'ion $Si_nHf_mO_pN_q^-$ divisée par l'abondance isotopique du composé $Si_nHf_mO_pN_q$. Encore une fois, une seule occurrence est utilisée pour chaque compose, et on évite au maximum les interférences de masse. Pour obtenir Q_{Hf}, Q_O and Q_N, on remplace simplement n par m, p et q, dans l'équation, le reste d l'équation restant identique. Les limites hutes des sommes sont déteriminées par l'intensité des ions secondaires : on arrête de sommer lorsque les ions ne présentent plus d'intensités suffisantes.
L'utilisation de ces quantités offre plusieurs avantage par rapport à de simples intensités d'ions secondaires. On peut en citer deux critiques pour notre application : (i) la réduction des effets dus au transitoire de surface et d'interface et (ii) la minimisation des effets de matrice. Cependant, même si ces quantités sont plus représentatives de la distribution des éléments de matrice dans le matériau, elles sont tout de même différentes de la distribution réelle [57]. Il est donc nécessaire de calibrer ces valeurs pour les convertir en concentration. Nous avons choisi une méthode de calibration originale, qui consiste à calibrer les profils ToF-SIMS sur des données acquises en XPS (et donc libres d'effets de matrice) [58]. On sait que l'aire d'un pic d'intensité en XPS peut s'écrire de la façon suivante avec une approximation de 10% [58-59]:

$$\mathrm{I_A(XPS)} = \mathrm{I_0} \cdot SF_A^{XPS} \int_0^{\infty} \frac{D_A(z) \cdot \exp\left(-\dfrac{z}{\lambda \cos(\theta)}\right)}{\cos(\theta)} dz \qquad \text{(IV.2)}$$

Où $I_A(XPS)$ est l'aire du pic XPS relative à l'élément A A, I_0 l'intensité originale du faisceau, SF_A^{XPS} la sensibilité XPS pour l'élément A dans une matrice donnée, $D_A(z)$ la distribution en profondeur de l'élément A, θ l'angle de détection des photoélectrons, λ la moyenne de la longueur d'atténuation pour les électrons de tous les éléments concernés dans la matrice, et z la profondeur. La distribution $D_A(z)$ peut être modélisée par l'équation suivante:

$$D_A(z) = Q_A(z) \cdot SF_A^{SIMS} \qquad \text{(IV.3)}$$

Où $Q_A(z)$ est une quantité définie en équation (IV.1), et SF_A^{SIMS} is le facteur de sensibilité ToF-SIMS que l'on cherche. En implémentant l'équation (IV.3) dans l'équation (IV.2), tous les paramètres deviennent connus sauf SF_A^{SIMS} que l'on cherche. On peut ensuite obtenir des profils quantifiés en multipliant chaque valeur vue en équation 5IV.1) par la valeur du facteur de sensibilité associée. Cette approche a l'énorme avantage d'être auto-calibrée, c'est à dire qu'elle ne requiert aucun échantillon de référence pour pouvoir être quantitative.

IV. 4. Développement d'une procédure de préparation face arrière adaptée à des empilements de grille ultra fins

Nous proposons ici une méthode simple pour une préparation face arrière adaptée à des échantillons montés sur substrat de Si pur et présentant des oxydes piédestaux d'épaisseurs nanométriques, comme par exemple les empilements de grille avancés. Cette méthode consiste en un polissage physique par abrasion jusqu'à quelques microns de Si restant, suivi par une attaque chimique au TMAH. Nous l'avons utilisée pour préparer des échantillons d'empilement

grille métal/diélectriques pour les CMOS du nœud 32 nm. Dans ces échantillons la couche d'arrêt de l'attaque chimique est constituée d'une couche de SiON de 1.5 nm d'épaisseur.
La préparation comporte quatre étapes principales. La première est la préparation de l'échantillon et de sa contre plaque support. La contre plaque peut être n'importe quel morceau de silicium, mais il est mieux qu'elle présente des formes colorées à sa surface pour permettre une meilleure visualisation de l'avancement de la préparation au fur et à mesure. Cependant il ne faut pas qu'il présente de topographie excessive car cela peut détériorer la qualité de l'analyse finale. Les deux morceaux sont nettoyés dans l'acétone et l'IPA pour retirer toute contamination de surface, puis sont collés à la glue en faisant attention de ne pas inclure de bulles d'air dans la résine. Après quoi les quatre côtés de l'ensemble sont polis pour retirer toute particule.
La seconde étape est le polissage physique, qui est réalisé de façon semi-automatique par le polisseur mécanique. A la fin de cette étape, il ne reste que 5 microns de Si sur les 800 à l'origine.
La troisième étape consiste à couvrir les quatre côtés de l'échantillon avec du platine afin de les protéger de l'attaque chimique. L'épaisseur des couches est de 100 nm environ.
La dernière étape est l'attache chimique au TMAH, qui se fait dans un petit volume et pour des temps courts étant donné la faible épaisseur de Si à enlever. Si toutes les étapes précédentes sont bien réalisées, il est aisé de choisir le bon moment pour stopper l'attaque car la couleur de l'échantillon change radicalement lorsque toute l'épaisseur de Si est enlevée. La durée totale d'une préparation ne dépasse pas une demi-journée.

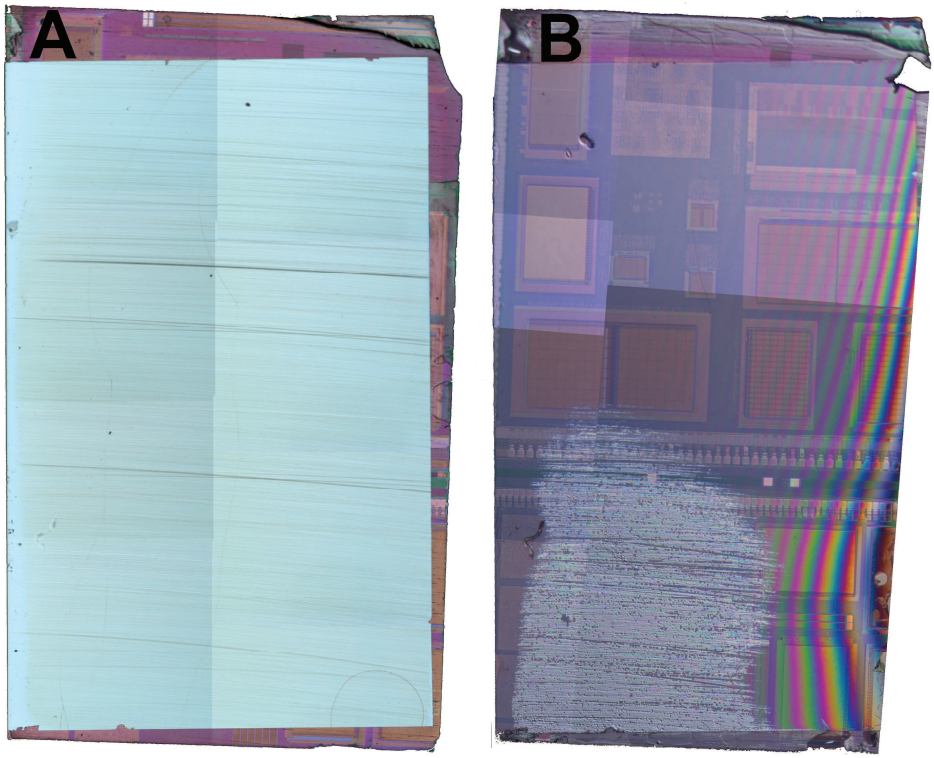

Figure IV.1 Image optique de l'échantillon avant (**A**) et après (**B**) l'étape d'attaque chimique au TMAH. Les franges d'interférence sont dues à une inhomogénéité de l'épaisseur de colle entre les deux échantillons.

Un des avantages de cette préparation est son fort taux de surface utile pour l'analyse. Sur la Figure IV.1 on voit des vues au microscope optique d'un échantillon juste avant et après l'étape d'attache chimique. A gauche on voit une surface grisée correspondant à l'échantillon à préparer. A droite, on voit la même structure, la surface de la contre plaque étant à présent visible par transparence à travers ce qui reste de l'échantillon à préparer et qui est maintenant exclusivement constitué des couches d'intérêt pour l'analyse. La moyenne de surface utile sur les échantillons

préparés par cette méthode est de 70%, ce qui permet l'utilisation d'un même échantillon pour plusieurs techniques d'analyse.
L'autre avantage de cette méthode est la grande qualité de surface après préparation. Des études AFM ont montré qu'en moyenne la rugosité RMS sur des scans de 10 × 10 µm était de 0.228 nm, ce qui est presque aussi bon que pour une surface de Si non traitée.
Enfin, elle permet de conserver presque entièrement les couches d'intérêt puisque les analyses ToF-SIMS, MEIS et AR-XPS de ces échantillons s'accordent pour sire que l'épaisseur moyenne de SiON restante après préparation était de 1.2 nm, ce qui représente plus de 80% de l'épaisseur originale de la couche. Cette préparation permet donc également de préserver la structure à analyser.

IV. 5. Améliorations apportées par les différentes solutions développées en application à des matériaux et structures d'intérêt

IV. 5. a- Améliorations apportées par le mode EXLE pour le profil de couches de SiON

Des profils ToF-SIMS ont été acquis sur des échantillons de couches ultra fines de SiON. Les profils obtenus dans la couche la plus épaisse (1.95 nm) avec un faisceau d'abrasion à 250 et 150 eV sont montrés en Figure IV.2. Ces profils représentent les distributions en profondeur des quantités Q_A/Q_{total}, c'est-à-dire la composition du faisceau d'ions secondaires comme défini par l'équation (IV.1). On observe une différence importante entre les profils obtenus aux deux énergies. D'un point de vue général, les profils obtenus à plus haute énergie sont beaucoup plus dilatés. Plus spécifiquement, les plateaux de Si et O sont bien résolus à l'intérieur de la couche d'oxyde à 150 eV mais présentent des pentes à 250 eV. La montée du signal de Si et la baisse du signal de O à l'interface présentent également des pentes plus faibles à plus haute énergie.

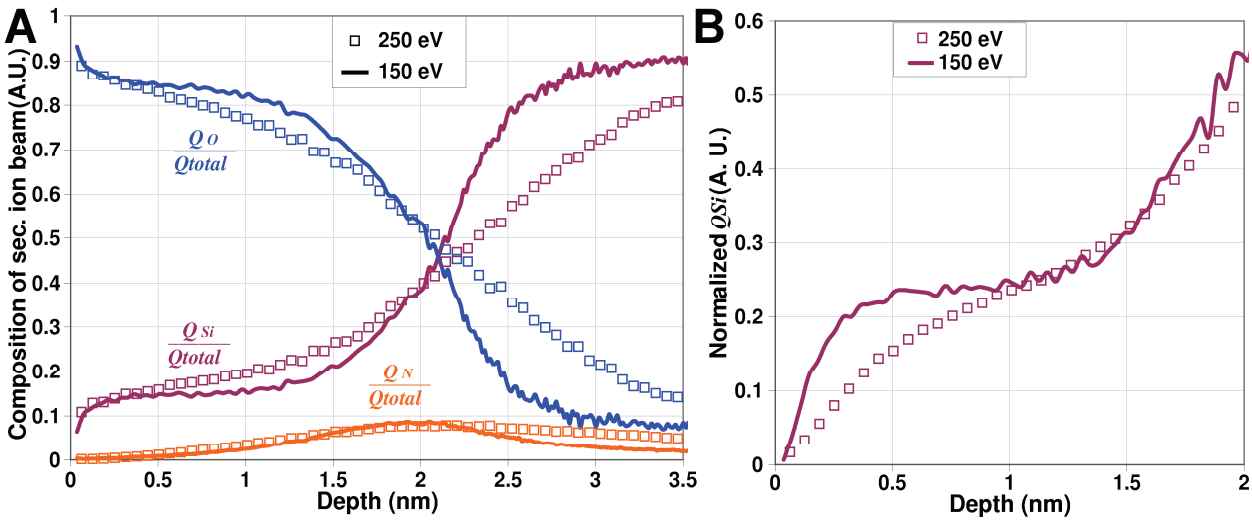

Figure IV.2.A Profils full spectrum d'un échantillon de SiO2 nitruré de 1.95 nm d'épaisseur obtenu avec une abrasion Cs de 250 et 150 eV, et une analyse avec15 keV Bi^+.

B Zoom dans la région de proche surface sur Q_{Si}. L'établissement du régime permanent est plus lent à 250 eV.

La largeur d'interface a ainsi été mesurée à 1.2 nm à 250 eV mais à seulement 0.75 nm à 150 eV. De plus, à l'intérieur du substrat de Si on constate une queue de N beaucoup plus persistante à 250 eV. Tout cela indique que la résolution en profondeur est nettement meilleure avec notre protocole EXLE. Cependant, ce protocole impose des vitesses d'abrasion extrêmement lentes, ce

qui augmente considérablement le temps d'analyse. Bien qu'il soit particulièrement indiqué pour l'analyse de couches ultra fines, nous allons donc utiliser une abrasion 250 eV par la suite.

IV. 5. b- Précision des profils acquis avec le protocole full spectrum dans des empilements de diélectriques haute permittivité

Une propriété intéressante des profils obtenus avec le protocole full spectrum est que le nombre de coups est optimisé pour chaque élément, et leur intensité est proche, avec une différence de moins d'une décade dans tous les cas. Ceci n'est pas usuel en ToF-SIMS puisque les intensités d'ions secondaires correspondant à des espèces différentes diffèrent souvent de plusieurs ordres de magnitude. En conséquence, les facteurs de sensitivité de Ge, Hf, O et N sont très proches de celui de Si. Ceci prouve par ailleurs que les effets de matrice sont bien minimisés en utilisant ce protocole. De plus ont s'aperçoit que ces facteurs varient également très peu d'un échantillon à l'autre pour un élément donné, bien que les structures et les compositions soient légèrement différentes.

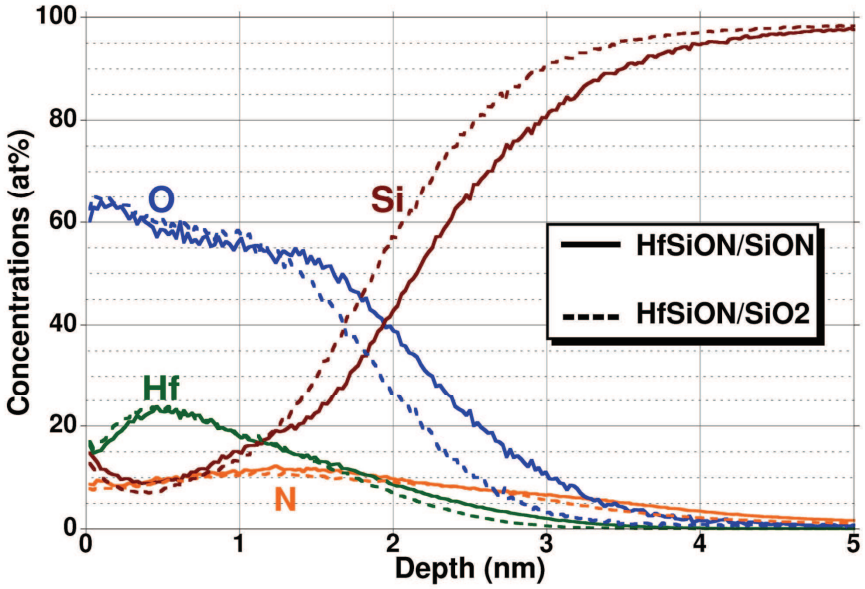

Figure IV.3 Profils full spectrum des échantillons HfSiON/SiO_2/Si et HfSiON/SiON/Si.

Les profils full spectrum d'empilements HfSiON / SiO_2 / Si et HfSiON / SiON / Si sont présentés en Figure IV.3. L'échelle de concentration est en at%, ce qui n'est pas usuel en ToF-SIMS et est une conséquence directe de mécanisme de quantification décrit en IV.2. Chacun des profils présente une structure caractéristique de l'empilement étudié, avec un plateau de O, Si et Hf correspondant au silicate d'hafnium, puis une région transitoire correspondant à l'oxyde piédestal et enfin une région riche en Si correspondant au substrat. L'oxyde piédestal est vu plus fin dans le cas de SiO_2, ce qui est bien en accord avec les valeurs nominales. De même, les compositions trouvées sont proches des compositions nominales des couches, ce qui tendrait à montrer que les profils sont justes. Pour le prouver il nous faut utiliser une autre technique.

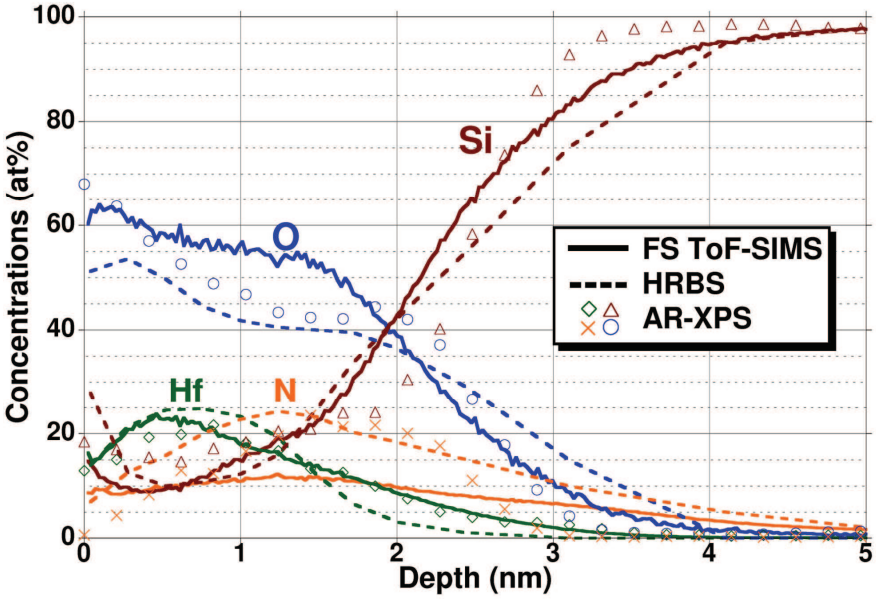

Figure IV.4 Superposition des profils ToF-SIMS, HRBS et AR-XPS sur l'échantillon HfSiON/SiON/Si.

Les profils obtenus en ToF-SIMS, HRBS et AR-XPS sur l'échantillon HfSiON/SiON/Si sont superposes en Figure IV.4. Premièrement on constate un assez bon accord des profils entre les trois techniques, autant en termes d'épaisseur de couches que de composition. En effet on trouve un accord sur les compositions avec une dispersion de ±2 at% pour Hf et Si ; et de ±5 at% pour O et N. Les stœchiométries partielles [Hf]/([Hf]+[Si]) obtenues avec les trois techniques s'accordent également bien sur une valeur de ~60% ±5%. Enfin les profils convergent sur le fait que le pic d'azote se situe à l'interface entre le silicate d'hafnium et l'oxyde piédestal.
Une observation plus précise de ces profiles montre tout de même des différences, et en particulier sur le profil de N qui présente une queue persistante en ToF-SIMS, ce qui est du à la migration de l'élément in-situ lors de l'analyse et qui ne peut donc pas être « rattrapé » par notre protocole de traitement de données.
En revanche, cette étude montre bien la faisabilité d'analyse quantitative des éléments de matrice dans des empilements de diélectriques hautes permittivité par ToF-SIMS.

IV. 5. c- Améliorations apportées par la préparation face arrière pour l'analyse d'empilements de grille HKMG ultra fins

L'utilisation d'une technique à faisceau d'ions implique l'abrasion, dans notre cas avec une espèce chimiquement active. Ceci génère deux effets: (i) la création de rugosité et le mélange à l'impact des couches sous la surface de l'échantillon, et (ii) : la modification de la composition des couches de surface par adsorption d'espèces chimiques, qui peuvent à leur tour provoquer la migration d'espèces à l'intérieur de l'échantillon. Pour remédier à cela et obtenir des profils de profondeurs fiables, on peut utiliser une préparation face arrière.
La Figure IV.5 montre les profils ToF-SIMS de même échantillon obtenu par approche classique et par face arrière. Les deux approches donnent le même profil dans la couche de TiN comme le montre le bon alignement des deux profils. Cependant dès que l'on pénètre dans la couche de silicate d'hafnium, il y a distorsion très importante du profil obtenu par analyse face avant, qui est un effet direct de la ségrégation d'Hf pendant l'analyse. On n'observe pas cet effet par analyse face arrière car le Hf est dans ce cas sur une couche métallique, ce qui l'empêche de ségréger au cours de l'analyse. En plus de la modification de vitesse d'abrasion, on assiste à une distorsion très importante des intensités d'ions secondaires qui montrent un changement brutal de

probabilités d'ionisations pour presque tous les éléments. La quantification est donc très difficile dans ce genre d'échantillons par analyse conventionnelle, tandis qu'une analyse face arrière permet de gommer une bonne partie des artéfacts observés.

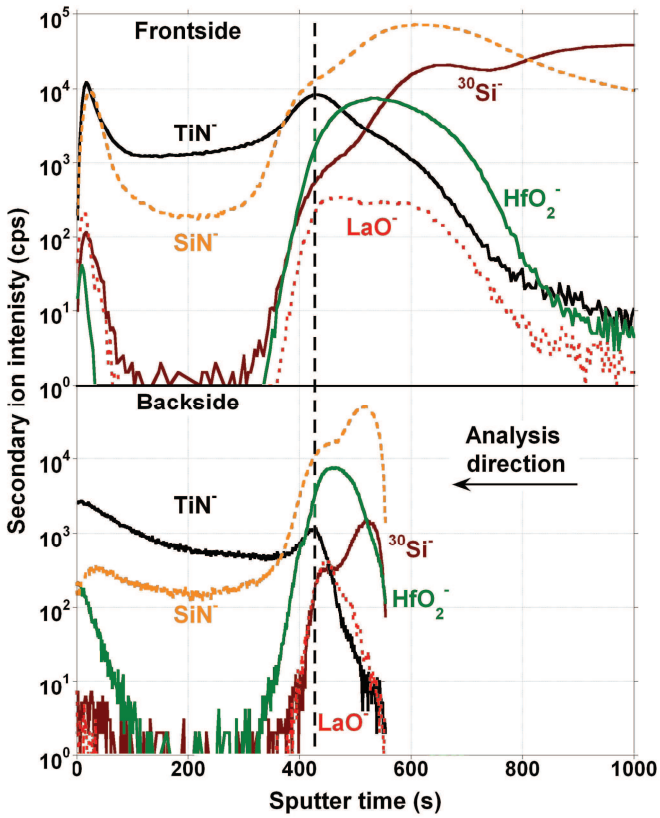

Figure IV.5 Profils ToF-SIMS du même empilement HKMG selon l'approche conventionnelle et l'approche face arrière.

En conclusion, nous avons développé différents protocoles originaux pour permettre l'amélioration de la quantitativité du ToF-SIMS pour les éléments de matrice dans des empilements HKMG. Nous avons testé ces protocoles dans des échantillons représentatifs de structures pour la microélectronique avancée et comparé ces analyses avec des analyses obtenues par d'autres outils de pointe. Nous avons montré qu'à chaque fois de bons résultats étaient obtenus avec les protocoles développés.

V Mise en place des solutions et résultats dans les matériaux et structures pour les USJ Arsenic pour les générations de CMOS post 32 nm

V. 1. Etude systématique des ions secondaires

Lors de l'analyse d'implants très basse énergie de As dans Si, on sait que les ions $AsSi^-$ ne présentent pas d'artéfact de mesure, alors que les ions As^- en présentent (et en particulier un pic de concentration irréaliste à l'interface oxyde natif/silicium [60-61]. Cet effet est très clairement observé dans le profil ToF-SIMS montrés en Figure V.1. Ce profil correspond à un échantillon d'implant As 1 keV dans Si(110) sans recuit. La forme de profil attendue est donc une convolution d'une gaussienne et d'une exponentielle décroissante pour former un profil en cloche. La distribution de l'ion $AsSi^-$ correspond assez bien à cette description, mais pas celle de l'ion As^-. En effet celle-ci montre un pic de concentration à environ 100 s d'abrasion, puis une double tendance exponentielle de chute de signal : une avant 250 s d'abrasion, une autre après.

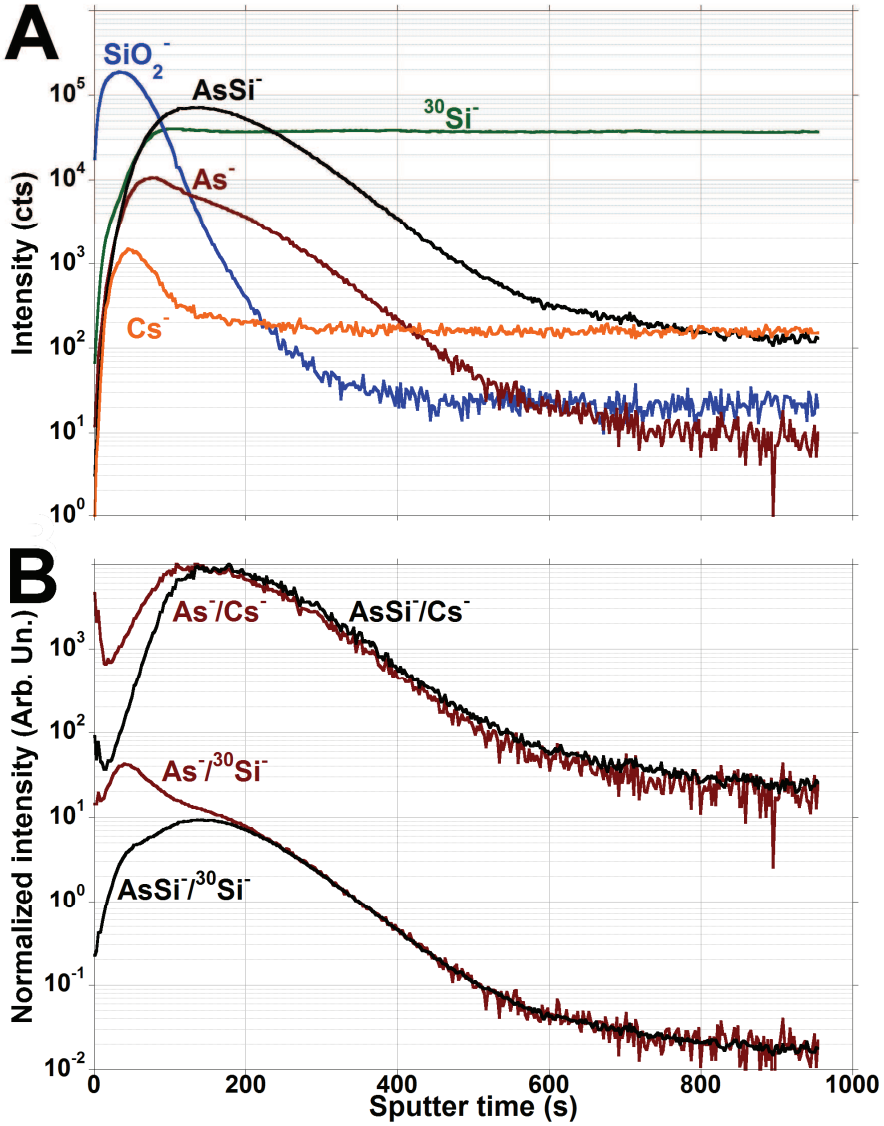

Figure V.1.A Profils d'intensités brutes dans un échantillon d'implant d'As dans du Si.
B Comparaison de différentes normalisations opérées pour minimiser les artéfacts de mesure. On observe une minimisation optimale en utilisant le signal Cs^-.

Le choix de l'ion $AsSi^-$ semble donc plus avisé pour caractériser ces échantillons. Cependant, étant donné l'intérêt de sources et drains sSiGe pour les prochaines générations de dispositif, il serait intéressant de trouver un protocole directement transposable dans ces matériaux. De facto, l'ion $AsSi^-$ ne peut pas être utilisé à cause de l'interférence de masse dans SiGe avec les isotopes SiGe-, qui requiert une résolution de masse bien supérieure à celle fournie par notre instrument pour être praticable [62]. Nous devons donc trouver un moyen de caractériser précisément ces échantillons en utilisant l'ion As^-.
Il faut se remémorer que les intensités brutes des ions secondaires ne sont pas nécessairement représentatives de la forme finale du profil quantifié, puisque l'on passe nécessairement par la normalisation par un signal représentatif de la matrice. On peut donc, via le choix d'un ion secondaire pour la normalisation du signal As^-, essayer de minimiser les artéfacts de forme observés sur le profil d'intensités brutes. Le signal Cs^- apparait comme un candidat intéressant car il possède une évolution d'intensité en profondeur qui semble compenser les évolutions irréalistes du signal d'As^- (voir Figure V.1). Les résultats de cette normalisation sont montrés en Figure V.1. On observe bien une diminution de la différence entre les signaux relatifs à As^- et $AsSi^-$ après normalisation, ce qui indique le bien fondé de notre approche. Cette normalisation, utilisée dans les échantillons d'intérêt et dans un implant de référence, permet d'obtenir une quantification en profondeur de la concentration d'As dans le matériau.

V. 2. Mise en place d'une échelle de profondeur

La façon la plus simple de rendre compte de l'évolution des vitesses d'abrasion dans SiO_2 et Si est de les mesurer dans des échantillons de référence et d'établir une phase d'adaptation entre les deux vitesses en normalisant un signal relatif à l'oxygène, comme proposé en partie IV. Cependant, pour le profilage des USJ à base d'As, on attend des effets de transitoire non linéaires en surface qui peuvent induire un shift important du pic d'As vers la surface. Ces effets sont dus à la phase d'accumulation du Cs en surface de l'échantillon et ne sont pas pris en compte par un modèle ne tenant compte que de vitesses moyennes dans Si et SiO_2. Pour corriger cela, nous avons mis au point une nouvelle composante variable du VSR, valable en proche surface:

$$VSR_{surface} = (SR_{SiO_2} \times M) \cdot \mathrm{e}^{-\frac{t \times SR_{SiO_2}}{D_c}} \qquad \text{(V.1)}$$

Où SR_{SiO2} est la vitesse moyenne dans SiO_2 déterminée dans l'échantillon de référence, M est un facteur amplificateur empirique et D_c une valeur empirique de profondeur critique d'atténuation des effets de transitoire. Après optimisation, nous avons sélectionné une valeur de 4 pour M, et de0.23 nm pour D_c.

V. 3. Améliorations apportées par les différentes solutions développées en application à des matériaux et structures d'intérêt

V. 3. a- Précision de l'échelle en profondeur

Pour évaluer la précision de notre échelle en profondeur, nous avons utilisé le protocole full spectrum pour quantifier le Si et l'O dans des échantillons d'implants d'As 1 keV dans du Si(110) et à travers un oxyde natif. Les épaisseurs d'oxyde ont été obtenues par NRA, en assumant une densité 2200 $kg.m^{-3}$ [46], par HRBS et ToF-SIMS en déclarant l'interface SiO_2/Si à mi-intensité du signal relatif à l'oxygène. Les épaisseurs trouvées par toF-SIMS à plusieurs

énergies d'abrasion se sont révélées être très proches l'une de l'autre, avec une variation ±0.15 nm autour de leur valeur moyenne. La comparaison des épaisseurs obtenues par les trios techniques est donnée en Table V.i.

	ToF-SIMS	HRBS	NRA
Echantillon non recuit	1.46 ± 0.15	1.48 ± 0.1	1.51 ± 0.15
Echantillon recuit	2.02 ± 0.15	2.07 ± 0.1	1.98 ± 0.2

Table V.i Epaisseurs d'oxyde obtenues par ToF-SIMS, HRBS and NRA dans l'échantillon recuit et non recuit. Les valeurs sont en nm.

On observe un accord excellent des trois techniques, ce qui montre bien la précision de notre protocole d'établissement d'échelle de profondeur.

V. 3. b- Améliorations apportées par le regime EXLE

Comme déjà démontré en partie IV, la meilleure résolution en profondeur peut être obtenue en utilisant le régime EXLE. Ceci se vérifie encore içi en comparant les profils full spectrum de concentration de Si et O obtenus à 250 et à 150 eV d'abrasion césium. On observe une fois encore une meilleure résolution du plateau de O et Si dans la zone correspondant à l'oxyde en descendant en mode EXLE. La largeur d'interface peut être calculée en faisant la différence entre les points d'intensité 20% et 80% sur le signal de Si. Les valeurs ainsi trouvées sont de 0.5 ±0.1 nm à 150 eV contre 0.9 ±0.1 nm à 250 eV. Malgré cette différence, les distributions en profondeur d'O obtenues aux deux énergies s'accordent bien dans une région située en plein milieu de l'interface (entre 1.8 et 2.0 nm). Par contre, la chute du signal d'O est bien plus rapide après ce point en utilisant le mode EXLE. La chute du signal mesurée dans le régime exponentiel de chute est de 0.45 nm à 150 eV contre 0.77 nm à 250 eV. Le protocole expérimental de profilage EXLE montre donc bien des améliorations importantes en termes de résolution en profondeur.

V. 3. d- Comparaison générale de profils obtenus avec différentes conditions expérimentales

Pour déterminer quel profil de concentration d'As est le plus juste, il nous faut d'abord déterminer au plus près cette distribution en utilisant une technique dont la précision est reconnue dans ce type d'échantillons. Pour l'échantillon non recuit, nous aurons donc recours à la simulation (Crystal TRIM), et à la HRBS pour l'échantillon recuit (tandis que la simulation du profil diffusé obtenu avec S-Process servira uniquement pour vérifier que la forme du profil ne soit pas aberrante). Une superposition des profils obtenus à 150, 250 et 500 eV par ToF-SIMS et par simulation ou HRBS dans les échantillons recuit et non recuit est présentée en Figure V.2.
Tout d'abord, si l'on compare les profils ToF-SIMS entre eux, on observe comme l'on pouvait s'y attendre une dilatation plus importante des profils obtenus à plus haute énergie d'abrasion. Ceci est particulièrement frappant sur les profils obtenus à 500 eV, qui ne résolvent même pas le pic d'As correctement, que ce soit avant ou après recuit. Ce pic est en effet confondu avec l'artéfact de surface, induit par le régime transitoire, qui provoque une surévaluation du signal d'arsenic dans les premiers nanomètres de l'analyse. Hormis ces différences, on observe tout de même un accord relativement correct entre les différents profils sur deux points : la position en profondeur du pic de concentration d'As et la queue du profil (après 8 nm).

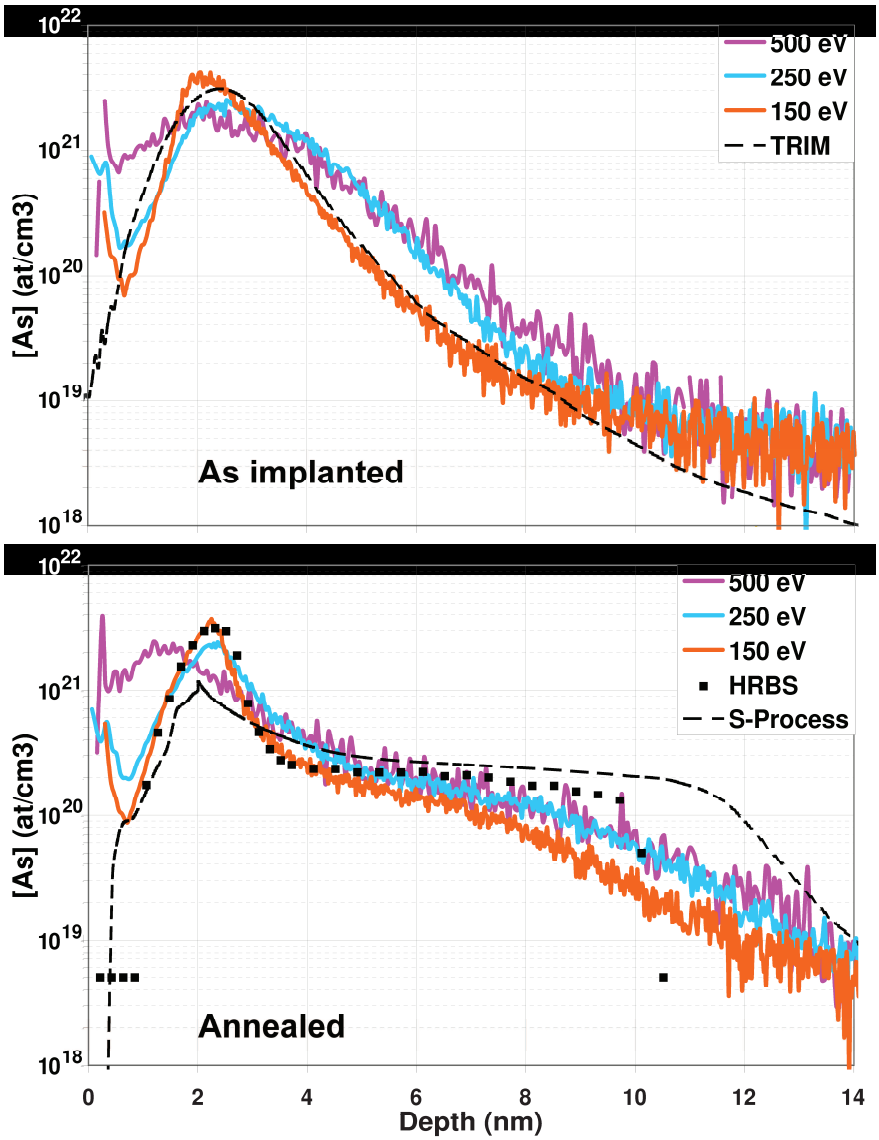

Figure V.2 Superposition des profiles de concentration ToF-SIMS, HRBS et simulation dans les échantillons recuit et non recuit.

Si l'on compare maintenant les profils ToF-SIMS avec ceux obtenus par les techniques de référence, on voit que les meilleurs profils sont toujours obtenus à 150 eV d'abrasion, que ce soit dans l'échantillon recuit comme non recuit. Bien que le plateau de concentration d'As dans l'échantillon recuit et les queues de profils montrent tous un accord avec les profils de référence, la finesse du pic de concentration maximum est bien meilleure à 150eV. Ceci est particulièrement flagrant sur le pic d'interface oxyde/silicium de l'échantillon recuit. On obtient donc la meilleure forme de profil à 150eV, quel que soit l'échantillon.
Pour aller plus loin, on peut également s'intéresser à la comparaison des doses totales d'As calculée à partir des profils ToF-SIMS et celle obtenue en RBS qui nous sert de référence. Ceci est réalisé en Figure V.3. De façon un peu surprenante, on voit que les profils donnant la meilleure forme de profil ne donnent pas systématiquement une dose juste. Par exemple, le profil obtenu à 150 eV sous-estime la dose d'As par rapport à la RBS. Au contraire, des profils dont on sait que la forme est fausse et déformée donnent des doses en accord avec la RBS, comme par exemple le profil obtenu à 500 eV. On peut en déduire que cette dose, artificiellement juste, n'est que le résultat d'une coïncidence d'un équilibre entre les zones où la concentration d'As est

surestimée et celles où elle est sous-estimée. Par conséquence, aucun des profils vus jusqu'ici ne permet d'avoir une description précise de l'échantillon sur tous les points nécessaires, à savoir forme de profil et dose totale. En revanche les profils obtenus en mode EXLE sont bien les meilleurs en ce qui concerne la forme du profil.

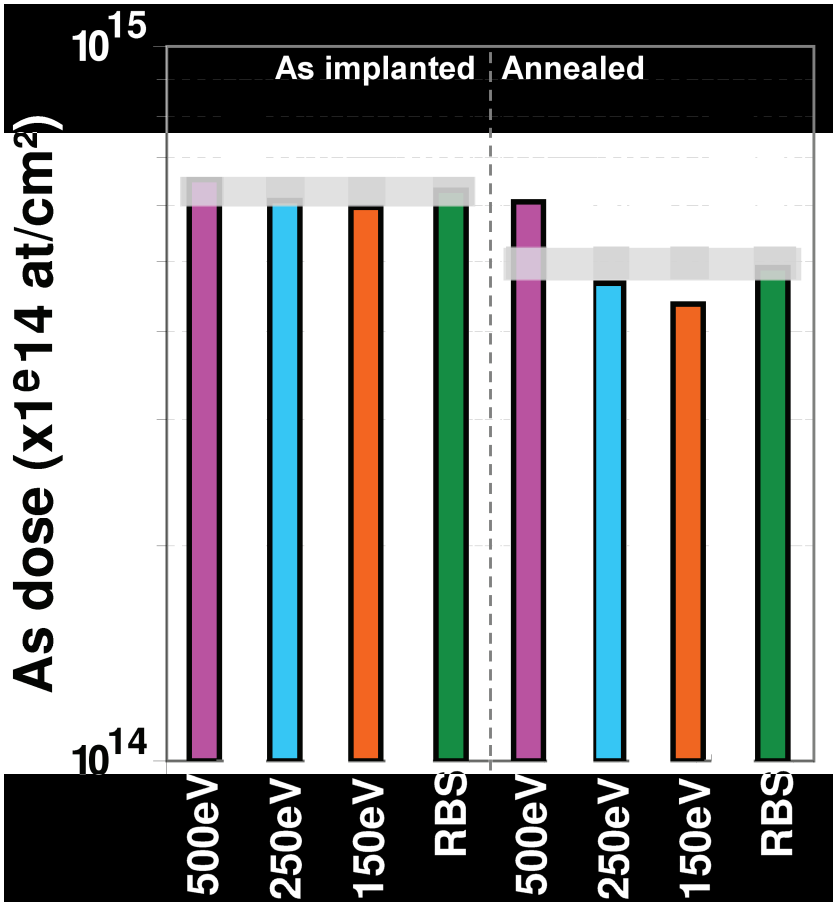

Figure V.3 Doses totales d'As calculées à partir des profiles ToF-SIMS et trouvées en RBS dans les deux échantillons. La marge d'erreur RBS est indiquée par une barre grisée.

En conclusion, nous avons développé différents protocoles originaux pour permettre l'amélioration de la quantitativité du ToF-SIMS dans les implants d'As dans Si. Nous avons également développé un nouveau protocole d'établissement d'échelle de profondeur. Nous avons testé ces protocoles dans des échantillons représentatifs de structures pour la microélectronique avancée et montré qu'à chaque fois de meilleurs résultats étaient obtenus avec le protocole de profilage EXLE. Cependant nous avons aussi démontré les limites de la technique puisqu'il a été impossible d'obtenir une dose juste et une forme de profil juste avec une seule analyse.

VI Mise en place des solutions et résultats dans les matériaux et structures pour l'électronique organique : application aux mélange PMMA-C_{60}

VI. 1. Etude des spectres de masse, sélection d'ions secondaires représentatifs

Il n'est à priori pas trivial de détecter des fullerènes, molécules organiques composées uniquement de carbone, dans une matrice polymère dont l'élément principal est également le carbone. Nous avons donc étudié les spectres de masse obtenus dans plusieurs conditions expérimentales pour essayer de trouver celle qui permettait une meilleure observation du C_{60} en séparant bien les contributions des fullerènes et celles du polymère. Nous avons obtenu des spectres de masse en utilisant les faisceaux primaires Bi_x^+ à 25 keV, dans lesquels x = 1 ou 3. Le suivi des ions secondaires positifs n'a pas permis la détection d'ions relatifs au fullerène dans des mélanges de faible composition de C_{60}. Par contre, les spectres obtenus en suivant les ions secondaires négatifs ont montré une forte signature à la masse 720 u, correspondant à $^{12}C_{60}^-$. Un spectre de surface d'un échantillon de PMMA - 10 wt% C_{60} est montré en Figure VI.1.

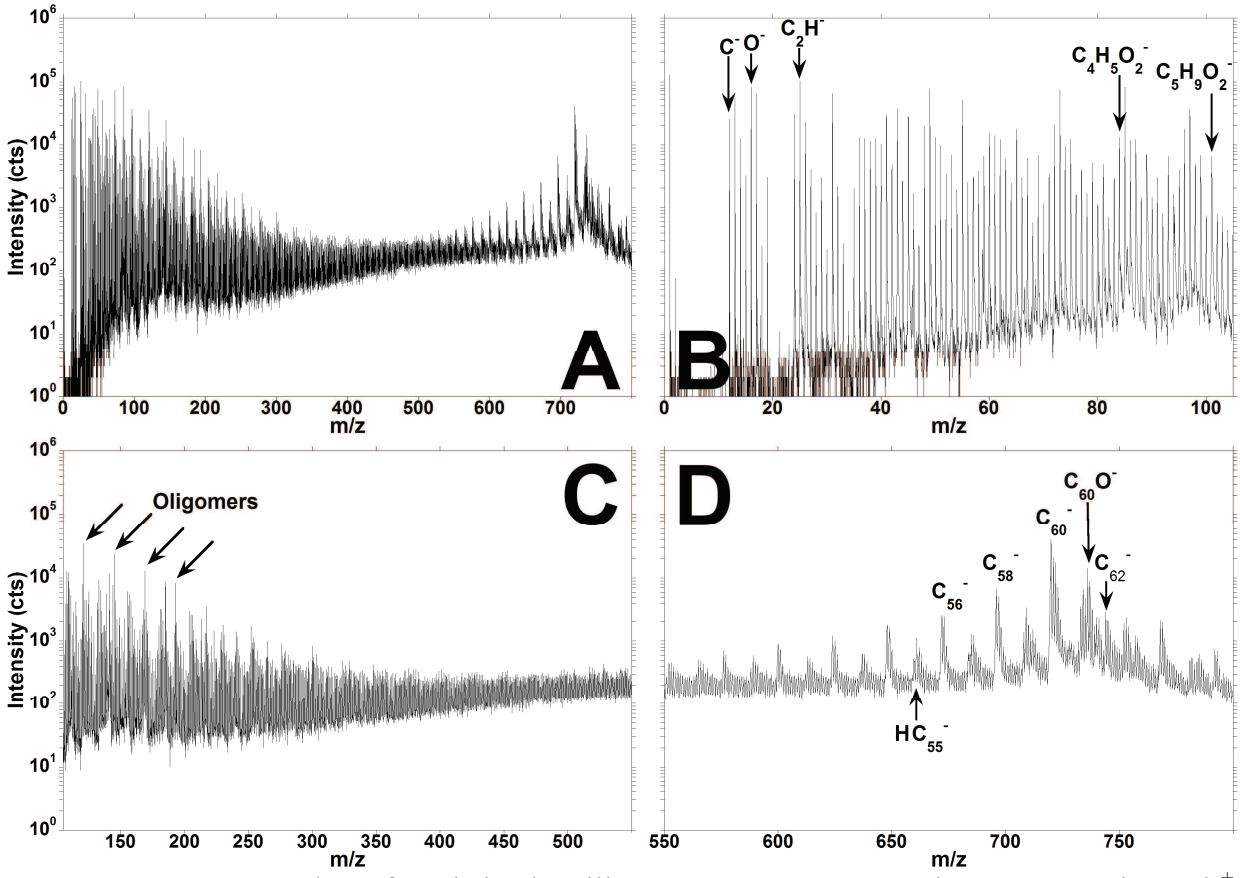

Figure VI.1.A Spectre de surface de l'échantillon PMMA-10 wt% C_{60} obtenu avec 25 keV Bi_3^+.
B Zoom sur la zone de faible masse du spectre, de m/z = 0 à 105.
C Zoom sur la zone de moyenne masse du spectre, de m/z = 105 à 550.
D Zoom sur la zone de haute masse du spectre, de m/z = 550 à 800.

Le groupe de masse du C60 apparait avec une intensité particulièrement forte dans le cadre de la Figure VI.1.D. Lorsqu'on regarde le spectre de masse complet (Figure VI.1.A), on observe en plus du groupe de C60 un nombre assez important de pics, parmi lesquels il est nécessaire de déterminer ceux qui sont caractéristiques du PMMA. On peut diviser ce spectre en trois groupes différents ; (i) le groupe de m/z < 50, qui correspond au pics d'ions monoatomiques (C, O, H) et

poly atomiques (résultant de la fragmentation de la matière organique mais aussi de la recombinaison à l'impact), (ii) le groupe $50 \leq m/z \leq 105$, qui correspond à la fragmentation de la chaine de PMMA en fragments caractéristiques, et au monomère de PMMA à $m/z = 101$ (Figure VI.1.B) et enfin (iii) le groupe $m/z \geq 105$, qui correspond à des ions oligomères contenant un nombre n de monomères et/ou des fragments lourds de chaine (Figure VI.1.C). Les ions secondaires caractéristiques du PMMA sont donc choisis dans le groupe (ii), dont l'analyse spectrale est facilitée par une littérature abondante. En partant de librairies de spectres et de la littérature disponible, nous avons donc sélectionné l'ion fragment $C_4H_5O_2^-$ (m/z=85 u) et le monomère du PMMA $C_5H_9O_2^-$ (MMA + H, m/z=101 u) comme ions caractéristiques du PMMA.

VI. 2. Mise en place d'un protocole de profilage minimisant les dommages

Du fait de la nature très fragile des matériaux organiques, ils sont très facilement endommagés par le bombardement des ions primaires, et ce même à faible dose. La plupart du temps, cela résulte en une perte rapide des signaux moléculaires, témoignant d'une destruction importante des couches. Pour éviter ce phénomène, il nous faut utiliser une énergie d'abrasion basse et retirer autant que possible le dommage infligé aux couches par les ions énergétiques du faisceau d'analyse. Pour réaliser cela nous opérons le ToF-SIMS en mode « non interlaced » avec illumination alternative de l'échantillon par le faisceau d'abrasion et d'analyse. L'utilisation de l'oxygène comme espèce d'abrasion ayant mené à la disparition quasi-totale des signaux relatifs au C_{60} après de très faibles doses, nous avons uniquement utilisé le césium comme espèce d'abrasion. Les meilleurs profils ont été obtenus en utilisant le protocole suivant : 25 keV Bi^+ ou Bi_3^+ pour l'analyse et 250 eV Cs^+ pour l'abrasion. Les courants primaires dans ce mode étaient de 15 nA en continu pour les deux faisceaux. Les tailles de balayage étaient de 300 µm × 300 µm et 100 µm × 100 µm pour l'abrasion et l'analyse respectivement. Le meilleur équilibre entre stabilité des signaux et statistique (nombre de points de donnée) a été obtenu en alternant 3 secondes d'abrasion et un cycle d'analyse avec une pause de 0.5 secondes.

VI. 3. Mise en place d'un protocole de quantification du C_{60} dans un mélange PMMA - C_{60}

La possibilité de quantifier le niveau de C_{60} dans les mélanges a été étudiée en utilisant différents ions secondaires caractéristiques du PMMA et en regardant l'évolution du ratio $I(C_{60}^-)/I(\text{fragment}^-)$ en fonction du taux nominal de C_{60} dans les couches. De manière générale, on s'aperçoit que plus on utilise un fragment massif du PMMA, plus on obtient une bonne corrélation linéaire entre la valeur du ratio d'intensité et la composition nominale. Cependant, au-delà d'une certaine masse, la reproductibilité diminue du fait des faibles intensités de signal. La meilleure corrélation a en effet été obtenue en utilisant l'ion secondaire $C_5H_9O_2^-$, qui est représentatif du monomère du PMMA. Le protocole de quantification choisi consiste donc à regarder l'évolution du ratio $I(C_{60}^-)/I(C_5H_9O_2^-)$ en fonction de la composition nominale en C_{60}.

VI.4. Améliorations apportées par les différentes solutions développées en application à des matériaux et structures d'intérêt

VI. 4. a- Avantage des ions poly-atomiques pour l'obtention de spectres de masse optimisés

Le spectre de masse de la surface d'un échantillon de mélange PMMA - 0.025 wt% C_{60} obtenu avec Bi^+ and Bi_3^+ est montré en Figure VI.2. Le groupe de masse correspondant au C60

apparait avec de beaucoup plus fortes intensités sur le spectre obtenu avec Bi_3^+. L'augmentation de sensibilité est d'environ 15 en passant d'un ion monoatomique à poly-atomique, tout en gardant la même tension d'accélération. De plus (non montré) les signaux moléculaires sont aussi améliorés, avec des pics de plus forte intensité aux masses m/z = 85 and 101 qui correspondent à des fragments caractéristiques de la chaîne de PMMA. Ceci montre que les ions primaires poly-atomiques sont les plus indiqués pour notre analyse car ils permettent d'optimiser les signaux d'ions secondaires caractéristiques des mélanges à étudier. Par comparaison les ions monoatomiques n'offrent qu'une très faible sensibilité.

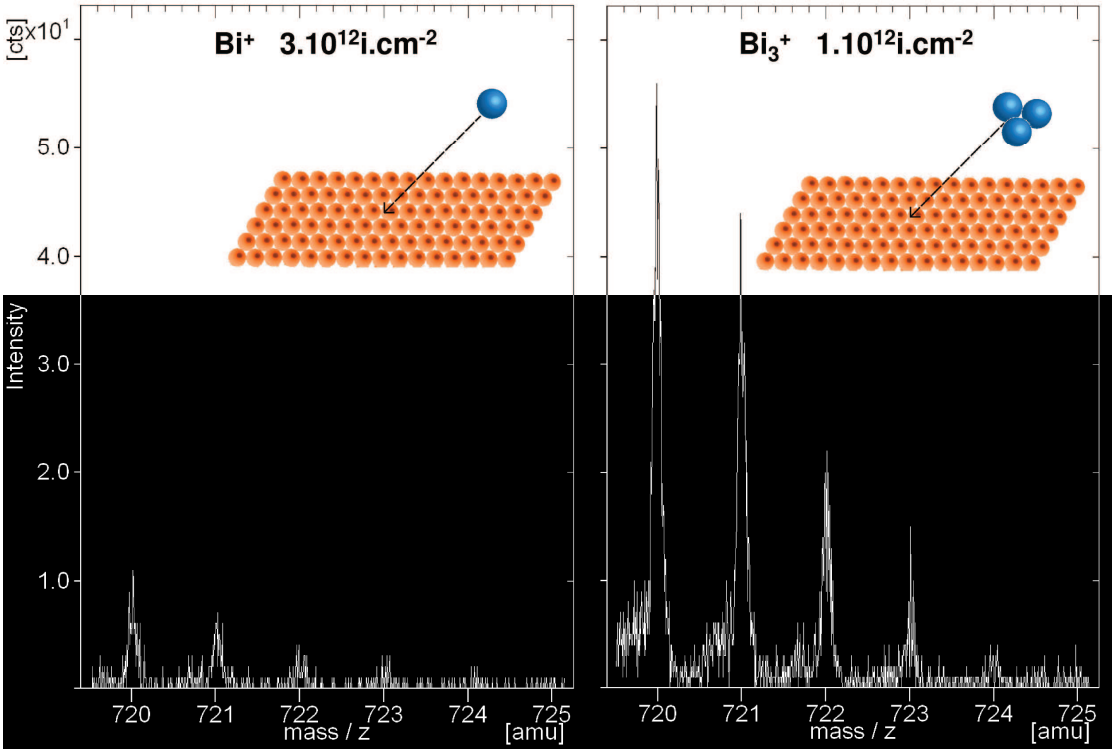

Figure VI.2 Zoom sur la zone m/z= 719 to 726 du spectre de surface de l'échantillon PMMA - 0.025 wt% C_{60} obtenus avec le même nombre d'atomes incidents de Bi^+ and Bi_3^+.

VI. 4. b- Propriétés des profils et quantification avec les protocoles développés

Le protocole de profilage développé en section VI.2 a permis d'obtenir des profils d'intensités de signaux organiques extrêmement stables en profondeur. La Figure VI.3 montre le profil obtenu sur l'échantillon PMMA - 0.015 wt% C_{60}. Après un court régime transitoire induisant une forme en « v » sur tous les signaux organiques, l'intensité des tous les fragments observés reste remarquablement stable tout au long de la couche organique. Cette stabilité, comparable à des résultats récents de la littérature [63], montre que presque aucune perte d'information chimique n'est à déplorer, c'est-à-dire que la destruction du matériau par le faisceau d'analyse est suffisamment compensée par le cycle d'abrasion basse énergie. Pour mesurer la perte de signal on peut utiliser le calcul de la section efficace d'endommagement, qui est inférieure à 0.001 nm² dans tous les échantillons, ce qui est plusieurs ordre de magnitude meilleur que ce que l'on trouve dans la littérature pour une abrasion au SF_5^+ à 5 keV [64].

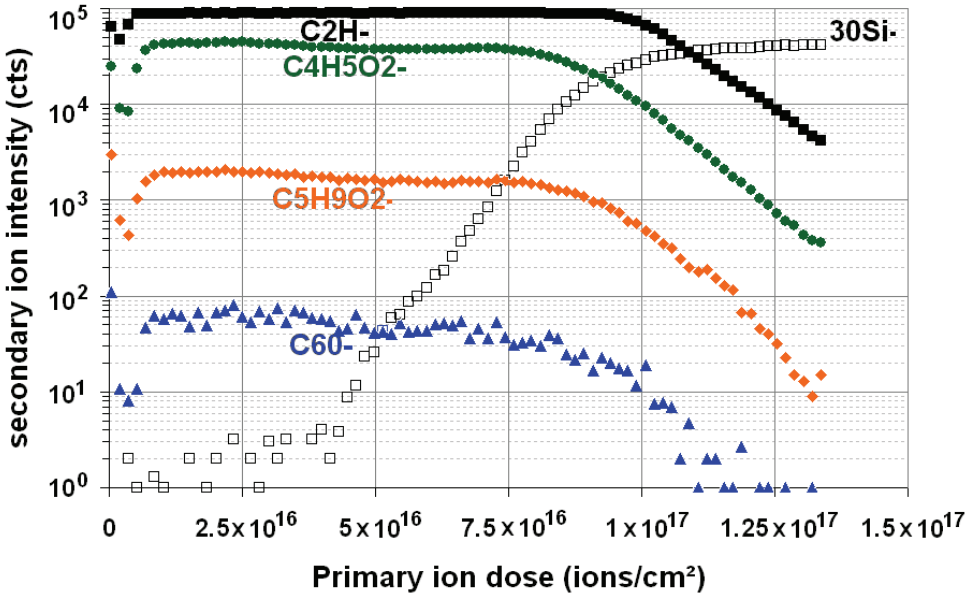

Figure VI.3 Profil en profondeur de l'échantillon PMMA - 0.015 wt% C_{60}. remarquez le transitoire court et la stabilité des ions secondaires organiques dans la couche organique.

Au plus le contenu de la couche en C_{60} est important, au plus l'interface couche organique/substrat silicium (et donc la résolution en profondeur) semble être améliorée, comme le montre la Figure VI.4. La décroissance exponentielle du signal de C_{60}^- varie de façon monotone avec le contenu en C_{60} des couches, de 550 secondes d'abrasion par décade dans l'échantillon PMMA - 0.015 wt% C_{60} jusqu'à 30 secondes d'abrasion par décade dans l'échantillon PMMA - 20 wt% C_{60}. Nous estimons que ceci est du au caractère de plus en plus conducteur des couches lorsqu'on rajoute du C_{60}, ce qui influe sur la formation de rugosité à la surface de l'échantillon.

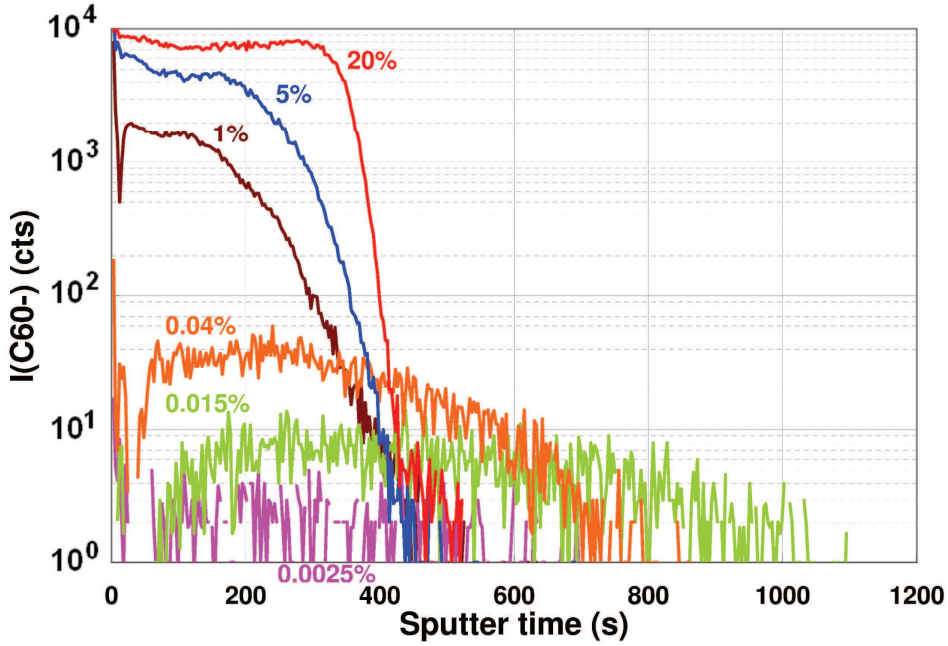

Figure VI.4 Profils d'intensité de C_{60}^- dans une sélection d'échantillons.

Enfin, nous avons utilisé le protocole développé en VI.3 pour obtenir une courbe de calibration de la concentration en C_{60} dans des couches de mélange dont la concentration en C_{60} variait de 0.0025 wt% à 20 wt% C_{60}. En traçant la variation de valeur du ratio $I(C_{60}^-)/I(C_5H_9O_2^-)$en fonction du contenu nominal des couches en C_{60}, on obtient une excellente régression linéaire comme démontré en Figure VI.5. Cela prouve la faisabilité d'obtenir de façon simple la quantification du contenu de ce type de mélange. De plus, cela donne la possibilité d'évaluer de façon très précise la concentration de C_{60} dans les couches, ce qui est intéressant d'un point de vue dispositif puisqu'une variation de concentration de C_{60} entraine un changement de comportement électrique.

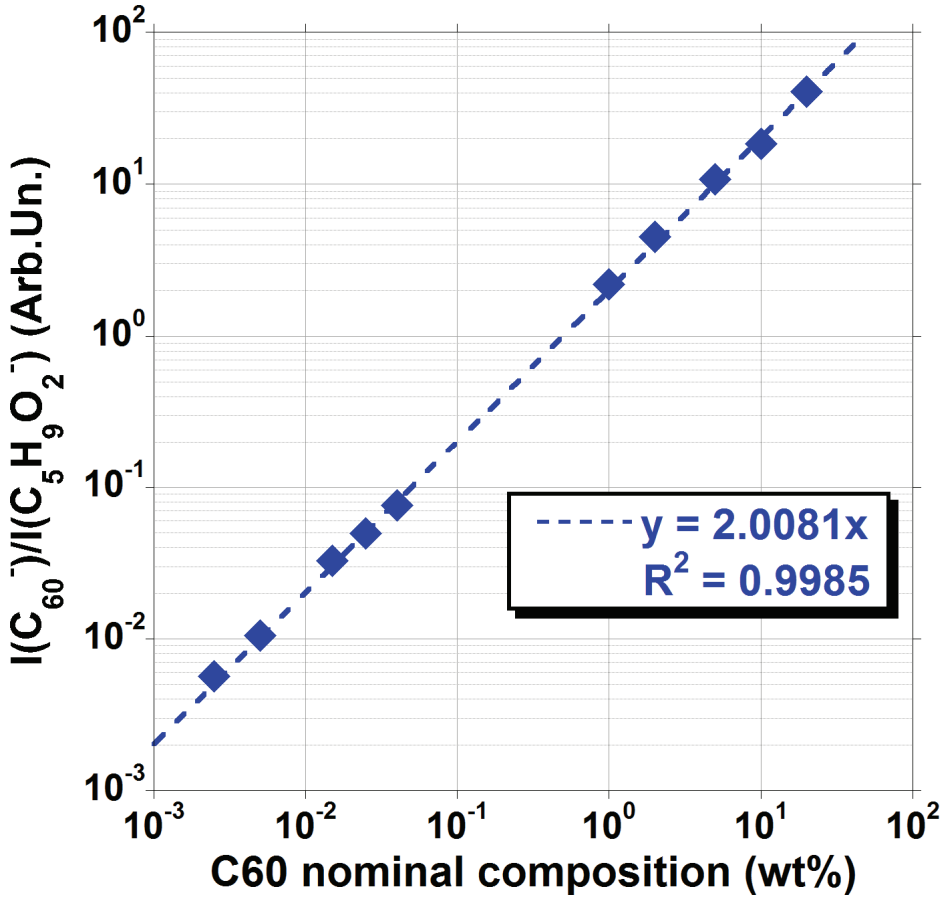

Figure VI.5 Evolution des ratios d'intensité $I(C_{60}^-)/I(C_5H_9O_2^-)$ avec le contenu nominal des couches en C_{60}.

En conclusion, nous avons développé différents protocoles originaux pour permettre l'obtention d'analyses quantitatives par ToF-SIMS dans des couches de mélange de PMMA et de C_{60} pour les mémoires organiques. Nous avons testé ces protocoles dans des échantillons représentatifs de structures pour la microélectronique avancée et montré que les ions poly-atomiques permettaient une amélioration forte de la sensibilité aux ions secondaires caractéristiques du C_{60} et du PMMA. Nous avons aussi montré que le protocole de profilage développé permettait d'obtenir des profils extrêmement stables et également de quantifier très précisément la quantité de C_{60} dans les couches, via un protocole de quantification simple.

CONCLUSIONS ET PERSPECTIVES

Au cours de ce travail de thèse, nous avons étudié les différentes façons de relever le défi de la caractérisation physico chimique de matériaux et structures pour les dispositifs de la microélectronique nouvelle génération à l'aide d'un instrument ToF-SIMS disponible commercialement. Nous avons proposé un survol des différentes ressources à notre disposition pour ce faire, et développé des protocoles spécifiques à chaque cas pour répondre aux besoins de caractérisation. Ces protocoles ont été utilisés pour améliorer la capacité de l'instrument à donner des informations quantitatives plus précises et mieux résolues en profondeur. Nous nous sommes en particulier concentrés sur les empilements à base de SiGe et de matériaux haute permittivité, sur les implants ultra basse énergie, et sur le matériaux organiques. L'utilisation combinée de plusieurs protocoles a souvent permis de dévoiler une approche nouvelle et donnant de meilleures analyses. Pour chacune des applications étudiées d'importantes améliorations ont donc été apportées. De plus, pour certaines d'entre elles il est encore possible d'avoir une marge de progrès pour améliorer encore plus les résultats.

Cependant, nous avons aussi mis en évidence des limitations dans certains cas, ce qui nous permet aussi de livrer des perspectives. Il serait par exemple possible de continuer l'étude sur la quantification des éléments de matrice en réalisant des tests de reproductibilité sur divers matériaux et dans diverses configuration afin d'étendre les possibilités de caractérisation à ces autres matériaux. Il serait également possible d'améliorer les résolutions en profondeur et la qualité des analyses en très basse énergie via une amélioration des faisceaux d'ions primaires, ce qui demande une modification de l'instrumentation. Enfin, l'émergence de nouvelles techniques de caractérisation telles que la sonde atomique tomographique permettent d'ouvrir le champ des possibles dans le domaine de la quantification à l'échelle nanométrique de dispositifs complets de la microélectronique dans leur environnement habituel.

BIBLIOGRAPHIE

[1] F.M. Wanlass, U.S. Patent n° 3,356,858, **1967**.
[2] H. Wong and H. Iwai, *Microelectron. Eng.*, 83 (**2006**) 1867-1904.
[3] International Technology Roadmap for Semiconductors: executive summary, (**2009**), http://www.itrs.net/Links/2010ITRS/Home2010.htm
[4] V. Fan, D. Harman, J. Jewett, J. Leet and D. Speranza, *Intel Technology Journal*, (**February 2008**).
[5] J.R. Bacon, K.L. Linge and L. Van Vaeck, *J. Anal. At. Spectrom.*, 20 (**2005**) 763-802.
[6] J.R. Bacon, K.L. Linge, R.R. Parrish and L. Van Vaeck, *J. Anal. At. Spectrom.*, 23 (**2008**) 1130-1162.
[7] A. Benninghoven, *J. Vac. Sci. Technol. A*, 3 (**1985**) 451-460.
[8] M.L. Pacholski and N. Winograd, *Chem. Rev. (Washington, DC, U. S.)*, 99 (**1999**) 2977-3006.
[9] A. Benninghoven, F.G. Rudenauer and H.W. Werner, Secondary Ion Mass Spectrometry: Basic Concepts, Instrumental Aspects, Applications, and Trends, Wiley, New York, **1987**.
[10] S. Hofmann, *Prog. Surf. Sci.*, 36 (**1991**) 35-87.
[11] P.C. Zalm, *Reports on Progress in Physics*, 58 (**1995**) 1321.
[12] S. Hofmann, *Reports on Progress in Physics*, 61 (**1998**) 827.
[13] T. Grehl, *Thesis work: Improvements in TOF-SIMS Instrumentation for Analytical Application and Fundamental Research*, University of Münster (**2003**).
[14] P. Williams, *Surf. Sci.*, 90 (**1979**) 588-634.
[15] K. Wittmaack, *Nuclear Instruments and Methods*, 168 (**1980**) 343-356.
[16] S.P. Smith, V.K.F. Chia, C.J. Hitzman and G. Mount, *Ion Implantation Technology. Proceedings of the 11th International Conference on*, (**1996**) 599-602.
[17] T. Grehl, R. Möllers and E. Niehuis, *Appl. Surf. Sci.*, 203-204 (**2003**) 277-280.
[18] J.F. Woitok, *Thin Solid Films*, 450 (**2004**) 138-142.
[19] D.G. Stearns, *J. Appl. Phys.*, 65 (**1989**) 491-506.
[20] J.M. Hartmann and et al., *Semicond. Sci. Technol.*, 15 (**2000**) 370.
[21] J.M. Fernández, L. Hart, X.M. Zhang, M.H. Xie, J. Zhang and B.A. Joyce, *J. Cryst. Growth*, 164 (**1996**) 241-247.
[22] J.M. Hartmann, A. Abbadie, D. Rouchon, J.P. Barnes, M. Mermoux and T. Billon, *Thin Solid Films*, 516 (**2008**) 4238-4246.
[23] P.M. Mooney and J.L. Jordan-Sweet, *JCPDS-International Centre for Diffraction Data*, (**1999**).
[24] M. Hytch, F. Houdellier, F. Hue and E. Snoeck, *Nature*, 453 (**2008**) 1086-1089.
[25] D. Cooper, J.-P. Barnes, J.-M. Hartmann, A. Beche and J.-L. Rouviere, *Appl. Phys. Lett.*, 95 (**2009**) 053501.
[26] M.J. Hÿtch, E. Snoeck and R. Kilaas, *Ultramicroscopy*, 74 (**1998**) 131-146.
[27] H. Lichte and M. Lehmann, *Reports on Progress in Physics*, 71 (**2008**) 016102.
[28] D. Briggs and J.T. Grant, Surface analysis by Auger and X-ray Photoelectron Spectroscopy, IM Publications and SurfaceSpectra Limited, **2003**.
[29] K. SIEGBAHN, C. NORDLING, A. FAHLMAN, R. NORDBERG, K. HAMRIN, J. HEDMAN, G. JOHANSSON, T. BERGMARK, S.E. KARLSSON, I. LINDGREN and B. LINDBERG, ESCA, Atomic Molecular and Solid State Structure Studied by Means of Electron Spectroscopy, Almquist and Wiksells, Uppsala, **1967**.
[30] D.A. Shirley, ESCA, John Wiley & Sons, Inc., **2007**.
[31] H. Basch, *J. Electron Spectrosc.*, 5 (**1974**) 463-500.
[32] L.C. Feldmann and J.W. Mayer, Fundamentals of Surface and Thin Film Analysis, North Holland, New York, **1986**.

[33] J.A. Leavitt, L.C. McIntyre and M.R. Weller, in, Materials Research Society, Pittsburgh, **1995**, pp. 37-81.
[34] H. Bubert and H. Jenett, Surface and Thin Film Analysis: Principles, Instrumentation, Applications, Wiley-VCH Verlag, **2002**.
[35] C.R. Brundle, C.A. Evans and S. Wilson, Encyclopedia of Material Characterization: Surfaces, Interfaces, Thin Films, Buttetworth-Heinemann / Manning Publications Co., Greenwich, **1992**.
[36] S. Selberherr, Analysis and Simulation of Semiconductor Devices, Springer-Verlag, Wien, New-York, **1984**.
[37] M. Stockinger, R. Strasser, R. Plasun, A. Wild and S. Selberherr, *SISPAD 98*, (**1998**) 77-80.
[38] W. Fang and E. Cumberbatch, *SIAM Journal on Applied Mathematics*, 52 (**1992**) 699-709.
[39] P. Pichler, H. Ryssel, R. Ploss, C. Bonafos and A. Claverie, *J. Appl. Phys.*, 78 (**1995**) 1623-1629.
[40] M. Posselt and J.P. Biersack, *Nucl. Instrum. Meth. B*, 64 (**1992**) 706-710.
[41] SYNOPSYS TCAD Tools.
[42] M. Perego, S. Ferrari and M. Fanciulli, *Surf. Sci.*, 599 (**2005**) 141-149.
[43] J.-M. Hartmann, A.-M. Papon, J.-P. Colonna, T. Ernst and T. Billon, *ECS Trans.*, 16 (**2008**) 341-351.
[44] M. Py, J.P. Barnes and J.M. Hartmann, *Surf. Interface Anal.*, 43 (**2011**) 539-542.
[45] J.P. Dismukes, L. Ekstrom and R.J. Paff, *J. Phys. Chem.*, 68 (**1964**) 3021-3027.
[46] K.E. Petersen, *Electron Devices, IEEE Transactions on*, 25 (**1978**) 1241-1250.
[47] J.M. Hartmann, L. Baud, G. Rolland, J.M. Fabbri and T. Billon, *ECS Trans.*, 3 (**2006**) 219.
[48] J.M. Hartmann, L. Clavelier, C. Jahan, P. Holliger, G. Rolland, T. Billon and C. Defranoux, *J. Cryst. Growth*, 264 (**2004**) 36-47.
[49] J.M. Hartmann, F. Gonzatti, F. Fillot and T. Billon, *J. Cryst. Growth*, 310 (**2008**) 62-70.
[50] M. Py, J.P. Barnes, P. Rivallin, A. Pakfar, T. Denneulin, D. Cooper and J.M. Hartmann, *Submitted for publication in Journal of Applied Physics*, (**2011**).
[51] M. Gavelle, E. Scheid, F. Cristiano, C. Armand, J.M. Hartmann, Y. Campidelli, A. Halimaoui, P.F. Fazzini and O. Marcelot, *J. Appl. Phys.*, 102 (**2007**).
[52] P. Holliger, F. Laugier and J.C. Dupuy, *Surf. Interface Anal.*, 34 (**2002**) 472-476.
[53] Z.X. Jiang, K. Kim, J. Lerma, A. Corbett, D. Sieloff, M. Kottke, R. Gregory and S. Schauer, *Appl. Surf. Sci.*, 252 (**2006**) 7262-7264.
[54] D. Marseilhan, J.P. Barnes, F. Fillot, J.M. Hartmann and P. Holliger, *Appl. Surf. Sci.*, 255 (**2008**) 1412-1414.
[55] W. Vandervorst, *Appl. Surf. Sci.*, 255 (**2008**) 805-812.
[56] A. Merkulov, P. Peres, S. Choi, F. Horreard, H.U. Ehrke, N. Loibl and M. Schuhmacher, *J. Vac. Sci. Technol. B*, 28 (**2010**) C1C48-C41C53.
[57] M. Py, J.P. Barnes and J.M. Hartmann, *Surf. Interface Anal.*, (**2010**) DOI: 10.1002/sia.3535.
[58] S. Ferrari, M. Perego and M. Fanciulli, *J. Vac. Sci. Technol. A*, 20 (**2002**) 616-621.
[59] C.J. Powell, A. Jablonski, I.S. Tilinin, S. Tanuma and D.R. Penn, *J. Electron Spectrosc.*, 98-99 (**1999**) 1-15.
[60] P.H. Chi, D.S. Simons, J.M. McKinley, F.A. Stevie and C.N. Granger, *J. Vac. Sci. Technol. A*, 20 (**2002**) 688-692.
[61] M. Tomita, T. Hasegawa, S. Hashimoto, S. Hayashi, Y. Homma, S. Kakehashi, Y. Kazama, K. Koezuka, H. Kuroki, K. Kusama, Z. Li, S. Miwa, S. Miyaki, Y. Okamoto, K. Okuno, S. Saito, S. Sasaki, H. Shichi, H. Shinohara, F. Toujou, Y. Ueki and Y. Yamamoto, *Appl. Surf. Sci.*, 203-204 (**2003**) 465-469.
[62] A. Merkulov, F. Desse and M. Schuhmacher, *Proceedings of the Third European SIMS Workshop*, (**2002**) 52.
[63] L. Houssiau, B. Douhard and N. Mine, *Appl. Surf. Sci.*, 255 (**2008**) 970-972.

[64] M.S. Wagner, *Anal. Chem.*, 76 (**2004**) 1264-1272.

APPENDIX II : PUBLICATIONS LIST

FIRST AUTHOR PAPERS

-1- *Investigation of fullerene depth distribution in PMMA-C60 blends using dual beam ToF-SIMS*
M. Py, J.P. Barnes, M. Charbonneau, R. Tiron, J. Buckley, **Surf. Interface Anal.**, 43 (2011) 179-182.

-2- *Quantification of germanium in Si1−xGex alloys by negative mode ToF-SIMS: the interest of the full spectrum method*
M. Py, J.P. Barnes, J.M. Hartmann, **Surf. Interface Anal.**, 43 (2011) 539-542.

-3- *Quantitative profiling of SiGe/Si superlattices by time-of-flight secondary ion mass spectrometry: the advantages of the extended Full Spectrum protocol*
M. Py, J.P. Barnes, D. Lafond, J.M. Hartmann, **Rapid Commun. Mass Spectrom.**, 25 (2011) 629-638.

-4- *Quantitative depth profiling of ultrathin high-k stacks with Full Spectrum ToF-SIMS*
M. Py, J.P. Barnes, R. Boujamaa, M. Gros-Jean, K. Nakajima, K. Kimura, C. Roukoss, B. Pelissier, N. Gambacorti, **J. Vac. Sc. Technol. B** 29, 032208 (2011).

-5- *Accurate depth profiling of dry oxidized SiGeC thin films by extended Full Spectrum ToF-SIMS*
M. Py, E. Saracco, J.F. Damlencourt, J.P. Barnes, J.M. Fabbri, J.M. Hartmann, **Applied Surface Science** 257, 9414-9419 (2011).

-6- *Characterization and modelling of structural properties of SiGe/Si superlattices for multi-channel devices upon annealing*
M. Py, J.P. Barnes, P. Rivallin, A. Pakfar, T. Denneulin, D. Cooper, J.M. Hartmann, **J. Appl. Phys** 110, 044510 (2011).

-7- *Advanced backside sample preparation for multi-technique surface analysis*
M. Py, M. Veillerot, J.M. Fabbri, F. Pierre, D. Jalabert, C. Roukoss, B. Pelissier, R. Boujamaa, C. Trouiller, J.P. Barnes, **Eur. Phys. J. Appl. Phys.**, 55, 3 (2011).

-8- *Accurate depth profiling of oxidized SiGe (intrinsic or doped) thin films by extended Full Spectrum ToF-SIMS*
M. Py, E. Saracco, J. F. Damlencourt, J.P. Colonna, E. Martinez, V. Delaye, J. M. Fabbri, J. P. Barnes, and J. M. Hartmann, IBA 2011 proceedings, in: **Nuclear Instruments and Methods in Physics Research Section B** (2011).

-9- *Ultimate Backside Sample Preparation For Ultra Thin High-k/Metal Gate Stack Characterization*
M. Py, M. Veillerot, E. Martinez, J.M. Fabbri, R. Boujamaa, J.P. Barnes, and F. Bertin, **FCMN proceedings, AIP** (2011).

CO-AUTHOR PAPERS

-1- *Diffusion and activation of Boron and Phosphorus in preamorphized and crystalline Germanium using ultra fast anneal*
V. Mazzocchi, X. Pages, **M. Py,** J.P. Barnes**,** K. Vanormelingen, L. Hutin, R. Truche, P Vermont, M. Vinet,C. Le Royer, K. Yckache, Proceedings of *Advanced Thermal Processing of Semiconductors, 2009* **RTP '09**.

-2- *Boron and Phosphorus dopant activation in Germanium using laser annealing with and without preamorphization*
V. Mazzocchi, C. Sabatier, **M. Py,** K Huet, C. Boniface**,** J-P Barnes**,** L. Hutin, V. Delayer, D. Morel, M. Vinet, C Le Royer, J. Venturini, K. Yckache, *Advanced Thermal Processing of Semiconductors, 2009* **RTP '09**.

-3- *Study on C60 Doped PMMA for Organic Memory Devices*
M. Charbonneau, R. Tiron, J. Buckley, **M. Py,** J. P. Barnes, S. Derrough, C. Constancias, C. Licitra, C. Sourd, G. Ghibaudo, B. De Salvo, ***MRS. Symp. Proc***. Vol. 1250, 2010, 1250-G04-07.

-4- *Cyclic Deposition/Etch Processes for the Formation of Si Raised Sources and Drains in Advanced MOSFETs*
J.M. Hartmann, **M. Py**, P.H. More, T. Ernst, B. Prévitali, J. P Barnes,N. Vulliet, N. Cherkashin, S. Reboh, M. Hÿtch and V. Paillard, **ECS Transactions**, 33 (6) 391-407 (2010).

-5 - *Low temperature, boron and phosphorous doped SiGe for recessed and raised sources and drains*
J.M. Hartmann, **M. Py**, J.P. Barnes, B. Prévitali, P. Batude and T. Billon, **Journal of Crystal Growth** 327, 68-77 (2011).

-6- *Evaluation of the substitutional carbon content in annealed Si/SiGeC superlattices by dark-field electron holography*
T. Denneulin, J.L. Rouvière, A. Béché, **M. Py**, J.P. Barnes, J.M. Hartmann and D. Cooper, in: **MSM XVII proceedings** (2011)

-7- *Annealed Si/SiGeC Superlattices Studied by Dark-Field Electron Holography, ToF-SIMS and Infrared Spectroscopy*
T. Denneulin, J.L. Rouvière, A. Béché, **M. Py**, J.P. Barnes, N. Rochat, J.M. Hartmann and D. Cooper, **FCMN proceedings, AIP** (2011).

-8- *Lanthanum diffusion in the TiN/LaOx/HfSiO/SiO2/Si stack*
E. Martinez, P. Ronsheim, J.-P. Barnes, N. Rochat, **M. Py**, M. Hatzistergos, O. Renault, M. Silly, F. Sirotti, F. Bertin, N. Gambacorti, **Microelectronic Engineering** 88, 1349-1352 (2011).

-9- *The reduction of the substitutional C content in annealed Si/SiGeC superlattices studied by dark-field electron holography*
T. Denneulin, J.L. Rouvière, A. Béché, **M. Py**, J.P. Barnes, N. Rochat, J.M. Hartmann and D. Cooper, Accepted for publication in **Semiconductor Science and Technology**, 2011.

-10- *Study of the La-related dipole in TiN/LaOx/HfSiON/SiON/Si gate stacks using hard X-ray photoelectron spectroscopy and back-side medium energy ion scattering*
R. Boujamaa, F. Pierre, E. Martinez, **M.Py**, O. Renault, B. Detlefs, J. Zegenhagen, V. Loup, F. Martin, S. Baudot, M. Gros-Jean, F. Bertin, C. Dubourdieu, Submitted for publication in **Journal of Applied Physics**, 2011.